LARGE TELESCOPE EXPERIMENT PROGRAM (LTEP)

VOLUME I PART 1

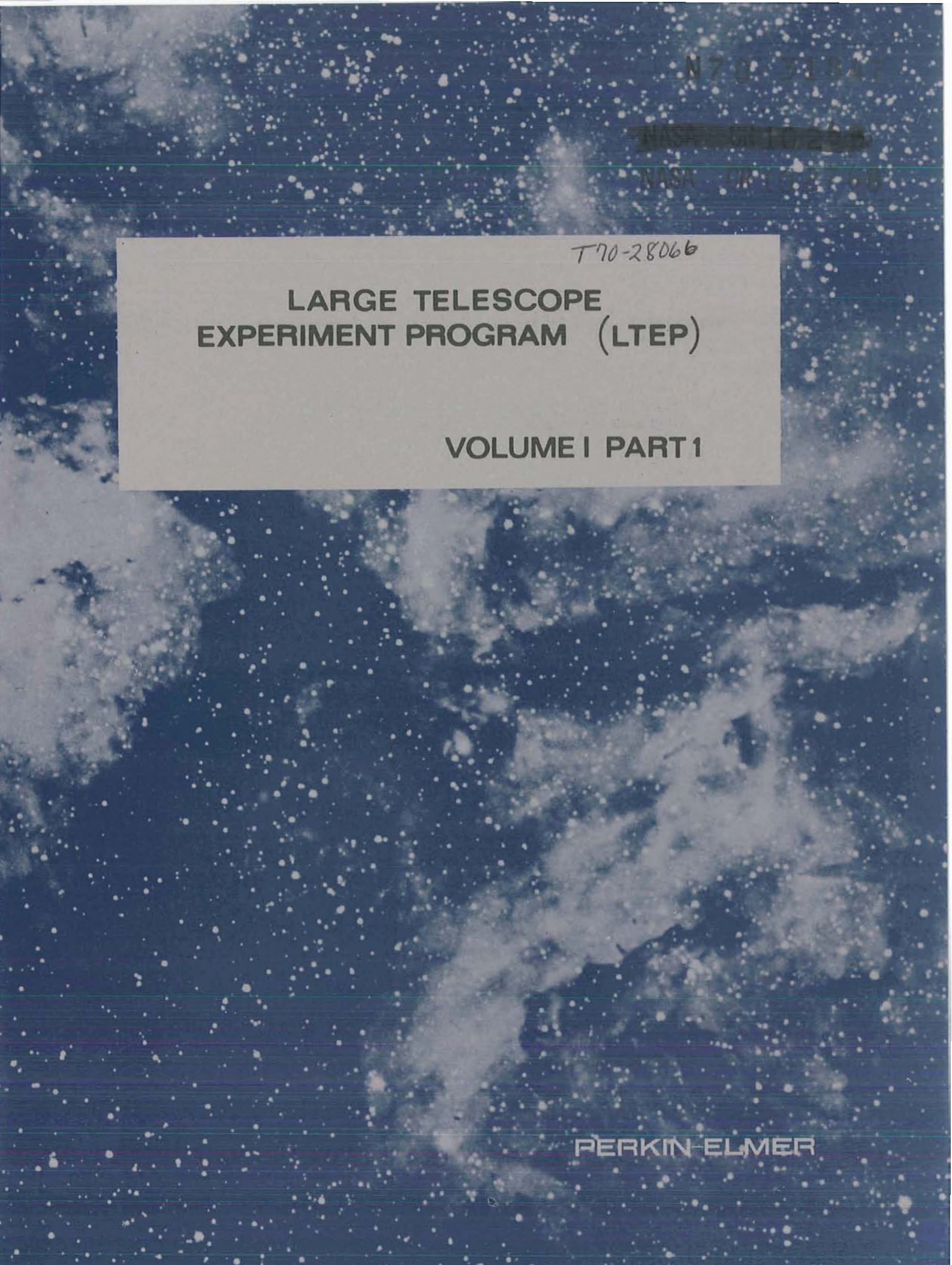

PERKIN-ELMER

N70-31847

PERKIN-ELMER

OPTICAL GROUP NORWALK, CONNECTICUT

ENGINEERING REPORT NO. 9800

LARGE TELESCOPE EXPERIMENT PROGRAM (LTEP)

VOLUME I PART 1

DATE: APRIL 24, 1970

PREPARED FOR: ASTRIONICS LABORATORY

MARSHALL SPACE FLIGHT CENTER

NATIONAL AERONAUTICS AND SPACE FLIGHT ADMINISTRATION

HUNTSVILLE, ALABAMA

Contract: NAS8-21497

Alan B. Wissinger, Program Leader

Approved:

Herbert F. Wischnia, Director, Optical Systems

COPY NO. 71

CONTRIBUTORS

THE PERKIN-ELMER CORPORATION

J. Bartas
Dr. C. Chi
H. Crane
C. Fencil
A. Ledger
D. Markle
Dr. C. McIntyre
W. Peters
H. Robertson
E. Schlesinger
H. Wischnia
A. Wissinger
Dr. C. Zanoni

LOCKHEED MISSILES AND SPACE COMPANY

R. Bullesbach
L. Chidester
C. Christman, Jr.
R. Clifford
J. Dodds
L. Hauben
D. Ingwerson
R. Jacobs
Dr. H. Johnson
S. Kay
Dr. H. Kindsvater
R. LeCount
G. Long
Dr. R. Martindale
W. Miller
W. Mimnaugh
W. Nelson
P. Paul
P. Pielich
R. Rolling, Jr.
S. Simson
Dr. M. Walt, IV
E. Webb
L. Wong
J. Wordsworth
Y. Yoshikawa

2-METER LTEP SPACE SHUTTLE APPLICATION

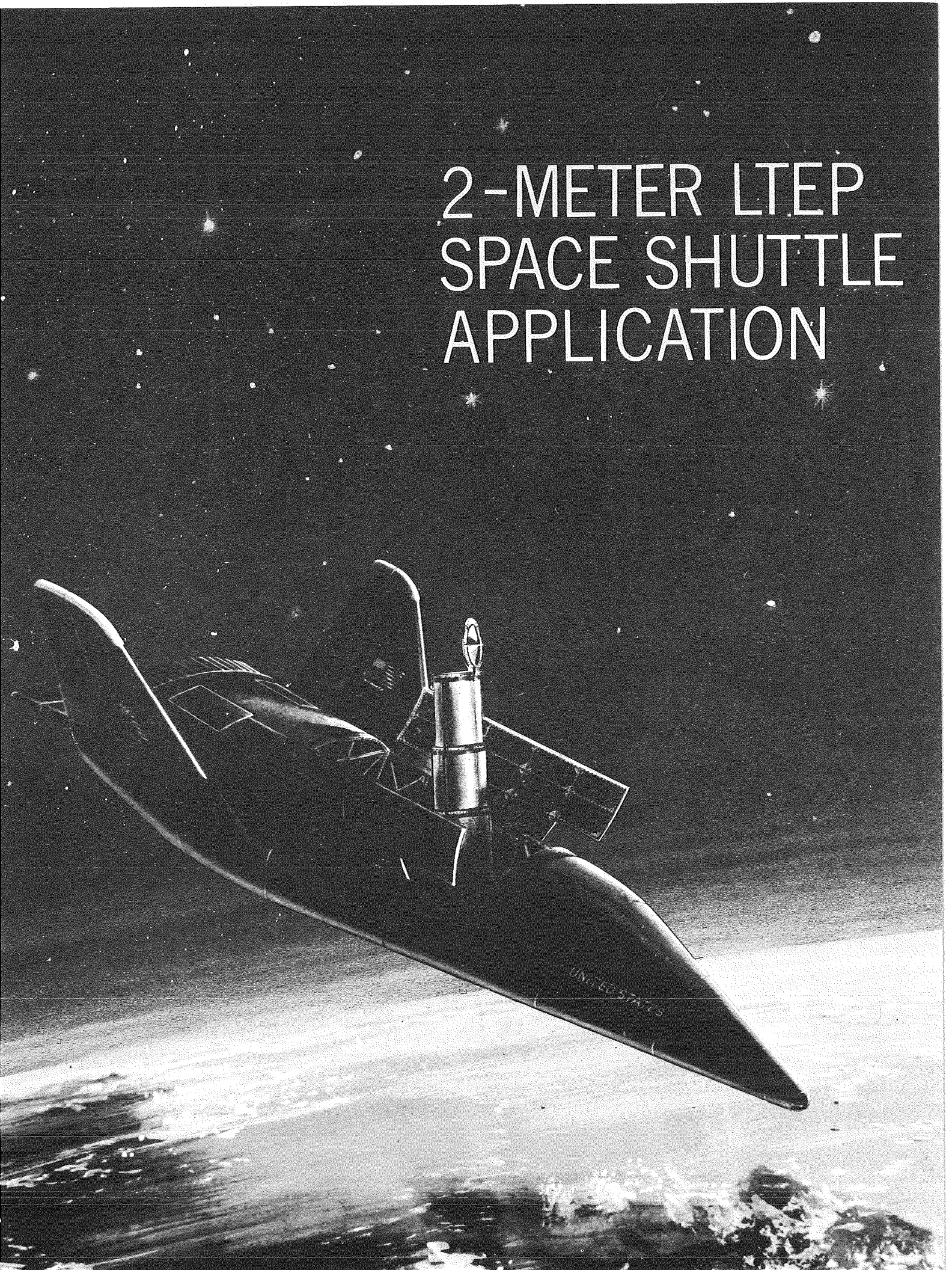

TABLE OF CONTENTS

TABLE OF CONTENTS (Continued)

TABLE OF CONTENTS (Continued)

TABLE OF CONTENTS (Continued)

TABLE OF CONTENTS (Continued)

TABLE OF CONTENTS (Continued)

TABLE OF CONTENTS (Continued)

TABLE OF CONTENTS (Continued)

TABLE OF CONTENTS (Continued)

TABLE OF CONTENTS (Continued)

LIST OF ILLUSTRATIONS (Continued)

LIST OF ILLUSTRATIONS (Continued)

LIST OF ILLUSTRATIONS (Continued)

LIST OF ILLUSTRATIONS (Continued)

LIST OF ILLUSTRATIONS (Continued)

LIST OF ILLUSTRATIONS (Continued)

LIST OF ILLUSTRATIONS (Continued)

LIST OF ILLUSTRATIONS (Continued)

LIST OF ILLUSTRATIONS (Continued)

LIST OF ILLUSTRATIONS (Continued)

LIST OF ILLUSTRATIONS (Continued)

LIST OF ILLUSTRATIONS (Continued)

LIST OF ILLUSTRATIONS (Continued)

LIST OF ILLUSTRATIONS (Continued)

LIST OF ILLUSTRATIONS (Continued)

LIST OF ILLUSTRATIONS (Continued)

LIST OF ILLUSTRATIONS (Continued)

LIST OF ILLUSTRATIONS (Continued)

LIST OF ILLUSTRATIONS (Continued)

LIST OF ILLUSTRATIONS (Continued)

LIST OF ILLUSTRATIONS (Continued)

LIST OF TABLES

LIST OF TABLES (Continued)

LIST OF TABLES (Continued)

CHAPTER 1 - PREFACE

The current program planning of NASA is seriously searching out meaningful goals for the Nation after the most successful Saturn-Apollo missions to the lunar surface. The areas of transportation such as space shuttle, space tug, nuclear stage, and lunar rovers are receiving prime attention. The new science and technologies of space labs and solar observatories are in the immediate future. As presented in the Space Task Group report to the President*, September 1969, the astronomy missions of the future are highlighted: "...both optical and radio astronomy have been stimulated by the opening of new regions of the electromagnetic spectrum and new fields of interest have been uncovered -- notably in the high energy x-ray and gamma-ray regions. Astronomy is advancing rapidly at present, partly with the aid of observations from space, and a deeper understanding of the nature and structure of the Universe is emerging ...about a variety of celestial objects, such as pulsars, quasars.... Astronomy has a far greater potential for advancement by the space program than any other branch of physics."

The long-range program in optical-stellar space astronomy is based on a 3- to 10-meter large space telescope with diffraction-limited optics to be placed in space in the early 1980's. The Astronomy Mission Board* on page 4 of its report states: "A telescope of 120-inch aperture above the earth's atmosphere has 10 times the resolving power of the 200-inch telescope on Mount Palomar operating under the best atmospheric conditions. Because of the very small image sizes that are possible with telescopes in orbiting observatories, a space telescope 120 inches in diameter should be able to detect stars 100 times fainter than the faintest detectable from the earth. Data on such faint objects are critical for settling major questions in cosmology, such as whether the Universe is infinite or not."

The optical technology required for the 120-inch space telescope has not been demonstrated in the following critical areas:

- Precision figuring of 120-inch mirrors to $\lambda/50$ rms
- Long-term substrate stability to $\lambda/50$ rms for 120-inch mirrors
- Long-life high-reflectivity ultraviolet mirror coatings
- Stellar pointing to 1/100 arc-second for a 120-inch space telescope
- Space maintenance of large astronomical telescopes by astronauts

---

*A Long-range Program in Space Astronomy. Position Paper of The Astronomy Missions Board, Doyle, Robert O., Ed., Scientific and Technical Information Division Office of Technology Utilization. National Aeronautics and Space Administration, Washington, D.C., July, 1969, p. 6 and 13.

Further optical engineering is required in the thermal design to achieve isothermal conditions in overlong periods of time, and the proper handling techniques of telescope film in repeated replacement/retrieval mode for a large space telescope must be developed. Imagery of faint objects (magnitude 27 to 29) whether by electronic sensors such as image tubes or astronomical plates is desired for the 120-inch instrument, and the technology to accomplish this imagery is not ready.

The ability for manned interfaces is not proven in the space environment. The intricate ground-based astronomy community has not yet been given any indication as to the proposed operational modes or their control position of the experimentations.

The Large Telescope Experiment Program (LTEP) initiated a systematic approach to the development of large space telescopes. The technological areas were thoroughly reviewed, advanced, and extrapolated wherever possible. The result of this thorough study has led to the formation of a logical large space telescope project plan for the future:

1. To phase-up in one step from a precursor 2-meter optical system LTEP (or OTES) to the 3-meter system. (The alternative 3-meter precursor mission is possible, but at higher cost and risks.)

2. To maximize the precursor flight to achieve the necessary optical technology and astronomical observations which in turn will be the foundation for the follow-on 3-meter system.

To achieve a configuration of the LTEP precursor mission, the following technological status had to be established in order to determine the precursor mission profile:

1. Optical material stability - - - the lack of adequate experimental data on stability has been one of the more formidable problems. There are a number of potential materials but it is not wise to extrapolate to large mirror sizes based on small mirror test data. An alternative is to use the concept of a segmented primary mirror with each segment controlled by a laser interferometer. Another concept is to use an Active Deformable Mirror. Both concepts have been sponsored by NASA and developed in the laboratories of Perkin-Elmer.

2. The ability to figure and coat a 120-inch monolithic diffraction-limited optics is again a very major development program.

3. The pointing of the large space telescope by use of a free-float technique, or by an all-wavelength transfer-lens approach can be done with a 2-meter telescope to prove capability in space of the 0.01 arc-second pointing. Also, the orbital altitude effects on stability can be evaluated for future flights.

4. The thermal requirement to maintain stable conditions is mandatory. The recording of faint objects over long periods of time requires that thermal disturbances of the optical systems and the telescope housing must be minimized. The concepts of thermal control are applicable to both 2- and 3-meter systems.

5. The ability to record imagery is a prime mode of operation for the LTEP. The high-resolution data will have flux ranges over 6 orders of magnitude and a spectral range of about 1 order of magnitude. A detector size of about 6 inches in diameter would be desired if it could be developed to have a resolution of 100 lines pairs/mm.

6. The ability to house multiple-application scientific instruments both for high spatial and spectra resolution has been investigated. The capability exists for both the 2- and 3-meter systems to house a variety of scientific instruments.

The precursor step to the 3-meter National Astronomical Observatory is basic and is on good mission status with the Space Shuttle/base missions envisioned. The purpose of the study is to give the best view of possibilities that can be accomplished in the decade of the 1970's.

CHAPTER 2 - SUMMARY

The Large Telescope Experiment Program is to identify and develop for NASA the technology necessary to realize the goal of the United States to operate a National Astronomical Space Observatory (NASO) in the late 1970's or early 1980's The technology identification objective is fulfilled by the study through:

1) A survey of the decisive experiments in astronomy which astronomers and astrophysicists have planned and are now planning, since the advent of space research has opened new vistas for our scientists.

2) A thorough and exhaustive reporting of the current state-of-the-art in optical technology, telescope systems technology (thermal control, pointing servos, alignment), spacecraft technology and currently possible operational modes.

3) Identification of the technology gap which the program will bridge prior to design of the large telescope for the NASO. The means for developing the required technology is a series of ground and space technology experiments embodied in a 2-meter aperture telescope designed for use with existing ATM hardware.

Interviews with prominent astrophysicists, surveys of planned astrophysical experiments, and reviews of publications of the various science and NASA Boards and committees have resulted in tentative specifications for the NASO Large Telescope suggesting that it:

- be operated in conjunction with a permanent space station in earth orbit, either docked or autonomously,
- have an aperture of 3 to 5 meters (as large as can be accommodated),
- have a distance penetration greater than that postulated by current cosmological theory (e.g., 29th-magnitude or dimmer stars corresponding to a universe radius of 10^{10} light years), to permit new extra-galactic exploration
- permit observations from the far ultraviolet region (800 Å) to the near infrared region (1 micron),
- achieve a quality of imagery corresponding to the diffraction limit of at least 3 meters (0.006 arc-seconds) at 1000Å,
- be designed so that the experiment packages can be changed to accommodate new astrophysical experiments conceived during the decade of life of the telescope.

It is sobering to contrast this list of specifications with the achievements of the present day in space astronomy. OAO-A2 is in orbit and Stratoscope II is being flown on balloons, but no appreciably larger diffraction-limited imaging space telescopes exist or are under construction. The specifications for the largest of these instruments are as follows:

- apertures - under 36-inch diameter

- distance penetration - stars brighter than 18.5th magnitude: $\sim 10^5$ light years
- spectral range - OAO's 1100Å - 4000Å
  - Stratoscope - 4000Å to 6000Å
- resolution - spatial 0.1 arc-second (Stratoscope)
  - spectral 0.1Å (OAO-C)
- operating time - 10 hours on balloons - about one year in orbit
- optical quality - Stratoscope II: $\frac{\lambda}{25}$ rms wavefronts
  - OAO-C: $\frac{\lambda}{5}$ rms wavefronts

It is obvious from these specifications that the accomplishments to date define a wide technology gap to be bridged before the NASO telescope reaches the firm planning stages. It is to close this gap that the LTEP espouses a 2-meter aperture precursor telescope experiment program to utilize existing space hardware from the Apollo Applications Program ATM. The LTEP telescope will advance the technologies required for the Space Observatory by designing and constructing a telescope twice as large as any space telescope existing today. This will implement advances into the new technology of active optics which has been demonstrated on the ground. Much new astrophysical research will also be possible using this instrument and it will prove invaluable to science in designing the astrophysical experiments and observations that will be carried out in the 80's.

The specifications for the LTEP precursor telescope, whose feasibility is studied in these volumes, are as follows:

- aperture - 2 meters
- central obscuration ratio - 0.2 (on diameter)
  4% (area)
- wavefront error - $\lambda/25$ rms
- field coverage - 30 arc-min
- pointing accuracy - 0.01 arc-sec rms (12th-magnitude stars)
  - 0.006 arc-sec rms (8th-magnitude stars)
- instrumental capability - can accommodate seven scientific instrument packages using film, plates, and photo-electric detectors
- spectral coverage - 800Å to 1μ
- thermal control - stabilized temperature at -80°C ± 5°C
- weight (telescope only) - 5500 lb
- distance penetration - 26th magnitude

A model of the 2-meter LTEP telescope is shown in Figure 1. A three-section telescoping shroud contains the telescope primary mirror, secondary mirror and the figure sensor used to measure and correct the figure of the primary mirror. The ATM Experiment Pointing Control (EPC) is adapted for use in some of the LTEP operations, while extra-fine pointing and stabilization techniques are embodied for other more critical astronomical operations. The CMG system is utilized for stabilization of the space station as in the AAP-ATM. Because the 2-meter telescope is just small enough to fit within the already developed ATM hardware, a substantial cost savings is possible over any larger aperture telescope that might be developed for use in conjunction with a space station. In comparison with a 3-meter telescope, for example, the 2-meter technology telescope would cost one fourth what the larger instrument would cost.

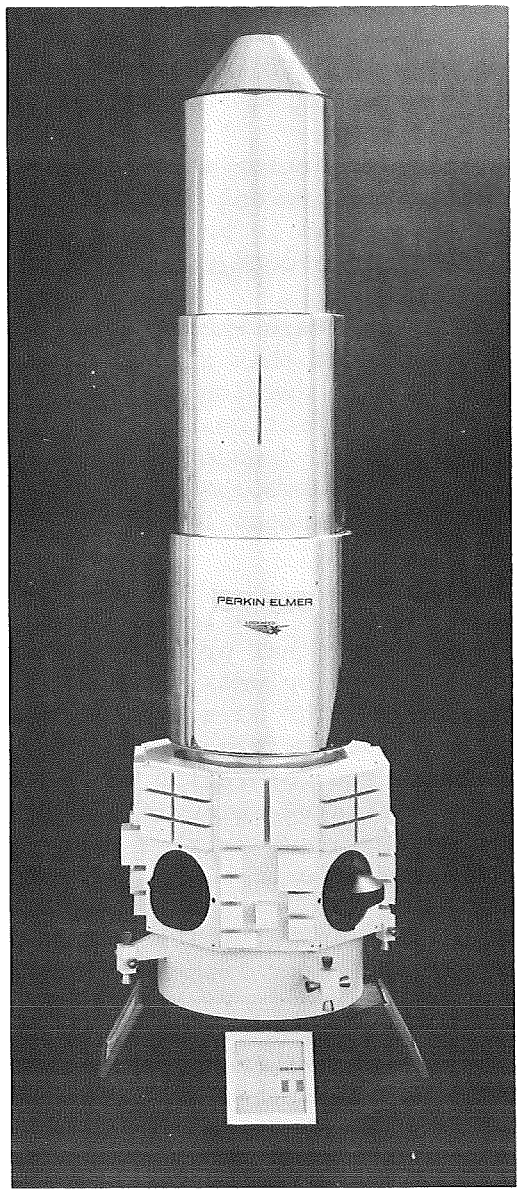

Figure 1. LTEP Model

There are many very difficult technical problems which must be overcome before a successful space telescope can be realized. Foremost among these is the problem of making, testing, launching, and finally operating in space a primary mirror accurate to one part in 10^8. Even if a perfect mirror survived the launch with no damage and the thermal control permitted near isothermal conditions, its optical performance could be seriously degraded by spontaneous relaxations of internal strains, perhaps affected by the cosmic radiation on the crystalline structure of the mirror material itself. Until a mirror of this size is placed in space with the high optical quality demanded by the astronomy mission and a means for measuring the optical performance with commensurate precision, there is really no way to determine the type or degree of degradation. There is, however, a means to continuously adapt to internal structural changes and at the same time, measure, record and transmit evidence of these changes to engineers on earth, through the application of the Active Optics servo control concept. Thus, a high degree of immunity to optical performance degradation, whatever the cause, with valuable technology contributions are afforded by the LTEP configuration.

The second most serious problem besetting a large space telescope is that of pointing with a stability sufficient to prevent blurring of the finest detail. For the two-meter telescope, this amounts to holding a given pointing direction with an error of no more than 1/100 arc-second for an orbital half period.

Third, it is no simple task to maintain the extremely close mechanical tolerances demanded by an optical instrument of this size and relative compactness. Nor, of course, is it a simple matter to develop optical designs which are tolerant of mechanical and fabrication imperfections. Since the alignment of the primary and secondary mirrors is so critical (amounting to tolerances on the order of tenths of thousandths of an inch), development of servo control of the optical alignment (first tried in the Stratoscope II telescope) for the space observatory is indicated.

These are the primary technology problems to which the LTEP two-meter telescope is addressed. There are a host of other problems in space optics technology which have been considered in these volumes, including thermal control, achievement of high optical efficiency at the wavelength extremes, optimization of the optical design for aberration-free performance over the widest possible telescope field, techniques for enhancing the resolution of telescope in specialized ways ("superresolution"), and the design of scientific instrumentation packages such as spectrographs and photometers to assure that the greatest possible scientific information is obtained from the telescope.

In volume II, the spacecraft and launch vehicles which are likely candidates for the LTEP launches are identified. Four launch vehicle/operational modes have been nominated. These are summarized in Figures 2, 3, and 4. The support structure, life cells for the astronauts, mission profiles and time lines, solar arrays, the propulsion and support modules for autonomous operations have been studied and feasible designs are reported. These are summarized in Figures 5, 6, 7, 8, and 9.

Thermal control of the telescope has also received special attention, with passive control using the Optical Solar Reflector (OSR) coatings developed by Lockheed and a more active control based on heat-pipe technology studied by Chrysler and reported on Volume I. Both techniques are feasible to provide the desired internal temperature at the primary mirror of -80°C ±4.5°C.

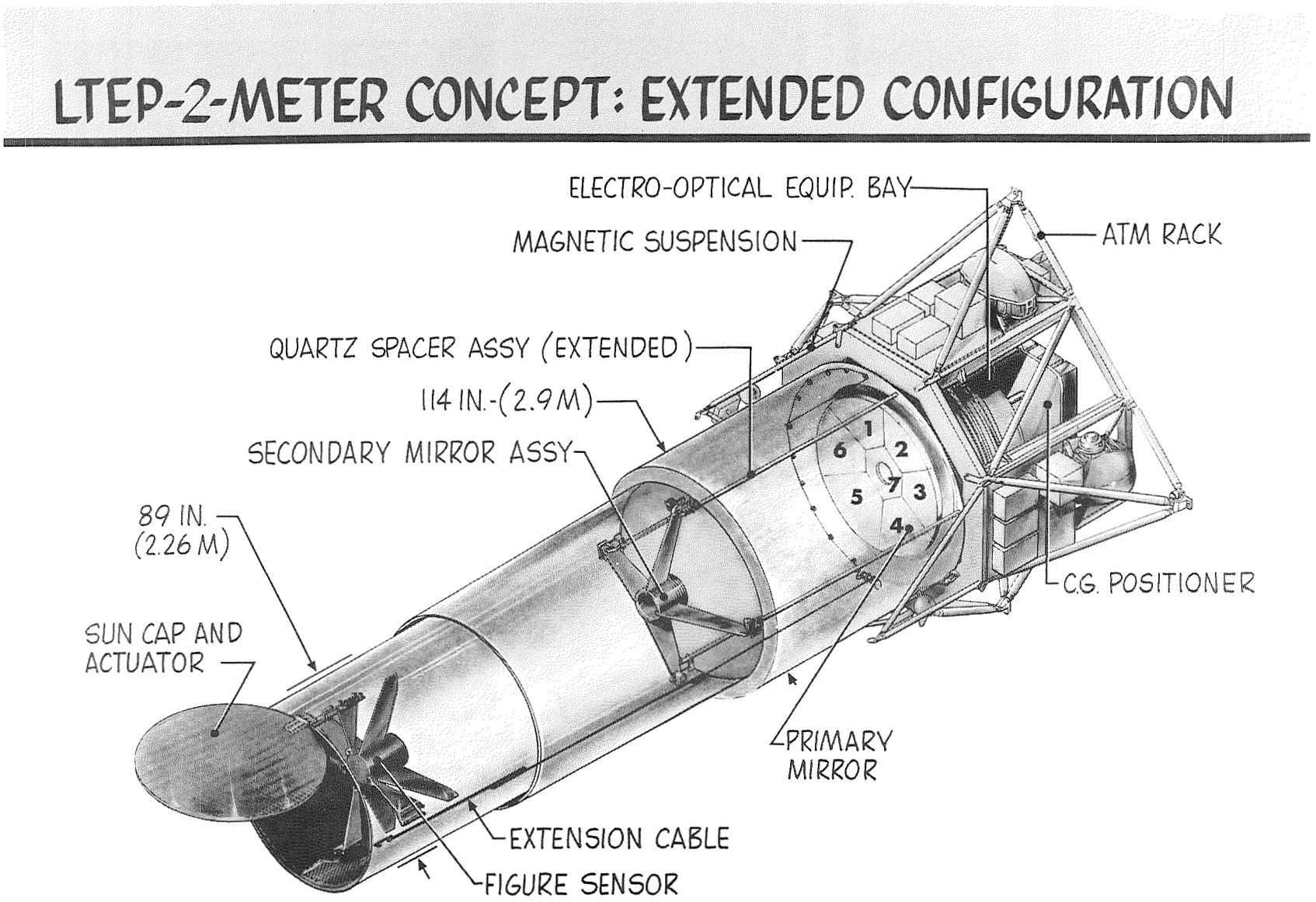

Figure 2. LTEP-2-Meter Concept: Extended Configuration

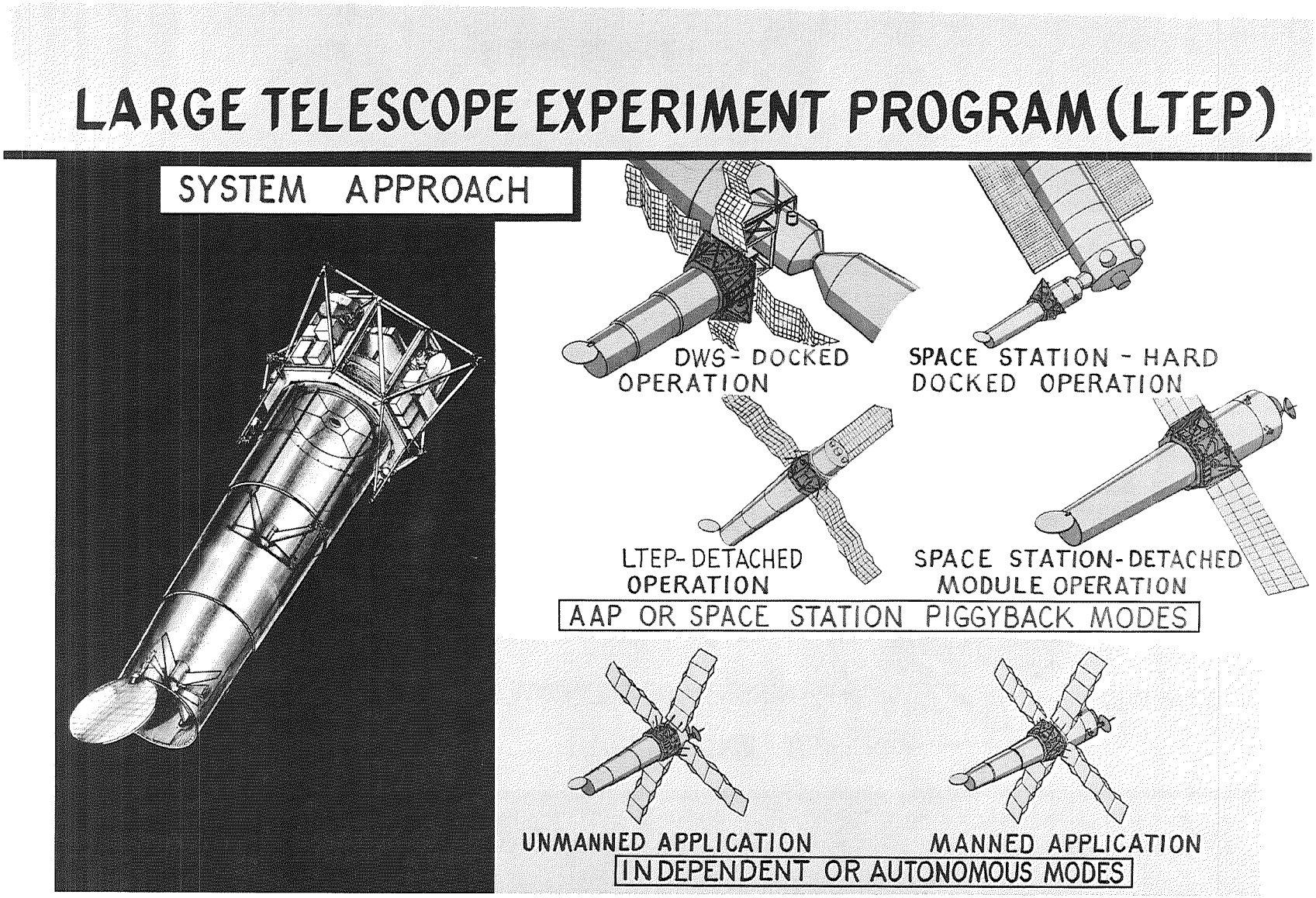

Figure 3. Large Telescope Experiment Program (LTEP)

LTEP OPERATIONAL MODES

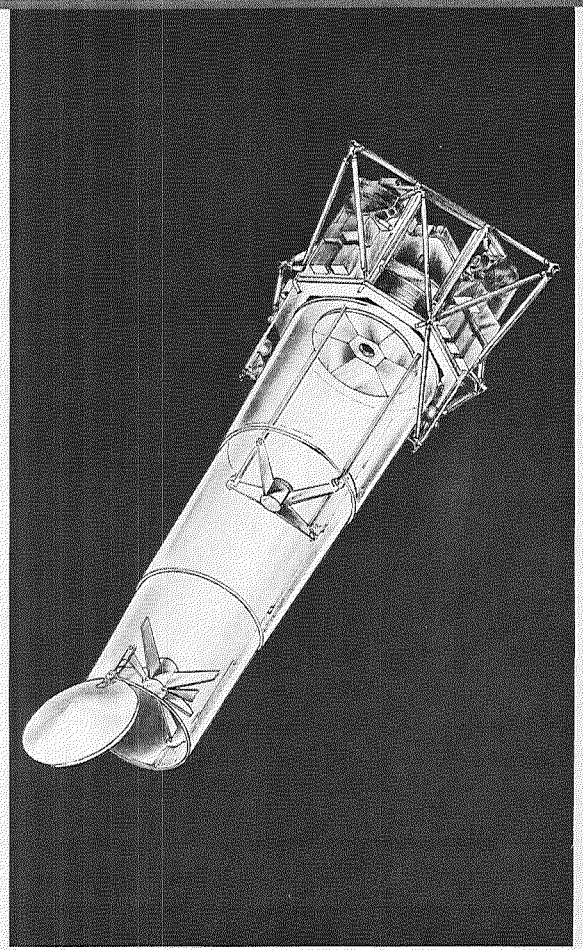

MODE	DESIGNATION	DEFINITION
1	THE SWS-II LTEP AAP SATURN WORKSHOP *	● LAUNCHED ON SAT. V WITH DWS-2 ● INITIAL OPERATION HARD-DOCKED; MANNED SUPPORT ● SUBSEQUENT OPERATION DETACHED (REMOTE) ● REDOCKING FOR MANNED RESUPPLY/ MAINTENANCE
2	THE TITAN III C LTEP INDEPENDENT/ UNMANNED	● LAUNCHED ON TITAN III C ● UNMANNED OPERATION (NO RESUPPLY OR FILM RECOVERY)
3	THE RENDEZVOUS LTEP INDEPENDENT LAUNCH-CLUSTER OPERATION	● LAUNCH ON TITAN III C ● DOCK TO AAP CLUSTER—MANNED OPERATION ● SEPARATE FOR UNMANNED REMOTE (DETACHED) OPERATION ● REDOCKING FOR MANNED RESUPPLY/ MAINTENANCE
4	THE SATURN IB LTEP INDEPENDENT LAUNCH-MANNED CAPABILITY	● LAUNCH ON SAT. IB WITH MOTEL ● MANNED OPERATION WITH CSM ● UNMANNED OPERATIONAL SPAN ● CSM RESUPPLY AND MAINTENCE

*THE CONCEPTUAL DESIGN IS INHERENTLY ADAPTABLE TO OPERATION AS A SPACE SHUTTLE OR SPACE STATION EXPERIMENT IN A MANNER SIMILAR TO THE SATURN/AAP SYSTEM

Figure 4. LTEP Operational Modes

LTEP SYSTEM CONFIGURATIONS

MODE →	THE SWS-II LTEP ① AAP SATURN WORKSHOP	THE TITAN IIIC LTEP ② INDEPENDENT UNMANNED	THE RENDEZVOUS LTEP ③ INDEPENDENT LAUNCH CLUSTER OPERATION	THE SATURN IB LTEP ④ INDEPENDENT LAUNCH MANNED CAPABILITY
LAUNCH ENVELOPE	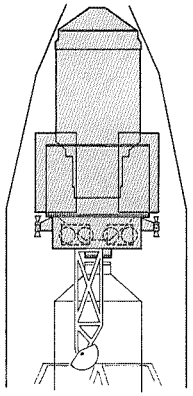	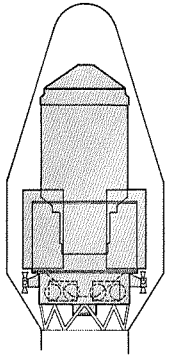	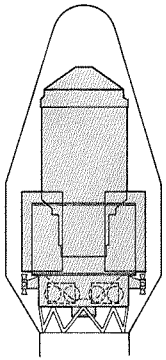	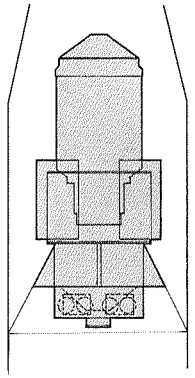
LAUNCH VEHICLE	SATURN V	TITAN IIIC	TITAN III C	SATURN I B
SYSTEM EQUIPMENT	2 METER TELESCOPE ATM RACK PROPULSION/SUPPORT MODULE	SAME AS MODE 1	SAME AS MODE 1	SAME AS MODE 1 PLUS MOTEL
MANNED SUPPORT	AAP SATURN IB LAUNCH	NONE	AAP SATURN IB LAUNCH	SATURN IB LAUNCH
KEY FEATURE	INTEGRAL CLUSTER EXPERIMENT	UNMANNED SIMPLIFIED EXPERIMENT	AAP EXPERIMENT AUTONOMOUS LAUNCH	AUTONOMOUS-MANNED SUPPORT CAPABILITY

Figure 5. LTEP System Configurations

MODE 1 - THE SWS-II LTEP

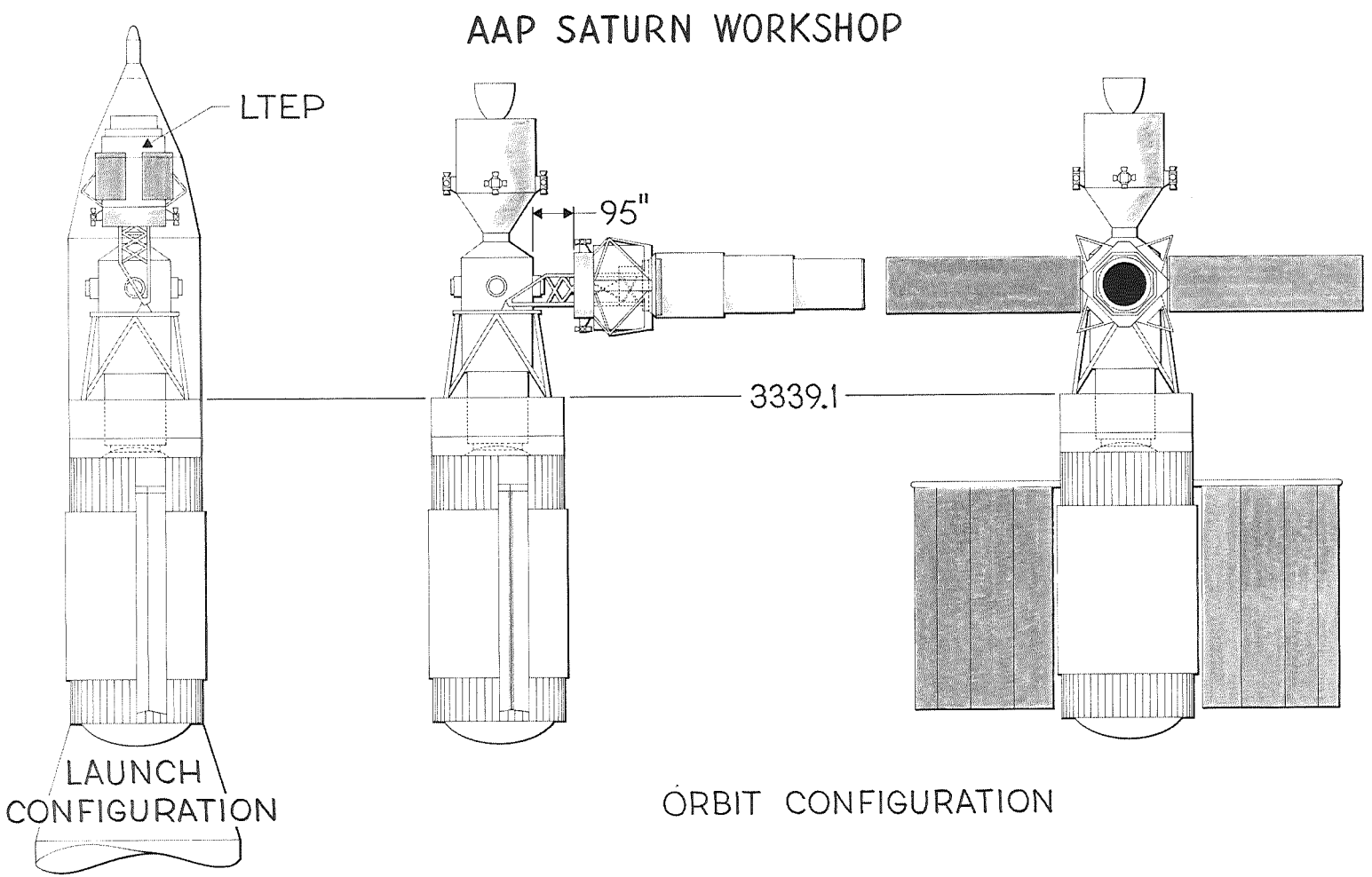

Figure 6. Mode 1 - The SWS-II LTEP

MODE 2 - THE TITAN IIIC LTEP

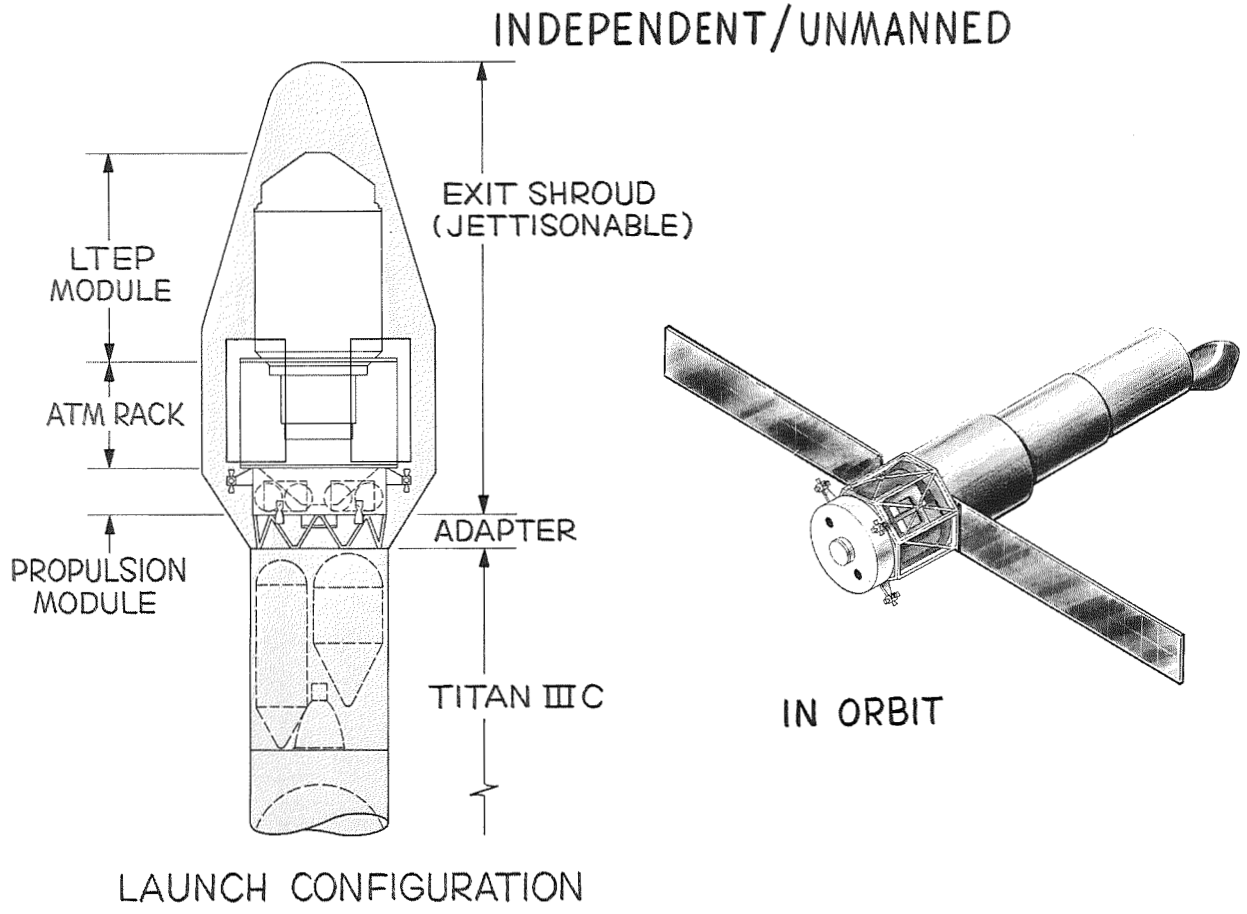

Figure 7. LTEP Mode 2-Independent/Unman

MODE 3 - THE RENDEZVOUS LTEP

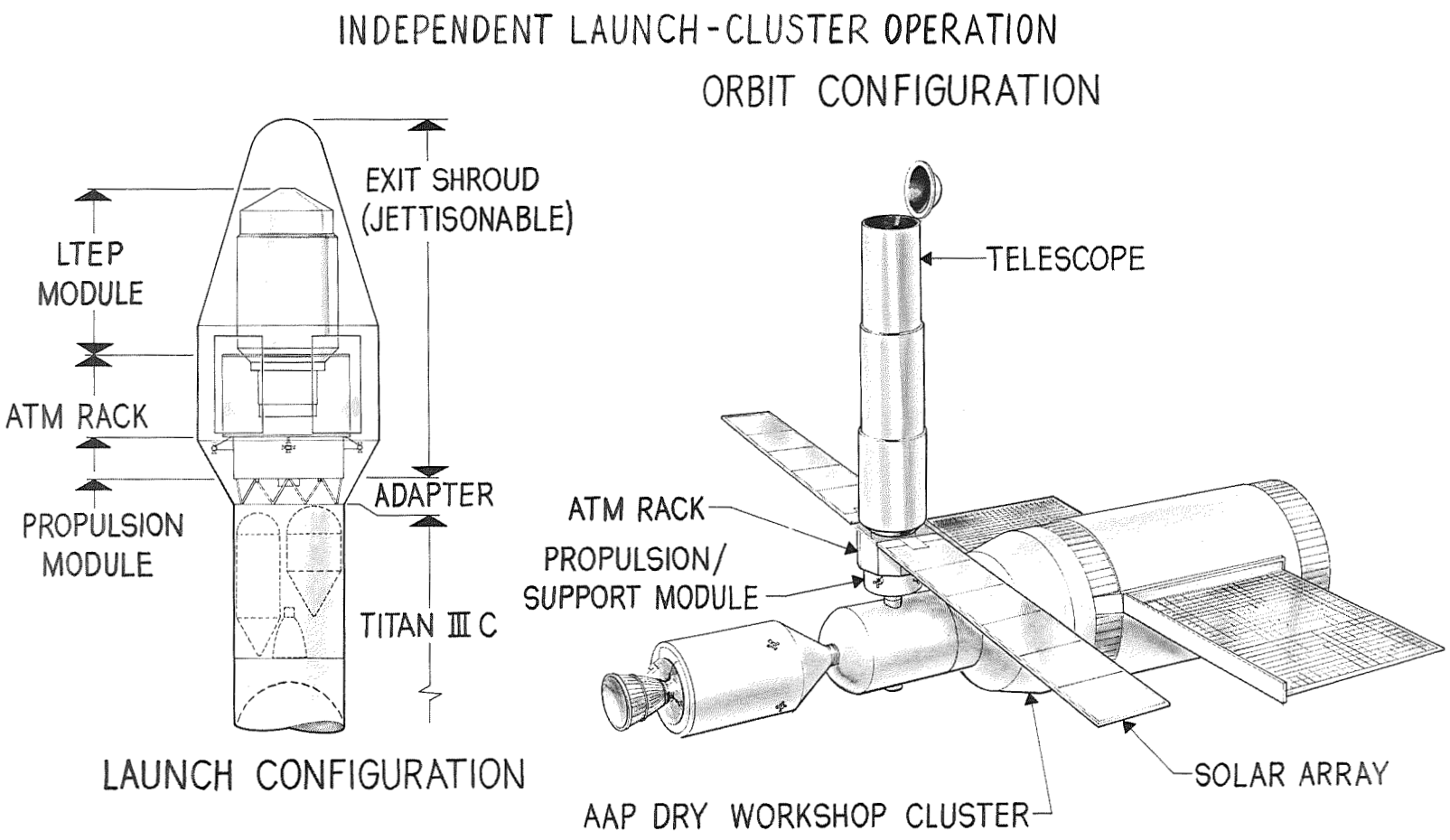

Figure 8. LTEP Mode 3-Independent Launch-Cluster Operation

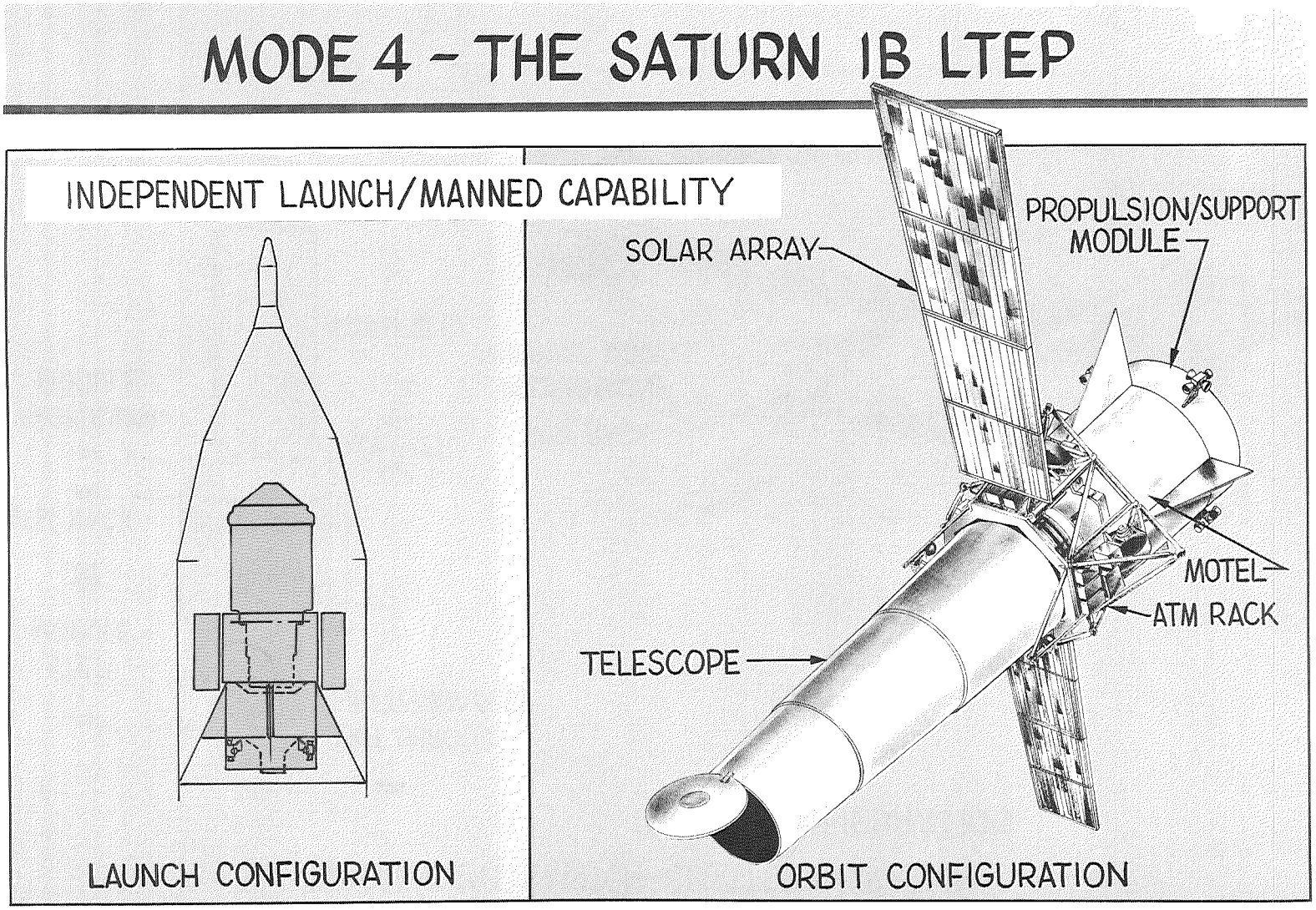

Figure 9. LTEP Mode 4 - Independent Launch/Manned Capability

Research in space is extremely expensive. Recognizing this, the Large Telescope Experiment Program has delineated a series of non-space experiments which will most economically accomplish the needed advances in technology which have been identified in this and the previous Optical Technology Extension System (OTES) and Optical Technology System (OTS). These experiments are of the supporting research and technology ilk, but because they are cast in the frame of reference of a particular telescope configuration and particular spacecraft parameters, are in reality the same as the development testing phase of a prototype design. This approach is designed to achieve highly productive and directed SRT without the inefficiencies, overruns, and schedule delays of the conventional aerospace program in which development and production are attempted concurrently.

These non-space experiments are:

- Fabrication and laboratory demonstration of a full-scale 2-meter aperture aspheric primary mirror utilizing the active optics principle
- Development of automatic alignment techniques for incorporation into the demonstration and development of the 2-meter mirror
- Full scale testing of fused silica, CerVit*, ULE* and other primary mirrors (some of which already exist) after exposure to the thermovacuum and vibration environment
- Operation of a ground-based Active Optics telescope for use by the astronomical community
- Additional laboratory development of the Free Float technique for achieving pointing control to 0.01 arc-second or better
- Development of silicon and beryllium "X" as primary mirror materials, and full scale thermovacuum and vibration testing
- Construction of high-efficiency echelle spectrograph and filter spectrometers for the ultraviolet and infrared regions based on new developments in grating and filter technology
- Further developments in image tubes and infrared detectors
- Fabrication and laboratory testing of large deformable mirrors
- Research in contamination control and contamination susceptibility in optical coatings to overcome the present outgassing problems in ATM
- Research in photographic films to reduce their susceptibility to radiation damage, thereby reducing the shielding requirements
- Information processing techniques to enhance the resolution of the telescope ("Superresolution"), extend the faint limit of telescopes, and apply the synthetic aperture concept to the problem of detecting faint companions of stars.

These non-space developmental activities are acheduled and costed in the Phase B recommendations contained in the section on Technology Planning and Resource Analysis. Accomplishment of these non-space experiments will require three years if funded for about $14,000,000. The interrelation of these experiments with the development of the LTEP two-meter telescope is shown in Figure 10.

* Product of Corning Glass Co., Corning, N.Y.

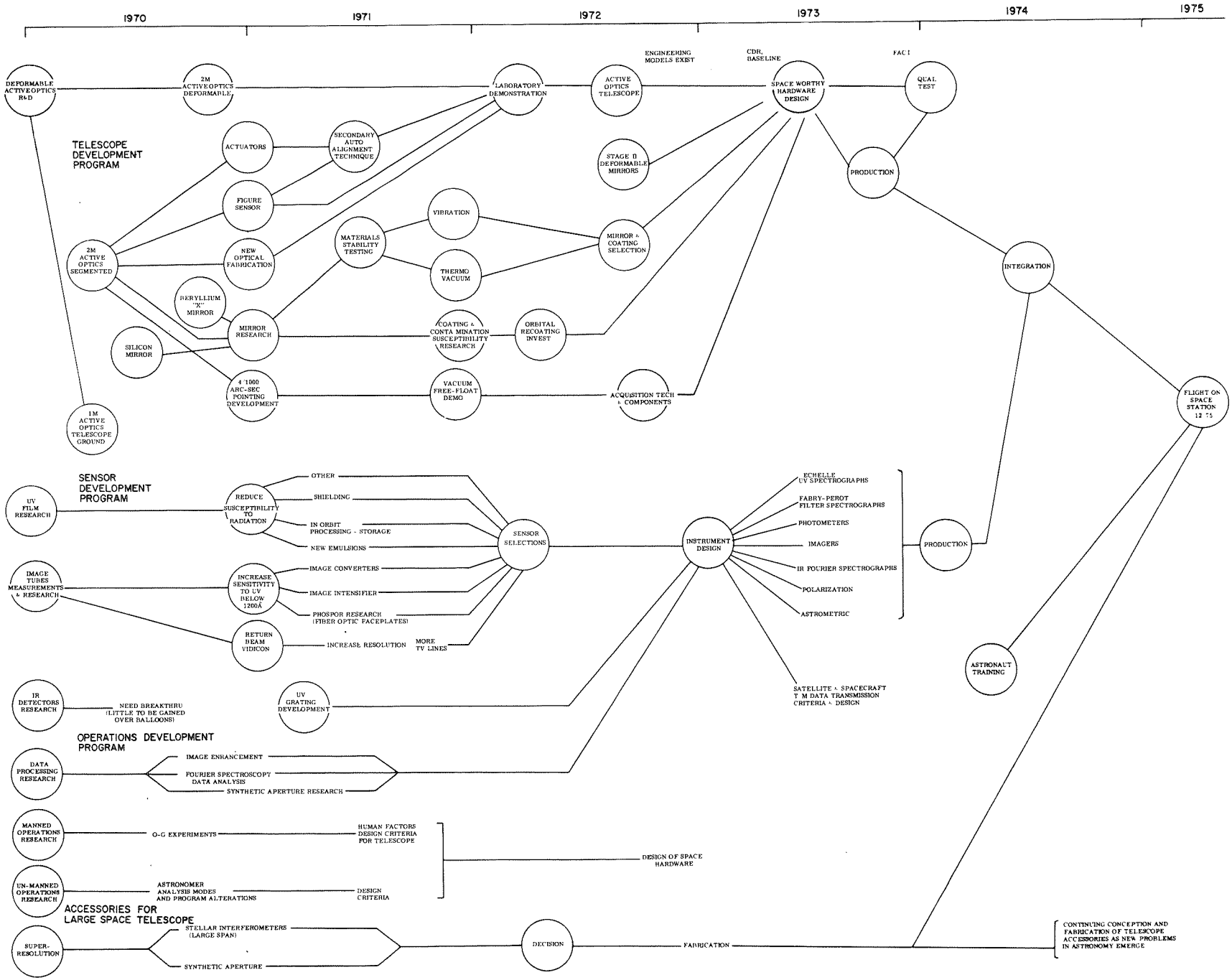

Figure 10. Large Telescope Experiment Program Technology Development Plan

CHAPTER 3 - ASTRONOMICAL UTILIZATION OF THE LTEP TELESCOPE

TECHNICAL CHARACTERISTICS OF THE 2-METER LTEP

A 2-meter diffraction-limited spaceborne telescope is a powerful tool for new astronomical research. Operating in orbit not only removes the atmosphere spectral window and the atmospheric image degradations, "seeing" scintillation, refraction and dispersion, but also provides access to more distant, faint objects of astronomical interest. The essential advantages in capability achieved by a large orbiting telescope are:

1) Wide spectral coverage

2) Very fine angular resolution

3) Marked improvement in faint limit

Because of the absence of the atmosphere, the technical capabilities of an orbiting telescope are the prime factors which limit the performance in each of the above three areas. To realize the potential improvements that are available from orbital operation, very stringent requirements are placed on: (1) the instrumental spectral bandpass, and (2) the optical imagery and tracking.

Spectral Coverage

Wide spectral coverage especially in the vacuum ultraviolet can only be achieved for large apertures using an entirely reflective optical system. The 2-meter LTEP optical configuration is described in detail elsewhere in this report. The telescope is a Ritchey-Chrétien employing an f/2 primary and a secondary with a magnification of 5. The optimum design for this two-reflecting element configuration yields a flat field of about 5.5 arc-minutes over which diffraction-limited images are produced. The 5.5-arc-minute field is limited by field curvature and astigmatism. In order to achieve this performance a primary mirror figure good to $\lambda/50$ rms is required. Since the 5.5-arc-minute field is much smaller than the 20- to 30-arc-minute diameter field required by the pointing system, it is necessary to extend the field further with a Ross type of refractive corrector situated near the focal plane. Ordinarily, the addition of refractive elements places narrow limits on the spectral bandpass of a telescope. However, this limitation is avoided in the present configuration by cutting a hole through the center of each of the corrector elements so that the center 5.5-arc-minute portion of the field remains all-reflective for imagery and spectroscopy in the vacuum ultraviolet. By coating the aluminized surfaces of the primary and secondary with LiF, the short wavelength limit of the telescope is about 1080Å.

Imagery and Angular Resolution

To realize the very fine angular resolution capability, it is necessary to require diffraction-limited performance over as large a field as possible. For ground-based telescopes, the stellar image diameters are determined by the atmosphere and are rarely less than 1 arc-second in diameter. For a 2-meter aperture, the diffraction-limited image size is about 0.05 arc-seconds. Thus, the potential exists for increasing by at least a factor of 400, the number of resolution elements recorded per unit area of the celestial sphere. Figure 11 shows the intensity profiles expected with 2-meter earth-bound telescopes and a 2-meter diffraction-limited orbiting telescope. In order to realize the 0.05-arc-second image size limit, stringent requirements are placed on the pointing accuracy. It is necessary to stabilize the field of view to a fraction of the diffraction-limited image size for periods which might typically be several hours duration. Thus, the pointing accuracy requirement is about 0.01 arc-second.

The only feasible method of achieving the 0.01-arc-second pointing requirement is to use stars within the telescope field of view as a pointing reference. Any other method, such as a separate boresighted guidance system, is prone to failure because of the thermoelastic deformations occurring in the entire telescope structure as the satellite sweeps in and out of the earth's shadow. With common pointing and imaging optics, it is possible to achieve a very high degree of immunity to structural changes since these produce identical changes in the pointing and image fields which are indistinguishable from pointing errors and which are nulled by the pointing system.

Faint Limit Performance

The faint limit of a telescope denotes the faintest visual magnitude accessible in a given integration time to carry out some specified observation with a given percentage of accuracy. A 10-percent accuracy is used for the analysis that follows.

When using photoelectric detection, the faint limit of an earth-based telescope is sky-background limited. This occurs for two reasons: (1) the night-time sky is equivalent to a background of a one 22.5th visual magnitude, (Mv), star per square arc-second of area on the celestial sphere whereas in orbit the background is equivalent to less than one 29th-visual-magnitude star per square arc-second of area, and (2) the atmospheric "seeing" broadens the image.

Using conventional photography, it is feasible for the 2-meter LTEP to work to about Mv = 25 with one day exposures.*

Using photoelectric detection, the faint limit of a 2-meter orbiting telescope is dark current limited.

*Tifft, W.G.: Space Astronomy of the Steward Observatory. Report T68-12, University of Arizona, Tucson, Arizona, 1968, p. 10.

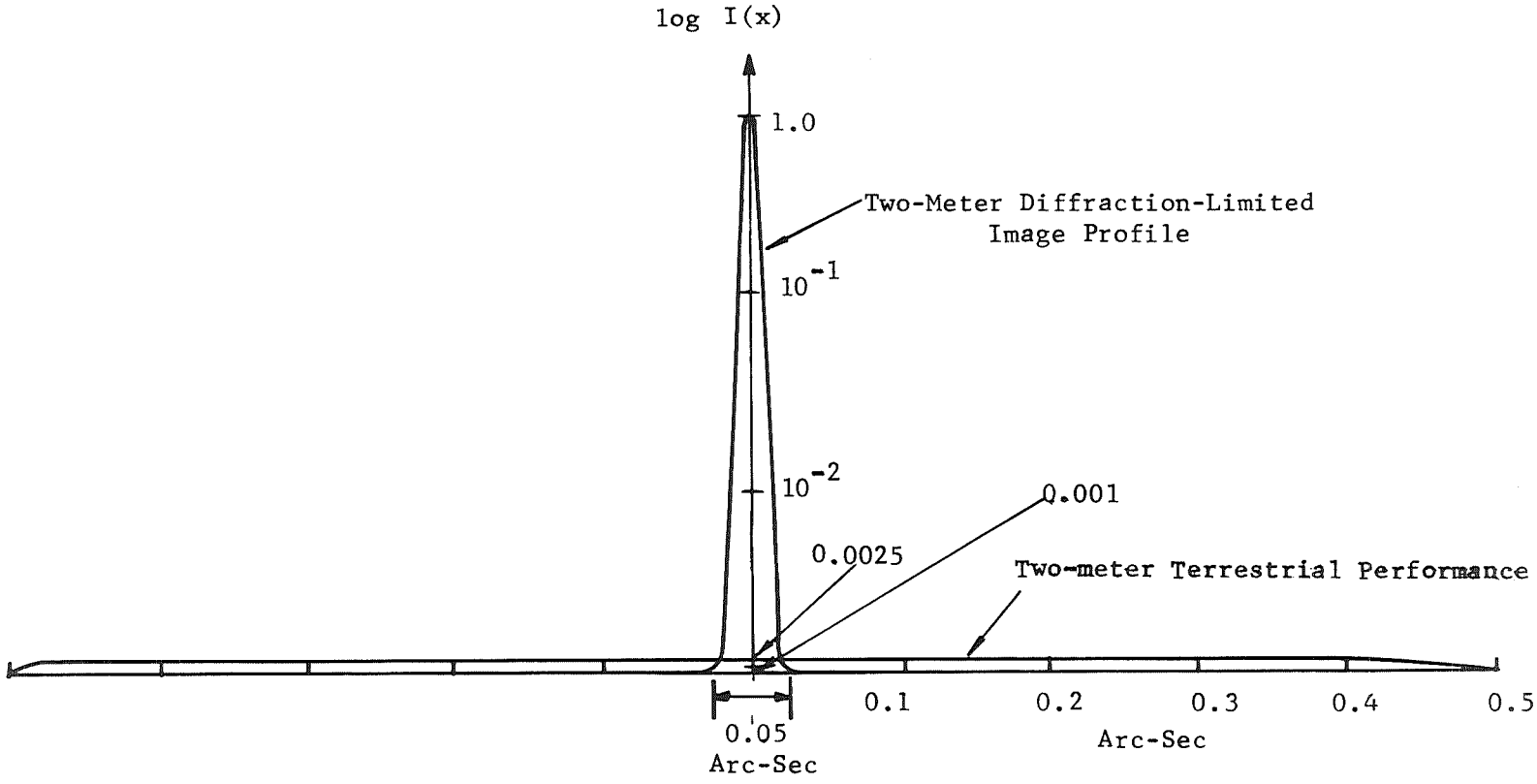

Figure 11. Diffraction-Limited Orbital Performance Compared with Terrestrial Performance for 2-Meter Telescope

Table 1 shows the comparative photoelectric performance of a 2-meter orbiting telescope and a 200-inch (5m) earth-based telescope.

TABLE 1. COMPARATIVE PHOTOELECTRIC PERFORMANCE

Visual Magnitude	2m Space	5m Earth-Based
	Integration Times (Signal to noise = 10)	
20.0	2.5 Sec	5.8 Sec.
23.0	1.1 Min	22.5 Min.
25.0	26.3 Min.	
27.0	15 Hours	

As indicated by Table 1, the advantages of a 2-meter space telescope are striking. For a Mv = 23.0, the integration time for the 2-meter space telescope is about 1/20 that for the 5-meter earth-based telescope. More important, the faint limit of the 2-meter space telescope is about 4 visual magnitudes fainter than that of a 5-meter earth-based telescope. This represents a factor of 40 lower level in stellar light flux of the telescope.

In summary, the 2-meter space telescope with the characteristics outlined above represents a potentially powerful instrument for exciting astronomical research. It could be of prime importance not only for astronomical research but also cosmological research. Undoubtedly, some of the most exciting results obtained by such an instrument are likely to be those which are not presently foreseen.

ULTRAVIOLET SPECTROSCOPY

The scientific importance of ultraviolet astronomy has been recognized for a long time and has provided the impetus for rocket and balloon-borne experiments. The wide wavelength coverage permitted above the atmosphere is a prime justification for spaceborne ultraviolet astronomy. Figure 12 depicts the spectral extinction of the earth's atmosphere in the ultraviolet region. This figure gives the altitudes at which normally incident radiation is reduced by a factor of e^{-1} of its initial intensity. From Figure 12, it is apparent that high altitude balloons operating between 30 to 40 km can conduct experiments in the 2000-3000Å region. In order to cover the entire ultraviolet region, it is necessary to use rocket vehicles to carry the instrumentation above 100 km. It is necessary to go above 200 km to conduct observations free of atmospheric extinction over the entire ultraviolet spectral region.

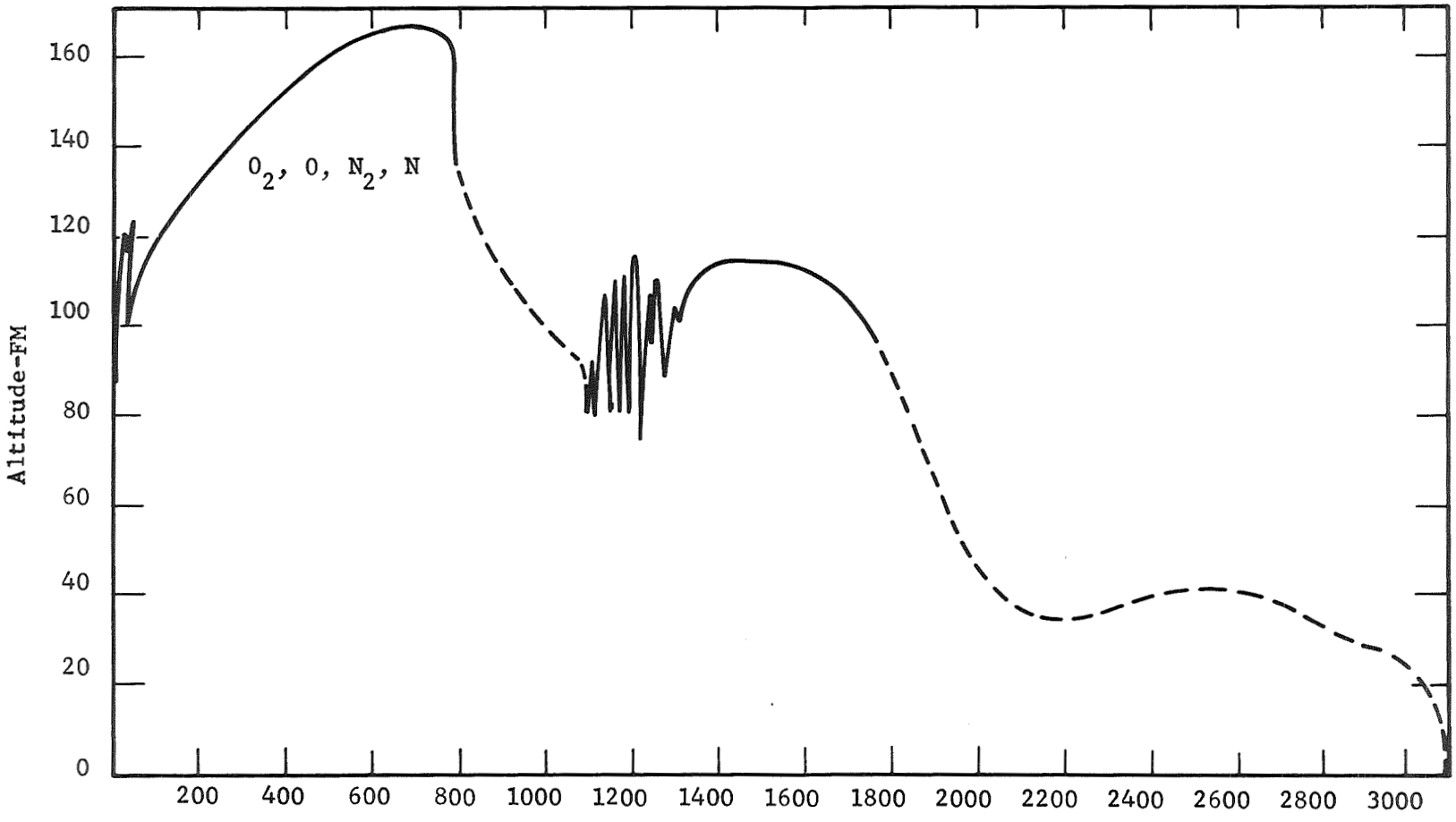

Figure 12. Altitude at which radiation incident normal to the Earth's atmosphere is reduced to e^{-1} of its initial intensity. (The chemical constituents that are the main contributors to the absorption in various spectral regions are shown on the curve.)*

*Wilson, R. and Bokensberg, A.: Ultraviolet Astronomy. Annual Review of Astronomy and Physics. Vol. 7, 1969, p. 422.

A wide range of important astrophysical investigations are of importance in the ultraviolet region. Table 2 gives some of the important phenomona, the important spectral ranges, and the spectral widths to be expected. It is evident from Table 2 that access to the full ultraviolet spectral range, i.e., 900Å to 3000Å, is extremely important and that for many investigations 0.1Å resolution is required.

The two ultraviolet instruments suggested as part of LTEP are 1) a Rowland circle spectrometer and 2) an echelle spectrograph.

Rowland Circle Spectrometer (Equipment Module E)

In the far ultraviolet region the efficiency of the best reflective coatings is very low. At 1200Å a reflectivity of better than 50 percent is considered excellent, and below 1000Å efficiencies are somewhat less than 20 percent, even if platinum or rhodium coatings are used. Figure 13 shows reflectivity for aluminum with MgF_2 and LiF over-coats. This absorption loss is further compounded by the large scattering losses which occur at these wavelengths. Even on good surfaces, the scattered radiation generally acts to obscure the desired images. It is therefore imperative that the number of optical surfaces be kept to an absolute minimum in instruments designed to operate in this region. The Rowland circle spectrometer fulfills this condition and, in addition, can be designed so that the inherently lower data rate of this type of instrument is partially offset by its versatility.

The OAO-C, built for Princeton University by Perkin-Elmer, is based upon the Rowland circle spectrometer. This instrument and an adaption for the LTEP are described elsewhere in this report. Some of the performance test data is becoming available, and in Figure 14 , spectral scans illustrative of the resolution are shown. As noted on the record, the 3131 Å Mercury doublet (0.28Å separation) is very well resolved, showing that 0.1Å will readily be accomplished by the instrument.

The potential advantages of including this spectrometer in a 2-meter telescope are clear: the photon gathering power is more than quadrupled, since the four-times-larger aperture of LTEP and the behind-the-mirror location for the spectrometer reduces the obscuration from 35 percent in OAO-C to only 4 percent in the LTEP configuration. The total net gain in photon collection, then, is a factor of 10 in favor of the LTEP over OAO-C.

Echelle Spectrograph (Equipment Module D)

Initially at least, the greatest need will be for an instrument of moderately high spectral resolution but capable of performing a spectrographic survey of a faint stellar spectrum in a minimum length of time.

This requirement appears to be met by an echelle spectrograph modified from the one developed by Perkin-Elmer in the Advanced Princeton Study and adapted to the LTEP. The echelle spectrograph is described in detail elsewhere in this report, but briefly, the spectrograph consists of two gratings ruled at right

TABLE 2 . AN INDICATION OF THE IMPORTANT SPECTRAL RANGE AND SPECTRAL WIDTHS TO BE EXPECTED IN UV SPECTRA FOR VARIOUS ASTROPHYSICAL GROUPS*

		Important Spectral Range	Spectral Widths	Remarks
Early-Type Stars	STELLAR PHOTOSPHERES (ABSORPTION LINE) O,B,A			
	Giants	1220-3000 Å (1)	Strong line 1-50 Å Faint line ~0.4 Å	Radiation damping; several resonance lines covered Turbulence broadening
	Broad line	1220-3000 Å (1)	Strong lines 2-50 Å Faint lines ~2 Å	Radiation damping; several resonance lines covered Rotation broadening
	Main Sequence Narrow line	1220-3000 Å (1)	Strong lines 1-50 Å Faint lines >0.05 Å	Radiation damping; resonance lines covered Lower limit from thermal broadening; no rotation or pole-on viewing
	Sub-main Sequence	1220-3000 Å (1)	Strong lines 1-50 Å Faint lines >0.05 (2)	Radiation damping; also Stark broadening in H, HeI, HeII Lower limit from thermal broadening
	EXTENDED ATMOSPHERES (Emission line) (3)			
	P. Cygni Stars (supergiants; expanding envelope)	912-3000 Å	Absorption line shift ~1 Å	
	Be Stars Shell Stars } (Rotating envelope)		Photospheric absorption line 4A Shell emission line ~2 A Shell absorption line >0.05 A	Emission generally variable on a time scale of some years
	Wolf-Rayet Stars	912-3000 Å	Emission lines ~20 Å	Energy in emission lines roughly equal to that in continuum
Late-Type Stars (F,G,K,M)	Chromospheric/Coronal Features	912-2000 Å (4)	MgII lines 0.3-3.0 Å (5) Coronal lines ~0.5 Å (6)	Lyman α, if observable ~1 Å
Variable Stars	Cepheid Variables	1500-3000 Å (7)	Strong lines 1-50 Å Faint lines >0.1 Å	Radiation damping; several resonance lines covered Lower limit mainly from turbulence
	βCephei Stars	1200-3000 Å	Strong lines 1-50 Å Faint lines 0.2-0.8 Å	Radiation damping; several resonance lines covered Rotation broadening
	Magnetic Stars	1200-3000 Å	Strong lines 1-50 Å Faint lines >0.1 Å	Radiation damping; several resonance lines covered Lower limit from thermal plus Zeeman broadening
Interstellar Medium	Novae	912-3000 Å	Various up to 20 Å	Great variations in spectrum; absorption and emission lines; complex structure
	Eclipsing Binaries	912-3000 Å	Strong lines broad Faint lines >0.1 Å	Radiation damping; several resonance lines covered Lower limit from turbulence broadening
	INTERSTELLAR DUST Early type O,B Stars (8)	1220-3000 Å (9)	Broad band ~100 Å	

*Wilson, R. and Boksenberg, A.: Ultraviolet Astronomy. Annual Review of Astronomy and Physics. Vol. 7, 1969, pp. 424-425.

TABLE 2 . AN INDICATION OF THE IMPORTANT SPECTRAL RANGE AND SPECTRAL WIDTHS TO BE EXPECTED IN UV SPECTRA FOR VARIOUS ASTROPHYSICAL GROUPS* (Continued)

		Important Spectral Range	Spectral Widths	Remarks
Interstellar Medium (Continued)	STELLAR PHOTOSPHERES (ABSORPTION LINE) O, B, A Giants			
	INTERSTELLAR GAS Nearest O,B Stars — Atomic Hydrogen	912-1220 Å	Lyman α~5 Å Lyman β~1.5 Å	Values for nearest stars, $N=10^{20}$ atoms cm^{-2}
	Nearest O,B Stars — Molecular Hydrogen	1040-1120 Å	$1\Sigma_a^+ - 1\Sigma_\mu^+$ ~0.5Å; HD Shift ~3Å	Abundance unknown, stated value for 10% of H (10) HD observation also possible if abundance significant
	Relatively near abundant elements O,B Stars C, N, O, Mg, etc.	1100-3000 Å	Resonance lines~0.1-0.4 Å (11)	Values for N = 5×10^{20} atoms cm^{-2}
Galactic Nebulae	Planetary Nebulae	912-3000 Å	Emission lines 0.1-0.3 Å (12)	Strong UV flux expected from nucleus
	Diffuse Nebulae	912-3000 Å	Emission lines ~0.1 Å	Kinetic temperatures $\sim10^4$ °K
	Crab Nebulae	912-3000 Å	Continuous synchrotron spectrum Emission lines split ~10 Å	Continuous spectrum mainly from amorphous center Emission lines mainly from expanding filaments
External Galaxies	Normal Galaxies	1250-3000 Å	Emission lines: Lyman α~1 Å Others~0.1Å	Lyman α flux $\sim10^{-12}$ erg cm^{-2} sec^{-1} (13)
	Abnormal Galaxies (Strong Radio Emitters, quasistellar objects, Seyfert Galaxies)	1250-3000 Å	Emission lines up to ~20 Å	Lyman α flux $\sim10^{-10}$ erg cm^{-2} sec^{-1} (13)

NOTES TO TABLE I

1. Heavy blanketing below 1220 Å from model atmosphere calculations for early B stars. This blanketing should extend to A-type but may be much lessened in O-type stars.
2. Lower limit ignores possible contribution of pressure broadening which may be significant for some lines.
3. Early UV spectra indicate presence of pronounced extended atmospheres in a number of early-type supergiants and giants. These are of the P Cygni type but with large expansion velocities of the order observed in Wolf-Rayet stars (3).
4. Chromospheric emission lines will probably be swamped by photospheric radiation at wavelengths above 2000 Å with the exception of Mg II resonance lines at 2796 Å and 2803 Å.
5. Obtained from Wilson-Bappu relation between width and luminosity for Ca II lines.
6. Obtained from values for the Sun.
7. Since the spectral types involved are mainly late A.K. and early F, photospheric emission should be appreciable only above 1500 Å. Observations of Mg II lines will be important
8. Early observations of UV stellar flux have already extended the interstellar extinction curved down to 1115 Å(4).
9. Observations below 1200 Å may be difficult for distant stars due to absorption of interstellar atomic hydrogen.
10. A UV stellar spectrum has placed an upper limit on the abundance of interstellar H_2 as 10% of H (5).
11. The intrinsic line widths of very faint lines are very narrow, but the components due to individual clouds are shifted by the order of 0.1 Å due to the random motions of the clouds.
12. These values are obtained from expansion velocities which often cause a splitting of the line into two components. In some cases, much higher velocities are observed for lines of low stages of ionization.
13. Estimated Lyman α fluxes obtained from Burbidge (6). The Galaxy will be transparent to this line for redshifts $\nu/c > 3\times10^{-2}$

*Wilson, R. and Boksenberg, A.: Ultraviolet Astronomy. Annual Review of Astronomy and Physics. Vol. 7, 1969, pp. 424-425.

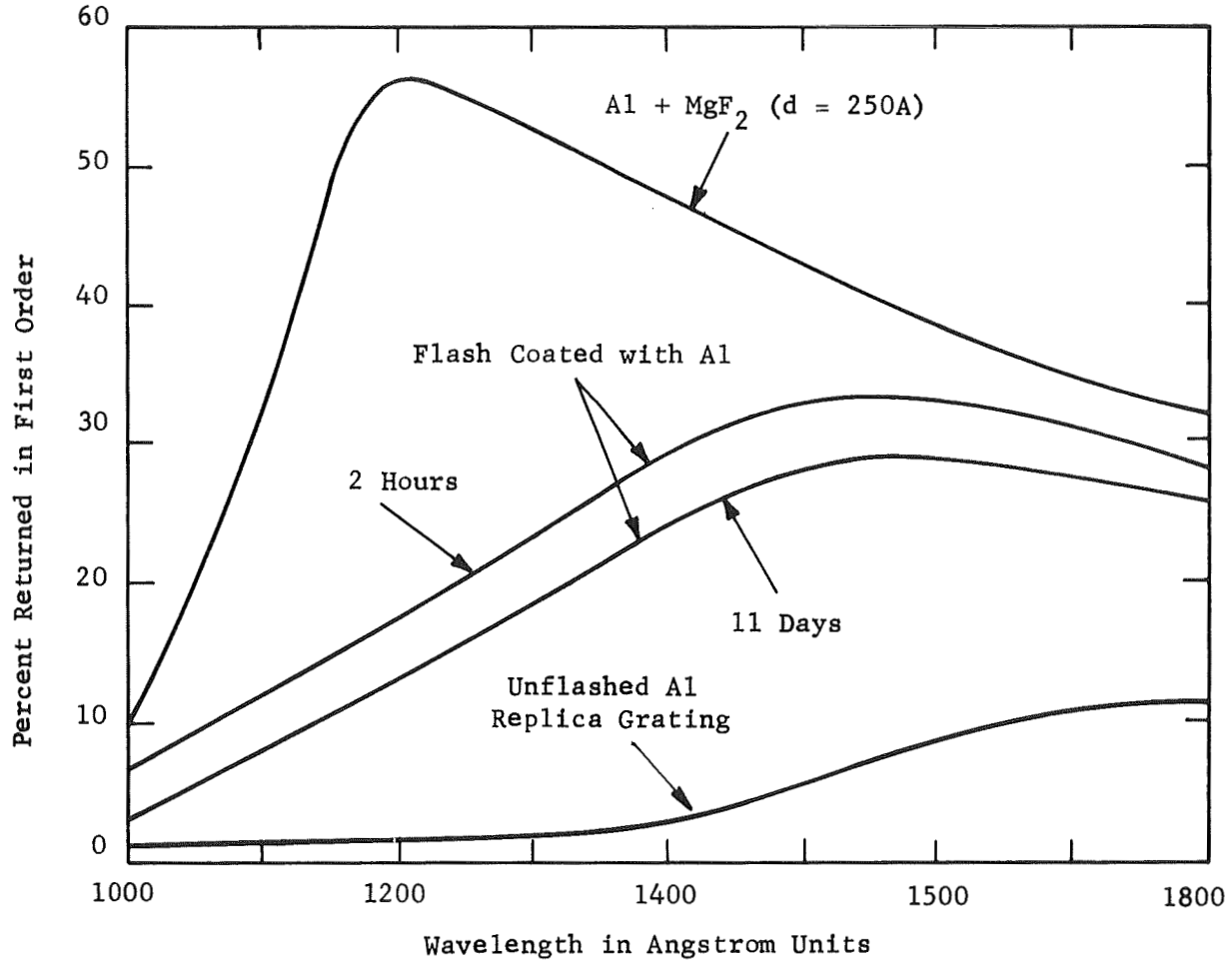

Figure 13. Improvement in efficiency produced by overcoating an aluminum replica grating with fresh aluminum and with fresh aluminum plus 250 A of MgF_2. (600 lines/mm grating at λ1200 A.)*

*Hass, George, ed.: Physics of Thin Films. Vol. 1, Academic Press, New York and London, 1963, p. 183.

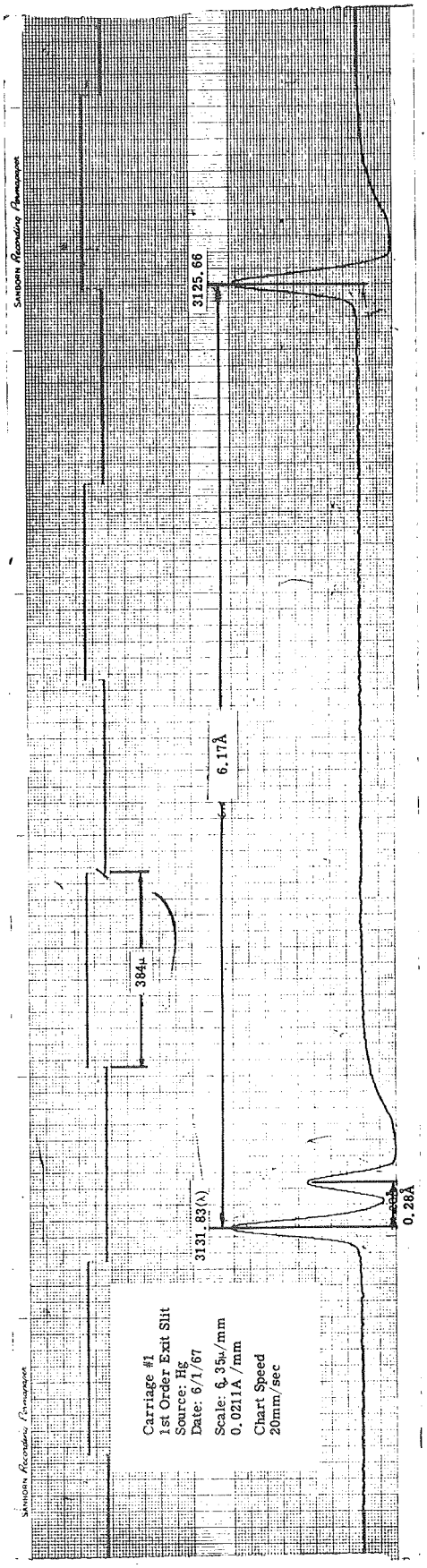

Figure 14, Spectrometer Resolution

angles to each other and a folding flat located near the vidicon image surface. The first grating is concave, operates in the first order, and yields a spectrum stretching from one side of the vidicon to the other. The second grating is flat, operates at very high orders typically between 10 and 40, and has a very high dispersion. The function of the first grating is to separate the overlapping orders of the second grating so that a nicely folded spectrum is formed at the vidicon much like the lines of type on a printed page. The vidicon axis is tilted with respect to the folded spectrograph axis in order that the astigmatic image plane containing the high dispersion focus coincides with the vidicon sensitive surface.

The vidicons are an ideal data transducer for a spectrographic survey instrument since they possess the quantum efficiency of a phototube yet have the capability of integrating the signals from a large number of resolution elements simultaneously. However, the spectral response of present tubes is limited to wavelengths longer than about 1250Å by the lithium fluoride window, the sensitivity can vary considerably from point to point on the photo-sensitive surface, and the size of the sensitive surface is limited to about 1.6 inches diameter for the largest. During the manned portion of the telescope operation program it may therefore be desirable to use film in the spectrograph as well as in the f/10 imagery package. This possibility could be incorporated in the design, probably without altering significantly the vidicon arrangement. The use of vidicons for astronomy is discussed in Appendix C.

For stellar spectroscopy an entrance slit is not required at all since the stellar image is extremely small (approximately 5 microns in the visible). However, with large nebula or star clusters, a variable slit serves to isolate the portion to be studied and also to determine the resolution.

PHOTOGRAPHIC PHOTOMETRY AND HIGH RESOLUTION IMAGERY (Equipment Module C)

The ability of the photographic plate to record simultaneously a large number of objects makes the use of photography an efficient method for gathering data on a large number of stars in a limited field. Photographic methods are useful in studies aimed at obtaining stellar statistics, variable-star surveys, or studies of rich star clusters.

The prime advantages of a spaceborne 2-meter diffraction-limited telescope when used in conjunction with photographic techniques are in the achievement of high angular resolution and the ability to measure the luminosity of fainter, more distant objects. Specifically, a 2-meter LTEP is of unique value in setting limits on the sizes of the compact nuclei of galaxies. In addition, it is possible to obtain photographic measures of the angular diameters of galaxies from detailed luminosity profiles which are unperturbed by the atmosphere. A further powerful photographic application of the 2-meter LTEP would be in the field of cosmology. In particular, it would be possible to detect and measure the luminosity of Cepheid variables at a distance of 10^8

light years, which is a distance 10 times greater than that attainable from earth. At distances of 10^8 light-years, the velocity of expansion is sufficiently large compared to the random galactic motions, that the two are sufficiently decoupled to permit deduction of a much more accurate Hubble constant.*

The application of the LTEP to the determination of the magnitudes and colors of stars and objects not accessible from the earth is most important. Figure 15 depicts the spectral curves for the various color assignments. Table 3 gives necessary plate-filter combinations required to carry out the measurements.

TABLE 3. PLATE-FILTER COMBINATIONS FOR VARIOUS MAGNITUDE SYSTEMS **

System	Plate-Filter Combination	λ_{eff} † (A)	$\Delta\lambda$ (A)
V	Kodak 103a-D+2-mm Schott GG11	5750	1400
B	Kodak 103a-O+2-mm Schott GG13	4330	950
U	Kodak 103a-O+2-mm Schott UG2	3540	600
B	Kodak 103a-O+2-mm Schott BG3+1-mm Schott GG13	4250	670
G	Kodak 103a-O+2-mm Schott GG5	4690	470
O	Kodak 103a-G+2-mm Schott OG5	5600	530
R	Astro Pan+2-mm Schott RG1	6340	400
I	Kodak IN+2-mm Schott RG8	8040	1600

ASTROMETRY

Astrometry deals with the precise measurement of position, changes in position, and dimensions of objects on the celestial sphere. The main areas of interest in astrometry are:

*Spitzer, L., Jr.: Science. Vol. 161, 1968, p. 225.

**Stock, J. and Williams, D.: Astronomical Techniques. W.A. Hiltner, ed., The University of Chicago Press, Chicago, 1962, p. 374.

†For equal energy at all wavelengths, neglecting telescopic and atmospheric absorption.

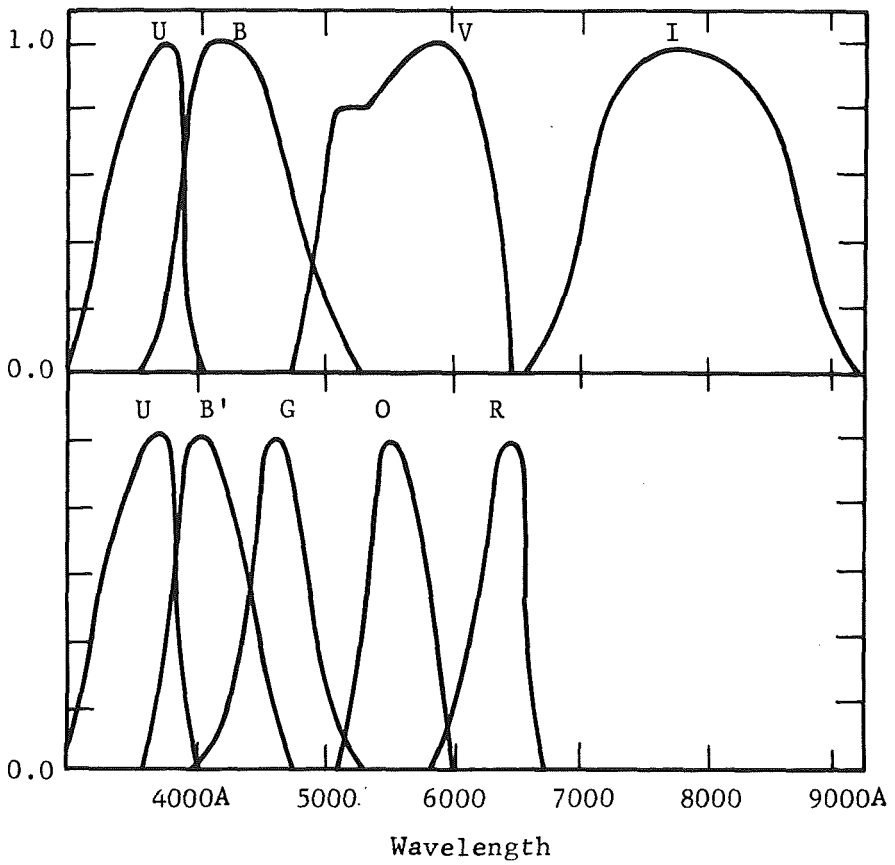

Figure 15. **Relative spectral responses of some typical plate-filter** combinations used for the determination of magnitudes and colors. (The curves have been plotted for equal energy at all wavelengths, neglecting absorption by the telescope and atmosphere and taking the maximum sensitivity of each combination as unity. The various combinations are tabulated in Table 1)*

*Stock, J. and Williams, D.: Astronomical Techniques. W.A. Hiltner, ed., The University of Chicago Press, Chicago, 1962, p. 374.

1. Measurement of proper motions of stars, nebulae, and galaxies.

2. Measurement of trigonometric parallaxes.

3. Measurement of double star orbits.

4. Search for planetary companions of stars.

5. Measurement of the dimensions of nebulae and diffuse objects.

Measurements of the proper motions of distant galaxies are important in order to establish the local inertial rest frame. This problem is frequently referred to as the determination of the constants of precession. The proper motions of distant galaxies should not be characterized by a systematic rotation with respect to the local inertial rest frame. Furthermore, proper motion data contribute to the knowledge of the true spatial motion of stars so that a more accurate understanding of galactic rotation, velocity dispersion as a function of spectral type, and the dynamic characteristics of star clusters is possible.

Parallax measurements are crucial to astrophysical theory because the stars of known trigonometric parallax are the means for calibrating the absolute stellar luminosities and bolometric corrections.*

Double star orbit and period determinations lead to direct values for stellar masses which can then be compared to those predicted mass-luminosity relations.**

Extra-Terrestrial Astrometry

A spaceborne, diffraction-limited 2-meter telescope operating at an f/10-f/50 configuration over a 5-arc-minute x 30-arc-minute field with zero coma is potentially an extremely useful source of astrometric data because:

1. The systematic atmospheric effects such as differential refraction and atmospheric dispersion are eliminated.

2. The stellar images are about 1/20 as wide because the widths are determined by the diffraction limit rather than by atmospheric "seeing".

---

*Schwarzschild, M.: Structure and Evaluation of the Stars. Princeton University Press, Princeton, N.J., 1958, Chapter 1.

**van den Bos, W.H.: Astronomical Techniques, W.A. Hiltner, ed., The University of Chicago Press, Chicago, 1962, p. 537.

3. Fainter objects can be photographed with exposure times shorter than those that must be used in earthbound photography.

4. It is possible to cover the Southern Hemisphere.

A spaceborne telescope is readily useful for obtaining relative coordinates and proper motions photographically. It is not as easily suited to the measurement of absolute coordinates which have been determined by meridian-type instruments.* A diffraction-limited telescope operating without atmospheric effects utilizing photographic plates, at least initially, would provide a large amount of new astrometrical data.

Since faint objects require exposure times that are considerably longer than the periods of good "seeing", i.e., stellar images one second in size, the atmospheric "seeing" thereby increases the exposure time required because of the image broadening. From a spaceborne diffraction-limited 2-meter telescope, it is possible to photograph stars of Mv = 23.0 in a time of 1.5 hr whereas terrestrially this would require a 5.0-m (200 in.) telescope with an 8-hr exposure.**

For astrometry, the atmospheric refraction of the star light produces two systematic effects. First, the differential refraction along a meridian

$$\Delta R_D = (n-1)\ (\sec^2 Z)\ \Delta Z,$$

where ΔR_D is the distance between two stars near a zenith angle Z but separated by an angle of ΔZ. At Z = 45 degrees, and Z = 1 arc-minute, ΔR_D = 0.03 arc-second. The differential refraction orthogonal to the observer's meridian is comparable to that along the meridian. For a 5-arc-minute field ΔR_D = 0.15 arc-seconds. In addition, atmospheric refraction is dispersive since it bends different colors by different amounts. This dispersion manifests itself as a lateral chromatic aberration.

$$\Delta R_c = \frac{dn}{d\lambda}\ (\tan Z)\ \Delta\lambda,$$

---

*Podobed, V.V.: Fundamental Astrometry. The University of Chicago Press, Chicago, 1962, p. 14.

**Tifft, W.G.: Theoretical Performance Capability of an Astronomical Optical Space Telescope for Photography and Photoelectric Photometry. Space Astronomy of the Steward Observatory, University of Arizona, Report T68-12, 1968, p. 7.

where ΔR_c is the angular separation of the images produced by light separated by a wavelength difference $\Delta\lambda$, and n is the refractive index of air. For example, at a zenith angle of 45 degrees, the red (7000Å) and blue (4000Å) images of a star are separated by 1.4 arc-seconds.

Thus, not only will the telescope provide improved astrometric data, but it can provide valuable new data for more distant stars. The extension of parallax measurements to a sphere of greater radius than is now available extends not only the number of calibration stars but also extends the range of spectral types and luminosity classes included in the calibration.

Instrumentation

The astrometric instrumentation is similar to that described in the instrumentation subsection of the Photographic Photometry and High Resolution Imagery section. A major difference, of course, is that for the astrometry, use is made of photographic plates rather than film. A common astrometric plate used for the visible is the Kodak 103-AD emulsion on a 1/16-inch thick glass backing. The plate sizes are 4 in. x 6 in. The fact that many exposures can be taken on a single plate reduces the amount of plate handling. A plate handling camera has not yet been designed for LTEP. However, a representative scheme is given in the paragraphs which follow.

Description of Shutter and Plate Magazine Arrangement

An arrangement of the plate camera assembly is illustrated in Figure 16. Light from the telescope optical system passes through the 1:1 transfer lens system to form an image at the focal plane. The main part of the light passes through the beam splitter and exposes the photographic plate during the interval in which the shutter is open. A reseau plate is fixed at the focal plane to enable recording plate calibration data as each photographic plate is exposed. A time presentation device, consisting of an illuminated clock and image-forming optics, identifies each plate exposed. Figure 17 provides two additional views of the plate camera. Additional details of the plate camera are provided in Figures 18, 19, 20, and 21.

The plate magazine assembly is bolted to the camera frame and is removable for loading. Plates are arranged in the magazine in two stacks of five plate assemblies each. Each plate assembly, illustrated in Figure 18, consists of a sheet metal container lined with foam-type material and the photographic plate. Plate changing is accomplished by lifting the plate assembly from the exposure position and actuating transfer mechanisms "A" and "B". This causes the top plate assembly in stack "A" to be shifted laterally to the top of stack "B"; at the same time, the bottom plate assembly (unexposed) on stack "B" is shifted to the bottom of stack "A". Figures 19, 20, and 21 illustrate this operation.

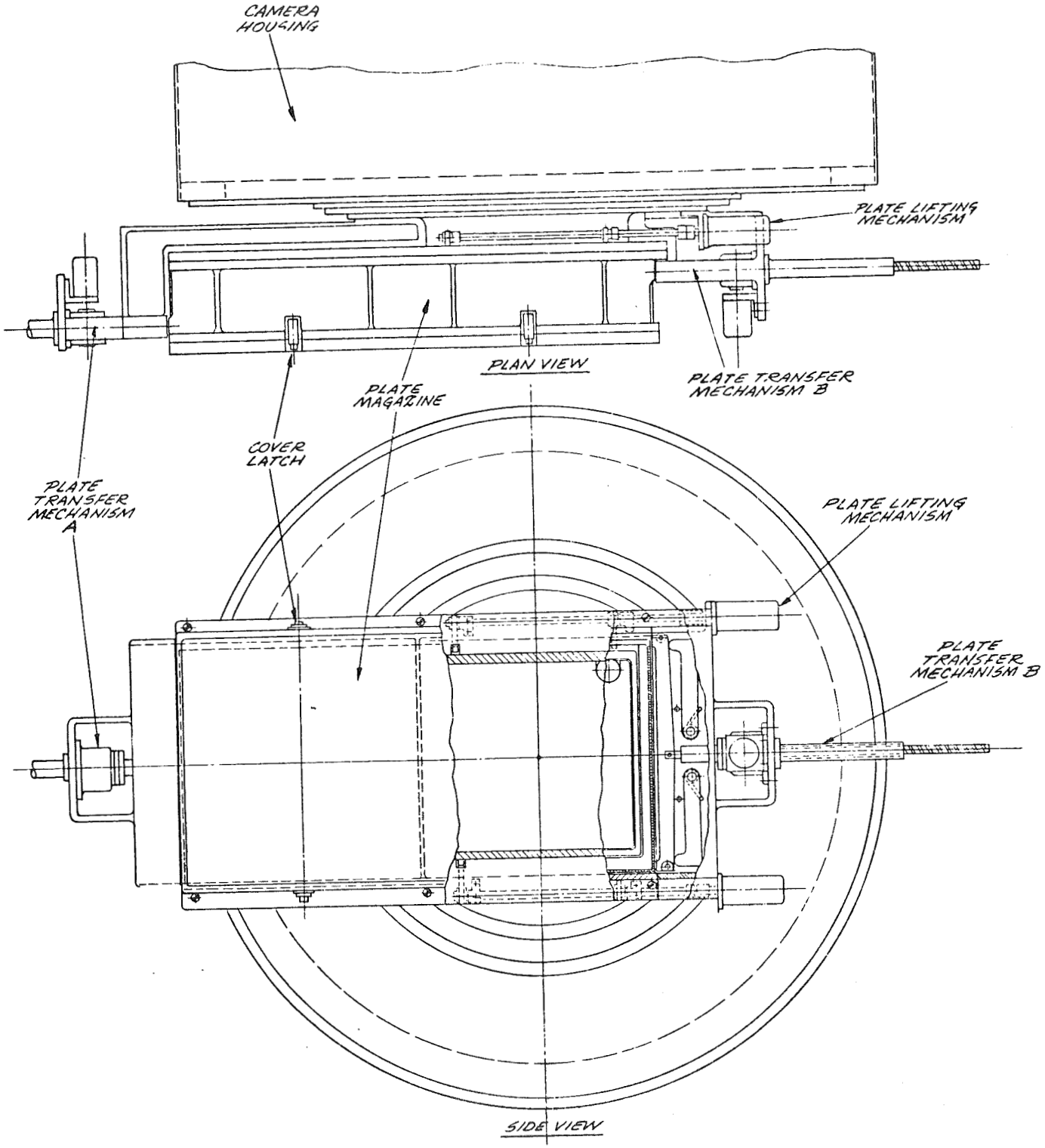

Figure 16. Arrangement of Camera

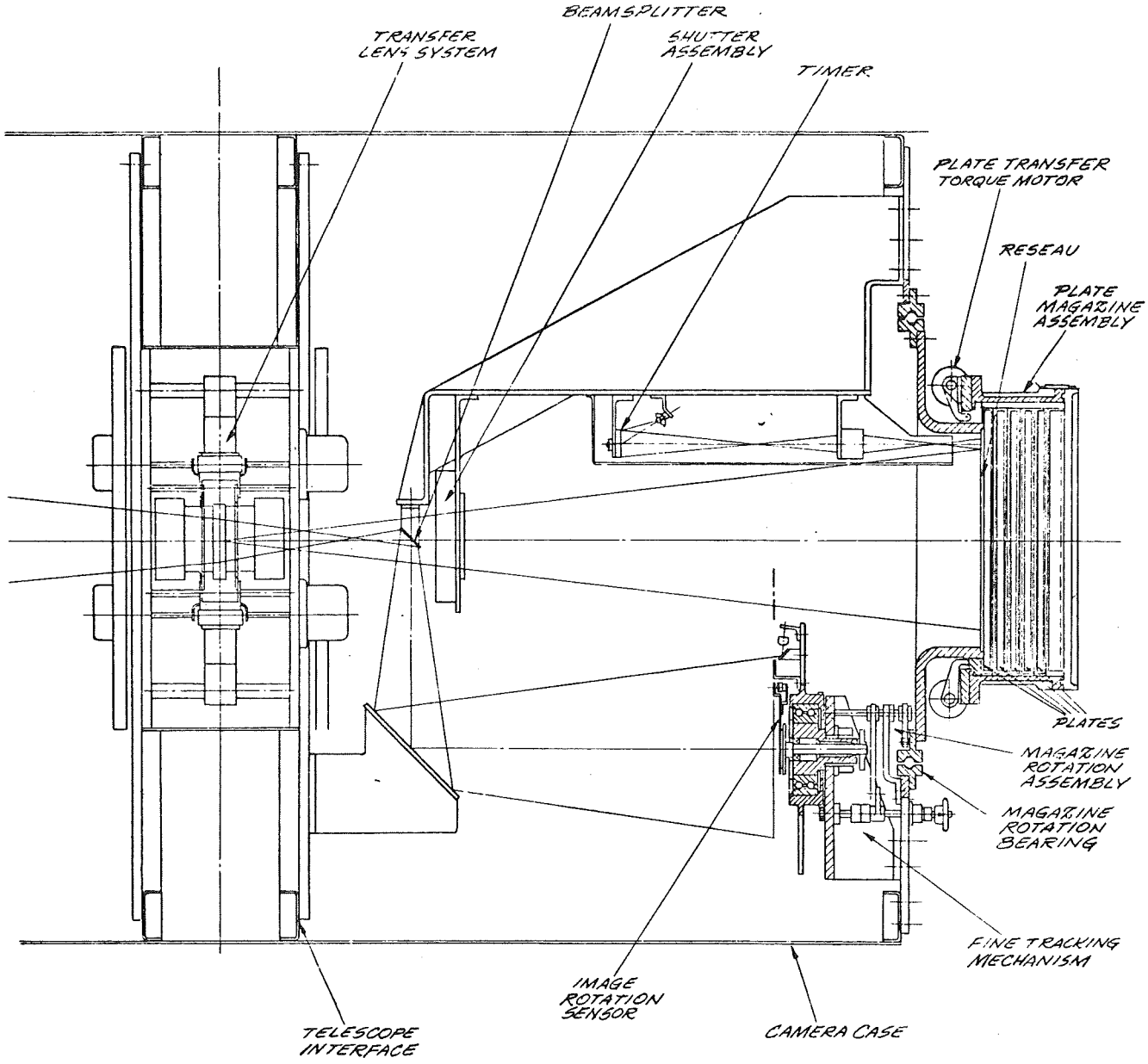

Figure 17. Plate Magazine and Change Mechanism

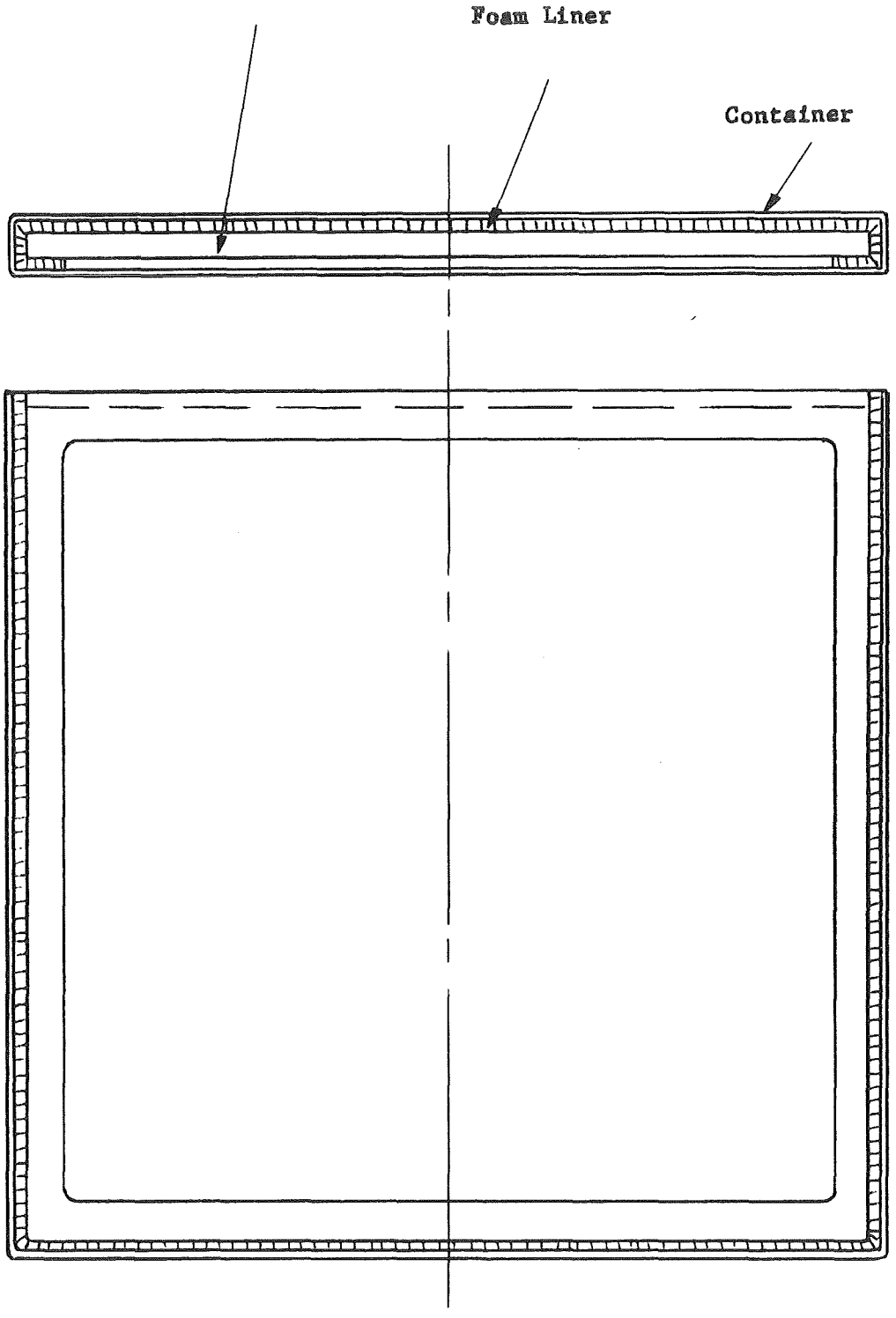

Figure 18. Photographic Plate Assembly

PERKIN-ELMER

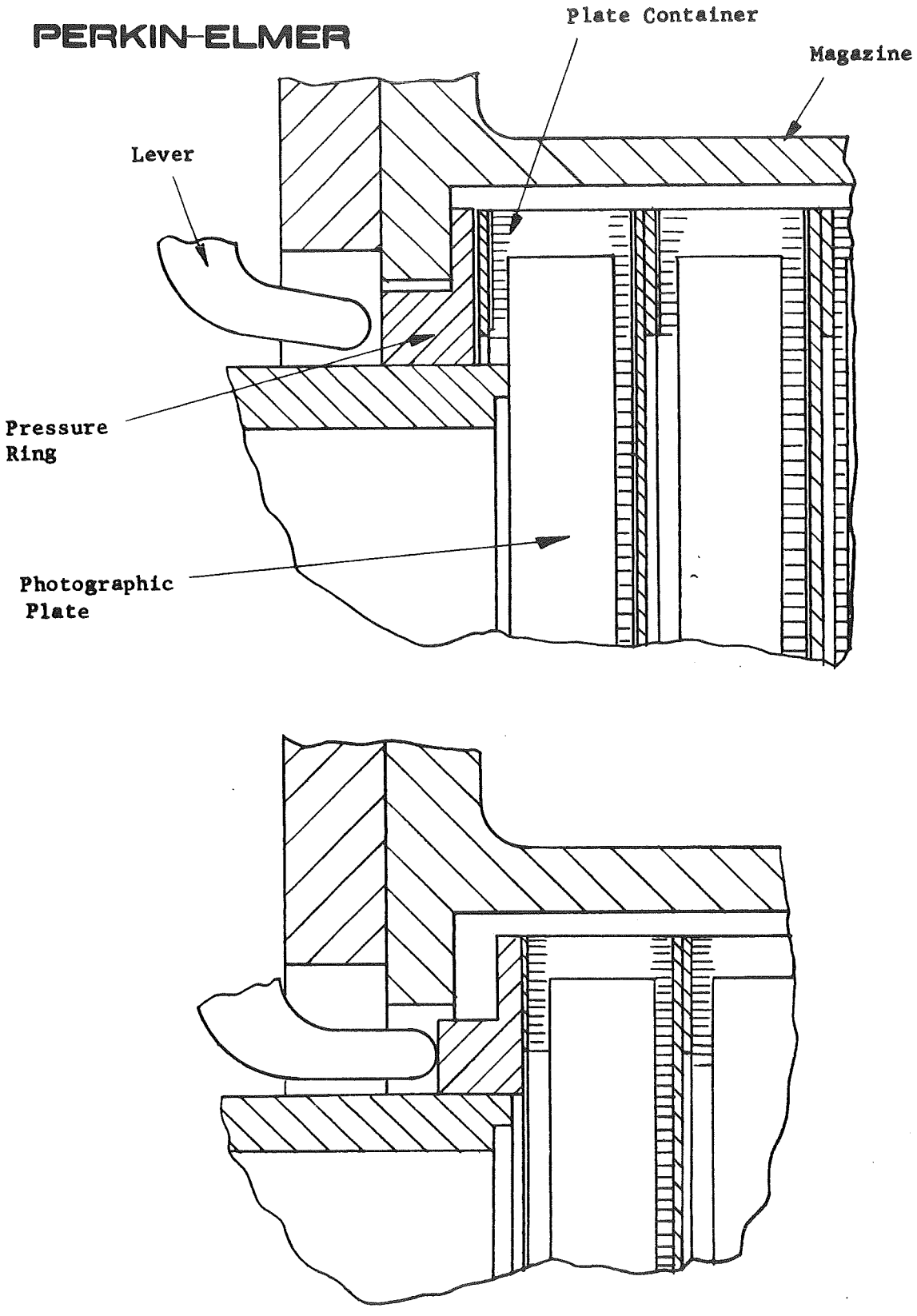

Figure 19. Exposure and Transfer Positions of Plates

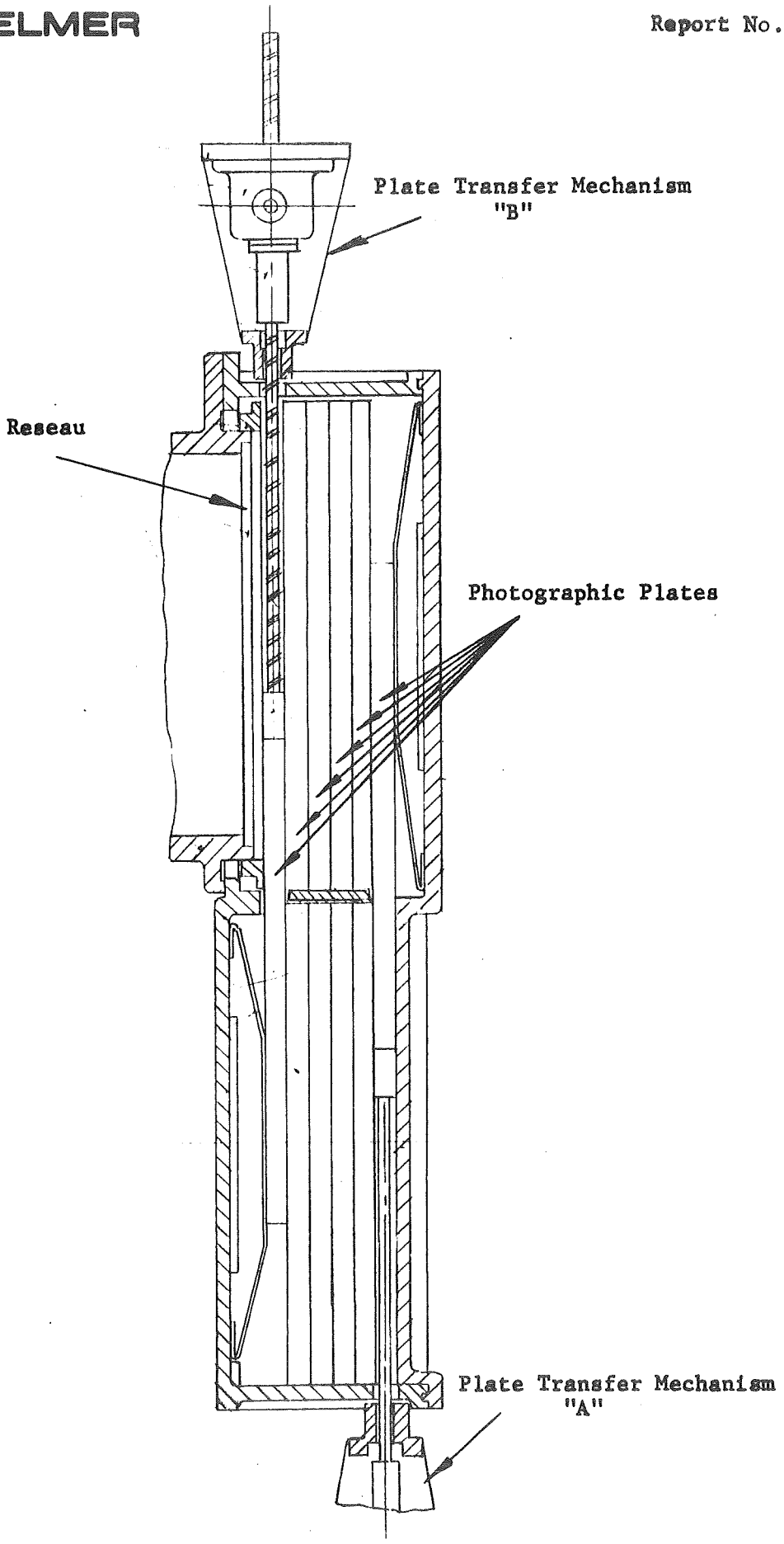

Figure 20. Plate Magazine and Transfer Mechanism, Transfer Stage

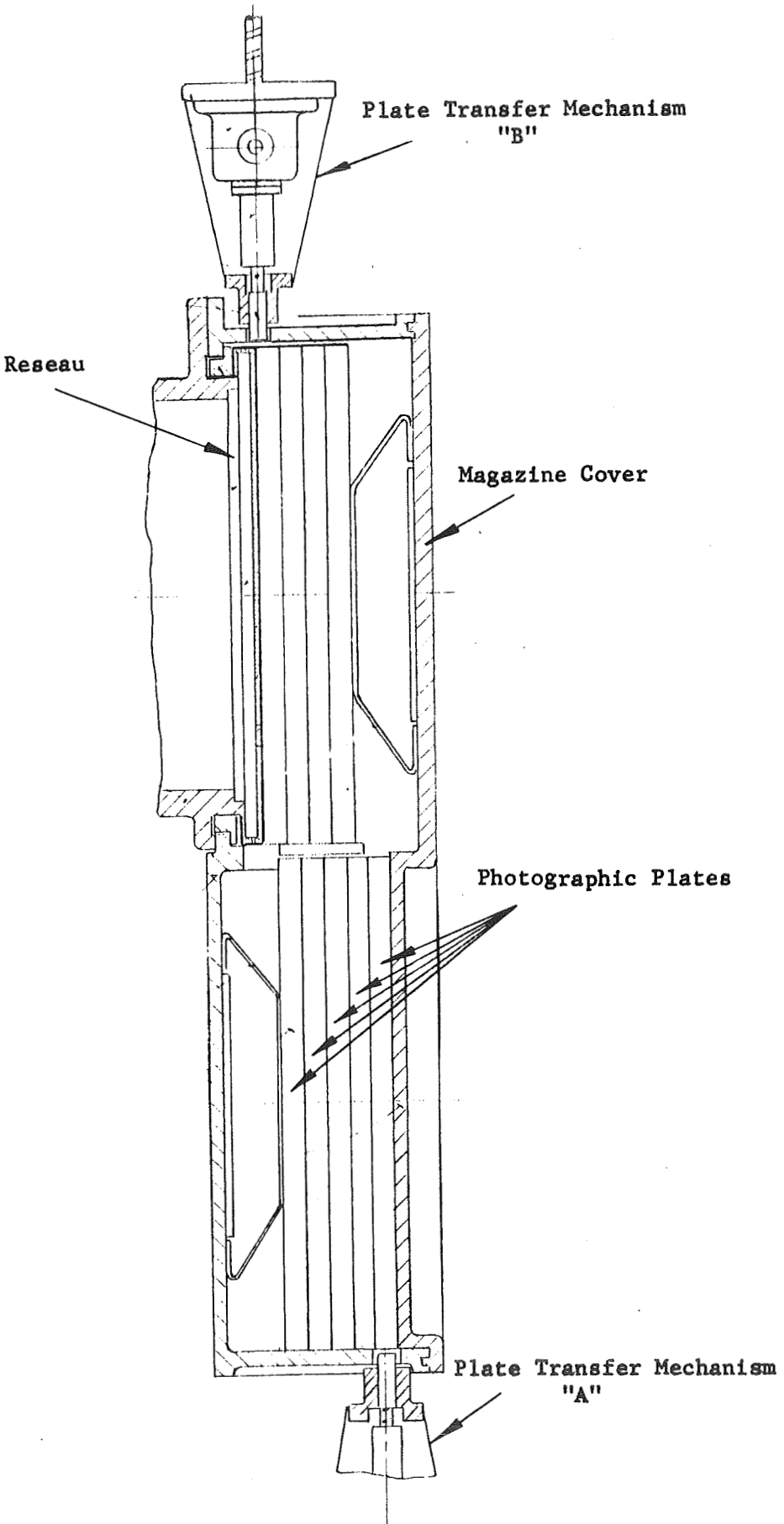

Figure 21, Plate Magazine and Transfer Mechanism, Exposure Position

POTENTIAL POLARIMETRY INSTRUMENTATION

During the past decade the measurement of polarization has become increasingly important in stellar astronomy. These measurements are usually made because of their usefulness in establishing the presence and nature of magnetic fields, either the general field of the galaxy or extragalactic nebulae or more restricted fields, such as that found in the Crab Nebula or in M87.*

The polarization state of starlight after passage through dust clouds is modified. The size, shape index, and orientation of particles can be estimated.** A wavelength dependence of polarization has been observed† so that broadband polarimeters are very useful. In the wavelength range 0.3μ to 1.0μ, particle diameters ranging from 0.17μ to 0.4μ are observed (n = 1.33 assumed). Larger and smaller particles, if present, can only be observed by longer and shorter wavelengths respectively.

Measurement Techniques

Polarizers which provide an undeviated beam such as the Rochon or Senarmont prism,†† a pile of plates,‡ or mirror systems‡‡ offer advantages in the

---

*Hiltner, W.A., ed.: Astronomical Techniques, University of Chicago Press, 1962, Chapter 10.

**Greenberg, J. Mayo, Meltzer, A.S.: Astrophysical Journal, Vol. 132, 1960.

†Coyne, G.V., Gehrels, T.: Astronomical Journal. Vol. 71, No. 6, June, 1966, pp. 355-363.

Gehrels, T., and Teska, Thomas M.: Applied Optics., Vol. 2, No. 1, January 1963, pp. 67-77.

††Steinmetz, D.L., Phillips, W.G., Wirick, M., and Forbes, F.F.: Applied Optics. Vol. 6, No. 6, June 1967, pp. 1001-1004.

‡Bird, G.R., Shurcliff, W.A. Shurcliff, J.: J. Opt. Soc Amer. Vol, 37, No. 818, pp. 235-237.

Walker, William C.: Applied Optics. Vol. 3, No. 12, December 1964, pp. 1457-1459.

‡‡Rosenbaum, G., Feurerbacher, B., Godwin, R.P., Skibowski, M.: Applied Optics, Vol. 7, No. 10, October 1968, pp. 1917-1920.

Hamm, R.N., MacRae, R.A., Arakawa, E.T.: J. Opt. Soc. Amer. Vol. 55, No. 11, November 1965, pp. 1460-1463.

techniques of detection and measurements.* These advantages relate to the fact that the polarizer can be rotated while the detector remains fixed, all without the use of auxiliary reflectors. See Figure 22 for the optical arrangement.

For internal calibration purposes a Lyot-type depolarizer** should be flipped in the beam between the telescope output and the polarizing prism.

A Lyot depolarizer consists of two retardation plates, one twice the thickness of the other, with the axis of one oriented at a 45- degree angle to that of the other. The depolarization is effective if the plates are thick enough to provide a 200π change in the retardation angle for changes in λ defined by the bandwidth. The Lyot depolarizer is not effective in monochromatic light.

Only the range of wavelengths from 0.13μ to 1.0μ will be considered. Because of the special nature and severity of the problems relating to wavelengths below 0.13μ, they will not be dealt with here.

Piles of plates or mirror systems, because of their inefficiencies, will not be considered and fortunately need not be considered because of recent developments in a 'double' Rochon prism.† This prism consists of MgF_2 crystals and is good for the range 0.13μ to 0.30μ. A double Rochon can be fabricated more easily and has a smaller optical path which allows less absorption loss.

For the wavelength range 0.30μ to 1.0μ, calcite is a good material. It has a high bi-refringence and consequently higher prism angles, which make for easier fabrication. The transmission is good for the whole range (0.3μ to 1.0μ). For color polarimetry it is desirable to provide five band pass filters, equally spaced in $1/\lambda$, that is, filters centered at: 0.322, 0.379, 0.463, 0.500 and 0.813 microns, all of half-width 0.47 recriprocal microns.

Measurements may be carried out with any one of the five filters or with the Lyot depolarizer.

---

*Pernicone, C.V., Hemstreet, H.S., Patrick, K.W.: Arizona Photopolarimeter Telescope - OAO. Vol. 1, Perkin-Elmer Engineering Report No. 8527 (I), October 26, 1966.

**Billings, Bruce H.: J. Opt. Soc. Amer. Vol. 41, No. 12, December 1951, pp. 966-973.

†Steinmetz, D.L., Phillips, W.G., Wirick, M., and Forbes, F.F.: Applied Optics. Vol. 6, No. 6, June 1967, pp. 1001-1004.

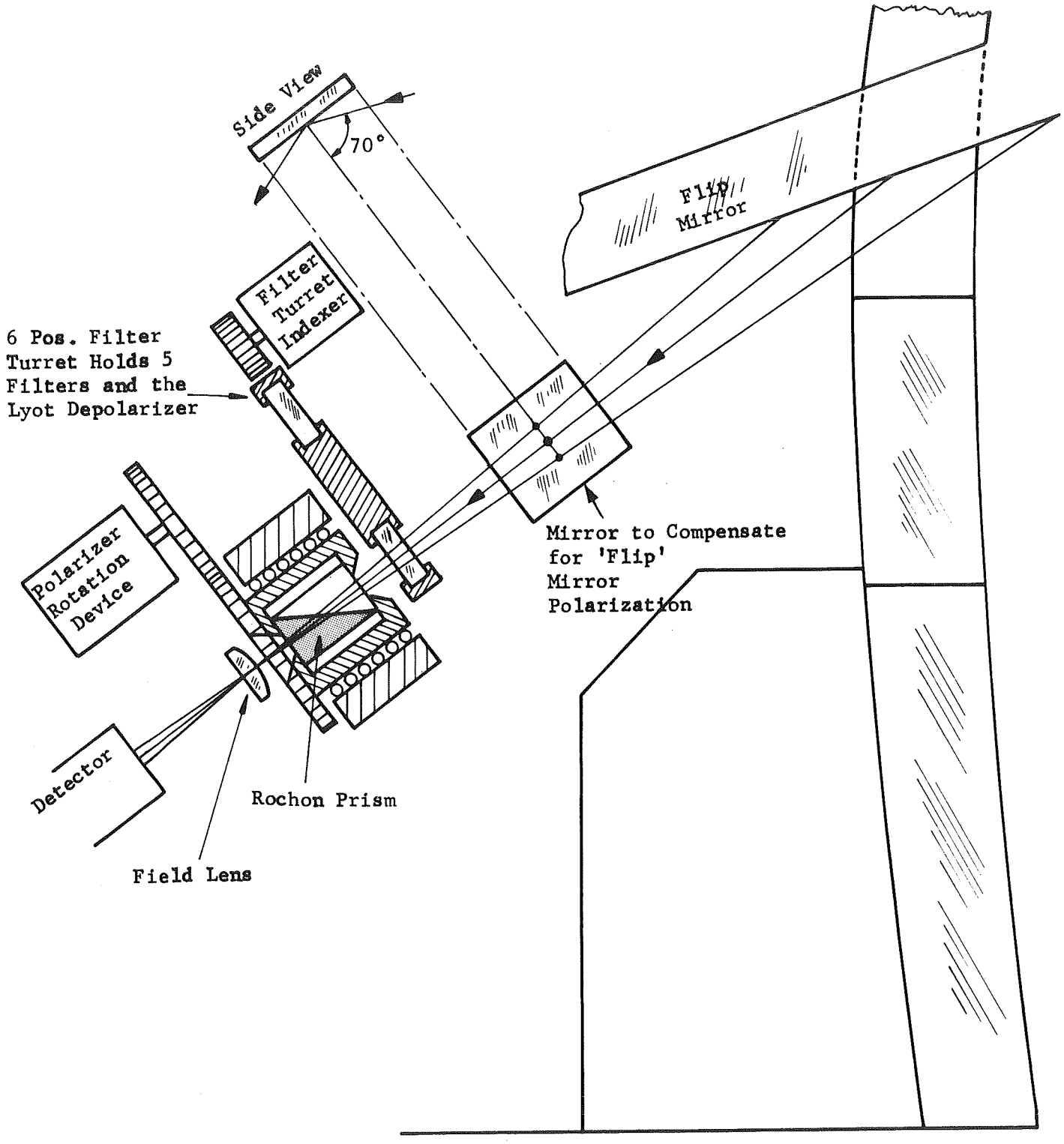

Figure 22. Optical Arrangement

Filters for the range 0.13μ to 0.3μ are difficult to make and require development. Metal-dielectric types have been made by Bates and Bradley,* and by Baumeister.**

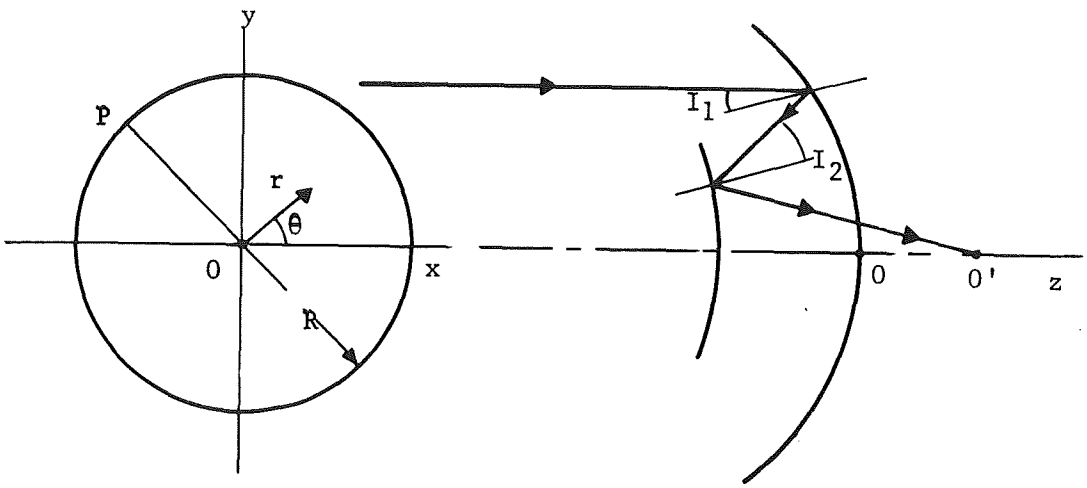

Figure 23. Polarization of the Telescope Mirrors

Consider the telescope system shown in Figure 23 with incidence plane defined by the lines $\overline{O\,P}$ and $\overline{O\,O'}$.† Note that the incidence angles I_1 and I_2 are independent of the azimuth angle θ, but are functions of the coordinate, r.

*Bates, B. and Bradley, D.J.: Interference Filters for the far UV(1700Å to 2400Å), J. App. Opt.Vol. 5 No.6, p. 971, June 1966.

**Baumeister, P.W., Costich, V.R., Pieper, S.C.: Paper WB11, Pres. Opt. Soc. Amer., October 7, 1964.

†Hiltner, W.A., ed.: Astronomical Techniques, University of Chicago Press, 1962, Chapter 10.

For an incoming beam polarized in the y direction, where E_y is the amplitude one has:

$$E'_y = \frac{E_y}{\pi R^2} \int_o^R \int_o^{2\pi} \left[\cos^2\theta\, R_{||}\,(r) + \sin^2\theta R_{\perp}\,(r)\right] r\, dr\, d\theta$$

$$E'_x = \frac{E_y}{\pi R^2} \int_o^R \int_o^{2\pi} \sin\theta\cos\theta \left[R_{||}(r) - R_{\perp}(r)\right] r\, dr\, d\theta$$

The complex reflectance amplitudes, $R_{||}$ and $R_{\perp}$ are independent of θ, so that:

$$E'_y = \frac{E_y}{R^2} \int_o^R \left[R_{||}\,(r) + R_{\perp}\,(r)\right] r\, dr = F(R)$$

$$E'_y = 0$$

The circularly symmetric system causes no polarization.

The Polarization of the Flip Mirror

The amount of polarization at wavelength 0.6μ introduced by the flip mirror is:

$$P = \frac{R_{||}}{R_{\perp}} = 0.92$$

This must be compensated for by another mirror using the same 70-degree incidence angle as the flip mirror but with its plane of incidence normal to that of the flip mirror. Electronic compensation is out of the question because the amount of correction is far greater than the polarization to be observed.

Special Mirror Coating

Any asymmetry introduced by the coating process will cause substantial polarization errors. If the evaporation sources do not provide enough symmetry under static conditions, the mirror must be rotated during evaporation. The evaporation times are very short so that high speed rotation would be needed. This requirement is relaxed if the asymmetry is periodic and of many periods in the course of 1 revolution.

Detection

The detection is accomplished by rotating the Rochon at a constant angular rate to provide an ac signal. The phase and amplitude of the frequency

component at a frequency of twice the polarization rotation rate, and the average value constitute the data from which the polarization $P = 2.5 \log(\frac{I_{max}}{I_{min}})$ and the plane of vibration can be calculated. Figure 24 shows the functional block diagram.

SATELLITE INFRARED ASTRONOMY

The atmosphere limits infrared astronomy in two ways: absorption of incoming light and background emission. Absorption decreases considerably at airplane altitudes (15 km or 50,000 ft) and is quite small (less than 10 percent) at balloon altitudes (30 km), except for a few narrow bands from water, carbon dioxide, and ozone. Atmospheric emission occurs as line emission and thermal graybody emission in the many absorption bands. Line emission, in particular OH, has been observed at heights of 60 or 70 km. If one goes to satellite infrared astronomy, one has zero absorption and zero emission in the pristine environment.

Current Problems in Infrared Astronomy

The present problems in infrared astronomy are:

(1) Interstellar line aborption and emission by ions and molecules.

(2) Planetary emission, both line and thermal, but predominantly thermal in the infrared region longer than a few microns.

(3) Thermal emission by gas clouds (protostars), and heated instellar grains.

(4) Cool stars and circumstellar dust (both of which imply "infrared stars").

(5) Cosmic blackbody background.

(6) Radiation from our galaxy and other normal and protogalaxies.

(7) Quasars, pulsars, and Seyfert galaxies.

Only problem (1) benefits greatly from the difference in absorption at balloon and satellite altitudes, and then only for those lines which are close to atmospheric absorption lines. The principal line which would be available only in a rocket or satellite telescope is the 28μ line of molecular hydrogen (H_2) which is very close (within 0.02μ) to a water vapor absorption line. Other lines which are close to atmospheric absorption lines are: (1) Ne^{++}, 15.38μ, near CO_2, 15μ and, of course (2) the water vapor and carbon dioxide lines themselves.

Problems (2) through (7) require only broadband measurements, and do not benefit very much from the lack of line absorption at satellite altitudes. These problems might benefit from the lack of background emission which would have two effects.

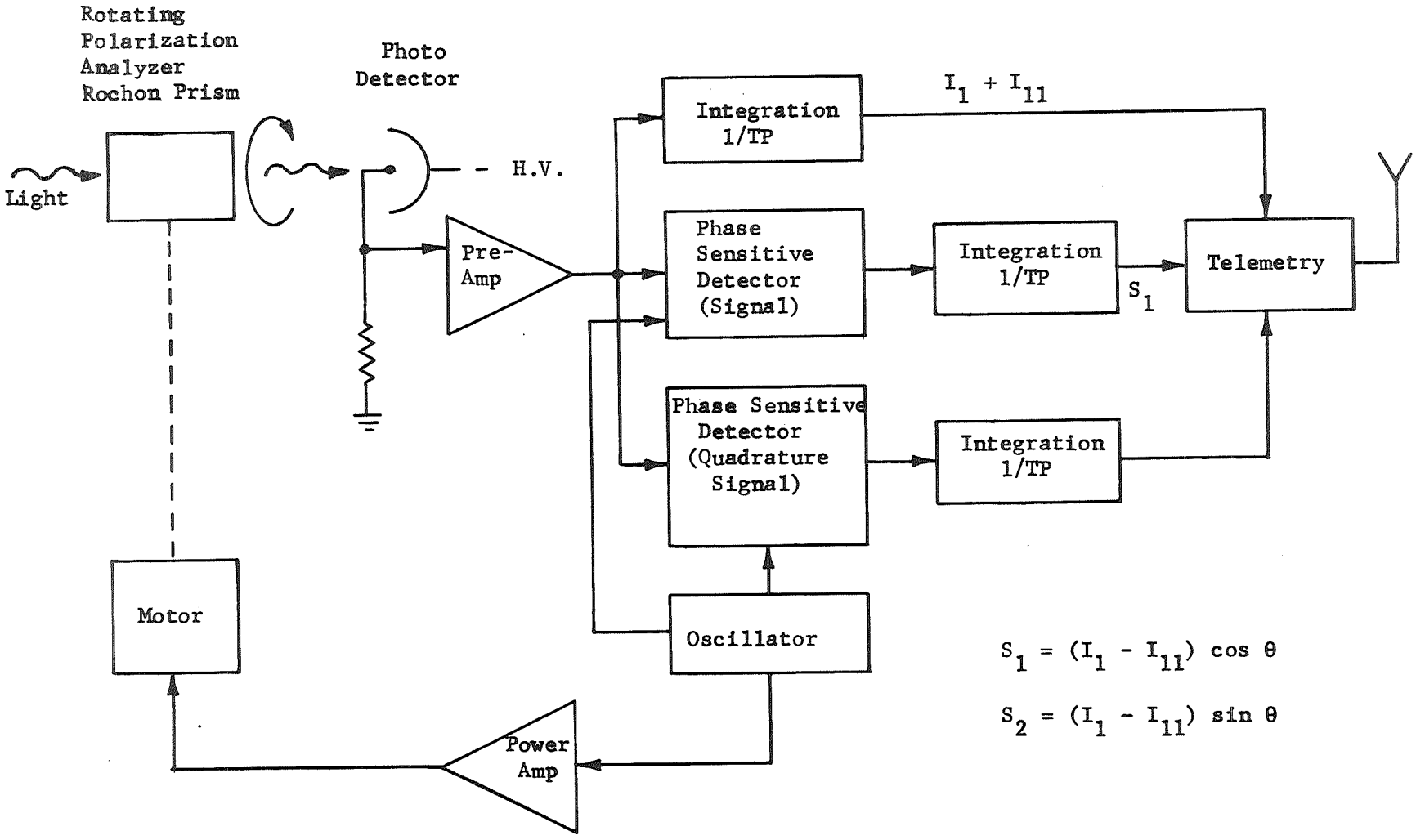

Figure 24. Polarization Amplitude and Phase Detection System

1) Reduction of shot noise allowing fainter sources to be seen, and

2) Elimination of atmospheric fluctuations from one position in the sky to another, allowing observation of diffuse sources and background radiation, as well as absolute flux measurements.

There is little or no quantitative experimental data on atmospheric emission as a function of height and wavelength. Order of magnitude calculations multiplying the absorptivity of the atmosphere by a blackbody spectrum at atmospheric temperatures are shown in Table 4 . These do not seem to conflict with the few other quantitative estimates.* Comparing these background radiances with typical (bright) infrared objects (Table 5), it appears at first glance that the background should mask even bright objects. But if we compute the "noise equivalent power", NEP, of this background radiation, which is the limiting number, we get much more reasonable values. Comparing these NEP's with those of good detectors (Table 6), we see that detector noise is of the order of, or much greater than, background noise.

Atmospheric fluctuations appear to be significant on the ground,** but no estimate is available of their magnitude at airplane and balloon altitudes.

All other things equal, a satellite infrared telescope would give increased signal-to-noise ratios of a maximum of 2 or 3 over airplane or balloon telescopes in absorption regions of the spectrum with present practical detectors. A reduction in NEP of detectors to 10^{-15} W $Hz^{-1/2}$ in the 5-200μ range would make the gain in signal to noise on the order of 10, rather than 2, in going from airplane to satellite altitudes. It would also be of significant help at that point to cool the telescope, since its thermal radiation is the same order of magnitude as that of the sky.

An indirect advantage of a satellite infrared telescope is the increased observing time available over an airplane or balloon telescope. Looking at Table 5 we see that the typical integration times necessary in infrared astronomy for one broadband measurement range from 10^{-3} to 10^{3} seconds. The upper limit for balloon observations is about 4×10^{4} seconds, and astronomers would be disinclined to use a balloon flight for one measurement of one object in one

---

*Wark, D.Q., Alishouse, J., and Yamsmoto, G.: Applied Optics. Vol. 3, 1964, p. 221.

Turon-Lacarrieu, P., and Verdet, J.P.: Annals d'Astrophysique. Vol. 31, 1968, p. 1.

Stein, W.: Astrophysics Journal. Vol. 144, 1966, p. 318.

**Becklin, E.E., and Neugebauer, G.: Astrophysics Journal, Vol. 151, 1968, p. 145.

TABLE 4

ATMOSPHERIC LIMITATIONS

Emission in watts and the corresponding noise equivalent power, NEP, at the detector for a 100-inch telescope with a 1-arc-minute diaphragm in the designated spectral bandwidth. NEP = $(h\nu \times \text{watts})^{1/2}$

SPECTRAL	SEA LEVEL		AIRPLANE-BALLOON (50-100K ft.)		SATELLITE
Band (μ)	Watts	NEP(watts $Hz^{-1/2}$)	Watts	NEP (watts $Hz^{-1/2}$)	0
2.0 - 2.5	1×10^{-11}	1×10^{-15}	10^{-13}	10^{-16}	0
10 - 12	2×10^{-6}	2×10^{-13}	10^{-7}	5×10^{-14}	0
80 - 120	100% absorption in this band		10^{-8}	4×10^{-14}	0
500-1500	3×10^{-10}	3×10^{-16}	10^{-11}	5×10^{-17}	0

TABLE 5

INTERESTING OBJECTS

Typical Signal Strengths of Interesting Objects and Integration Times Necessary for S/N = 10*

Object	BAND (Microns) 2-2.5μ	10-12μ	80-120μ	500-1500μ
K or M Star (m_v = 4)	10^{-8} w, 10^{-4} sec	10^{-10}, 10^{-1} **		
K or M Star (m_v = 9)		10^{-12}, 10		
K or M Star (m_v = 14)		10^{-14}, 10^{3}		
Saturn			5×10^{-9}, 10^{-2} †	10^{-9}, 10^{-1}
Galactic Center	10^{-10}, 10^{-2} ††	greater than 10^{2}	5×10^{-13}, 10 ‡	
Planetary Nebula (NGC 7027)		3×10^{-11}, 10^{-1} ‡‡	2×10^{-11}, 10^{-1}	
Seyfert Galaxy (NGC 1068)		3×10^{-12}, 1 ‡‡	2×10^{-12}, 1	

* Allowing for practical filter transmittances and non-optimum detector operation with the same telescope parameters as for atmospheric emission (units, watts, and seconds).

** Allen, C.W., ed.: Astrophysical Quantities. Athlone Press, London, 1963, p. 125.

† Aumann, H.H., Gillespie, C.M., and Low, F.J.: Astrophysics Journal Letters. Vol. 157, 1969, p. L69.

†† Stein, W.: Astrophysics Journal. Vol. 144, 1966, p. 318.

‡ Hoffman, W.F., and Frederick, C.L.: Astrophysics Journal Letters. Vol. 155, p. L9.

‡‡ Low, F.J., and Kleinmann, D.E.: Astronomical Journal. Vol. 73, 1968, p. 868.

TABLE 5 (Continued)

Object	BAND (Microns) 2-2.5μ	10-12μ	80-120μ	500-1500μ
Quasar (3C273)		3×10^{-12}, *	2×10^{-12}, 1	
Interstellar Grains in the Galaxy				5×10^{-13}, ** 10
Grains Near Stars (Trapezium in Orion) (15-arc-sec Diaphragm)		3×10^{-11} † 10^{-1}		
Max 28μ H_2 Emission		10^{-11}, 10^{-1} **		
12.8μ Ne Line		10^{-12}, 10 ††		

*Low, F.J.: Astrophysics Journal. Vol. 142, 1965, p. 1287.

**Stein, W.: Astrophysics Journal. Vol. 144, 1966, p. 318.

†Stein W.A., and Gillett, F.C.: Astrophysics Journal. Vol. 155, 1969, p. L197.

††Gillett, F.C., and Stein, W.A.: Astrophysics Journal. Vol. 155, 1969, p. L97.

TABLE 6

INFRARED DETECTOR SUMMARY*

Detector and Detecting Mechanism	Wavelength Range (μ)	Noise Equivalent Power (watts)	Size	Temperature (°K)
S-1 PM Tube Photoemissive	0.6-0.9	2×10^{-16}		200
Doped Germanium Inverse Photocond.	0.7-1.7	10^{-16}		4
PbS	1.2-3.5	10^{-14}	$(0.25mm)^2$	78
Hg or Au doped Ge Photoconductive	5-15	$10^{-12} - 10^{-13}$	$(0.25mm)^2$	20
Cu doped Ge** Photoconductive	<26			4
Ga doped Ge** Photoconductive	<120			4
InSb Photoconductive	<2000	10^{-11}	$(1.0cm)^2$	4
Ge Bolometer Thermal	5-20	2×10^{-13}	$(1.0mm)^2$	4
Ge Bolometer Thermal	1000-1500	4×10^{-14}	$(0.25mm)^2$	2
Theoretical Bolometer	<1>,1000	10^{-14}	$(0.25mm)^2$	2
Theoretical Bolometer	<1>,1000	2×10^{-15}	$(0.25mm)^2$	0.9

*Unless otherwise stated, from Low, F.: Infrared Detection. Space Research Directions for the Future. National Academy of Science, Woods Hole, 1965.

**Harwit, Houck, and Fuhrmann : Rocket-Borne Liquid Helium Telescope. Applied Optics. Vol. 8, No. 2, February 1969, p. 475.

wavelength band. In the next few years interest will probably turn to other than the brightest infrared sources as represented in Table 5 , and also to narrower bandwidths than 2 to 20 percent, and an increase in integrating time will be mandatory.

The advantages of satellite infrared astronomy over airplane astronomy at the present time are then:

1) Slightly reduced absorption and background noise, together allowing a gain in signal to noise of perhaps 2 in many but not all observations.

2) Ability to observe very broad sources and make absolute flux measurements (given a telescope cooled to at least 10°K).

3) Longer available observing time.

4) Greater platform stability.

Conclusions

There are two major areas which require substantial development effort before the potential usefulness of orbital infrared astronomy can be realized.

1) Presently available detectors: even when cooled, present day detectors exhibit noise equivalent powers comparable to atmospheric background, and

2) Cryogenic Telescopes: The primary mirror and telescope temperature, if over 10°K, yields a large background comparable in magnitude to the atmospheric background.

Tables 6, 7, 8, and 9 show that in the best cases, the three noise sources, the detector, the telescope, and the atmosphere, contribute equal amounts of background. Furthermore, the sizeable background due to hot telescope is clearly evident in Table 9 .

The interest in infrared astronomy will mount as successes in the shorter wavelengths are achieved. The areas where technology must be developed are clearly identified. A breakthrough in low-noise detectors or imagers, as well as in long-life, cryogenically cooled telescope mirrors and structure must be achieved before significant new information contained in the infrared spectrum will become available. Successes in the development of IR technology in all disciplines should be closely watched, so that new techniques can be applied to benefit astronomy.

TABLE 7

ATMOSPHERIC ABSORPTION*

Ground	Airplane	Balloon	Satellite
(See Table 8 - Atmospheric Windows			
1-15μ windows (20-50% absorption) in 50% of spectrum 90-100% absorption in rest of spectrum.	15% absorption in 90% of spectrum 80% absorption in bands, 10% of spectrum.	5% absorption in 90% of spectrum 30% absorption in bands, 10% of spectrum.	No absorption.
15-1000μ virtually 100% absorption in all of spectrum.	40% absorption in 50% of spectrum. 80% absorption in 30% of spectrum. 100% absorption in remaining 20% of spectrum.	10% absorption in 50% of spectrum. 30% absorption in 30% of spectrum. 100% absorption in remaining 20% of spectrum.	No absorption.

*Turon-Lacarrieu, P., and Verdet, J.P.: Annals d'Astrophysique. Vol. 31, 1968, p. 1.

Kondratiev, K., Nicolsky, G.A., Budinov, I., and Andreev, S.P.: Applied Optics. Vol. 6, 1967, p. 197.

Gates, D.M., Murcray, . ., Shaw, C.C., and Herbold, R.J.: J. Opt. Soc. Amer. Vol. 48, 1958, p. 1016.

Murcray, D.G., Murcray, F.H., and Williams, W.J.: Applied Optics. Vol. 6, 1967, p. 191.

Valley, Shea L., ed.: Handbook of Geophysics and Space Environments. Air Force Cambridge Research Laboratories, United States Air Force, 1965, pp. 3-37.

Kuhn, P.M., Lojko, M.S., and Petersen, E.W.: Nature. Vol. 223, 1969, p. 462.

Allen, C.W., Ed.: Astrophysical Quantities. Athlone Press, London, 1963, p. 125.

TABLE 8

ATMOSPHERIC TRANSMISSION "WINDOWS"

0.3 - 1.1 microns

1.2 - 1.3 microns

1.5 - 1.7 microns

2.0 - 2.5 microns

3.3 - 4.0 microns

4.4 - 4.8 microns

8.0 - 13 microns

22 microns

1000 and up microns

TABLE 9

BACKGROUND FROM TELESCOPE THERMAL EMISSION

		Telescope Temperature	
λ (microns)	0°C (λ_{peak} = 11μ) Background at Detector* (watts/micron)	-80°C (λ_{peak} = 14.8μ) Background at Detector* (watts/micron)	-150°C (λ_{peak} = 23.2μ) Background at Detector* (watts/micron)
2	2×10^{-11}	Negligible	
3		0.72×10^{-11}	
4	1.6×10^{-6}	0.72×10^{-9}	Negligible
5			0.38×10^{-11}
8	0.32×10^{-5}	0.24×10^{-6}	
10		0.44×10^{-6}	0.76×10^{-8}
11	0.4×10^{-5}		
14.8		0.72×10^{-6}	
20	1.8×10^{-6}	0.50×10^{-6}	
23.2			0.76×10^{-7}

*Assuming an emissivity of 0.01 and 1-arc-minute cooled diaphram for an f/10 configuration.

CONSIDERATIONS FOR A MICHELSON INTERFEROMETER EXPERIMENT ON LTEP

Introduction

The basic usefulness of a Michelson Stellar Interferometer lies in the following areas.

1. Measurement of apparent angular diameters of stars.

2. Measurements of brightness distribution, i.e., limb darkening, at various wavelengths across the Red Giants.

3. Search for features, e.g., dark spots or regions of increased brightness, on the surfaces of the Red Giants.

4. Set limits on the shape, i.e., oblateness, of the Red Giants.

5. Search for features on the surfaces of the planets.

6. Set limits on the apparent angular size of the nuclei of Seyfert Galaxies.

7. Set limits on the apparent angular size of quasi-stellar sources, e.g., 3C273B.

8. Measurements of the separation of binaries.

The requirements on a Michelson are dictated, of course, by the task to which it is oriented. In particular, some of the potential applications require large separations of the external mirrors and relatively small light collecting aperture areas. In contrast, other applications require only modest separations but large light collecting apertures. The applications which can be carried out with small apertures afford the possibility of implementation terrestrially. However, the atmosphere places a severe limit on the size of the aperture areas which can be used. $0.1m^2$ is the largest used on the brightest stars. The aperture areas on the proposed large separation terrestrial Michelsons range from $0.01m^2$ to $0.1m^2$. The small apertures limit the domain of usefulness to relatively bright objects.

The foremost advantage of an extra-terrestrial Michelson is the ability to use light-collecting aperture areas limited only by the size of the optics, i.e., the telescope primary, and not by atmospheric considerations. For a 2-m primary used extraterrestrially, the collecting areas of the Michelson can be $0.75m^2$. This number represents an increase in signal by a factor of at least 7.5.

Besides being able to investigate faint objects, a spaceborne Michelson possesses the following advantages:

1. Removal of the atmospheric spectral window so that the interferometer can work in the ultraviolet region below 3000Å and can also work continuously throughout the infrared region to 1.1μ.

2. Elimination of the atmospheric seeing and scintillation which degrade the fringe visibility.

Conclusions

Of the eight potential uses of a Michelson given in the introduction, a spaceborne interferometer of moderate size used in conjunction with a 2-meter telescope primary would be of unique applicability for the implementation of Items 2 through 7. Operating at a wavelength of 5000Å, a 20-meter interferometer can resolve angular diameters of 0.006 arc-second. Since resolutions of 0.01 arc-second are extremely useful for Items 2 through 7, a moderate size denotes an external mirror separation of 10 to 20 meters.

In the calculations which follow, it will be shown that to significantly increase the astronomical data on measured stellar-apparent angular diameters, a 100- to 200- meter external mirror separation is required. Even at these separations, the stars accessible are relatively bright, i.e., brighter than $M_V = +6$ and, therefore, such measurements are feasible with a small aperture, large-separation terrestrial Michelson.

With a resolution of 0.006 to 0.01 arc-second and with the capability of measuring the relative phase and amplitude of the partial coherence function, Items 2,3,4 and 5 can be implemented in orbit. The large collection aperture is the key to establishing the implementation of Items 6 and 7 since the brightness of these objects is less than or equal to $M_V = +13$.

In summary, a 10-to 20-meter Michelson used extra-terrestrially with a 2-meter telescope primary is valuable from the astronomical viewpoint because:

1. It is capable of generating a significant amount of new and useful astronomical data, Items 2 through 7 on page 57.

2. The engineering and instrumentation experience gained on a 10-to 20-meter interferometer serves as a milestone for larger Michelsons which will be of great interest as larger primaries are placed in orbit.

However, since a 10- to 20-meter Michelson is a complex and sizeable instrumentation package whose integration with the LTEP constitutes a major impact on the LTEP concept, it is not recommended to include such a package in the initial flight package. Furthermore, it is quite possible that installation of a 10-to 20-meter Michelson on the LTEP could be affected during a separate piggy-back operation.

The utility of a much smaller Michelson, i.e., 2- to 3-meters, is extremely marginal. It is difficult to justify the expense and effort required for the rather limited new data since the resolution is only slightly above that of the primary.

Calculations and Operation of the Spaceborne Michelson Interferometer

The fundamental principle underlying the operation of the Michelson stellar interferometer is a consequence of the Zernike-vanCittert Theorem.* This theorem gives the complex degree of coherence between two points in an optical field coming from a quasi-monochromatic-incoherent extended source. The theorem states that the degree of partial coherence, $\gamma(x,y)$, between two points, P_1 and P_2, illuminated by an extended, non-coherent source is given by the normalized Fourier transform of the intensity distribution $I_s(\alpha,\beta)$; where $I_s(\alpha,\beta)$ is the source intensity as seen from P_1 and P_2.

$$\gamma(x,y) = \frac{\iint_{\text{source}} I_s(\alpha,\beta)\, e^{ik(\alpha x + \beta y)}\, d\alpha d\beta}{\iint_{\text{source}} I_s(\alpha,\beta)\, d\alpha d\beta} \qquad (1)$$

For a distant star of angular radius $\alpha/2$ and I_s = constant, one gets $\gamma(x) = 2J_1(\pi \times \alpha/\lambda) / (\pi \times \alpha/\lambda)$, where J_1 = Bessel function of first kind. From this relation it is possible to make a plot of $\gamma(x)$. (Figure 25.)

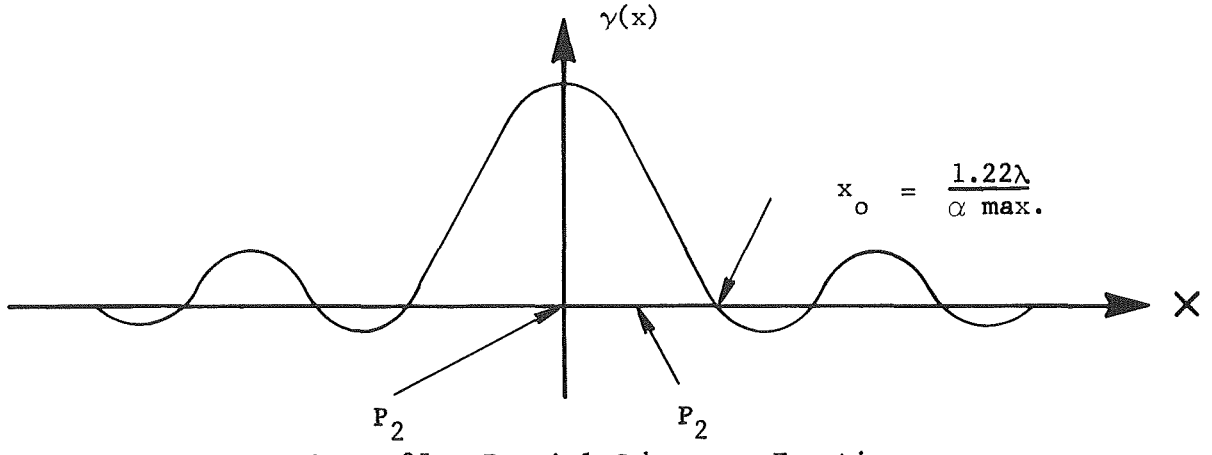

Figure 25. Partial Coherence Function

When the distance between P_1 and P_2 is zero, the degree of coherence is maximum. As P_1 and P_2 become increasingly separated, the degree of coherence decreases and goes to zero at a spacing of $x_0 = 1.22\lambda/\alpha$. It is possible

*Born, M. and Wolf, E: Principles of Optics. Pergamon Press, London, 1959, p. 510, pp. 271-276.

to use this behavior of the degree of coherence, γ, to measure the angular diameter of a distant extended source. To do this, a Young's double slit experiment is set up using light from the distant source. As long as the two slits in the Young's experiment are separated from each other by less than the distance $x_0 = \frac{1.22\lambda}{\alpha_{max}}$, then the Young's fringes will exist and have a visibility directly proportional to the degree of complex coherence, γ, i.e., when the two slits are at zero spacing, the Young's fringes are of maximum visibility. As the spacing of the Young's slits is increased, the visibility decreases and goes to zero when:

$$D = \frac{1.22\lambda_0}{\alpha}, \qquad (1A)$$

where D = spacing of Young slits for zero visibility, λ_0 = effective operating wavelength, and α = angular diameter of star. Since both D and λ_0 are measurable quantities, α can be inferred from the measurement of D which yields zero fringe visibility.

From the relation $x_0 = \frac{1.22\lambda}{\alpha}$, it is clear that the smaller the angular diameter one wishes to measure, the larger x_0 will be. Michelson's Stellar Interferometer is illustrated in Figure 26.

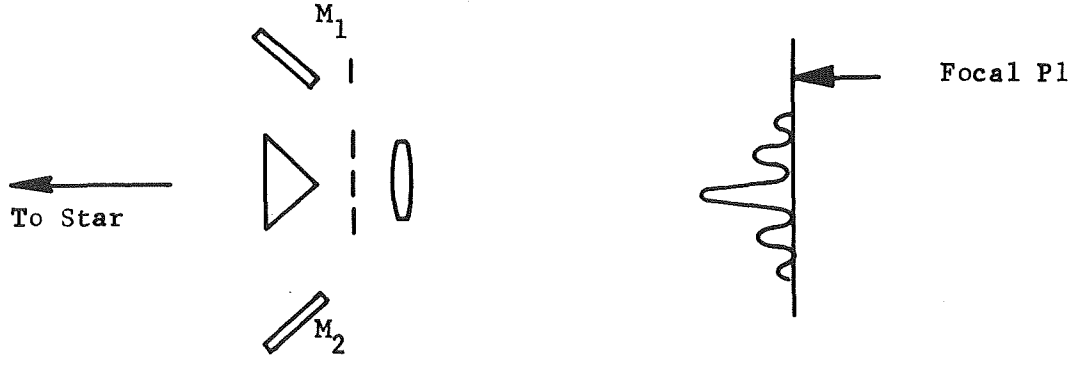

Figure 26. Michelson's Stellar Interferometer

Rather than use the Young slits to measure the spatial extent of coherence from the star, the side mirrors, M_1 and M_2, which feed the Young's double slit setup, are used to probe the extent of spatial coherence. This obviates the need for a large objective, and, of equal importance, it permits independent selection of slit separation so that the Young's fringes are spaced suitably far apart to facilitate their resolution. As one separates the Young's slits, the Young fringes become more closely spaced so that measurement of the fringe visibility is impaired. If $\underline{a}$ denotes the spacing of the Young's slits, then the spacing of the Young's fringes is:

$$\Delta = \lambda/\underline{a}. \tag{2}$$

The Young's fringes are modulated, i.e., have the envelope, dictated by the single slit intensity pattern. The form of the envelope is:

$$[\sin(\pi bx/\lambda)]^2/[\pi bx/\lambda]^2, \tag{3}$$

where b = slit width.

If $\underline{n}$ indicates the number of Young's fringes in the main, central image peak, then

$$\underline{n}\,(\lambda/\underline{a}) = \lambda/\underline{b}, \tag{4}$$

or

$$\underline{b} = \underline{a}/\underline{n} \tag{5}$$

In order to collect as many photons as possible, one would like to have $\underline{b}$ as large as possible. Furthermore, if $\underline{n}$ is too large, i.e., $\underline{b}$ small, (or $\underline{n}$ too small, i.e., $\underline{b}$ large), then ascertaining fringe visibility is difficult. $\underline{n}$ = 5 is a reasonable value. Therefore, one has five Young's fringes in the central image peak, and the area of the Young's slits constitute about 25 percent of the total aperture area. For a 2-meter aperture, this gives about $0.75m^2$; for a 3-meter aperture, the value is $1.8m^2$. These values are to be compared to $0.1m^2$ which is the maximum aperture area used through the atmosphere.

Applications - Apparent Angular Diameters of Stars

A basic application of a Michelson Stellar Interferometer lies in the measurement of apparent angular diameters of single stars.* Other techniques are superior to the Michelson for measuring the separation of binaries. An alternate technique for measuring stellar diameters is the intensity interferometer

*Miller, R.H.: Science 153. 1966. p. 581.

of Brown and Twiss.* Therefore, this discussion will address itself not only to the potential of a large spaceborne Michelson interferometer, but it will also specify the areas of exclusive accessibility by the Michelson as opposed to an intensity interferometer.

The desire to measure apparent angular diameters is very strong because in conjunction with parallax measurements, stellar diameters can be deduced. If a star has a measured angular diameter, α, in arc-seconds, and a parallax, p, then its diameter, D, in solar diameters is:

$$(D/D_0) = 107\ \alpha/p \qquad (6)$$

Knowing both apparent and actual diameters is extremely important for checking mass-luminosity-size-magnitude-spectral-type relations and predictions for stars and predictions for stars and stellar models.

Assuming a star is a sphere emitting as a blackbody with a blackbody temperature, T_{peak}, apparent visual magnitude, M_V, and apparent angular diameter, α, the following relation holds.**

$$M_V = K_1/T_{peak} - 5 \log_{10}\alpha - K_2 \qquad (7)$$

where K_1 and K_2 are constants typically equal to 29400 and 15.25, respectively. Since M_V and T_{peak} are readily accessible, a measurement of α can be a further check on the details of stellar behavior and properties.

Table 10 lists the results obtained with the 6.2m and the 15.2m Michelson interferometers at Mount Wilson.

TABLE 10. MT. WILSON INTERFEROMETER RESULTS

6.2m Michelson Interferometer

Star	Spectrum	Angular Diameter	Visual Magnitude
ε Bootis	K1	0.020 arc-second	0.24
ε Tauri	K5	0.020 arc-second	1.06
α Orionis	M2	0.047 arc-second	0.92
β Pegasi	M2	0.021 arc-second	2.61
α Herculis	M5	0.030 arc-second	
0 Ceti	M6	0.047 arc-second	2.00
δ Scorpii	M1	0.040 arc-second	1.22

*Brown, Hanbury, R.: Annual Reviews of Astronomy and Astrophysics. Vol. 6, 1968, p. 13, (Edited by L. Goldberg).

Brown, Hanbury, R. and Twiss, R.Q.: Proceedings of the Royal Society of Astronomy. 1958, p. 248, pp. 199-221.

**Russell, H.N., Dugan, R.S., Steward, J.O.: Astronomy II. Ginn and Co., 1927, p. 738.

TABLE 10 (Continued)

15.2m Michelson Interferometer

Star	Spectrum	Angular Diameter	Visual Magnitude
β Andromeda	M0	0.0108 arc-second	2.37
α Ceti	M2	0.0115 arc-second	2.82
ν Aquilae	K3	0.0084 arc-second	2.80
ε Pegasi	K2	0.0084 arc-second	2.54
α Orionis	M2	0.0340 arc-second	0.92
α Bootis	K1	0.0190 arc-second	0.24
α Scorpii	M1	0.0290 arc-second	1.23

Table 11 lists the results of measurements of apparent stellar diameter using the Narrabi Observatory intensity interferometer. This list is current through February 1967.

TABLE 11. NARRABI OBSERVATORY INTENSITY INTERFEROMETER RESULTS

Star	Spectrum	Angular Diameter	Visual Magnitude
β Crusis	Bo5	0.000705 arc-second	1.50
γ Orionis	B2	0.000740 arc-second	1.70
ε Canis Majoris	B2	0.000780 arc-second	1.63
α Pavonis	B3	0.000770 arc-second	2.12
ε Orionis	B0	0.000700 arc-second	1.73
α Eridani	B5	0.001086 arc-second	0.60
α Gruis	B5	0.000980 arc-second	2.16
α Leonis	B7	0.001033 arc-second	1.34
β Orionis	B8	0.002074 arc-second	0.34
α Canis Majoris	A1	0.005085 arc-second	-1.58
α Lyrae	A0	0.003310 arc-second	0.14
χ Piscus Austrini	A3	0.001980 arc-second	1.29
α Carinae	F0	0.006480 arc-second	-0.86
α Aquilae	A7	0.002790 arc-second	0.89
α Canis Minoris	F5	0.005310 arc-second	0.48

The results of the 15.2-m Michelson were, in some cases, quite different from those obtained with the 6.2-m interferometer. Much difficulty was encountered in attempting to use the 15.2-m Michelson.

The results from the Narrabi Observatory are quite good. However, since the intensity interferometer is quite insensitive, it can study only stars brighter than $M_V = +3$ and hotter than 4500°K. This conclusion holds true and does not change as one increases the size or spacing of the intensity collectors. Therefore, the domain where the Michelson is of unique importance lies in the measurement of apparent angular diameters for stars of: 1) any spectral type with magnitudes fainter than $M_V = +3$ and 2) all stars in the K or M spectral type.

In order to ascertain the population of stars accessible to measurement with a potentially large orbiting Michelson interferometer, it can be shown that:

$$M_{V\ \text{limit}} = \frac{29400}{T_{peak}} - 5 \log_{10} \frac{2.44\lambda_0 \times 10^5}{D} - 15.25 \qquad (8)$$

T_{peak} is the effective blackbody temperature of the star and is fixed for a given spectral type. λ_0 is the effective operating wavelength of the interferometer. D is the separation of the two outer mirrors of the Michelson. λ_0 and D must be in the same units. Since λ_0 and $\lambda_{peak} = \frac{Rw}{T_{peak}}$ are not necessarily the same, several modes of operation, i.e., $\lambda_{peak} \leq \lambda_0$ or $\lambda_0 \leq \lambda_{peak}$ must be considered. Rw is the constant in Wein's displacement law.

Figure 27 illustrates a representation of Equation (8) giving $M_{v\,limit}$ for various spectral types and interferometer sizes. Clearly, if $\lambda_0 = \lambda_{peak}$ for the ultraviolet region, the resolution of the interferometer is improved and the number of photons available is maximum.

In the infrared region, it may be desirable to keep λ_0 in the visible. The graphs are not corrected for possible spectral variations in quantum efficiency of photo-detectors. The domain accessible to the intensity interferometer is given for comparison.

From Tables 10 and 11, it can be concluded that about 25 apparent stellar diameters are presently known. A survey of The Yale University Observatory Catalog of Bright Stars, 1964 indicates that there are about 480 stars brighter than or equal to $M_V = +6$ in the K and M spectral classes which have measured parallaxes. These include some M-type dwarfs within 10 parsecs. Therefore, it is possible to conclude that a Michelson interferometer with 100- to 200-meter external mirror separation used in orbit can increase the number of measured apparent stellar diameters by a factor of

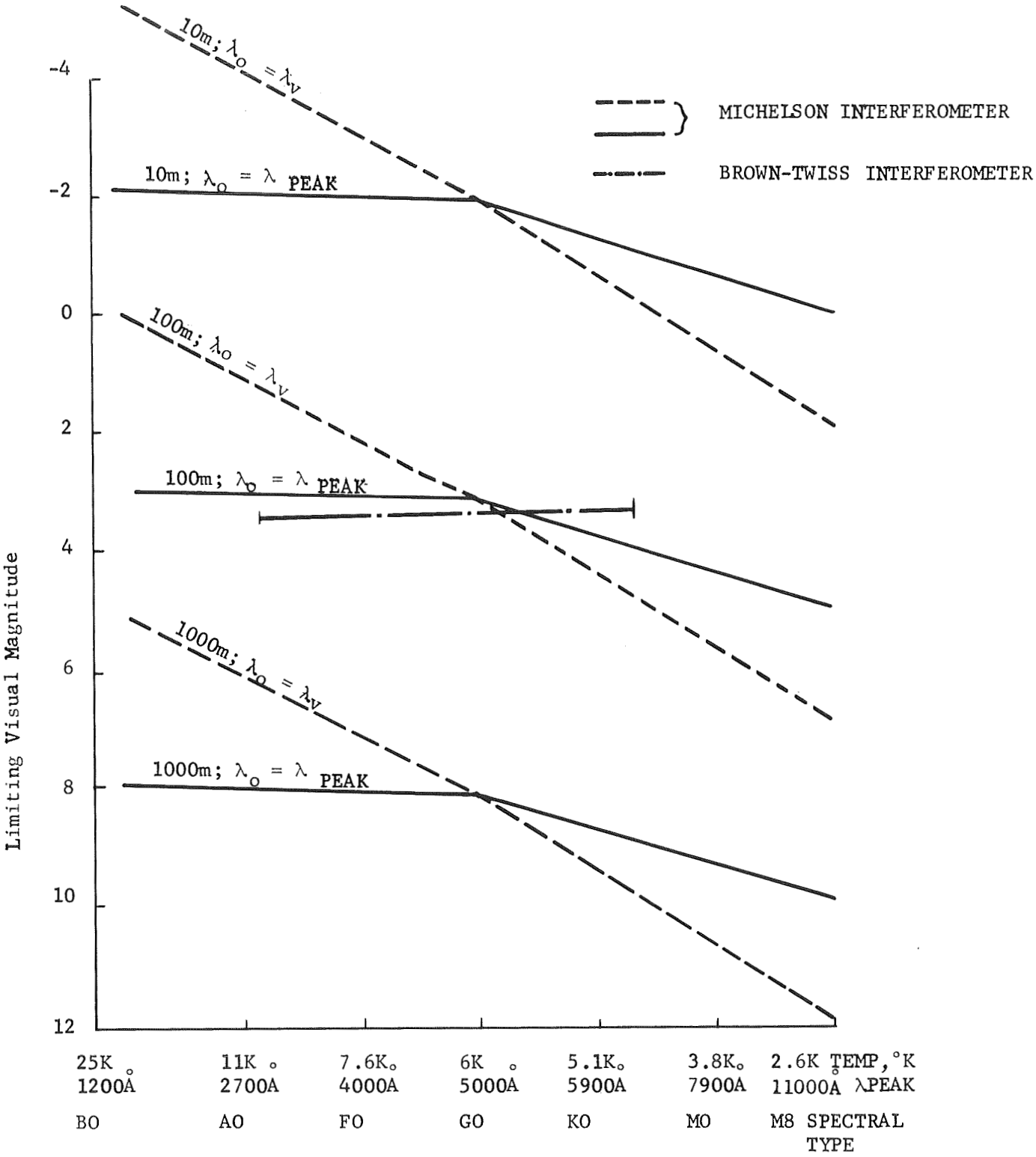

Figure 27. Detectability Curves For Interferometers

about 20. A 10-meter interferometer would be of little, if any, value in providing an increase in astronomical data. A 50-meter size is also of marginal return because the K and M spectral type stars of measured parallax with M_V fainter than +4 exceed those brighter than M_V = +4 by about 10 to 1. The 100- to 200-meter interferometer can reach the K and M spectral types to M_V = +6.

In order to obtain complete information about a general brightness distribution, it is necessary to measure the relative phase of the visibility function, i.e., the partial coherence function. The presence of the atmosphere severely limits the phase measurements.* Above the atmosphere, techniques have been proposed** which are applicable to the determination of the amplitude and relative phase of the visibility function.

Pluto has an apparent angular diameter of about 0.2 arc-sec. This number is quite uncertain because Pluto's apparent visual magnitude, M_V, is +14. The mean density of matter on Pluto is uncertain because of an apparent discrepancy between the presently estimated diameter of 0.2 arc-sec and the mass as determined from celestial mechanics. A firm measurement of Pluto's diameter would contribute significantly either to bracketing the density of matter on Pluto or to giving insight into some presently uncertain factors contributing to its apparent mass.

Since quasi-stellar sources and Seyfert galaxies are quite faint objects, $M_V \approx 14$, terrestrial observations require long exposure so that upper limits on their apparent angular size are only about 1 arc-second. A Michelson with a 10- to 20-m mirror separation used with a 2- to 3-m primary in orbit could improve these upper limits by one or two orders of magnitude.

---

* Beavers, W.I.: Interferometric Investigation of Arcturus. Thesis, Indiana University, 1965.

Elliot, J.: A Stellar Interferometer for Faint Astronomical Objects. Thesis, Massachusetts Institute of Technology, 1965.

** Rogstad, D.H.: 1967 Woodshole Summer Study: Synthetic Apertures. VII, p. 85.

Preliminary Design for Michelson Stellar Interferometers

This section will discuss some of the advantages and problems of such an undertaking and will present an optical design utilizing prisms which significantly relaxes some of the system tolerances. The original Michelson experiment was an impressive accomplishment because of sophisticated optical instrumentation and as a fundamental demonstration of optical coherence theory. An optimist will argue that the original results of Michelson can be easily extended by an orbiting system because of the absence of perturbing atmospheric effects in space. The pessimist will also quite correctly argue that to launch, erect, and operate an instrument of dimensions exceeding 300 feet to sub arc-second accuracy, wavelength tolerances will be exceedingly difficult.

The following discussion will present a system with supporting preliminary calculations which is a viable alternative to the classic configuration for the Michelson interferometer (Figure 28). The technique utilizes the class of prisms which has a constant deviation property. The two prisms which were considered in this analysis are the penta prism and roof penta prism (penta prism with one reflecting surface replaced by a roof prism). Using matrix notation, the requirement of a prism system for the application being considered is

$$\bar{I}_o = \bar{P}_2 \cdot \bar{P}_1 \cdot \bar{I}_i \qquad (1)$$

where $\bar{I}_o$ and $\bar{I}_o$ are 3 vectors representing the direction cosines of the input and output, respectively.

$\bar{P}_1$, $\bar{P}_2$ are the matrix operators for the prisms of Figure 28 .

The Michelson stellar interferometer will have no errors if the prisms P_1 and P_2 have the following property;

$$\bar{P}_2 \cdot \bar{P}_1 = \bar{I} \qquad (2)$$

where $\bar{I}$ is the identity matrix

By calculation one determines that pairs of penta prisms (as in Figure 28) or pairs of roof penta prisms have the property required by Equation (2). However, this property in itself is of no consequence since two properly oriented mirrors of the Michelson stellar interferometer have the same property as Equation (2). The advantages of the prism system are realized when one introduces errors into various elements of the system and then notes the change in system performance.

Before presenting results of this analysis, a cursory discussion of errors for a ground-based Michelson stellar interferometer will be presented.

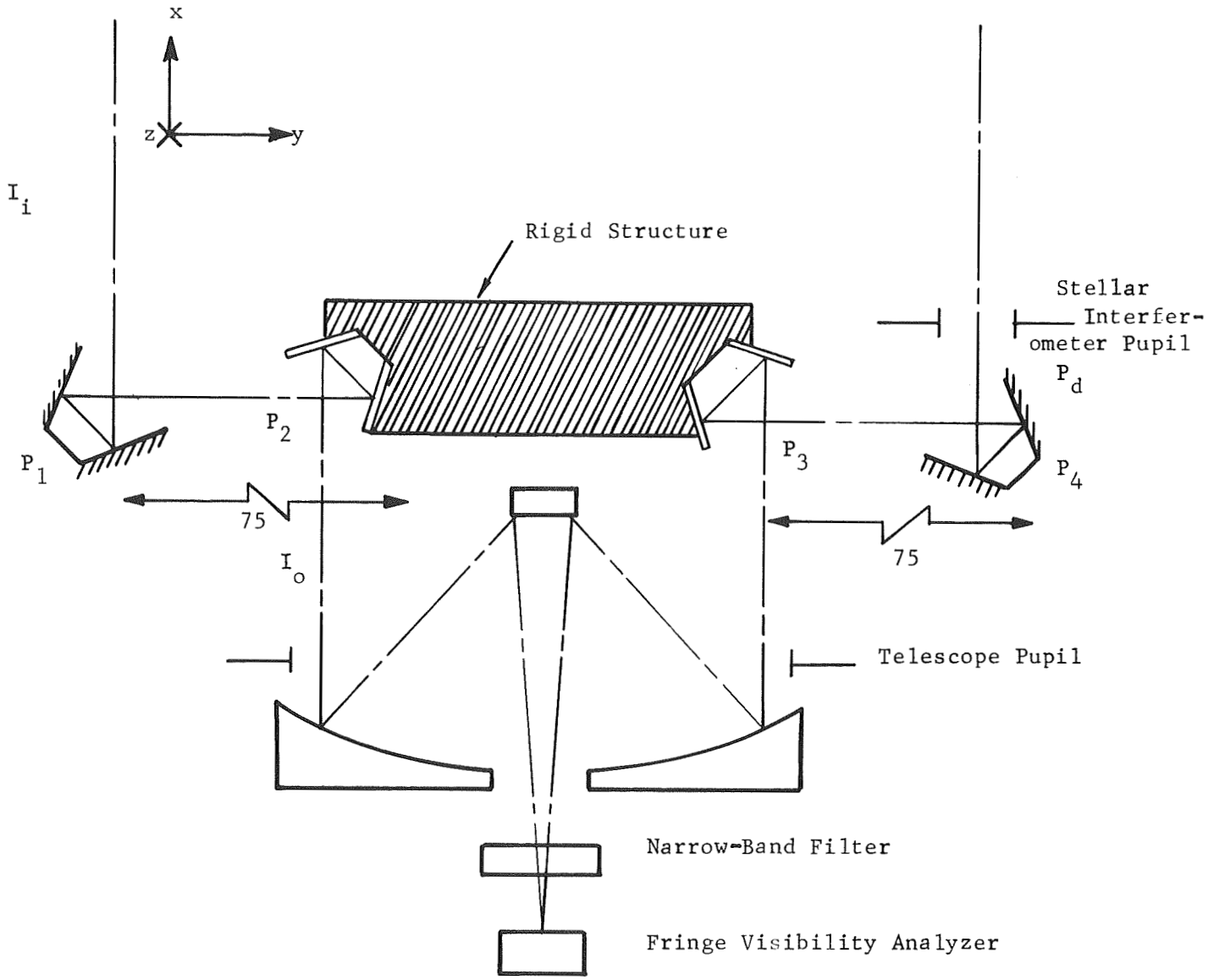

Figure 28. Stellar Interferometer Utilizing Prisms

Atmospheric

The error caused by atmospheric turbulence are classified in the following categories.

a) Amplitude variations (fading)

b) Phase variations (change in effective path length)

c) Angle of arrival

d) Correlation distance which limits the upper diameter of the remote mirror over which the incident light is spatially coherent (typically 10 cm).

The above effects are eliminated by orbiting the instrument and thus will not be considered further.

Polarization

Since the polarization perturbation caused by the atmosphere is on the order of arc-minutes, it is excluded as a source of error from all interference experiments.

Mechanical Disturbances Within Instrument

The problems of both "high" frequency (<1 Hz) vibrations and structural bending and rotation of the elements in Michelson's experiment were circumvented by using a very stiff (and heavy) structure for positioning the remote mirrors. This luxury cannot be accepted in a space mission. Also, it can be inferred from the increased baselines being discussed for orbiting stellar interferometers that a major source of error is expected to result from the displacement and rotation of the remote mirrors.* The compensation of this error is the motivation for developing the design of Figure 28 .

The mirror angular alignment tolerances of the classic Michelson interferometer are a fraction of λ/d, where d is the entrance pupil (typically the diameter of the remote mirror). Linear motion parallel to the optic axis will, in general, introduce vignetting. As will be discussed, the interferometer has the additional constraint that both optical path lengths must be equal to within tens of hundreds of wavelengths. Thus, angular tolerances are on the order of

*Factors such as gravity gradient may introduce significant torques on the structure.

a fraction of an arc-second and linear dimensional tolerances possibly as small as 0.001 inch can be expected.

The discussion of alignment tolerances for the proposed orbiting system requires several assumptions;

1) Each penta prism has no intrinsic errors.

2) Prisms P_2 and P_3 are oriented within rigid structure such that all mirror normals are coplanar.

3) The limiting aperture of P_2 and P_3 is sufficiently large to obviate vignetting.

4) Only errors caused by translation or rotation of remote prisms are significant.

Although realization of these tolerances is by no means trivial, the technique of utilizing prisms has transferred the difficulty of maintaining two mirrors separated by over 100 feet to accuracies of arc-seconds (ground based instrument) to the problem of maintaining alignment of the mirror surfaces of the individual prisms and the alignment of D_2 to D_3 to typically arc-seconds (orbiting instrument).* The resulting trade of increased complexity for relaxed tolerances for the alignment of the remote mirrors (Prisms P_1 and P_4) is thus justified.

The remaining factor to be considered in the system error trade-off is the bandwidth of the narrow band filter. Brown * shows that the fringe visibility is increased for the case when small errors exist between the path lengths of the two interferometer "arms". For example, an optical bandwidth of 1000Å (Figure 28) requires that the total optical path lengths through the two arms of the instrument may not vary more than 1 or 2 waves. This is increased to over 1,000 waves if a 1Å narrow-band filter is utilized. This is feasible, however, since the development of the solid spacer Fabry-Perot filters (which were fabricated for the ATM Hydrogen-Alpha Telescope).

Conclusion

A complete error analysis including both fabrication errors of the individual prisms and structural errors is required to verify the system design. Assuming positive results from this analysis, the proposed technique provides an auxilliary experiment which will provide significant new data on stellar diameters with an acceptable change in the basic LTEP hardware.

---

*Preliminary analysis of a similar optical system (Perkin-Elmer Engineering Report No. 8949) verifies this conclusion.

Brown, R.H.: Annual Review of Astronomy and Astrophysics. Annual Reviews, Inc., Palo Alto, Calif. 1968.

CHAPTER 4 - LTEP TELESCOPE OPTICAL SYSTEM

DIFFRACTION - LIMITED SPACE TELESCOPES

A 2-meter, diffraction-limited, spaceborne telescope will be capable of resolving detail between 10 and 50 times finer than that obtainable from earth. No one can guess the extent or the nature of the knowledge that will be gained from such a close-up, sparkling view of the universe but it is certainly one of the most exciting possibilities that the space program has to offer mankind.

The 10- to 50-fold increase in resolution comes about partially because diffraction rather than atmospheric turbulence limits seeing in space and also because the shorter ultraviolet wavelengths accessible in space diffract less, thus forming images with finer detail. There is a wide variety of tasks for which a 2-meter, diffraction-limited telescope might be used. They include spectroscopy, polarimetry, metrology, interferometry, and many others, but as long as the 2-meter telescope remains the largest spaceborne instrument, its primary goal will almost certainly be imagery. When larger spaceborne telescopes become available, then the role of the 2-meter instrument can be expected to evolve into one of the astronomical specialties, such as, perhaps, spectroscopy.

Along with the great potential benefits of a large spaceborne telescope come a host of difficult technical problems. Foremost among these is the problem of making, testing, launching, and finally operating in space a primary mirror with a figure accurate to one part in 10^8. Even if a perfect mirror were to be placed in orbit and somehow be completely isolated from thermal inhomogeneities, its optical performance could be severely affected by spontaneous relaxation of internal stresses accelerated by radiation effects. Until a mirror this size is placed in orbit, it is impractical to determine the type or degree of degradation, but it is possible, by means of a figure sensing and control system, to continuously adapt to structural changes, thus achieving a high degree of immunity to figure degradation, whatever the cause.

The second most serious problem besetting a large telescope is that of pointing with a stability sufficient to prevent the blurring of the finest detail. For the 2-meter telescope this amounts to holding 1/100-arc-second stability for half an orbital period. Third, it is no simple task to develop a telescope that is sufficiently near perfection that diffraction rather than aberrations or optical imperfections limits the performance. Good optical systems are not simply based on computer-optimized optical designs although computer designs that take into account practical realities such as tolerances, and optical fabrication and testing difficulties are prime requisites.

A substantial portion of the technology necessary to achieve a diffraction-limited space telescope has already been employed on the 36-inch-diameter, balloon-borne, Stratoscope telescope of Princeton. The Stratoscope primary mirror was figured to $\lambda/50$ rms and thus paved the way for other large, diffraction-limited optical systems. Similarly, the stabilization techniques that

would be used on a satellite telescope are essentially the same as those that have been proven capable of stabilizing the field of view of Stratoscope to within $\lambda/50$ arc-sec rms. The decision to use a servo mechanism for maintaining the alignment of the optical system on Stratoscope, has proven to be sound and now every spaceborne optical system is active to some degree. The extension of active control to the figure of the primary mirror is not without precedent, but rather is a natural extension of the techniques developed on Project Stratoscope to maintain diffraction-limited imagery. This approach is inherent in the LTEP.

The evolution of a spaceborne telescope was taken one step further during the Princeton Advanced Satellite Study (NASA-NGR-31-001-044). This study resulted in a 1-meter telescope that could be fitted within the limited geometry of an OAO satellite package to yield diffraction-limited imagery and high-resolution spectroscopy in the 1000Å to 3000Å spectral region. This amounts to shrinking the length of the Stratoscope telescope by a factor of three while at the same time increasing the aperture from 36 inches to 1 meter and adding a spectroscopic capability. A high degree of reliability was planned by using two image tubes, either of which could be used for imagery or spectroscopy, and also by using redundant phototubes in the pointing system.

The key optical features originated in the Princton Advanced Satellite that impact on the LTEP Design Concept are:

- A very short Cassegrain telescope having refractive corrector elements to produce a sufficiently large well-corrected field for finding at least two guide stars suitable for guidance.

- A hole through the refractive corrector elements, which passes the central field, therefore is not spectrally limited and is of prime interest for imagery or spectroscopy in the far ultraviolet region.

- Two very compact optical relay systems that fit between the last telescope corrector and the focal plane and allow two guide stars in arbitrary positions in the telescope field to be positioned at fixed locations close to the central field. These are called "Image Movers" or "Guide Star Positioners".

- A two-element, all reflective, off-axis microscope capable of reimaging the small central image field as well as the guide star images on either image tube and its associated image dividers.

- An echelle spectrograph capable of producing a folded spectrum on either image tube, thus permitting a large spectral range to be integrated and read out in a single step.

Taken together these features result in an extremely useful, compact astronomical instrument that undoubtedly will be closely related to the large-aperture imaging telescopes in the coming generation. Thus, the baseline design for the LTEP configuration, is a scaled-up version of the Princeton Advanced Satellite Experiment Package which has been modified for other astronomical observations.

APERTURE SELECTION

Larger apertures collect more light and, providing the optics can be made diffraction-limited, provide greater resolution. The only rationale for the selection of an aperture size is, therefore, to use the largest possible aperture within the economics or physical bounds imposed on the telescope. For the LTEP experiment package, the economical and physical bounds are the ATM gimbals and LM rack. These limit the aperture size to 2 meters, a rather modest size with respect to some of the larger ground-based telescopes, but, in fact, a daring and exciting step for space astronomy. For example, at 2000Å, the theoretical resolution of a 2-meter telescope is 1/50 arc-seconds. This is a factor of 50 greater than the resolution for a ground-based telescope even when the seeing is good, and is even beyond the limits of the Stratoscope telescope by a factor of 5, since the upper atmosphere still limits the uv spectral region from balloon-borne telescopes.

THE PRIMARY MIRROR

Surely one of the soundest technical predictions that can be made in this age is that astronomers will always need larger apertures and greater resolution. The 2-meter telescope will inevitably be followed by a 3- or a 5-meter telescope which, in turn, will be succeeded by still larger telescopes until perhaps economics and advancing technology permit very large space telescopes to be fabricated in situ. Fairly early in this progression, the size of the telescope aperture will exceed the maximum allowable payload diameter* and it will be necessary to assemble the primary mirror out of a number of pieces carefully nested together to survive the rigors of launch. At this stage, segmented mirrors and "active" optical systems will be a vital necessity. The evolution of this technology might start with the addition of a few actuators to a small monolithic mirror to correct for any astigmatism. It might proceed to a very thin, medium-sized primary having an array of actuators on the back and then to an array of segments launched in their correct relative positions but requiring small adjustments prior to use, and finally culminate in the very large primary mirror that is launched as a group of nested elements. Of course, there are many other development paths, and the choice depends upon how technology and astronomy are apportioned at each step and also on the relative technical difficulties. For example, the 2-meter LTEP mirror could be either a single monolithnic mirror that is bent into shape

*For example, even the new Space Shuttle is limited to 15 feet in diameter.

by an array of actuators behind it, or an array of seven hexagonally shaped mirrors each of which is optimally aligned by three actuators. Only three actuators are required since the other three degrees of freedom can be taken care of by mechanical restraints that locate the segment within about ±0.005 inch of its nominal position. Both approaches involve a comparable number of actuators and offer a substantial technological gain and improvement in figure compared to what might be expected from a single monolithic mirror. Furthermore, monolithic segmented or flex mirrors must be fabricated with new techniques.

Distortion due to stress relief can be minimized to some extent by the use of carefully annealed glasses selected for very low residual stress. Advances in the state-of-the art may make it possible to figure segments separately or to fabricate and test a thin mirror without first making a thick mirror. Clearly in making any choice between monolithic, thin or segmented mirror approaches, environmental, fabrication, and testing problems must be considered. The monolithic and thin mirrors require no ambiguity sensors, and even without active control would function as a light bucket. For reliability, the deformable mirror approach offers technical advantages over monolithic. The actuators in a deformable mirror do have the capability of partially compensating for a failure of a neighboring actuator since there is a force interaction between adjacent actuators.

STRUCTURAL DEVELOPMENT

In comparison to the exotic possibilities afforded by active interferometric sensing and figure correction in an astronomical telescope, the problems of structural design seem mundane. However, if the structural design is not carefully attuned to the strengths and weaknesses of the active optics approach, many of the advantages can then be lost through a pedestrian, inefficient structural design. The active telescope concept permits a much different basis for the structural design, emphasizing load carrying capability (through the launch phase) rather than rigidity as in the conventional approach. More conventional materials such as aluminum can be used for the structure since absolute stability is no longer a prerequisite.

The most important part of the telescope structure is the primary mirror cell. The telescope tube and the scientific instruments will be coupled to the mirror cell and the center of gravity of the telescope will therefore be very close to the primary mirror. For this reason, the structural connections for launch caging will also be made to the primary mirror cell.

Launch and boost conditions are the primary factors governing the design of the primary mirror cell. These conditions are, for the Saturn Work Shop launch environment: 6.0g longitudinal steady-state acceleration, 2.0g

lateral steady-state acceleration, with the vibratory conditions described by NASA/MSFC document 50M02408 superimposed. The maximum acceleration under this set of conditions would be 7.0g. Thus, the main structural members of the primary cell, for example, would be designed to support loads in the neighborhood of 23,000 pounds. This is based on a mirror weight including actuators of 1400 pounds, experiment weights totalling 1000 pounds, electronics weight of 200 pounds, and structure weight of 500 pounds, for a total weight of approximately 3300 pounds. To these loads must be added the necessary structural safety factors and any vibration magnification factors.

Figure 29 shows a concept for the primary cell structure. The basic load-carrying member is a ring with rectangular cross section. The closed cross section is chosen to optimize the rigidity of the ring. The ring cross section is 12 inches deep and 5 inches wide, and has wall thickness of 1/4 inch. As shown in Figure 29 , the backing plate for the mirror extends across the midplane of the basic ring structure. The backing plate is stiffened by webbing that extends between the mirror segments. These stiffening webs are carried through the experiment instrument compartments, forming closed cells of high rigidity. The overall telescope configuration is shown in Figure 30.

An important aspect of the mirror cell design is the method for vibration isolation (if any) or of designing for survival if there is no vibration isolation. From the standpoint of simplicity, a configuration that would permit caging of the entire telescope system during launch on damper struts (similar to aircraft landing gear) is attractive. A sway space of only ±0.5 inch would permit attenuation of frequencies above approximately seven cycles per second. This would permit rejection of a great portion of the vibration spectrum, as shown in Figure 31.

If this is not feasible (which can only be determined in conjunction with NASA), the local vibration magnification factors for the mirror structure must be computed, which is a difficult process. Once the local load factors are known, the strength of the structure can be increased as required. In the case of glass components, this cannot be done, of course. In those instances when the material properties and function cannot accommodate an increase in strength to withstand the local vibration environment, a vibration isolation scheme will be necessary. If individual isolators are required, then mechanisms to disconnect the isolators and optically align the component in orbit will also be required. It is this complication that vibration isolation of the entire package would avoid.

In Volume II of this study, Lockheed has explored in detail many of the features of the telescope mechanical configuration, including the means for erecting the telescope tube. The reader is referred to this section of the report for the details of the configuration.

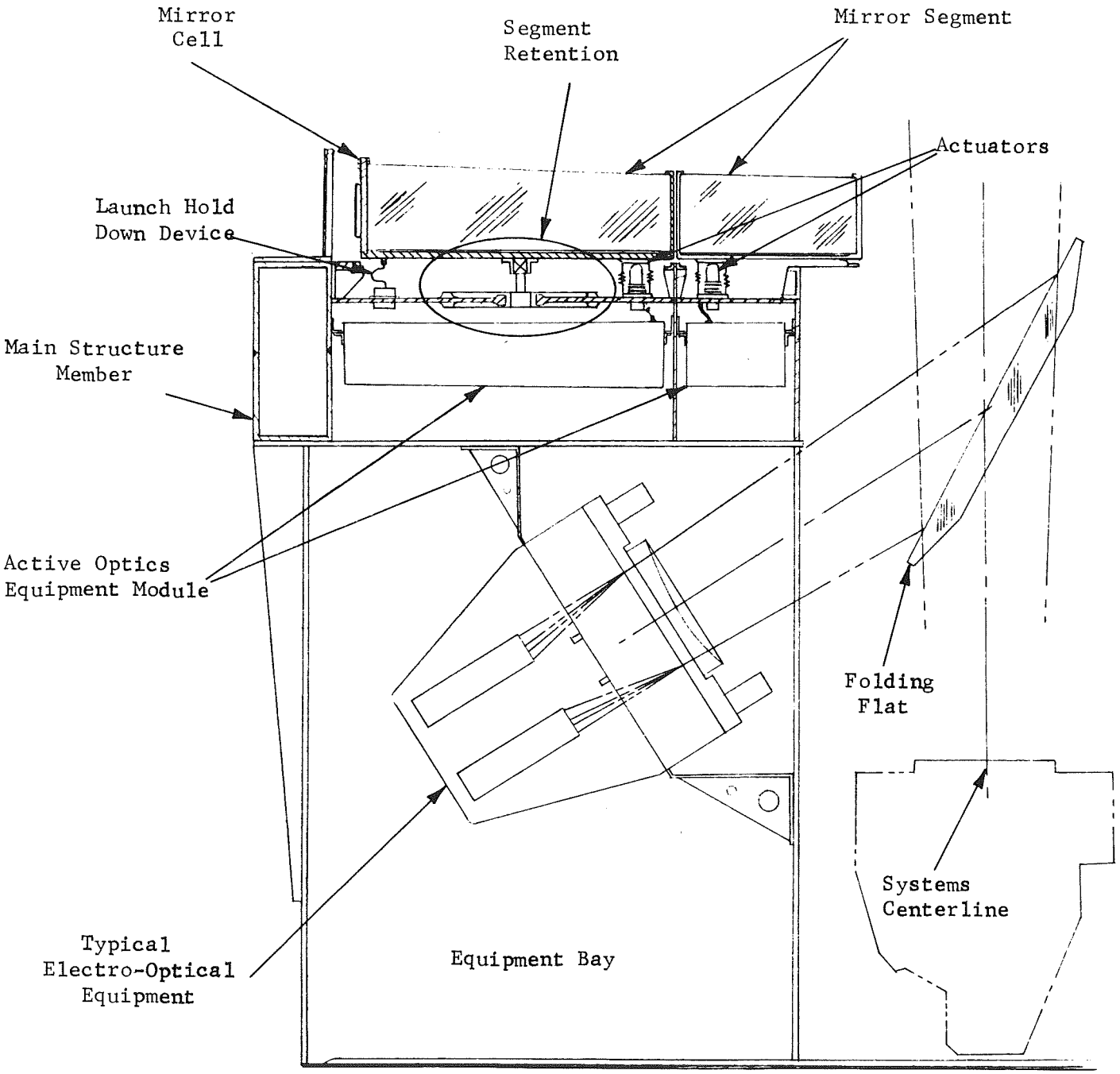

Figure 29. Cross Section through Primary Mirror Cell

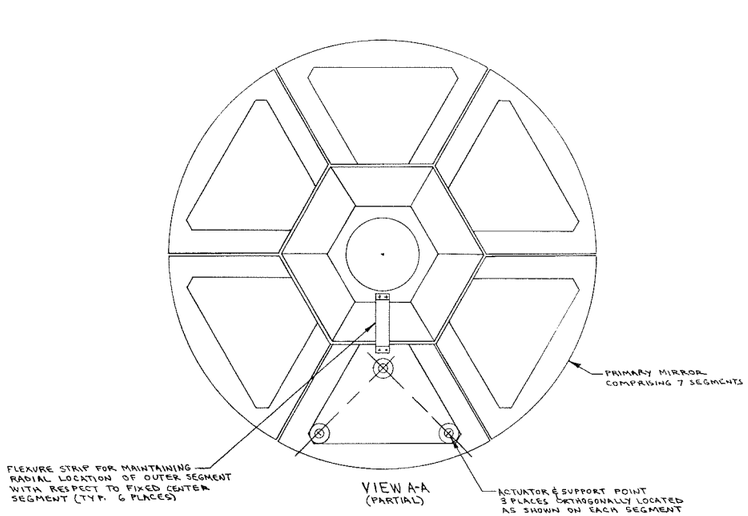

VIEW A-A
(PARTIAL)

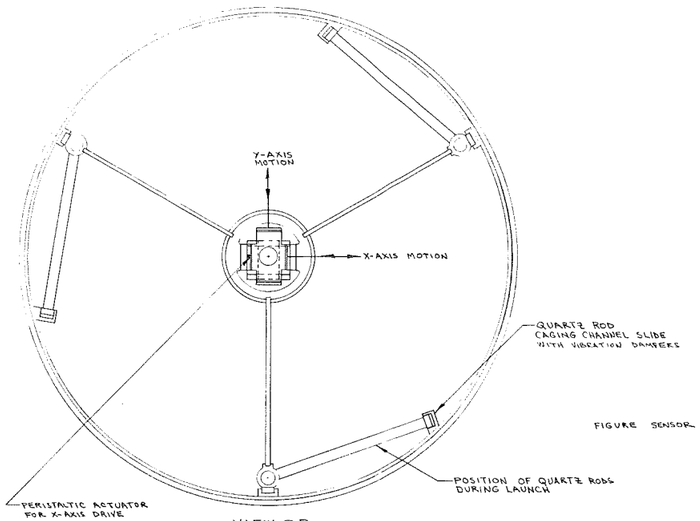

VIEW B-B
(PARTIAL)

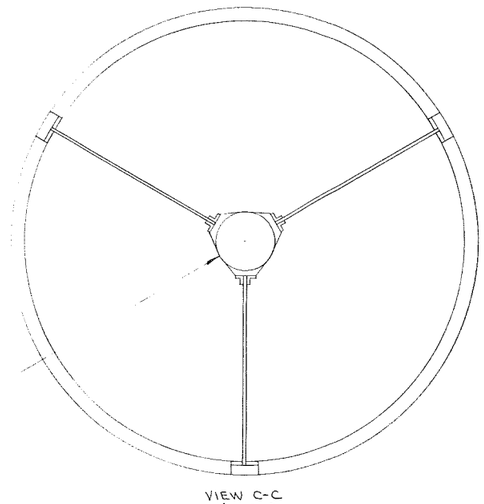

VIEW C-C
(PARTIAL)

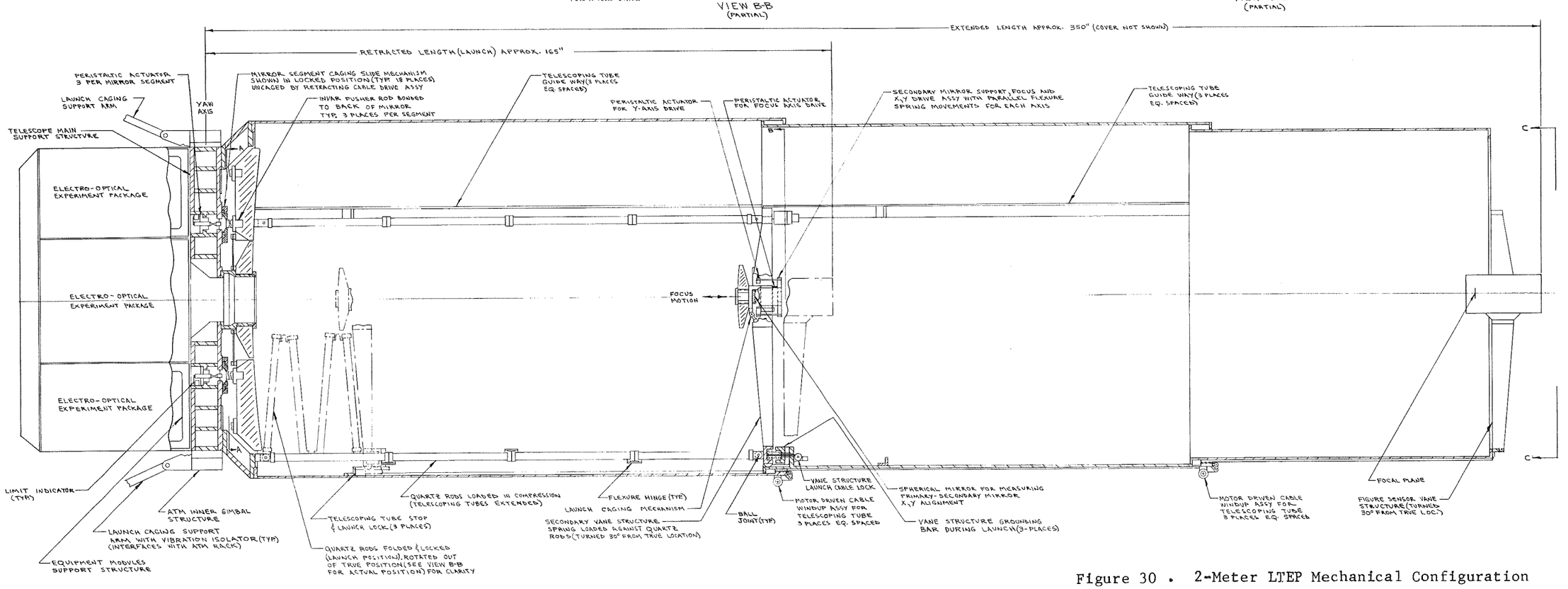

Figure 30 . 2-Meter LTEP Mechanical Configuration

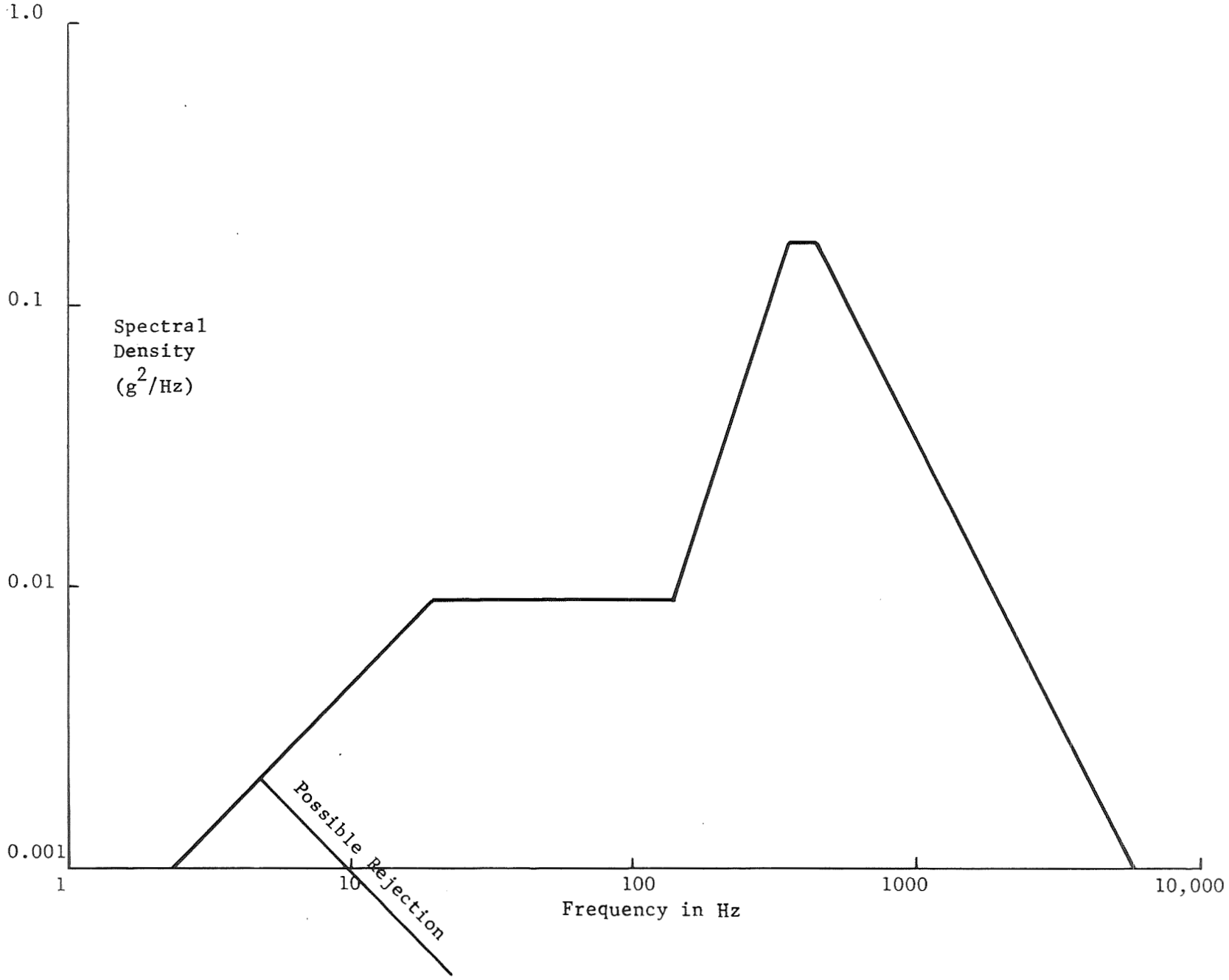

Figure 31. High Level Random Vibration Criteria Test Curve

The optical parameters used in the development of the LTEP optical design are listed in Table 12.

TABLE 12.

LTEP OPTICAL PARAMETERS

Telescope	
Type	f/10 Ritchey-Chrétian Cassegrain
Primary f/number	f/2
Secondary Magnification	5
Obscuration Ratio	0.2
Uncorrected Field	5-arc-minutes diameter
Uncorrected Focal Length	20 meters.
Telescope Corrector	
Number of elements	4
Magnification	1.12
Corrected Field	30-arc-minutes diameter
Image Mover	
Number of elements	6
Acceptance Cone	f/3.9
Useful Instantaneous Field	2-arc-minutes
5X Microscope	
Type	Off-axis, All reflective, 2-element
Magnification	5
Acceptance Cone	f/3.725
Image Field Position	1 inch off-axis
Guide Star Field Position	1.28 inches off-axis
Image Field	52.2 seconds diam on a 1-inch diam vidicon

OPTICAL CONFIGURATION

The essential components of the LTEP experiment are a Cassegrain telescope having a rotatable flat near the focal plane, and seven hexagonally shaped experiment packages grouped behind the primary mirror. Six of the experiment packages can be optically linked to the telescope by indexing the folding flat about the optical axis, and the seventh experiment package, which is in the center of the cluster, is accessed by flipping the folding flat out of the optical path. Each of the seven experiment packages contains a fine pointing error sensor, an optical instrument (microscope, spectrograph, etc.), and a data transducer such as an image tube or phototube. For diffraction-limited imaging it is essential that the telescope field be stabilized by boresighting on two guide stars within the telescope field. For spectroscopy it is sometimes possible to use the same star as is used for pointing.

A Cassegrain telescope arrangement was selected for the LTEP configuration primarily because this arrangement provides a maximum amount of room for the experiment packages. In addition, the Cassegrain has a small obscuration ratio and provides a conveniently large f-number for guidance or image relay systems. By using a Ritchey-Chretien modification of the Cassegrain, it is possible to obtain a diffraction-limited image field of about 5 arc-minutes in diameter. This is substantially larger than can be handled with present image tubes but is too small by a factor of 6 if two guide stars of sufficient brightness are to be found in the field of view when the telescope is oriented toward the poles of the galaxy. Figure 32 shows a refractive corrector system added to the telescope to yield a well-corrected, 30-arc-minute guidance field. A hole through each of the refractive corrector elements passes the small useful central field of the telescope so that the far ultraviolet portion of the spectrum is available in this field. This optical arrangement is utilized for the imagery experiments which require diffraction-limited stabilization for the study of far ultraviolet sources. The 6-inch space between the last corrector element and the focal plane is sufficient for two small optical relay systems which can be oriented so that the two guide stars in the telescope field appear to be located in two fixed positions on either side of and close to the central image field. This greatly reduces the space required for pointing sensing and also permits the pointing and imaging systems to share the same microscope. Thus, any displacement of a microscope component during an exposure results in an error detected by the guidance system which is nulled. Since the pointing star relay systems are not common to both pointing and image trains, any motion of the component parts of these systems produces image blur. Careful design of these components is therefore extremely important.

The lower experiment shown in Figure 32 is the f/50 image system which, being all-reflective, is capable of imaging the far ultraviolet region. The upper experiment is for f/10 film imaging in the visible and near ultraviolet region. In this case, an all-reflective path is not warranted and the telescope corrector elements pass both pointing and imaging beams.

LTEP OPTICAL DESIGN

Telescope and Pierced Corrector

A Ritchey-Chretien telescope was selected for the LTEP mission after comparison with alternative systems such as the Baker three-mirror telescope. In general, the Cassegrain has few reflections, a small obscuration, a conveniently large f-number, and a configuration that permits a large multi-purpose instrument package. Unlike the Baker system, the Cassegrain does not have a large well-corrected field. The minimum acceptable field size is determined by the probability of finding at least two guide stars of sufficient brightness sufficiently close to an arbitrary image field that they may be used for pointing. For a 2-meter aperture telescope operating on 12th and lower magnitude pointing stars, a pointing field between 20 and 30 arc-minutes in diameter is required. This is a rather large field for a 2-meter, diffraction-limited telescope, especially if it has to have a fast, f/2 primary in order to keep the overall length within bounds. Without the refractive elements the primary-secondary combination is free of spherical aberration and coma but is limited by field curvature and astigmatism. Using the Rayleigh quarter wavelength tolerance criterion and a wavelength of 0.5 micron, the uncorrected field is about 5.5 arc-minutes in diameter. This is increased to 30 arc-minutes in diameter by a four-element refractive corrector array positioned a short distance in front of the focal plane. The corrector details are shown in Figure 33.

Ordinarily, the addition of refractive components places narrow bounds on the spectral range of a telescope, but this can be avoided by cutting a hole through the center of each of the corrector elements so that the center portion of the telescope field, used for imaging or spectroscopy, remains all-reflective, and the outer portion of the telescope field, used for pointing, and for some of the imaging systems contains the refractive components.

A well-corrected Ritchey-Chretien telescope might typically have an image size of about 1 arc-second at the edge of a 1/2-degree field. This is adequate for earth-based astronomy, but is too large by a factor of 20 for diffraction-limited imagery in a 2-meter aperture spaceborne telescope. Since the guidance error is directly proportional to the image size, a 1-arc-second image size would be prohibitive on any but the brightest stars of which there are too few. Previous optical design on a similar optical system* had indicated that very significant improvements could be obtained on the field performance of the Ritchey-Chretien design. Continuation of this work on an appropriately scaled system finally led to a four-element corrector design which is close to diffraction-limited out to the edge of a 30-minute diameter field.

The large well corrected field yielded by this corrector design is particularly remarkable since the position of the refractive elements in the design were constrained to places between the present position of the first and last

*Wissinger, A.B.: Advanced Princeton Satellite Study. Perkin-Elmer Engineering Report No. 8688, June 1967.

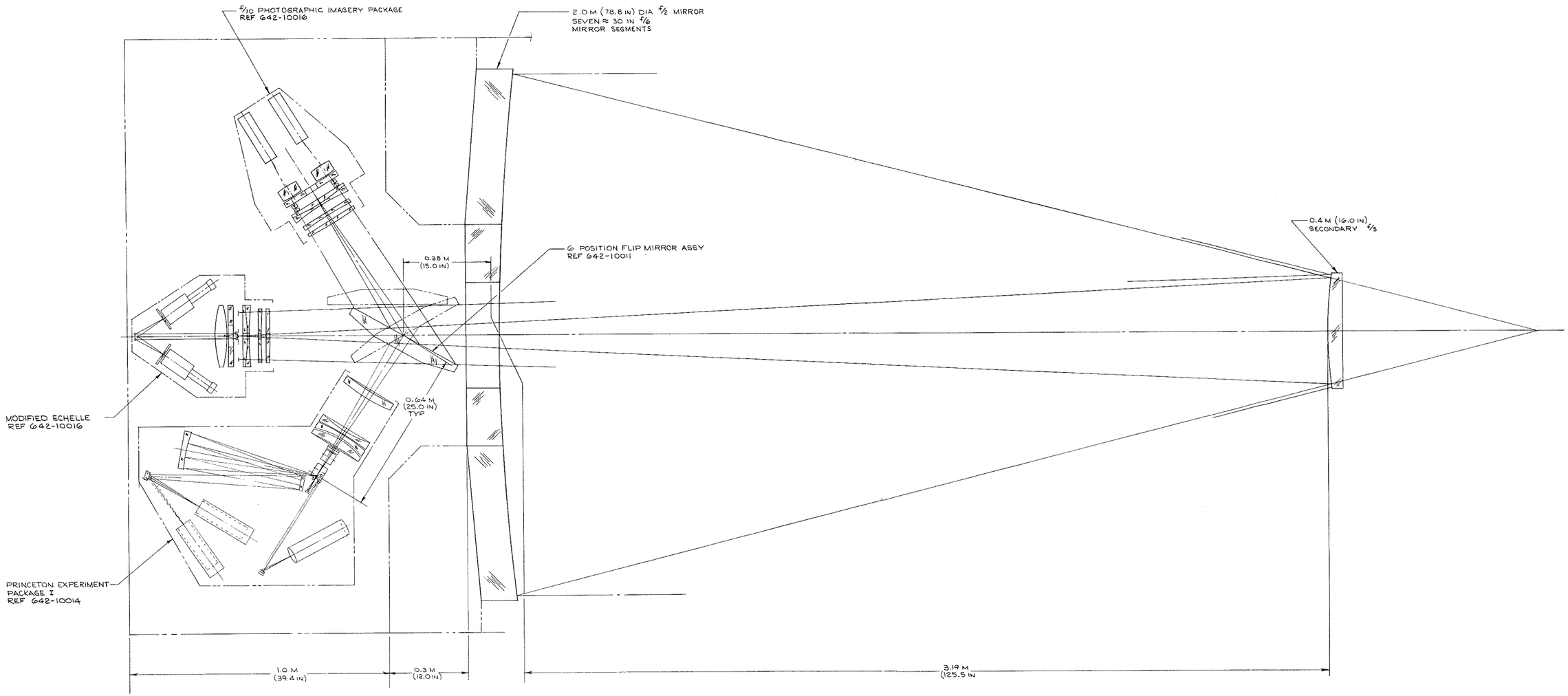

Figure 32 . LTEP 2-Meter Telescope Optical Schematic

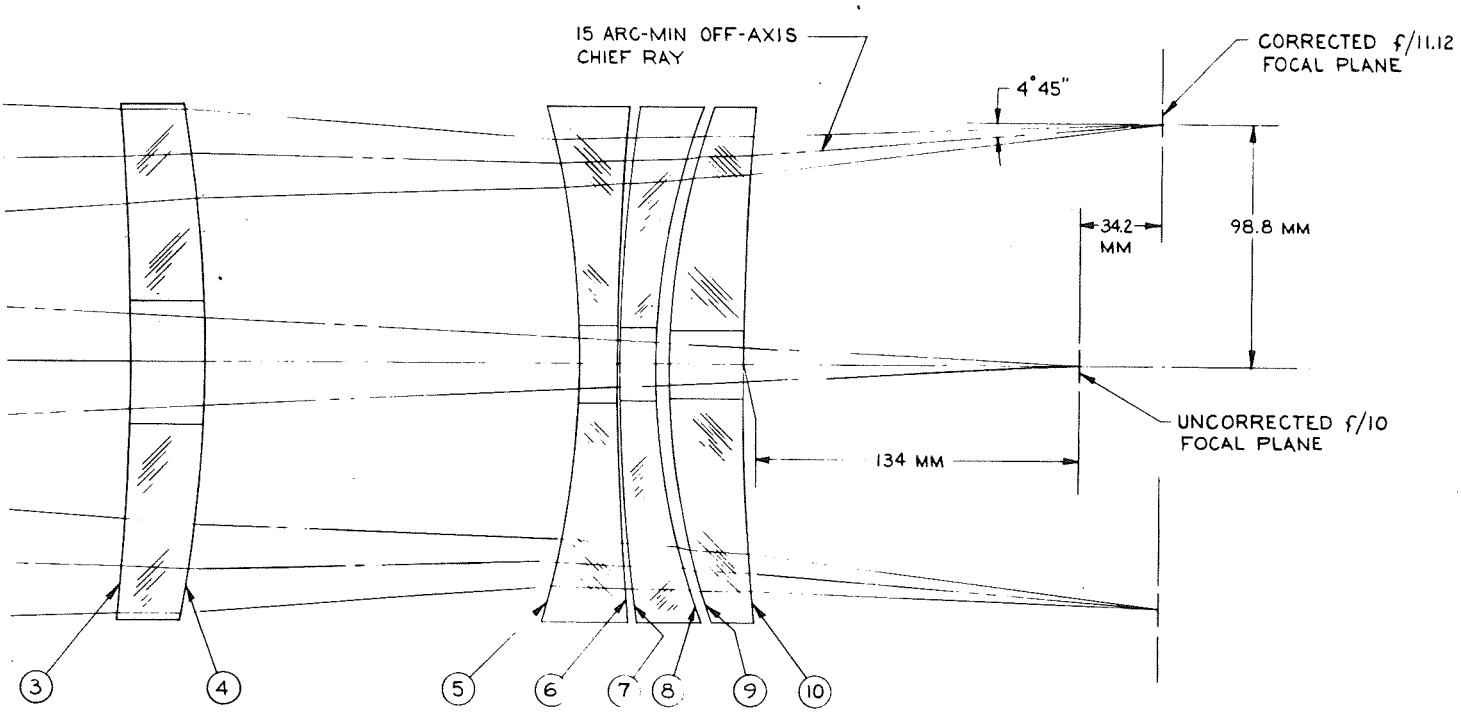

Figure 33. Telescope Corrector Details

element; and the exit pupil was limited so that the chief ray at the edge of the field did not exceed the 4 degrees - 45 minutes shown in Figure 33 . The reason for these constraints, which undoubtedly limit the degree of correction, is that they have a very beneficial effect on the remainder of the optical system and therefore on the complete system. For example, the space between the last corrector element and the uncorrected f/10 focal plane is used by the image movers which position the two guide stars in the fixed field of the pointing system. The space between the first corrector element and the focal plane is kept short to keep the transition between the corrected and uncorrected fields small and also to avoid mechanical interference with the flip mirror. One of the properties of the image movers is that they move the apparent position of the stellar image without affecting the angle between the chief ray and the optical axis. This angle must therefore be incorporated into the f-number or the field coverage of the microscope and has a marked effect on the microscope performance.

Figure 34 shows the results of an exact geometrical ray trace through the Ritchey-Chretien telescope and corrector. The meridional and skew ray fans used in the ray trace are illustrated schematically in Figure 35 . The field angle is assumed to lie in the y-z plane and is defined as the angle between the optical axis and an incoming chief ray which passes through the center of the entrance aperture. In most astronomical telescopes (the Schmidt being an obvious exception) the primary mirror acts as the entrance aperture. The aberrations are calculated by subtracting the focal plane coordinates of the chief ray $\bar{x}_k$, $\bar{y}_k$ from the coordinates of a skew or meridional ray. Since meridional rays are confined to the y-z plane by definition, the aberrations of these rays are given by $\bar{y}_k - \bar{y}_k$. In general, the coordinates of skew rays differ from those of the chief ray in both x and y directions. However, the x-direction aberration usually predominates and since $\bar{x}_k$ equals zero, the skew ray aberrations are described approximately by x_k. The skew fan plots cover only half of the aperture since the aberrations are symmetrical across the aperture. The aberrations of colors on either side of the central 4861A color for which the system is corrected are also shown in Figure 34 . In this case, the chief ray is defined from the central color only and the central rays for the other colors do not pass through zero because of chromatic aberrations.

There are several ways of assessing image quality. One of the simplest is to compare the geometrical image size with the diffraction image size. At 0.5 micron wavelength the latter is about 6.8 microns radius or 13.6 microns diameter at the first diffraction-limited dark-ring. This compares favorably with a geometrical image size of 12 microns at 10.2 arc-minutes off-axis and less favorably with an image size of about 20 microns at 15 arc-minutes off-axis. The comparison depends on the focal plane chosen and could be altered so that the image size at both off-axis positions were equal to 15 microns.

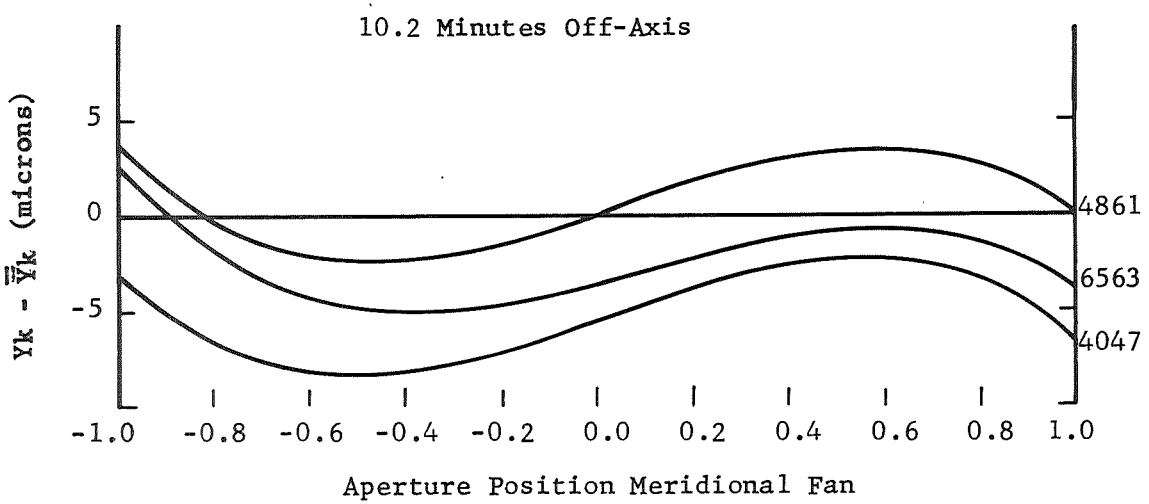

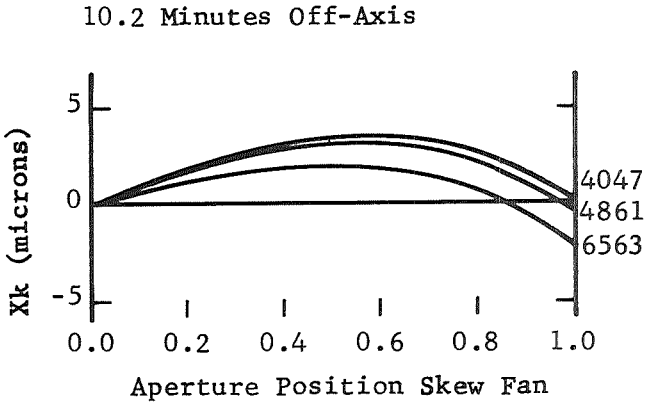

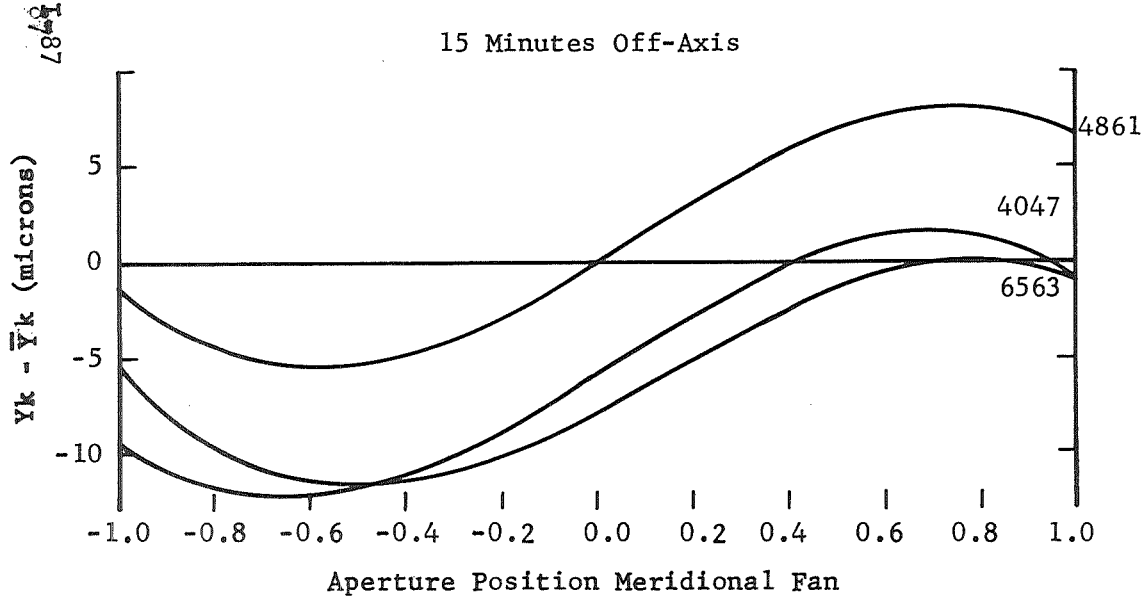

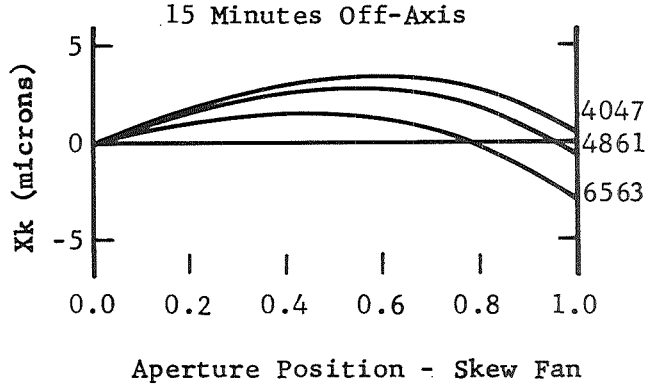

Figure 34. 2 Meter Telescope
Geometrical Image Size

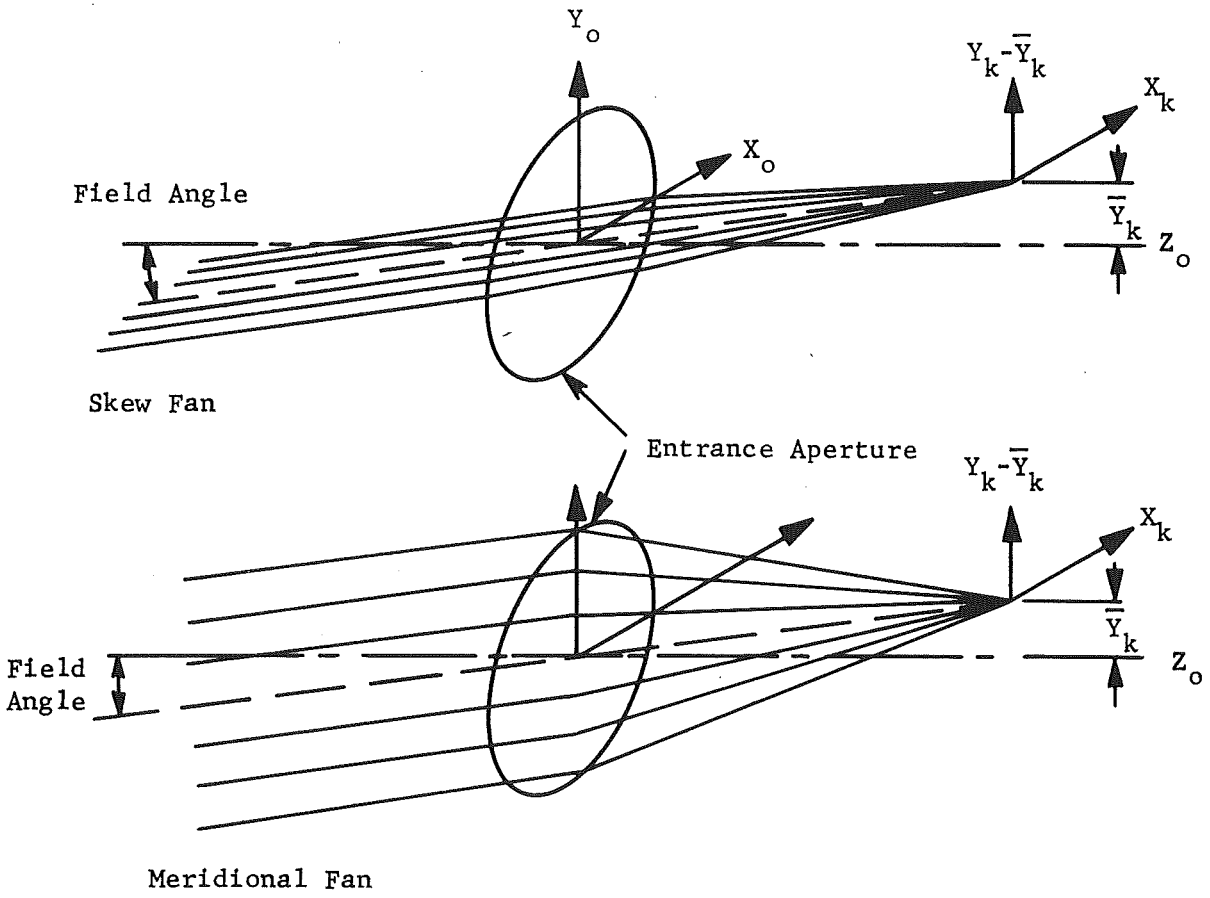

Figure 35. Meridional and Skew Ray Fans

An alternate method of assessing the effects of aberrations on the theoretical diffraction-limited performance is to compare the aberrations with the tolerances derived by Rayleigh on the basis of a 1/4-wavelength wave front deformation. In the presence of several aberrations this technique breaks down somewhat but is still useful if applied to the predominant aberrations. At the edge of the field the worst aberration appears to be lateral color which amounts to about 8 microns. This compares to a 1/4-wave tolerance of 5.5 microns for lateral colors. It may therefore be concluded that although the present corrector does not quite meet the most stringent criteria for imagery at the edge of the field, it does provide adequate imagery for pointing error sensing.

Image Movers

One of the prime requirements on the LTEP telescope is a pointing system capable of providing image stability of 0.01 arc-second over very long time periods. The only operational system coming close to fulfilling this requirement is Stratoscope II, a 36-inch-aperture balloon-borne telescope designed and built for Princeton University Observatory by Perkin-Elmer. Pointing on Stratoscope II is achieved by splitting two guide star images in the telescope field on the apex of prisms set to coincide with the image center. The logic system compares the intensity in each image quadrant with the intensity of the other image quadrants thereby deriving pitch, roll, and yaw pointing signals.

The principle advantage of the Stratoscope scheme is that it does not depend on the relative alignment between different optical systems. Both pointing and image systems utilize the same optical elements so that thermoelastic deformations in the telescope structure produce identical effects in both systems. If the null seeking pointing system is operational, then image displacements due to deformations in the telescope structure are immediately compensated by changes in the pointing direction of the telescope.

The difficulty of implementing a similar scheme on a satellite-borne telescope is the large volume of space required. A 30 arc-minute diameter field corresponds to a circular area 87 cm in diameter in a 2-meter, f/50 telescope. Furthermore, keeping the relay microscope field angle in bounds would probably require about 8.7 meters between focal planes.

The image mover is the ingenious scheme which retains the common telescope and microscope optics principle built into Stratoscope but also permits the size of the microscope to be reduced to a convenient, easily packaged size. The principle on which it operates was first reported by Perkin-Elmer in Report 8346 for Princeton University. Much of the description which follows is adapted from the Advanced Princeton Satellite Study Report No. 8688.

In its original form the image mover device consisted of a very simple system of lenses and mirrors which could be arranged to shift a guide star image from an arbitrary position to a fixed position. The optical arrangement required to achieve this is illustrated in Figure 36 .

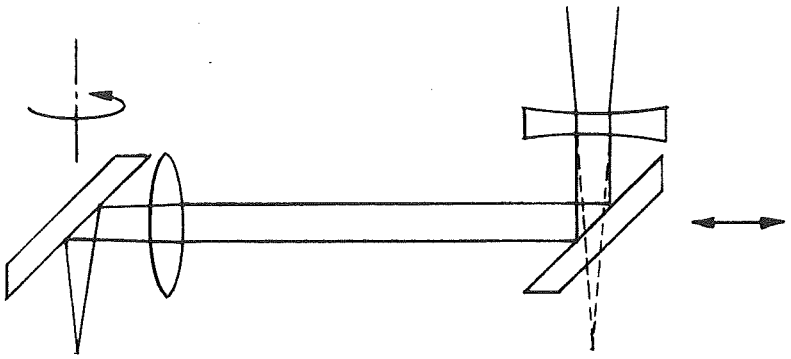

Figure 36. Image Mover Concept

A converging bundle of light from a star to be used as a pointing reference is intercepted before coming to a focus by a negative lens that renders the rays parallel. A small diagonal mirror turns the collimated beam through a right angle that intersects a positive lens. This refocuses the bundle so that after reflection from a second diagonal mirror the guide star image lies in the same focal plane as before. The image mover can be adjusted to shift star images from arbitrary positions by moving the negative lens and its diagonal mirror toward or away from the positive lens and by rotating the entire image mover assembly about a vertical axis through the shifted image position. In this way a star image may be moved from an arbitrary point in the outer portion of the telescope field to a fixed point close to the telescope optical axis and on the uncorrected f/10 focal plane. In this way, both the pointing stars and the uncorrected telescope image field can be handled with the all-reflective f/50 microscope, thus producing magnified star images on either side of the vidicon. At this point, the pointing star images are divided into four parts which are continuously compared to derive pitch, yaw, and roll pointing error signals.

The LTEP image mover mechanism design concept, which affords a number of advantages to the pointing system at the cost of additional optical surfaces, is shown in Figure 37. There is no requirement for a sliding mechanism in the arrangement shown which uses a second pivot axis. Both pivot axes are parallel to the telescope optical axis and also coincide with optical axes of the positive and negative lens groups. The main axis, about which the entire image mover rotates, passes through the small folding flat. The upper arm pivot axis, about which only the long prism and the negative doublet rotate, passes through both folding prisms. Each axis has associated with it a motor and an encoder which position the image movers with respect to the telescope axis in analogous fashion to the known position of the guide stars and image field center.

An important advantage of the two-axis LTEP design shown in Figure 37 is that it provides coverage over a large portion of the telescope field and a large acquisition zone around the nominal position of the pointing star image. The size of the acquisition zone required by the telescope is determined by the angular-position and velocity errors expected from the coarse pointing system. A 2-arc-minute diameter acquisition zone, which is provided in the present design, is about that required for compatibility with the small star trackers in the OAO series of satellites. In the event that coarse pointing is markedly better in the LTEP package, then the pointing star acquisition zone may be reduced with a corresponding beneficial reduction in background illumination. The portion of the telescope field that can be covered by the image movers is shown in Figure 38, along with the various orientations of the image mover mechanism required to cover the field extremities. Most of the central portion of the field that is not accessible would be badly vignetted by the hole of the telescope field corrector elements and would therefore not be usable anyway.

As might be expected, a small rotation of the image mover about the telescope axis or a small shift in the position of the negative doublet with respect to the positive triplet can produce a relatively large pointing error. It is therefore essential that the mechanism that positions the image mover elements be designed so that such motions can be minimized during the operation of the telescope. This can probably be achieved most easily by a mechanical design that locks the elements with respect to each other and the instrument package frame once they have been positioned correctly. Small translational displacements of the entire image mover system have a negligible effect on the quality of the guide star images if the f-numbers of the incoming and outgoing image beams are equal. In this case, the image mover system is analogous to a window in a collimated light path; it introduces an amount of parallax depending on the angular orientation, but translational motions have no effect since the optical power is unity. This advantage is utilized in the present design with the exception that the field-correcting elements are assumed part of the image moving system, thus yielding equal f-numbers for the uncorrected on-axis image beam and for the star beams emerging from the image movers.

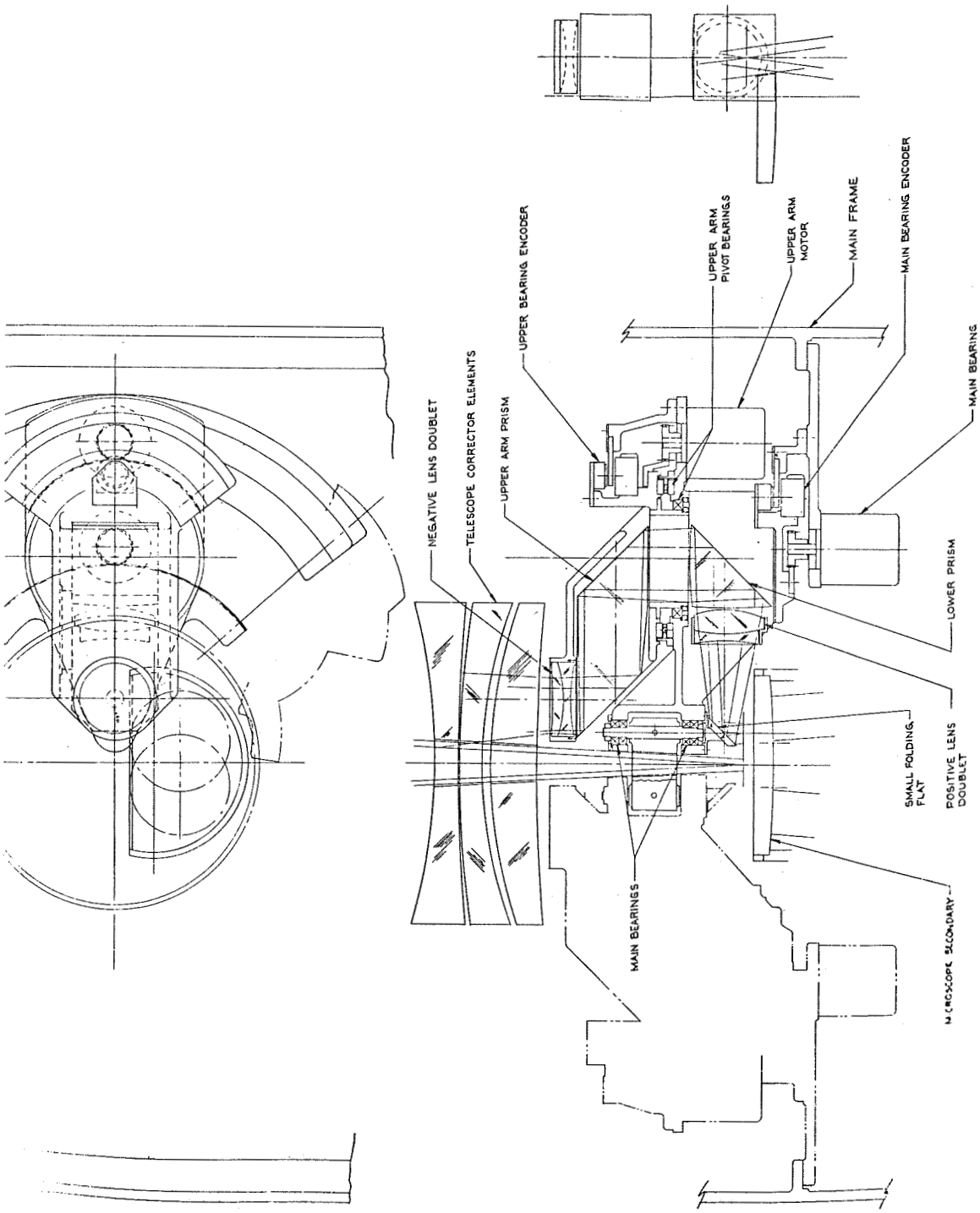

Figure 37. OTES Image Mover Mechanism

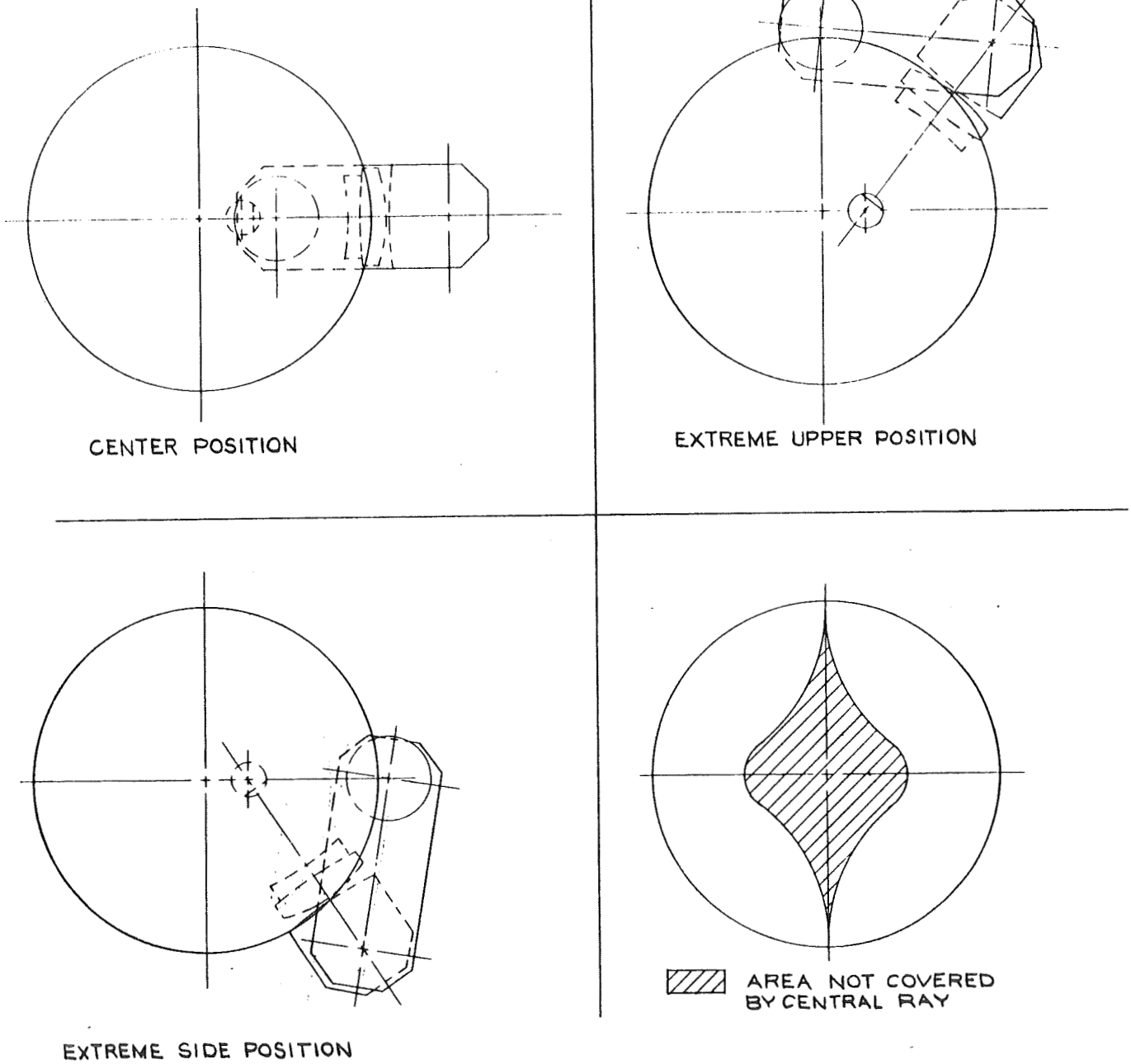

Figure 38.. OTES Image Mover Field Coverage

When additional design work is done on the image movers, attention should be given to reducing the number of optical surfaces and finding an arrangement that will lock the elements tightly together once they have been positioned correctly. Since the total optical path between elements does not vary in the two-pivot design, it may be possible to achieve the same correction with fewer elements by eliminating the collimated path between negative and positive elements. Since the outer portion of the image mover field is used only during acquisition, the only important optical aberrations that need be considered in the image mover design are spherical aberration and longitudinal color.

f/50 Imaging Microscope

The main purpose of the microscope is to relay the central, all-reflective portion of the telescope field to the image surface of a vidicon or image orthicon. Some magnification is required since the limiting resolution at 2000Å imaged at f/10 is 500 cycles (line pairs)/mm and 1000Å imaged at f/10 is 1000 cycles/mm, whereas the resolution of present day vidicons is typically 25 cycles/mm. Clearly, if we wish to record the highest theoretical spatial frequencies passed by the telescope at 1000Å, a magnification of about 40 is required for present vidicons but this is likely to decrease with the development of better image tubes. A magnification of five was selected for the LTEP microscope predicated on an eight-fold increase in vidicon resolution. In the event that vidicon development does not progress as far as anticipated before a design freeze is necessary, then a higher magnification will be necessary.

In order to prevent slowly changing temperature distributions in the instrument package from misaligning the pointing and imaging systems, it is also necessary that the microscope relay the guide star images positioned on either side of the image field. This is a more difficult requirement, since the microscope must operate farther off-axis and at a much lower f-number in order to accommodate the tilt imparted to the guide star image beams lying on the periphery of the telescope field. The 4-degree 45-arc-minute tilt imparted to the marginal chief ray by the present corrector system increases the acceptance angle from f/10 to f/3.725.

A microscope containing refractive elements is not feasible since it would restrict the spectral range of the telescope. Furthermore, the number of reflective microscope designs is extremely limited either because it is physically impossible to incorporate them into the present system, or because they suffer from a high obscuration ratio. A large obscuration would seriously compromise the overall optical performance of the telescope imaging system.

A unique Perkin-Elmer image microscope* having none of the above objections is shown in Figure 39 . It consists of two axially aligned surfaces of

*The optical design of this imaging microscope was invented by D. Markle and L. McCarthy and is not included in this report because it is proprietary to The Perkin-Elmer Corporation.

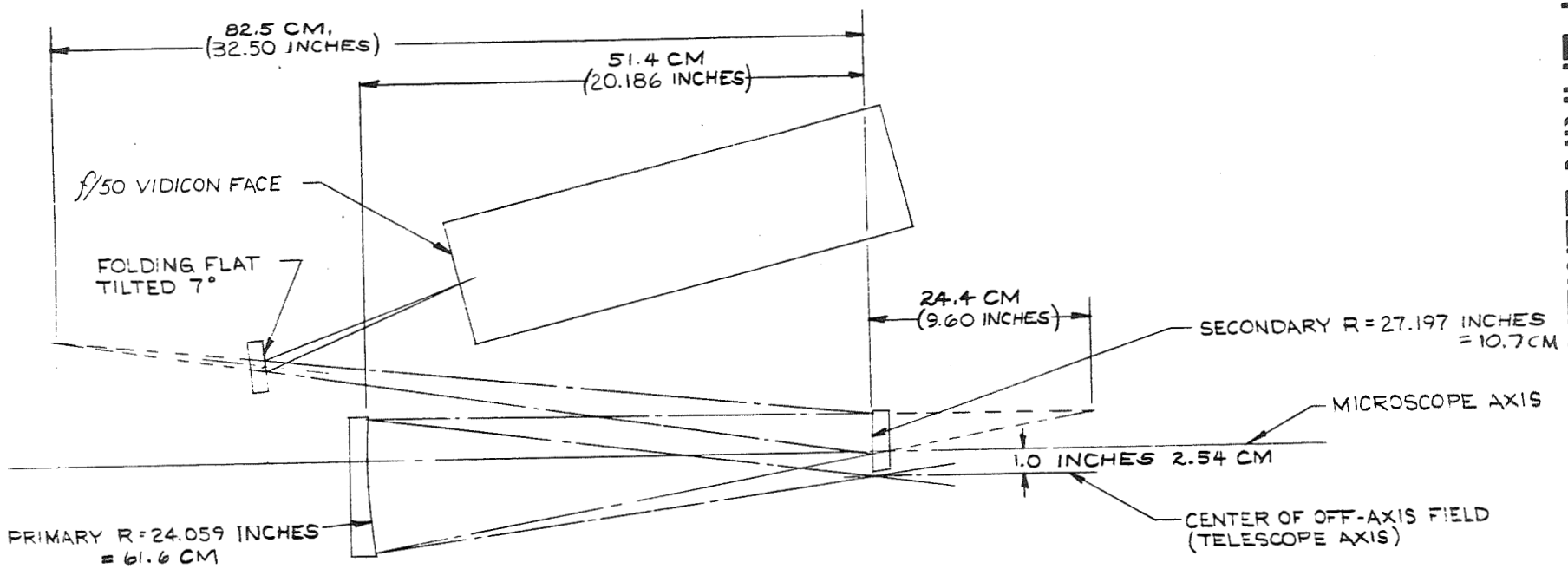

Image Dividers
and Photomultipliers

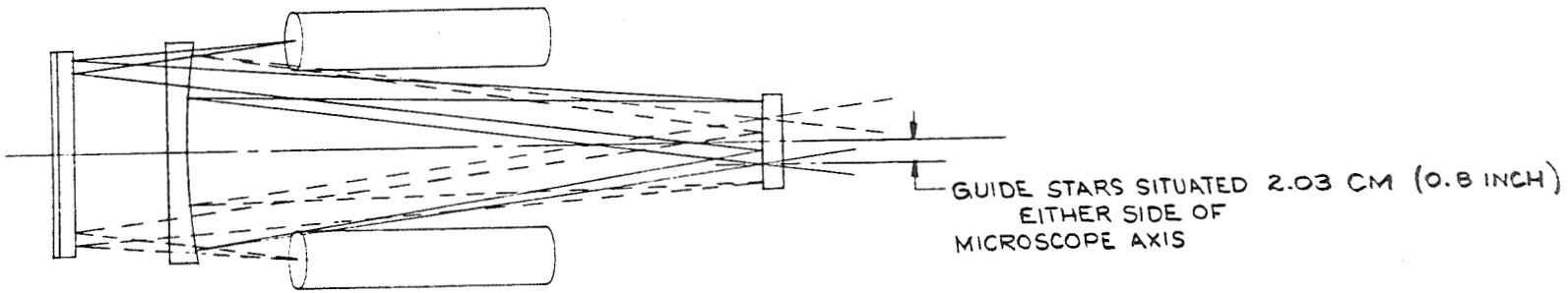

Figure 39. OTES Reflecting Microscope

revolution. A small folding flat is also included, but this has no effect on the optical performance and serves only as a packaging convenience.

Since the microscope is employed off-axis, there is no obscuration. The f/10 focal plane of the telescope and the effective f/3.725 plane of the image movers is situated adjacent to the reflecting microscope secondary mirror - a position that minimizes the extent to which the telescope must operate off-axis. The vidicon or orthicon position shown in the top view of Figure 39 is folded along the side of the microscope. If more room were available in the instrument package, this fold might be eliminated and the overall optical efficiency in the far ultraviolet region enhanced. The guide star image dividers are situated on either side of the vidicon about 8 inches apart (bottom view of Figure 39). The aberrations of the two-element microscope are illustrated in Figure 40 which shows the geometrical image size at two field positions on a curved focal plane. The ray fans shown in Figure 40 extend over an f/3.725 aperture so as to accommodate the tilt imparted to the guide star beams by the telescope corrector. In practice, only about a third of the aperture is used by pointing star beams, but the section used varies depending on the position of the pointing star in the telescope field. The on-axis telescope field that is relayed by the microscope to the vidicon or orthicon does not move around but always occupies the central third of the total aperture.

f/50 Telescope and Microscope Combination

The overall performance of the f/50 telescope-microscope combination is illustrated by the modulation transfer curves shown in Figures 41 and 42. These show the transfer functions for both radial and tangential directions in various positions of the vidicon field. The 1-inch decenter between the telescope and microscope axis is in the radial direction. No refractive components, which would limit the spectral response, are contained in the vidicon optical path which consists of five reflective surfaces up to the front surface of the vidicon. The obscuration due to the secondary and the baffles, which are necessary to shield the image and guidance fields from directly incident light, has a marked effect on the shape of the MTF curves. In the present design this obscuration would amount to about 23.1 inches out of the 78.8 inches total aperture. A central obscuration has much the same effect as optical aberrations would have on a system with a clear aperture. In both cases, it is the intermediate spatial frequencies that are attenuated the most.

At the center and to each side of the 1.6-inch diameter vidicon face the MTF curves are identical to the theoretical diffraction-limited response of an obscured f/50 optical system. At the top and bottom of the vidicon field some defocusing occurs because of the curved field produced by telescope and microscope combination. The field curvature of the telescope is opposite to and slightly stronger than the curvature produced by the microscope. Because of the misalignment between the axes of the two systems their field curvatures do not cancel as well as might otherwise be expected.

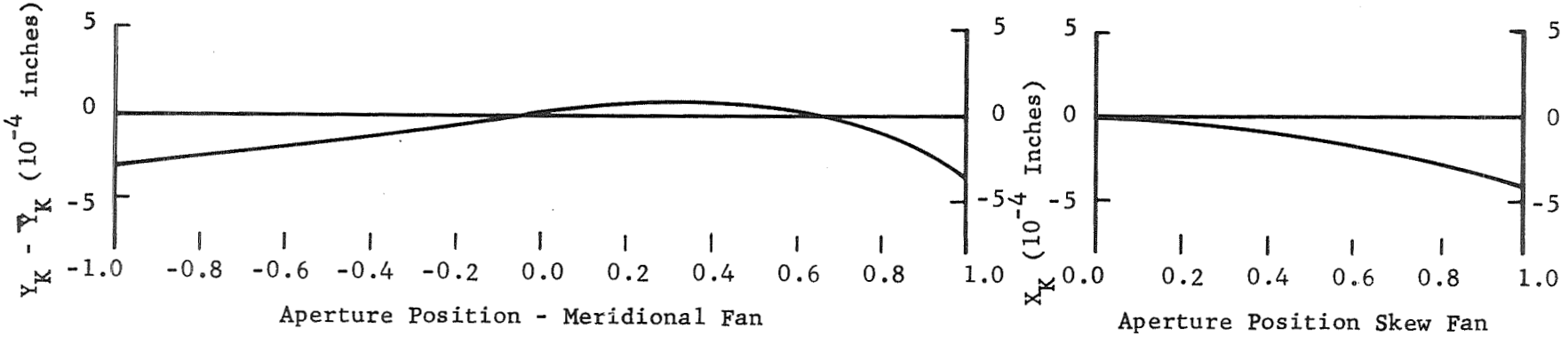

-1.28 Inches Off-Axis

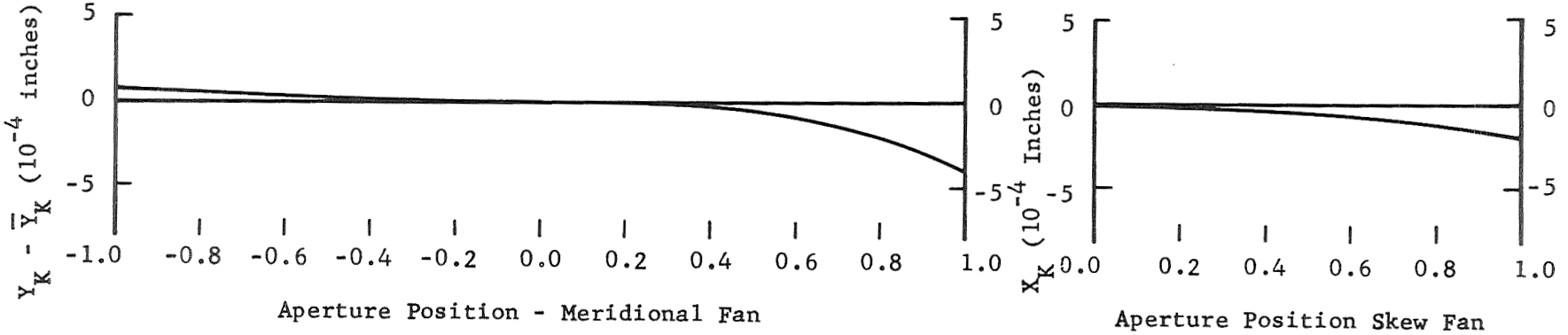

-9.0 Inches Off-Axis

Figure 40. LTEP REFLECTIVE MICROSCOPE
X5 Magnification (f/3.723 - f/18.63)

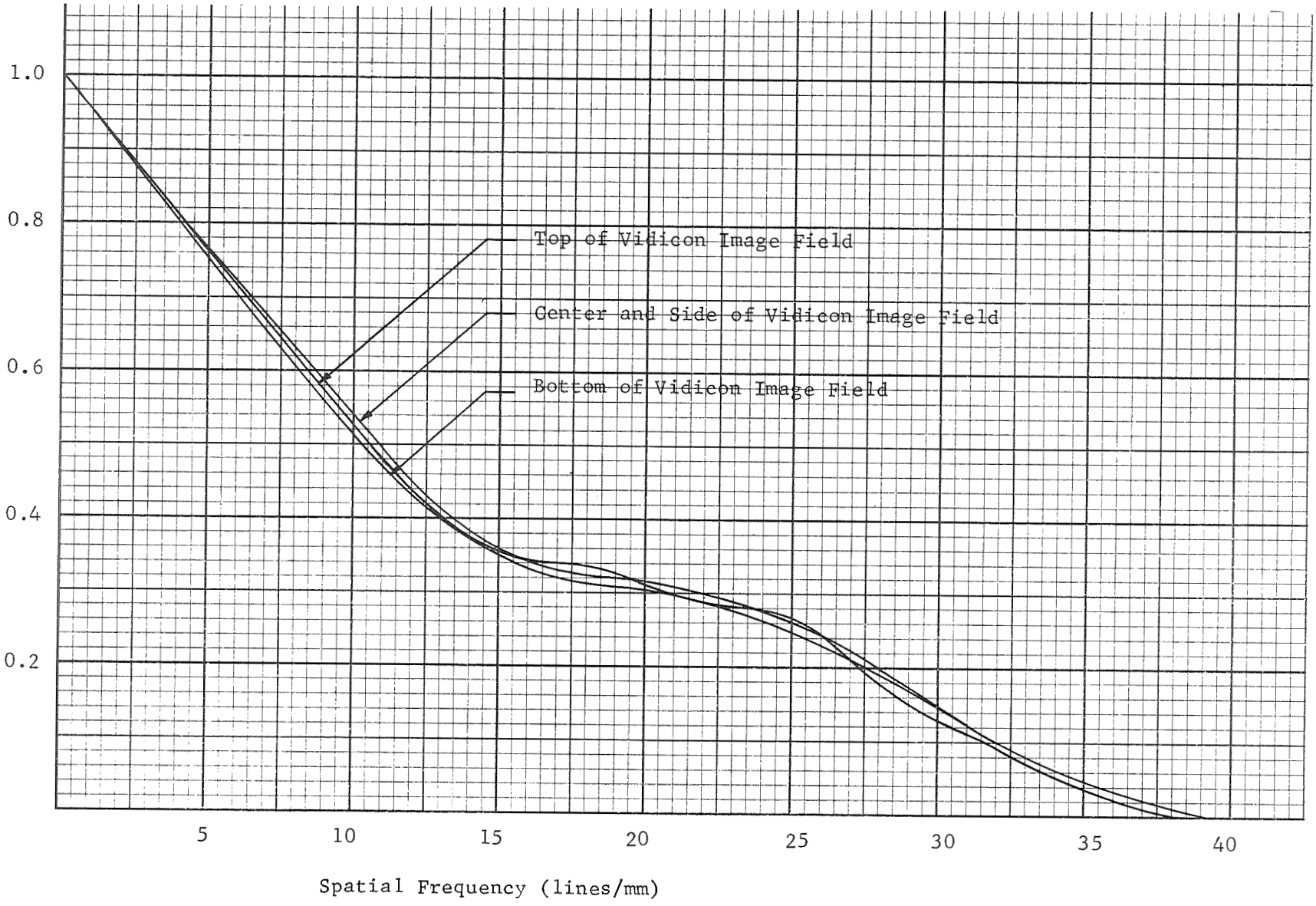

Figure 41. LTEP 2-METER TELESCOPE
f/50 Vidicon Image Field M.T.F.
5000Å Radial Direction

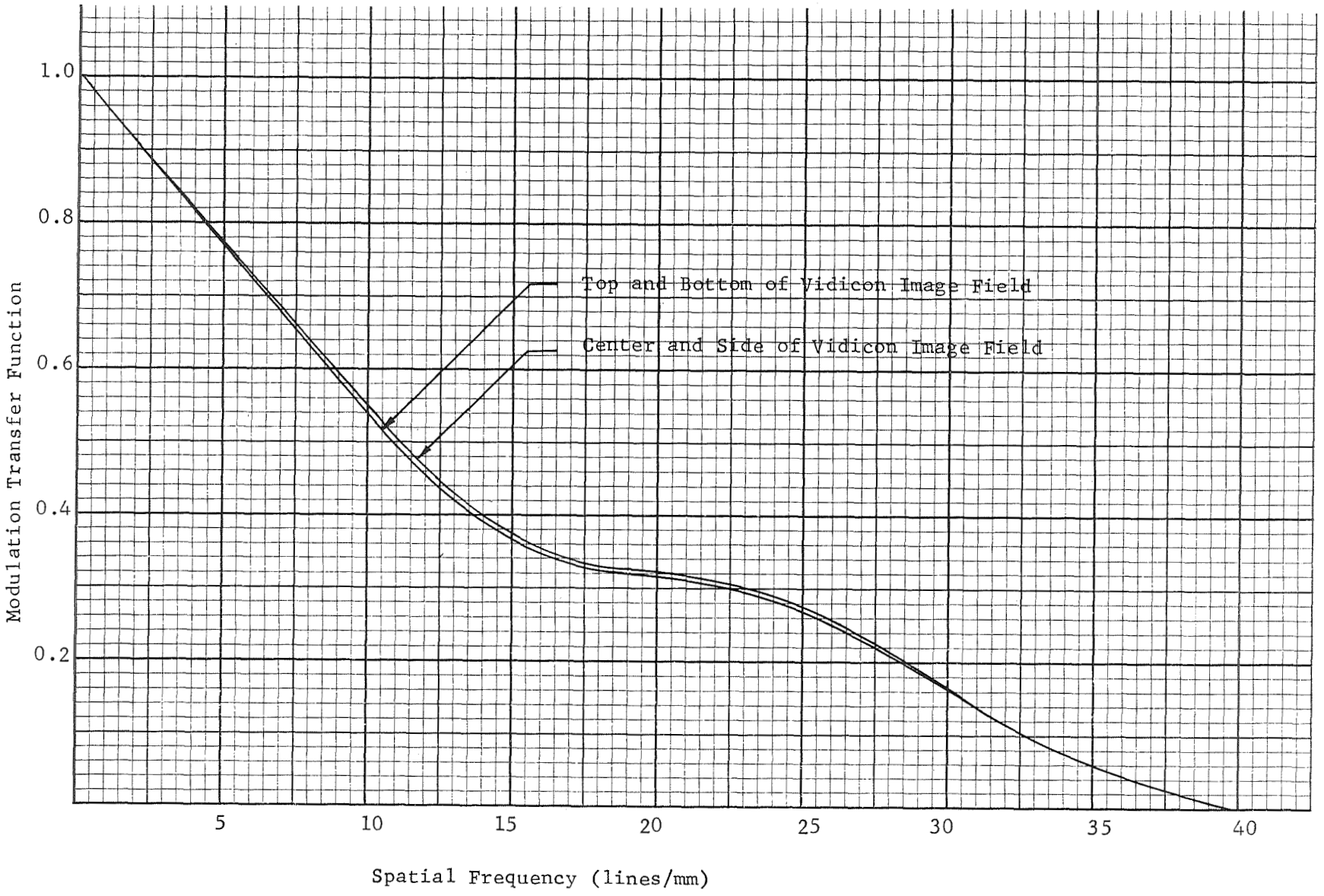

Figure 42. LTEP 2-METER TELESCOPE
f/50 Vidicon Image Field M.T.F.
5000Å Tangential Direction

The decenter between the telescope and microscope also affects the limiting frequency of the MTF curves. At the center of an f/50 system the limiting frequency would normally be $1/\lambda f = 40$ cycles/mm at a wavelength of 0.5 microns. In a decentered configuration the exit pupil is foreshortened when viewed along the telescope axis, the distance between the center of the exit pupil and the center of the field is slightly different from the nominal position, and the incidence angle of rays striking the focal plane is also altered. The effect is noticable on the radial MTF curves and probably accounts for most of the very small difference between the top and bottom field position curves.

As the wavelength decreases, the effect of aberrations increases and more pronounced differences between the actual and theoretical diffraction-limited MTF's can be expected. This is illustrated in Figures 43 and 44 which show the radial and tangential MTF's at the top and center of the vidicon field for a wavelength of 0.25 microns. Even at this wavelength the optical aberrations have little effect and the design may be termed "diffraction limited".

The transfer function at shorter wavelengths was not investigated since it is apparent that the resolution of the vidicon, alignment and the surface quality of the optical components will ultimately limit the resolution rather than the optical aberrations.

f/10 (Photographic Imagery System)

Photographic emulsions have become firmly entrenched as a recording medium in many of the disciplines comprising modern astronomy and will continue to remain so for many years to come. In general, photographic emulsions have quantum efficiencies under 1 percent, whereas image tubes have efficiencies above 10 percent, but films are available with a wide range of resolution capability extending into the hundreds-of-lines-per-millimeter region and may be obtained in virtually any size. Films also tend to yield cleaner pictures than vidicons but on the other hand are susceptible to radiation fogging and require developing.

In the LTEP configuration where man is available for changing cassettes and developing photographs the particular advantages of film can be put to good advantage. For example, a 70-mm-wide strip of film at the f/10 image plane can record a field some 2000 times larger than a vidicon. Furthermore, there is no need for a microscope or for image movers, and the telescope corrector can be considerably simplified. A conceptual design is shown in Figure 45. The photographic telescope corrector elements shown are representative but have not been designed since feasibility has been well established by the more difficult vidicon system corrector. For example, with the photographic corrector it is not necessary to restrict the divergence angle or to leave a large space between the last corrector element and the focal plane. This will probably result in a reduction in the number of elements from four to three, and an extension of the corrected spectral range into the ultraviolet with fused

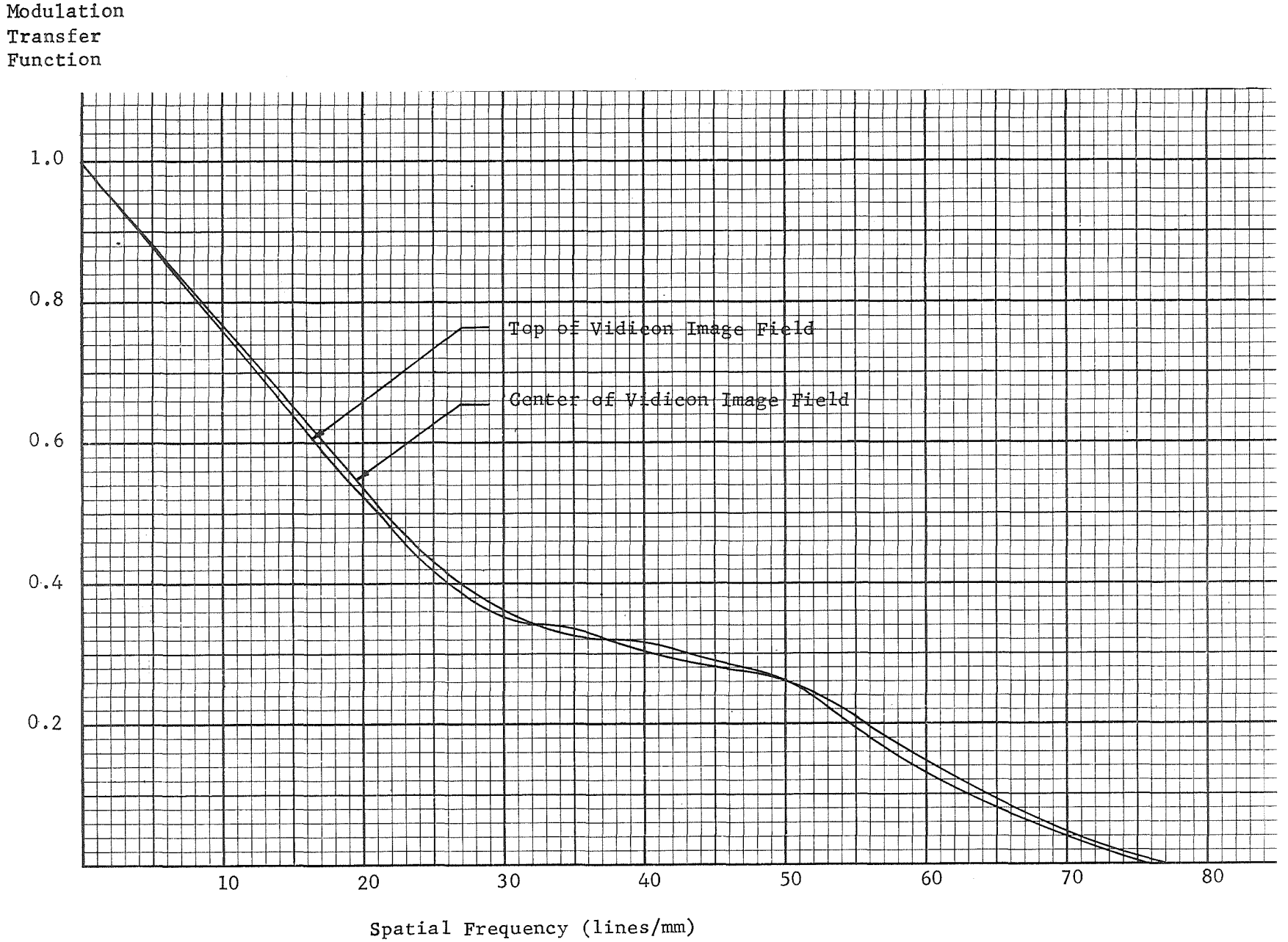

Figure 43. LTEP 2-METER TELESCOPE
f/50 Vidicon Image Field M.T.F.
2500Å - Radial Direction

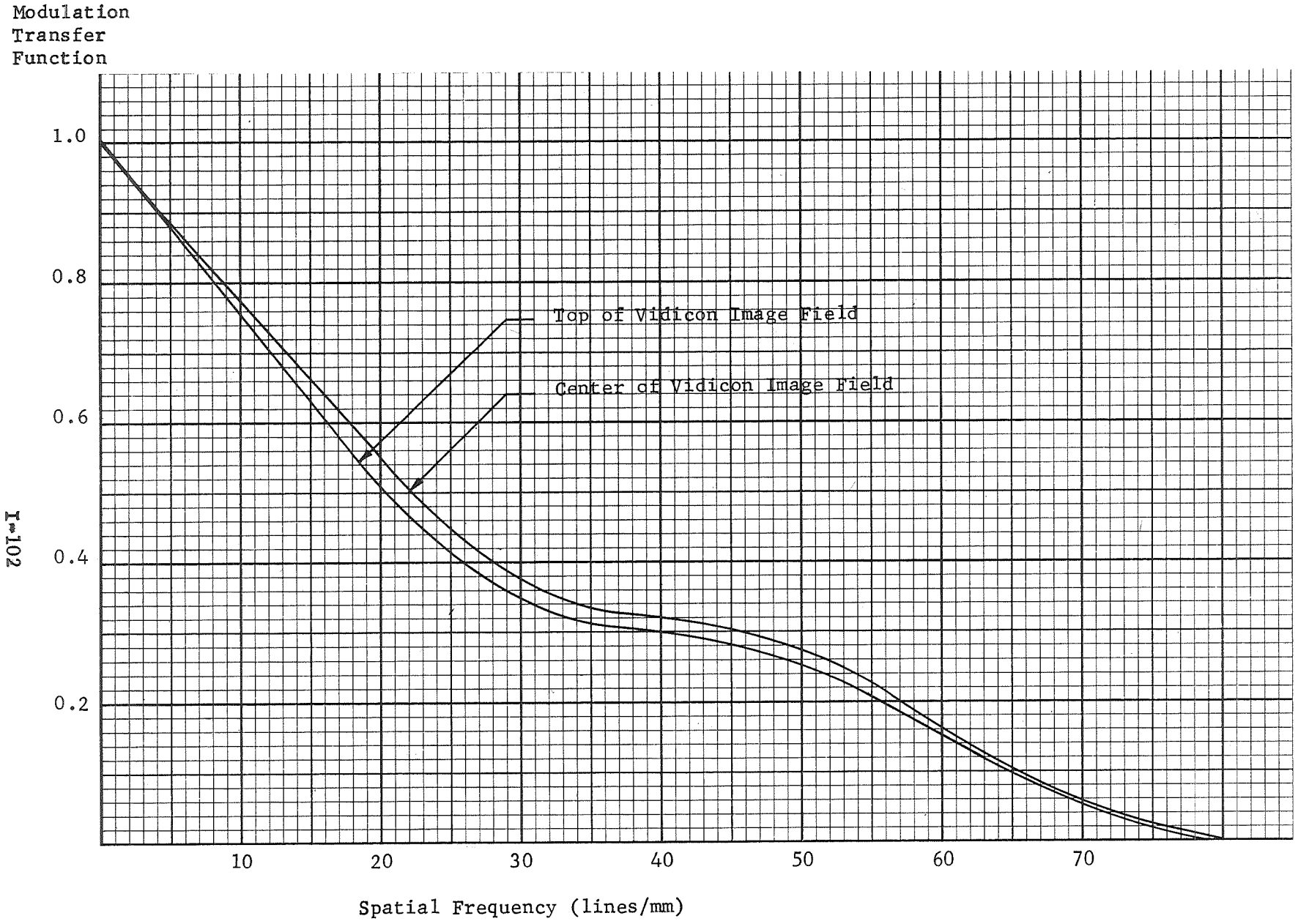

Figure 44. LTEP 2-METER TELESCOPE
f/50 Vidicon Image Field M.T.F.
2500Å - Tangential Direction

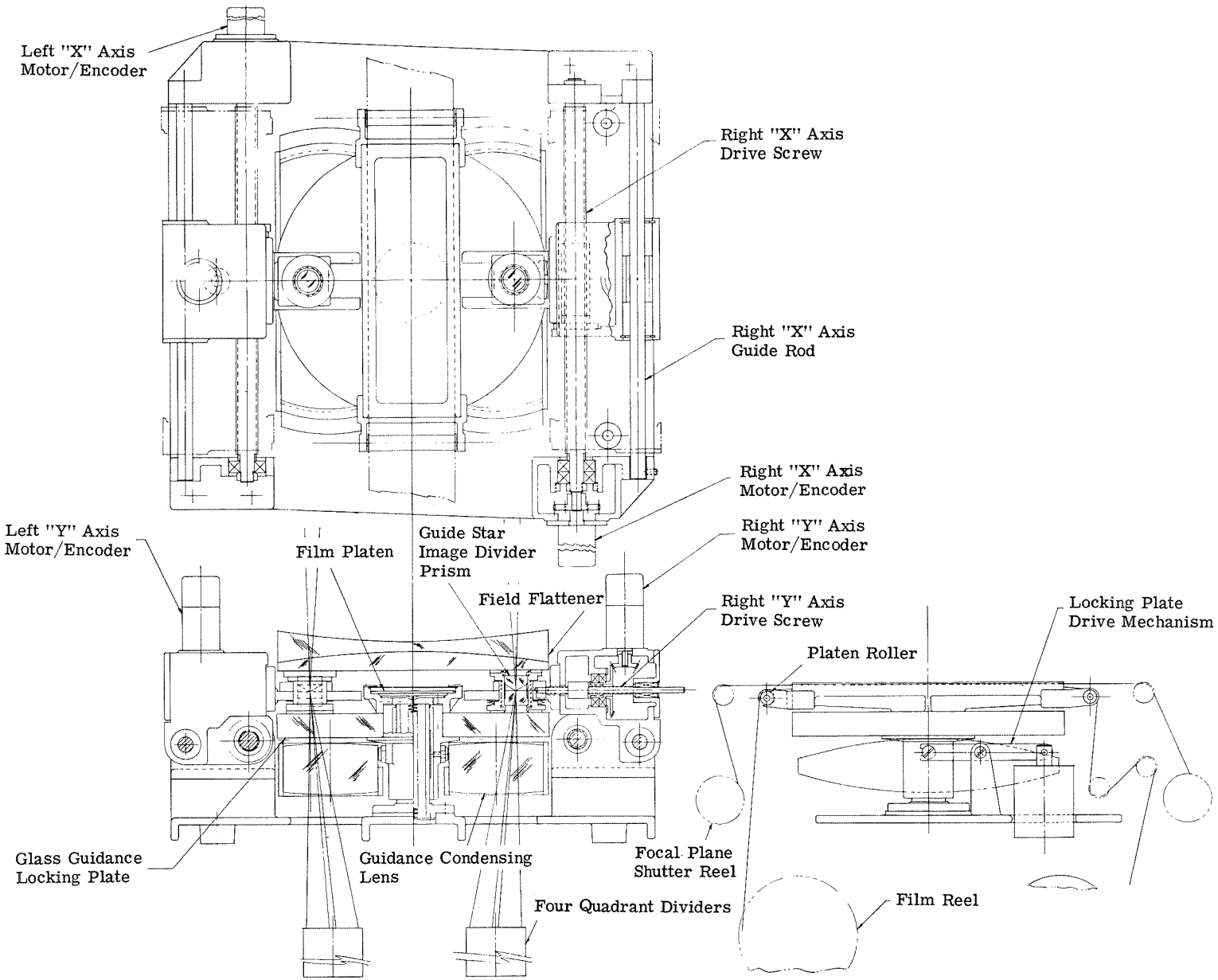

Figure 45 . LTEP Photographic Image Package

silica, lithium fluoride, or similar optical materials that transmit in this region. The last two corrector elements, which act primarily to flatten the field, are illustrated in the side view of Figure 45 .

The corrected f/10 focal plane is about 17.8 cm in diameter and situated midway between the last corrector element and a glass window. The photographic field is a 70-mm strip through the center of the corrected focal plane from one side to the other. The film rests on a platen immediately below a focal plane shutter. Take-up reels for the film and the shutter are shown in the side view.

The pointing field consists of two D-shaped sections on either side of the photographic field. Each "D" section contains a four-quadrant image divider consisting of two prisms oriented so that the roof of one faces the roof of the other, but with a 90-degree angle between the apex lines. When suitably positioned, the image divider splits a guide star image into four separate beams which exit through the window (locking plate) below the dividers. A field lens below the window of each section directs the four separate beams onto a four-quadrant photomultiplier from which signals are derived.

Pointing Error

The position of each image divider along the x direction is determined by a screw-driven fork which straddles the divider assembly. The y direction position is controlled by a screw captured in each divider assembly which is driven back and forth by a threaded collar geared to a drive motor and encoder. The x motor and encoder are fastened to the fork and travel with it along the x axis. Because it is not necessary to split both stars into four parts, but only to split one into four and the other into two for roll correction, the positional accuracy required of the prism mover mechanism is not extreme. For example, a 0.004-inch error corresponding to about a 1-arc-second in the telescope field would serve only to decenter the actual position of the photographic field from its planned position by a comparable amount. A 1-arc-second offset in a 1800 by 700-arc-second field would hardly be noticeable.

Although the positioned accuracy of the mover mechanism is not critical, its stability once positioned is critical. In order to keep image blur to a tenth of the image size, the relative separation between the photographic emulsion and the image divider must be maintained to about 1 wavelength or 0.00004 inch. This is approximately 1.5 parts in 10^5 and is achieved with the present design despite the moderate temperature variations which are inevitable in a practical system. When the dividers are being positioned in the pointing field, the locking plate is pulled away from the corrector, and the divider assemblies move easily toward the new positions. Once in the new position, the dividers are clamped tightly between the locking plate and the corrector plate so that they cannot move during the exposure period. The clamping mechanism for the locking plate is shown in the side view. A spring-load in each of the divider assemblies prevents the assembly from cccking and binding

between the two glass surfaces when in the unclamped position and also provides a smooth transition to the clamped position and back. The glass plates on either side of the divider assemblies provide an optical path for the star beams, and, equally important, provide a rigid mechanical link between the pointing and imagery portions of the telescope field which is relatively immune to thermal changes. If fused silica is used ($\alpha \approx 5 \times 10^{-7}/°C$), the allowable temperature change is about 13°C.

Princeton Experiment Package

One of the building blocks of the spaceborne stellar telescopes which evolved in the Advanced Princeton Satellite Study (NASA NGR-31-001-044) was a very compact echelle spectrograph (see Figure 46). The echelle arrangement produces a spectrum folded like the lines of type on a printed page, thus permitting a large wavelength increment to be integrated and read out on an image tube in about the same time as might be required for a single wavelength with a conventional scanning monochromator (see Figure 47*). Since the spectrograph was intended to study the 1000Å to 3000Å spectral region, refractive components could not be used and the number of reflections had to be minimized since losses as high as 50 percent per surface are common at the shorter wavelengths.

The first spectrograph arrangement to be considered in detail was a 30-inch long, two-element echelle employing a spherical predisperser grating operating in the first order and a flat echelle grating operating in the 14th through to the 39th orders. Both gratings were very tiny elements about 1/4 inch in diameter and situated very close to the f/10 Cassegrain telescope focal plane. The beam leaving the predisperser and echelle elements was made f/150 in order to minimize aberrations and diffraction effects. Good correction over the vidicon field was obtained by tipping the vidicon with respect to the telescope axis and by making the predisperser element slightly torroidal. Details of the design may be found in Perkin-Elmer Engineering Report No. 9149** and the measured efficiencies in Report No. 9608†. The efficiency at 1600Å was found to be only about 3 percent.

The poor efficiency is predictable on the basis of diffraction theory. If each grating groove is to diffract light so that the diffraction maximum falls on the same point, then with spherical gratings, it is necessary to vary the blaze angle from side to side across the grating so that each facet is aimed at a common point on the Rowland circle.

Although the efficiency of the f/10 echelle might be increased by a more precise blaze, and especially by a variable blaze, the simplest and most practical means of achieving higher efficiencies is simply to add additional elements, thus changing the two-element spectrograph into a three or four-element spectrograph. In fact, a cursory examination of several three-element

---

*Illustrative of Echelle format. Exposure was made with large image size.

**Markle, D.A : Optical Design of a Two-Element Spectrograph. Perkin-Elmer Engineering Report No. 9149, January 22, 1968.

†Grosso, Ronald P.: Measurement of Efficiency of the Two-Element Echelle Spectrograph. Perkin-Elmer Engineering Report No. 9608. March 2, 1969.

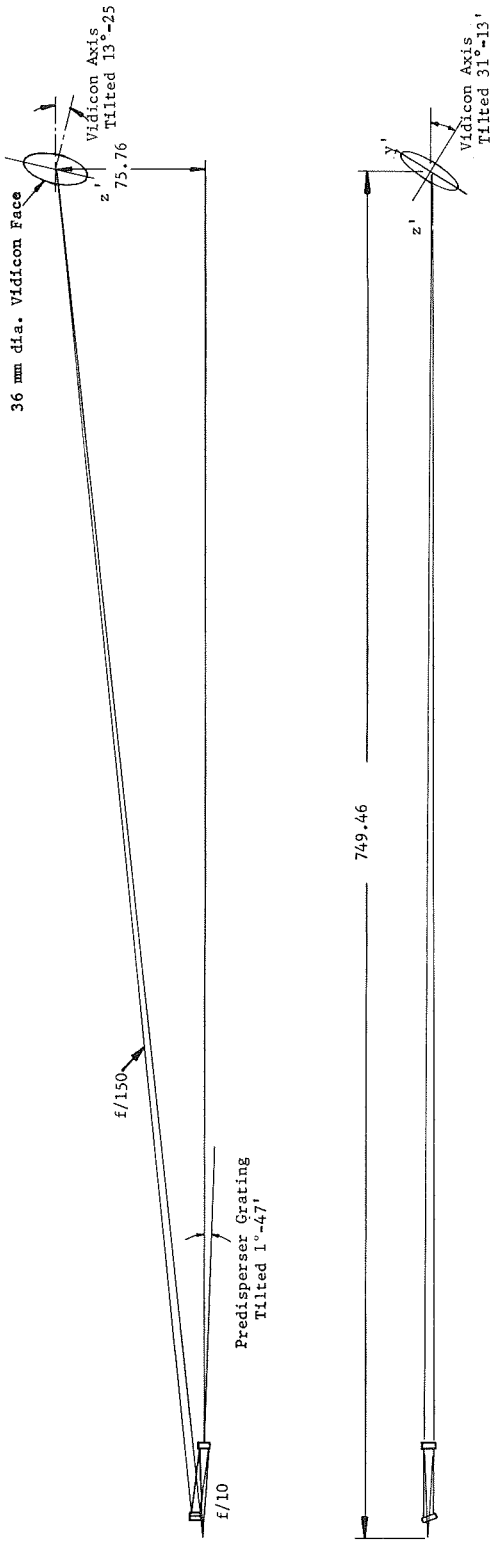

Figure 46. Princeton Advanced Satellite Spectrograph Layout

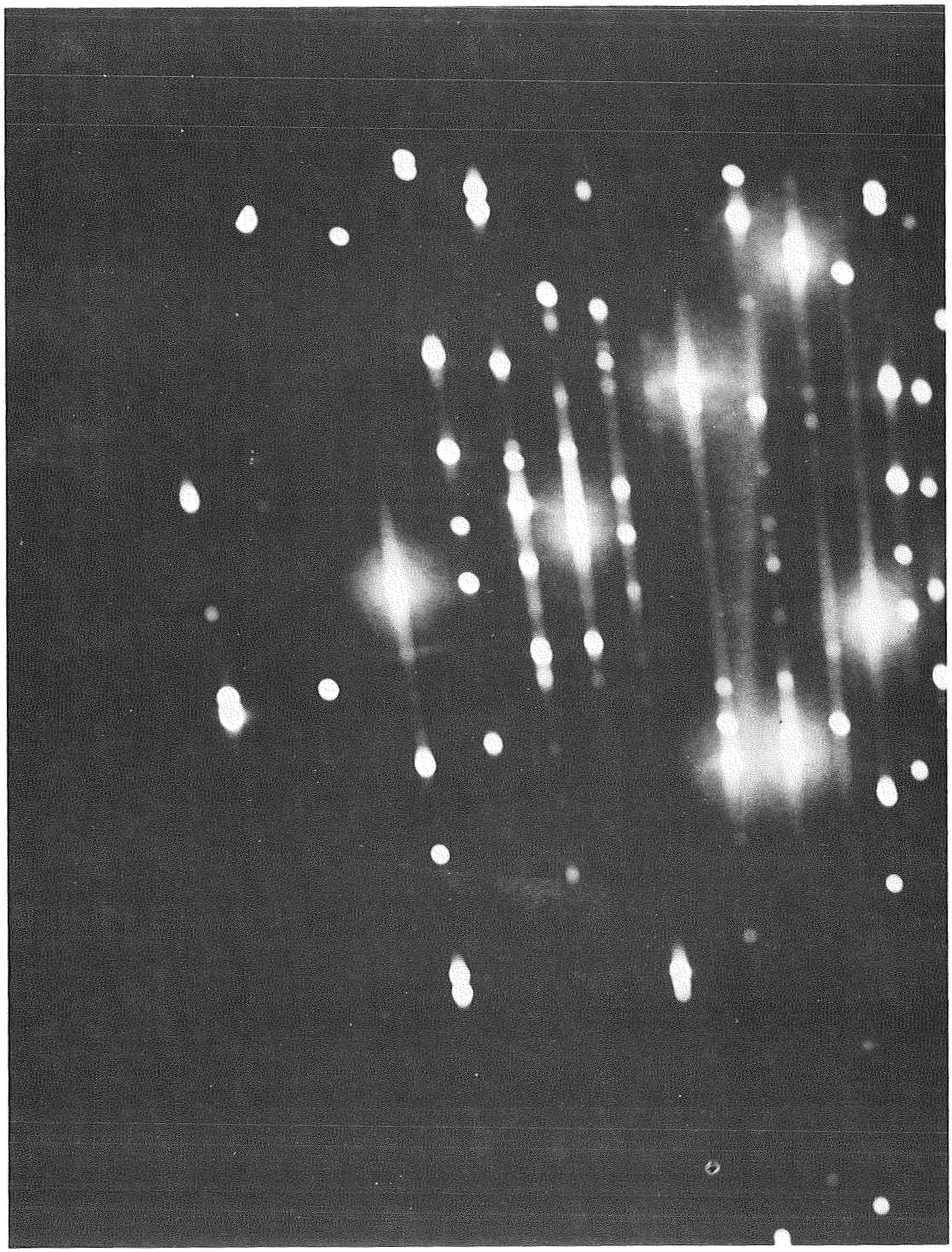

Figure 47 . Echelle Spectrograph Format

echelle spectrograph arrangements indicates that, theoretically at least, these have considerably higher efficiencies at Lyman alpha, even allowing for an additional 20-percent loss from the extra surface.

One way in which the experiment package developed on the Princeton Advanced Satellite study could be packaged in the LTEP configuration is shown in Figure 48. The telescope, correctors and image movers are nearly identical except for scaling. The central image field and the two guide star image fields are folded away from the optical axis and into an all-reflective microscope by a flat which cuts across the f/10 focal plane. A rotatable folding flat near the microscope focal plane directs the on-axis image field into one of two vidicons and the off-axis guide star fields into pointing star divider systems on either side of the appropriate vidicon.

A small hole in the f/10 folding flat passes the field required for spectroscopy to an off-axis paraboloid. Collimated light from the paraboloid strikes a flat echelle near the f/10 focal plane and a curved postdisperser which focuses the spectrum on a vidicon. The postdisperser operates in the first order, and yields a spectrum stretching from one side of the vidicon to the other. The echelle grating is flat, operates at very high orders typically between 10 and 40, and has a very high dispersion. The function of the postdisperser is to separate the overlapping orders of the echelle grating so that a nicely folded spectrum is formed at the vidicon much like the lines of type on a printed page. The vidicon axis is tilted with respect to the folded spectrograph axis in order that the astigmatic image plane containing the high dispersion focus coincides with the vidicon surface.

The vidicons are an ideal data transducer for a spectrographic survey instrument since they possess the quantum efficiency of a phototube yet have the capability of integrating the signals from a large number of resolution elements simultaneously. However, the spectral response of present tubes is limited to wavelengths longer than about 1250Å by the lithium fluoride window. The sensitivity can vary considerably from point to point on the photosensitive surface, and the size of the sensitive surface is limited to about 1.6 inches diameter for the largest. During the manned portion of the telescope operation program it may, therefore, be desirable to use film in the spectrograph as well as in the f/10 imagery package. This possibility is not illustrated in Figure 48, but could be incorporated in the design, probably without altering significantly the redundant vidicon arrangement shown.

The performance of this three-element spectrograph has not been analyzed and it may well prove to have some shortcomings. However, sufficient work has been done to indicate that a three element echelle spectrograph is preferable to a two element when starting with an f/10 beam. Furthermore, this general layout is amenable to quite a variety of spectrograph designs since different vidicons are used for imaging and spectroscopy. In fact, the small size of the vidicon would permit 2 vidicons to be used for spectroscopy as well as for imagery.

Similarly, there is no need to use a 5X microscope. The 20X microscope developed for the Princeton Advanced Satellite could be employed just as readily, and, in fact, it may even be possible to use microscopes of much

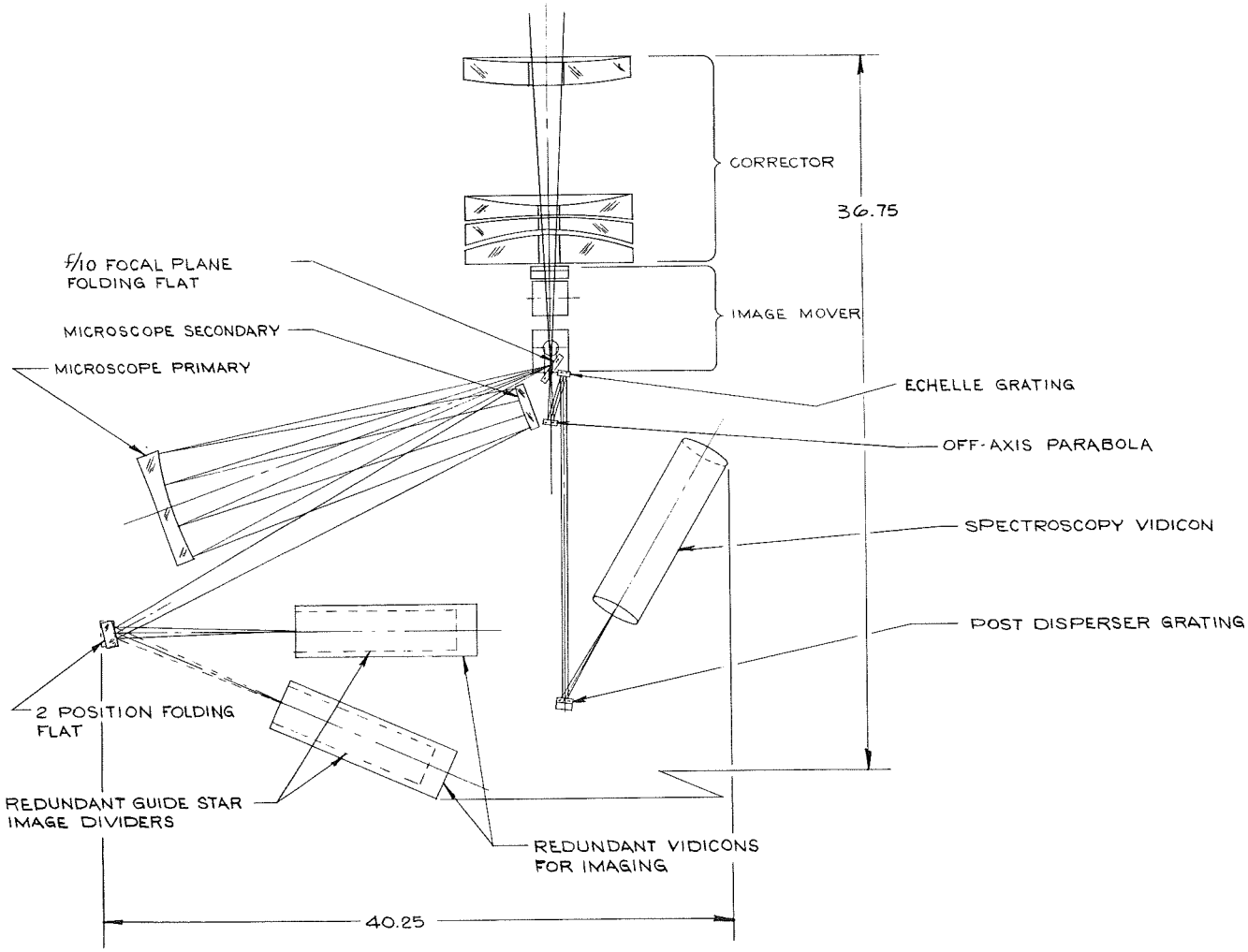

Figure 48. 2-Meter Telescope Princeton Experimental Package 1

higher magnification than this. Slight changes in the present microscope design are required to avoid interference between the microscope secondary and the spectrograph. It is also necessary to modify the image mover design somewhat to avoid mechanical interference between the pivoting image mover mirror and the f/10 folding flat. The main problem area in the Princeton package is separation of the image and pointing star beams from the spectrograph beam. An alternate method is illustrated in Figure 49. In this case the image-forming beams pass through the f/10 focal plane directly into the microscope whereas the spectrograph beam is extracted by an extremely tiny flat extending a short distance into the image field. The extracted beam is handled by a three-element spectrograph analogous to that in the first design. The principal difference between the two methods is that the first one has an extra reflection in the image path whereas the second one has an extra reflection in the spectrograph path.

Modified Echelle

The central package in the LTEP configuration must be smaller than the six outer packages but has one less reflection since the indexing flat is folded out of the optical path when the central package is used. Since the number of reflections becomes extremely important below 1000Å where even a 20 percent reflectivity is high, it would be advantageous to use this space for spectroscopy primarily in the 800Å to 1200Å region. The optimum instrument for this purpose would therefore be a Rowland circle grating operating near glancing incidence. The instrument shown in Figure 49 is a three-element echelle containing an off-axis ellipse a few inches below the f/10 focal plane, an echelle grating near the focal plane and a postdisperser at the very back of the experiment package facing the vidicon. The echelles, postdisperser and vidicons are duplicated on either side of the optical axis so that in the event of a vidicon failure, the ellipse may be rotated 180 degrees about the optical axis bringing into play the duplicated portion of the spectrograph.

An imaging capability is also provided in this instrument so that in a dense stellar cluster the star or stars within the spectrograph field can be easily identified. The image field is separated from the spectrographic field by a field mirror in the f/10 plane which passes the spectrographic field through a small hole and reflects the remainder. Two mirrors which would probably be aspherics magnify the image field and focus on either vidicon depending on the orientation of the last microscope mirror.

Neither the spectrograph nor the microscope contained in this instrument package has been designed. However, the spectrograph shown is related to one of the three-element spectrographs that were recommended for further analysis in the last Princeton Spectrograph Study* Furthermore, the microscope is required only to handle the image field, which is much smaller and has a much larger f-number than that required of the microscope in the Princeton experiment package.

*Markle, D.:Theoretical Efficiency of the Princeton Two-Element Echelle Spectrograph. Perkin-Elmer Engineering Report No. 9746, September 1969.

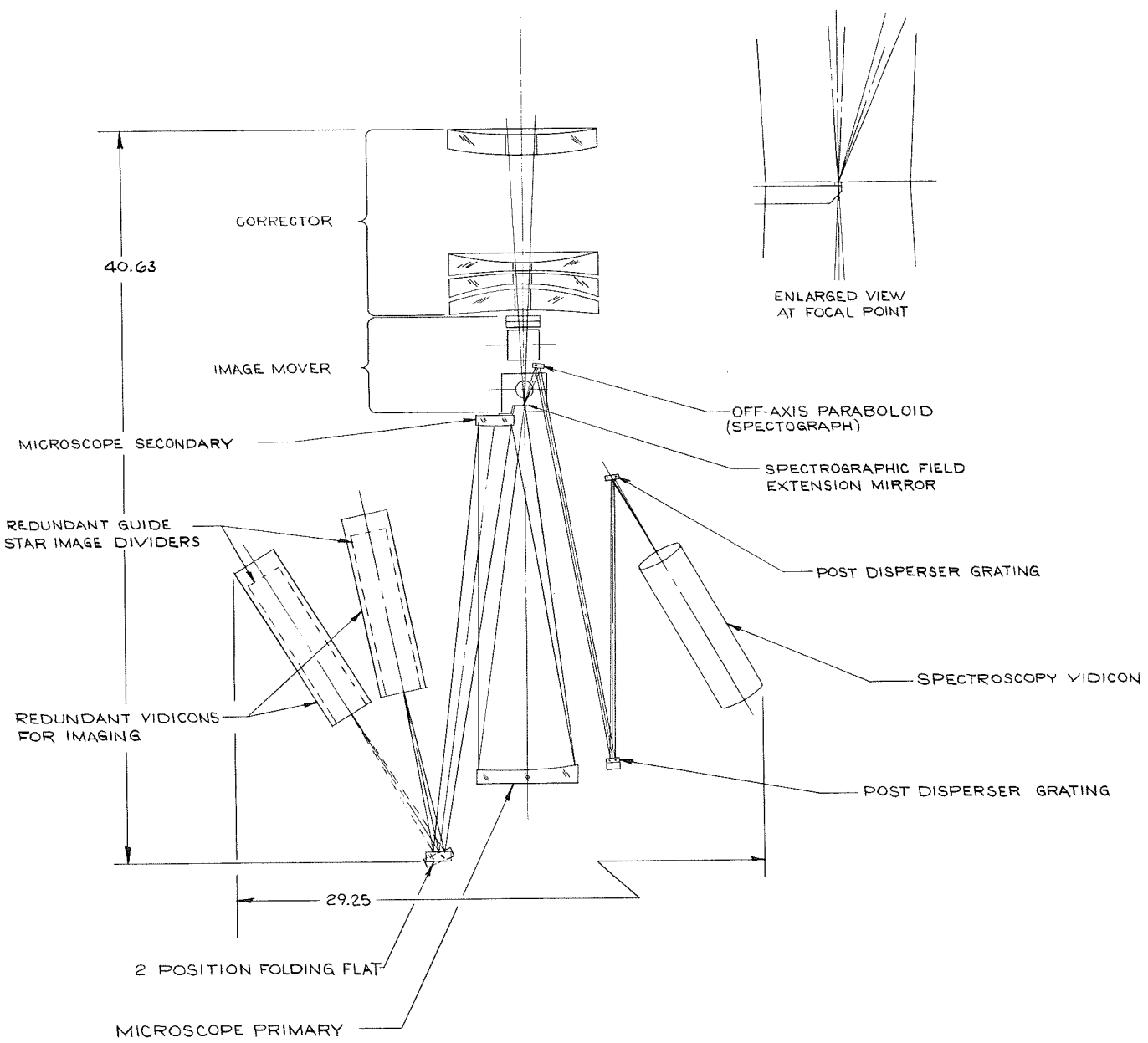

Figure 49. LTEP 2-Meter Telescope Princeton Experiment Package II.

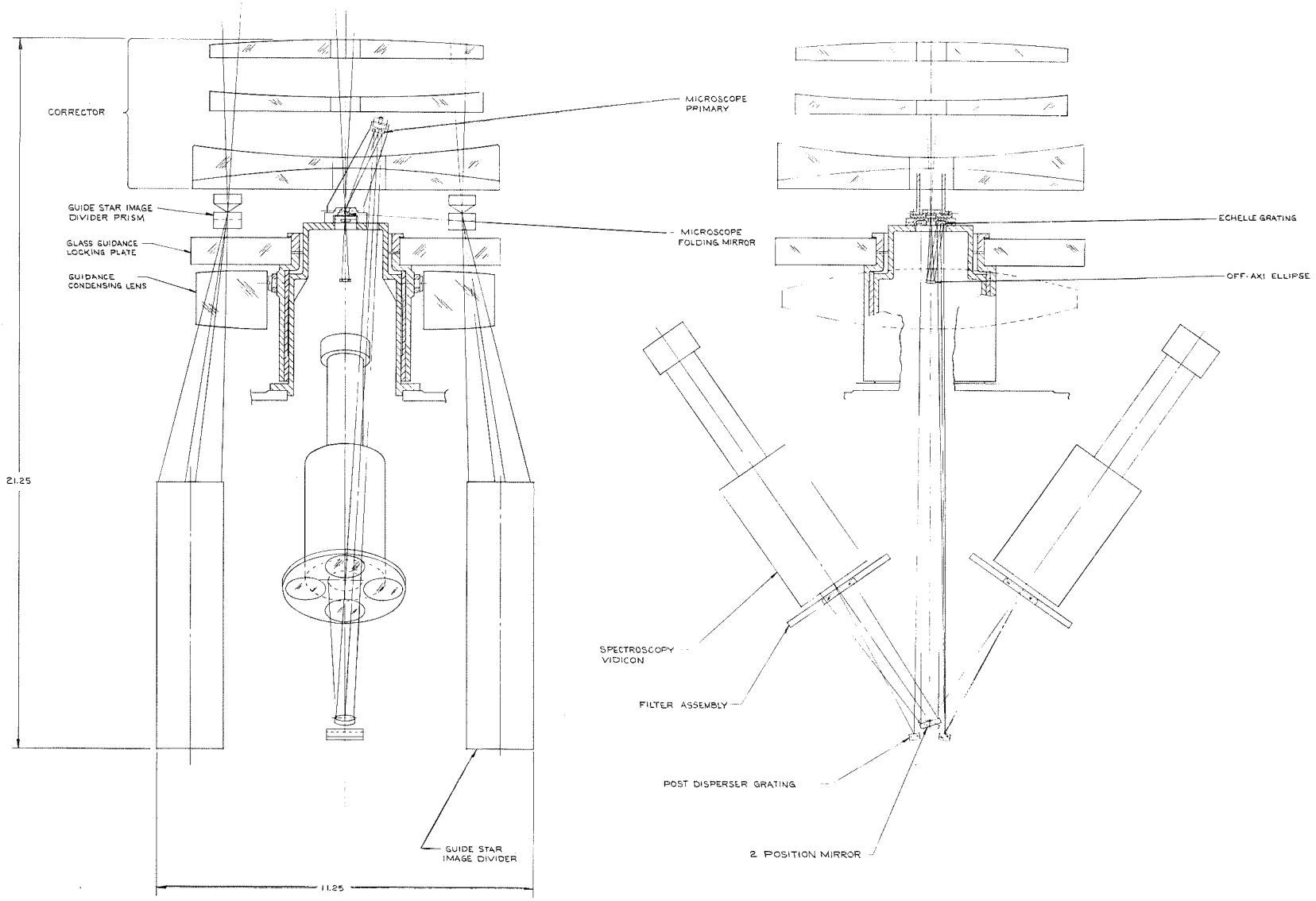

Figure 50 . LTEP 2-Meter Telescope Modified Echelle

Although it may appear that the modified echelle package has all the capability of the Princeton package, this is not strictly the case. It is possible that both packages could cover the same spectral regions with similar spectral and spatial resolutions, but the Princeton package is capable of much greater long term stability in the image train. This comes about by using the microscope to carry imagery as well as the guide stars in the Princeton package, whereas the guidance is done in the f/10 plane in the modified echelle package. Separate guidance and imaging systems leave the imagery susceptible to slight changes in the position of the microscope elements.

Rowland Circle Spectrometer (Equipment Module E)

In the far ultraviolet region the efficiency of the best reflective coatings is very low. At 1000Å a reflectivity of 50 percent is considered excellent, and below 1000Å, efficiencies are somewhat less than 20 percent, even if platinum or rhodium coatings are used. This absorption loss is further compounded by the large scattering losses which occur at these wavelengths. Even on good surfaces, the scattered radiation generally acts to reduce image contrast. It is therefore imperative that the number of optical surfaces be kept to an absolute minimum in instruments designed to operate in this region. The Rowland circle spectrometer fulfills this condition and, in addition, can be designed so that the inherently lower data rate of this type of instrument is partially offset by its versatility.

A Rowland circle spectrometer patterned after the Perkin-Elmer designed OAO-C, the Princeton Experiment Package, is shown in Figure 51 . This contains a reflective entrance slit that shears a portion of the energy from each side of the image focused upon it and directs this energy into a relay lens followed by a simple pointing error sensing system. Unlike the previous instrument packages, the Rowland circle spectrometer does not require two pointing stars or a large telescope field, but it does require fairly bright stars since the same star is used for pointing and spectroscopy.

The spectrum imaged along the arc joining the entrance slit and grating is scanned by two arms which pivot about the main bearing assembly. Each arm contains two exit slits, one slit for the first order spectrum in the 1600Å and 3200Å region which is detected with a conventional trialkali phototube, and the other slit for the second order spectrum in the 800Å to 1600Å region, which is sensed with an open cathode type of detector. Each arm may be operated independently of the other so as to provide redundancy in the event of a failure of the detector tubes or seizure of one of the arms. Mechanical interference between the arms is avoided by folding the exit slits on arm No. 2 out of the Rowland circle plane with a small optical flat. In this way arm No. 2 may pass in front of arm No. 1 with only a small amount of the spectrum being obscured.

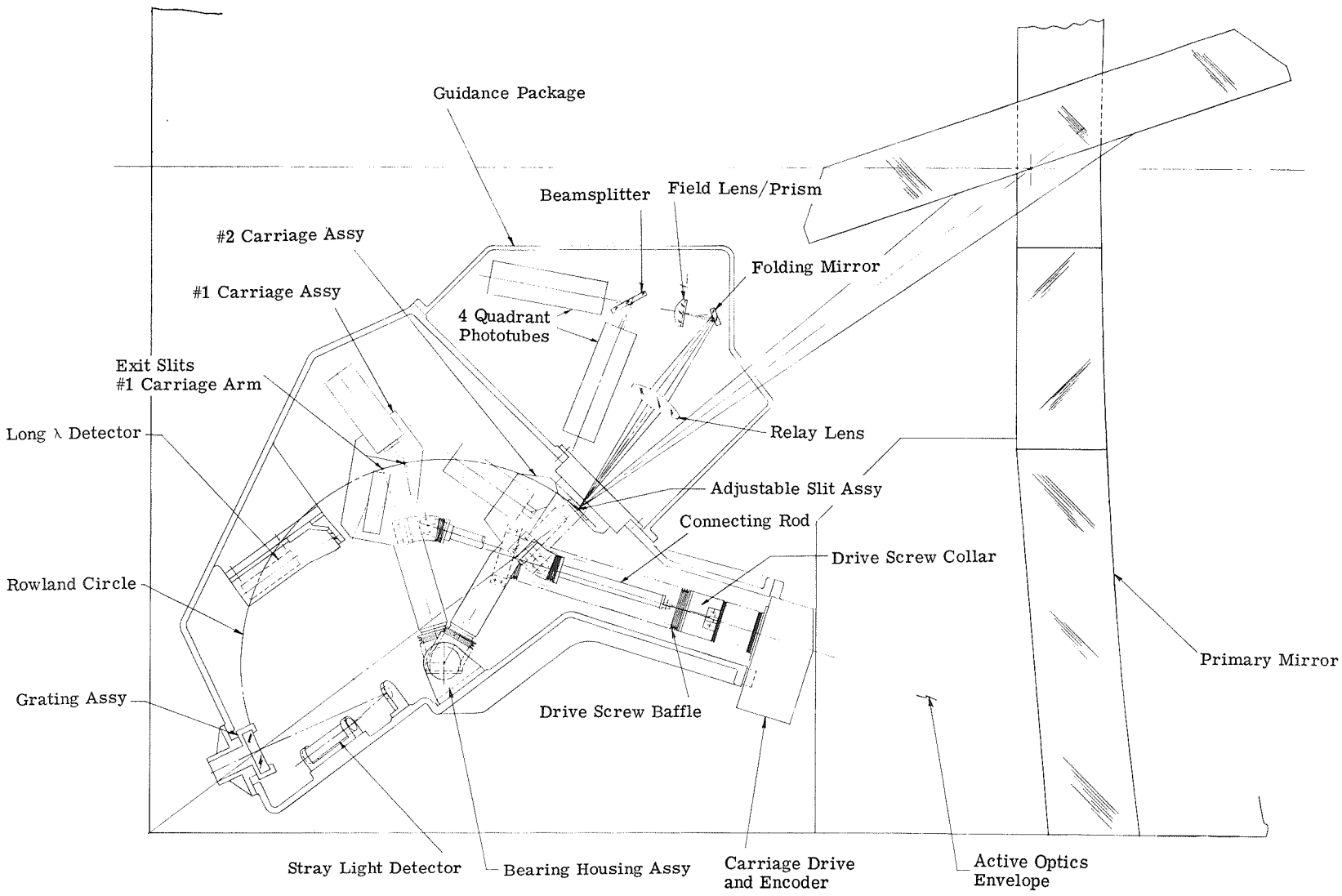

Figure 51 . LTEP Rowland Circle Spectrograph

Each arm is activated by a drive screw coupled to the arm by a collar and connecting rod. The main bearing, one of the connecting rod joints, and the drive screw are sealed in a bellows assembly which contains a lubricant under a low pressure inert atmosphere. As the collar is driven from one end of the lead screw to the other, the bellows on one side expands and the bellows on the other side contracts. The joint between the connecting rod and the screw collar is simply a flexible steel spring.

In the OAO-C spectrometer, the entrance slit and the exit slits on carriage No. 1 are about 25 microns wide, yielding about a 0.1Å resolution with a 1-meter radius grating. The slit widths on carriage No. 2 are four times as large, making it more useful for spectrographic survey work. In the event that the optical system should fail to produce suitably small images, or if it becomes desirable to sacrifice resolution in favor of speed, then the entrance slit may be opened to match the second set of exit slits. In this case, some defocusing may also be necessary so that part of the image is returned to the guidance system. The space envelope in the LTEP package requires a reduction in the size of the Rowland circle from 1 meter used in OAO-C to about 60 cm. This also reduces the resolution proportionally. However, it is probably preferable to suffer reduced resolution rather than the high absorption and scattering losses attendant upon folding flats. The decrease in size, and also the thermally isolated position of the spectrometer behind the primary mirror, help to reduce the thermoelastic deformations in the spectrometer structure, which must be kept to a very low level if the inherent resolution is to be achieved. The main sources of error are believed to be irregularities and wear in the drive screw and thermal effects from the drive motors.

The long wavelength and stray light detectors shown in Figure 51 are typical examples of peripheral instrumentation, which may be added to this type of equipment to enhance the data acquisition capability. Monitors centered on lines of astronomical interest can be used to extend the spectral coverage on either side of the nominal range covered by the spectrometer. The stray light monitor detects both the scattered radiation and the penetrating radiation components which might otherwise prove misleading. With this type of instrument it is also possible to incorporate calibration sources which can be scanned periodically to ascertain changes caused by wear or material instabilities.

The guidance sensor associated with the LTEP spectrometer is very similar to one half of the pointing system employed in the f/10 imaging system (Module C) and the echelle spectrograph (Module D). The faces of the entrance slit are highly polished and tilted slightly with respect to each other so that they act like one of the prisms in the pointing star divider assembly. If the stellar image falls on one side of the slit, it passes through the pointing system and falls on a corresponding side of a four-quadrant image tube. A relay lens provides a second focus where a prism oriented at right angles to the slit direction splits the image into up and down direction components which also have corresponding quadrants on the image tube. The pointing electronics sequentially samples each phototube quadrant and compares opposing halves to derive the pointing signals. A beamsplitter and second phototube provide redundancy in the event of a phototube failure.

RELIABILITY CONSIDERATIONS

Figure 52 presents a functional block diagram of the active optics system. In a 20-inch deformable mirror system or in a seven-segment mirror system there would be 19 or 21 channels of control electronics, respectively, required to operate the system.

Studies have shown that up to half of the actuator channels can fail before the imagery degrades to a point where the system has failed its mission. This is of course dependent upon the pattern of the failed actuator channels on the mirror matrix. There is also compensation and interaction from adjacent unfailed actuator channels which tend to cancel out the effects of a particular single actuator failure.

In systems where there is so much interaction, loading and compensation among the various components it is often difficult to formulate a reliability model. It therefore becomes necessary to analyze the system to determine the component failures that are critical to system operation. Critical components are those for which a single failure renders the system inoperative. In the case of certain components a single failure only degrades system performance and these components must be considered critical only when they fail in pairs, triplets or n-tuples.

In the system shown in Figure 52 the critical single point failures are the laser and the scanning detector.

Perkin-Elmer is currently developing a space-qualified laser which has operated for 11,000 hours before failure of the cathode. As development of this laser continues it is expected that longer laser life will be attained. If we assume that this point estimate of one sample is the present MTBF of the laser and we installed redundant cathodes we could expect an MTBF of

$$M_{redundant} = \frac{3M}{2} = 16500 \text{ hours}$$

The scanning detector presently used is an image dissector television camera. By the use of redundancy and established reliability parts the criticality of the scanning detector can be controlled so that its probability of success will be high for a lengthy mission time.

If we assume a conservative estimate of 1/3 of the actuator channels required to fail for system failure and assume that each channel is identical and independent the reliability model is the binomial distribution. That is, 14 out of 21 channels must succeed for system success. Then accordingly

$$P_s = \sum_{k=14}^{21} \binom{21}{k} P^k (1-P)^{21-k}$$

where P_s = Probability of success of the system

P = Probability of success of each actuator channel

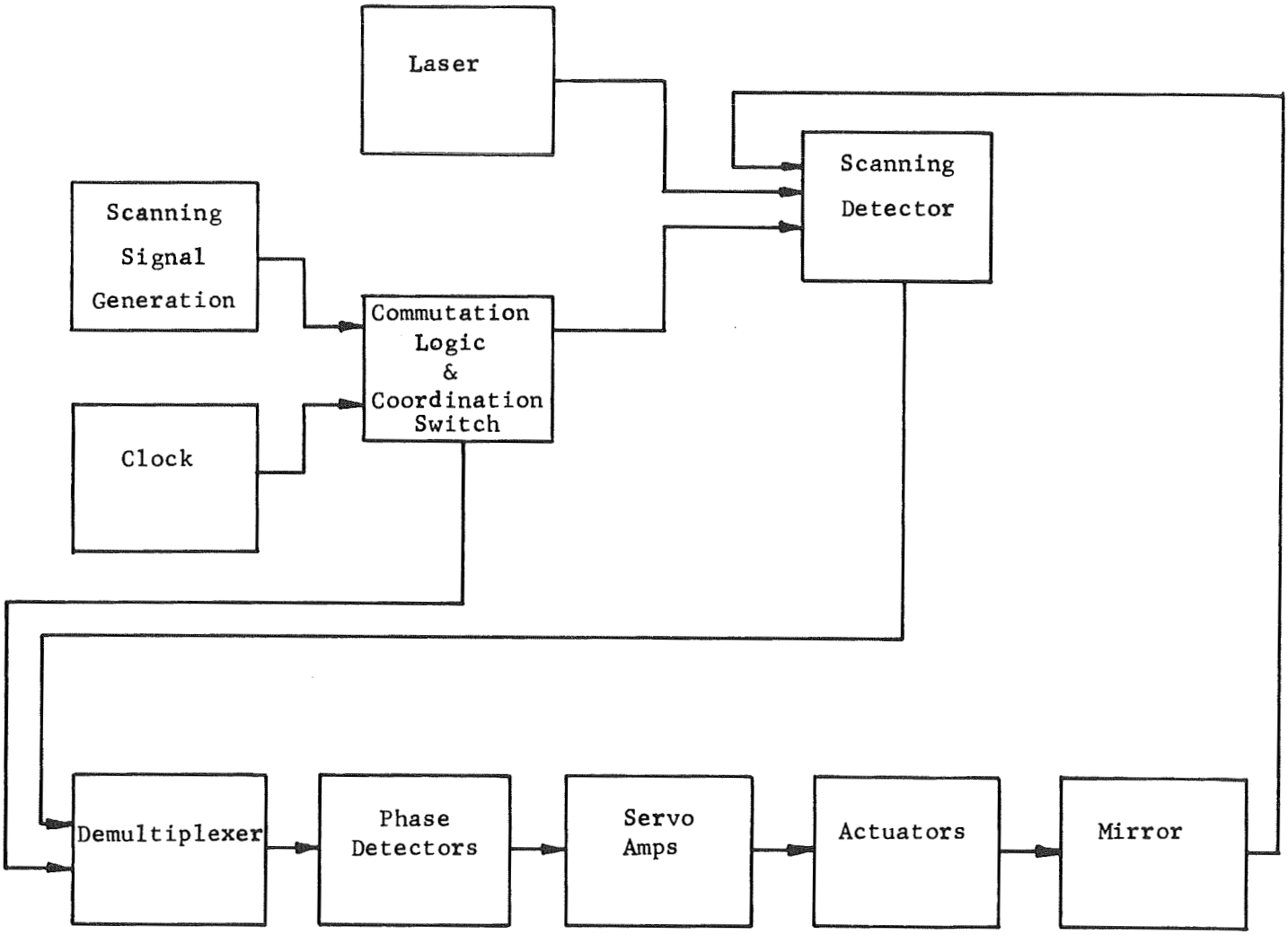

Figure 52. Functional Block Diagram - Active Optics System

Since the major parts of actuator channels are electronics, the use of screened integrated circuits and established reliability parts will make P sufficiently high for confidence in system success.

Recommendations

In order to evaluate the reliability of the system, it is recommended that a failure-mode, effect and criticality analysis be performed to single out all the critical components and effect improvement in their reliability or eliminate them altogether. A stress analysis should also be performed and corrective action implemented wherever there are overstressed or low-reliability parts in use.

The laser and scanning detector should be made redundant to increase their reliability.

The system design should be made maintainable and scheduled replacement of life-limiting items such as the laser and scanning detector should be analyzed and implemented. This will require that the system be designed so that this replacement cycle can be performed by an astronaut in space using basic tools and a minimum amount of energy.

CHAPTER 5 - OPTICAL ALIGNMENT AND TOLERANCE STUDY

It is inevitable that the primary and secondary mirrors will experience some misalignment after the telescope is in orbit and that the relative positions of these elements will change during orbit. If nothing is done about these inevitable alignment changes, the result will be defocused, comatic and astigmatic images and the performance capability of the telescope will be seriously degraded. A penalty paid for compactness in telescope length is an extremely tight requirement on the position of the secondary mirror. The tightness of the tolerances coupled with the physical size of the two-meter telescope rule out almost any possibility for a passive structure to accommodate the necessary alignment requirements.

Experience with the only existing, large diffraction-limited telescope (Stratoscope II) has indicated a definite need for inflight alignment detection and correction capability.* This need is intensified by the faster primary (an f/2 as opposed to an f/4 for Stratoscope II) and the large mirror size (80 inches versus 36 inches for Stratoscope II).

The paragraphs that follow present an analysis of the possible modes of alignment control and conclusions are drawn as to those that will be mechanized.

MODES OF ACTIVE CONTROL REQUIRED

If they are to be considered rigid bodies, both of the mirrors are limited to a maximum of six degrees of freedom relative to the figure sensor - three degrees in translation and three in rotation. In the case of a system with aspheric components, different positions about the optical axis are indistinguishable from each other for an axi-symmetrical primary mirror. The off-axis elements of a segmented aspheric primary require lateral positioning with respect to the optic axis, but these alignments are not sensitive enough to require continuous control and can be gaged mechanically. This leaves five degrees of freedom to be controlled, three in translation and two in rotation. The degrees of freedom described are not equally critical but calculations show that all of them are sensitive enough to make active control more than desirable. The degrees of control of the primary mirror, secondary mirror, and figure sensor are illustrated in Figure 53. As the secondary and primary are controlled relative to the figure sensor, it is possible to transfer some of the degrees of freedom, where convenient, to the figure sensor. Thus, the axial and lateral translation and two degrees of tilt of the primary mirror relative to the figure sensor are most conveniently managed by tilting and translating the figure sensor with respect to the primary.

*McCarthy, Daniel: Operating Characteristics of the Stratoscope II, Balloon-borne Telescope. I.E.E.E. Transactions on Aerospace and Electronic Systems, Vol. AES 5, No.2, March 1969.

Figure 53. Degrees of Freedom for Alignment

SECONDARY ALIGNMENT

The front surface of the secondary mirror cannot be used directly for alignment to the phase measurement interferometer with the present figure sensor scheme. An alignment surface must therefore be generated on the back of the secondary mirror to intercept a portion of the test wavefront from the figure sensor. The problems of determination of the optimum figure of this alignment surface, the interference technique for sensing misalignment, and the data reduction technique for producing alignment signals are presently being investigated and experimentally verified at Perkin-Elmer under NASA contract. The design employed to implement the proposed secondary control system will draw on the results of this program. Several novel methods are being considered. A relatively straightforward approach (Figure 54) consists of an almost parabolic secondary alignment surface that returns the wavefront from the figure sensor back through the same null corrector used to accommodate the aspheric primary mirror, such that it returns to a focus at the focal point of the interferometer decollimating lens when the secondary is aligned properly. The image of the secondary at the output of the interferometer is monitored to determine the phase of the returning wavefront from several different points of the secondary alignment surface. Three points that do not lie on a straight line provide information to determine orientation of the secondary mirror in tilt; another point is required to provide information about axial translation and two additional points can provide information about the two degrees of lateral translation.

PRIMARY LATERAL ALIGNMENT

The techniques of alignment of the primary mirror in tilt and axial translation have already been developed in the previous Active Optics programs. Because of the relative sizes of the primary mirror and the figure sensor unit, it is much more convenient to tilt the figure sensor rather than translate the primary mirror to correct for lateral mispositioning of the primary with respect to the secondary mirror. For the same reason, requisite tilt and axial translation of the primary mirror, with respect to the figure sensor, are also corrected at the figure sensor. This leaves only segment actuation to be accomplished at the primary mirror, so that the primary mirror, wide field correction elements, and focal plane instrumentation can be fixed to a common frame in company with a minimum number of mechanical displacement devices.

Thus, by considering the primary mirror as the system reference, all of the necessary alignment adjustments can be made at the figure sensor and secondary mirror.

The optical arrangement of automatic lateral alignment of the secondary mirror is shown in Figure 55. The Twyman-Green Phase-Measuring Interferometer requires a change in the lenses (Lenses 1 & 2) located in the collimated laser beam with the diameter no greater than the equivalent obscuration of the secondary mirror.

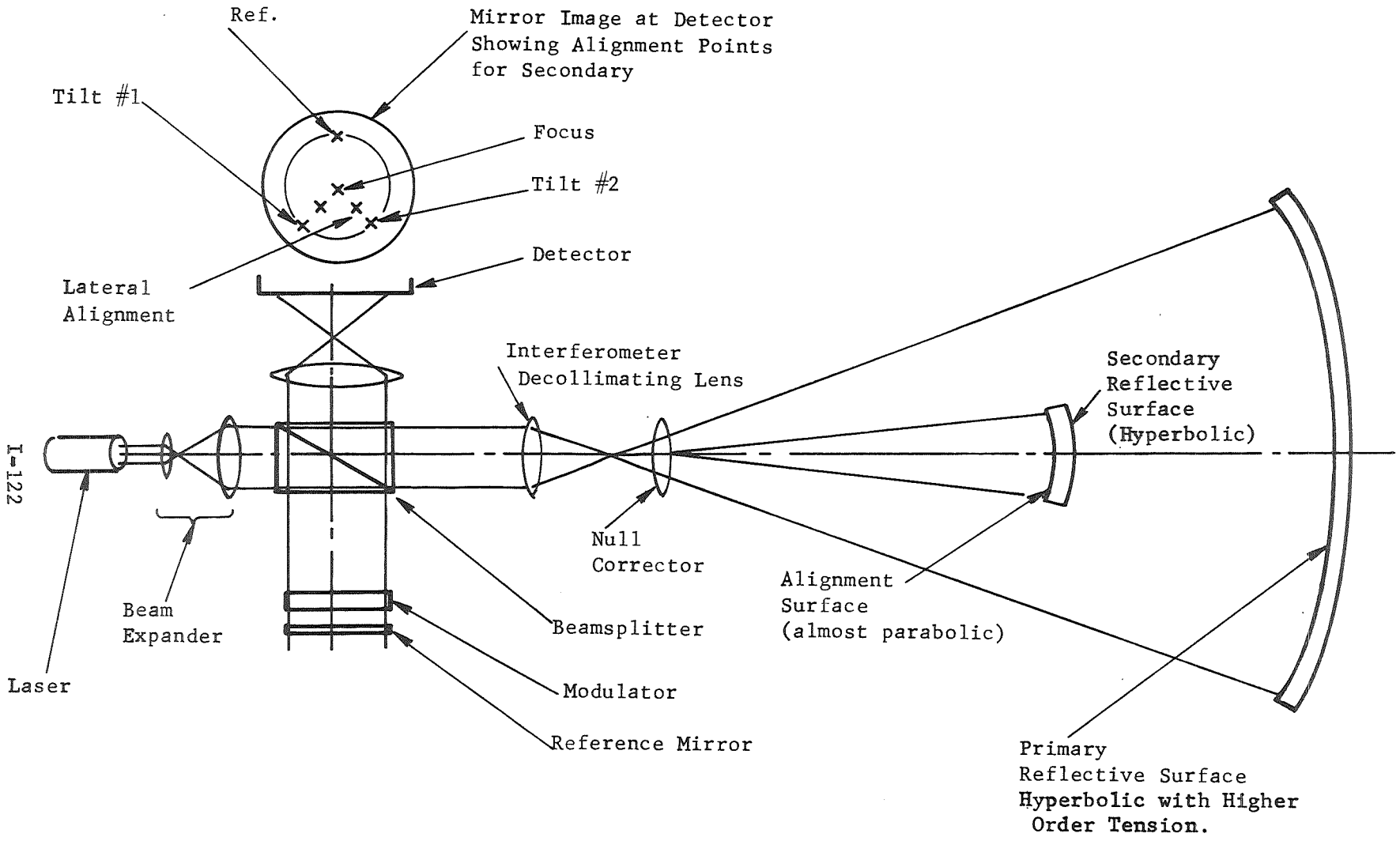

Figure 54. Secondary Mirror Alignment Detection Arrangement

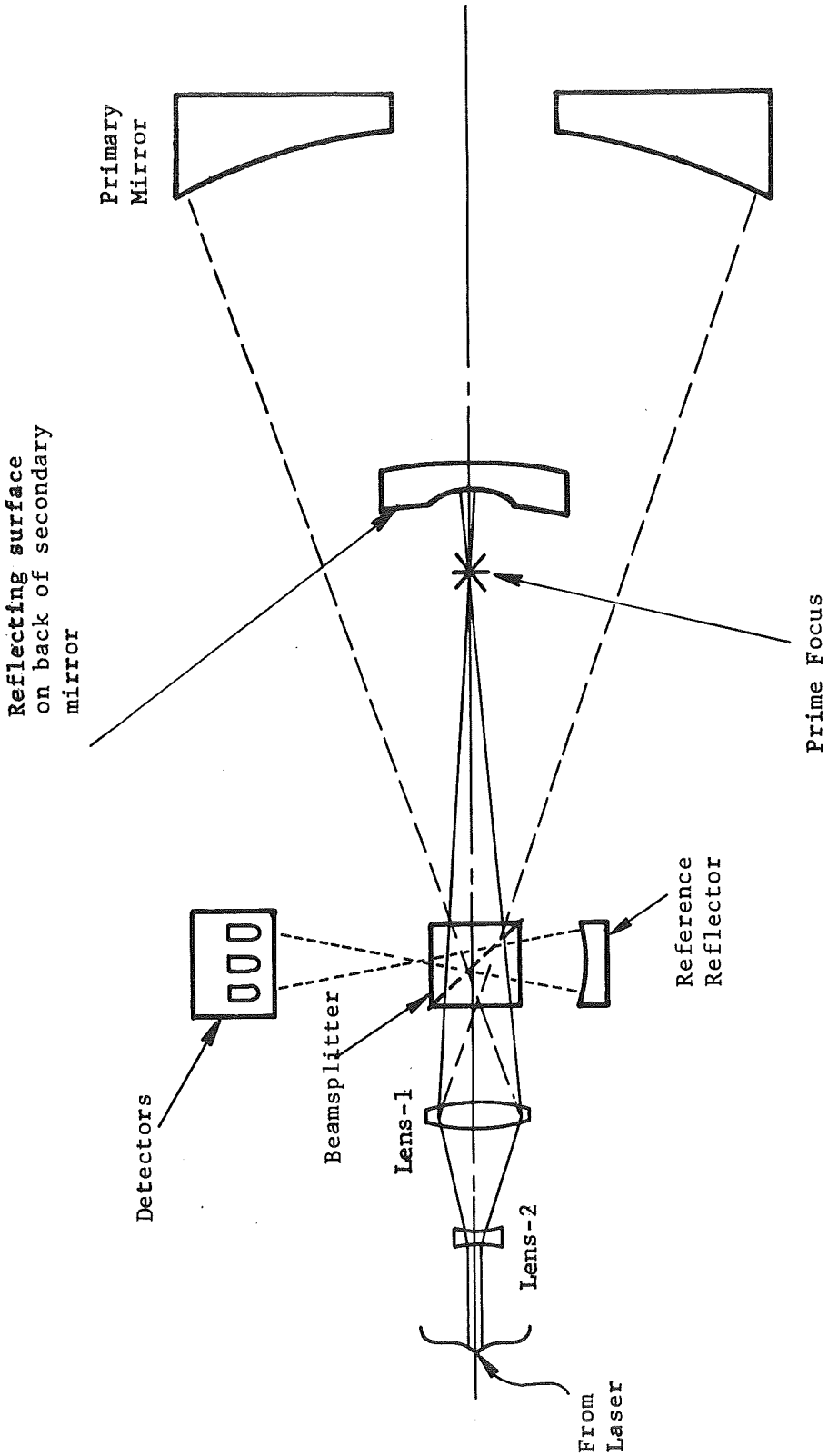

Figure 55 - Optical Arrangement for Measuring Secondary Mirror Misalignment with the Figure Sensor

The lenses will make the central p tion of the laser beam converge at the prime focus of the primary mirror. The spherical surface added to the back of the secondary is designed with its center situated at the prime focus. The figure sensor then measures the lateral displacement of the spherical mirror relative to the prime focus. (Note that the lateral translations of the secondary manifest themselves as tilt errors at the figure sensor.)

The geometry illustrating this concept further is shown in Figure 56 using a Cassegrain telescope. Rays arriving at the telescope from a remote on-axis point source will be converted by the primary mirror into a wavefront that converges at the prime focus. The secondary mirror then relays the point source from the prime focus to the Cassegrain focal point. To perform this function accurately, secondary focus must remain aligned with the prime focus. Studies conducted during the Stratoscope II Project showed that all other factors are of secondary consequence compared to this requirement.

Aspheric considerations are not necessary in this case. The mirror, which is mounted on the secondary, and the reference mirror are both spherical, resulting in common fringe patterns.

The alignment of the secondary rear spherical mirror to the optical axis of the hyperbola is required to be set and maintained to within the specified tolerance. Figure 57 summarizes this and the other alignment tolerances for the Ritchy-Chretien system.

Typical values obtained in an analysis of this system show that a secondary lateral displacement of 0.0012 inch causes approximately a full wavelength (1λ) of relative tilt in one beam of the interferometer. This is well within the sensitivity of the figure sensor.

Two peristaltic actuators, one for each axis, drive the secondary mirror in X and Y lateral directions.

LONGITUDINAL (FOCUS) ALIGNMENT OF THE SECONDARY MIRROR

As mentioned previously, the longitudinal alignment of the secondary mirror must be held to ±1 micron. This statement is true for an axially fixed focal plane. Focus of the telescope can actually be accomplished in two ways: by moving the secondary mirror or by moving the focal plane axially. Motion of the secondary mirror is much more sensitive than motions of the focal plane, being related by the square of the optical magnification of the secondary mirror. Thus, if the secondary magnification is ten, the ±1 micron tolerance at the secondary translates to ±100 microns at the focal plane. If both the secondary mirror and the focal plane were adjusted simultaneously for best focus, diffraction-limited imagery would be possible over a fairly wide range, perhaps as large as 0.2 to 0.3 millimeter at the secondary. It is evident, therefore, that only one adjustment capability need be provided, and because of the

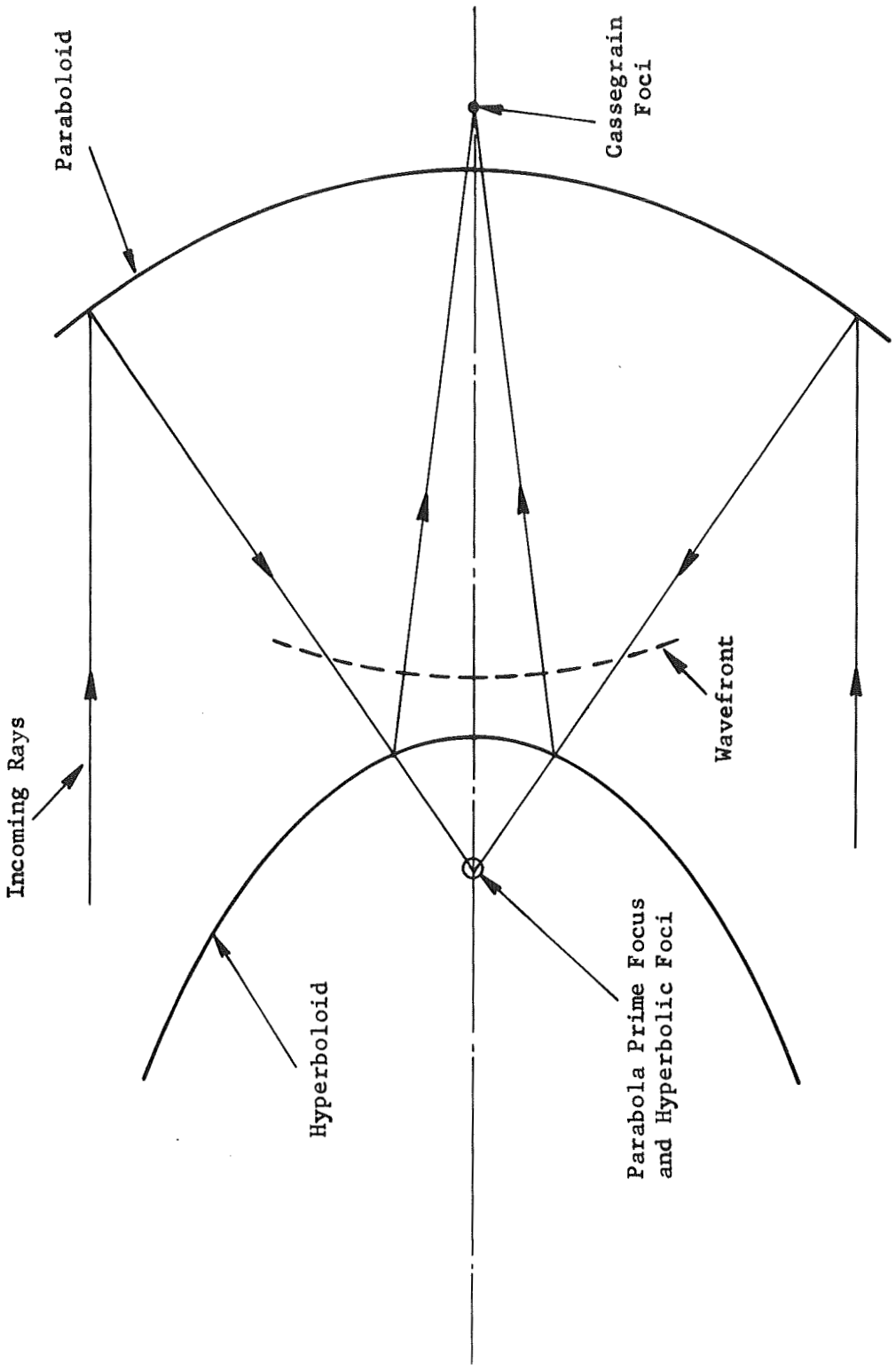

Figure 56. Geometry of Secondary Mirror Alignment Showing Coincidence of Primary Prime Focus and Secondary Foci for a Cassegrain Telescope System

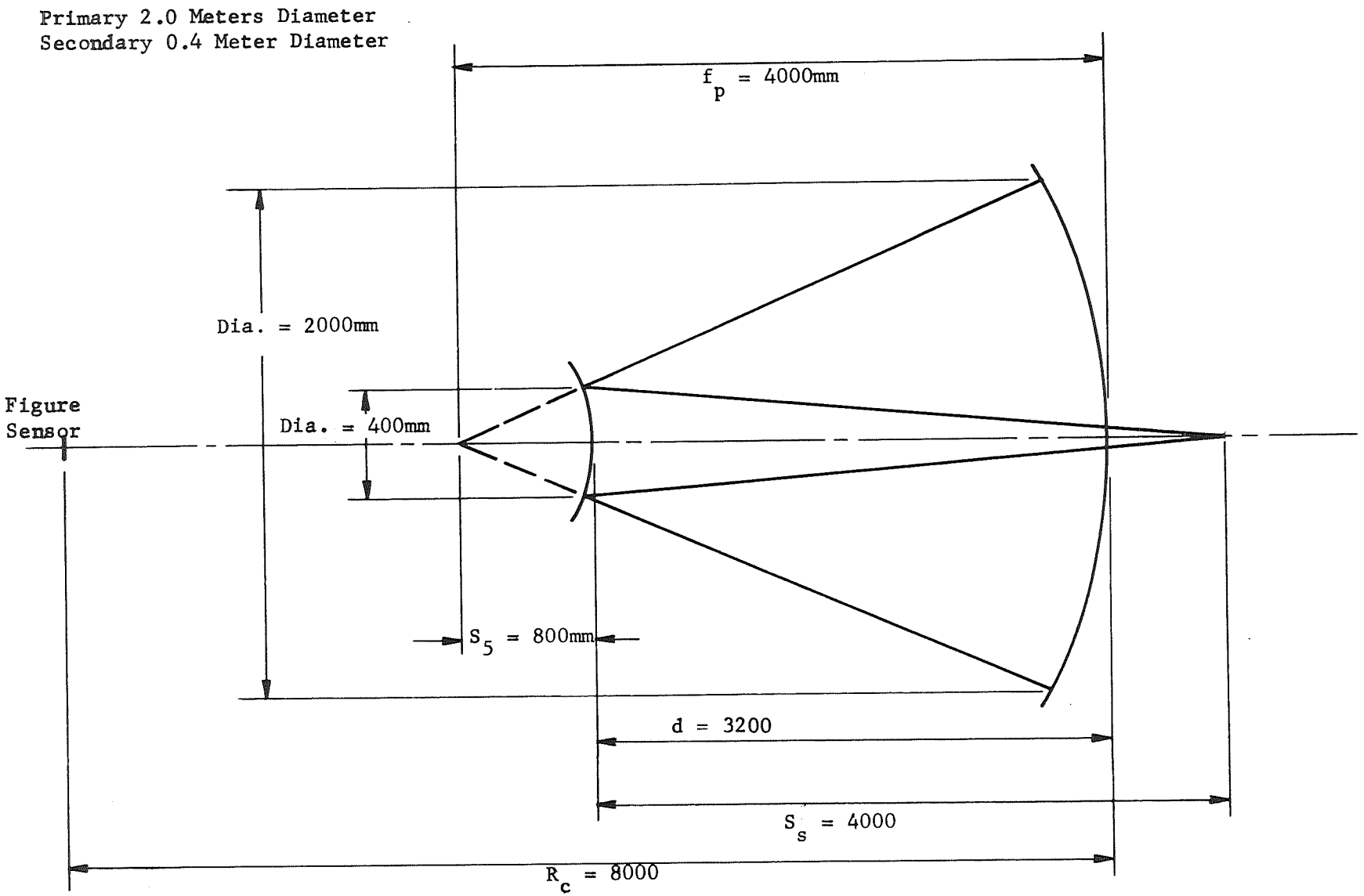

Figure Sensor	Secondary Mirror	Primary Mirror
2 Lateral Translation-$\lambda/6$	2 Lat. Transl. $\pm$ 20μ	Rotation
1 Axial Translation-$\lambda/2$	1 Axial Transl. $\pm$ 1μ	14 (2 per Segment)
2 Rotation-2.4×10^{-5}Rad.	2 Rotation-5×10^{-5} Rad.	$\pm \lambda/50$

Figure 57 . Basic Optical Alignment Tolerances

potential difficulty in adjusting a large sensor package at the focal plane (compounded by multiple instrumentation), the adjustment of focus at the secondary mirror is attractive, particularly since drive capabilities must already be incorporated into the secondary mirror assembly for lateral alignment.

Sensing of longitudinal alignment of the secondary mirror using the figure sensor is not feasible, unfortunately. This was shown in Perkin-Elmer Report No. 9575, prepared for NASA E.R.C. on January 13, 1969, titled "Interim Report - Advanced Figure Sensor". This report shows that a 0.005-inch axial misalignment produces a figure sensor signal of only $\lambda/50$. An axial alignment requirement of ±1 micron (±0.00004 inch) would produce only $\pm\lambda/5000$ of interferometer signal, clearly not usable.

An independent means of sensing best focus (or primary-secondary axial alignment) must be incorporated. Operating experience for two systems for achieving this already exists: one is the In-Flight Alignment (IFA) system of Stratoscope II, and the other, the Telescope Alignment System (TAS). The IFA system produces a graphical cross section of the image at the final focal plane for operator analysis; the TAS makes an optical measurement of the relative positions of primary, secondary, and focal plane, and provides a null signal when the optics are at a pre-determined relative distance. The TAS system lends itself to servo control, but does not necessarily optimize the imagery. The IFA system would be much more complicated to automate, but a skilled operator is able to check lateral alignment (by observing asymmetry in the image profile) as well as to optimize focus. It is assumed that the users will wish to participate in the focusing operation, and the TAS will supply valuable independent monitoring data on the operation. The TAS system description follows. A description of the IFA-system will be found in Appendix F.

CHAPTER 6 - GENERAL ANALYSIS OF THE PERFORMANCE LIMITATION OF THE TELESCOPE ALIGNMENT SYSTEM AUTOFOCUS DEVICE

The Telescope Alignment System (TAS) generates a signal which indicates the amount and direction of focus error in an optical system. The mechanization involves the transmission of light from a desired image plane within the optical system, out into object space where it is retroreflected by two penta prisms back through the optics to the image plane. At correct focus, the transmitted image and the returned image are superposed at the desired image plane and a null signal is generated. Figure 58 shows the general hardware arrangement and light paths corresponding to a focused condition. The arrangement is a balanced one wherein light from two images is transmitted from the nose of a slit prism in opposite directions around the indicated optical paths. At correct focus the light from source number 1, modulated to produce a square wave output, reforms an image at the nose of the prism as does light from source number 2 which is modulated at 180 degrees relative phase to source number 1. The detectors view light coming from the reflective sides of the roof prism which under focus conditions receive nominally equal amounts of diffraction spill-over light from each image. Since the sources are modulated out of phase, each detector thus receives a small amount of dc light.

Defocus is detected by sensing the lateral separation of the two images which exists ahead of and behind focus. This is illustrated in Figure 59 which delineates inphase light (by lines slanting up and to the right) from out-of-phase light (by lines slanting up and to the left). Figure 60 indicates how the detector light balance is affected by misfocus with, for example, detector 1 receiving more inphase than out-of-phase light in the ahead-of-focus condition. Since detector 2 receives more out-of-phase light under the same focus conditions, the detector output signals may be subtracted to obtain net focus error signal in electrical form.

The TAS principles as previously described have been utilized to control the focus of an f/3 optical system. The optical arrangement (shown in Figure 61) and associated electronics, including source lamp balance and source intensity (AGC) control circuits, were designed for long term use in hard vacuum (orbital application) and exhibit a signal-to-noise ratio of 500 per root cycle. Here the signal is that corresponding to about an eighth wave ($\frac{\lambda}{8}$ at 0.9μ) aberration criterion while the predominant noise source was found to be the Johnson noise associated with the detector load resistor.* The following paragraphs present an analysis of the focus performance limit imposed by noise on a general optical system employing the aforementioned techniques.

DERIVATION

Signal and Signal-to-Noise Ratio Required

The first step in the analysis will be the approximation of the sensing scale factor; that is, the amount of signal generated per unit departure from perfect focus. Assuming that images are uniformly bright, the lateral displacement, d_y of the center of illumination can be expressed as

*Signal preamplifier noise was not considered

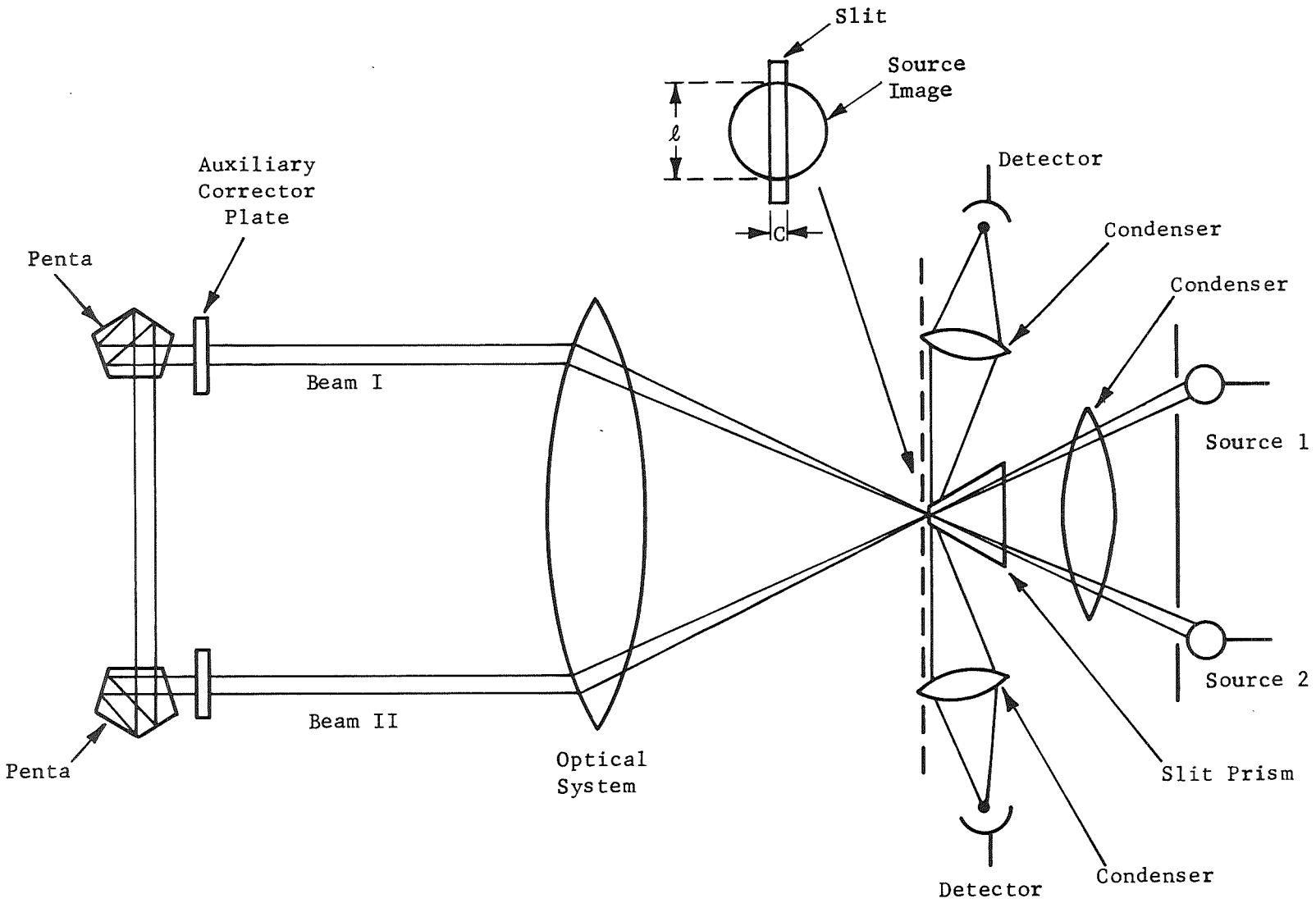

Figure 58. Telescope Alignment System - Schematic

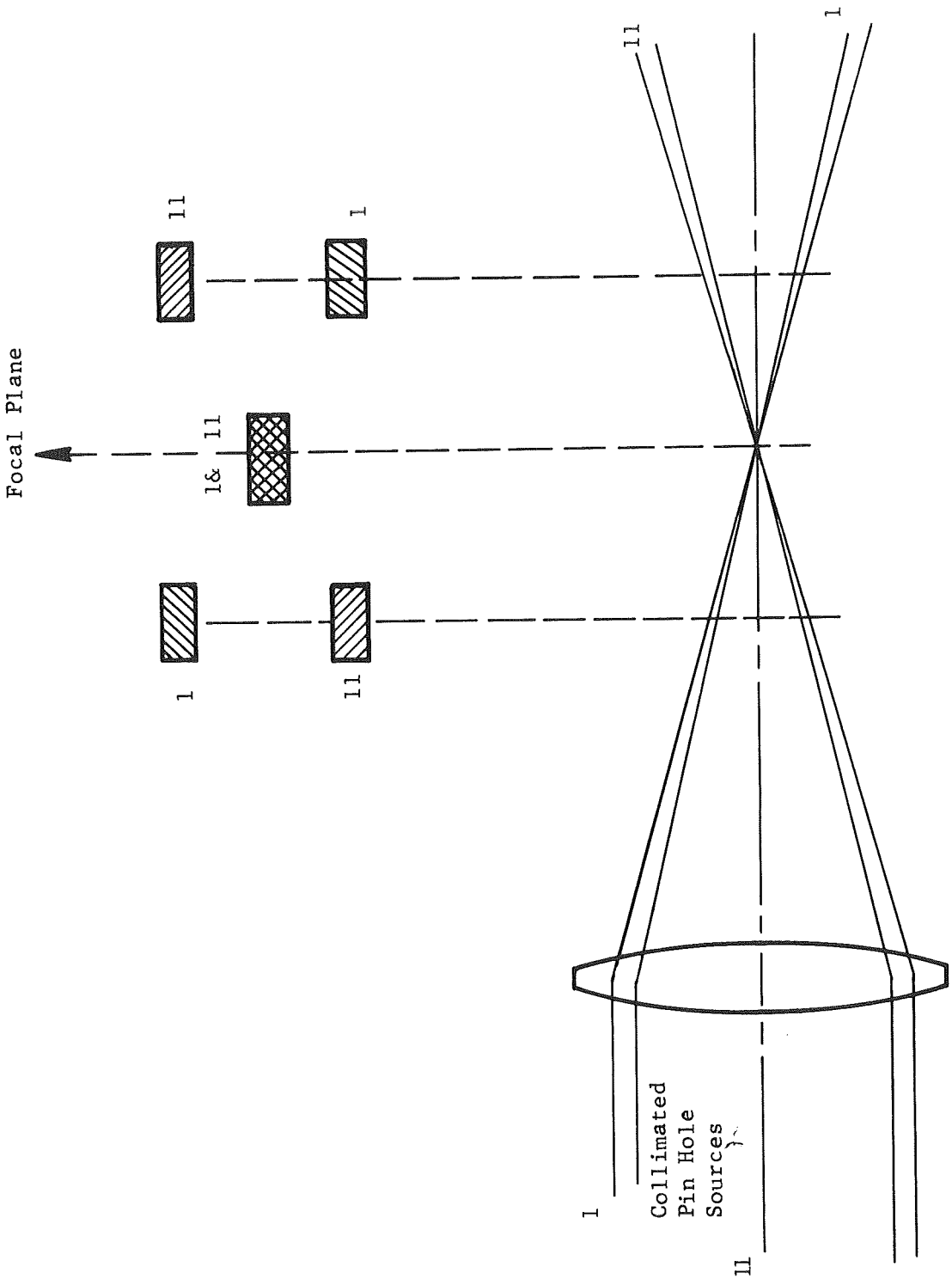

Figure 59 . Lateral Image Separation

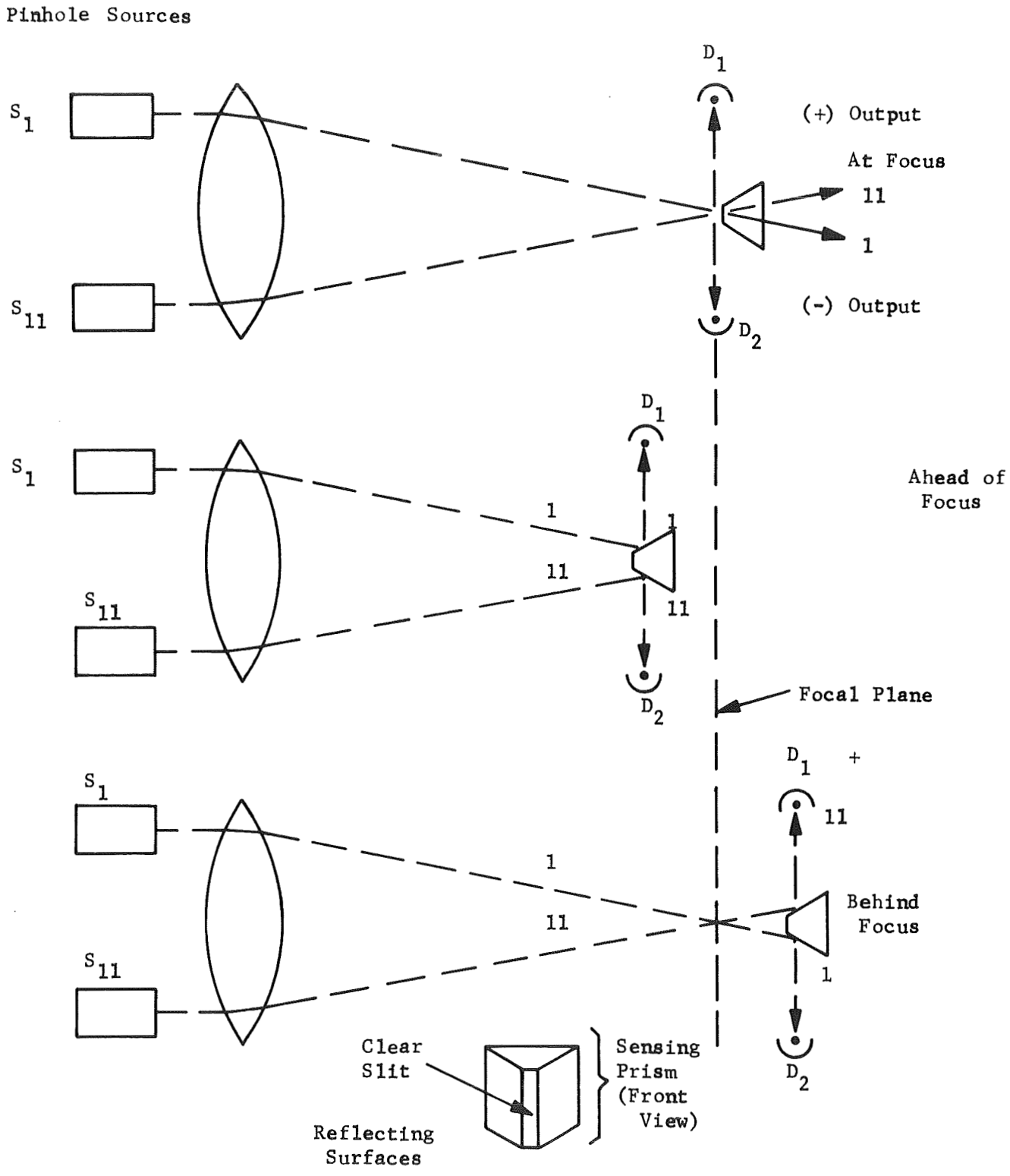

Figure 60. Detection of Out-of-Focus Conditions

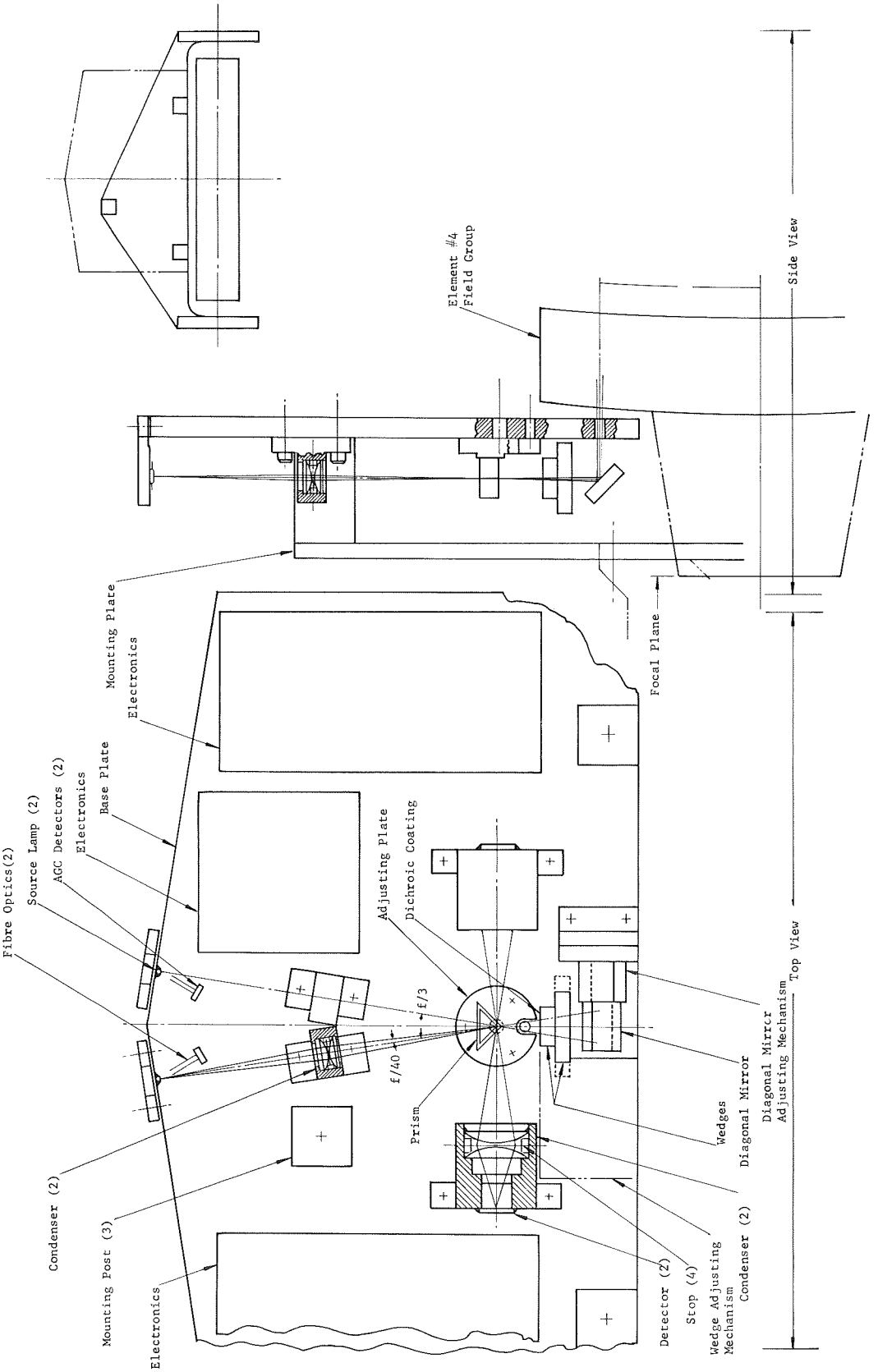

Figure 61. Sensor Optical Schematic

$$d_\ell = \delta \frac{D_{a/2}}{D_a F} \qquad \text{(refer to Figure 62),}$$

where δ is the distance between the in-focus position and the focus position being considered. The distance between the prism and the perfect image plane which results in one half the light falling on the reflecting side surface of the prism is then approximately that for which

$$d_\ell = C/2$$

or

$$\delta\left(\frac{D_{a/2}}{D_a F}\right) = \frac{C}{2}$$

or

$$\delta = CF$$

If we now assume that the signal magnitude is linear with displacement, then the signal scale factor will be such that sensor saturation occurs at $\delta = 2CF$.

Figure 63 illustrates that a shift of the prism nose from the infinity focus position by an amount CF will result in a displacement $\delta = 2CF$ between the prism nose and the reimaged light. This occurs basically because the light traverses the system twice and the lateral, and therefore traverse, magnification is essentially unity. It is thus concluded that the scale factor is such that the full or maximum signal would be generated when departure from infinity focus is CF.

Let us now express the maximum magnitude of the electrical signal as a function of system parameters: i.e., the source irradiance times the solid angle subtended by the penta times the illuminated area of the slit prism nose times the optical system transmission from source to detector times the detector conversion factor: i.e.,

$$S_e = 2\, C\ell I_s \frac{D^2 \frac{\pi}{4}}{(D_a F)^2} \, TK \qquad (1)$$

Where:

- $C \times \ell$ is the illuminated area of the slit prism nose
- I_s is the source brightness
- D_p is the penta aperture diameter
- T is the optical transmission
- K is the detector conversion factor
- D_a is the main aperture diameter
- F is the system f-number

and where the factor of 2 is introduced to account for the use of two sources.

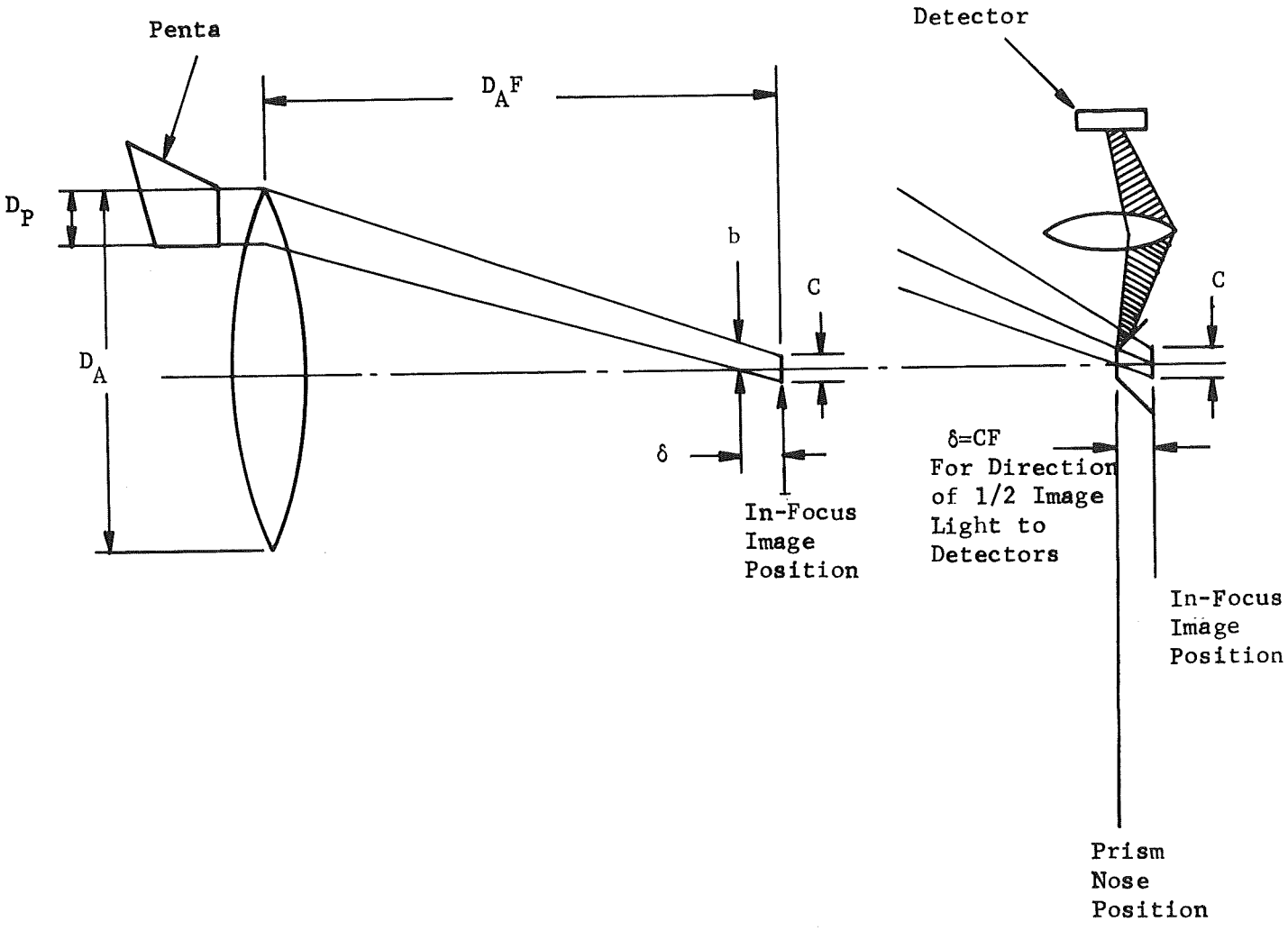

Figure 62. Sensor Image Geometry

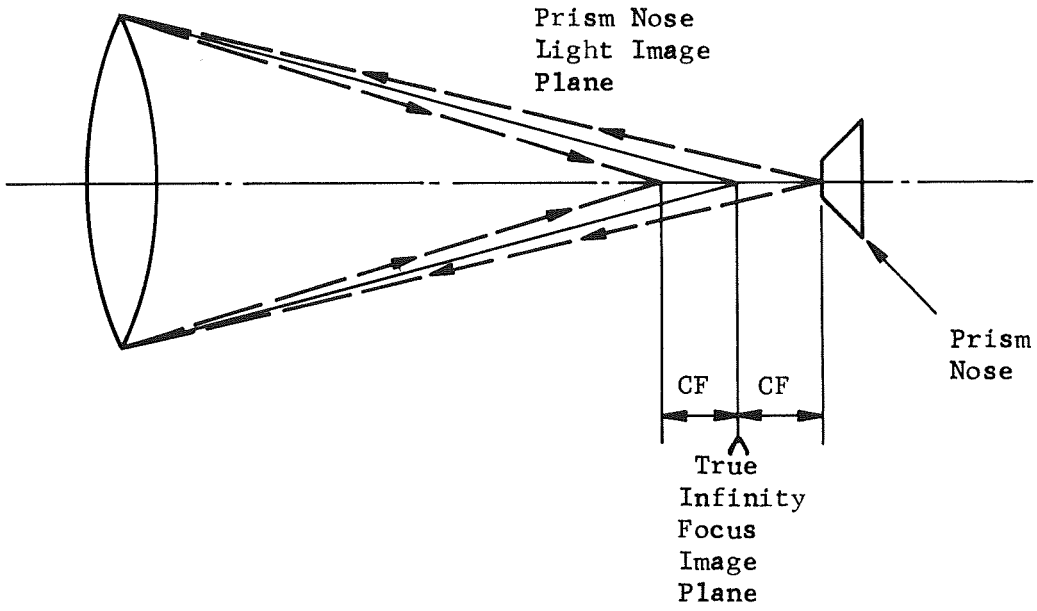

Figure 63. Defocussed Image Geometry

The sensing signal scale factor, detector current per focus shift, is thus

$$\frac{S_e}{CF} = \frac{2\ell I_s D_p^2 \frac{\pi}{4} TK}{D_a^2 F^3} \qquad (2)$$

The allowed maximum defocus error, on the other hand, can be expressed as

$$E_{max} \triangleq \frac{8\lambda_R}{n} F^2$$

where λ_R is the wavelength of the data field radiation (viz, approximately 0.1 micron when viewing stellar ultraviolet sources)

and n is selected in accordance with the optical degradation considered acceptable (i.e., n = 10 for 1/10 wave performance)

The signal corresponding to this amount of defocusing is then

$$\frac{S_e E_{max}}{CF} = \frac{16\ell I_s D_p^2 \frac{\pi}{4} TK \lambda_R}{n D_a^2 F} \qquad (3)$$

It may also be stated that the minimum signal-to-peak-noise ratio required in the system is

$$\frac{S}{N_p}\Big|_{min} = \frac{CF}{\frac{8\lambda_R}{n} F^2} = \frac{CN}{8\lambda_R F} \qquad (4)$$

Sources of Noise

The following sources of noise for the focus sensor shall now be discussed in the order indicated.

1. Noise in Signal
2. Detector leakage or dark current noise
3. Johnson noise of detector load resistor

The rms noise associated with the signal (Equation 1) can be expressed

$$i_{ns} = \sqrt{2eS_e \Delta f} = \frac{D_p}{D_a F} \sqrt{C\Delta f C\ell I_s \pi TKP} \qquad (5)$$

The expression includes the factor P which represents the fraction of total light falling on the detectors. P will be unity when all the light impinges on the prism sides and will take on lesser values as null is approached and more light returns to the nose of the prism.

Since the detector dark current is not modulated, only its fluctuation components will affect the sensor performance. The value of the dc dark current i_{dc} as well as the accompanying ac components i_{nd} depends upon the area of the detector, A ; i.e.,

$$\begin{aligned} i_{dc} &= K_d A_d N \\ i_{nd} &= \sqrt{2ei_{dc}\Delta f} = \sqrt{2eK_d A_d N \Delta f} \end{aligned} \tag{6}$$

where K_d is the leakage current per unit area and N is taken as two for the case of two detectors.

Theoretically, optics can be utilized to concentrate the light on the prism and allow the use of extremely small detectors. More practically, the collection optics will be limited in f-number and place a constraint on the optical reduction. The dark current estimated for PIN diode detectors is in the order of 10^{-7} amperes per square centimeter.
Load resistor noise component can be expressed as

$$i_{nR} = \sqrt{\frac{k\bar{T}\Delta F}{R}} \tag{7}$$

where k is Boltzman's constant
$\bar{T}$ is temperature in Kelvin
and R is resistance value

The value of R must be maintained low enough so that the time constant it represents when acting with stray and detector capacitances does not prevent passage of modulated signals. The PIN detector capacitance is estimated at 750 pF per square centimeter while a practical value of stray capacitance might be 20 pF.

The modulation frequency, it should be noted, is usually maintained above the frequency range where excess (or 1/f) detector noise prevails (viz, ≈100 Hz for PIN diodes).

Light Source

The light sources used in the autofocus sensor should be spectrally matched to the detectors and be sufficiently intense to provide an adequate signal-to-noise ratio in the system. In this connection it is important to realize

that sources often are limited in useful output radiation because of their inherent brightness (I_s, $W/cm^2/sr$) which cannot be increased by conventional optical means. Hence, if gallium arsenide diode emitters are used to illuminate the prism nose, the amount of potentially useful light from each will be in the order of

$$L = (15W/cm^2/sr)(c\ell) \left(\frac{\frac{\pi}{4} D_p^2}{D_a^2 F^2} \right)$$

where the first bracketed term represents the inherent brightness of a gallium arsenide source,* the second term is the illuminated area of the prism nose, and the third term represents the steradians of light intercepted by the retrodirecting pentaprisms.

Of this, the actual amount of light used depends upon the detector response and the optical transmission characteristics of the system.

Performance of an f/10 system

The arrangement of Figure 61 utilizes gallium arsenide light sources and PIN diode detectors since these components are small and reliable in a hard vacuum environment. The performance of the autofocus sensor in the LTEP application where the f-number is 10 rather than 3 shall now be assessed. The assumed parameters are given in Table 13.

The allowed maximum signal current is from Equation (3)

$$\frac{SE_{max}}{CF} = \frac{16 \ell I_s D_p^2 \frac{\pi}{4} TK\lambda_R}{n D_a^2 F} \triangleq S$$

which for the assumed parameter values reduces to

$$S = \frac{16(0.25cm)\ (15W/cm^2/sr)\ (\frac{4\ in.}{80\ in.})\ (0.4)\ (0.3\frac{A}{W})\ (0.5x10^{-4}cm)}{10 \times 10} = 9\ na\ p\text{-}p$$

$$S = 9 \times 0.45 \frac{Arms}{Ap\text{-}p} = 4.05 \approx 4\ nArms$$

The noise in signal can be estimated with the aid of Equation (5)

$$i_{ns} = \frac{2D_p}{D_a F} \sqrt{e\Delta f C \ell I_s TKP} = \frac{200}{2000} \sqrt{1.6x10^{-19} C(0.25)15(0.4)(0.3)} = 27x10^{-13} C^{1/2}$$

where P has been pessimistically assumed as 1.

*Based upon T.I, type PEX1203 unit which produces a minimum of 40mw into a 130-degree cone, via a lens, from a 0.012-inch diameter region.

TABLE 13

ASSUMED PARAMETER VALUES FOR f/10 TAS SYSTEM

Parameter	Value
λ_R, recorded field wavelength	0.5μ
n	10 ($\frac{\lambda}{10}$ criterion)
ℓ, roof prism nose length	0.1" =0.25 cm
T, optical transmission	0.4
I_s, source brightness	15 watts/cm^2/steradian
K, detector conversion factor at 0.9μ	0.3 ma/mw (PIN DIODE)
D_p, penta aperture (assume square so $\frac{\pi}{4} \rightarrow 1.0$)	4" = 10 cm
D_a, main aperture diameter	80" = 200 cm
F, f-number	10
P	1.0
Δf, noise bandwidth	1.0 Hz

On the other hand, dark current noise is in the order of

$$i_{DN} = \sqrt{2eI_D\Delta f} = \sqrt{2e10^{-7}C\ell} = 0.89 \times 10^{-13} C^{1/2}$$

This value of dark current noise is based upon the assumption that the cell is equal in area to the prism nose. While smaller cells might be used or larger cells may be required, it is apparent that, for the assumed parameters, noise in signal predominates over detector dark current noise.

Johnson noise current of a 1-megohm load resistor is expressed by

$$i_{gn} = \sqrt{\frac{4KT\Delta f}{R}} = 1.28 \times 10^{-13} \text{ amperes at } 25°C$$

The associated shunt capacitance of approximately

$$20\text{pf} \times C\ell \left[750\text{pf/cm}^2\right] \leq 207\text{pf}$$

obtained for $\ell = 0.25$cm and $C \leq 1$ cm will act with the load resistor to produce a single order lag at over 700 Hz which permits optical chopping at over 100 Hz to avoid detector 1/f noise components.

While either noise in signal or Johnson noise may predominate, depending for example upon the actual value of C, it is clear that the signal-to-noise ratio of the system is adequate even for bandwidths substantially in excess of the assumed one cycle and/or with smaller retrodirecting penta prisms.

The foregoing paragraphs describe the TAS autofocus sensor and indicate that solid state electronics including emitters and detectors offer adequate focus accuracy when operating at an f-10 image plane of an 80-inch aperture diameter LTEP telescope. This was shown to be the case for a reasonable set of assumed parameters. The general equations and approach to assessing performance when operating at even higher f-numbers have been shown from which trends can be established. For example, the maximum allowed signal (Equation (3))

$$\frac{S_e E_{max}}{CF} = \frac{16\ell I_s D_p^2 \frac{\pi}{4} TK \lambda_R}{nD_a^2 F} \text{ ; amperes p-p}$$

can be divided by the square root of Equation (1)

$$\sqrt{S_e} = \sqrt{2C\ell I_s \frac{D_p^2 \pi/4}{D_a^2 F^2} TK}$$

noise amperes rms to obtain the following equation for signal-to-noise-in-signal ratio trend as a function of parameter variations:

$$\frac{S_{pp}}{n_{rms}} = \bar{1}0 \sqrt{\frac{\ell I_s Tk}{C}} \frac{\lambda_R}{n} \frac{D_p}{D_a}$$

This indicates that "noise in signal"-limited performance is not really a function of f-number but rather will tend to remain constant. One final word of caution is that, since the derivations are based on geometric optics, both C and ℓ should be chosen to be larger than the resolution of the penta optics. Hence,

$$C, \ell > \frac{\lambda}{D_p} (D_a F)$$

where λ is the wavelength of gallium arsenide radiation.

For the preceding calculations,

$$\frac{\lambda}{D_p} \quad D_a F \approx 0.9 \times 10^{-4} \times 20 \times 10 = 0.018\text{cm}$$

which is sufficiently smaller than the assumed C and ℓ values.

CHAPTER 7 - THE TELESCOPE POINTING SYSTEM

There are significant space experimental tasks that can optimize precision pointing of large telescopes. A number of techniques for accomplishing the required milli-arc-second-range type of precision pointing have been developed, including the techniques that have been employed in balloon-borne telescopes such as Stratoscope II. Space operational experience is needed in pointing the astronomy telescope that is feasible today in order to know how to best point the giant space telescopes of the future.

It is to this end that the Large Telescope Experiment Program has determined the feasibility of a pointing configuration which embodies a number of candidate pointing techniques. These techniques have been integrated into an experimental program wherein each technique will be evaluated when utilized as the primary mode of pointing for the seven different astronomy missions. In addition to the valuable engineering and technological data which will be gathered by comparative in-space performance data, the configuration offers backup redundancy modes since one pointing technique could substitute for another in the event of failure of a single pointing experiment. Thus, the astronomy mission will be safeguarded by the multiplicity of pointing techniques.

The pointing techniques considered in this section are:

- ATM Gimbals - updated Experiment Pointing Control System (EPC) as used in Apollo Telescope Mount.
- Transfer Lens - servo-controlled optical element positioned to current pointing errors of the main telescope optical system.
- "FREE FLOAT" - Zero gravity magnetic suspension and isolation servos.
- Image plane stabilization (for roll) - servo-driven single-axis stabilization for experiment packages.

As the basis for the various pointing system analyses, the disturbances arising from spacecraft motions and electronics are first analyzed. Since the independent modes will not involve crew motions, the disturbances expected in those modes are significantly fewer than those anticipated in the AAP Cluster mode of operation. For this reason, only the Cluster configuration is studied under "disturbances". This section is followed by a discussion of the performance requirements for the various scientific instrumentation packages. Finally, the mechanization of the pointing configuration is discussed in detail.

SPACECRAFT - INDUCED DISTURBANCES

The LTEP pointing control system will consist of several major subsystems that must be mutually, comparably, and appropriately designed if required performance is to be achieved. The spacecraft attitude control, in either clustered or autonomous mode (refer to Figure 64), will be provided by the ATM rack Control Moment Gyro (CMG) subsystem. This subsystem provides coarse pointing during acquisition and track modes and serves as a support base for the gimbal control subsystem or Experiment Pointing Control (EPC) or, alternatively, as a force reaction base for the telescope when magnetically suspended. With EPC loops operative, a piggy-back arrangement exists wherein the spacecraft motions are attenuated in amplitude but not in frequency. Spacecraft angular motions must be amplitude-limited because gimbal bearing spring constants introduce undesired torques into the EPC loops. High frequency components are particularly undesirable in this respect since the EPC loop has finite bandwidth and hence becomes ineffective at higher frequencies. The resulting telescope motions are limited mainly by the self-stabilizing effect of telescope inertia.

Disturbance torques also enter the telescope when its c.g. is not coincident with the gimbal axis intersection point if the telescope is translationally accelerated. Such motions naturally arise when spacecraft rotations are about a point not coincident with the gimbal axis. The separation between these points is not expected to be zero and, in clustered configuration, is on the order of twenty to thirty feet. Telescope translational accelerations particularly at higher frequencies, also cause bending of the telescope structure with attendant optical and pointing effects. Lateral motions of the secondary mirror with respect to the primary mirror axis, for example, will cause optical image degradation (coma) and change the line-of-sight direction. These considerations set upper limits on spacecraft motions during fine pointing.

Motions of the figure sensor, which is even farther from the primary mirror, are also undesired. While active positioning controls are contemplated to maintain these elements in precise alignment, the large bandwidths required to provide high frequency corrections are undesired.

During magnetic suspension mode, the spacecraft-induced disturbances described above are avoided but the spacecraft motional amplitudes and frequencies must still be constrained. The amplitude of high frequency translation motion determines the magnetic torquer air gap dimensions, which should be kept small to minimize weight, stray field, and required power. Low-frequency components of translation are not as troublesome, since the telescope can be translationally controlled by low bandwidth servos to maintain centered conditions. In effect, forces are applied to the telescope to translate it in unison with the local spacecraft structure. Low bandwidth is chosen to avoid high frequency forces which can introduce troublesome telescope tube bending and disturbance torques.

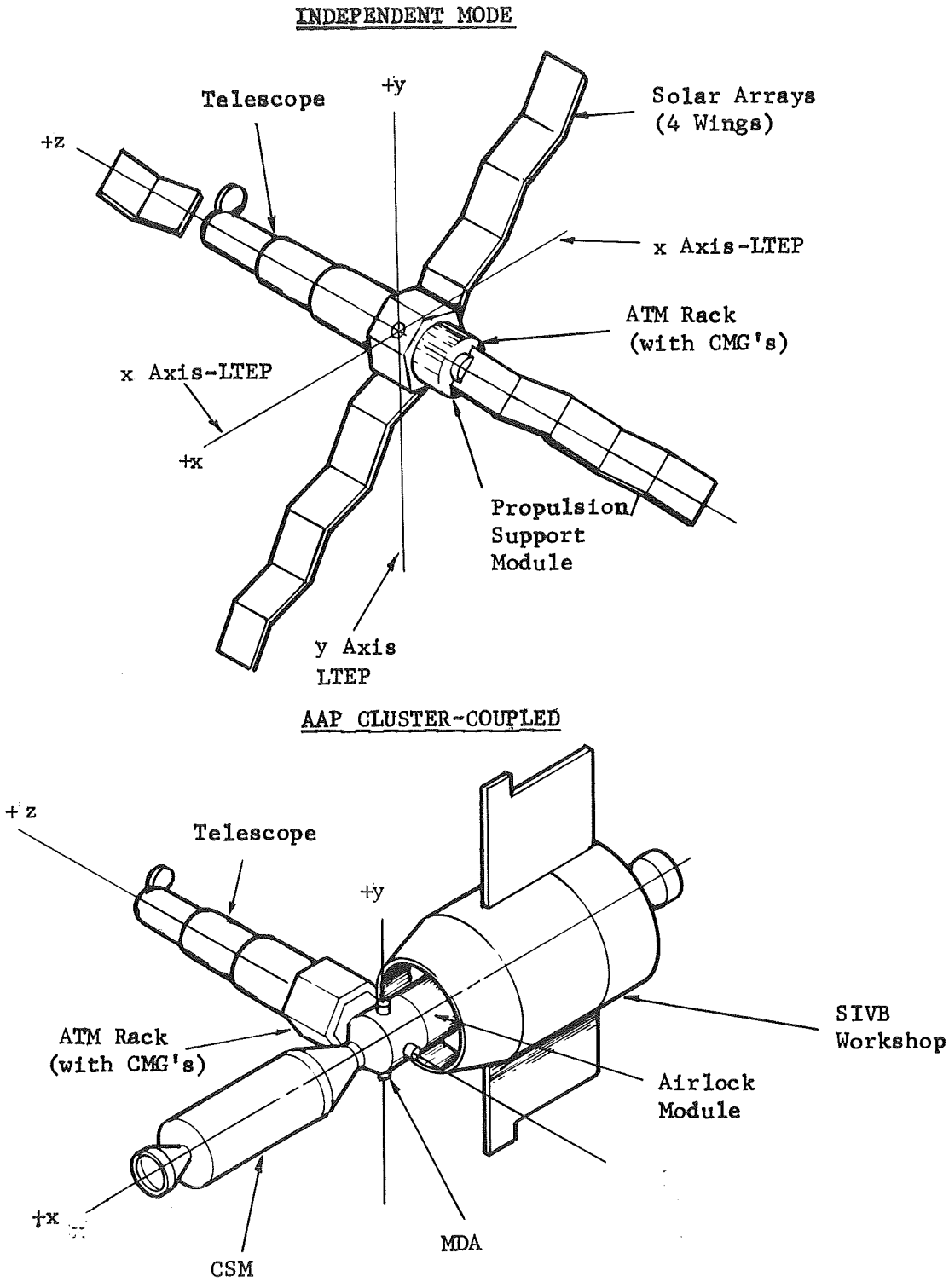

Figure 64. Configurations and Reference Axes

Hence the CMG control subsystem supports either the magnetic suspension subsystem, which has three control axes, or the EPC, which has only two (cross line of sight, CLOS) control axes. When rotation control, more precise than that provided by the CMG, is an experimental requirement when using the EPC subsystem, the equipment at the final image plane of the telescope will be rotated to compensate for roll motions as they appear. Under such conditions, it is desired that the CMG input amplitude be small to limit the magnitude of equipment motions. The component frequencies, moreover, should be limited so that rotation control loop bandwidth is limited. The noise degradation effects of the signals from the rotation error sensors, which are of the guide star image-splitting type, can thus be maintained within acceptable bounds.

The telescope will also contain transfer "lens" subsystems which can be applied to reduce the cross line-of-sight (telescope structual pointing) errors even further than is accomplished by the CMG and EPC or magnetic suspension subsystems. One obvious constraint on the latter two subsystems, then, is that their residual errors be limited so that transfer "lens" corrections are not so large as to cause excessive optical image degradations.

A basic premise in estimating spacecraft motional disturbance parameters is that they will be essentially the same as those expected for the ATM CMG subsystem. Furthermore, the performance of the existing ATM (EPC) gimbaling control subsystem was also considered representative. Moderate design changes, it was decided, would be considered for either system, if necessary, to obtain a satisfactory interface between the CMG subsystem and the LTEP telescope.

Pointing Requirements

Table 14 summarizes the subsystem combinations recommended for pointing each of the experiment modules. Subsequent paragraphs will discuss the detailed guidance requirements of each based upon estimated parameters for the LTEP baseline design.

Tables 15 and 16 present both the required and estimated performances of the EPC and CMG subsystem for ATM. The required performance values were developed to accommodate the various individual experimental packages supported by the solar-oriented spar. The estimated values, indicated in parenthesis, are results of NASA analyses made with hybrid computer simulations of the system and represent the present two-sigma capability. Pointing uncertainty components are those which are, in effect, dc or bias errors, while the stability components are those which change with time.

The CMG Stability figures include a 5.3-arc-minute error that is due to a wall pushoff cycle generated by an astronaut when pushing himself off one wall with a subsequent push to stop at the opposite wall. Other components include a 0.86-arc-minute gravity gradient error, an aerodynamic component (about one tenth

TABLE 14. REQUIRED POINTING ACCURACIES

Experiment Module	Experiment Description	Pointing Requirements* (Arc seconds rms) CLOS	Pointing Requirements* (Arc seconds rms) RLOS**	Error Sensing Means	Control System CLOS	Control System RLOS
A	-			-	-	-
B	-			-	-	-
C	F/10 Film Imagery(visible)	0.006	0.34	2 Guide Stars	(A)Free Float (B)Trans.Lens	Free Float Image Plane Rotation
D	Echelle Spectograph(uv)	0.0015	(See Note 3) ***	2 Guide Stars	Free Float	Free Float
E	Rowland Circle Spectrometer(uv)	0.006	N.A.	Target Star	Gimbals	None
F	F/50 Electronic Imagery (uv)	0.0015	0.464	2 Guide Stars	Secondary Tilt	Image Plane Rotation

*Note 1: Pointing requirements for uv-oriented experiments are based upon wavelength of 0.125μ. Pointing requirements as given are based upon 1/10 diffraction-limited resolution per each axis.

**Note 2: RLOS Requirement as stated is about the nominal line of sight.

***Note 3: RLOS Requirement is not critical if star is on axis.

TABLE 15. EPC CONTROL SYSTEM POINTING CAPABILITY 2σ

System Axis	Pointing Uncertainty	Stability for 15 Minutes
EPC X	±2.5 arc-sec (1.77 arc-sec)	±2.5 arc-sec (0.63 arc-sec)
EPC Y	±2.5 arc-sec (1.77 arc-sec)	±2.5 arc-sec (0.63 arc-sec)
EPC Z Roll Reference	±10 arc-min (±7.0 arc-min)	CMG control system

TABLE 16. CMG CONTROL SYSTEM POINTING CAPABILITY 2σ

System Axis	Pointing Uncertainty	Stability for 15 Minutes
CMG X	±4 arc-min (±2.75 arc-min)	±9 arc-min (±3.6 arc-min)
CMG Y	±4 arc-min (±2.75 arc-min)	±9 arc-min (±5.7 arc-min)
CMG Z (Roll)	±10 arc-min (±0.624 arc-min)	±7.5 arc-min (±5.0 arc-min)

that due to gravity gradient, and an acquisition sun sensor (drift) error of 2 arc-minutes. Only the crew disturbance generates high frequency error components. It is possible to reduce gravity gradient and aerodynamic error components, according to NASA engineers, by including an integrator in the CMG control electronics. Subsequent work shall assume that it is possible to thereby reduce the non-crew-induced spacecraft motions to approximately ±5 arc-seconds. It is worth noting at this point that LTEP pointing accuracy as will be discussed is not strongly dependent upon this assumption. The reason for this is twofold. First, for short exposure, the full error due to gravity gradient and aerodynamic effects will not be incurred, since their periods are 2700 seconds or more. More important, the control systems proposed for LTEP fine line-of-sight correction are such that a small bandwidth increase will allow significantly larger disturbance magnitudes to be banded. For example, a doubling of bandwidth will increase the noise-induced errors by $\sqrt{2}$ and provide disturbance attenuation increases of 4, 8, or 16 times, with the exact value depending upon the slope of the open loop gain characteristic (-12, -18, -24 dB/oct) at the disturbance frequency.

The EPC pointing uncertainty includes a ±1.2 arc-second fine sun sensor (FSS) static error, a gyro bias of ±0.248 arc-second and an ATM computer offset. The stability components include wire torque creep (0.3 arc-second), amplifier drift (0.5 arc-second), fine sun sensor stability (0.1 arc-second), and thermal gradient effect (0.5 arc-second). These figures are the estimated EPC pointing errors which appear in a 15-minute time interval. The wire torque creep term is the error introduced by torque variations with time of the wires crossing the gimbal axes and is in addition to torques arising from wire bundle spring constant. The only other source of varying error estimated is 0.2 arc-second peak amplitude induced by the wall pushoff cycle. This error increases to peak value in 12 seconds and then decays as a result of CMG and EPC corrective actions. All the EPC errors given above apply when the CMG subsystem is also operative.

LMSC estimates of LTEP expected disturbances include 0.2 to 1.5-arc-second and 25-arc-second disturbances due to crew movements. These are estimated values anticipated during clustered and autonomous configurations with both the present CMG and EPC loops operating. Solar pressure, gravity, and aerodynamic gradient torques acting directly on the LTEP telescope are reportedly about 0.62, 1.5, and 2.95 millifoot-pounds, respectively. Noise from the rate gyros (within the ATM loop) and acquisition sensors within the spacecraft control loop, although previously thought to be a major error contributor, is now reported to be effectively filtered out electronically.

The present CMG and EPC bandwidths are approximately 0.03 and 2.5 Hz, respectively. The latter bandwidth was chosen to satisfy an ATM experiment requirement to settle out all disturbances within 10 seconds of time.

Requirements for Imagery

The pointing requirement associated with film or electronic imagery is that the line of sight be stable during exposures. Static or bias errors do not result in image degradation but merely in an altered position in the format area. Such errors must simply be small compared to the format size so that the desired targets appear somewhere in the pictures. Non-static pointing errors, on the other hand smear the images and result in loss of fine detail. The pointing constraint usually imposed is to limit the overall rms motions to approximately 20 percent or less of the telescope resolution. Stratoscope II, for example, has an estimated 0.016-arc-second rms error about the cross lines of sight when guiding on ninth-magnitude stars. Assuming an equal roll axis error, the overall rms error is 0.0277 arc-second, or approximately 23 percent of the 0.12-arc-second resolution at one-half micron. It is thus seen that the allowed rms error about each axis is 13.3 percent of the telescope resolution. For the LTEP instrument where each axis has two mispointing components (random noise and sinusoidal motion or torque-induced), each component must be held to approximately 10 percent of the telescope resolution. Accordingly, the criterion followed in establishing the LTEP guidance requirements was that the rms noise should not exceed 10 percent of the telescope noise when operating on the dimmest available guide stars, and the peak amplitude of sinuosidal error should be similarly constrained. Better performance is then obtained on brighter stars since the noise-induced errors become smaller. Optimum performance in such a case is obtained, then, by increasing the bandwidth sufficiently to reduce the sinusoidal error without excessive increase in the error due to noise.

Requirements for the Rowland Circle Spectrometer

The Rowland circle spectrometer (Figure 65) places several requirements on its associated guidance system. Mispointing in the case of a single point source will cause the image to move around in the plane of the entrance slit. In the case of a small slit, the motions can cause light level fluctuations within the spectrometer. If the image moves off the slit, as an extreme example, the light at the spectrometer detectors will drop sharply. While peripheral equipment could include, say, a zero order detector whose output signals indicate required data correction, such fluctuations are clearly undesirable. Use of a large slit, on the other hand, will avoid the light loss, but the image motion will cause relative motion of the spectrum with respect to the detectors. This of course will degrade the resolution of the instrument and is equally undesired.

Operation on extended sources requires line-of-sight stability to allow good spatial resolution and permit use of small entrances to exclude adjacent and undesired targets.

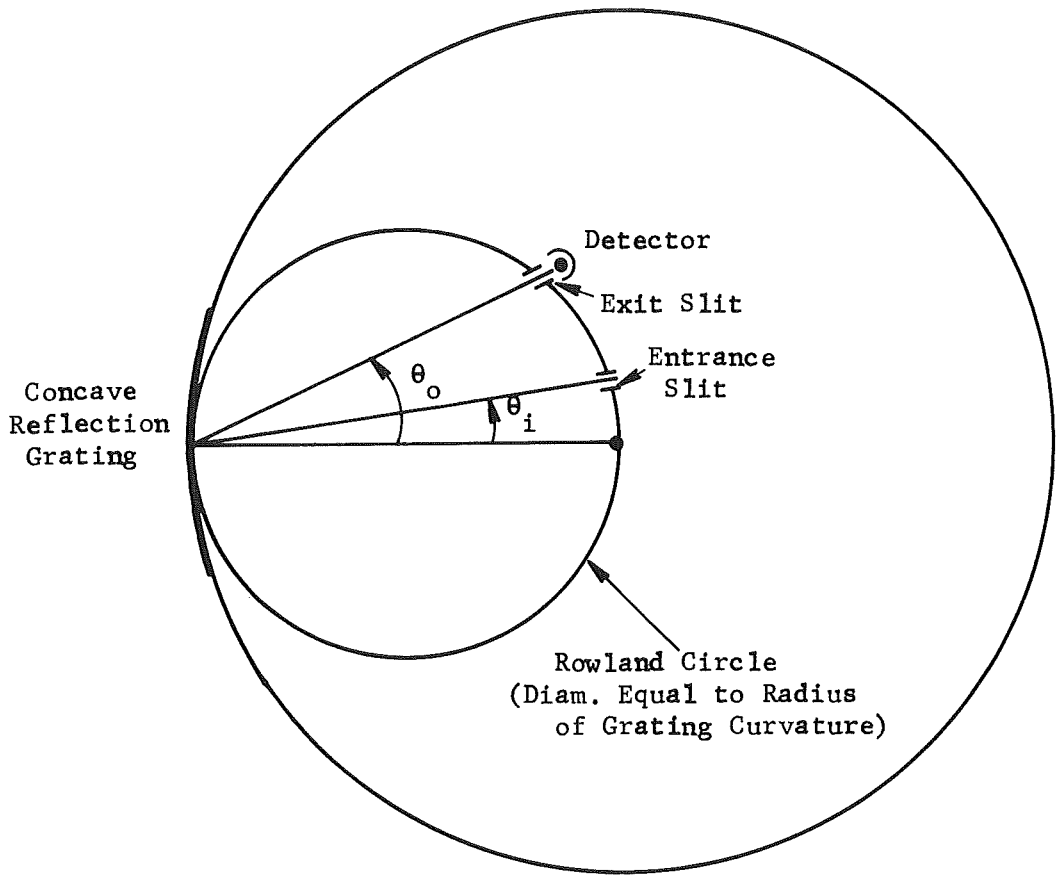

Figure 65. Rowland Circle Spectrometer

Spectrometer Operation Constraints - The Rowland circle spectrometer utilizes a reflection grating to disperse light in accordance with the relation

$$M\lambda = d(\sin\theta_i + \sin\theta_o)$$

where d = spatial distance for one grating cycle

M = order number

The curvature introduced simply acts to focus the light from the entrance slit on the Rowland circle to another point on the circle. Hence the expressions for resolving power and angular dispersion derived for flat-reflection gratings are still valid: i.e.,

$$\text{angular dispersion} \triangleq \frac{\Delta\theta_o}{\Delta\lambda} = \frac{M}{d\cos\theta}$$

$$\text{resolving power} \triangleq \frac{\lambda}{\Delta\lambda} = MN$$

where N = total number of grating cycles used

The Perkin-Elmer designed OAO-C Princeton Experimental Package utilized a 2400-line-per-millimeter grating, a 1-meter Rowland circle diameter and an f/20 bundle. The theoretical resolving power of that instrument was thus

$$\frac{\lambda}{\Delta\lambda} = MN = M\left(2.4 \times 10^6 \frac{\text{lines}}{\text{meter}}\right)\left(\frac{1 \text{ meter}}{20}\right) = 0.12\times10^6 \times M$$

which offers 0.005Å resolution at 1000Å in second order. The 25-micron entrance slit subtends an angle of 25 microradians at the grating and limits achieved resolution to 0.05 and 0.1Å in second and first orders respectively; viz,

$$\Delta\lambda = \frac{\Delta\theta_o d\cos\theta}{M} = \frac{\Delta\theta_o d}{M} \simeq \frac{25\times10^{-6}}{1\times24\times10^6} = 0.1\text{Å} \Big|_{M=1}$$

The proposed instrument with its 0.6-meter circle diameter and f/10 bundle will utilize nearly the same total number of lines of such a grating and hence have the same basic resolution. The entrance slit size, if chosen as 1.22 λ/D at, say, 0.5 micron, will be approximately 6 microns wide. This subtends 10 microradians at the grating and will lower the resolution in first (λ = 1600 to 3200 Å) and second (800 to 1600Å) orders to

$$\Delta\lambda = \frac{10\times10^{-6}}{M\times2.4\times10^{6}} = \frac{4.2\times10^{-12}}{M} = \begin{matrix}0.042\text{Å}; \text{ First Order}\\ 0.021\text{Å}; \text{ Second Order}\end{matrix}$$

Hence, this instrument will be comparable resolution-wise with the OAO-C scientific payload with slit sizes up to twice that considered above.

Pointing Performance with Slit Jaw-Reflected Visible Light - The technique of utilizing visible light reflected from the slit jaws is similar to that which uses the roof prism. (See Figure 66.) For the roof prism, the slit width is essentially zero and all the light is reflected (or directed) to the guidance photosensors. When the slit width is non-zero, this is not the case and the sensing characteristic (signal versus angle) is altered. Figure 67 shows such characteristics for various slit width sizes and indicates that the sensor scale factor (signal-per-unit angular error) at null is reduced as the slit width is increased. Pointing accuracy can be estimated for several slit widths and compared to that for the standard roof prism. This shall be accomplished with the aid of Figure 67 and a previously derived expression (refer I-257).

$$E_p = \left(\frac{\text{Linear Range}}{2}\right)\left(\frac{S}{N}\right)^{-1}$$

Here E_p is the telescope pointing error and S/N is the system signal-to-noise ratio. Linear range is the angular distance between saturated signal level ($\pm S$) intercepts obtained by a straight-line approximation to the sensor curve at null.

Results are presented by Table 17 and were computed assuming that the maximum pointing error angle never exceeds $1/4(1.22\lambda/D)$. This constraint was imposed so that sensor light level and its associated noise component would be determinable. Also shown is the guide star magnitude increment required when working with the slit to obtain the same guidance accuracy as without the slit. A reasonable slit width range for the spectrometer appears to be $1.22\lambda/D$ to $2.44\lambda/D$ since the magnitude increment is reasonable.

TABLE 17: PERFORMANCE OF SPECTROMETER GUIDANCE SENSOR RELATIVE TO ROOF PRISM SENSOR

Slit Width (λ=.5μ)	0	0.61λ/D	1.22λ/D	1.83λ/D	2.44λ/D
Linear Range, LR (Relative)	1	1.25	2.86	9	16.7
S/N (Relative)	1	1.29	1.82	2.9	3.78
$\left(\frac{LR}{2}\right)\left(\frac{S}{N}\right)^{-1}$ (Relative)	1	0.97	1.57	3.1	4.4
Guide Star Mag. Increment	0	--	-0.98	-2.45	-3.24

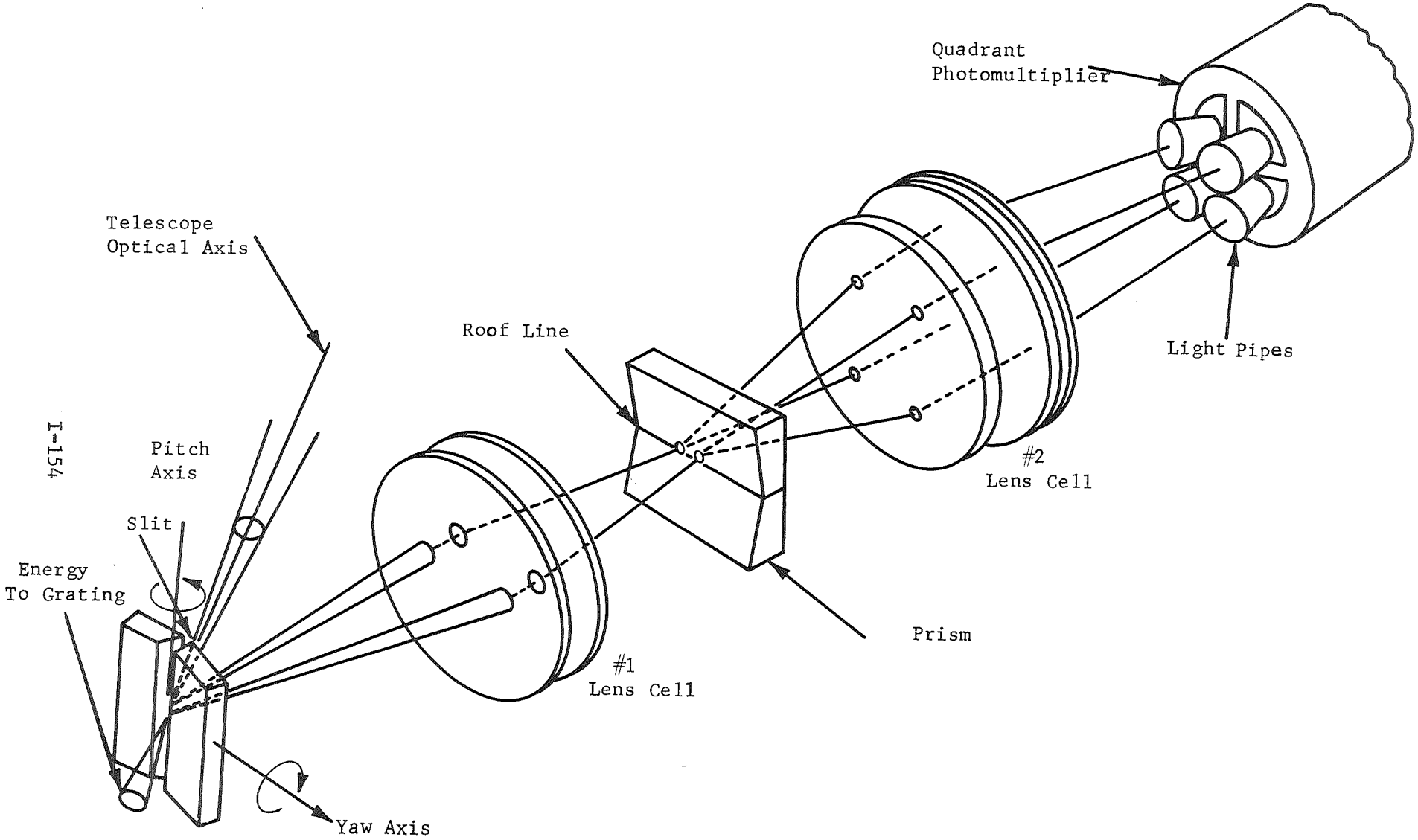

Figure 66. Guidance Optics Schematic (Null Condition Shown)

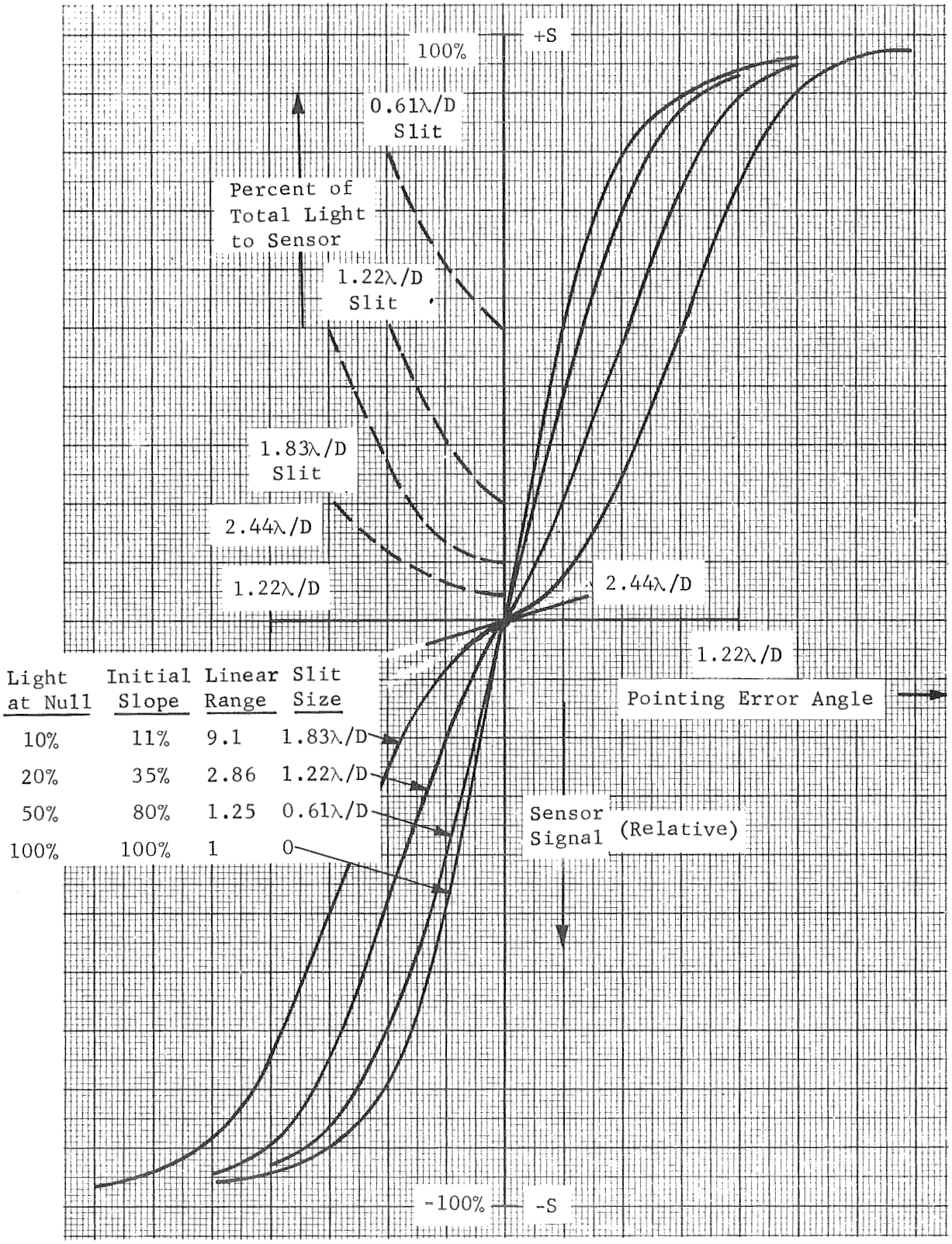

Light at Null	Initial Slope	Linear Range	Slit Size
10%	11%	9.1	1.83λ/D
20%	35%	2.86	1.22λ/D
50%	80%	1.25	0.61λ/D
100%	100%	1	0

Figure 67 Pointing Error Sensor Characteristics for Various Slit Widths. (Diffraction-Limited Star Image)

Signal versus Angle (Solid Curves)
Light Used versus Angle (Dashed)

It should be noted that this width is based upon guidance photosensor wavelength; hence, the spectrometer entrance expressed in terms of telescope resolution units is larger in the ultraviolet region. It is important to note that this results in reduced ultraviolet light loss within the instrument due to diffraction effects at the entrance. Also recorded light levels will be less susceptible to variations with mispointing.

The peak allowed mispointing of the instrument could be based upon avoiding light level changes greater than a certain percentage within the spectrometer itself. Considered shall be 2500Å ultraviolet images whose shape could be nearly diffraction limited, it being assumed that images at shorter wavelengths would be no larger in size. If the slit width corresponds to $1.22\lambda/D$ at 0.5 microns (0.06 arc-second), then a peak error of nearly 0.03 arc-second is tolerable for any allowed light variation if the ultraviolet image is a point. Since the actual image is not a point but rather is assumed to have a diffraction-limited shape, it is expected that allowed mispointing will increase as greater light level fluctuations are permitted. This is shown by computed results, as depicted in Figure 68, corresponding to the 2500Å ultraviolet diffraction-limited image.

This figure indicates that if spectrometer fluctuations are to be limited to 1 percent, then the guidance errors for 3,6, and 9-micron slits should not exceed 0.0015, 0.006 and 0.0233 arc-second, respectively. This is shown by Table 18 together with previously derived values of relative pointing error.

TABLE 18. SPECTROMETER SIGNAL FLUCTUATIONS VS SLIT WIDTH

Slit Width (Micron)	δ, Maximum Arc-Seconds Mispointing For Light Fluctuation		E_n, Relative Pointing Error (Due to Noise In Signal)	δ/E_n, Figure of Merit		Percent Guidance Light At Null
	1%	5%		1%	5%	
3	0.0015	0.003	0.97	0.00155	0.0031	50
6	0.006	0.0127	1.57	0.00382	0.0081	20
9	0.0233	0.0285	3.1	0.0075	0.0092	10
12	≈0.038	≈0.043	4.4	0.0086	0.0097	5

The indicated figure of merits obtained by dividing allowed mispointing by relative pointing error, are highest for larger slit sizes. Hence, were it not for the pointing degradations of background light and pointing sensor noise, the larger slit sizes are to be preferred.

Spectrometer Energy

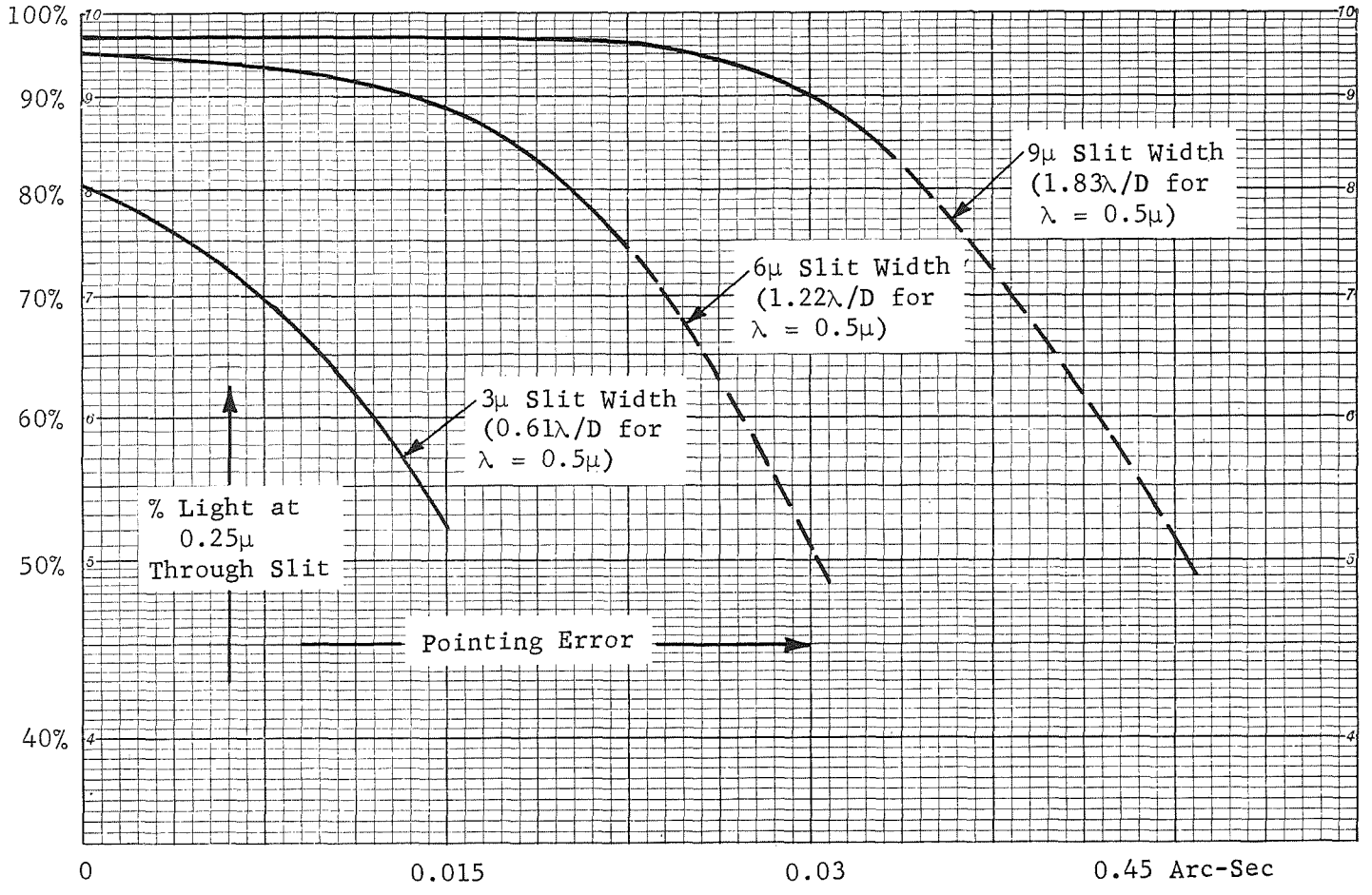

Figure 68 . Spectrometer Energy at 2500Å
Versus Pointing Error and Slit Width

The optimum slit size for guidance purposes is thus expected to be in the 6- to 12-micron range with a value dependent upon actual conditions and other considerations. To meet the 1-percent fluctuation criteria with a 9-micron slit, a guide star bright enough to provide 0.00382 peak (0.0013 rms) arc-second with the standard roof prism sensor must be employed. This must be reduced in magnitude to compensate for degradations.

Disturbances due to gravity gradient are slowly varying and by themselves are readily correctable with data obtained from an auxiliary light level monitor. However, such error will displace the nominal operating error from zero and result in greater than 1-percent light variation on similar polarity noise-induced peaks. A like situation arises in the event of unequal background light levels on opposite sides of the slit. These bias effects will not be serious if the light fluctuation rates are modest (permitting corrections), or if the integration time at each wavelength is great enough to reduce the peak fluctuation error via averaging. Further work will be required to establish the scientific requirements of the instrument and develop the associated guidance performance demand. It should be noted that there was no motivation, from the guidance standpoint, to investigate performance with defocused images at the entrance slit; i.e., the ultraviolet image approaches the visible image size and makes it more difficult to avoid the aforementioned light level variations.

Applicability to the Echelle Spectrograph - The previous results are almost directly applicable to the echelle spectrograph payload. For example, if a slit width and a peak fluctuation are specified, peak pointing error is determinable. Since separate guidance sensors are employed, the remainder of the procedure is essentially identical with that for the imaging instruments. More specifically, the peak error is divided into a tolerable disturbance peak component and a peak (3σ) noise-induced component. Bandwidth and stellar magnitude requirements are then derived.

DISTURBANCE EFFECTS ON SYSTEM

Pointing errors will arise in any stellar guidance system from many causes including external and internal torques, motional disturbances, and noise from photosensors and electronics. Previous work on the OTES program has shown that, given certain disturbances and the form of the control system, there exists a reasonable approach to pointing performance optimization. In the case of a telescope with an internal transfer lens to compensate for given structure motions, for example, the approach basically involved:

- providing sufficient open loop gain at the disturbance frequency to adequately suppress the motion-induced errors
- minimization of bandwidth to minimize noise-induced errors.

A similar procedure is followed in the case of a telescope torqued to maintain pointing when stray torques are present. In either case, the fastest falloff of gain with increasing frequency, compatible with stability, is sought to achieve desired gain at the disturbance frequency with the minimum (equivalent noise) bandwidth practical.

The addition of electronic integration circuits to the basic control system is an effective means to accomplish such ends.

Knowledge of the required bandwidth then permits determination of the guide star magnitude required to limit "noise-in-signal" induced mispointing to equal that due to torque (or motion) disturbance. The total telescope field over which guide stars of this magnitude (or brighter) are viewable is then determined from star occurrence probability statistics. For the case where two guide stars are required, a possible criterion might be to have a field large enough to encompass two guide stars 90 percent of the time at, say, the galactic poles.

It should be clear that high frequency disturbance components are undesirable since they force the use of higher bandwidths and, therefore, brighter guide stars. A larger optical field of view is then required in order to assure a sufficient probability that the desired number of guide stars will indeed be present. The net effect of high frequency disturbance components, then, can be an impractical optical design problem. Considered separately below are the guidance systems associated with each of the experiment modules. Individual coverage is necessary since the disturbances, suspension systems, accuracy requirements, and pointing error sensors are not the same in all cases and acquisition problems are, in general, different. Table 19 presents a capsule summary of the guidance performance for the various modules as evolved below. Listed are the predominating disturbances, the guidance loop gain crossover frequencies required for adequate disturbance attenuation and the guide star magnitude required to avoid excessive noise-induced error. Figure 69 shows what pointing performance improvements are attainable, for each module, when using brighter stars. The solid curves indicate the variation of the noise-induced error component for the condition of maintained bandwidth. The particular bandwidth in each case is that which results using the crossover frequency of Table 19. The dotted curves, on the other hand, indicate the variation of noise-induced error for the condition where the bandwidth is increased to maintain the same ratio of noise to disturbance-induced error components (as shown in Table 19). The latter curves are applicable when bandwidth is increased in effect by a horizontal shift of the open loop gain characteristic upward in frequency. The corresponding mechanization would involve both a gain increase and simultaneous reduction of all control system time constants.

TABLE 19 : SUMMARY OF ESTIMATED GUIDANCE PERFORMANCE CHARACTERISTICS

Stabilization Means	Transfer Lens and Counter Rotating Image Plane Equipment		Gimbals	Magnetic Suspension	
Module	F (Electronic Imagery)	C (F/10 Photographic Imagery)	E** (Rowland Circle Spectrometer)	C (F/10 Photographic Imagery)	D (Echelle Spectrograph)
Predominating Disturbance Amplitude (Period in Seconds)	5 Arc-Seconds (2700)	5 Arc-Seconds (2700)	0.6 Foot-Pounds of Wire Creep Torque in Fifteen Minutes	1.5×10^{-3} Pound-Foot ..... Grav. Grad. 29.5×10^{-3} Pound-Foot ..... Aerodynamic	
Crossover Freq (Hz)					
x-y	0.018	0.013-0.018	0.58	0.1	0.1
Roll	0.004	0.0028	NA	0.02	0.017
Equivalant Noise Bandwidth (Hz					
x-y	0.045	0.033-0.045	1.45	0.25	0.25
Roll			NA		
Guide Star Visual Magnitude	12*	13.5*	9	13.5*	12*
Noise-Induced Pointing Error in Arc-Seconds rms					
x-y	0.0015	0.0037	0.0062	0.01 ***	0.0032
Roll	0.0015	0.0007	NA	<0.01 ***	<0.0032
Disturbance-Induced Pointing Error in Arc-Seconds Peak					
x-y	0.0015	0.006	0.01	0.006	0.006
Roll	0.00065	0.0018	NA	0.006	0.006
Allowed Pointing Error In Arc-Seconds Due to			0.028 Total Peak Error in Slit Width Direction	0.006	0.028 Total Peak Error for <5% Spectrograph
Noise (rms)	0.0015 each axis	0.006 each axis	For <5% Spectrometer		
Disturbance (Peak)	0.0015 each axis	0.006 each axis	Light Level Reduction	0.006	Light Level Reduction

*Based upon 90% probability of simultaneous occurance of two stars of this magnitude (or brighter) at galactic poles.

**Estimates based upon use of 9-micron slit width.

***Use of 12.9-magnitude guide stars will reduce noise-induced mispointing to 0.006 arc-seconds.

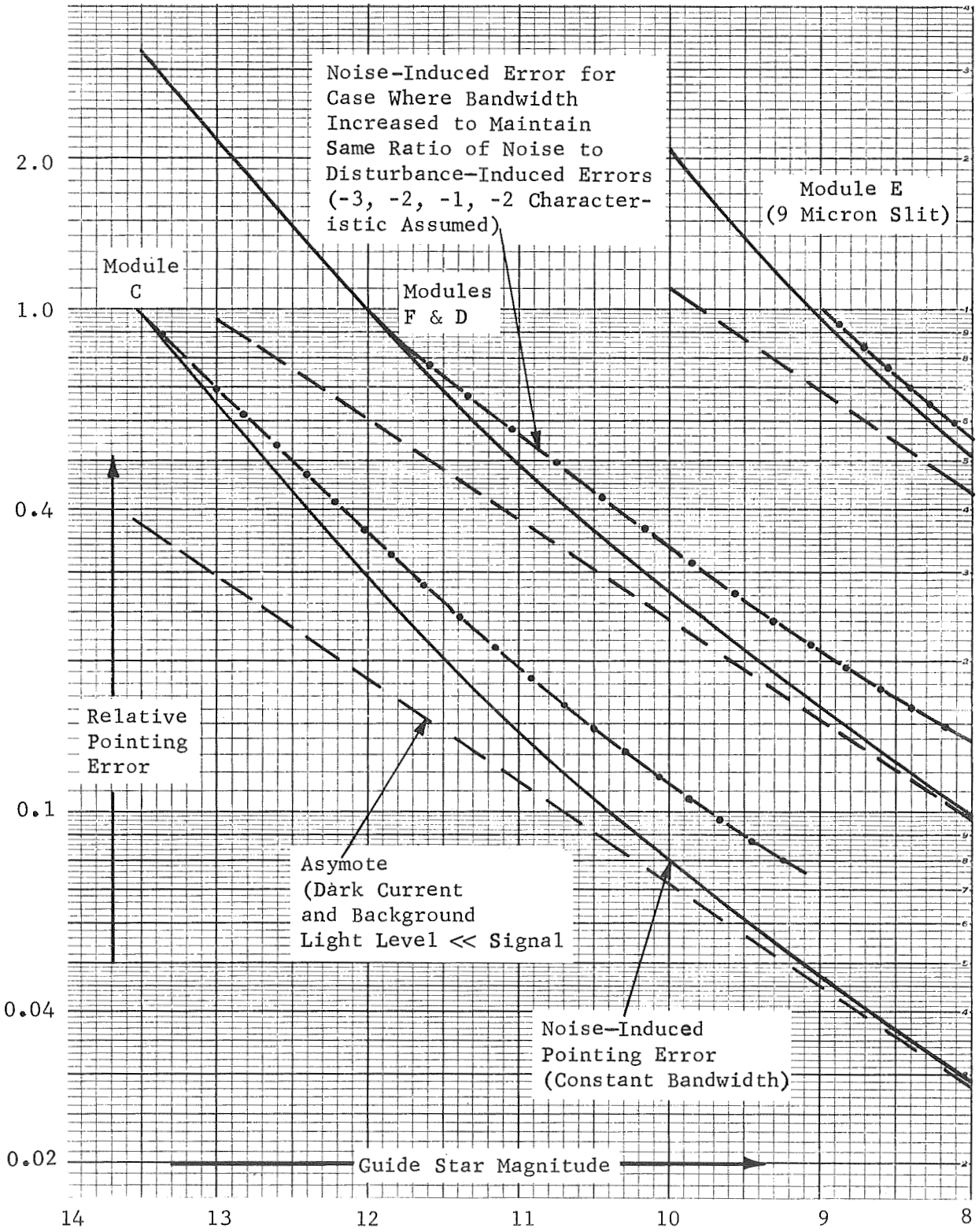

Figure 69 Variation of Noise-Induced Pointing Error With Guide Star Magnitude.

Assumed: 2 Arc-Minute Diameter Guidance Field and Dark Current Degradation Equivalent to that from Four RCA-Type 7265 Phototubes (275°K). Bandwidth Maintained Constant.

Stabilization for Modules C and F (f/10 film and f/50 electronic imagery)

The originally recommended pointing stabilization method for these modules was a transfer lens for x-y stabilization and rotation of equipment at the final image plane to compensate for spacecraft motions. Use of the gimbal axis loops was not proposed. Estimated spacecraft motions of 7.5 arc-seconds at a frequency of twice per orbit (1 cycle per 2700 seconds) were assumed and the required field of view and stellar magnitudes were derived. The present spacecraft motions, corresponding to the baseline ATM CMG performance, are different and will be considered in order to determine their impact upon telescope pointing system design.

The two-sigma pointing and stability errors of the CMG subsystem are listed (in Table 16) as ±165 and ±342 arc-seconds, respectively, for the y axis while the x axis has smaller stability error. The transfer lens must be able to compensate for motion in the order of 5 arc-minutes or more. While this could be accomplished, as envisioned, by controlled secondary mirror motions, the optical degradation associated with this magnitude of correction is prohibitively large: i.e., the size of the uncorrected optical field at f/10 is 2.75 arc-minutes in radius, and transfer lens compensation simply shifts the image without significant effects on the optical quality. A correction of 5 arc-minutes, for example, thus shifts points with excessive optical degradation onto the recorded field area. It is significant that the components of error include a 5.25-arc-minute peak astronaut-induced mispointing (due to the one wall pushoff cycle) plus other errors which are either of the static type or slowly vary with time. The acquisition sun sensor, for example, contributes 2 arc-minutes in a 15-minute time period while gravity gradient and aerodynamic effects contribute less than 1 arc-minute total.

An approach to a workable transfer lens guidance scheme might be to utilize the EPC system to remove the spacecraft x-y angular motion. An alternate and the presently recommended approach would be to avoid astronaut disturbances during telescope operation, and, in addition, alter the existing CMG subsystem to include integration and to avoid bias and drift error components. This would reduce the CMG mispointing to a few arc-seconds of static error plus a total ac component which shall be taken as ±5 arc-seconds.

Equally significant is that the motional disturbance frequencies are then primarily limited to one and two cycles per orbit plus possibly some CMG noise-induced motions which are within the CMG 0.03-Hz bandwidth.

Hence the roll as well as the CLOS pointing control loops can offer adequate pointing stability without resorting to high bandwidths.

Table 20 presents the parameters for the field-of-view and pointing analysis which follows.

TABLE 20 : TWO-METER TELESCOPE PARAMETERS FOR POINTING CONTROL

CMG POINTING ERROR		
ACQUISITION		1 arc-minute
TRACK		
Amplitude		5 arc-sec
Frequency		1 cycle per 2700 seconds
RECORDED FIELD SIZE	MOD F	5.5-arc-minute diameter
	MOD C	11.6 x 30 arc-minutes
RECORDED FIELD WAVELENGTH		Module C 0.5μ (Visible)
		Module F 0.125μ (uv)
TELESCOPE APERTURE DIAMETER		2 meter
GUIDE STAR OPTICAL EFFICIENCY		n_o = 31.6 percent
GUIDANCE SENSOR QUANTUM EFFICIENCY		n_q = 10 percent
STRAY BACKGROUND LIGHT		225 11th magnitude stars per square degree

The basic pointing requirement is to hold the rms error due to noise and motional disturbances about each axis down to one tenth of the telescope's diffraction-limited resolution.

The cross line-of-sight error magnitudes tolerable are thus 0.006 and 0.00015 arc-second for modules C and F, respectively. The allowed roll rotation is 0.725 arc-second for module C and 0.308 arc-second for module F. The latter figures were determined by assuming that roll occurs about the x-y guide star image and that the resulting rms motion at the recorded field extremity should not exceed an amount equivalent to the tolerable x-y motion.

The required transfer lens open loop gain at the disturbance frequency as has been shown previously, is equal to the ratio of the disturbance motion to the tolerable error or in this case

$$\frac{\text{Disturbance Angle}}{\text{Allowed error}} \approx \frac{5 \text{ arc-sec}}{0.006 \text{ arc-sec}} = 833$$

for module C and 3350 for module F.

Figure 70 shows that this can be obtained for module F with an open loop characteristic (-3,-2,-1,-2) which has a zero dB gain crossover of 0.018 and an estimated equivalent noise bandwidth of 0.045 Hz. The last figure, together with optical and quantum efficiencies, is used to determine the guide star magnitude required to maintain noise in signal error within the allowed 0.0015 arc-second. This is readily accomplished with the nomograph of Figure 71 using the quantity

$$\frac{n_o\, n_q}{\Delta F} = \frac{0.1 \times 0.316}{0.045} = 0.7$$

It is found that an error of 0.00015 arc-second can be obtained using stars whose visual magnitude (M_v) is 13.3. Use of this stellar magnitude would, were it not for other noise sources (viz, PMT dark current and background light) provide a safety factor of 10 .

The associated area of total field based upon the requirement of module F can now be estimated with the aid of Figures 72 through 75 . Figure 72 shows the average number of guide stars per square degree as a function of galactic latitude and star magnitude (viz, approximately 240 per square degree for Mv = 15.4 at 90-degree latitude). Figures 73 and 74 indicate the probability statistics of star occurrence in the field assuming a Poisson occurrence spatially (viz, from Figure 74 , the area of field required for 90-percent probability is $\frac{\pi}{4}(8.6)^2$ square arc-minutes). Figure 75 shows the results based upon 90-percent coverage. The total field of view of the 2-meter LTEP (φ_T) must be somewhat larger than the recorded field φ_R to ensure a reasonably high probability of containing at least two guide stars. The guidance field must be large enough so that the guidance photosensors can see the guide stars with the maximum initial mispointing angle of the telescope. The diameter of the guidance field during tracking (φ_{GT}) may be smaller than the guidance field required for acquisition (φ_{GA}) in order to avoid excessive degradations due to stellar background light (see Figure 76). Since the total field area available for selection by the guidance is not $\frac{\pi}{4}(\phi_T)^2$ but rather

$$\frac{\pi}{4}\left[(\phi_T - \varphi_{GA})^2 - (\varphi_R + \phi_{GA})^2\right]$$

at most, the actual value of φ_T depends upon the required values of φ_R and φ_{GA}. φ_R shall be assumed as 5.5 arc-minutes while a φ_{GA} of 2 arc-minutes is appropriate with the assumed initial structural pointing error of ±1 arc-minute. The values of φ_T required are then approximately 21.5 and 26 arc-minutes for 90-percent and 99-percent probability, respectively, at the galactic poles. A field of view of 30 arc-minutes will provide a 90-percent probability of obtaining two guide stars of 12th magnitude when viewing at the galactic poles. This would increase to over 90 percent at zero-degree galactic latitude. The use of 12th magnitude stars will tend to improve pointing precision by a factor of near 1.8 while the background light in the 2-arc-minute diameter guide field, being equivalent to 1/2 of twelfth-magnitude starlight will degrade this by a factor of $\sqrt{1 + 0.5} = 1.23$. Phototube dark current noise will also degrade pointing. RCA type 7265 S20 phototubes operating at 300°K (200°K) offer dark currents equivalent to 4×10^{-14} (1×10^{-15}) incident watts per tube at 5500Å or 2.76×10^{-11} (6.9×10^{-13}) lumens.

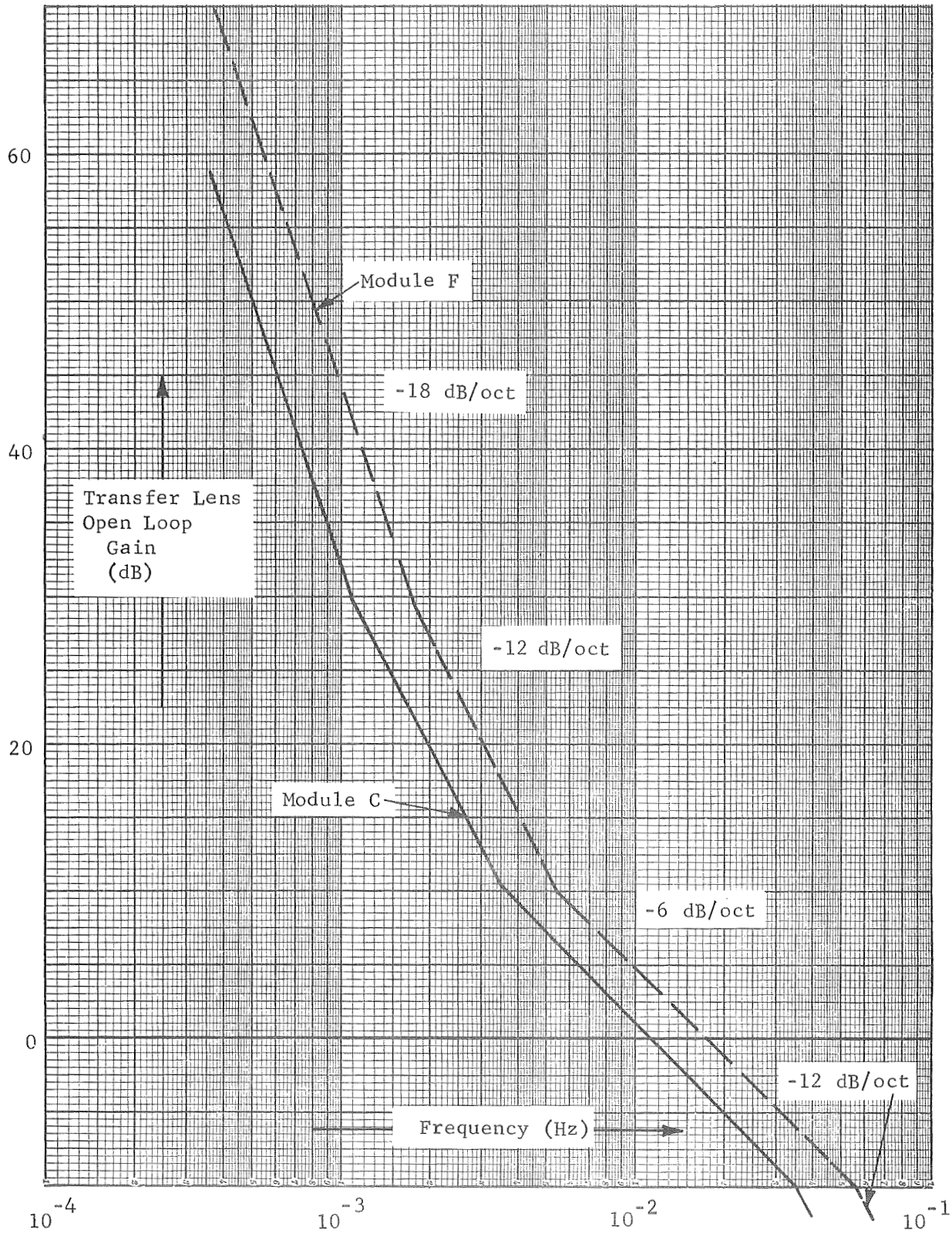

Figure 70 Transfer Lens Open Loop Gain versus Frequency Characteristic

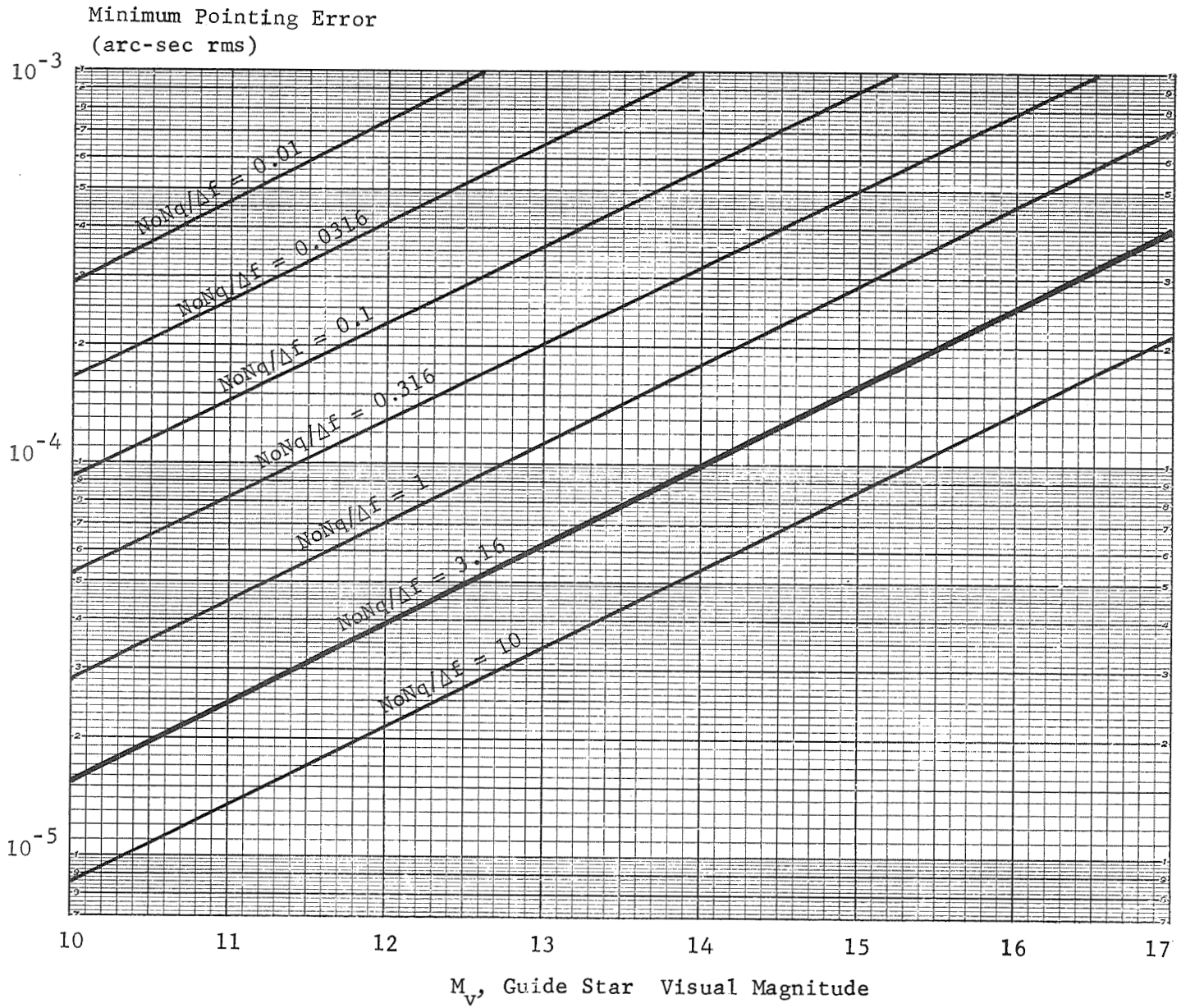

Figure 71. Guide Star Effect on Pointing Error for Two-Meter Aperture Telescope

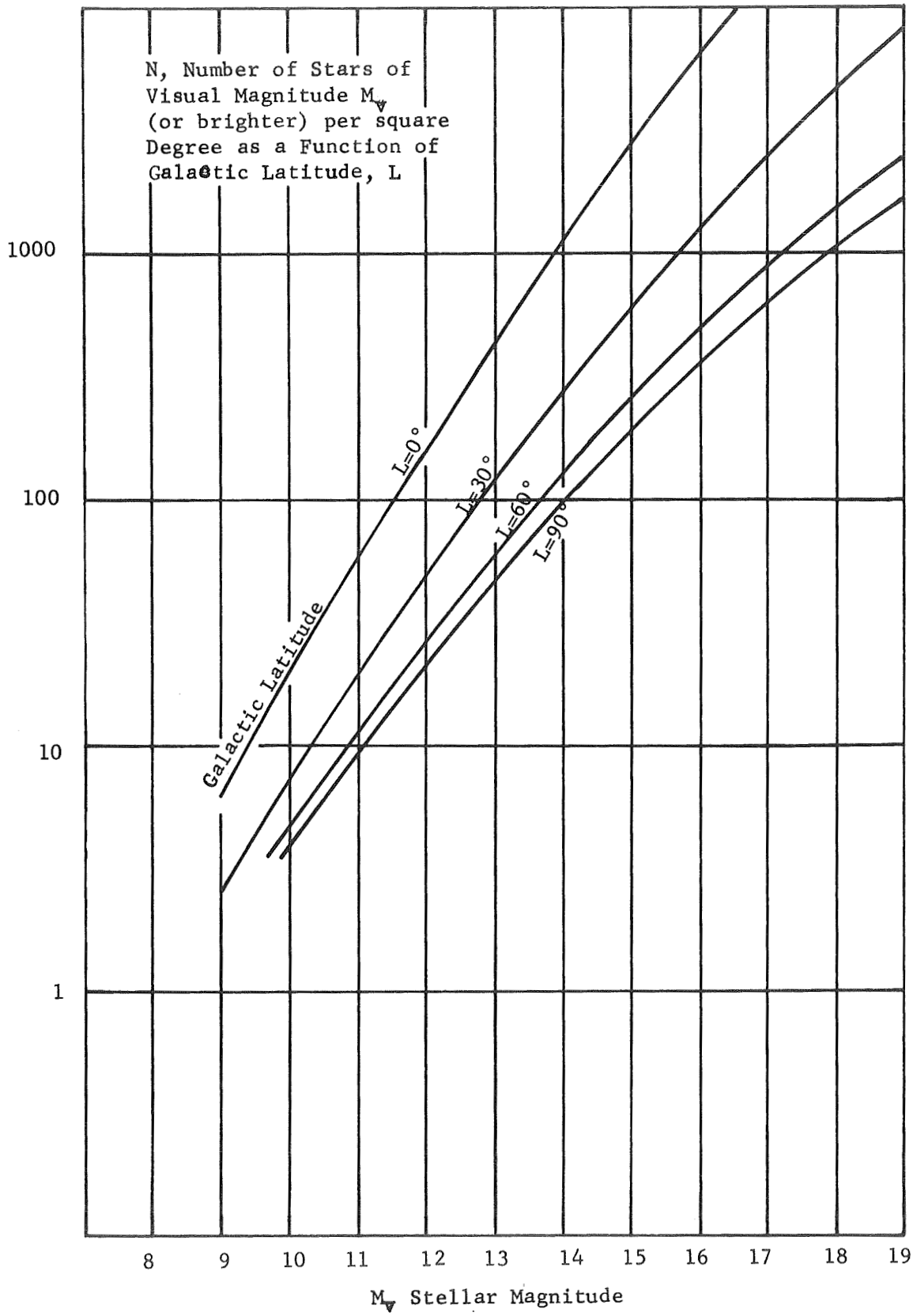

Figure 72. Availability of Guide Stars

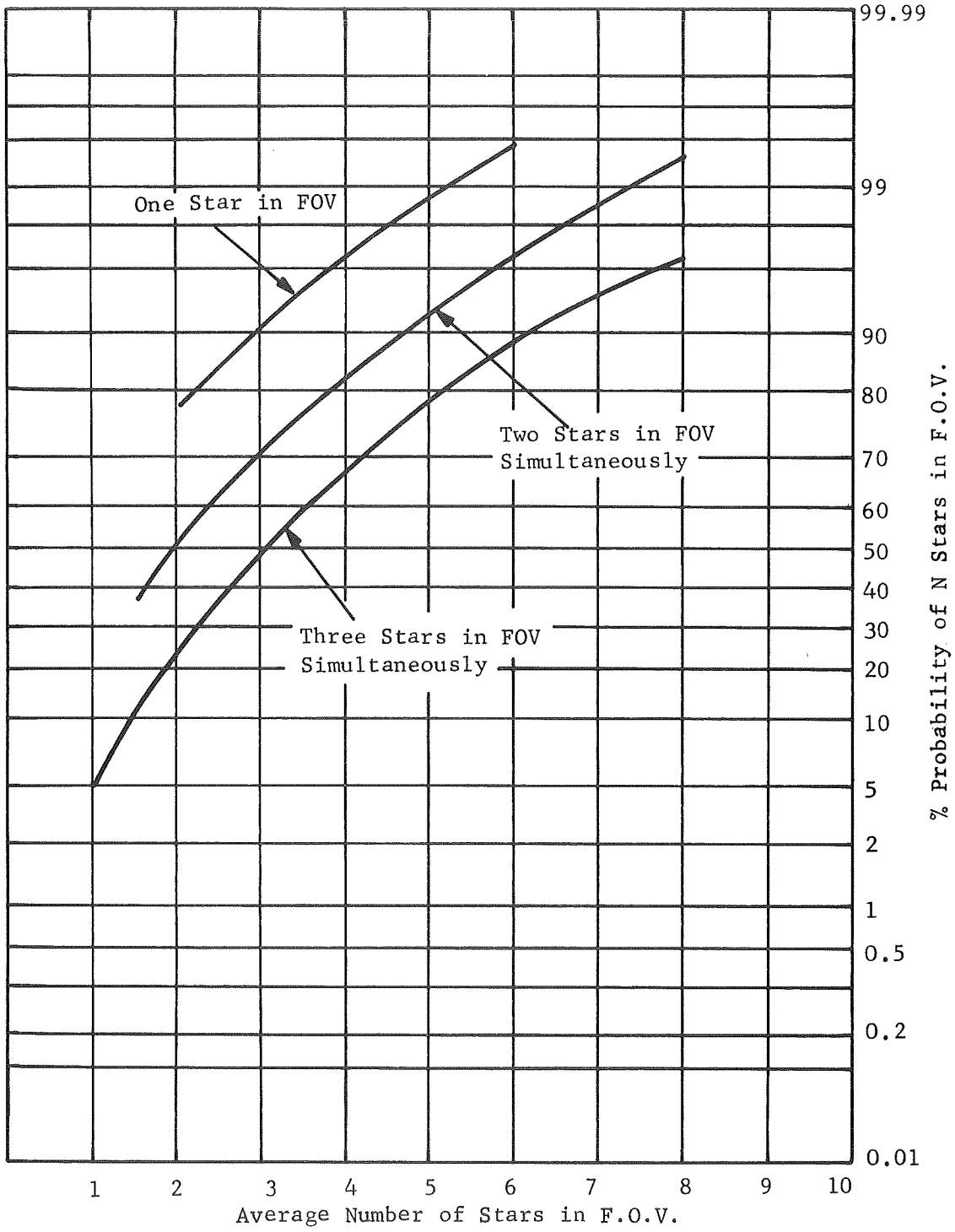

Figure 73. Guide Star Probability

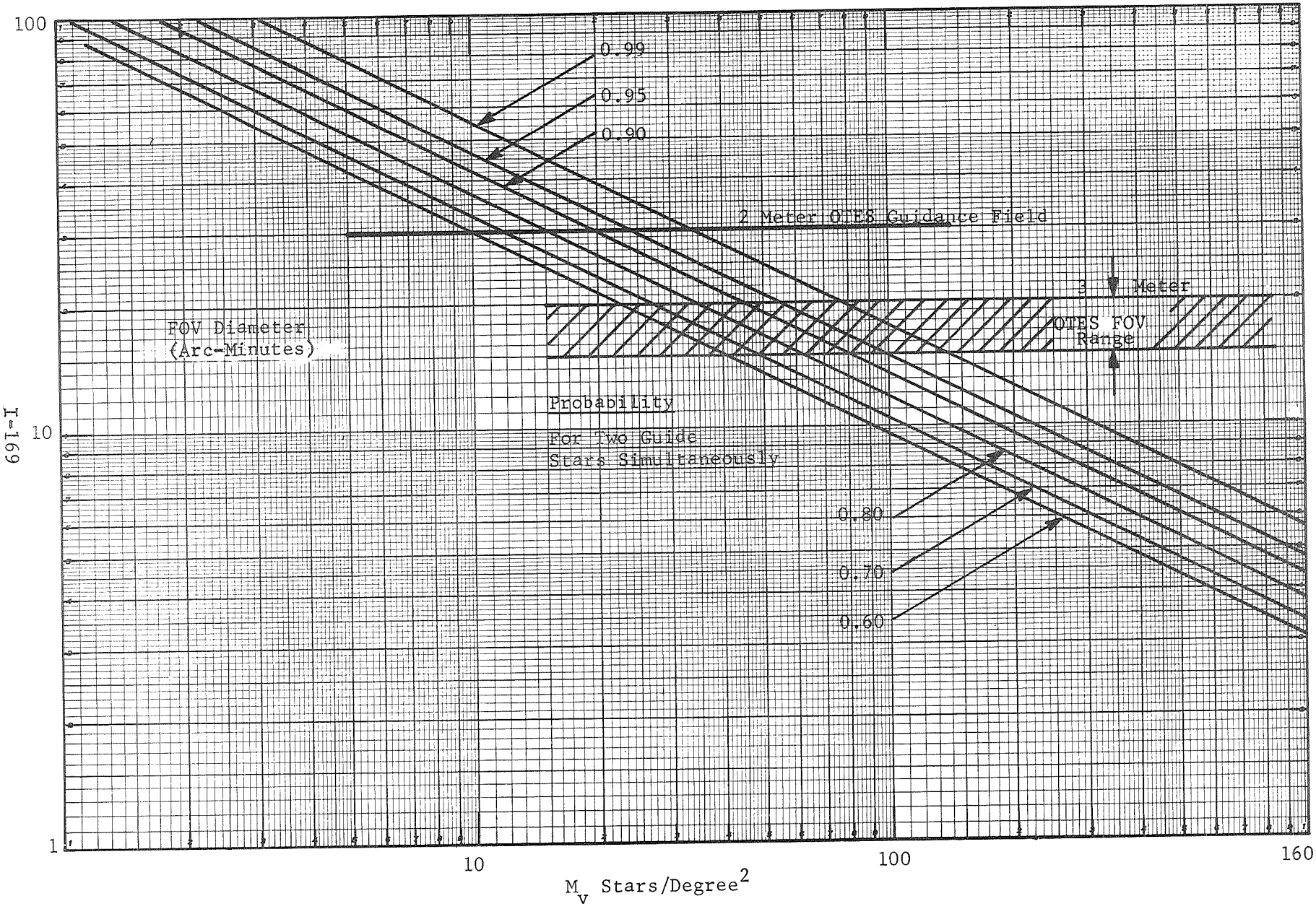

Figure 74. 2- and 3-Meter Telescope Guidance Field of View

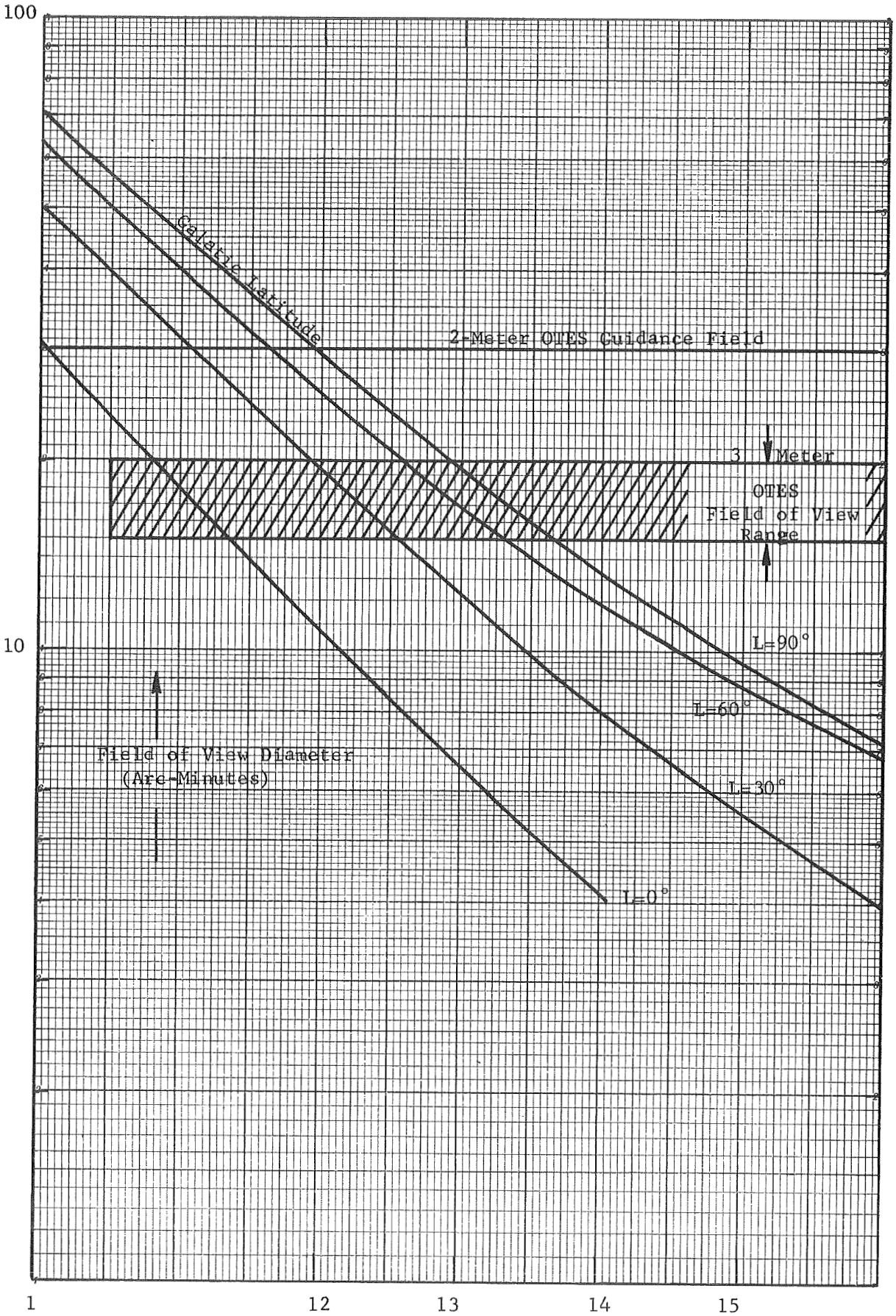

Figure 75. 90% Probability of at Least Two Guide Stars

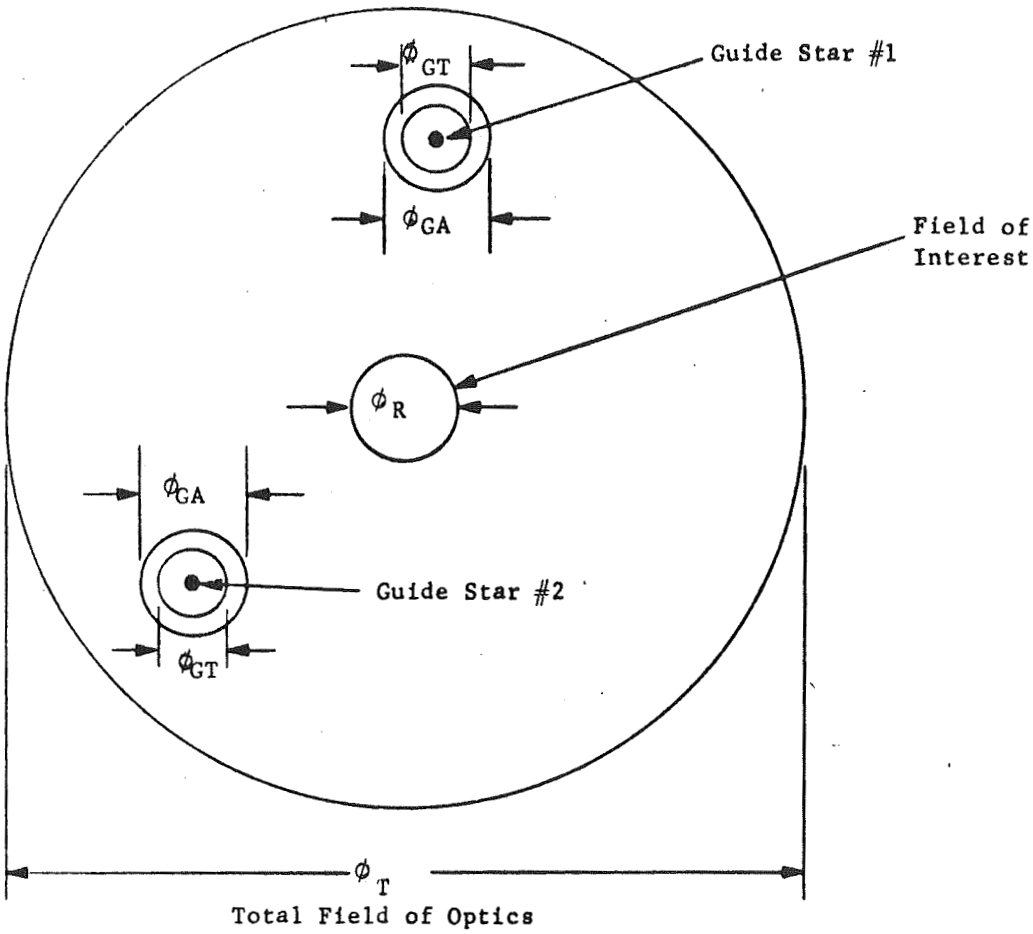

Figure 76. Diagram Illustrating Field Relationships

The light from a 12th-magnitude star is approximately

$$\frac{\left(2.4\times10^{-6}\ \frac{\text{lumen}}{\text{meter}^2}\right)\left(\frac{\pi}{4}D_A^{\,2}\right)n_o}{2.51^{M_v}} = 3.77 \times 10^{-11}\ \text{lumens}$$

The pointing degradation factor, corresponding to the use of four tubes, would be

$$\sqrt{\frac{4\times2.76}{3.77}+1} = 1.98$$

It is therefore recommended that the tubes be operated in a below-room-temperature ambient. Figures 77 and 78, which show the variation of phototube dark current and the equivalent background light it represents versus temperature, indicate that a 275°K ambient is appropriate.

Performance corresponding to that of nearly 13.3 magnitude should be thus achievable when guiding on 12th magnitude stars.

The performance obtainable with Module C, whose film strip is 11.6 arc-minutes wide and runs across the f/10 field, is based upon use of stars of 13.5 magnitude This is the stellar magnitude corresponding both to the reduced field available for placement of the guidance photosensor and 90-percent probability of simultaneous occurrence at the galactic poles. The associated pointing error, assuming the 0.011-Hz crossover frequency of Figure 70 and an equivalent noise bandwidth of 0.0275, is 0.00135 including the usual safety factor of ten. Background light and degradation due to the dark current of four phototubes (275°K) would increase this error to 0.0037 arc-second. This increases the open loop gain crossover frequency at which the components are equal, from 0.011 to 0.013 where the magnitudes are each 0.004 arc-second. It is worth noting that the rms error summation has a rather broad null when plotted versus crossover frequency, and bandwidths up to twice the above value will yield nearly the same mispointing. This means that disturbances over ten times larger can be handled by doubling the bandwidth with an attendant pointing error overall increase of about 40 percent (refer to Figure 79). Hence the sensitivity of the system performance to the 5-arc-second assumption is very low. The ultimate CMG pointing requirement will undoubtedly arise from optical degradations associated with off-axis positioning of the transfer lens.

Roll Pointing Precision

Up to this point only cross line-of-sight pointing errors due to motional disturbances and noise have been considered. The roll (about the line of sight) telescope error is equally important and magnitude constraints can be computed based upon the assumption that recorded image smear due to roll should be no larger than that due to cross line of sight errors. If one assumes that the x-y guide star is directly on axis and the diameter of the recorded field is θ_R, then a telescope resolution of

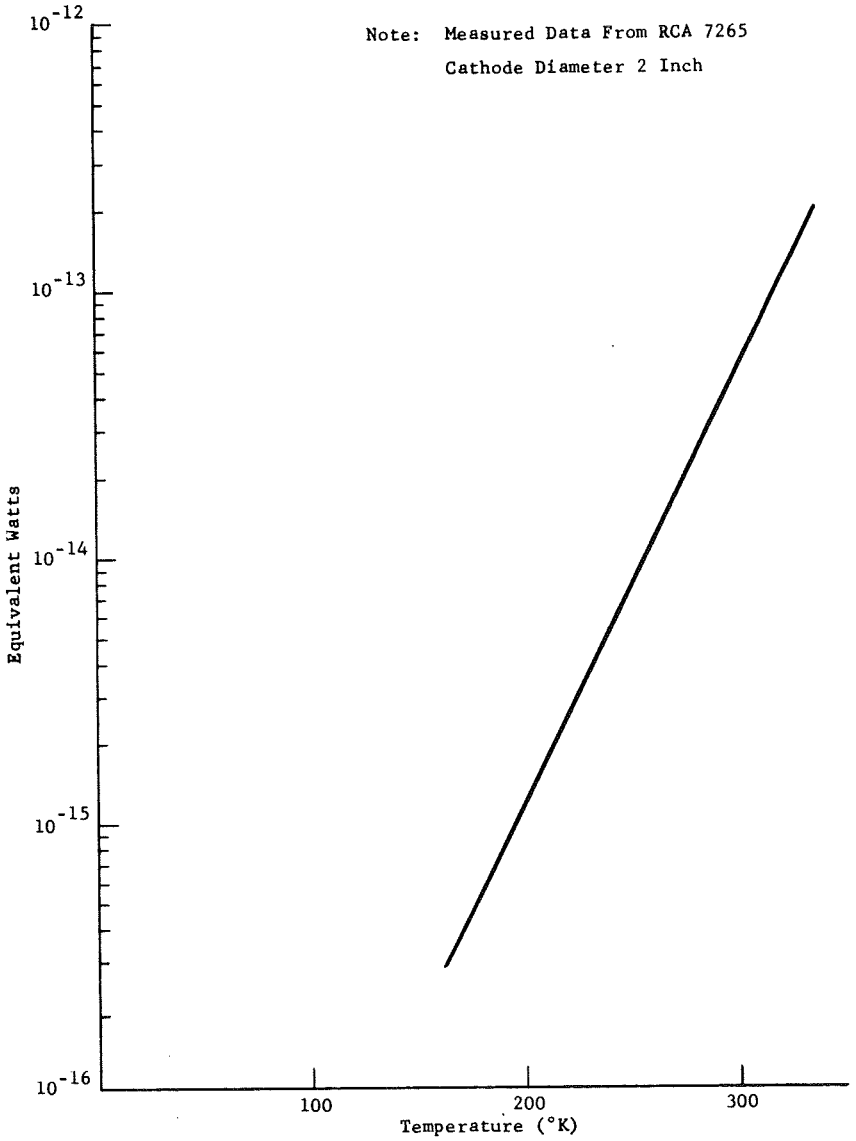

Figure 77 . Photomultiplier Cathode Dark Current Equivalent Watts

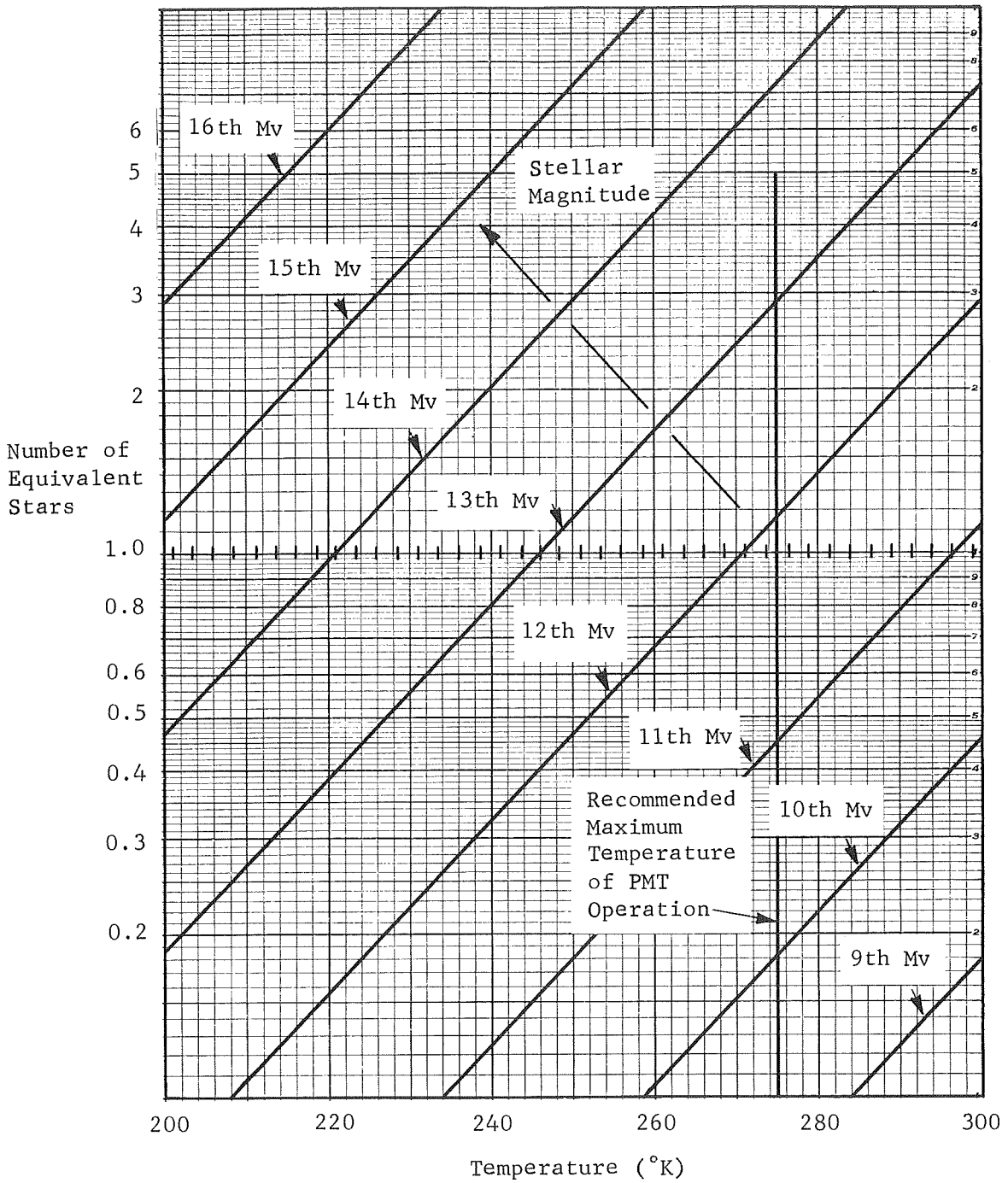

Figure 78. Dark Current in Equivalent Background Stars Versus Temperature

Four RCA 7265 Tubes, n_o = 31.6%
Aperture Diameter = 2 Meters

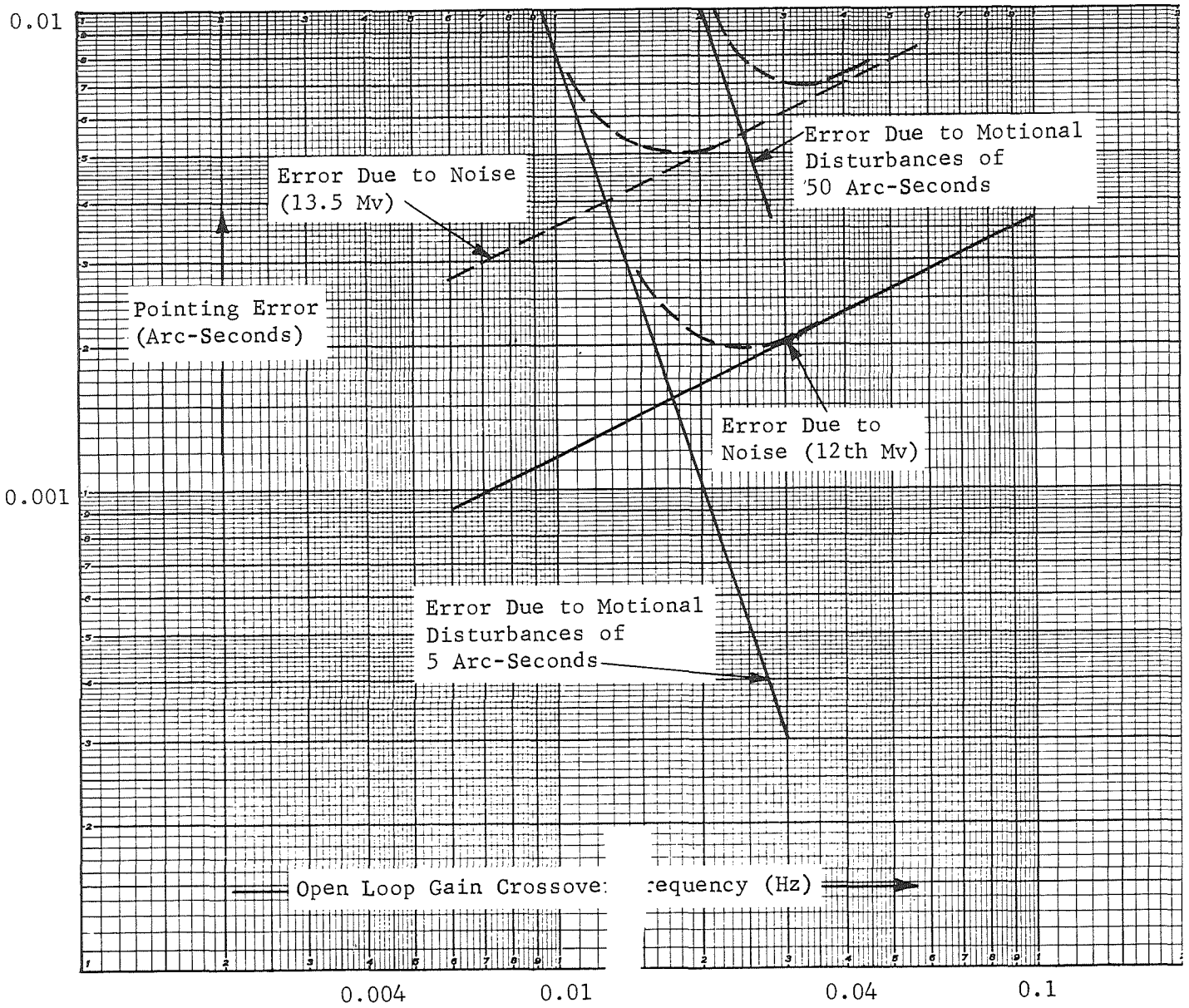

Figure 79. Estimated Errors Versus Transfer Lens Open Loop Gain Crossover for Module C

$$\frac{1.22\lambda_R}{D}\ ; \qquad \lambda_R = \text{Wavelength of recorded image} \tag{1}$$

implies that x and y pointing errors should be

$$\frac{1.22\lambda_R}{KD} \tag{2}$$

Roll motion of the image θ_V, which causes an equivalent photographic degradation, can now be determined from the expression,

$$\frac{\theta_R}{2} \sin \theta_V = \frac{1.22\lambda_R}{KD} \tag{3}$$

which reduces to

$$\sin \theta_V = \frac{2.44\lambda_R}{KD\ \theta_R} \tag{4}$$

The foregoing expression can be utilized to determine the roll servo pointing requirements for both modules C and F, whose f/10 fields are depicted in Figure 80 . Assuming D = 2 meters, K = 10, and θ_R = 15 and 2.75 arc-minutes for modules C and F, respectively, then

$$\theta_V = \frac{2.44\lambda_R}{KD\ \theta_R} = \frac{2.44 \times 0.5 \times 10^{-6}}{10 \times 2 \times 15} \times 60 \times 57.3 = 1.38 \text{ arc-seconds}$$

for module C (λ_R= 0.5μ) and

$$\theta_V = \frac{2.44(0.125)\times 10^{-6}}{10\times 2\times 2.75} \times 60\times 57.3 = 1.875 \text{ arc-seconds}$$

for module F (λ_R= 0.125μ).

Even greater roll stability is required if one considers the case where the rotations occur about the (cross line-of-sight or) translational guide star image, which is some angular distance from the center of the recorded field. Such a situation arises, as in the Stratoscope II system, when transfer lens corrections are made much more rapidly than roll corrections. With such an arrangement, the telescope required roll stability is

$$\sin\theta_V = \frac{2.44\lambda_R}{KD(\theta_T - \theta_{G_A} + \theta_R)} \triangleq \frac{1.22\lambda_R}{KD\ \theta_{X_{max}}} \tag{5}$$

where θ_T is the total field angular diameter

θ_{G_A} is the pointing photosensor acquisition field diameter

$\theta_{X_{max}}$ is the maximum distance of the translation star from the film. (see Figure 80).

The most stringent requirements arise for each module with the x-y guide star sensor locations shown (Figure 81) for which

$$\theta_v = \frac{1.22\lambda_R}{KD\theta_{x_{max}}} = 0.725 \text{ arc-second for module C and}$$

$$= 0.308 \text{ arc-second for module F.}$$

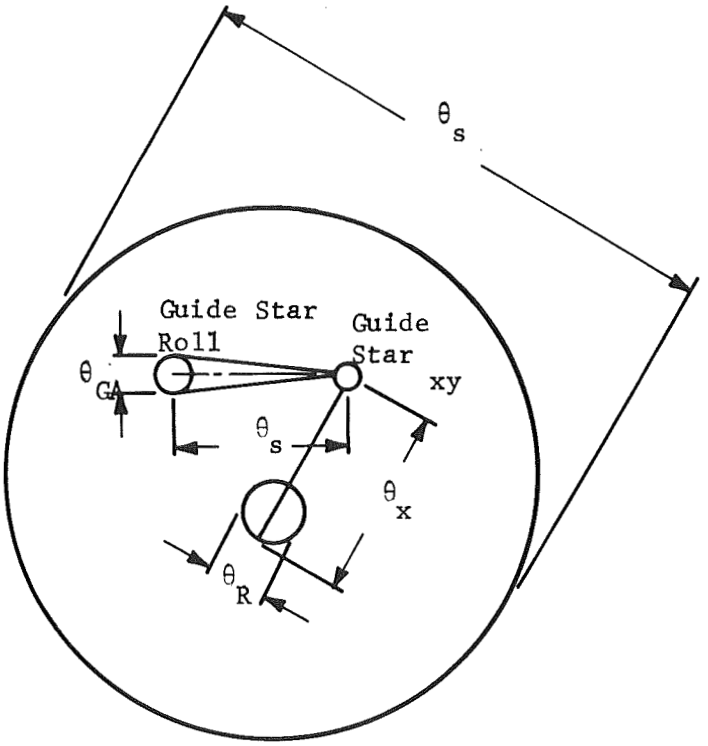

Figure 80 . Guide Star Image Geometry

Achieving Required Accuracy - The roll stabilization geometry indicates that the linear sensing range available with the roll star a distance θ_s from the xy star is equivalent to (refer to Figure 81)

$$\frac{\frac{1.22\lambda_G}{D}}{\theta_S} = \text{Linear Range, L.R.} \qquad (6)$$

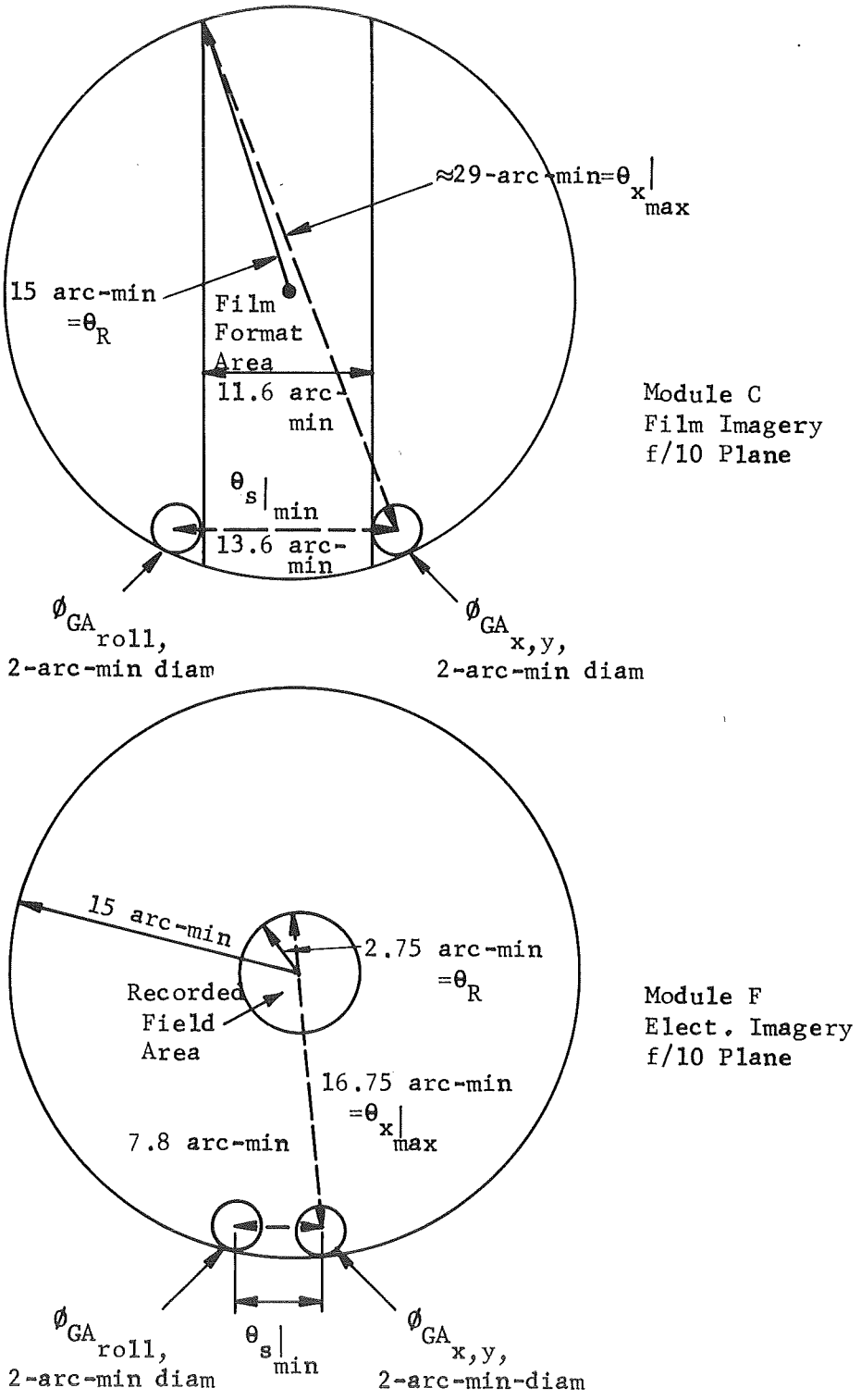

Figure 81. f/10 Image Plane Arrangement for Modules C and F

where λ_G is the wavelength of light forming the guide star image.

The minimum signal-to-noise ratio required to achieve the desired accuracy can be determined from the following relation relating pointing error to linear range and signal-to-noise ratio (refer to page I-257).

$$E_p = \frac{1.22\lambda_G}{2D}\left(\frac{S}{N}\right)^{-1} \tag{7}$$

$$\frac{S}{N_{min}} = \frac{LR/2}{E_p} = \left(\frac{0.61\,\lambda_{G/D}}{\theta_S}\right) \Big/ \frac{4.22\lambda_R}{KD\theta_{X_{max}}}$$

$$\frac{S}{N_{min}} = \left(\frac{K}{2}\right)\left(\frac{\theta_X}{\theta_S}\right)\frac{\lambda_G}{\lambda_R} \tag{8}$$

Based upon the same criterion, the signal-to-noise ratio required for translational pointing is simply

$$\frac{S}{N_{min}} = \frac{0.61\,\lambda_{G/D}}{\frac{1.22\lambda_R}{KD}} = \frac{K}{2}\,\frac{\lambda_G}{\lambda_R} \tag{9}$$

Since the S/N ratio for a given magnitude guide star varies as the square root of the bandwidth, the roll bandwidth must differ from the translation bandwidth by the factor

$$\left(\frac{\theta_X}{\theta_S}\right)^2$$

Assuming, then, the worst case conditions presented in Figure 81, it is found that the roll crossover frequencies should not exceed 1/4.6 times that (0.018 Hz) required in the transfer lens loops or 0.004 Hz for both modules. The motional disturbance of 5 arc-seconds will be attenuated by a factor of 37 if the roll and translation loops have similar shapes. This should suffice since the C and F modules require roll disturbance attenuations of only 6.9 and 16.3, respectively.

Module E, Rowland Circle Spectrometer

Roll stabilization requirements for this module are quite crude and are only necessary to avoid false signal fluctuations, when observing partially polarized sources, due to reflectance changes with angle within the instrument. These arise primarily from the metalized flip mirror which receives light at nearly 70 degrees from the normal and, hence, will have different reflectances (Rp and Rs) for the electric field vector components parallel to and in the plane normal to the surface. Figure 82 illustrates the nature of the phenomena for evaporated aluminum. If it is assumed that typical

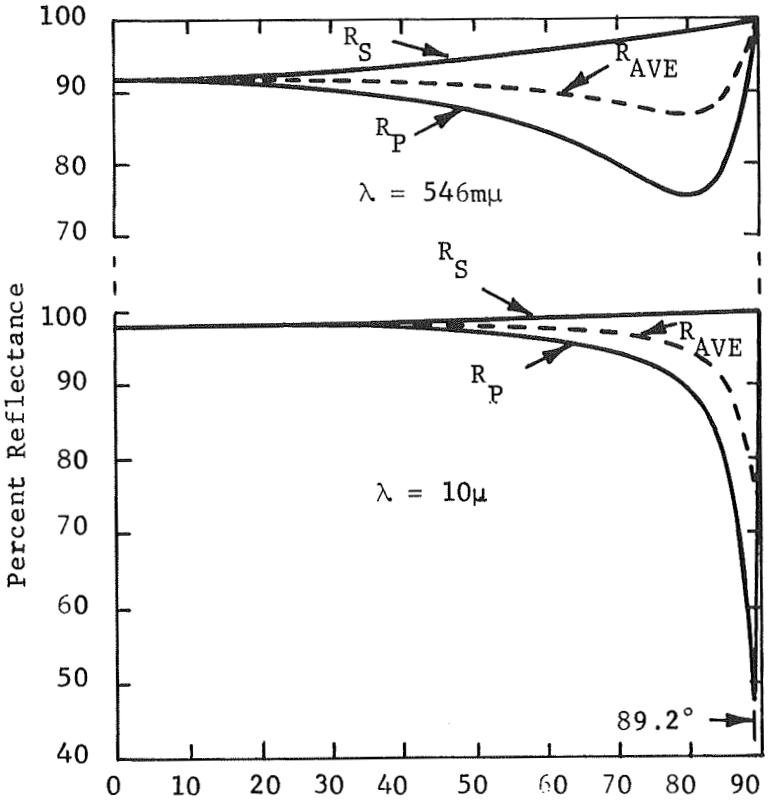

Figure 82. Calculated Reflectance of Evaporated Aluminum as a Function of Angle of Incidence for λ = 546mμ and λ = 10μ*

* Kingslake, R.: Applied Optics and Optical Engineering, Academic Press, VIII, 1965, p. 318.

sources will be 10 percent polarized, then a roll of 1 degree might cause a one tenth percent effect in the data. The 300-arc-second (2σ) stability quoted for the CMG control system thus appears to be adequate in itself, obviating the need for an auxiliary roll control loop. The performance of the EPC loop (1.77-arc-second pointing uncertainty and 0.63-arc-second stability errors) can be increased by 0.2 arc-second of peak error induced by crew movements. This occurs with the CMG and EPC loops operating, the latter with a bandwidth of near 2.5 Hz. Hence x-y spectrometer pointing utilizing the proposed stellar image-splitting error sensor and a gimbal axis suspension, must either

- resort to bandwidths well over 1 Hz in order to adequately suppress the (0.1 to 1 Hz) spectral components of astronaut disturbances, or
- be isolated from such disturbances by essentially removing the astronaut during module operation.

A consequence of the first alternative is a high equivalent noise bandwidth and the requirement to work on relatively bright stars to avoid excessive noise-induced mispointing. For example, if we optimistically assume a noise bandwidth of only 10 Hz, a guidance accuracy of 0.01 arc-second, $n_o = 31.6$ percent and $n_q = 10$ percent, then

$$\frac{n_o n_q}{\Delta_F} = 0.00316$$

from which it is determined that guide stars brighter than 11th magnitude are required. Moreover there is serious doubt whether sufficient isolation against the disturbance can be obtained without resort to bandwidths so high that the 18-Hz estimated (first bending mode) resonance of the structure presents insurmountable stability problems. The problems become insurmountable in the independent mode where the estimated disturbances are almost two orders of magnitude larger due to the lower system moments of inertia.

The choice of the second alternative, for this and other reasons presented elsewhere, is appropriate. The ac disturbances, T_A, which must still be handled then include gravity gradient (1.5×10^{-3} pound-feet) and aerodynamic torques (9.5×10^{-3} pound-feet) acting directly on the telescope and torques due to spacecraft motions, θm. The expected 5 arc-seconds of CMG loop motion due to gravity gradient (and other torques with the same period or greater) will couple torques, T_G, into the telescope via the gimbal spring constant K_g of 150 inch-pounds per radian: i.e.,

$$T_G = K_G \theta m \sin \omega t$$

The other component of torque, T_C, due to c.g. placement error can be expressed

$$T_C = \ddot{\theta}_M L M_T \delta = -\omega^2 \theta_M L M_T \delta \sin \omega t$$

where

L is the distance from the gimbal axis intersection to spacecraft rotational center,

M_T is the mass of the telescope,

δ is the distance from the telescope c.g. to the gimbal axis intersection, and

ω is the disturbance frequency corresponding to twice the orbital frequency.

The pointing error resulting from telescope torque disturbances is reduced by servo loop action by the servo loop gain at the disturbance frequency: i.e.,

$$\theta_D = \frac{T_D/JS^2}{1+G/JS^2} = \frac{T_D/JS^2}{G/JS^2} \; ; \quad \text{when } \frac{G}{JS^2} \gg 1$$

The pointing error due to the aforementioned torque components can thus be expressed as

$$\theta_D = \frac{[T_A + K_G \theta_m - \omega^2 L M_T \delta \theta_m] \frac{1}{J\omega^2}}{G/J\omega^2}$$

Quantitatively, gravity gradient torque predominates over bearing spring constant torques with the latter being one fifth as large for the expected ±5-arc-second vehicle variations. Moreover T_C is found to be only 8.5×10^{-6} pound-foot for L = 20 feet, θm = ±5 arc-seconds, δ = 1 inch, J = 15,000 slug-ft^2, M_T = 6000/32 slugs, and with ω=0.00232 corresponding to half the orbital period. Hence, gravity gradient effects will tend to predominate and cause a pointing error of

$$\theta_D = \frac{1.5 \times 10^{-3}/15{,}000(0.00232)^2}{G/JS^2} = \frac{3820 \text{ arc-seconds}}{G/JS^2}$$

This indicates that an open loop gain of 382×10^3 at 0.00232 radians per second (f = 0.00037 Hz) is required to attenuate the associated error to 0.01 arc-second. Similarly, the aerodynamic torque, if assumed to be sinusoidal at the orbital frequency, can be reduced in effect to 0.01 arc-second if the loop gain is 30×10^6 at 0.00116 radian per second.

Wires crossing the gimbal axes, in the ATM application, can introduce a non-constant disturbance torque which leads to more stringent requirements. This is termed wire torque creep and has been measured by NASA as a 0.6 - pound-foot change in 15 minutes. The effect on a lead-lag stabilized torqued inertia control system is an error which constantly increases with time. The inclusion of an integrator in the loop, however, can reduce the effect of the torque creep to a steady state offset error. The expression for the minimum required open loop gain crossover frequency , ω_{co}, of a reasonable characteristic is presented in Figure 83. Taking the torque creep as 0.6 pound-foot per 15 minutes, telescope inertia of 15,000 slug-ft^2 and the maximum allowed steady state error as 0.01 arc-second, it is found that

$$\omega_{co} = \sqrt{3}\left[\frac{10A}{J\theta_{D(t)}\Big|_{ss_{max}}}\right]^{1/3} = 1.732\left[\frac{10 \times 0.67 \times 10^{-3} \times 206{,}000}{15{,}000 \times 0.01}\right]^{1/3} = 3.64 \text{ rad/sec}$$

or

$$F_{co} = \frac{\omega_{co}}{2_T} = 0.58 \text{ Hz}$$

The associated loop gains 6×10^7 and 53.6×10^7 at gravity gradient and aerodynamic frequencies are sufficient to reduce these error components to negligible levels.

The equivalent noise bandwidth of the servo would be about 2 Hz. If we assume that a 9-micron slit is used and mispointing should not cause spectrometric light variations in excess of 5 percent, then peak errors of 0.0285 arc-second are allowed (see page on Pointing Requirements). The allowed rms error due to noise then becomes equal to one third of (0.0285 - 0.01) or 0.0062 arc-second. As has been shown previously, the guide star magnitude required to accomplish this in the absence of dark current and background light degradations, is equal to that which provides 3.1 times less error with a roof prism sensor. Accordingly, the stellar magnitude is 9.8. Background light and dark current degradation factors, based on the fact that only about 10 percent of the starlight is available to the pointing sensors at null, are found to be 1.3 (2-arc-minute diameter field) and 1.5, respectively.

A ninth-magnitude star, on the other hand, offers roof prism pointing of 0.00195-arc-second rms (noise component) including degradations, and hence appears to be approximately the limiting usable guide star.

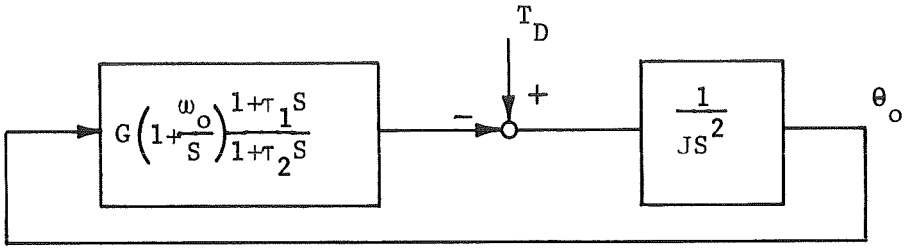

$$\theta_{o(S)} = \frac{1/JS^2}{1 + \frac{G}{JS^2}\left(\frac{1+\tau_1 S}{1+\tau_2 S}\right)\left(1 + \frac{\omega_o}{S}\right)} \quad T_{D(S)}$$

$$\theta_{o(\tau)}\Big|_{SS} = \lim_{S\to 0} S\theta_{o(S)} = \frac{A}{G\omega_o} \text{ ; for } T_{D(S)} = \frac{A}{S^2}$$

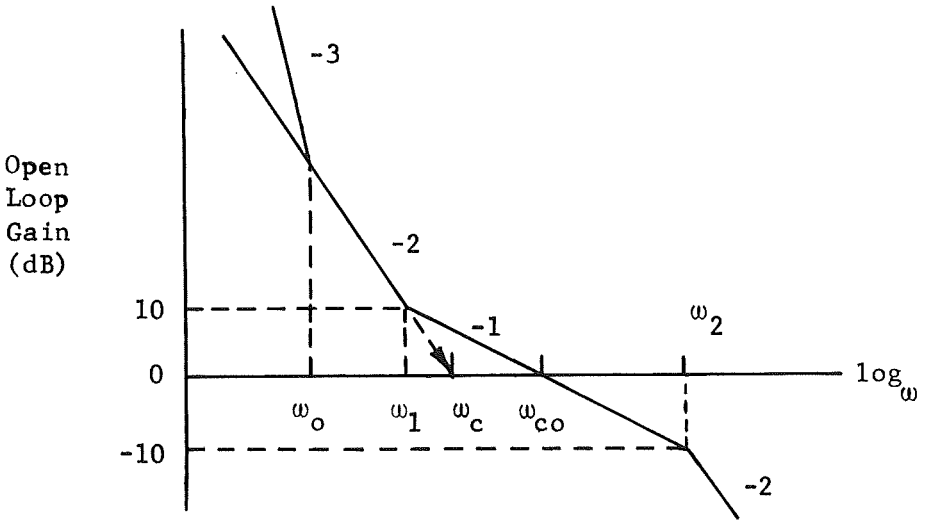

Now $G = J\omega_c^2$ and if $\omega_o = 0.1\ \omega_c$

Then $$\theta_{o(\tau)}\Big|_{SS} = \frac{10A}{J\omega_c^3} \quad \text{or} \quad \omega_c = \left[\frac{10A}{J\theta_{o(\tau)}\Big|_{SS}}\right]^{1/3}_{\max}$$

Hence $$\omega_{co} = \sqrt{3}\left[\frac{10A}{J\theta_{o(\tau)}\Big|_{SS}}\right]^{1/2}_{\max}$$

Figure 83. Gimbal-Axis Servo Mispointing Due to Torque Ramps

If wires across the gimbal axes are eliminated, or other means incorporated to avoid the wire torque creep disturbance, then aerodynamic torques will predominate. In this event, the crossover frequency of the proposed system could be reduced by a factor of 2.94 and the required guide star magnitude could be increased.

The attainable magnitude increment thus allowed would be less than the theoretical 1.17 due to the effects of background light and dark current.

Module D, Echelle Spectrograph

Use of free float suspension plus two star image-splitting error sensors is the recommended approach for stabilization using this module and represents an alternate method to the transfer lens approach for Module C, the f/10 film imagery package. With either module, the use of chain link transformers, capacitive-type position sensors, magnetic pushers, and other devices for achieving a high degree of isolation from vehicle disturbances, is suggested. The wire torque creep disturbance is thereby avoided and gravity gradient (1.5×10^{-3} pound-feet) and aerodynamic (29.5×10^{-3} pound-feet) torques predominate. These were shown to produce motional disturbances of 3,820 and 300,000 arc-seconds respectively in the unstabilized telescope at the associated disturbance frequencies. Loop gain requirements of module C are thus

$$\frac{3{,}820 \text{ arc-seconds}}{0.006 \text{ arc-seconds}} = 0.637 \times 10^{6};$$

$$\frac{300{,}000}{0.006} = 50 \times 10^{6}$$

at two and one cycles per orbit, respectively. Figure 84 indicates the crossover frequencies which then result from the use of certain characteristics. Illustrated are 10:1 lead-lag stabilized torqued-inertia systems with zero, one, and two low frequency integrations. It should be noted that the loop gains at the two disturbance frequencies are somewhat more than computed above so that total peak error is maintained at 0.006 arc-second. The integrations whose break frequencies are placed to contribute 5.7 degrees of extra lag at the crossover frequencies, have a small effect upon the noise bandwidth which in each case is approximately 2.5 times the corresponding crossover frequency. While the particular characteristics are by no means unique, two conclusions can be drawn. The use of at least one integrator is worthwhile to reduce the noise bandwidth and, the crossover frequency will be in the order of 0.1 Hz. While the dimmest guide star offering 0.006-arc-second accuracy (from Figure 71) is 14.4, background light (2-arc-minute field) and dark current (275K) degradation factors would be 2 and 3.3, respectively.

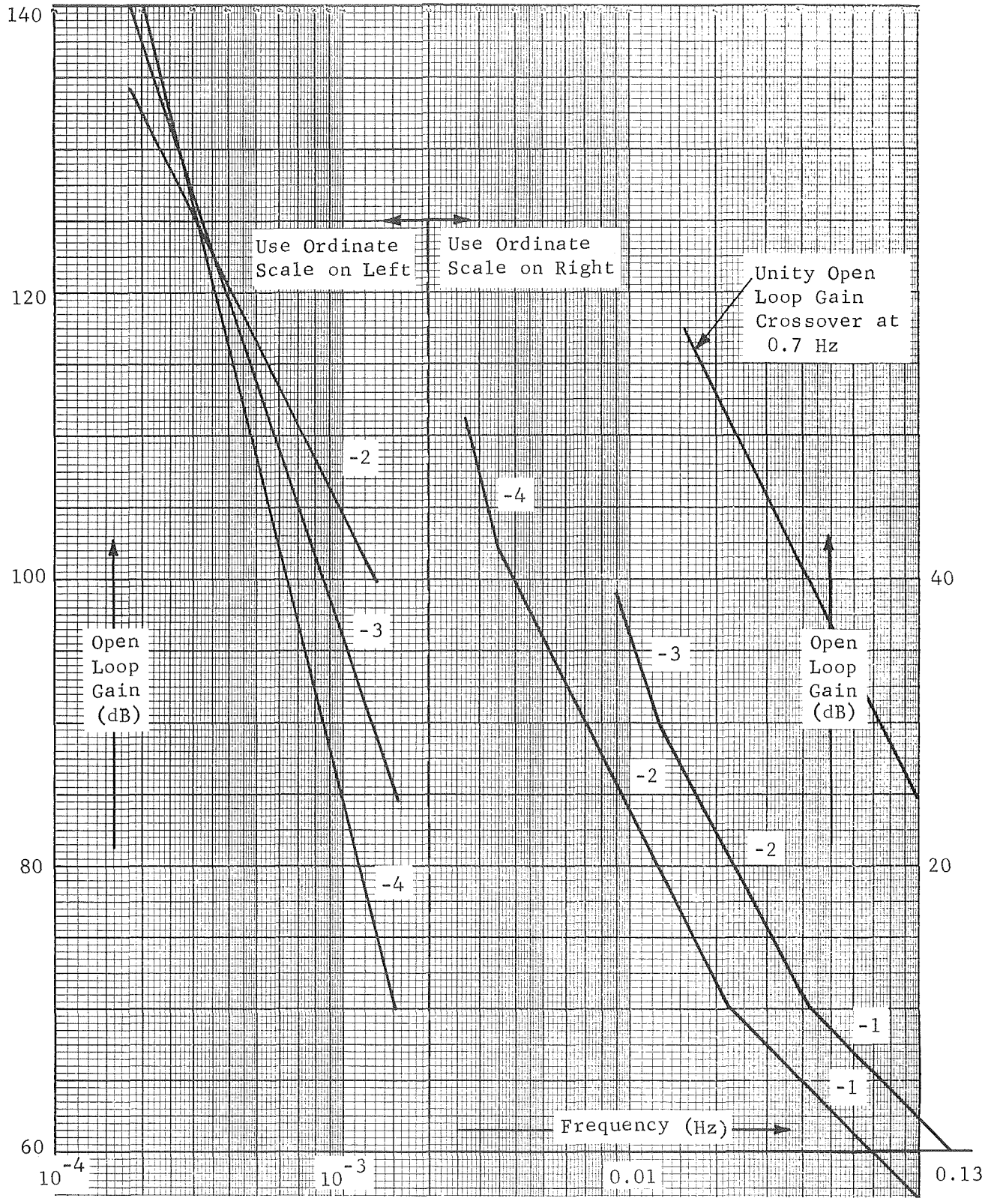

Figure 84. Open Loop Gain Characteristics for Module C.

Assumed Disturbances: Gravity Gradient of 1.5×10^{-3} pound-foot at Two Cycle per Orbit Plus Aerodynamic Torque of 29.5×10^{-3} pound-foot at One Cycle per Orbit

Operation with 11.5-magnitude stars, on the other hand, corresponds to 0.0038 arc-second which is graded to 0.01 arc-second by the background light (1.7) and dark current (2.34) degradation factors. Since this magnitude guide star has an associated 90-percent probability of dual occurrence in the guidance field of module C, it is concluded that brighter stars with corresponding lower occurrence probabilities shall be required. Twelfth-magnitude stars, offering probabilities of 37 percent at L = 90 degrees and 99.7 percent at L = 0 degree, will have an associated noise-induced error of 0.0032 arc-second including degradations.

The echelle spectrograph, module D, shall have a larger field of view allowing these brighter stars to appear about 90 percent of the time. If it is assumed that the associated guidance uses the same loop gain characteristic as for module C, then the peak x and y pointing errors shall each be

$$0.006 + 3\ (0.0032) = 0.0156 \text{ arc-second}$$

This shall be increased somewhat by a roll error component but should be adequate to avoid excessive light level variations within the spectrometer, due to mispointing, provided entrance diameters or slit widths of about 9 microns or larger are used. It should be recalled that total pointing error of 0.0233(0.0285)- arc-second peak corresponds to a one-percent (five percent) spectrometric light reduction for a slit width of 9 microns (refer to POINTING REQUIREMENTS).

As was indicated previously,* the roll pointing requirement for module C is 0.725 arc-second. While the disturbance torque-to-inertia ratio for roll is expected to be much less than for x and y, the same ratio shall be assumed. Accordingly, the roll gain requirement is $\frac{0.725}{0.006}$ = 120 times less than for translation. The crossover frequency for a (-3, -2, -1, -2) characteristic will then be ($\sqrt[3]{120}$ =) 5 times less or 0.02 Hz.

For module D, the roll error allowed for disturbance is 1.2 arc-seconds,** hence the gain requirement is $\frac{1.20}{0.006}$ = 200 times less and the crossover frequency is (5.9 times less or) 0.017 Hz. Since the same equivalent noise induced error in roll and cross line of sight occur when the bandwidths differ by

$$\left(\frac{\theta_X}{\theta_S}\right)^2 = \frac{\text{cross-line-of-sight bandwidth}}{\text{roll channel bandwidth}}$$

then assumption of the worst-case conditions presented in Figure 81 leads to

---

* Refer to section which discusses rotational aspect of module C stabilization when using transfer lens CLOS guidance.

** Taken as approximately four times the value required for module F since f/10 field utilization is about the same while permissible disturbance-induced error is here taken as 0.006 rather than 0.0015 arc-second.

required bandwidth ratios of 4.6. Hence it is concluded that roll performance shall be slightly better than required (i.e., 5.9 > 4.6 and 5 > 4.6).

Star Finding

The vehicle control concept for the LTEP spacecraft will be similar to that for the AAP but will differ in that star trackers rather than sun sensors will provide fine attitude commands. This is required since the LTEP experiments are not solar but stellar oriented. A possible configuration is depicted in Figure 85 and uses a roll star tracker plus two star sensors for pitch-yaw reference. The roll and coarse "pitch-yaw" sensor gimbal angles would be programmed to permit guide star tracking with the vehicle in any desired nominal attitude. The field of view of the sensors would be relatively large in order to ease the initial star acquisition in tasks. Operation on sixth-magnitude stars or brighter would require the use of ±15-degree gimbal angle ranges to obtain a 99-percent star occurrence probability when operating at or near the galactic poles. An optical field of a few degrees would be compatible with this since the probability of its viewing two bright stars simultaneously is extremely low: viz, the probability of observing one sixth-magnitude or brighter star in a 1-degree field is less than 10 percent at low latitudes. The fine sensor would be similarly gimbaled to work on like-magnitude guide stars. However, this sensor will be attached to the figure sensor support to minimize its boresight errors with the LTEP telescope. The field of view of the fine sensor must be large enough to permit it to capture its guide star in spite of boresight errors with the coarse sensor when the latter is controlling the vehicle.

The ATM gimbal ring zeroing mechanism has an estimated error of approximately 5 to 10 arc-minutes which sets the minimum field diameter to 10 to 20 arc-minutes. This can be reduced to about 2 arc-minutes by correcting the coarse sensor gimbal angles to compensate for ATM gimbal zeroing errors. This is possible since the ATM gimbal angle sensors are accurate to 1 arc-minute. Even with such correction and careful structural design to minimize additional boresight error components, a larger field - in the order of 10 arc-minutes - can be anticipated. Smaller fields could be used if the coarse sensor line of sight is perturbated to cause vehicle gyrations until the fine sensor sees its guide star, but this is considered an unnecessary complication. When available, signals from the fine sensor would be used to control the vehicle and so obtain fine sensor null. The LTEP instrument thereby has its line of sight controlled and will be able to acquire its (different) guide stars if directed within 1 arc-minute, the minimum proposed radial size of the various experiment guidance sensors. The predominating error in this regard is that due to the imperfections of the fine sensor gimbals whose angles must thus be within 42 arc-seconds. This level is attainable utilizing either available precision encoders (2^{18}) or synchros (20 arc-second available in size 15) in closed-loop servo control arrangements. Figure 86 shows one conceptual approach for accomplishing this with digital input commands and synchro shaft position sensors. Here the data storage registers (pictured from simplicity as relays K_1 through K_n)

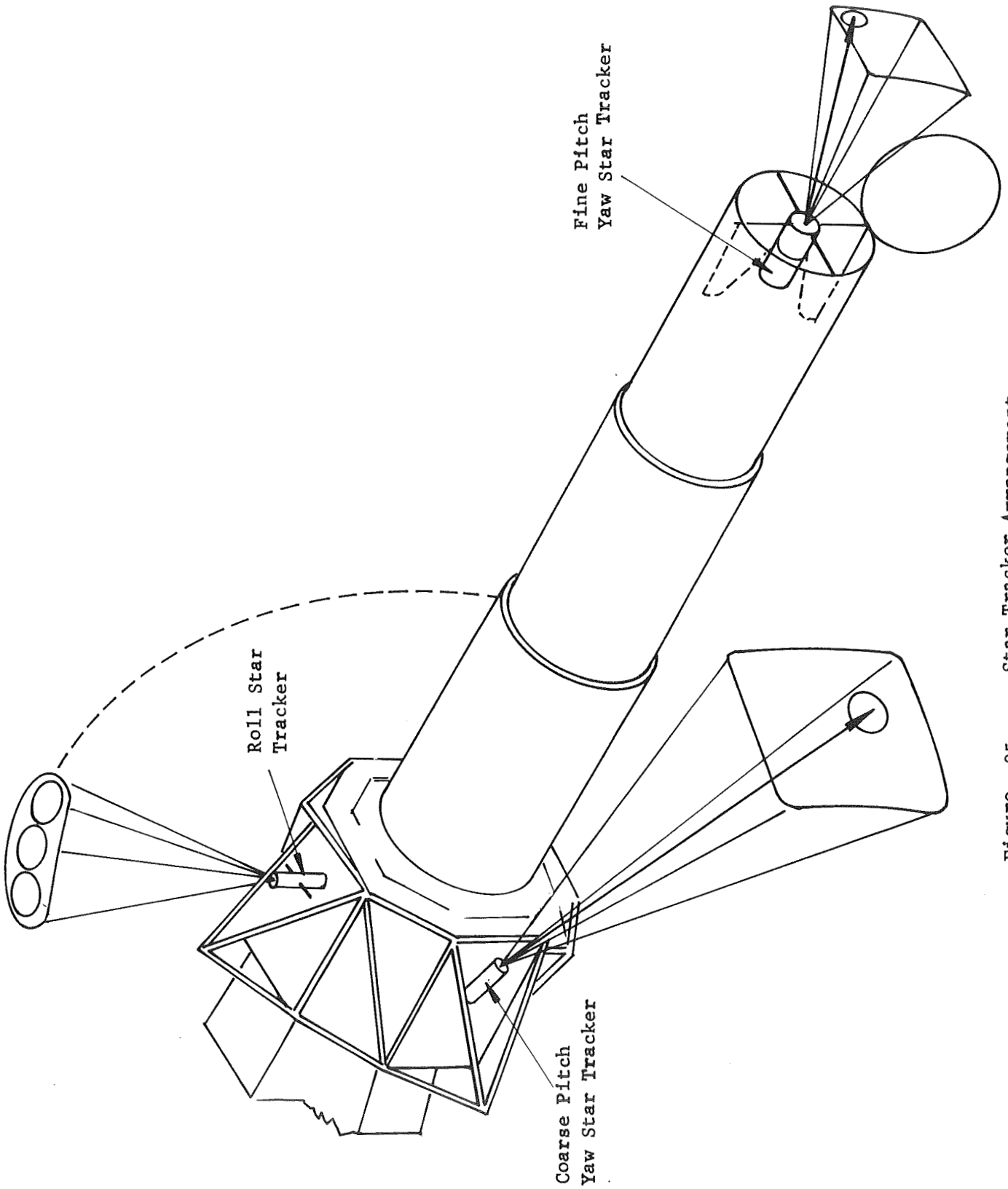

Figure 85 • Star Tracker Arrangement

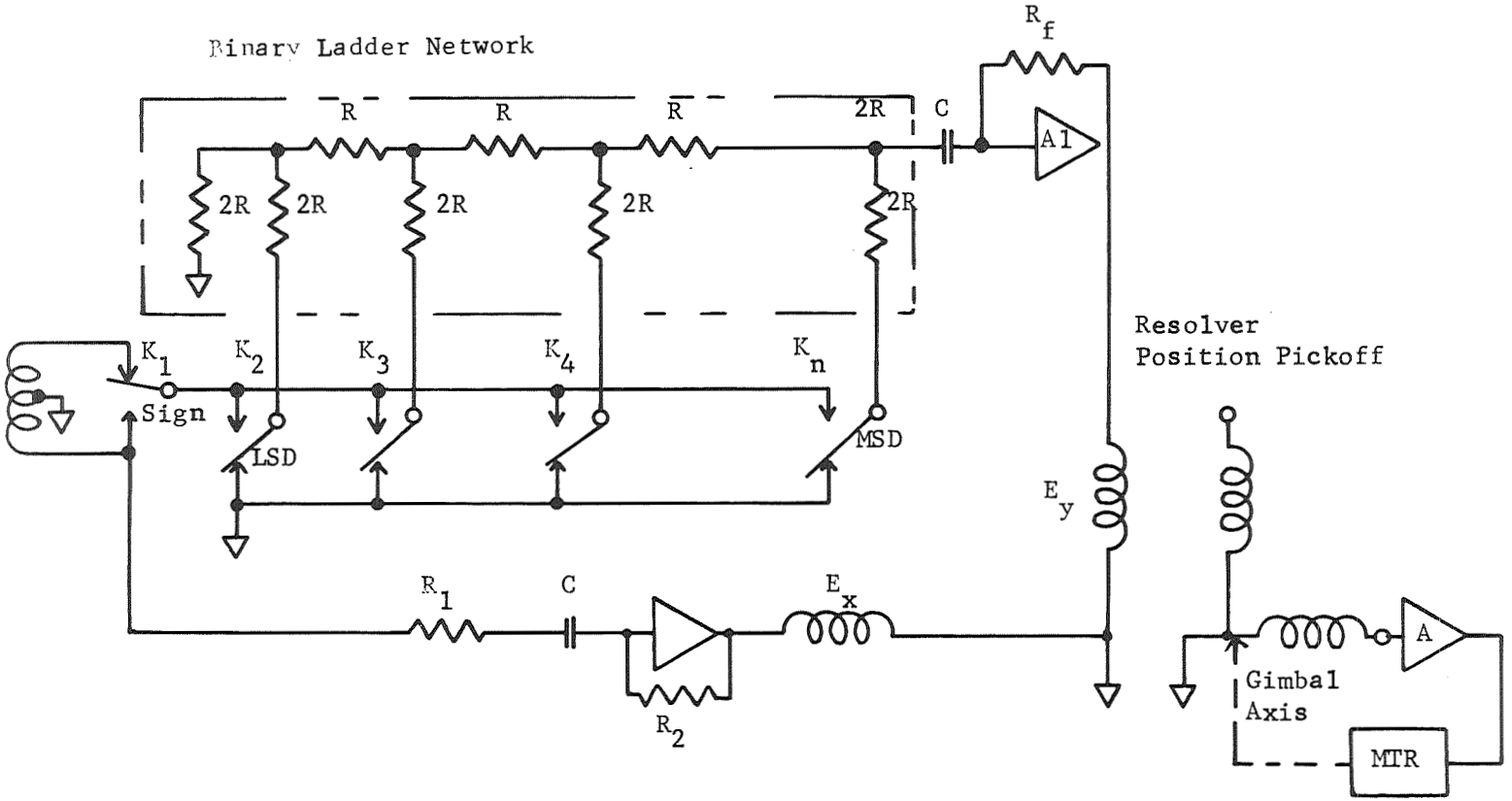

Figure 86. Possible Gimbal Axis Controller

operate in conjunction with the binary ladder network energized with ac, to convert the digital command to an ac analog output signal. This signal is applied to one resolver winding via amplifier A1 while amplifier A2 applies a fixed reference E_x to the other winding. The arrangement is such that the input digital command precisely determines the flux field direction set up within the resolve, and, therefore, the shaft orientation at which a null in the error signal is obtained; i.e.,

$$\varphi = \tan^{-1} \frac{E_y}{E_x}$$

where E_x is constant and the sign and magnitude of E_y is ground-command to obtain desired angles in the range of up to ±15 degrees. The servo sensitivity (volts per angular error from null) is directly proportional to $\sqrt{E_x^2 + E_y^2}$ and so will increase with gimbal angle magnitude ($S = K/\cos \varphi$) but should present no real servo design problems. The circuitry for controlling the motor to attain null is straightforward. A command word length of 16 bits, corresponding to an accuracy of one part in 65,536, will be required to quantize the 30-degree angular range into 16.5-arc-second increments.

Whatever the implementation, there appear to be only two ways to avoid the relatively stringent accuracy requirements. Either the radial size of the various LTEP pointing sensors could be increased or the fine star tracker line of sight could be perturbated to force vehicle search manuevers. The former alternate is rather strongly constrained in that the potential field available in which to position the LTEP experiment image-splitting prism is fixed by optical considerations. Hence, as the splitting prism size is increased, the apex cannot be positioned as close to the edge of the overall field. This in turn forces the use of dimmer guide stars to maintain a reasonable occurrence probability. The latter alternative, while undesirable, might be rather readily accomplished with existing star trackers such as the ITT OAO sensor, whose characteristics are given in Table 21. The unit provides acquisition-mode all-electronic scanning, and features detection of angular deviation of target star from sensor line of sight. Either error gradient-modifying bias signals or the electronic gimbaling (offset) feature offers convenient means for introducing search commands, without requiring associated gimbal axis motions.

SUMMARY OF POINTING IMPLEMENTATION

The coarse star tracker provides initial spacecraft pitch-yaw control, which is later provided by the fine pitch-yaw star tracker, while the roll star tracker controls the roll axis. The error signals generated by sensors internal to the LTEP telescope will then control either the transfer lens or gimbal axes to further refine the LTEP line of sight. When the transfer lens is operating, its position pickoff signals will be used to bias the vehicle position to maintain device operation around null. Such signals will be alternately derived from the gimbal angle sensors during gimbal operation and from the capacitive position sensors during magnetic suspension mode.

TABLE 21 . ITT OAO SENSOR CHARACTERISTICS

Star Magnitude Sensitivity	+6
Field of view	10 arc-minutes
Tracking accuracy	1 1/2 arc-seconds RMS
Error Filter Bandwidth	0.5 Hz
Error Gradient	1 v/arc-minute
Photo Surface	S-20
Weight Total	25
Optics	4.85 inches - F/1.85
Electronic Gimbaling (Offset)	±1.5 degrees in 15 arc-second steps
Voltage	±28 VDC ±10V
Power	7.7 Watts
Sensor Size	3 x 15 inches
Electronics Size	5 inches x 11 inches x 12 inches

The signal flow corresponding to the approach described above is shown in Figure 87 . During coarse star track control, the roll star tracker output signals are used directly to torque the vehicle's integrating rate gyros. It should be noted that the roll star tracker will be nearly coincident with the vehicle roll axis; viz, a ±0.5-degree gimbal range and 360 degrees of vehicle roll provide a potential guide star region of 360 square degrees. The signals from the coarse star tracker, which generally guides on stars offset from the LTEP telescope and vehicle roll axis, must be corrected to avoid interaction with the roll channel. For very small offset angles the correction components are as shown, the roll error signal times the sines of the appropriate star tracker gimbal offset angles.

The resulting pitch, yaw, and roll error signals are then used to torque the vehicle's Integrating Rate Gyros (IRG), and therefore the whole vehicle, to the correct position. Stability compensation feed back, indicated by dashed lines in Figure 87 , can be incorporated to obtain desired response characteristics. When the fine star tracker acquires its guide star, IRG corrections are obtained from this sensor whose signals are similarly corrected by processed roll error signals and, in addition, coordinate converted by a resolver into the vehicle

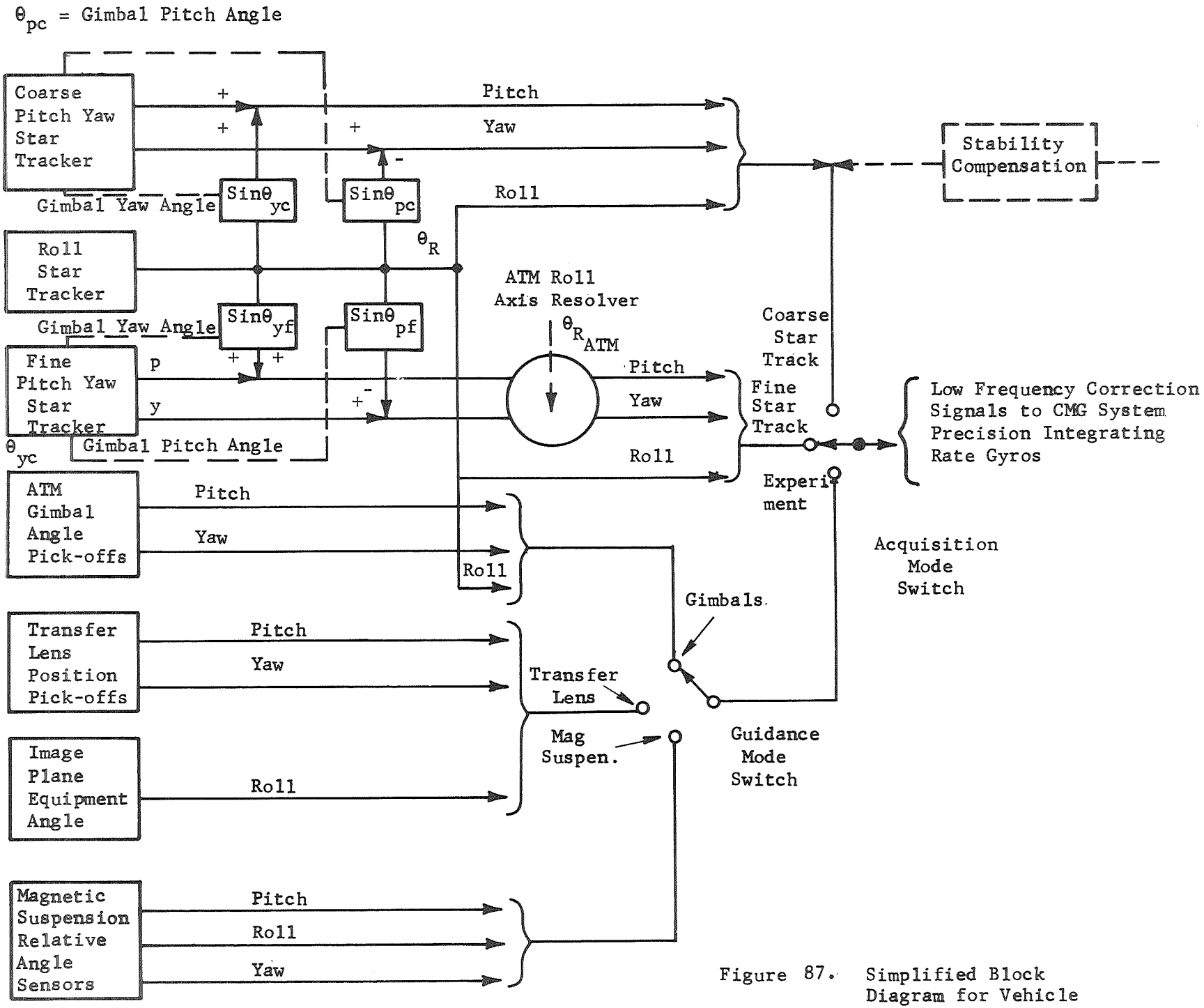

Figure 87. Simplified Block Diagram for Vehicle Control

coordinate system. During experiments, signals derived internal to the LTEP instrument from various sensors, depending upon the pointing control mode, are heavily filtered and used as a long term reference for the vehicle IRG units. The star trackers can be operated during this time in a self-nulling mode to remove boresight errors and hence provide more rapid reacquisition should this be subsequently required.

An inseparable aspect of acquisition and tracking is whether the main optical elements, which are separated by relatively large distances, will retain their required positions. Motion of the secondary with respect to the primary will not only cause excessive optical degradations, but in addition, will change the line of sight, thus compounding the acquisition and tracking tasks. The acquisition technique described above, for example, assumes that the fine star tracker and the LTEP line of sight are coincident within 1 arc-minute with most of this error attributable to sensor gimbal imperfections. The whole question of acquisition and tracking performance in the presence of mechanical and thermal disturbances to the optical elements will now be considered. This is appropriately done now, before discussing the separate LTEP pointing mechanizations, since all such arrangements are crucially dependent for success on the Active Optic controls to be described.

The allowed figure sensor and secondary mirror radial deflections are determinable from previously derived equations and are summarized in Figure 88. In the case of the figure sensor, tolerable axial motions, expressed in wavelength units, were shown to be

$$\Delta x = 16F^2\Gamma\left(1 + \frac{1}{16}F^2\right)^{\frac{1}{2}}$$

where F = mirror f-number

and Γ = fringe measuring accuracy of the phase measurement interferometer

adial translational tolerances were given as

$$\Delta y = \pm 8F\Gamma\left(1 + \frac{1}{16}F^2\right)^{\frac{1}{2}}$$

or an f/2 primary, an alignment requirement of $\Gamma = \frac{1}{50}$ wave leads to axial and adial tolerances of 1 and 1/4 wave, respectively (or 20 and 5 microinches for = 0.5 micron).

he secondary mirror on the other hand, has a radial (coma) constraint of

$$\Delta y = 64\frac{\lambda}{n}F^3$$

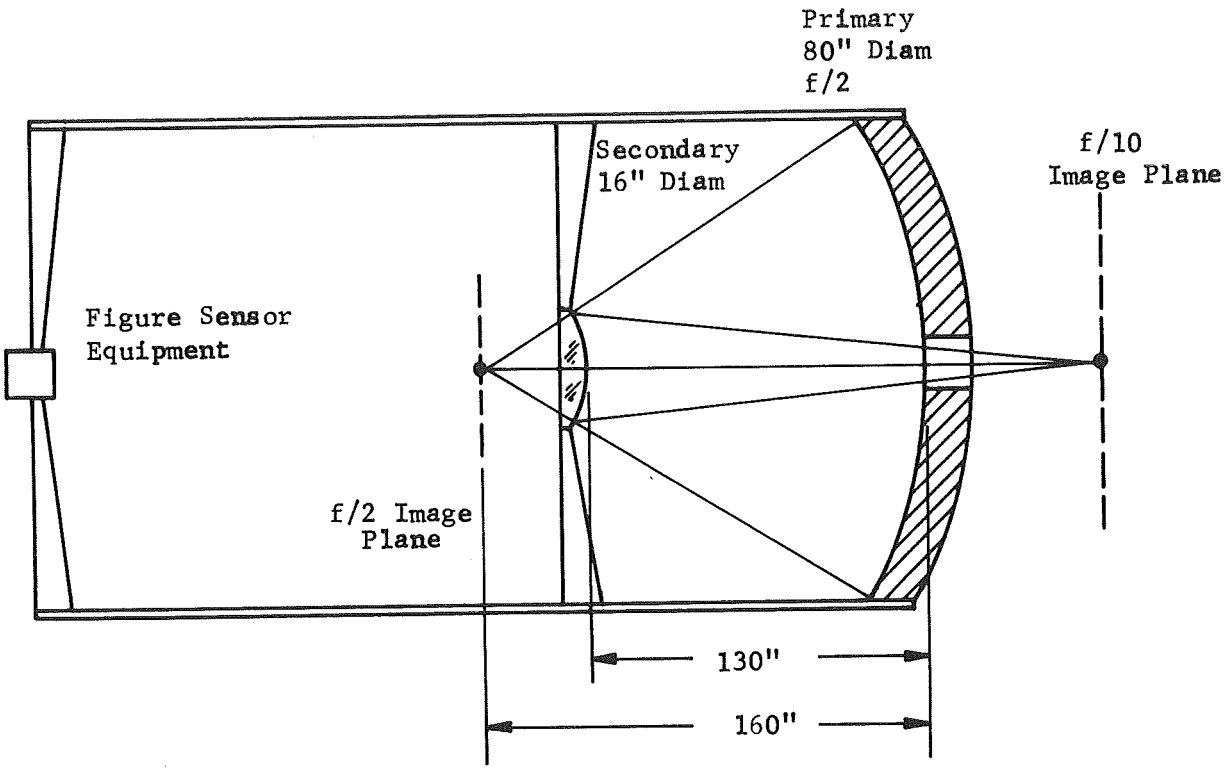

Constraints on Secondary Mirror Motion

A) Radial Motion = $64\frac{\lambda}{\eta} F_P^3$; $\frac{\lambda}{4}$ Coma Effect

B) Radial Motion = $\theta D_p F_p \frac{m}{m+1}$; Line-of-Sight Change

C) Axial Motion = $8\frac{\lambda}{\eta} F_p^2 \frac{m^2}{1+m^2}$; Defocusing

where F_p = primary mirror f-number

λ/η = wavefront deviation permissible

θ = allowed line-of-sight change

D_p = primary mirror diameter

m = secondary mirror magnification

Figure 88. Effects of Secondary Mirror Motion

which leads to a tolerance of about $\frac{1}{1000}$ inch to maintain coma degradation within $\frac{1}{10}$ wave at 0.5 micron.

The axial constraint

$$\Delta x = 8\frac{\lambda}{n} F^2$$

is much tighter amounting to 64 microinches for a 1/10-wave criterion at the same wavelength.

An appropriate tolerance for the angular alignment of the figure sensor structure to the LTEP would be a few arc-seconds, a value appreciably smaller than the total assumed 1 arc-minute of boresight error.

Structural Translation Acceleration Tolerance

LTEP telescope structure translational accelerations appear at the gimbal axes, whether free or clamped, due to vehicle rotations about some other point. The tube structure will deform, due to bending and shear deflections, and both the secondary mirror and figure sensor will depart radially from the primary mirror axis. While the secondary mirror is located by means of quartz spacers, the figure sensor is not so constrained, and angular as well as translation motions will appear.

The magnitude of the deflections may be estimated by considering the structure to be a simple beam, fixed at the primary mirror end, with the secondary and figure sensor located at the midpoint and free end, respectively. This shall be done with the aid of the simple beam formulae of Table 22, assuming that the first resonant bending mode is 18.8 Hz, as computed previously by LMSC (for a distributed lumped-mass model).

An expression for EI/m^3 in terms of w_n can be obtained from the resonant mode equation and substituted into the end deflection formula to obtain

$$y_B = g/w_n^2$$

in the case of an end-loaded beam. A similar expression

$$y_B = 1.55\ g/w_n^2$$

results in the case of a uniformly-loaded beam.

These equations indicate that the allowed translational acceleration can be expressed as

$$a = \frac{y_B w_n^2}{C}$$

where y_B is the maximum allowed end deflection

and C is a constant; unity for end-loaded beam and 1.55 for uniformly-loaded beam.

TABLE 22.. CANTILEVER BEAM FORMULA

		End Loaded	Uniform
First Resonant Bending Mode, w_n		$w_n = 1.732\sqrt{\frac{EI}{m\ell^3}}$	$w_n = 3.52\sqrt{\frac{EI}{\mu\ell^4}}$
Max Bending Deflection y_B	End	$y_B = \frac{1}{3}\frac{w\ell^3}{EI}$	$y_B = \frac{1}{8}\frac{w\ell^3}{EI}$
	Other	$y_B = \frac{1}{6}\frac{w}{EI}(X^3-3\ell^2X+2\ell^3)$	$y_B = \frac{1}{24}\frac{w}{EI\ell}(X^4-4\ell^3X+3\ell^4)$
	Mid	5/16 of end	$\frac{17}{48}$ of end
Max Slope θ, Due to Bending	End	$\theta = \frac{1}{2}\frac{w\ell^2}{EI}$	$\theta = \frac{1}{6}\frac{w\ell^2}{EI}$
Shear Deflection,	End	$y_S = \frac{\ell w}{AM_S}$	

E = Young Modulus, pounds/inch^2

m = load mass, slugs

ℓ = beam length, inch

x = distance from free end of beam, inch

I = area moment of inertia, inch^4

w = mg (or mass times gravity)

μ = beam mass per unit length

y = deflection in inches

θ = angle in radians

M_S = shear modulus (1/2 to 1/3 E)

A = cross sectional area of beam

Since the mid point and end deflections are proportionally related, the same expression applies with modified C values; i.e., $\frac{16}{5} = 3.2$ end-loaded and $1.55 \times \frac{48}{17} = 4.38$ for uniform loading cases.

A similar acceleration constraint can be derived from the shear deflection formula; i.e.,

$$a = \frac{y_S A M_S}{\ell m}$$

where y_S is the maximum allowed shear deflection.

The maximum tolerable accelerations, based upon estimated parameters and the foregoing formulae, can now be determined. The values of C shall be taken as the average of the stated extremes in the end and midpoint deflection formulae; i.e., 1.25 and 3.8, respectively. Accordingly, the maximum acceleration based on the figure sensor tolerable radial deflection is

$$a = \frac{5 \times 10^{-6}(18.8 \times 6.28)^2}{1.25} = 0.0556 \text{ inch/sec}^2$$

or about 1.44×10^{-4}g.

Similarly, for the case of the secondary mirror,

$$a = \frac{1 \times 10^{-3}(18.8 \times 6.28)^2}{3.8} = 3.67 \text{ inch/sec}^2$$

or about 0.114g.

Shear deformation constraints will be based upon a 100-inch diameter 0.03-inch-thick aluminum tube structure ($A = 9.42$ square inches and $M_S = 3.8 \times 10^6$ pound/inch^2). The estimated length and mass shall be taken as 130 inches and 750/32 slugs in computing the secondary mirror constraint; i.e.,

$$a = \frac{1 \times 10^{-3} \times 9.42 \times 3.8 \times 10^6 \times 32 \times 12}{130 \times 750} = 141 \text{ inch/sec}^2$$

or 0.365g.

Computation of the figure sensor constraint, based upon an estimated mass-length product of (1m =) 500 slug inches, yields

$$a = \frac{5 \times 10^{-6} \times 9.42 \times 3.8 \times 10^6 \times 12}{5000}$$

or 0.0011g.

The vehicle motional constraints imposed are presented in Figure 89 which relates rotational peak amplitude and associated frequency to translational acceleration at the gimbals, assumed to be 20 feet from the center of rotation. The allowed acceleration levels, as computed above, are presented as horizontal lines (based upon the use of scales A). It is seen that the most stringent requirements arise from bending-induced radial deflections at the figure sensor. For example, only 1 arc-minute of peak vehicle motion at 0.14 Hz, or 6 arc-seconds at 1.4Hz, is tolerable. Thus the astronaut wall pushoff cycle disturbance of 5.3 arc-minutes, with frequency components in the 0.1 to 1.0Hz range, is seen to be excessive unless the figure sensor position is actively controlled. While such control is contemplated, it is doubtful whether control loops with bandwidths in the 10Hz range (to offer sufficient attenuation at the disturbance frequencies) are practical. This is another reason for the elimination of astronaut disturbance during intervals when precise pointing is required.

Referring again to Figure 89, it is seen that the allowed disturbance magnitude at gravity gradient frequency is very large with a 10-arc-minute peak amplitude causing 10^{-8}g, and acceleration 1.44×10^4 times less than allowed. Equally significant is the fact that disturbance amplitudes over 10-arc-minutes peak at 0.03 Hz, the vehicle bandwidth, are tolerable. Hence, vehicle mispointing due to sensor noise can be expected to have negligible effects from the standpoint of structural rigidity.

Line-of-Sight Restrictions

The aforementioned constraints, evolved to avoid excessive optical degradations, also place implicit restrictions on associated LTEP line-of-sight deviations: that is, a secondary mirror radial translation of δ deviates the line of sight by

$$\theta = \frac{\delta \frac{m+1}{m}}{D_P F_P}$$

where m is the secondary mirror magnification

D_P is the primary mirror diameter and

F_P is the primary mirror f-number

For $m = 5$, $D_P = 80$ inches, and $F_P = 2$, it is found that

$$\frac{\theta}{\delta} = \frac{6}{5 \times 2 \times 80} = 0.0075 \frac{\text{rad}}{\text{inch}} = 1{,}545 \frac{\text{arc-seconds}}{\text{inch}}$$

Since the secondary mirror radial translation due to 0.000144 g (the figure sensor constraint for bending) is only about

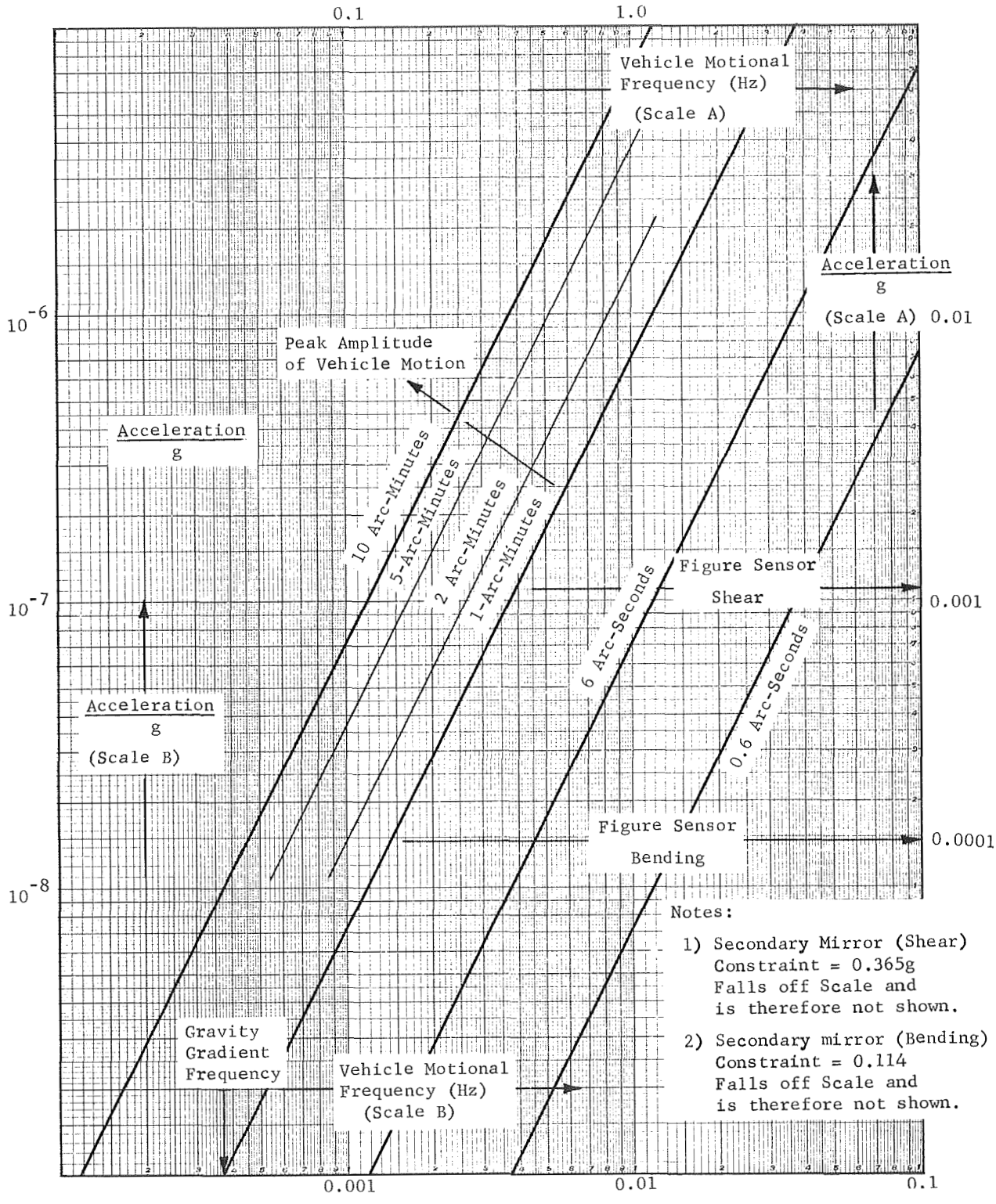

Figure 89. Translational Acceleration At ATM Gimbals Due to Vehicle Rotation

Distance From Rotation to Gimbal Axis Assumed as 20'

$$y_B = \frac{1.44 \times 10^{-4} \times 32.2 \times 12}{3.8\ (18.8 \times 6.28)^2} = 2.04 \text{ microinches}$$

then the implied line-of-sight constraint is only 0.00315 arc-second.

Line of Sight - Figure Sensor Misalignment

The misalignment between the LTEP line of sight and the figure sensor structure due to this same acceleration level can be readily evaluated since (refer to Table 23) the end slope and deflection of a simple beam are simply related. For an end-loaded beam

$$\theta = \frac{3}{2} \quad y_{B/\ell},$$

while for uniform loading

$$\theta = \frac{8}{6} \quad y_{B/\ell}.$$

Since the figure sensor allowed y_B was taken as 5 microinches, the end slope would be in the order of

$$\theta = 1.5 \times \frac{5 \times 10^{-6}}{320} \times 206{,}000 = 0.0047 \text{ arc-second}$$

which is also an implied constraint when limiting the translational acceleration to 1.44×10^{-4} g.

It is thus concluded that the mechanical disturbances introduced by vehicle motions should not betroublesome provided the astronaut is not present.

Thermally Induced Disturbances

Active alignment means are nevertheless required to combat the thermally-induced disturbances. Lockheed studies* have indicated that temperature gradients due to solar heating can induce worst case deflections well in excess of allowed levels (refer to Table 23).

TABLE 23: ESTIMATED VALUES FOR SOLAR RADIATION INDUCED DEFLECTIONS

Component	Amount of Deflection/rate of motion		
	Radial Translation	Axial Translation	Angular
Figure Sensor	1 inch / 0.00067 in./sec.	0.058 inch	800 arc-second / 0.5 arc-sec/sec
Secondary Mirror	0.23 inch / 0.00015 in./sec.	NA (See Note 1)	NA (See Note 1)

Note 1: Secondary to primary spacing and angle constrained by four quartz spacer rods.

*LTEP thermal/structural distortion effect on optical alignment and pointing. LMSC LTEP Report 4.5-2, July 31, 1969.

The angular motion and radial translations are induced by temperature differences of almost 65°F across the tube. The approximate rates of temperature change were 65°F per 1500 seconds (buildup) and -65°F per 1800 seconds (cooldown). The axial translation was due to an 11-degree estimated average temperature variation of the structural tube.

The results given by Table 23 can be used to determine some of the requirements for the active control loops. For example, if the temperature difference variation is taken to be sinusoidal, then the temperature extremes and rates determine an equivalent frequency: viz.

$$\theta \Big|_{max} = \frac{65}{2} (\sin\omega t) \Big|_{max} = \frac{65}{2} \ ^\circ F$$

$$\dot{\theta} \Big|_{max} = \frac{65}{2} \omega(\cos\omega t) \Big|_{max} = \frac{65}{1500} \ ^\circ F/sec$$

$$\therefore \omega = \frac{2}{1500} \quad \text{or} \quad f = 0.0084$$

Since radial translation is proportionally related to temperature difference, then the figure sensor radial translation can be expressed as

$$y_T \doteq \frac{1}{2}'' \sin 2\pi (0.0084)\, t, \text{ inch}$$

To reduce this to 5 microinches peak with an active control loop requires a minimum open loop gain of

$$OLG = \frac{500{,}000 \text{ microinch}}{5 \text{ microinch}} = 100{,}000$$

at 0.0084 Hz. This can be achieved with a (-2, -1, -2) system, provided the crossover frequency is in the order of 4.7 Hz. Resort to systems with steeper low frequency slopes, for example (-3, -3, -1, -2) or (-4, -2, -1, -2) systems, can reduce this to near 1.4 and 1.1 Hz. The associated actuators must be capable of increments of less than 5 microinches and must provide a total travel of 2 inches (a ratio of 4×10^5).

Less stringent requirements apply to both the angular correction loop which acts to reduce 800 arc-seconds to less than 1 arc-second, and the axial correction loop which must reduce 58,000 microinches, to under 20 microinches. Approximate crossover frequencies assuming the same loop characteristic shapes are given in Table 24 .

TABLE 24 : ESTIMATED CROSSOVER FREQUENCIES FOR ACTIVE OPTIC CONTROL LOOPS

Loop		Type of Characteristic			Accuracy Criterion	Disturbance Peak Ampl.
		(-2,-1,-2)	(-3,-2,-1,-2)	(-4,-2,-1,-2)		
Figure Sensor	Radial Positioning	4.7 Hz	1.4 Hz	1.1 Hz	5μ"	0.5 inch
	Axial Positioning	0.81	0.24	0.19	20μ"	0.053 inch
	Angular Positioning	0.45	0.134	0.10	1 arc-sec	800 arc-sec.
Secondary Mirror	Radial Positioning	0.23	0.069	0.051	10^{-3} inch	0.23 inch

This tabulation also indicates the crossover frequencies required for the secondary mirror control to reduce 0.23 inch of motion to a thousandth of an inch.

Further investigation will be required to establish whether these requirements can be met as is or can be conveniently relaxed. The use of secondary-to-figure sensor spacer rods, for example, would significantly reduce, or possibly eliminate, the axial and angular positioning requirements for the figure sensor. The signal to noise ratios available from the active control loop sensors should be assessed to determine whether acceptably low noise-induced errors will exist in the various loops. It is also recommended that serious consideration be given to structural-thermal design modifications which reduce the basic deflections caused by non-uniform solar heating. Other optical arrangements of figure sensor, secondary mirror and primary mirror should be sought to determine alternate forms which are inherently less sensitive to structural deflections.

TELESCOPE TRANSFER LENS SYSTEM

Final refinement of the LTEP line of sight, utilizing transfer lens techniques, has been recommended for modules C and F, the f/10 film and f/50 electronic imagery instruments. The particular mechanization proposed for the latter module involved controlled rotations of the secondary mirror about its short conjugate point, which is simultaneously maintained in coincidence with the prime focus. Since the secondary mirror magnification is 5X, an angular motion of 5 arc-seconds, for example, would compensate for a 1 arc-second line-of-sight mispointing. While this hardware approach would suffice for other modules, alternate arrangements can be considered. Possible configurations, in this regard, would include x-y translations of the equipment at the f/10 image plane to match image motion and thereby avoid optical degradations due to relative motion effects. In the event of a payload utilizing the f/10 as intermediate image plane, either refractive or reflective transfer lenses

working in either collimated or uncollimated beams, are possible alternates. The exact choice would depend upon the particular experiment requirements and image movers could be considered to reduce the required size of optical elements subsequent to the f/10 image plane. Motional compensation subsequent to the f/10 plane is an attractive approach since the associated optical elements would be much smaller, permitting use of more compact and efficient actuators, sensors, and other related hardware. As will become apparent later, this also facilitates temporary use of the transfer lens in a high bandwidth mode to obtain better acquisition characteristics (viz, reduced acquisition time). Presented below are the general considerations involved in the use of transfer lens stabilization for LTEP.

Concepts and Equipment

Figure 90 indicates the interaction of the vehicle control system and a transfer lens subsystem when the latter provides low frequency correction signals to the vehicle's IRG torquers.

The vehicle control system operates to maintain a given pointing direction, θ_{ref}, which can in general differ from required LTEP line of sight θ_s by an amount θ_n. The transfer lens compensates by introducing line-of-sight corrections θ_{TL} which differ from θ_n by the residual LTEP pointing error, θ_o. If the transfer lens is held on axis, then the vehicle dynamics are determined by its controller. If the transfer lens is now allowed to move off axis, its output signals to the vehicle's IRG will torque the gyro to reduce θ_n to zero. Since the correctional rate is proportional to θ_{TL}, the effect is equivalent to the signal path represented by the integrator. Moreover, the transfer lens loop, shown encircled by the dashed line, can be represented as unity transfer function for frequencies well within its bandwidths. In effect, then, the transfer lens path driving the IRG torquer constitutes the addition of an integration in parallel with the unity transmission path of the vehicle control loop. Adverse stability effects, under such circumstances, can be avoided by limiting the gain of the integration path to unity at a frequency well below the vehicle bandwidth. If this frequency is one tenth the vehicle 0.03Hz bandwidth, the integration which then results will reduce the vehicle mispointing at the gravity gradient frequency. This was mentioned before, in connection with vehicle disturbances, as the assumed approach to reduce vehicle mispointing to approximately 5 arc-seconds. The required integration gain ($\approx$0.02) is implemented by adjusting the system so the gyro is torqued at the rate of 0.02 arc-second /sec per arc-second of transfer lens compensation. Gyro dc rate error, it should be noted, will then be counteracted by a decentered nominal operating position of the transfer lens.

Secondary mirror correction of the LTEP line of sight is especially attractive since it avoids the use of extra optical elements and control signals can be developed in any of the various experiment payloads.

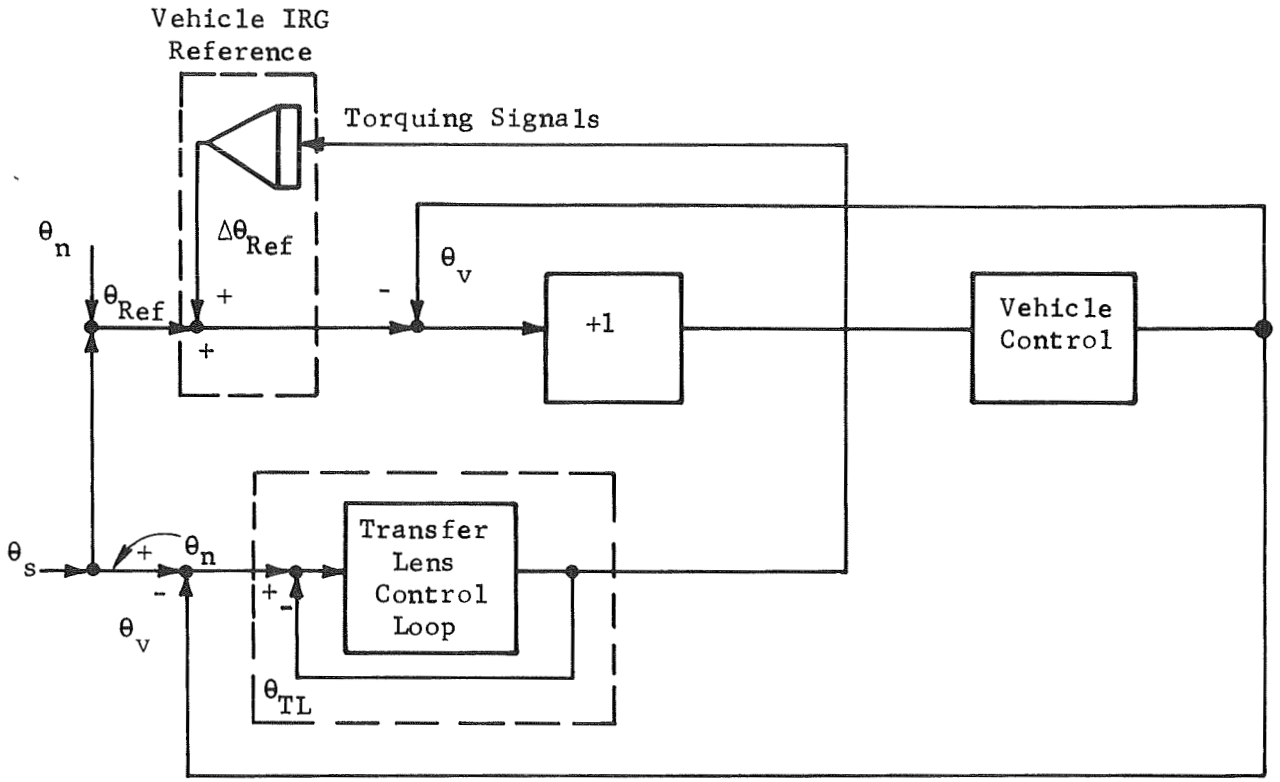

which reduces to:

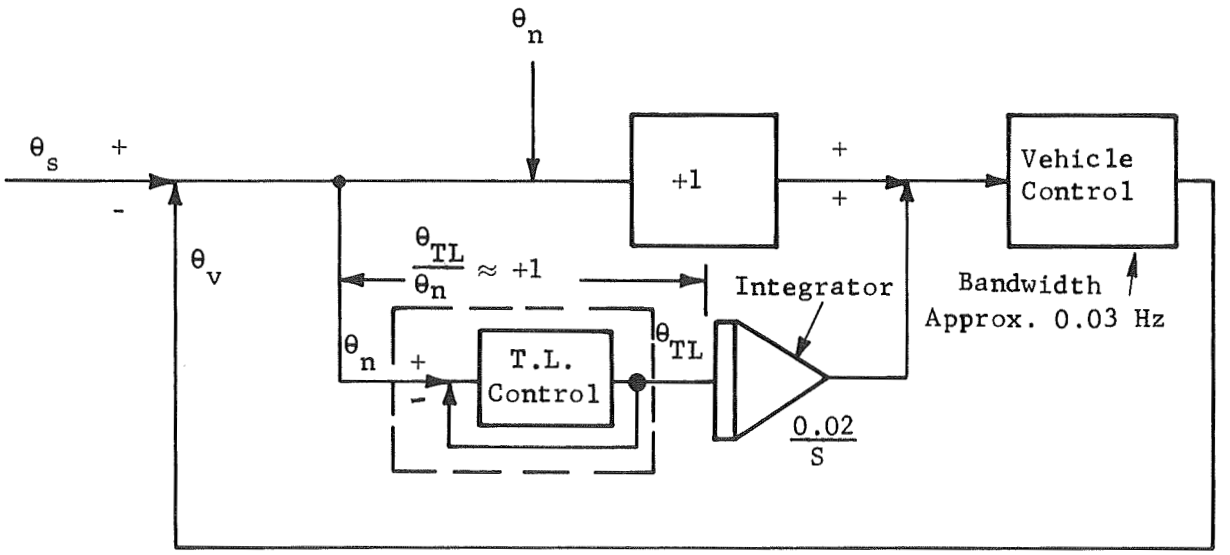

Figure 90. Interaction Between Vehicle and Transfer Lens Control Systems

As in all transfer lens mechanizations, it is particularly important to avoid ill effects arising from unintentional motions either accompanying corrective actions or existing independently. In the case of the secondary mirror approach, the secondary mirror conjugate and prime focus points must remain radially coincident within $64 \lambda F^3/n$ to avoid excessive coma. Variations in the axial direction must be within $8 \lambda F^2/n$ to maintain reasonably good focus. While quartz rods are proposed to maintain secondary-to-primary axial spacing, an active control is also advised and could take one of several forms. The Stratoscope II system, for example, accomplished this (focusing) by either of two methods, each of which involved examination of a star image at an equipment image plane. The first method utilizes orthogonal slit scans of the image to detect focus conditions by intensity versus position (time) variation and, in addition, the presence of coma evidenced by unsymmetrical responses. The second method involves the injection of electrical dither signals into the transfer lens control electronics. The servo responds by driving the transfer lens to generate compensating error signals. In-focus conditions are indicated by the minimum excursions which are required when the image is sharpest. While both of these methods have involved the use of operators in control of focus, automatic equivalents are possible. A third method, entirely automatic and already demonstrated with spaceworthy hardware, resorts to light projected from the desired image plane out through the optical system where it is redirected by two penta prisms back to the image plane. This method is known as the Telescope Alignment System (TAS).

The TAS arrangement features a roof prism at the image plane with a blunt nose through which two beams emerge, one toward each penta. These latter elements, positioned at diametrically opposite locations in the main aperture, receive the emergent beams and direct them across to each other where the light is then redirected back into the optical system. The two beams thus travel opposite paths to return reimaged onto the roof prism nose, provided good focus exists. Under poor focus conditions, the returning light strikes the sides, rather than the nose, of the prism and is reflected therefrom to two photodetectors whose outputs are differenced to obtain a focus error signal. This is possible since the two beams are temporally coded, 180 degrees out of phase, and strike opposite sides of the prism, each shifting from one side to the other as perfect focus is traversed. The system features ac - excited gallium arsenide emitters and solid state photodetectors and offers adequate signal-to-noise ratios even with bandwidths in the order of 10 Hz. The TAS arrangement is analyzed in detail in Chapter 6 starting on Page 129.

Active control of the secondary mirror lateral position is also planned, mainly to counteract bias errors and thermally-induced misalignments. The control concept involves the establishment of an optical image, at a point nominally coincident with prime focus, to serve as a reference from which departures of the secondary can be monitored. The image is generated by light from the figure sensor as indicated by Figure 91, that normally does not reach the primary but is intercepted by the secondary mirror rear surface. It should be noted that the figure sensor monitors the primary mirror and provides the required actuator signals while maintaining its laser light image at point Q, the primary mirror center of curvature. This latter function is

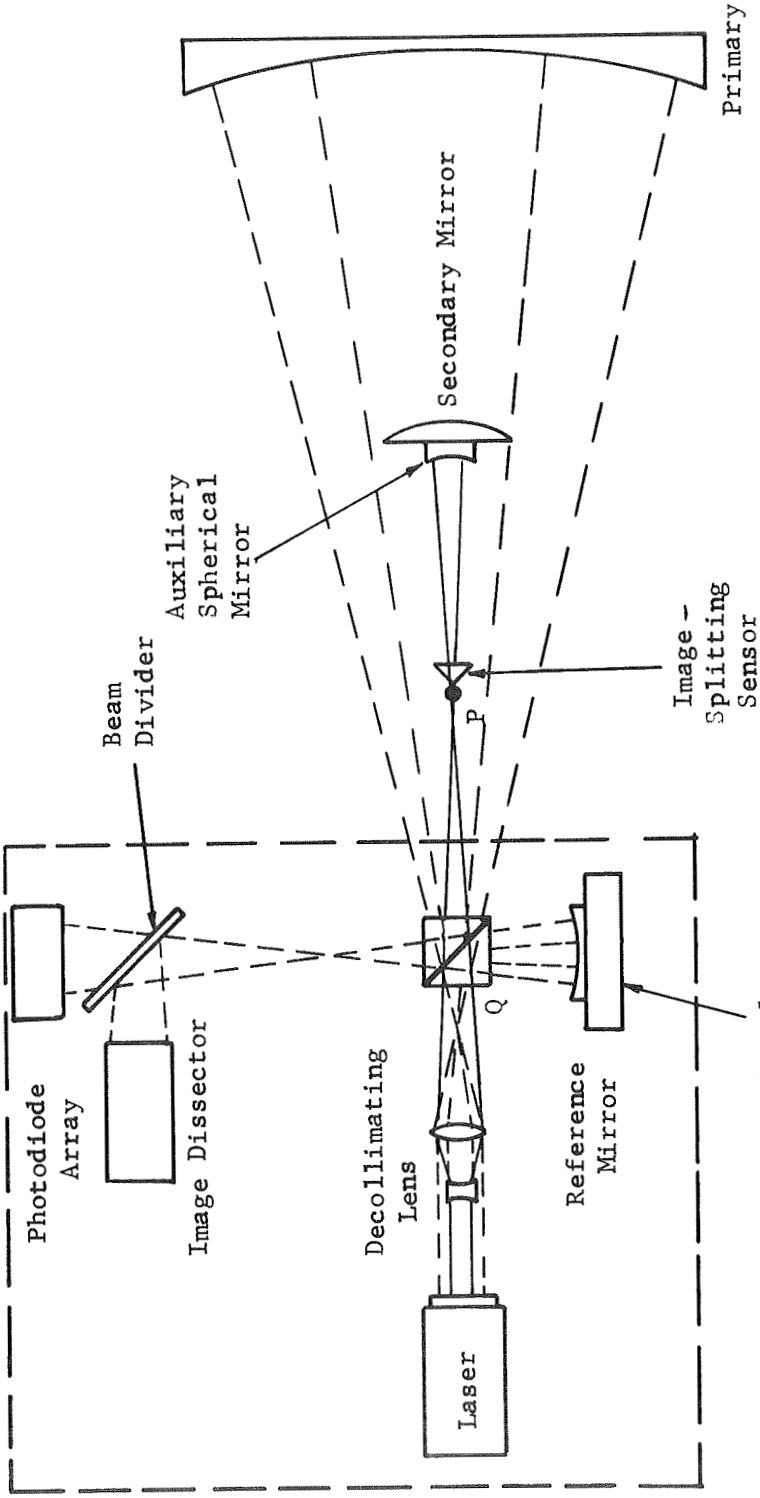

Figure 91. Generation of Reference Image by Figure Sensor

accomplished by figure sensor radial positioning to null the tilt signals and axial positioning to null "radius of curvature" error signals. These operations are not significantly sensitive to figure sensor rotations about point Q. However, such rotations do cause significant movements of the image at point P and must be avoided. Whether this is affected by additional quartz spacers between secondary and figure sensor and/or with active control loops, the angular accuracy requirement is in the order of

$$\Delta\theta < \frac{\frac{64\lambda}{n} F^3}{160} = \frac{64 \times 2 \times 10^{-6} \text{ inch}}{160 \text{ inch}} = 6.4 \text{ microradians}$$

$$\Delta\theta < 1.32 \text{ arc-seconds}$$

when $\lambda = 0.5$ microns and $n = 10$.

This precision is commensurate with the requirement, arising from acquisition considerations, that the fine star tracker attached to the figure sensor structure be supported with small boresight error to the LTEP line of sight.

The comparison of secondary mirror conjugate and prime focus positions can be accomplished by any convenient means. For example, a four-quadrant image divider (and associated sensors), with apex held with respect to the secondary at the latter's conjugate, could sense radial misalignment by conventional star tracker techniques. An alternate method would use an auxiliary spherical mirror fastened to the secondary mirror. This element would intercept the light diverging from P, and reflect the beam back to the figure sensor. Since its center of curvature would coincide with the secondary conjugate point, reimaging at P would take place provided the secondary is in the correct lateral position. When radial misalignment exists, the light is reimaged elsewhere and the figure sensor can be mechanized to sense the error in much the same way that primary mirrory tilt is detected.

Either lateral control method as described above or some alternate will be required to maintain alignment between the major optical elements, whether or not the secondary mirror is used as a transfer lens. The preceding discussion was nevertheless presented to clarify the interrelationship between the alignment and transfer lens loops associated with the secondary. In connection with this, several points are now worth noting:

- Either of the radial control methods described above are insensitive to small rotations of the secondary mirror about its conjugate (viz, in the case of an auxiliary spherical mirror, such rotation has no effect on where its reflected light is reimaged).

- If the radial and axial control loop bandwidths are substantially larger than that associated with the rotation control loop, then motions of the secondary conjugate point accompanying rotation will effectively be compensated out by the action of the alignment loops.

- Since the presently estimated transfer lens bandwidths are less than 0.1 Hz, this bandwidth relationship can be attained for the focus control loop (with the automatic scheme outlined above) and is a good possibility for the radial control loops.

Line-of-Sight (LOS) Stabilization

Control of the secondary mirror can be accomplished as shown in Figure 92. The secondary mirror could be gimbal-supported in a counter weighted arrangement with flexure bearings used to provide translational constraint but permitting rotation. Torques for angular positioning could be supplied using electromagnetic torquers mounted on the gimbals, or loudspeaker drive elements. The design would feature the use of capacitive position sensors which offer essentially infinite resolution and excellent reliability in a small size. These elements would be used in a feedback arrangement to form a minor loop which permits holding the secondary mirror at zero position during acquisition until control signals are available from the LTEP pointing sensors. The minor loop is also attractive, as shall be shown, in that it can suppress the effect of flexure-bearing spring constants without resorting to high major loop bandwidths.

Let us now consider this approach in detail, selecting where possible typical characteristics corresponding to available hardware. The flexture bearing axes should be coincident with the secondary mirror conjugate in order to avoid introducing unwanted translation with the desired rotation. The associated tolerances, in this regard, are not overly stringent amounting to about ±0.68 inches axially and 0.044 inches radially. These values were computed assuming that the ±5 arc-minute rotations (required for ±1 arc-minute LOS compensation) should not cause axial and radial shifts exceeding $\lambda/10$ degradations, at 0.5 micron, from defocus and coma: i.e.,

$$\theta\Delta x \leq 64\,\frac{\lambda}{n}\,F^3 \quad \text{or} \quad \Delta x = \frac{64\,\frac{\lambda}{n}\,F^3}{\theta} = \frac{64\text{x}2\text{x}10^{-6}\text{x}8}{5(57.3\text{x}60)^{-1}} = \frac{1.02\text{x}10^{-3}\,\text{inch}}{1.46\ \text{milliradian}} = 0.68$$

$$\text{and} \quad \theta\Delta y \leq 8\,\frac{\lambda}{n}\,F^2 \quad \text{or} \quad \Delta y = \frac{8\,\frac{\lambda}{n}\,F^2}{\theta} = \frac{64\text{x}10^{-6}\,\text{inch}}{1.46\text{x}10^{-3}\,\text{rad}} = 0.044$$

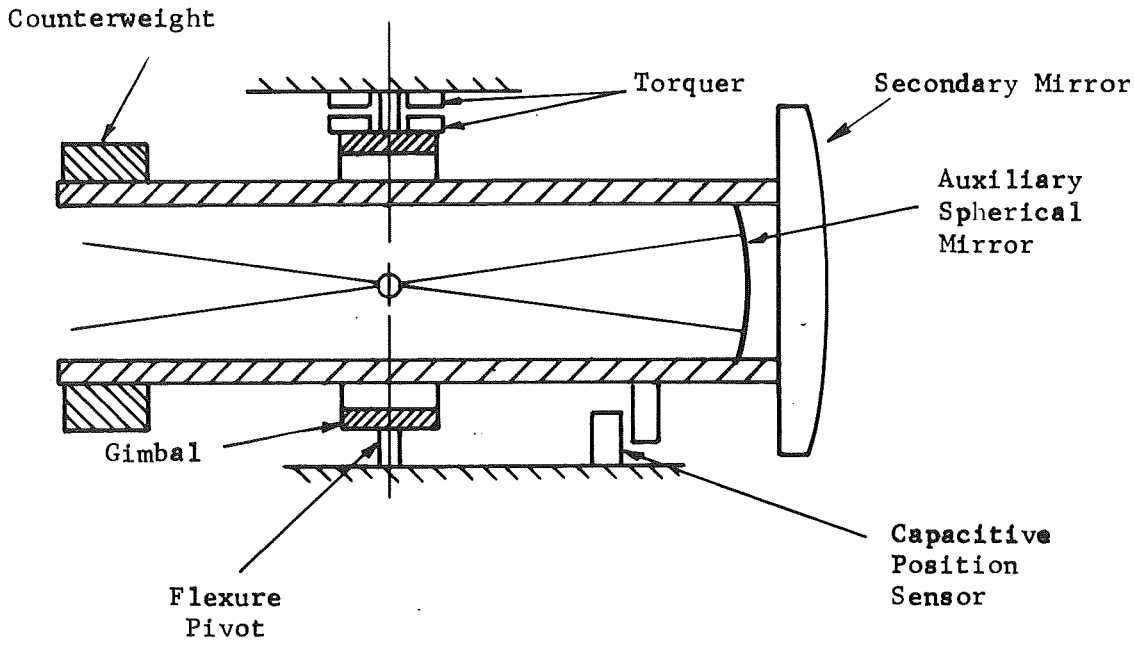

Figure 92. Secondary Mirror Line-of-Sight Control Concept

Actual translations should be much less than this, of course, to allow for other sources of error. The expected motions during track, it should be noted, are only in the order of 25 arc-seconds peak and primarily occur at gravity gradient frequency. Hence tolerances given above are increased accordingly (X12) and the alignment loops should be very effective in removing errors. Appropriate flexure pivots for use in this application are Bendix cantilevered standard pivots type 5032-600 which are 1 inch in diameter, and can provide at least 800-pound load-bearing capacity and a 0.15 foot-pound/degree spring constant per axis. The center shift of these units with angular deflection is less than 1.0 microinch at 9 arc-minutes as can be seen from Figure 93, and hence is expected to be significantly less than even the ±64 microinch axial motion constraint. The low spring constant of the bearing places minimal demands on the actuator and its input power. Even higher efficiencies would result using overcenter spring compensation of the flexures to reduce the net spring restraint of the gimbals. Reduction factors exceeding ten times are readily achievable as demonstrated by existing ATM gimbal flexures which exhibit a net 1/25th of their uncompensated rate.

The holding torque required to maintain a 7.5-arc-minute deflection, for example, will be only 0.0018 pound-foot with a tenfold bearing compensation. The foregoing angular deflection, which allows 2.5 arc-minutes for mechanical zeroing error, corresponds to an arc length of ±0.0262 inch per foot of radius. Hence, if magnetic pushers positioned for a two-foot level arm are used, the holding force required will be less than 0.001 pound and the motional range will be ±0.052 inch. While the current necessary to develop this force is a function of actual design parameters, some idea of required motor size and current level is obtained by examination of the hardware shown in Figures 94 and 95. Pictured are two views of a refractive transfer lens assembly used for line-of-sight stabilization of a laboratory model deep space optical communication telescope. The motor scale factor of 3 pounds per ampere was achieved, without serious attempts at optimization, over a working range of ±0.07 inch for each cross line-of-sight direction. Figure 96 presents a simplified sketch of the motor which illustrates the construction and principle of operation.

Only 1/3 milliampere through the 50-ohm actuator coil would be required with this design to produce the aforementioned 0.001-pound holding force. Greater efficiency and compactness are attainable through use of Alnico VIII (with a higher energy product) and a change of size and configuration to take advantage of the smaller motional range while significantly reducing stray field levels.

Also visible in Figure 95 and illustrated in Figure 97 is a form of capacitance position sensor which would be suitable for secondary mirror position sensing. As shown, the design features a bridge arrangement and plate sizing which makes the unit sensitive to motions only in the desired direction and, in addition, basically insensitive to external electric fields. The small inherent size

Loads and Spring Rates for Bendix Cantilever Standard Pivots

Catalog Number 5000 Series	D Dia.- Size	θ Maximum Deflection ± Degrees	Loads- Pounds Vc*	Vt*	Rate** lb-in. per radian	Loads- Pounds Pc*	Pt*
5020-400	5/8"	7-1/2	625.0	625.0	106.0	442.0	442.0
5020-600	5/8"	15	221.0	312.0	13.3	156.0	221.0
5020-800	5/8"	30	27.6	87.8	1.69	19.5	62.0
5024-400	3/4"	7-1/2	900.0	900.0	182.0	636.0	636.0
5024-600	3/4"	15	318.0	450.0	22.8	225.0	318.0
5024-800	3/4"	30	38.9	127.0	3.85	27.5	89.5
5028-400	7/8"	7-1/2	1220.0	1220.0	289.0	863.0	863.0
5028-600	7/8"	15	431.0	610.0	36.1	305.0	431.0
5028-800	7/8"	30	53.0	172.0	4.44	37.5	121.0
5032-400	1"	7-1/2	1600.0	1600.0	431.0	1131.0	1131.0
5032-600	1"	15	566.0	800.0	53.8	400.0	566.0
5032-800	1"	30	70.7	225.0	6.73	50.0	159.0

* Symbols designate the direction of applied load

** Rates are nominal, computed with pivots under no load

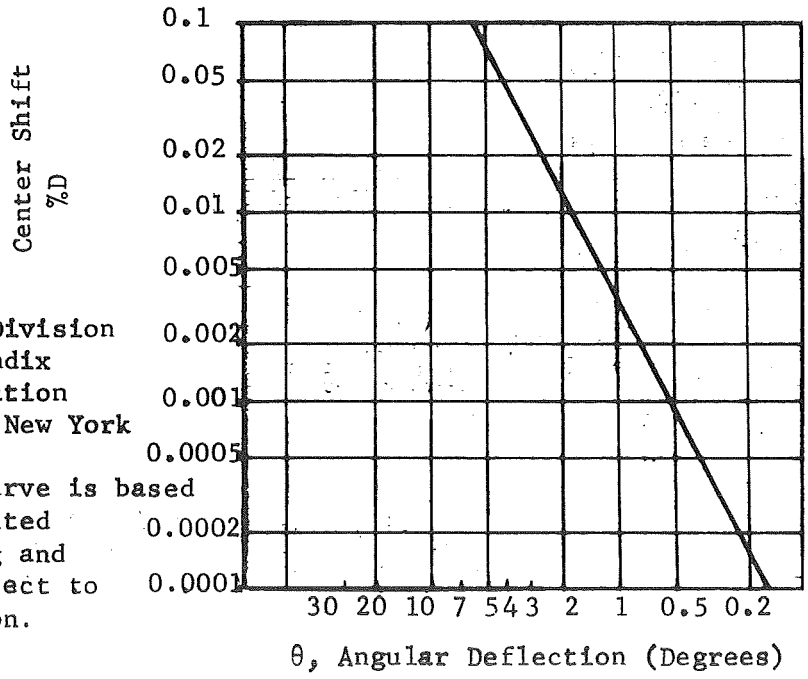

Utica Division
The Bendix
Corporation
Utica, New York

This curve is based on limited testing and is subject to revision.

Center Shift vs Angular Deflection For Cantilever and Double End Supported Flexural Pivots Under No Load Conditions

Pivots Made to Standard Dimensions

Figure 93 . Flex Pivot Center Shift vs Angular Deflection

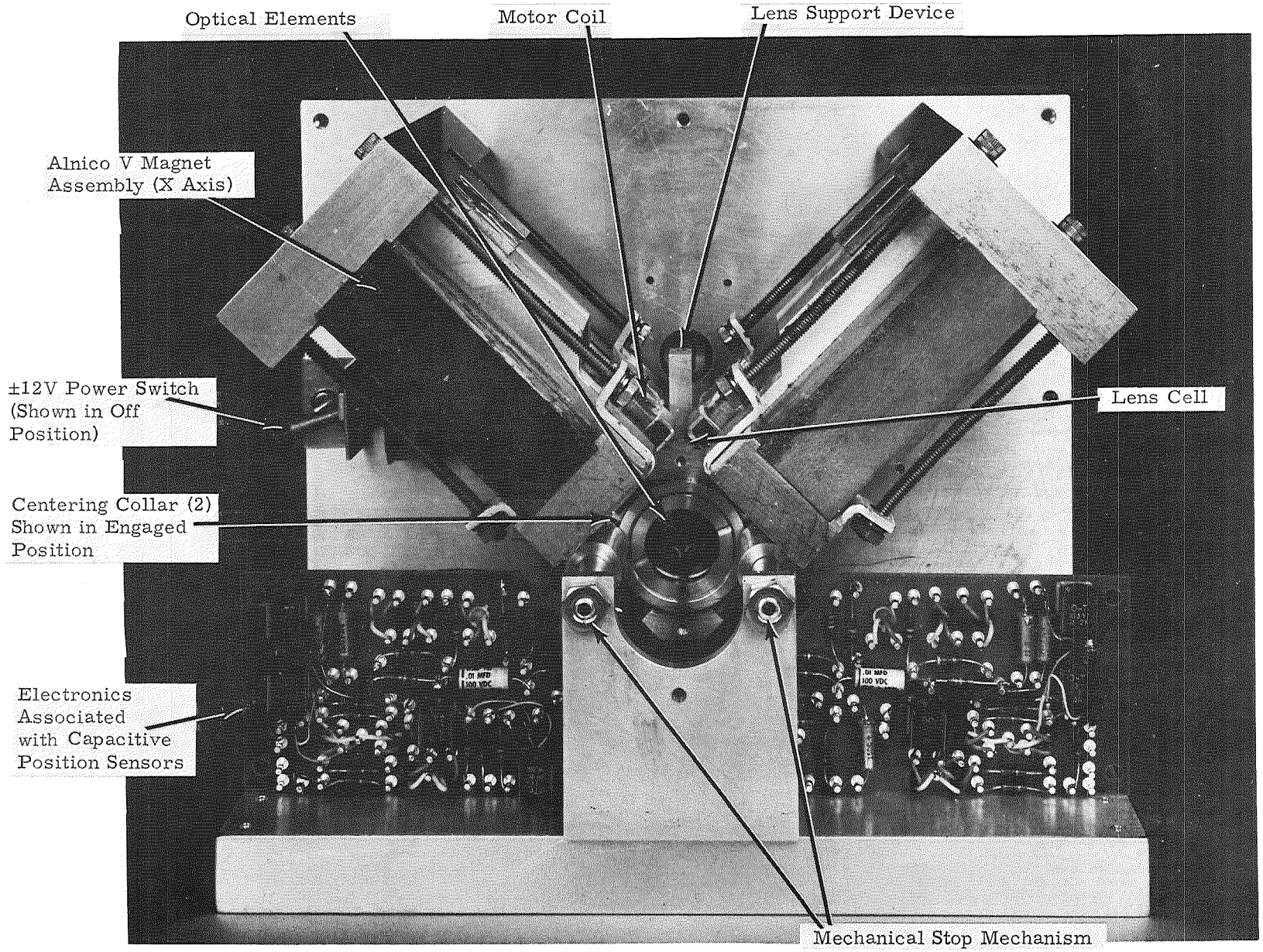

Figure 94 . Transfer Lens Mechanical Subassembly, Front View

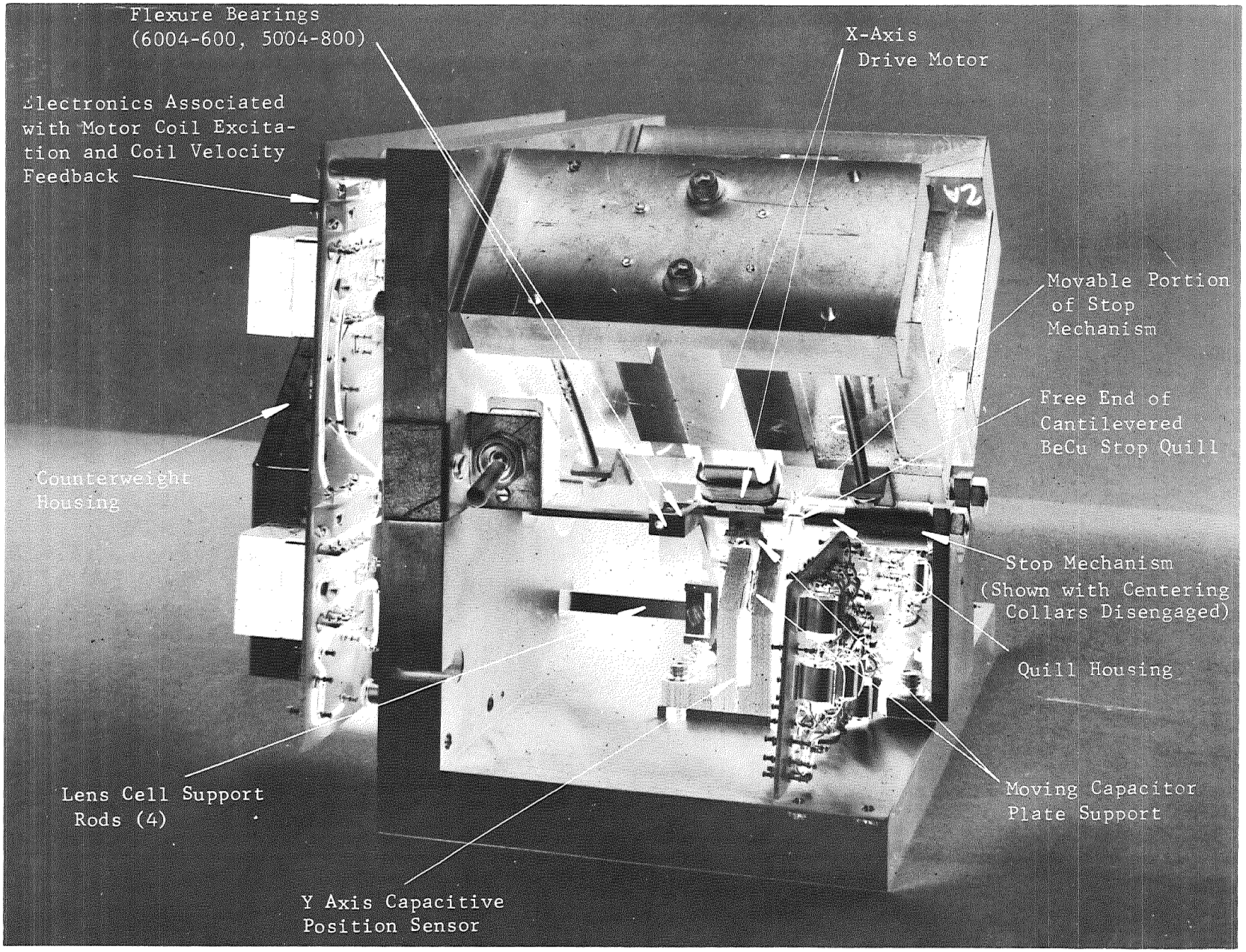

Figure 95 . Transfer Lens Mechanical Subassembly, Side View

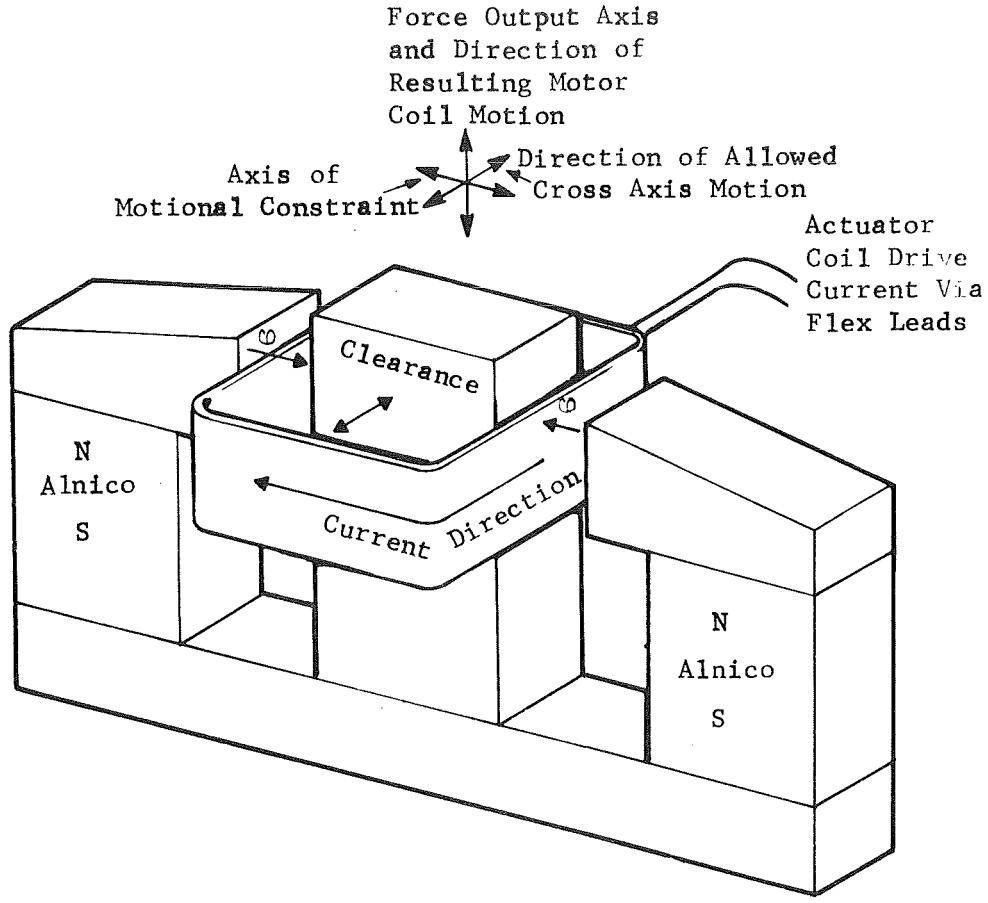

Figure 96. Magnetic Pusher Actuator Concept

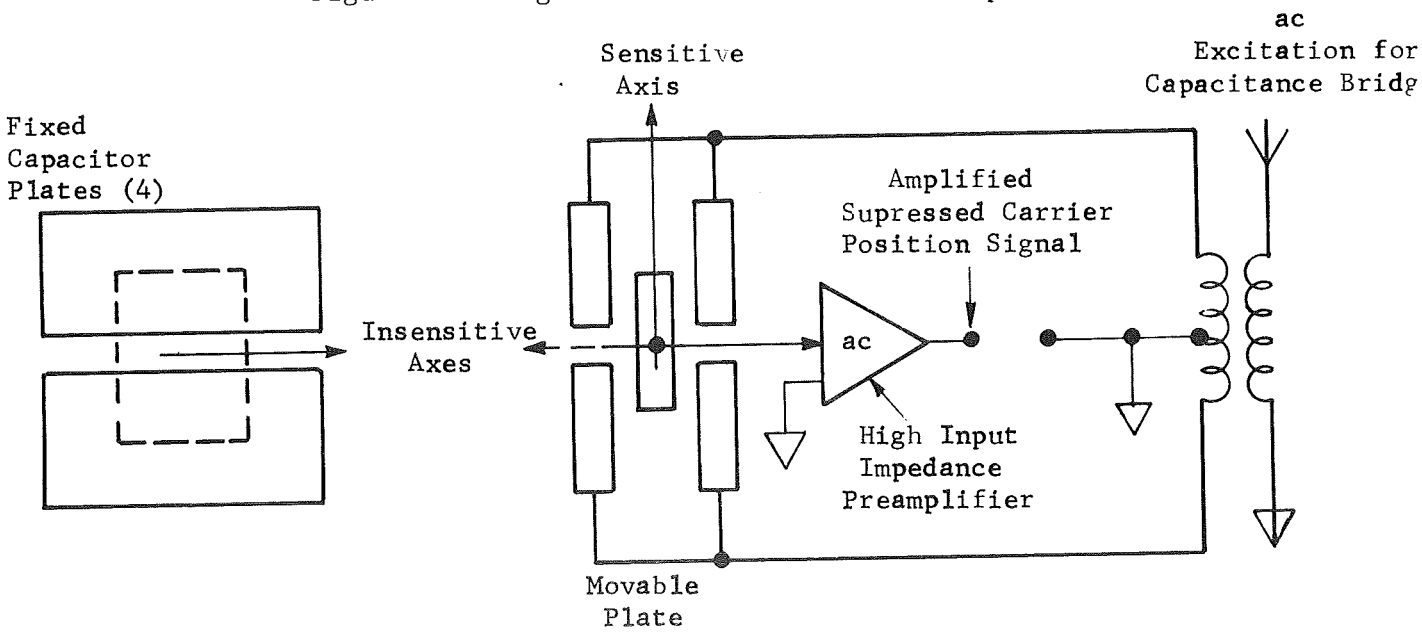

Figure 97. Capacitance-Operated Position Sensor Arrangement

of the unit (most volume being consumed by support structure) plus its insensitivity to both ac and dc magnetic fields makes the sensor ideally suited for use near the motors, into which it might even be designed. High output scale factor (30 Vdc/cm) and good linearity (refer to Figure 98) were achieved with this particular design.

The basic secondary control loop implementation following the aforementioned concept and featuring these components is shown in Figure 98. The mirror loop is used for zero positioning, prior to track, by feeding back the position sensor output signal, as well as its derivative for damping. During track mode, only derivative feedback is used and the minor loop transfer function becomes an integration. This is basically the same technique as used both on Stratoscope II, which utilizes separate rate and position sensors, and for control of the transfer lens equipment pictured previously. The latter arrangement resorts to a lead network and an operational amplifier, to develop a filtered (AtS/1+tS) position derivative with high scale factor but uncorrupted by operational amplifier offset. This is accomplished with a circuit, as shown below (Figure 99), which utilizes a lag-lead feedback network to produce a lead-lag transfer function. Following this is a high pass R-C section to produce an overall response increasing uniformily at +6 dB/oct to a gain of 10 and, in addition, to block any amplifier output bias voltage. A similar approach would be recommended for obtaining LTEP secondary mirror rotational rates. The remainder of equipment (in Figure 98) is straightforward in design and includes a four-quadrant photomultiplier and associated switching and decoding electronics for the recovery of tracking error signals. A gain control to allow compensation for guide star brightness differences, and integration networks, for low frequency gain enhancement while tracking, are also indicated.

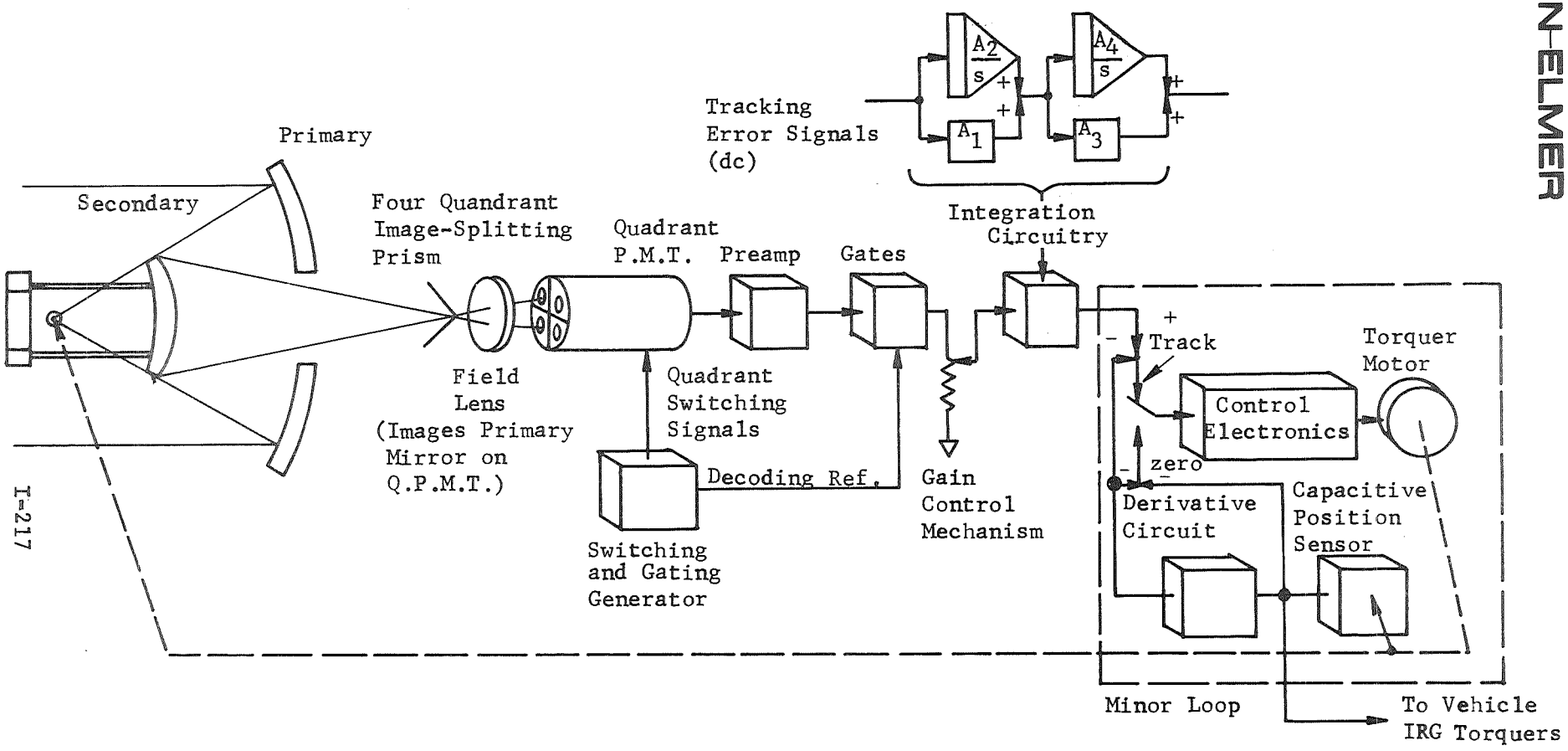

Figure 98. Single Axis Block Diagram for Secondary Mirror (Transfer Lens) Control

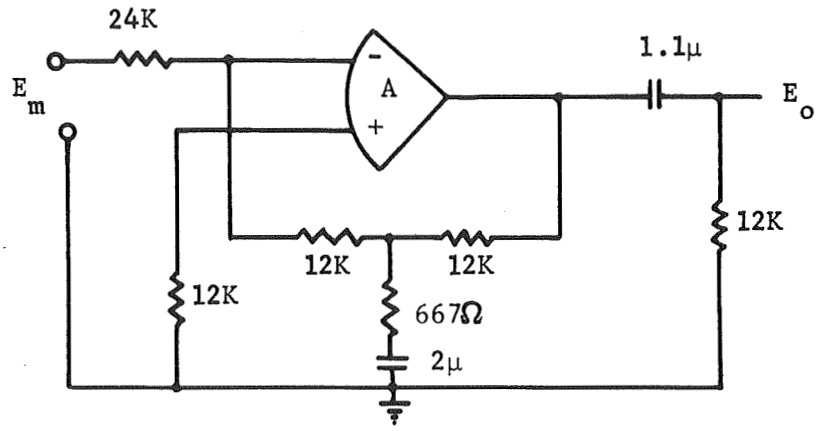

$$\text{Transfer Function} = \frac{E_o}{E_{in}} = \frac{1 + S/2\pi 12}{1 + S/2\pi 120} \times \frac{S/2\pi 12}{1 + S/2\pi 12} = \frac{10\,\frac{S}{2\pi 120}}{1 + S/2\pi 120}$$

Figure 99. Differentiation Circuit

CHAPTER 8 - GIMBAL POINTING SYSTEM

As described in an earlier section of this report, the gimbal system is to be used in technology experiments associated with a Rowland circle spectrometer (Experiment E). As shown in the analysis, the pointing accuracy required during Rowland circle spectrograph operations is in the order of 0.0285 arc-second peak. One of the ground rules for the LTEP study is that the present ATM hardware be assumed wherever possible as the baseline design. In previous sections, the servo system requirements for pointing with the gimbal system were set forth. In the present section we shall examine in detail the ATM Experiment Pointing Control (EPC) and Roll Positioning Mechanism (RPM) which Perkin-Elmer designed and manufactured for Marshall Space Flight Center under Contract NAS8-20772. The ATM specification calls for an rms pointing error of 2.5 arc-seconds. The LTEP requirements are for the accuracy to be improved by approximately 2 orders of magnitude. We shall examine, therefore, the hardware and design as it presently exists and attempt to set forth changes which may be required, or additional areas which should be studied in order to accomplish the pointing error budget required by the LTEP Program.

Before proceeding into the analysis of the hardware from the standpoint of the LTEP pointing system, a brief description of the ATM EPC and RPM gimbaling system as delivered to MSFC will be presented here.

The general arrangement of the system (refer to Figure 100) includes launch locks, a roll drive subsystem, and the pitch and yaw actuator packages. The purpose of the launch locks is to unload the gimbal rings from the ATM experiment loads (≈50,000 lb) experienced during boost phase. (Some analogous launch caging system will be required for the LTEP but is not germane to this discussion.) This reduces the strength requirements not only for the gimbaling itself but also for the pitch and yaw actuators.

The yaw actuator packages join the ATM experiment canister (or spar) to the pitch-yaw gimbal ring while the pitch actuators join the gimbal ring to the roll ring. These actuators are identical, and two are supplied in each axis to provide standby redundancy in the event of failure of one actuator.

Figure 101 shows the assembled actuator and its compensated flexure bearing blade arrangement. Figure 102 is a side view showing the relative location of some of the major components, including the 7-lb-ft limited rotation (brushless) dc torque motor. The concentric multispeed (16x and 1x) resolver can be seen in Figure 103 which shows all the parts of the actuator in their functional relationship.

The flexure bearings are important and will be discussed further since they serve the purpose of providing a support system with mechanical rotation similar to the ball bearings but with several unique advantages. A flexure bearing functions much like a torsional spring but can be designed to have a low torsional spring rate. There is no friction. These bearings have no radial and axial play and have no moving parts in the sense of rotating balls in a ball bearing race. They are eminently suited for space application since

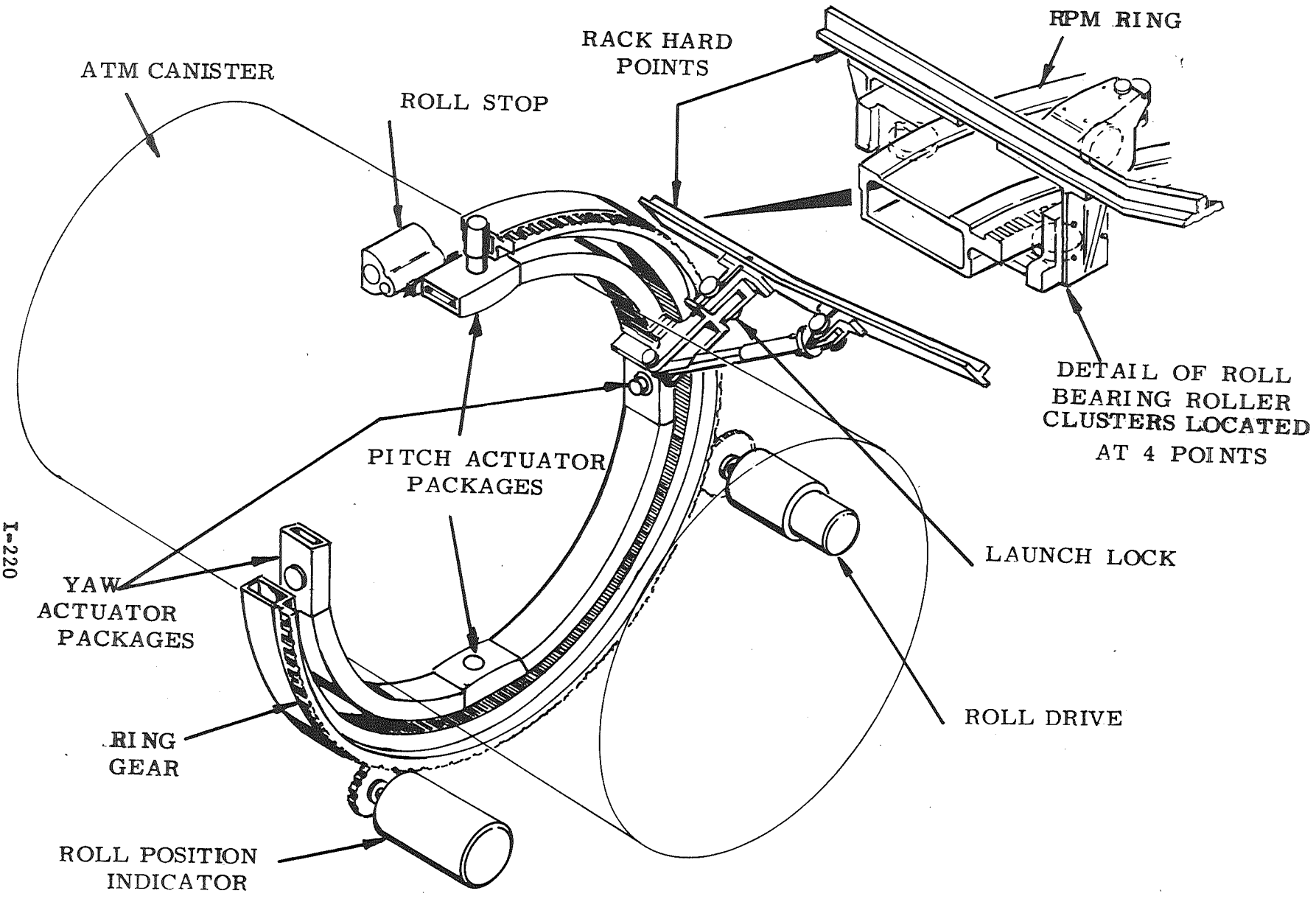

Figure 100. Arrangement of ATM EPC and RPM

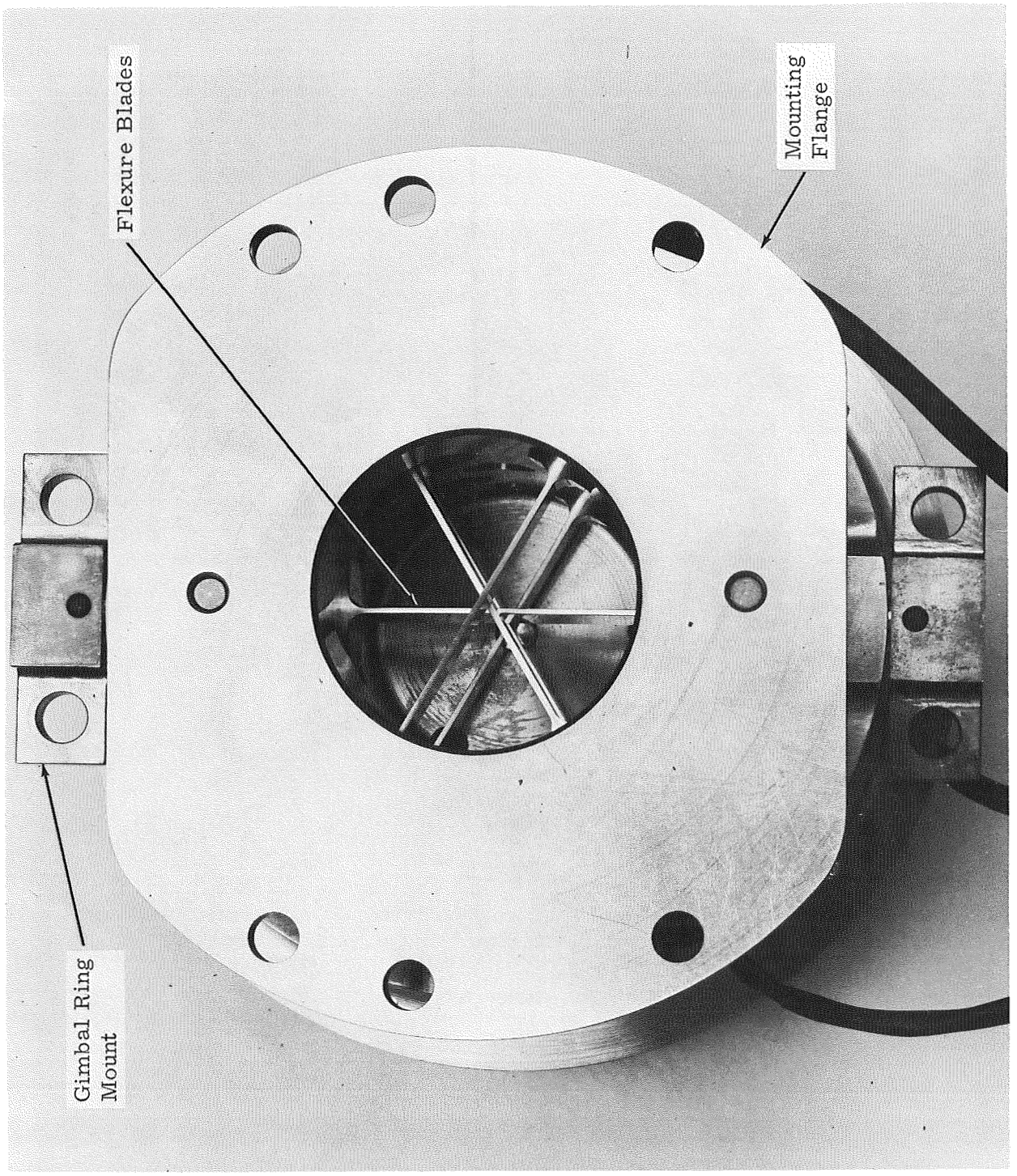

Figure 101 . ATM Flexure Bearing

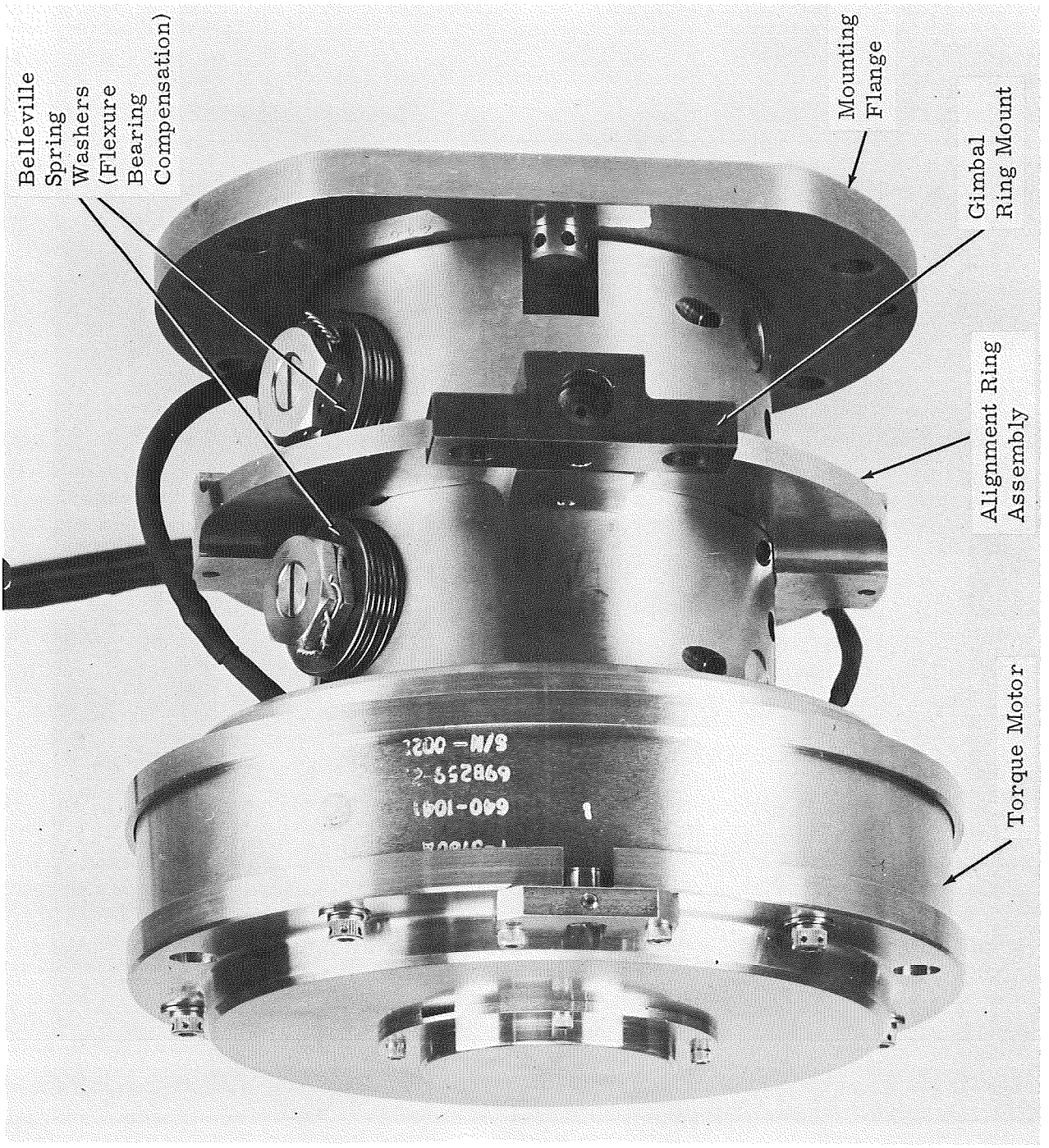

Figure 102 . ATM Pitch/Yaw Actuator Assembly

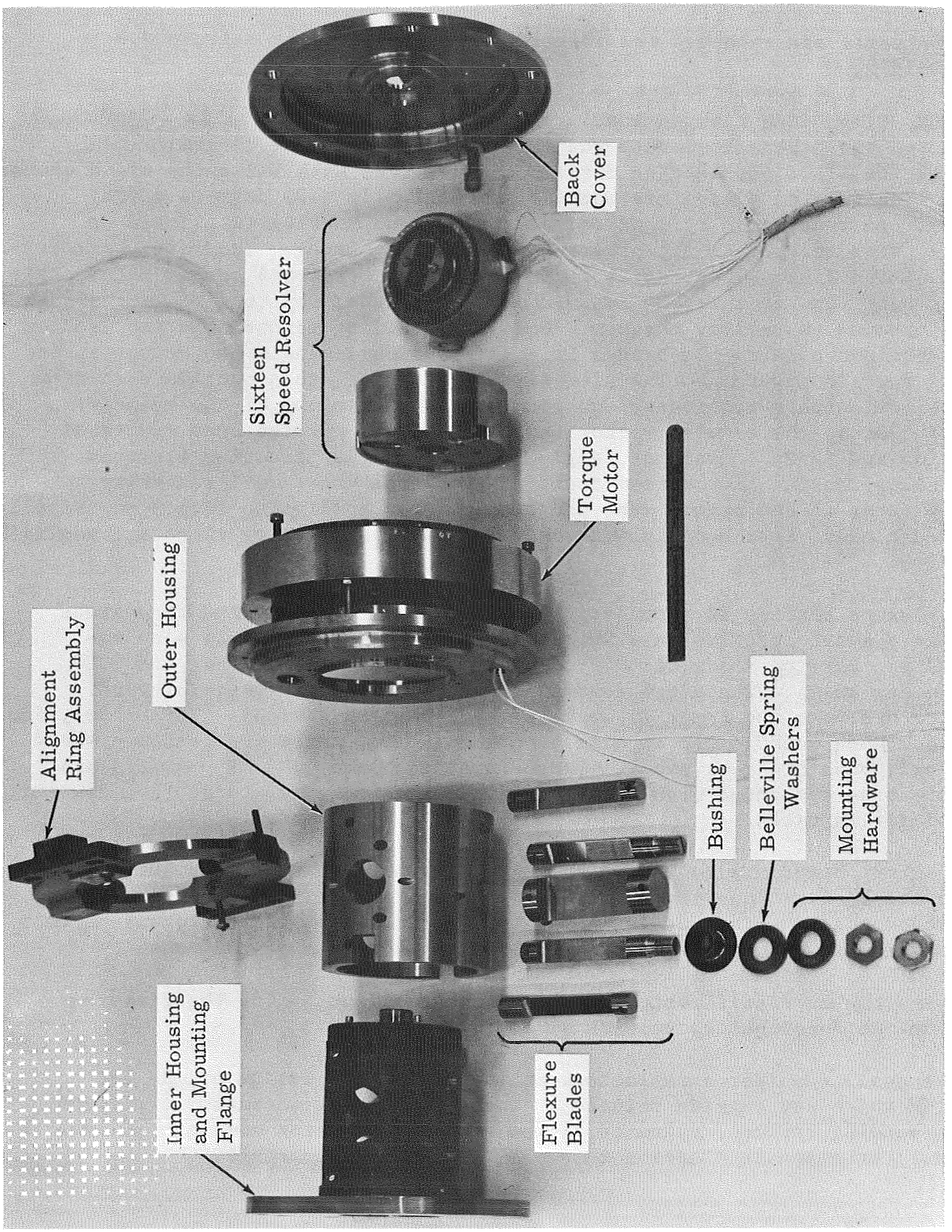

Figure 103. Pitch/Yaw Actuator for ATM

no lubricants are required and there is no possibility of seizure due to cold welding.

The ATM five-blade flexure bearing, as shown in Figure 104, is symmetrical about a plane perpendicular to the axis of rotation. The central blade of each "half" of the bearing forms a single blade with twice the width of the other blades. The blades are mounted symmetrically (120 degrees apart) between two concentric cylindrical housings. One housing is allowed to rotate with respect to the other by bending the blades. The main characteristic of the flexure bearing is therefore one of torsional spring rate. This spring rate can, in turn, be reduced or "compensated" by toggling techniques which provide cancelling torques. One such toggling method, the one used on ATM, requires placing the blades in equal tension as indicated by the spring and vectors in Figure 104. The situation is identical to a cantilevered beam (the blade) with a transverse end load. As the free end of the beam (or blade) flexes, the tension vector (end load) moves off the beam center of rotation and tends to pull or toggle the beam in the direction it moved. The static tension in the beam therefore opposes the normal restoring spring force of the beam.* The net result, when applied to five symmetrically located blades, is a bearing with very low torsional spring rates and negligible friction.

This flexure bearing is much larger than most. It is required to operate with very small friction in a weightless environment but it is also required tc survive loads of 4040 pounds in gravity (per bearing, or 8080 pounds per axis). These two conditions are basically incompatible and lead to problems not found in small flexure bearing designs. The blades, for instance, are much larger in size than need be for space applications where external loads are very small. Large internal blade bending moments must therefore be contended with in the design and compensated to achieve low torsional spring rates.

The flexure bearing also incorporates an alignment feature, the purpose of which is to accommodate angular misalignment between the pair of flexure bearings on either the ATM pitch or yaw axis. Angular misalignment can occur between two bearings due to manufacturing tolerances or thermal expansions.

The performance specifications for the actuators, utilizing the flexure bearings as described above, are given in Table 25.

Now we shall consider some factors in the mechanical design of the EPC and RPM which may degrade pointing. These factors are actuator striction, cable bending torques, dynamics of the ring-torque motor combination, and the residual uncompensated spring torque of the flexure bearings.

*Additional discussion of the theory will be found in Perkin-Elmer Engineering Report No. 9532.

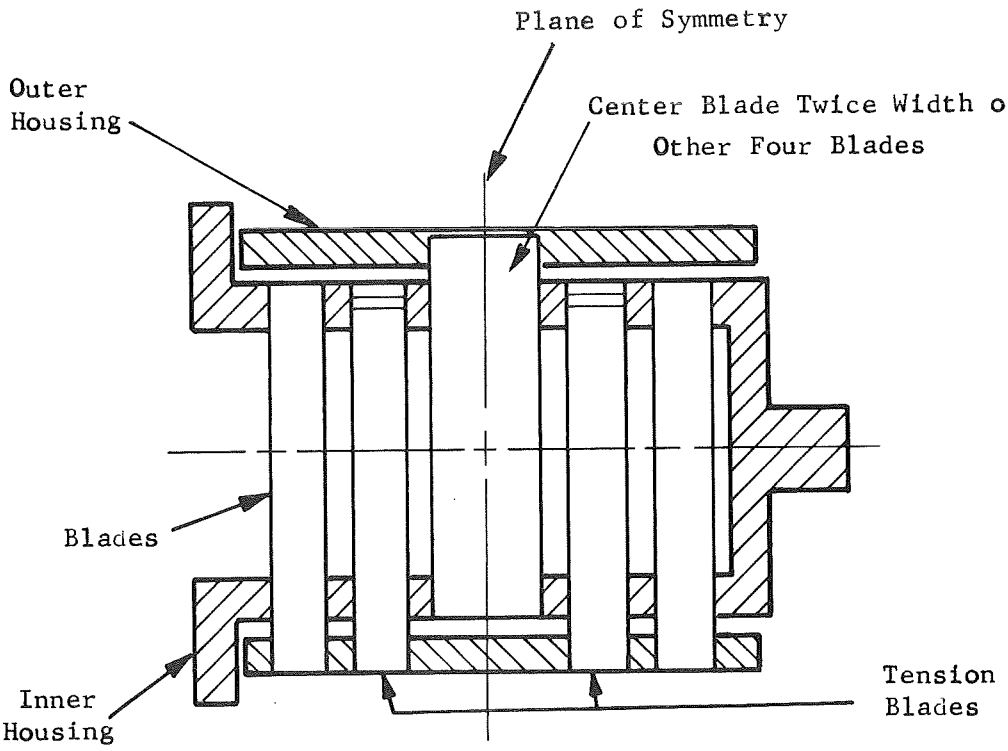

SIDE VIEW

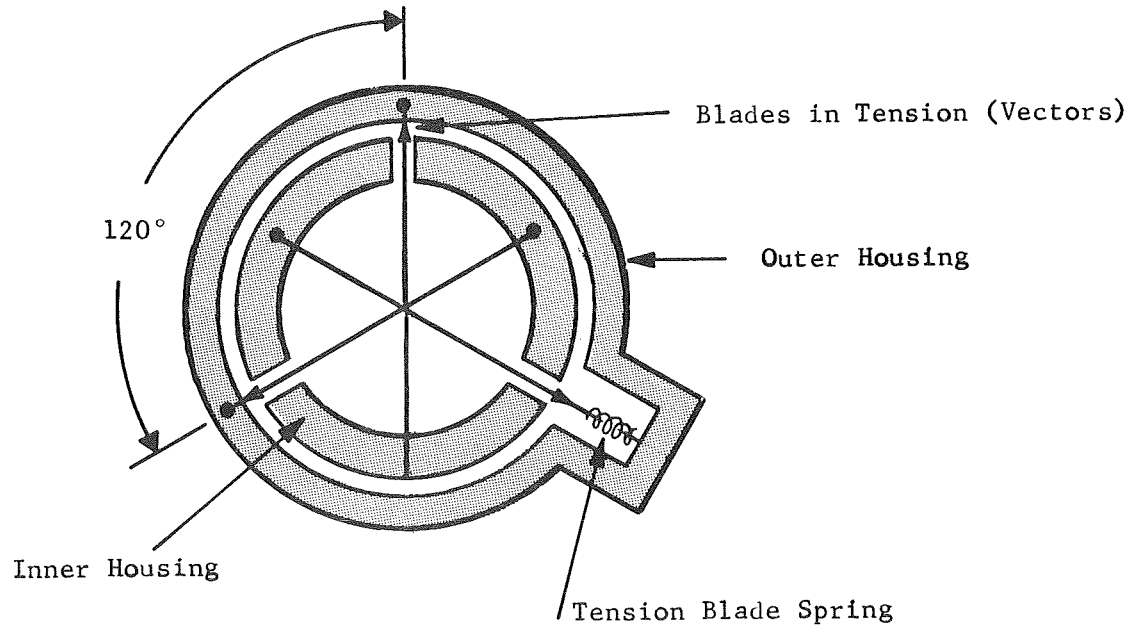

END VIEW

Figure 104. Schematic-Five Blade Flexure Bearing

TABLE 25. ACTUATOR PACKAGE FINAL DESIGN PARAMETERS

A.	Residual Flexure Bearing Spring Rate	-40 lb-in/rad
B.	Rotational Range	-±2.0 degrees
C.	Breakaway Torques	-0.002 lb-ft (Mechanical Assembly) 0.080 lb-ft (Electrical and Mechanical Assembly)
D.	Load Carrying Capability (Nonoperational)	-4040 lb (Vertical)
E.	Load Carrying Capability (Operational)	- 340 lb (Vertical)
F.	Residual Flexure Bearing Spring Rate Change Due to Misalignment (Over the angular misalignment range of ±0.5 percent)	- Neglibible (<<40 lb-in./rad)
G.	Motor Torque	±7.0 lb-ft (±12.5%)
H.	Power	- 140 watts
I.	Resolver Accuracy (Including center shift effect of rotation and bearing misalignment)	-30 arc-minutes (single space) 1.0 arc-minutes (sixteen speed)
I-1	Rotational Axis Center Shift	- Less than 0.001 inch
I-2	Center Shift During 1/2 Degree Bearing Misalignment	-0.002 inch at Resolver gap
J.	Adjustment Capabilities	-±1.0 degree (Resolver centering) ±50% residual spring rate adjustment
K.	Compliance Data	-20×10^{-6} in./lb (Verticle) -2.2×10^{-4} in./lb (Axial) 12×10^{-6} in./lb (Lateral) 0.50×10^{6} lb-in./rad (Torsional)
L.	Thermal Operating Range	-70 degrees F to +150 degrees F
M.	Package Weight	-33 lb

ACTUATOR STICTION EFFECTS

The present ATM EPC actuators contain 7 ft-lb dc torque motors. These motors have a characteristic (which is termed friction breakaway by the manufacturer) that is closely akin to "stiction" which would be detrimental to fine pointing control. In Perkin-Elmer laboratory measurements, this effect was measured to be 0.03 ft-lb per actuator. Since there are two actuators in each axis (to provide redundancy), a total of 0.06 ft-lb of stiction would be present in each system, a value which is double the aerodynamic torque considered previously. The exact nature of this stiction or friction effect is not clearly established but is believed to be caused by residual magnetism effects in the rotor. The manufacturer estimates that it can be reduced 50 percent by changing to a low-hysteresis ferrous material and, in addition, indicates that the absolute magnitude could be reduced if a smaller torquer could be employed. It appears as though the maximum torque disturbances on the LTEP will not exceed 1 ft-lb. Hence, the present motors can probably be replaced with smaller motors to reduce the stiction effect by a factor of approximately 7 to 14, from the present 0.06-ft-lb value to 8.6- to 4.3- millifoot pounds. We are quite confident that this reduction will in fact be meaningful in terms of total effect since the flexure bearing breakaway is negligibly small; i.e., the breakaway friction forces of the bearing with no motor are lower than 0.002 ft-lb as determined by test data.

DISTURBANCE TORQUES ARISING FROM THE CABLING SYSTEM

A factor which required a large torque motor for ATM is that the motor must bend the electrical cables as they cross the gimbaling system bearings. In the present ATM the torque required to overcome the steady state bending of the cables as they loop across the EPC actuators is approximately 1.5 ft-lb (Figure 105 illustrates the size of the cable bundle). To the extent that this torque can be reduced, the size of the torque motor can be reduced and the magnetic stiction effect mentioned above can be minimized.

There are a number of ways of doing this. One straightforward approach would be to build an auxiliary servo system which would measure and mechanically provide the cable-bending torques so that none were experienced by the gimbaling system. Such a servo system would consist of a sensor which measures the extension of a molded cable loop and an actuator both to maintain this shape and provide an equal and opposite force, thereby removing the force required to bend the cable from the pointing actuator torque motor load. This scheme is shown in Figure 106.

A second approach would be to use a time-sharing system, such as time or frequency multiplexing, to reduce the number of conductors required. In the solar ATM, a total of approximately 1200 conductors are required. If this number were reduced to 300-400 in LTEP by a multiplexing scheme, then perhaps a commercial item such as the Aeroflex "Data Bridge" could be used to reduce the cable torques. A version of this device utilizes flat cable, rolling between two concentric cylinders, as shown in Figure 107 .

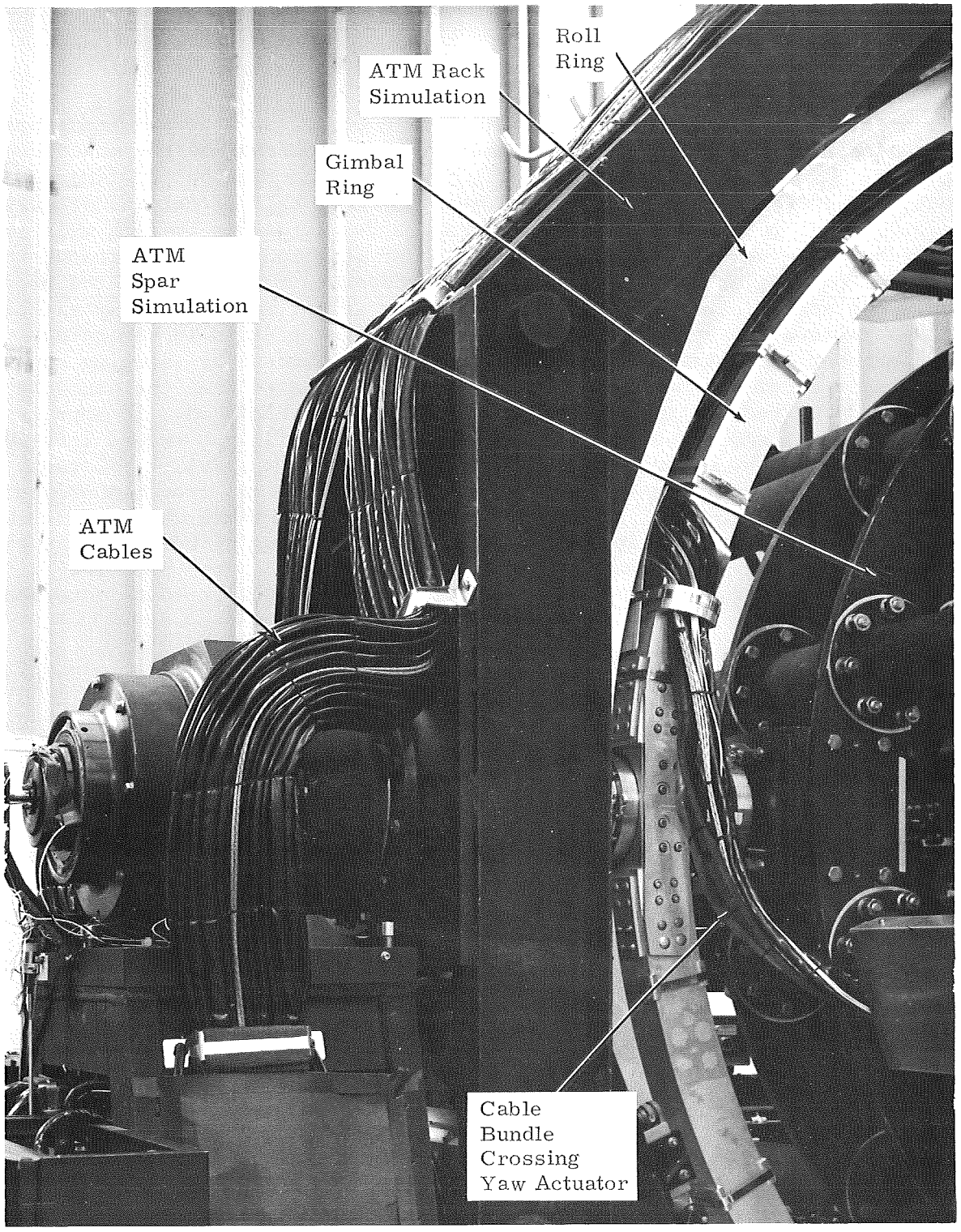

Figure 105. EPC and RPM Installed in Zero-G Simulator for Pointing System Testing

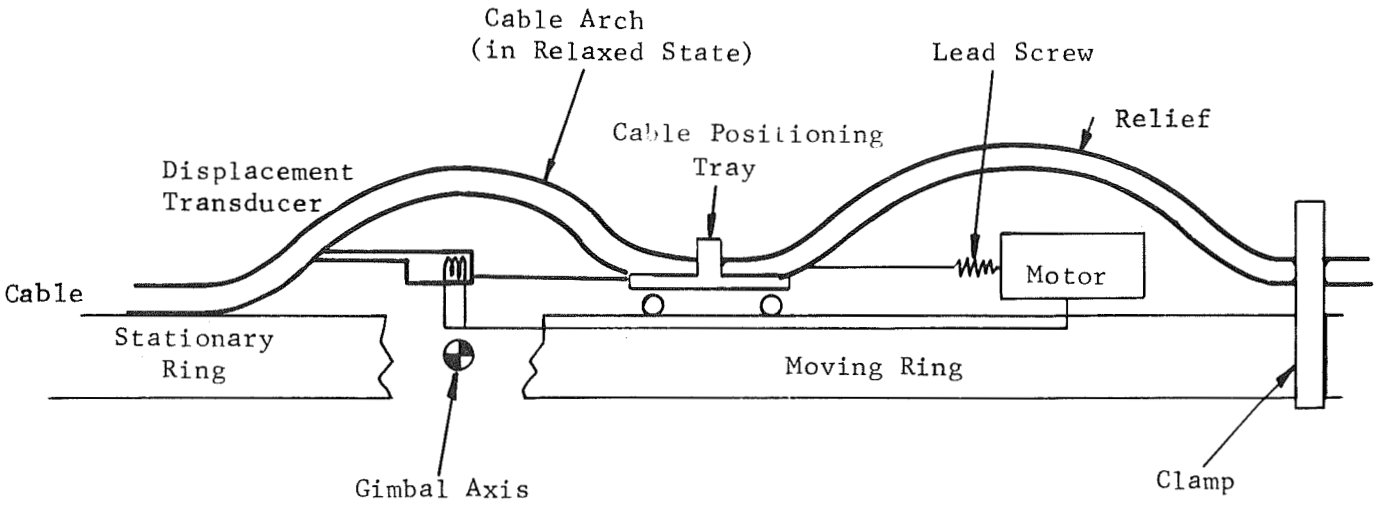

Figure 106. Techniques for Low-torque Axis Crossing For Cables

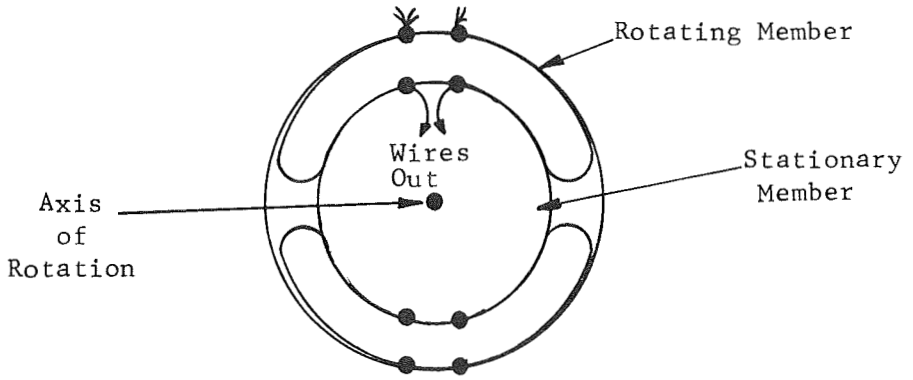

Figure 107. Principle of "Databridge"

Manufacturer's data shows extremely low rolling torques (1 in-oz), and the design could readily be adapted to the existing ATM design, by fitting the unit outside of, and concentric with, the torque motors on the pitch-yaw actuators.

A third alternative is to use the chain link transformer to transmit power (up to 100 watts) and multiplexed signals across the gimbals. The chain link transformer will be discussed in detail in the section which follows covering the free-float pointing system. This approach will reduce the cable torques to zero.

Future efforts should include a closer consideration of the LTEP cabling system requirements to select a suitable and practical approach to gimbal axis crossings. One motivation for this is the desire to reduce, for example, wire torque creep disturbances. Other important benefits would be a reduction of torquer motor size (and required power) with an attendant reduction of hysteresis effects, as described above. Some further investigation would also be in order to determine the nature of the hysteresis phenomena and whether alternate motor designs could effectively avoid the effect. This could be followed by a reanalysis of pointing performance including the disturbances arising from hysteresis effects which, it should be noted, were ignored elsewhere in this report.

MECHANICAL RESONANCE MODES

While the usage of the gimbaling system is in space, it is ground handling considerations which largely governed the design of the gimbal rings. When the telescope or experiment canister is in orbit it is, of course, weightless and the strength requirements for the gimbal rings are quite modest. However, on the ground, the gimbaling system is called upon to support the full weight of the telescope or ATM experiment package. The ground handling requirements, then, set the strength, geometry and materials used in the gimbal rings and all other parts which form the load paths for the gimbaling system when in the earth's gravity environment. As a result, the gimbal rings are heavier than they would be if they did not need to meet this requirement.

From the servo analysis point of view the dynamics of the gimbal ring appear in the servo loop analysis. That is, if there are any energy-storage elements between the torque motor where corrective torques are generated and the error sensor, the resulting dynamics must be taken into account in the stability analysis and performance analysis of the closed loop servo. The gimbal ring constitutes a distributed mass and spring system which will interact with the moment of inertia of the torque motor and the inertia of the pointed body to form a dynamic system whose characteristics may effect the pointing performance. The gimbal rings are all welded construction and, hence, do have fairly high mechanical Q. If the resonant peak is close enough in frequency to the crossover of the closed-loop pointing servo and if the phase is correct, an unstable mode in which the torque motors and gimbal ring combination are involved could occur.

No test data exists as to what the natural frequency of the torque motor-gimbal ring combination is. However, using a simplified model of the torque motor-gimbal ring system, a natural frequency of 90 Hz has been calculated. It is believed that this is sufficiently far removed from the crossover frequency of the ATM application (2.5 Hz) and even farther removed from the 0.58 Hz contemplated for the LTEP to be of any harm.

Another possible resonant mode can be conceived in which the torque motor is locked and the telescope or experiment canister is caused to resonate against the spring of the gimbal ring. In this mode the natural frequency would be only 1.5 to 2 Hz. However, since the torque motor is driven by electronics having extremely high output impedance (e.g. current drive electronics), such a mode would not appear in the loop closure. This is because the torque generated is not a function of torquer motor velocity. To the extent that the gimbal ring inertia is not a significant fraction of the body to be pointed, torques generated by the torque motor are immediately applied to the pointed body. Therefore, there are no dynamic effects around 2 Hz which enter into the servo stability analysis.

RESIDUAL UNCOMPENSATED FLEXURE BEARING SPRING EFFECTS

The net spring rate for the compensated flexure bearing is not a constant value, but rather follows a square law as shown in Figure 108 . (This figure is the theoretical net spring rate.) The important point to note is the changing slope of the curve, which is the instantaneous spring rate.

Some test data is now available for various operational conditions of the flexure bearing actuator. Representative data is shown in Figure 109. It will be noted that a hysteresis effect exists, and because of this, the effective spring rate becomes quite high near the reversal point.

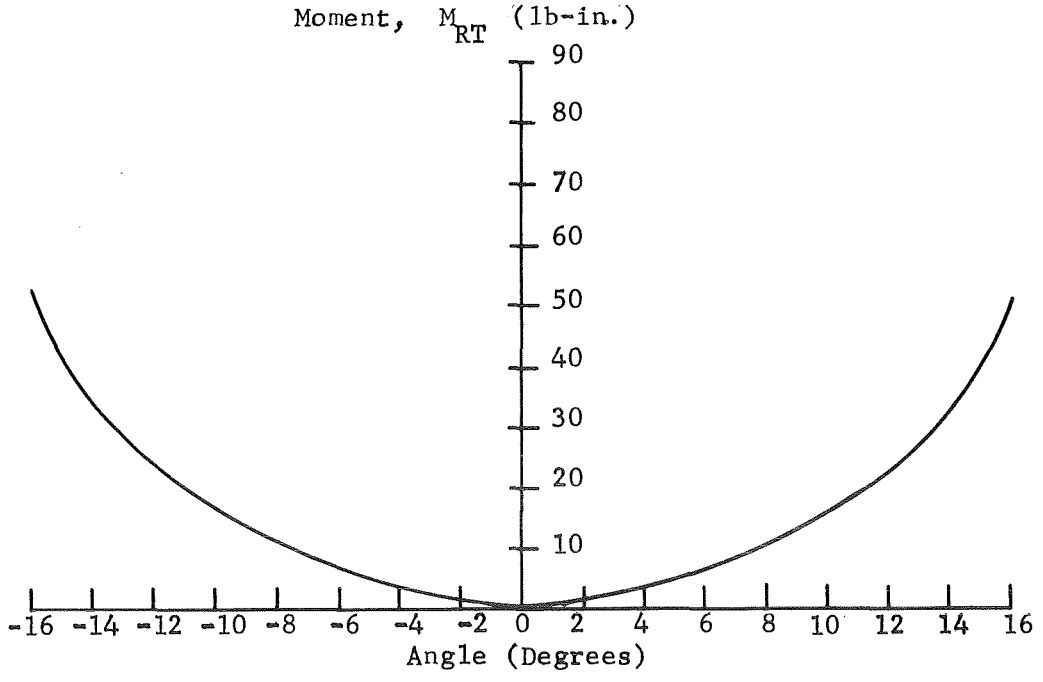

Figure 108. Theoretical Moment vs Angle

● - Data Point

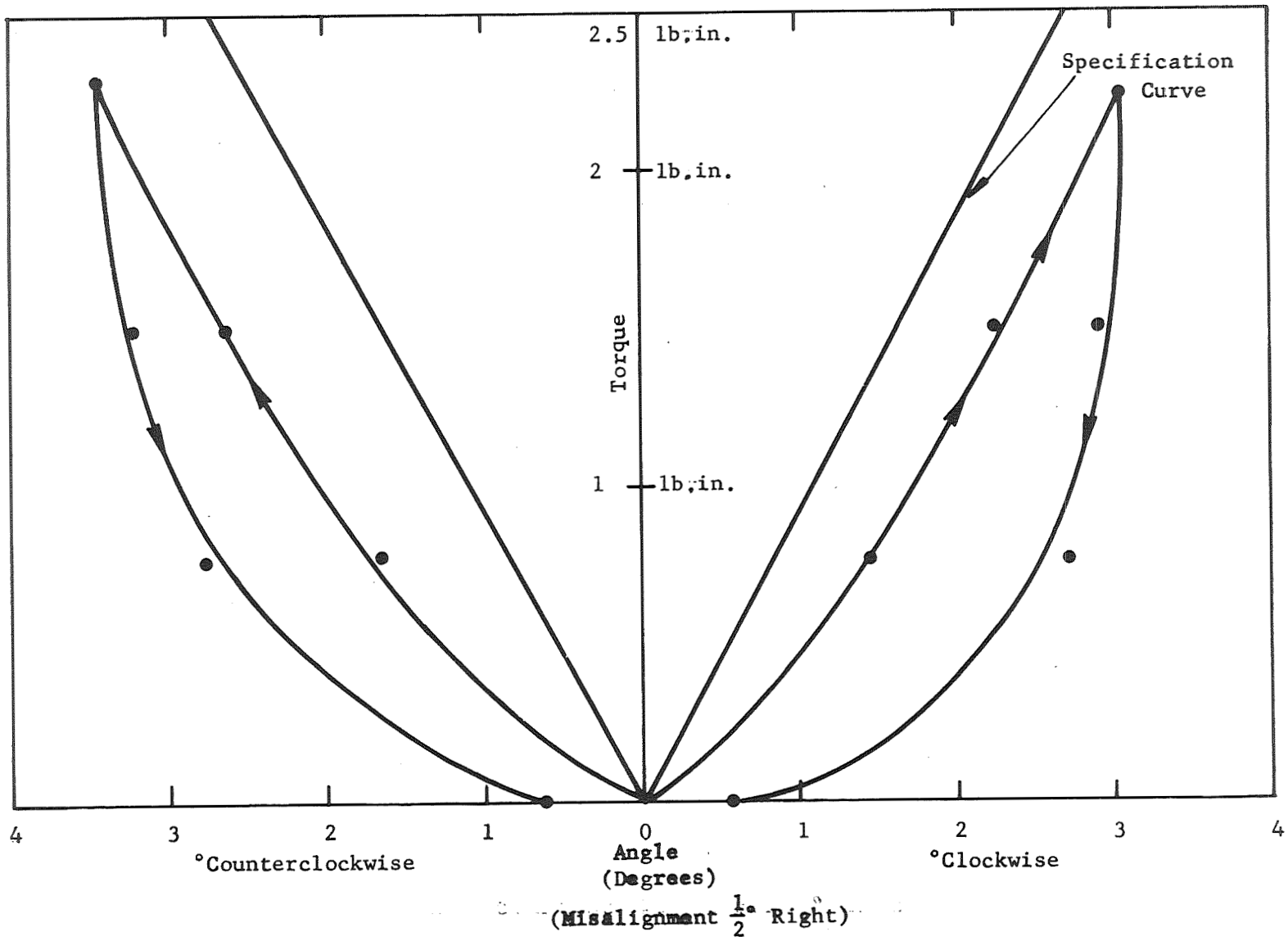

Figure 109. Restoring Torque versus Angle of Rotation

The exact cause for the hysteresis is not positively known. The most likely cause is the coulomb friction between the flexure blade and the retention bushing at the location of the Belleville spring washers (refer to Figures 102, and 103). Friction will cause fluctuations in the compensation tension in the blades, which results in under-compensation when the friction is working against the belleville Spring washers, and over-compensation when friction aids. If the total force exerted by the spring washers (approximately 160 lb) were reacted by the friction in the bushing, then there would be no compensation. The spring rate of the uncompensated flexure blades sets the maximum slope of the hysteresis loops. No data is presently available for hysteresis caused by small angular changes and the actual effect of hysteresis on pointing corrections can only be estimated. For ATM, the hysteresis is negligible. In the worst case, the hysteresis loops should be bounded by the large loops shown on the Figure 109. If the flexures are operated in the central $\pm 1^{\circ}$ of travel, then the maximum hysteresis effect would be ± 0.083 in-lb. The angular range over which the torque change would occur is harder to estimate. However, the spring rate cannot possibly exceed that of the flex blades with no compensation at all as mentioned previously. This rate is 443 in-lb per radian or about 2.3×10^{-3} in-lb/arc-second. At this spring rate, the ± 0.083 in-lb hysteresis effect would take place over 36 arc-seconds. For the 5-arc-second wander of the stabilized vehicle, the maximum disturbance torque the hysteresis effect could cause is ± 0.012 in-lb, and if the effect were actually measured, it most likely would be considerably smaller. If the hysteresis is indeed caused by a stick-slip at the compensator, then the effect will result in actual torque pulses. If, however, the hysteresis is due to internal hysteresis of the flexure blade material (another possible cause) then the effect is merely to change the spring rate, depending upon the direction of rotation. This would not cause torque pulses but would merely change the amount of coupling between spacecraft motion and telescope pointing.

Now to evaluate the effect. The worst case discussed above could result in disturbance torques of ± 0.012 in-lb, or 0.001 ft-lb. This is approximately the same as the gravity gradient disturbance torques discussed earlier. However, the frequency would be the same as for the vehicle motions. If these frequencies are characteristic of astronaut movements, then modifications to the flexure bearings to reduce hystersis should be undertaken. (These modifications would be to eliminate the sliding bushings and subsititute a flexure type retention for the load-carying flexure blades, or substitution of low-hysteresis material for the present flexure blade material.)

If astronaut motions can be reduced, then the most likely frequency of spacecraft motion would be the same as that for the gravity gradient. In that case, the hysteresis disturbances will be negligible. In any event, it would be well worthwhile to fully assess the nature of the effect and to make measurements to determine representative hysteresis values for use in the LTEP pointing analysis.

CHAPTER 9 - GIMBAL POINTING TEST CONSIDERATIONS

The task of demonstrating precise closed-loop pointing accuracies in earth's gravity environment for large hardware which is designed for space usage can be a formidable one, as will be discussed below. The task is further compounded by the judgments which must be made as to how much testing is enough. At one extreme there is the possibility of testing only sub-systems, assembling them, and first closing the pointing servo loop when in orbit. At the other extreme is to assemble all the flight hardware and unload, or support the various functional components on very low friction bearings so that all functional modes can be operated in the 1-g environment. An intermediate approach is to design the system so that performance is unaffected by gravity. The first approach is risky while the last two are costly or weighty. If it is NASA's judgment that closed loop testing of the large telescope experiment program in the 1-g environment be performed, then some development in fluid bearing (i.e., an appropriate gravity-compensating support-bearing technology will be required in order to accomplish this end. Otherwise, the pointing system must be redesigned to work the same in earth's gravity as in space. Final judgments will weigh the cost-effectiveness of ground testing versus the probability of failure and the costs of launch.

As the large telescope experiment program moves into the detail design phases, the problems of doing the system testing in the earth's gravity environment should be fully recognized and the necessary decisions made as to what the nature of pointing system testing shall be, and what accommodations should be made in the telescope configuration to permit the testing that is deemed adequate.

A few possible approaches to ground testing will now be discussed.

ZERO-G SIMULATION

All present zero-g simulations are achieved using very low friction support bearings arranged so that the effective center of suspension coincides with the center of gravity of the body under test.

Candidate bearings which would have sufficiently low friction levels to afford a good zero-g simulation are air bearings, and mercury floatation bearings. Both of these approaches are being utilized on the current ATM program. The air-bearing principle is utilized by MSFC in an EPC test fixture which will be described later. The mercury floatation approach is used in the Dynamic Test Fixture which was designed and fabricated by Perkin-Elmer as part of the ATM EPC-RPM Program. This device was constructed to permit closed loop EPC servo testing and features an ATM spar simulation as well as structure to simulate the ATM rack (support) and its expected angular motional disturbance.

Mercury has attractive physical characteristics for a floatation bearing. Its high density, as shown in the tabulation below, allows a relatively small device to support significant loads. The other listed characteristics indicate that mercury also offers a minimal drag relative to that of most other liquids.

Mercury Characteristics

a)	Density:	847 lb/cu ft
b)	Viscosity:	3.22×10^{-5} lb sec/ft^2
c)	Kinematic Viscosity	0.123×10^{-5} (i.e., approx 1/10 that of water)
d)	Typical Reynolds No:	88×10^5
e)	Fluid Friction Factor:	0.2

The basic principle in utilizing the mercury floatation bearing is to arrange to have the center of gravity of the telescope which is undergoing pointing testing to coincide with the effective center of bouyancy of the mercury floatation bearing. In addition, the center of rotation (e.g., point of intersection of the gimbal axis) should coincide with the center of bouyancy and center of gravity to avoid translation motions of the float with respect to its container. Figure illustrates this principle. Any subsystem whose weight would impair system operation can similarly be reacted by a separate bouyancy force acting on a float immersed in mercury. An example of the ratio of supported weight to bearing size is the ATM experiment canister whose 5500 pounds can be supported on a 27.8-inch diameter spherical bearing.

Another advantage of the mercury floatation bearing is that the parts need not be manufactured to very close mechanical tolerances as is the case of an air bearing. Figure 110 illustrates the mechanization reached on the ATM program. It was necessary to float or unload the gimbals as well as the mass representing the ATM experiment canister. The simulated canister was floated on a spherical float as shown in Figure 111. The two separate mercury floatation bearings were concentrically arranged and each mercury container was supported by structure connected to the floor. Figure 112 shows the float and structure used to support the weight of the gimbal ring. Figure 113 shows the installed gimbal and its support structure. Figure 114 is an artist's concept showing the overall general test configuration. A significant specification for the ATM Dynamic Test Fixture is that the residual unbalance of the simulated 3000-pound experiment canister be less than 0.01 ft-lb, a value corresponding to the equivalent of only 1/300,000 ft c.g. error

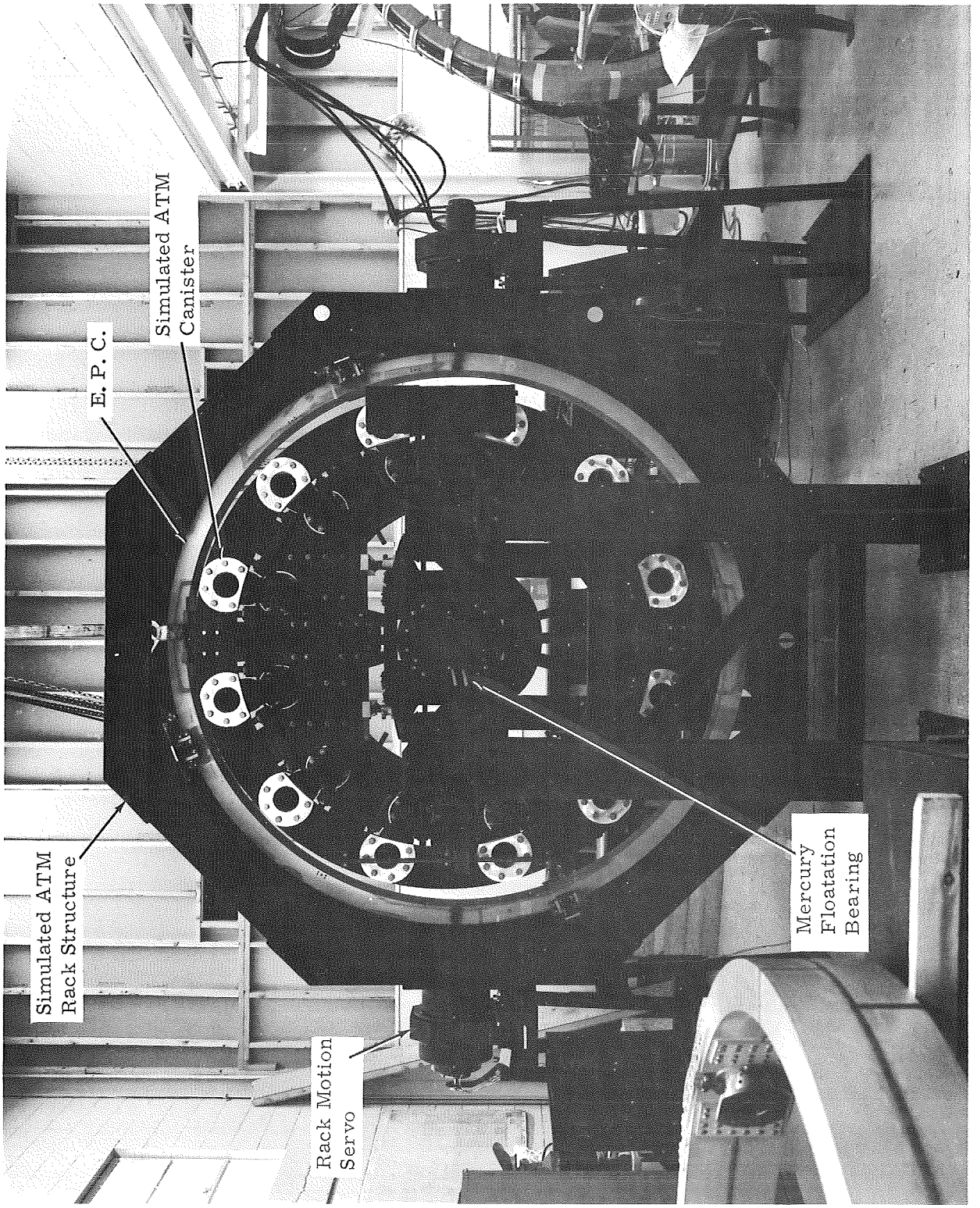

Figure 110 • ATM-A Zero Gravity Simulation for EPC Pointing Tests

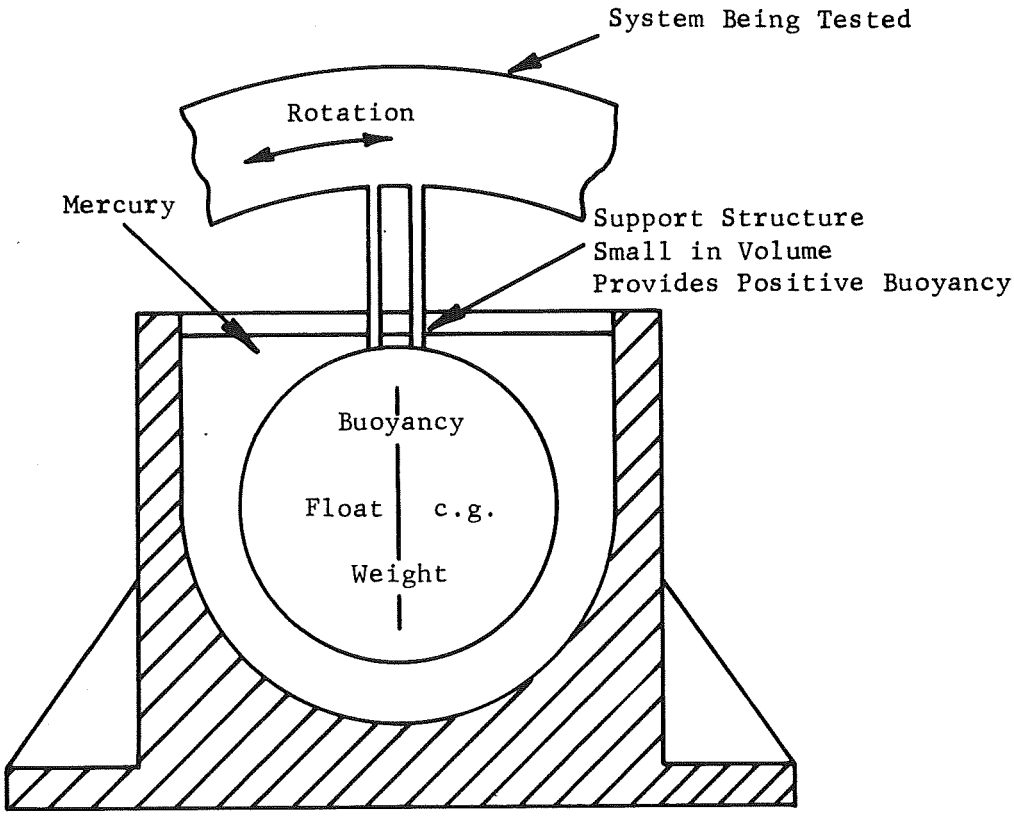

Figure 111. Mercury Bearing Concept

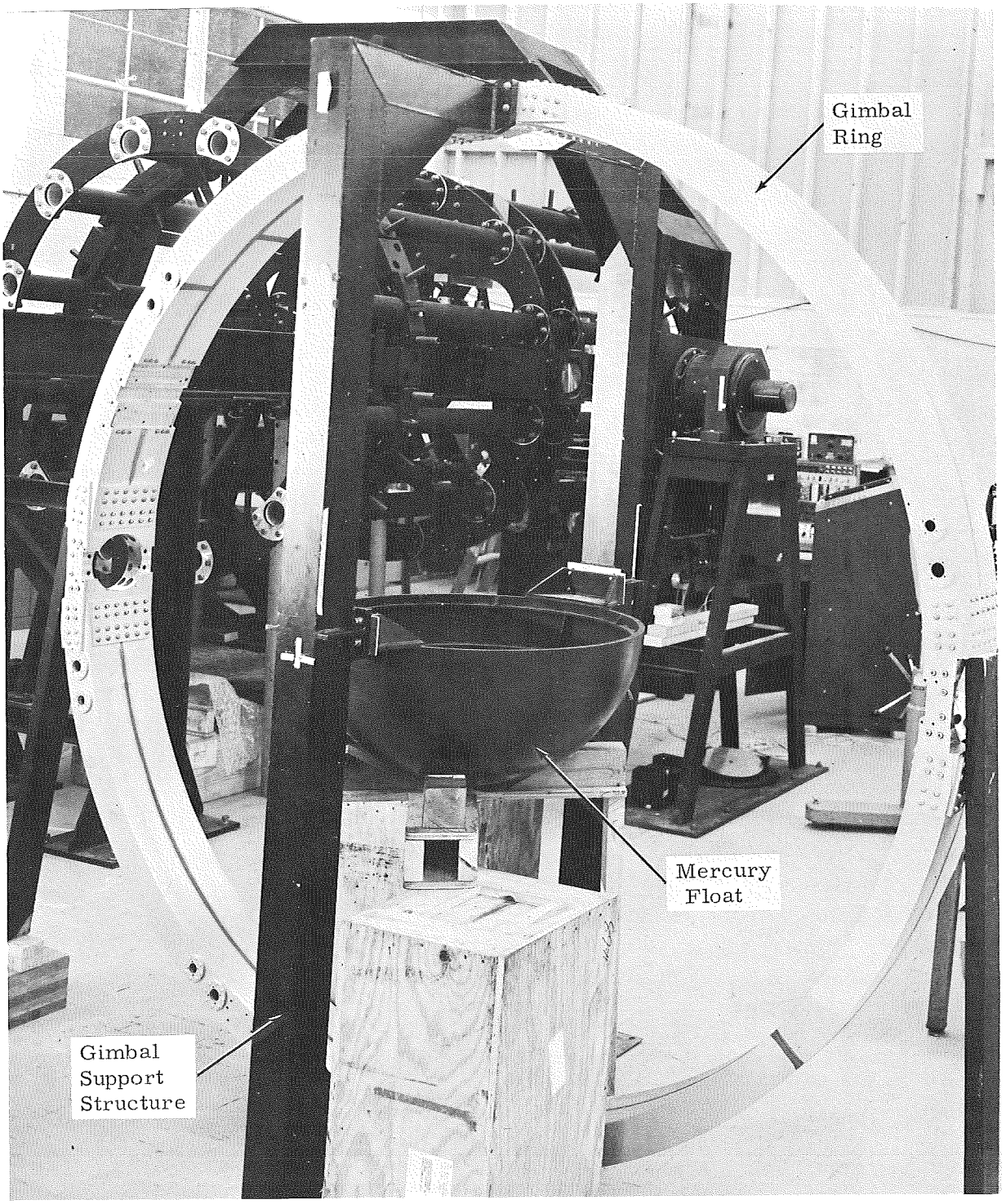

Figure 112. Gimbal Support Structure and Mercury Float

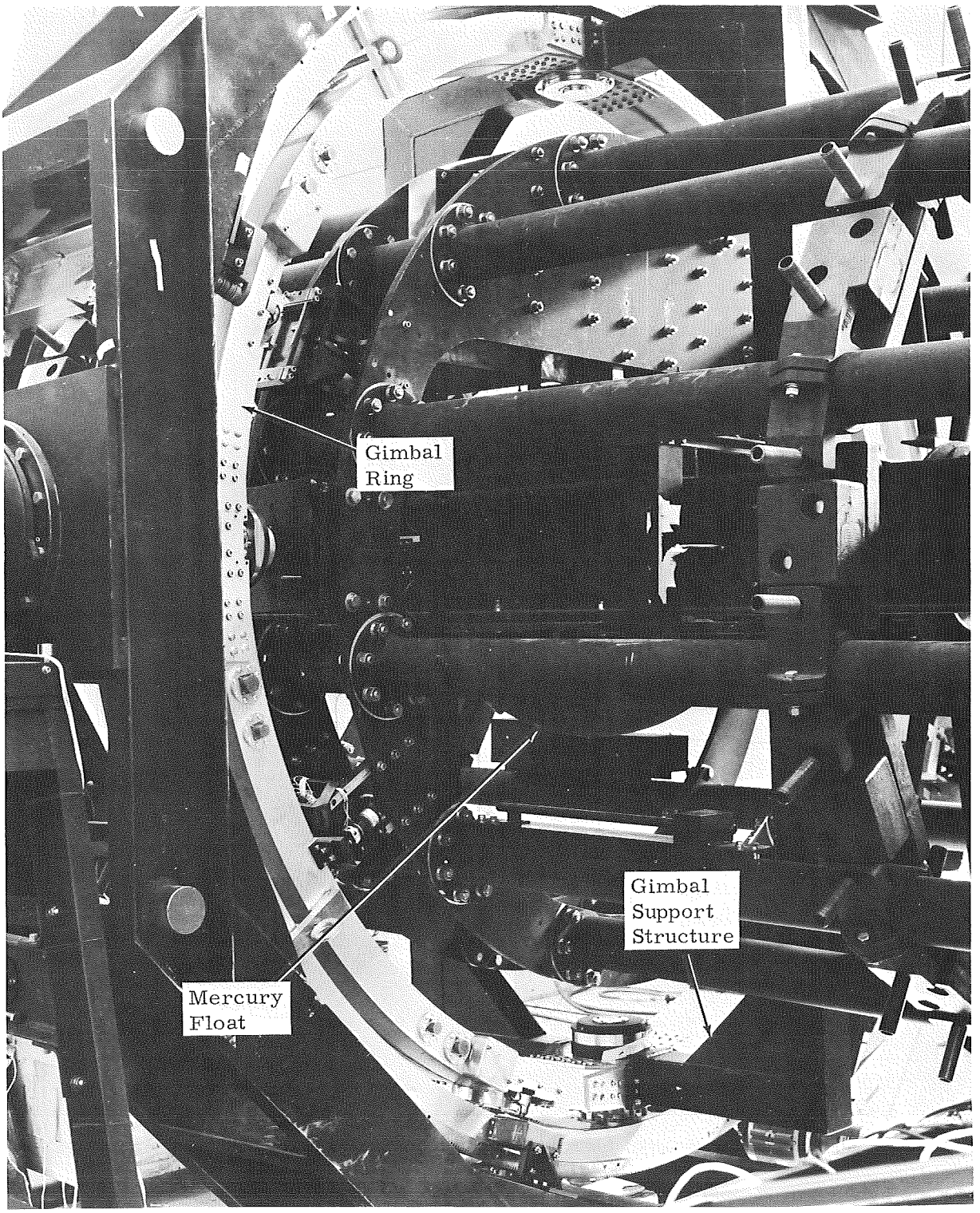

Figure 113. Gimbal and Support Installed in Test Fixture I-240

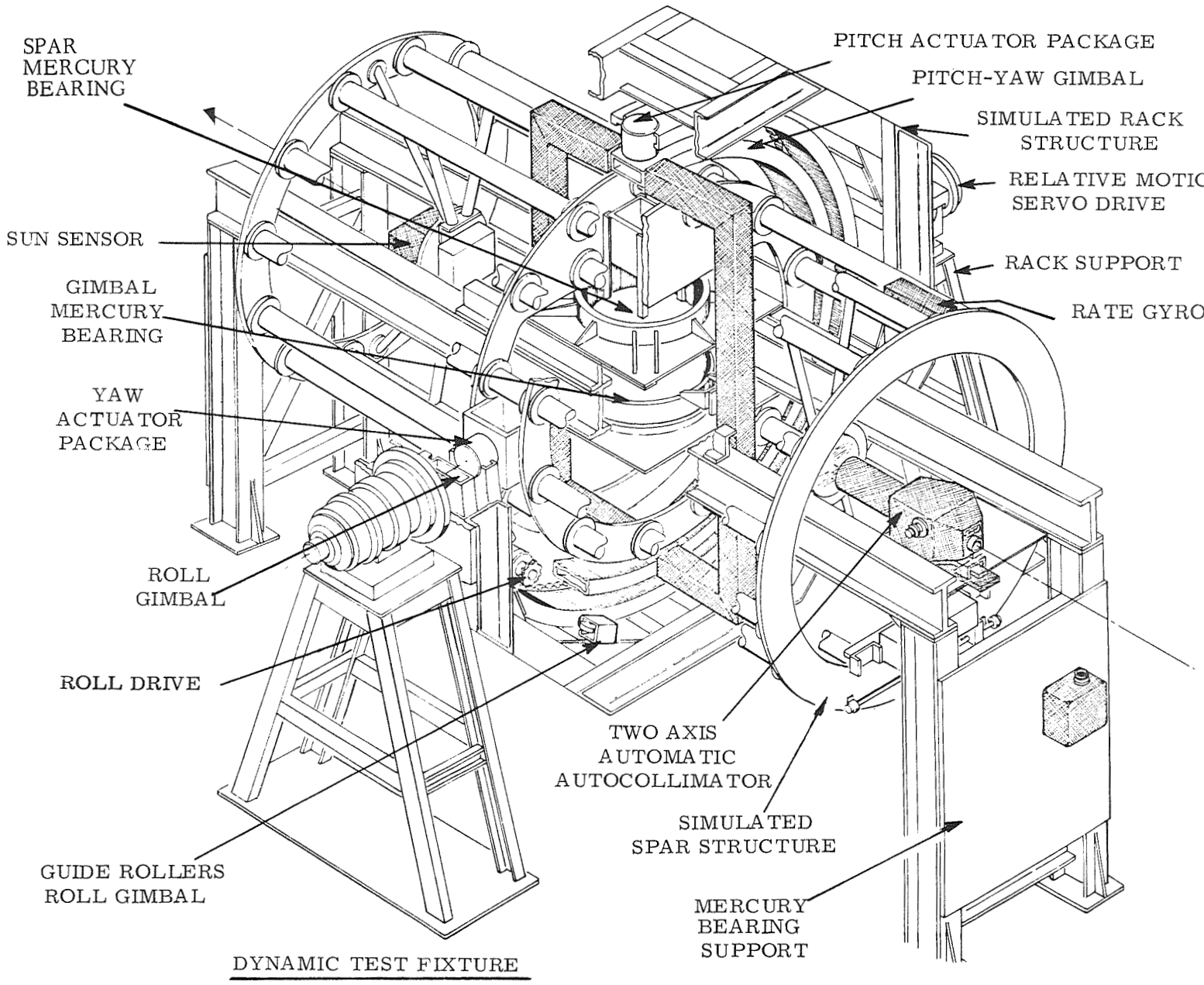

Figure 114 . Dynamic Test Fixture

It is not always possible to arrange to have the center of bouyancy of a mercury floatation bearing coincide with the center of gravity and the center of rotation. In these cases, the air bearing is attractive. For example, the MSFC air bearing arrangement shown in Figure 115 is to be used in ATM prelaunch gimbal checkout where it would be quite impractical to utilize a mercury floatation bearing. The bearing is a compound air bearing. Items (1) and (2) constitute a spherical air bearing to permit two-axis rotation of the system about its c.g. (shifted 7.5 in. downward by the addition of air bearing components), and items (2) and (3) constitute an air slide bearing. The latter degree of freedom is required to allow for horizontal translations due to rotations about the gimbal axes which are non-coincident with the air bearing center of rotation. The gimbal axes and the air-bearing centers cannot be made coincident (by counterweighting in this case to avoid the 7.5-in. shift) since the ATM actuators could not then rotate the experiment canister. This is because the actuator torque required to rotate the air bearing-supported canister would be the 7.5-in. arm times the weight times the angle, or

$$T = 7.5 \times 6240 \times \theta$$

Since only 7 lb-ft of torque can be generated by the actuators, the maximum angle the torquer can produce would be only

$$\theta = \frac{7}{\frac{7.5}{12} \times 6240} = 0.0018 \text{ radians or } 0.1 \text{ degree}$$

This is obviously incompatible with the requirement to demonstrate operation over the full ±2-degree gimbal angle. The illustrated configuration avoids this problem since the effective rotation is about the c.g. The associated 0.005-in. vertical displacement component causes no ill effects.

The schemes which we have been discussing are illustrative of the problems encountered when trying to test a pointing system in earth's gravity. It should be emphasized that the particular air bearing scheme (Figure 115) discussed was not designed to permit closed-loop testing, but is intended only for prelaunch checkout of gimbal freedom. It cannot in its present form be used for servo testing because the line of sight of the fine sun sensor is obscured by the air bearing, and the vertical motion requirement, discussed above, caused configuration changes in the torque reaction path incompatible with pointing servo operation. (The details of these changes are not germane and will not be described here.) The problems of suitable test fixturing are not necessarily insolvable but there is a tendency both for the fixtures to become more complicated, and/or to introduce other effects which may obscure phenomena that would be puzzling or even catastrophic when later encountered in space.

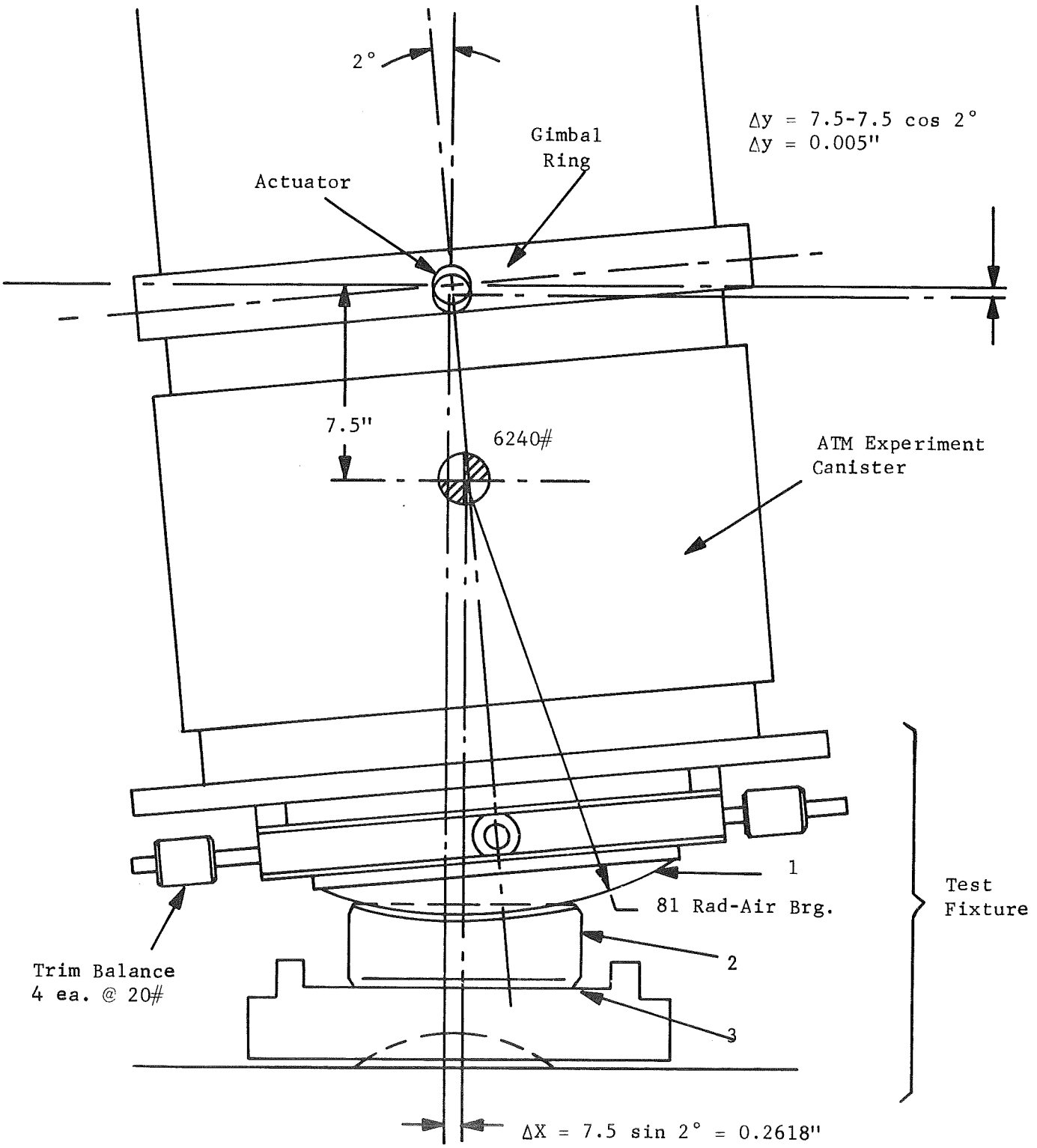

Figure 115. MSFC Air Bearing For ATM Checkout

A way of avoiding many of these difficulties and problems might be to redesign the gimbal system so that it is unaffected by the removal of gravity. The need for redesign under such conditions is illustrated by the following.

It is axiomatic in structural design that it is much easier to achieve a given strength requirement that it is to achieve a particular rigidity requirement. This can be illustrated by considering the ATM EPC gimbal ring. Figure 116 is a photograph of this ring. It has the strength capability of supporting 8000 lb and it weighs only 192 lb. However, under the 1-g weight of 5500 lb of the ATM experiment canister, the deflection of the ring is approximately 0.5 in. Figure 117 (A) shows the geometry of the deflected gimbal ring. It will be noted that the yaw axis has settled 1/2 in. below the pitch axis due to the weight of the experiment canister and earth's gravity.

In order for the outermost actuator to rotate the package about its axis, it must overcome the couple that is generated by the weight of the experiment canister and the 1/2-in. arm generated by deflection of the ring. Figure 117 (B) illustrates this geometry. For typical torque motor capability (e.g., 7 ft-lb), motions of only 0.03 degrees are possible in earth's gravity in the face of this ring deflection. In order to function in earth's gravity, it would be necessary to reduce these deflections by several orders of magnitude. If a large ring type of structure were designed to do this, the weight and size of the ring would increase substantially.

This is in marked contrast with, for example, the effects encountered with the Stratoscope II configuration. Here the telescope is "L" shaped, as illustrated in Figure 118, to place the c.g. out of coincidence with structure. This permitted the use of a compact, relatively light weight, yet highly rigid gimbaling mechanism, one with very small deflections and hence more compatible with test and operation in earth's gravity.

If the LTEP telescope were to be operated only on a gimbal system, a radical change in the configuration in line with the above discussion would be recommended. However, the free-float pointing mode is the method of choice for high resolution imagery. Many of the problems of mechanical suspension are avoided by the free-float pointing system, and test requirements are therefore eased (e.g., the problem of structural resonance interaction with the telescope is eliminated.)

In Chapter 10 Page 249 means for testing the free-float system will be discussed.

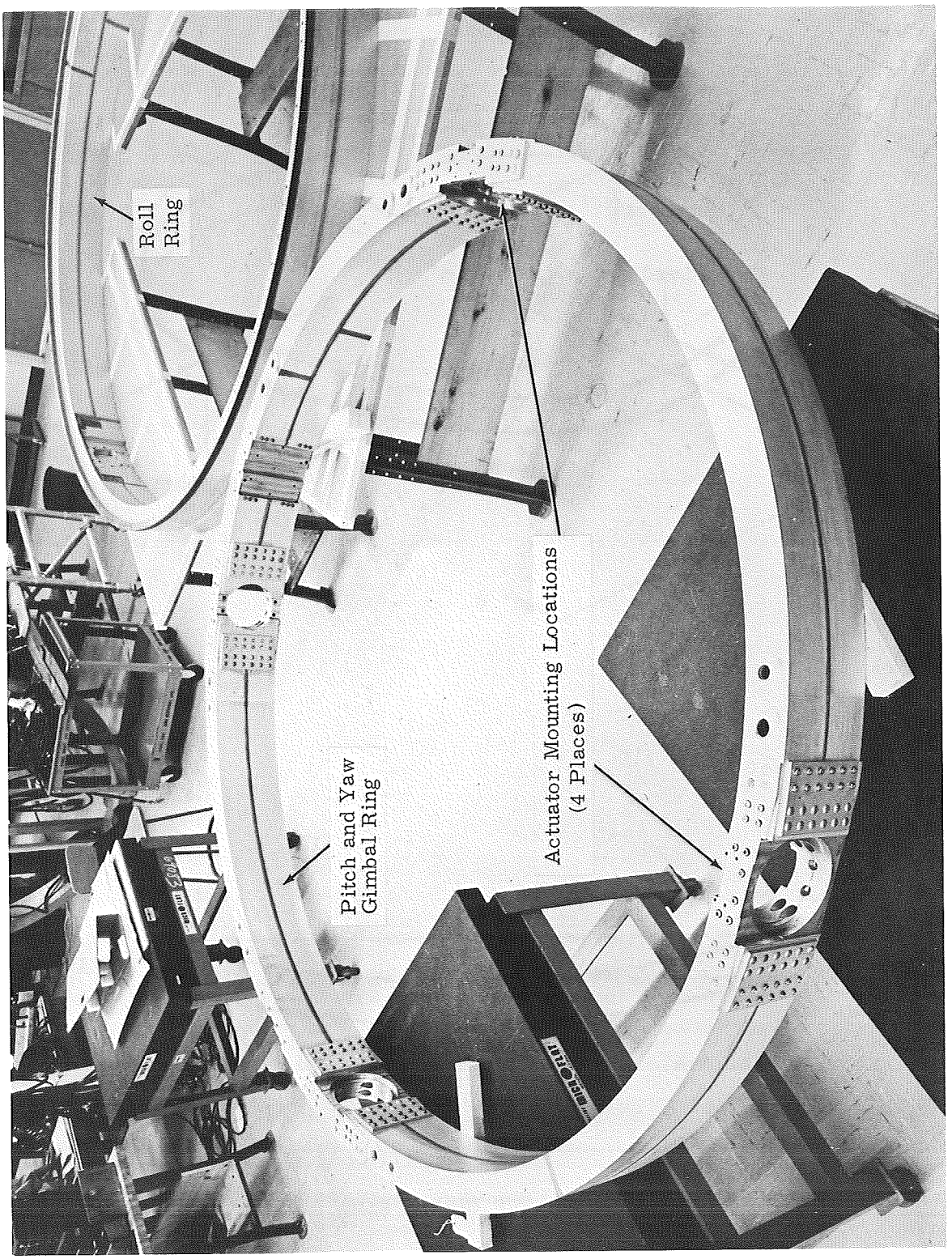

Figure 116. EPC Gimbal Ring

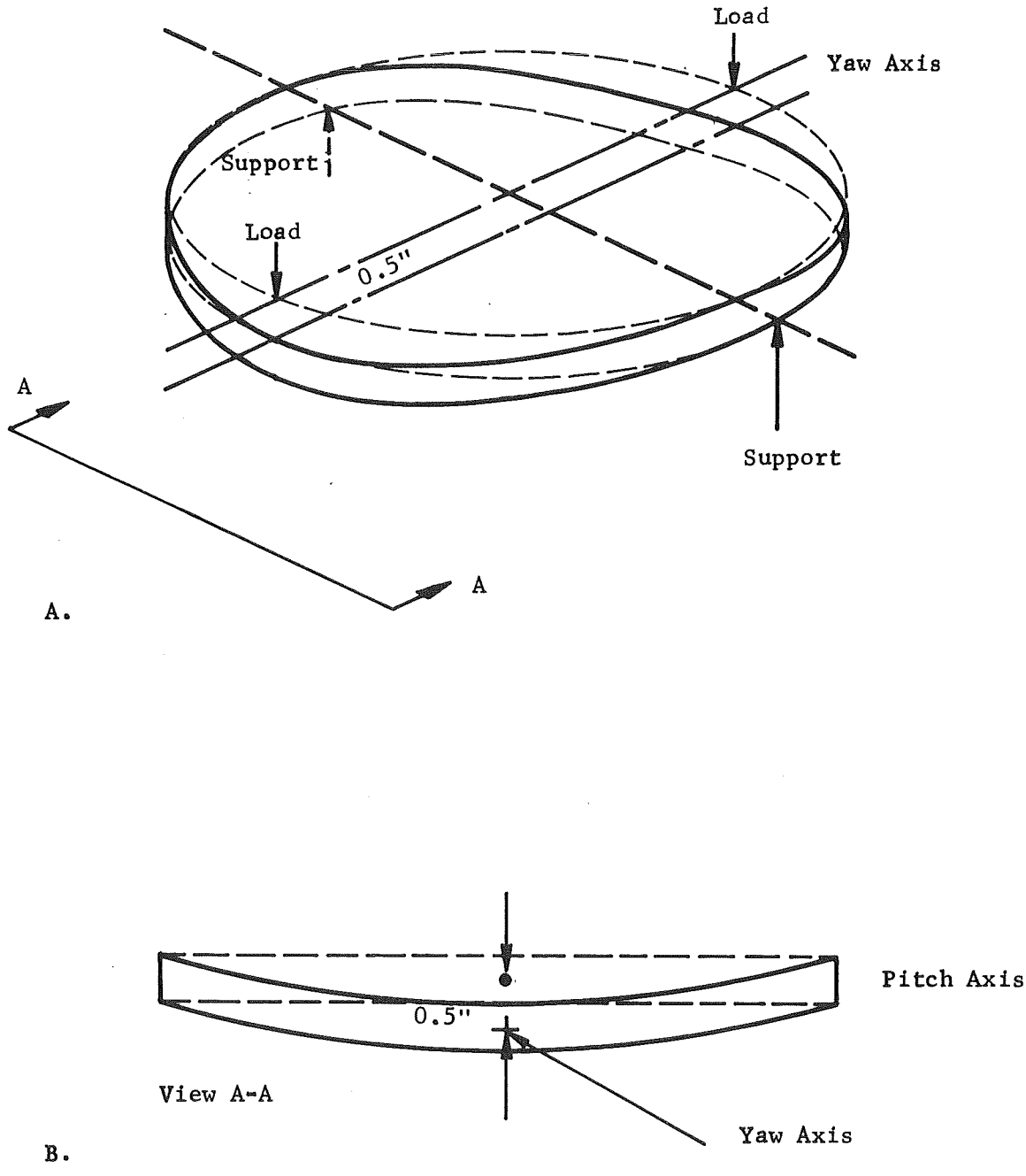

Figure 117. EPC Gimbal Ring Deflection Geometry

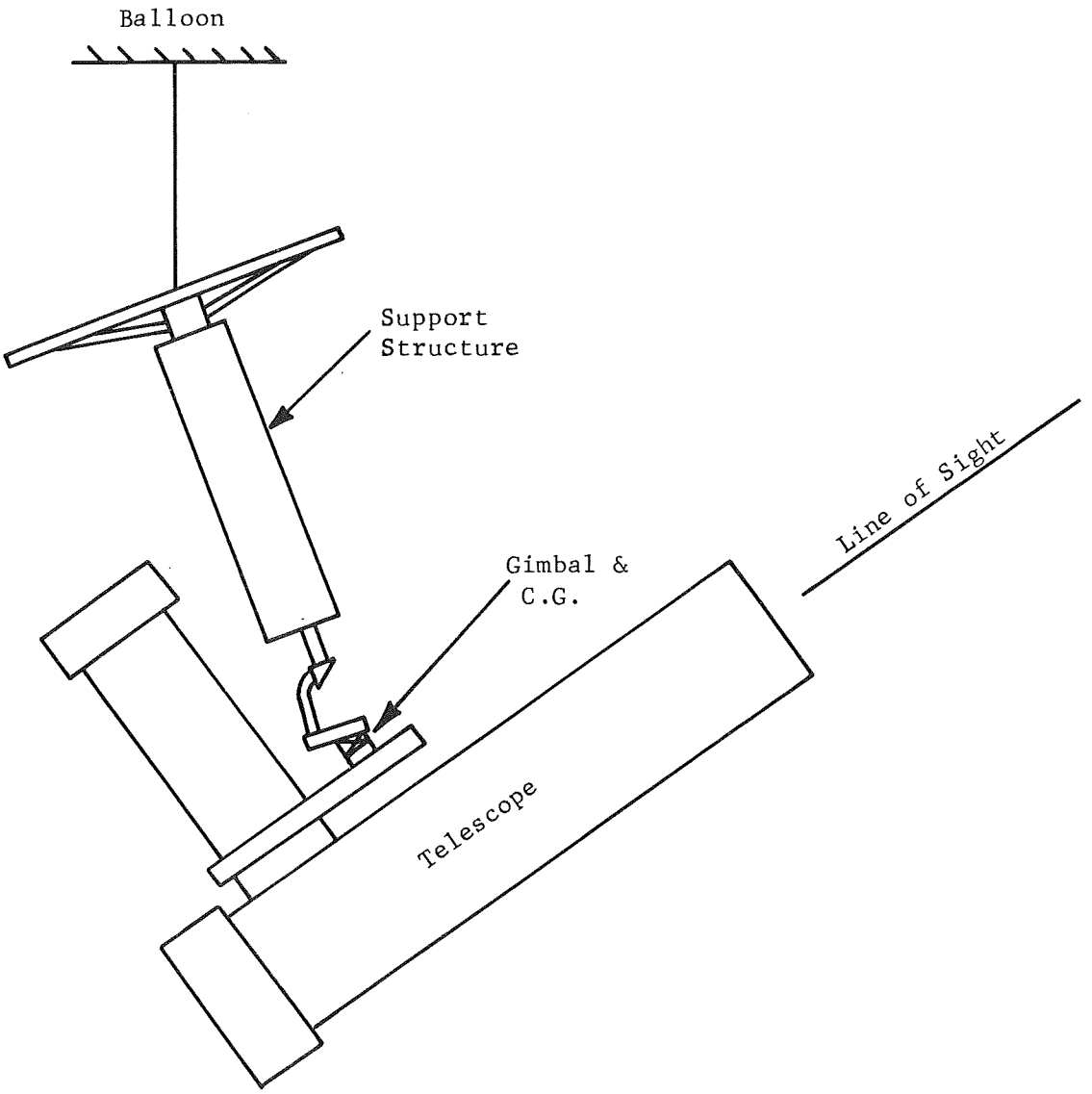

Figure 118. Stratoscope II Structural Arrangement

CHAPTER 10 - FREE FLOAT POINTING SYSTEM

DESCRIPTION

Fine angular pointing of the LTEP for both the CLOS and the RLOS, utilizing the free float technique, is recommended for Modules C and D, the f/10 film and echelle spectrograph (uv) instruments. In the free float or magnetic suspension pointing configuration, the LTEP telescope is completely isolated mechanically from the surrounding spacecraft by taking advantage of the weightlessness on orbit. The free float offers subfractional arc-second pointing accuracy capability. Its unique advantage is nearly complete isolation from external disturbances. High gain, high bandpass servo systems can normally cope with large external disturbances, but not without sacrificing performance because of increased susceptibility to random noise sources. The free float control system can be designed to perform at very low bandpass frequencies thus taking advantage of its isolation features.

External disturbances are not completely absent of course, but those torque disturbances affecting the system are low frequency once-or-twice-per-orbit types, such as gravity gradients and aerodynamic disturbances. The estimated magnitudes of these disturbances have been itemized in Table 26 where gravity gradients contribute 1.5×10^{-3} lb-ft of torque, and aerodynamic disturbances contribute 29.5×10^{-3} lb-ft. The minimum angular pointing accuracy requirements for Modules C and D in arc-seconds rms are, for noise-induced errors, 0.0032 for CLOS and 0.0032 or less for RLOS. For external torque disturbance-induced errors, the accuracy requirements are 0.0060 arc-second (peak) for both CLOS and RLOS. Noise-induced errors are simply those errors caused by noise or random inputs such as photon shot noise at the output of the guide star sensors.

The free float pointing system has six degrees of freedom to control since it is fully isolated from the outer spacecraft. There are three degrees of linear translation (x,y and z) and three degrees of angular motions (Ψ, ϕ, and β) as illustrated in the simplified sketch of Figure 119.

The line of sight (LOS) lies along the z axis. The cross line of sight axes (CLOS) are defined as β and Ψ and the roll axis (RLOS) defined by the angle θ.

The CLOS and RLOS axes mispointing errors are sensed by pointing error sensors located within the telescope structure, one sensor for the CLOS and one for RLOS. The translation axes errors are sensed by capacitive sensors mounted between the telescope and the outer spacecraft. These sensors, two per (translation) axis, monitor the relative position of the telescope with respect to the outer spacecraft for the purpose of maintaining the telescope centered in three directions with respect to the outer spacecraft.

The pointing error sensor, a two-axis device, utilizes a dividing prism and photomultiplier tubes located at the focal plane of the LTEP optical system. The sensor is shown schematically in the sketch of Figure 120.

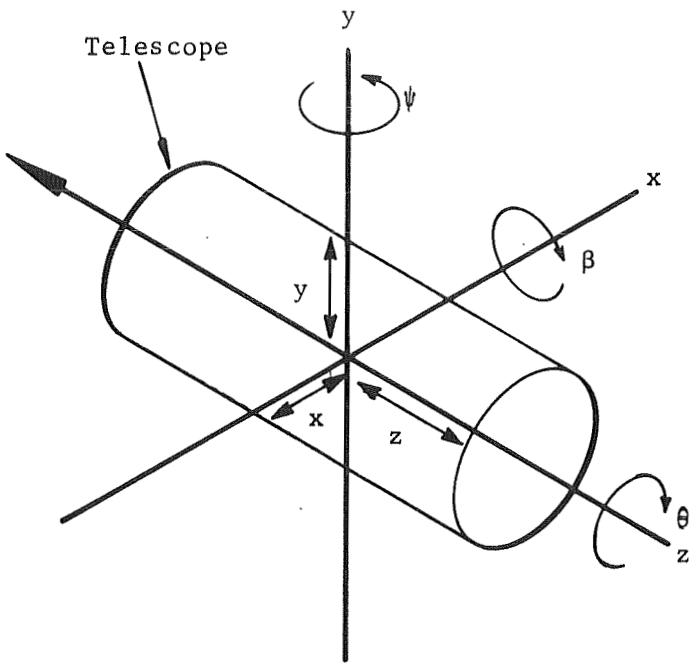

Figure 119. Free Float Degrees of Freedom

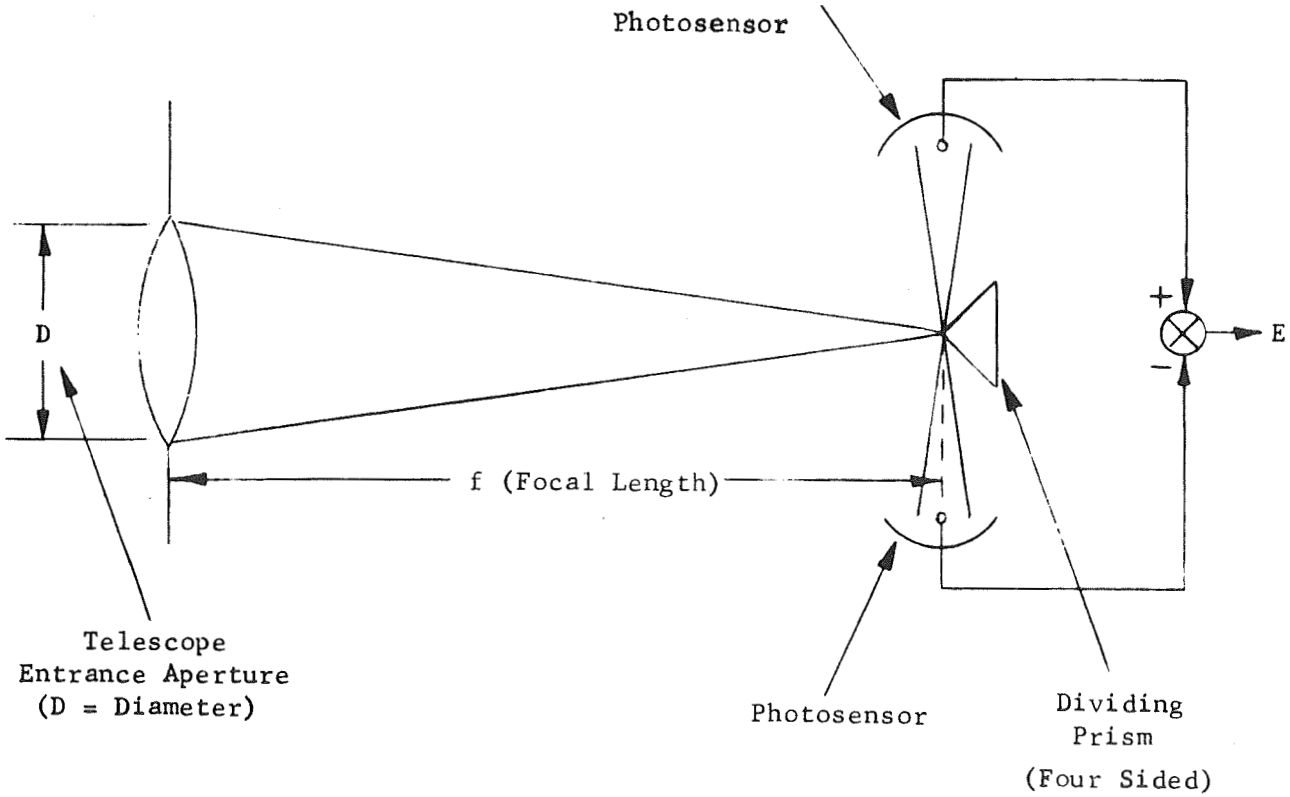

Figure 120. Single Axis Tracking Sensor Utilizing Diffraction-Limited Optics

Starlight entering the optical system converges at the apex of a four-sided prism where a focused image is formed and divided into two parts per axis. Each divided image is collected by a photomultiplier tube which produces electrical outputs proportional to light intensity. With correct angular alignment or pointing in a given axis, the two-photomultipliers receive equal quantities of light and, if their electrical outputs are differenced, the net output is zero. Mispointing upsets the light intensity division and causes the electrical output signal to depart from null.

In a practical configuration of the sensor, an optical chopper is used to modulate the light prior to entering the photocathode surfaces of the phototubes. The photomultiplier current outputs are therefore also modulated and signal processing is accomplished using an ac carrier. Modulation techniques eliminate the difficulty of maintaining balanced outputs in the dual sensing multiplier tubes as shown in the above sketch of Figure 120 . The effects of photomultiplier dark currents, electronic biases, etc., and their time variations would cause mispointing but these effects can be either minimized or completely eliminated in an ac system.

The capacitive sensors consist of two parallel plates, one mounted on the telescope and the other mounted on the spacecraft, forming a capacitor where the capacitance is determined by $c = eA/d$. The term "d" is the separation between plates or a measure of the relative spacing between the telescope and spacecraft. As "d" changes, so does "c", the capacitance. The change in capacitance is then converted into a proportional change in voltage.

Both the error sensor and capacitive displacement sensor electrical output signals are processed through electrical integration circuits prior to arriving at the magnetic pushers. The magnetic pushers, two per axis, six total per pointing system, are key components in the free float pointing system. They are used to simultaneously control both centering and angular motion of the telescope with a pair of pushers controlling one angular degree of freedom and one centering degree of freedom.

A single magnetic pusher consists of a permanent magnet, which is mounted on the outer spacecraft and a wire-wound coil located on the telescope. The coil is placed in the uniform radial flux field created by the permanent magnet and oriented to produce a linear output (magnetic reaction) force when current is applied to the coil windings. The concept is illustrated in Figure 121.

This type of dc force actuator has several unique features; first, the coil and permanent magnet are mechanically isolated in three translational directions with travel capability of at least $\pm 1/2$ inch in all three directions. Thus, the telescope is provided with a force actuator that preserves the free float mechanical isolation feature. Second, the telescope is not disturbed by motions of the permanent magnet with respect to the coil. Current can be applied to the magnetic pusher coil while the permanent magnet is in motion without coupling any of these spacecraft motions into the telescope. Both mechanical and magnetic isolation are therefore obtainable with this type of actuator.

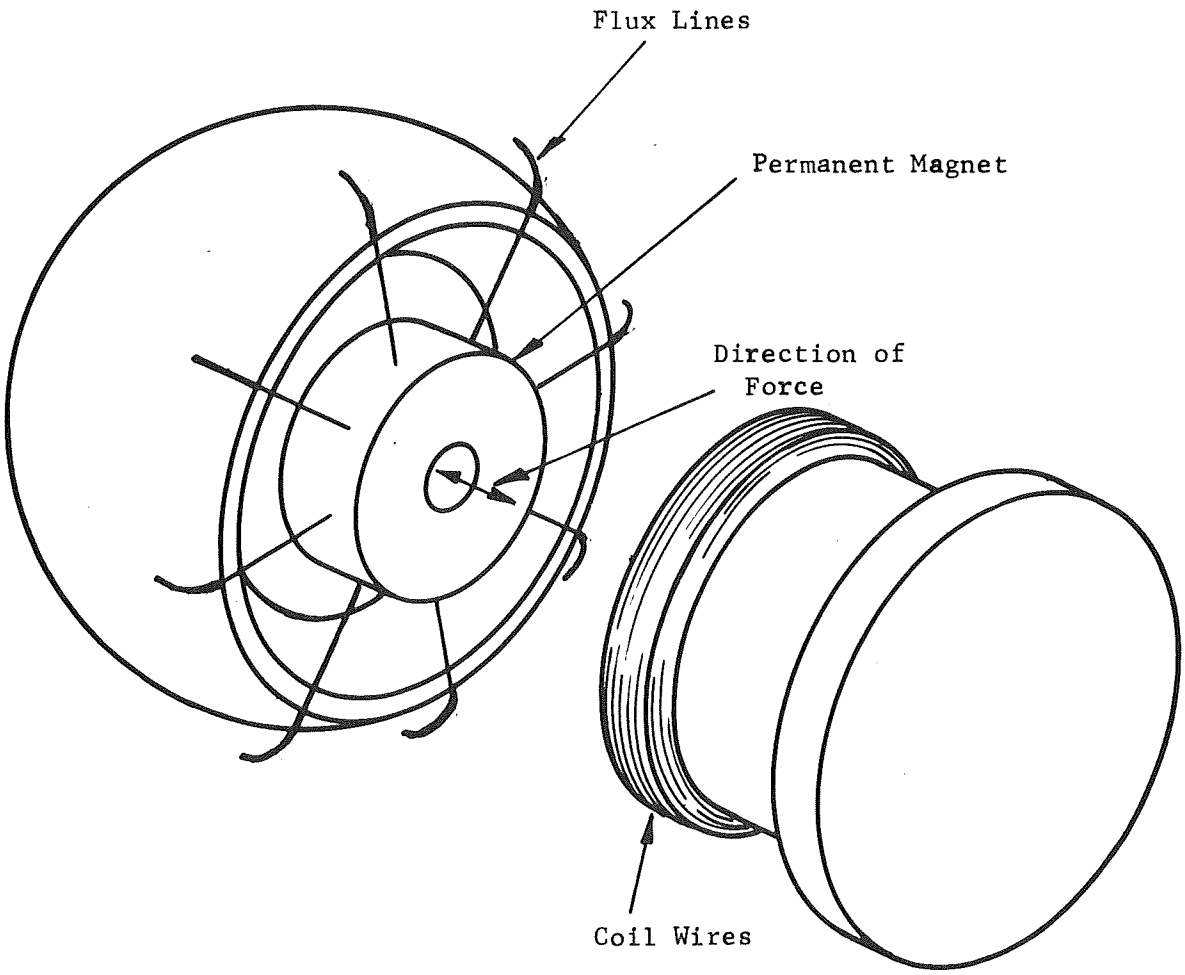

Figure 121. Exploded View of Magnetic Pusher

A pair of magnetic pushers is used to control a single axis of translation and also a single degree of angular freedom. Two actuators spaced equally apart about the center of rotation axis of the telescope will form a couple or moment when the magnetic reaction forces are in opposite directions. When the force output of both actuators is in the same direction, translation of the telescope will occur.

The integration circuits through which the optical star tracker output signals are processed serve to stabilize the pointing system control loops in both the CLOS and RLOS axes. These RC-type electrical networks provide the high gain required to combat disturbances at low frequency. This avoids the necessity of using angular rate gyros as minor loop feedback elements to achieve a high isolation from torque disturbances as is usually done with inertial platforms. Rate gyros are in themselves a source of noise and drift, creating errors detrimental to achieving the precise 0.0032-arc-second(rms) pointing accuracy required for modules C and D. Other rate stabilizing devices such as velocity generators or tachometers are also undesirable since they must achieve their reference from the spacecraft. Outer spacecraft velocities therefore would be coupled directly through the tachometers to the telescope.

The signal integration circuits also include proportional feedforward electrical paths to add leading phase shift at servo crossover frequencies to satisfy servo loop stability criteria. A typical pointing loop is shown in Figure 122.

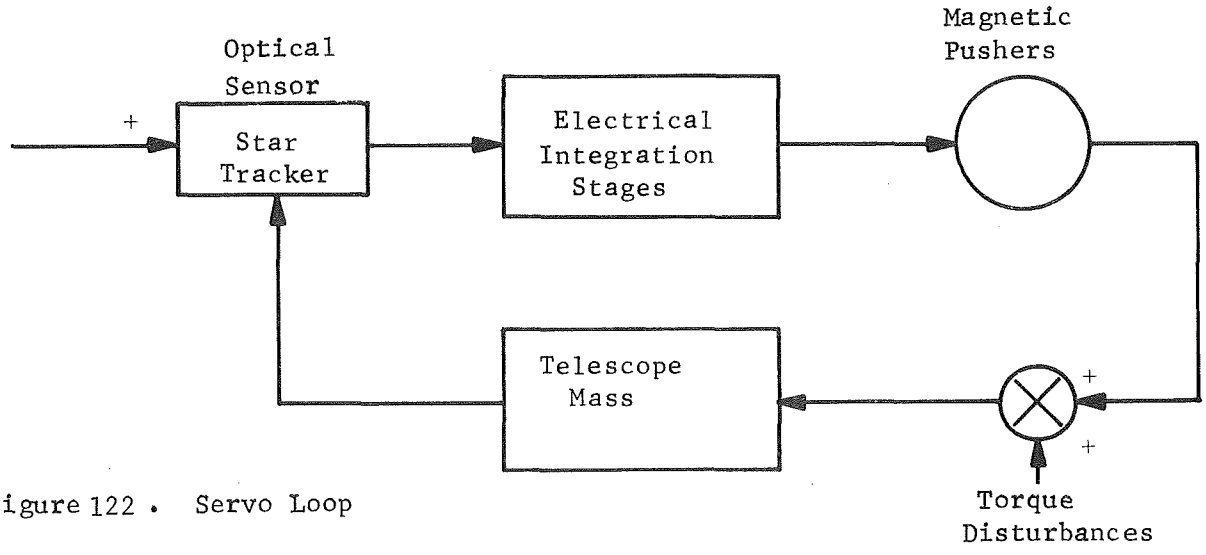

Figure 122 . Servo Loop

The advantage of using integration in the signal paths lies in the ability to achieve low servo loop bandpass frequencies, while still achieving extremely high gains at external disturbance input frequencies. On the other hand, low bandpass frequencies heavily filter noise inputs reducing noise-induced pointing errors to acceptable levels.

To maintain complete physical isolation between the telescope and spacecraft, wire crossings for electrical signals and power are avoided. To transfer electrical power to the telescope from the spacecraft for instance, a chain link transformer is used. This device consists of a toroidal wound primary through which a secondary coil is wound. The unit is shown below in Figure 123

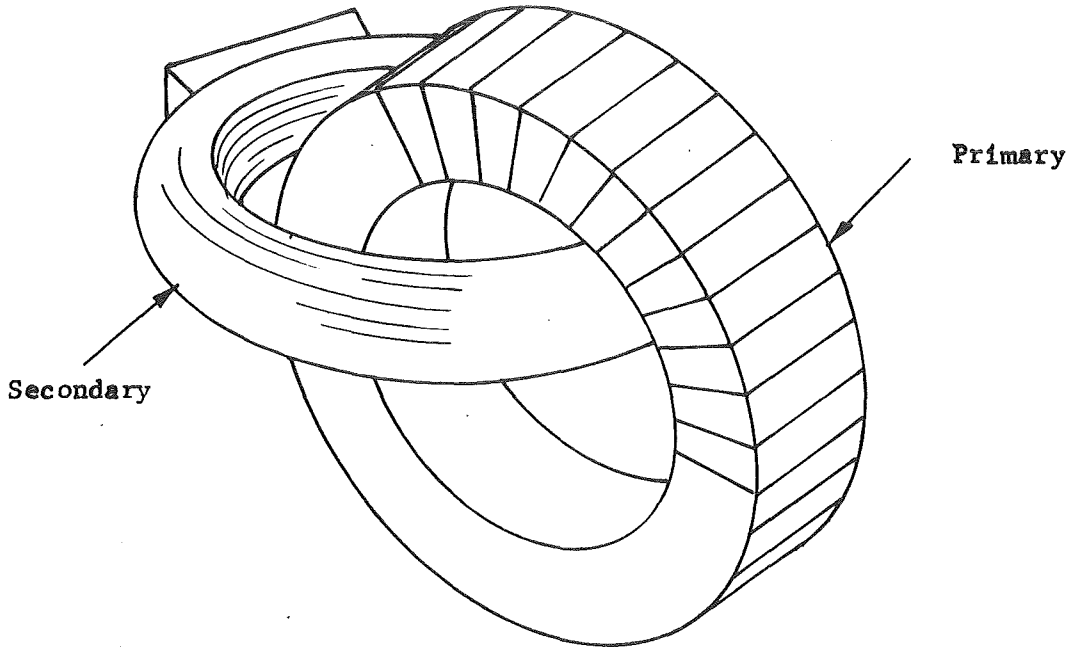

Figure 123. Chain Link Transformer

The secondary winding and the primary windings are physically separated by a 1/2 inch gap in all directions and the two windings are situated at right angles to each other. The right angle orientation of the secondary winding with respect to the primary winding cancels magnetic reaction forces between the primary and secondary when power is applied to the transformer. Experimental results with this device have shown force levels to be no greater than 1×10^{-4} lb with 100 watts of applied electrical power. The disturbance torque levels caused by these forces can potentially be minimized by locating the transformer at the center of mass of the telescope. The chain link transformer primary/secondary magnetic reaction forces will therefore act through only a small moment arm.

This type of transformer proved to be very efficient. At power levels of 40 watts, experimental tests revealed efficiencies in the order of 90 percent at 100 ac and 400 Hz.

External input commands and output signals can also be sent back and forth between the telescope and spacecraft using chain link transformers. Signal and command electrical power levels are small and the physical size of the transformers used for this purpose can be very small. The gap size limits the overall size of the transformer rather than the physical dimensions of the primary and secondary coils. An experimental low power chain link transformer weighing only a few ounces was tested in the laboratories at Perkin-Elmer

with successful results. A single chain link transformer can also transfer several signals at once using techniques such as phase modulation. Two signals phased 90 degrees apart can be fed into a chain link transformer simultaneously for instance, and separated at the output by demodulators--operating 90 degrees apart. This technique was used during the free float experiment (see "Experiments Results").

THEORETICAL CONSIDERATIONS

LTEP fine pointing control is achieved by using two preselected guide stars located in proximity to the stellar source being observed. The star trackers, as described in the previous section, angularly determine the location of the stars within the sensor field of view and produce error signals proportional to mispointing which, via the servo loop electronics and magnetic pushers, hold the telescope pointed at the object of interest. A minimum of two guide stars is necessary in order to achieve pointing information for both the CLOS axes and the RLOS axis.

External disturbance torques cause pointing errors as explained but equally important, noise-induced errors can also prevent the control systems from achieving pointing specifications. Fundamentally, the star tracker provides the pointing controls with commands in the form of error signals and there is no method of distinguishing between output tracker error signals caused by torque disturbances or those caused by internal star tracker noise. Although there are several sources that can cause excessive noise at the star tracker output, such as electrical circuit noise, most of these sources can all be reasonably minimized by proper circuit design with one exception; the fundamental "noise in signal" due to random photon arrival rates from the guide stars. This noise is ever present. Random photon noise cannot be eliminated, only minimized, by filtering,i.e., by integrating the output signals, or, in the case of a closed loop servo system, by using low bandpass frequencies. All methods achieve the same result; fundamentally, sampling the tracker output over a period of time to enable the detection of the signal in the presence of noise. The key parameter used in signal detection is the ratio of signal to noise (S/N). The first important step in determining servo pointing errors involves signal-to-noise calculations and in particular, signal-to-noise calculations based on expected guide star magnitudes. Large magnitude, low-intensity stars produce greater noise.

In order to calculate the star tracker and pointing system S/N ratio, a relationship between tracker receiver characteristics, power density at the receiver collector, noise due to background illumination, photon discreteness or shot noise, detector noise contributions, and servo response bandwidth must be developed.

The analytical relationship between the star tracker output signal and the angular pointing error for the dividing prism type of sensor is determined from the Airy diffraction pattern of the star image formed at the dividing prism. From the diffraction pattern, the image energy transfer curve is derived as a function of the pointing error which can be measured in terms

of a fraction of the Airy disk diameter. The image transfer curve is shown in Figure 124. It plots light intensity versus angle as related to wavelength (λ) and the aperture (D) of the optical system.

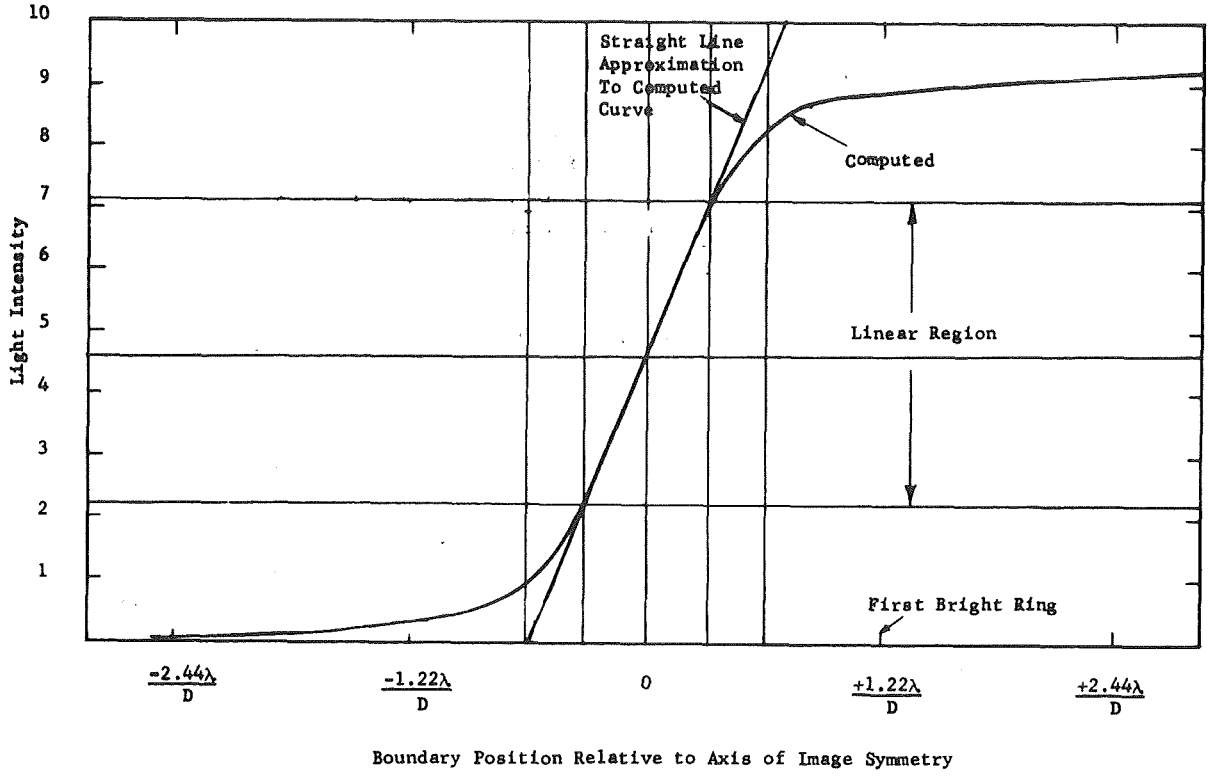

Figure 124 . Image Light Energy on One Side of a Knife Edge Boundary

Using a straight line approximation to the energy transfer curve, it is evident that the energy transfer at null position is equivalent to the total energy transferred for an angular motion of 1.22 λ/D (λ = wavelength, D = aperture diameter, both in meters). Such an angular motion results in the first bright ring of the diffraction pattern being moved to the apex of the image-dividing prism. Then, since the output of the photosensors are differenced,

$$E_{total} = 2S \qquad (1)$$

where S is signal in terms of angular pointing error relative to the diffraction pattern, and E is the electrical signal in the photosensor.

Assuming prior knowledge of the S/N ratio in a particular response bandwidth, an rms noise of N in this same bandwidth will, therefore, cause the system to have an rms pointing error (E_p) described by

$$E_p = 1.22\ \lambda/D \left(\frac{N}{S}\right) \tag{2}$$

for pointing errors close to null.

This expression is correct even when fairly large central obscurations are present, provided, in all cases, that the S/N ratio is reasonably large (viz, S/N $\leq$ 10). As the S/N ratio is lowered, the expression becomes optimistic (due to greater departures of the straight line approximation from the energy transfer curve) and more accurate results can be obtained with other than simple slope approximations.

The S/N ratio is derived statistically from analysis assuming Gaussian conditions and can be calculated from a knowledge of the optical transmission and photocathode quantum efficiencies, background illumination, photon discreteness, star irradiance and bandpass frequencies. The final expression for the S/N ratio can then be substituted into Equation (2) which would complete the relationship necessary to determine the magnitude of the mispointing caused by noise.

The relationship for the signal-to-noise ratio is given by

$$\frac{S}{N} = \frac{P_S \eta_Q \Delta t}{\left[\left(P_S \eta_Q + \epsilon_n\right) \Delta t\right]^{1/2}} \tag{3}$$

where

$$P_S = \eta_o I_m \epsilon_q A \tag{4}$$

Terms are defined as follows:

P_S = Arrival rate of signal photons at the photon detectors (photons/second)

η_o = System optical transmission efficiency

I_m = Star irradiance for a specific photomultiplier spectral range (watts/meter^2)

ϵ_q = Photon quantum energy at a specific wavelength (photons/second/watt), 1/hf

A = Entrance aperture area for the optical system (meter^2), $\frac{\pi}{4} D^2$

Mv = Guide star visual magnitude

η_Q = Photocathode quantum efficiency

ϵ_n = Equivalent photomultiplier quantum energy (rms pulses contributed by dark current), background illumination, and cosmic ray variations (photons/second).

Δt = Bandwidth period (second) or sampling interval which equals $\frac{1}{2 feq}$ where feq(Hz) is the equivalent system bandwidth.

If the background illumination, dark current, and other noise sources are neglected, i.e., $\epsilon_n = 0$, the relationship for the theoretical maximum S/N ratio is obtained.

If the maximum S/N ratio is then substituted into Equation (2), the final rms pointing error relationship is obtained. In this case, $\epsilon_n = 0$ and E_p is therefore considered the minimum pointing error that can be obtained.

The expression for E_p (min.) is plotted logarithmically against star magnitude (Mv) in Figure 125. Values of parameters used were as follows:

$$I_m(Mv = 0) = 3.8 \times 10^{-12} \text{ watts/cm}^2\text{/micron at 0.55 microns over a 0.10 micron spectral range}$$

$$\epsilon_q = 2.76 \times 10^{18} \text{ photons/sec/watt}$$

The E_p (min.) relationship derived using the above values is shown in Figure 125.

The E_p (min.) relationship clearly indicates the effect of aperture diameter on pointing accuracy. It is obviously more difficult to obtain a given pointing accuracy with a 1-meter aperture diameter than to obtain the same accuracy with a 3-meter aperture diameter for the same stellar magnitude and servo bandwidth.

If the dark current and other noise-contributing sources inherent in ϵ_n are included, the S/N will be reduced, resulting in an increased rms error. This is particularly true if, for instance, dark current variations due to thermal emission produce photocathode currents not much smaller than those due to signal. However, the amount of E_p increase due to all the ϵ_n factors can be minimized by using reduced temperatures for the photosensors, minimal field of view, etc. Dark current, for example, due to thermal emission appears as a photocathode output current level which may exhibit a slow drift rate. Cooling the photocathode markedly reduces these current levels. This was shown in Figure 77. where data was obtained using S-20-type photomultiplier tube. Cooling to 200°K (-73°C), if practical, can reduce the dark current by a factor of nearly 40:1.

Another technique for eliminating the dc component of thermal dark current is optical or electrical chopping of the light signal. The photocathode output current can be made to appear in a coded ac form and, with proper electrical processing techniques, photocathode dc or very low frequency variations can be rejected. Photocathode spectral sensitivity and gain changes that normally would produce electrical imbalances resulting in pointing errors for a two-tube per axis type of sensor would be eliminated.

Optical chopping has another significant advantage. One tube per axis can be eliminated which, in turn, directly eliminates the effects of tube imbalance. The single tube concept is accomplished by directing each divided image to a common optical chopper and phototube combination as shown in Figure
Several signal chopping techniques are feasible that capture 100 percent of the entering starlight to maintain maximum signal-to-noise ratio. By proper phase synchronization in the sensor electronics, the intensity of each divided star image is differenced to accomplish the same purpose, i.e., to make pointing error proportional to image intensity variations across a dividing prism. A typical optical chopping scheme is described below.

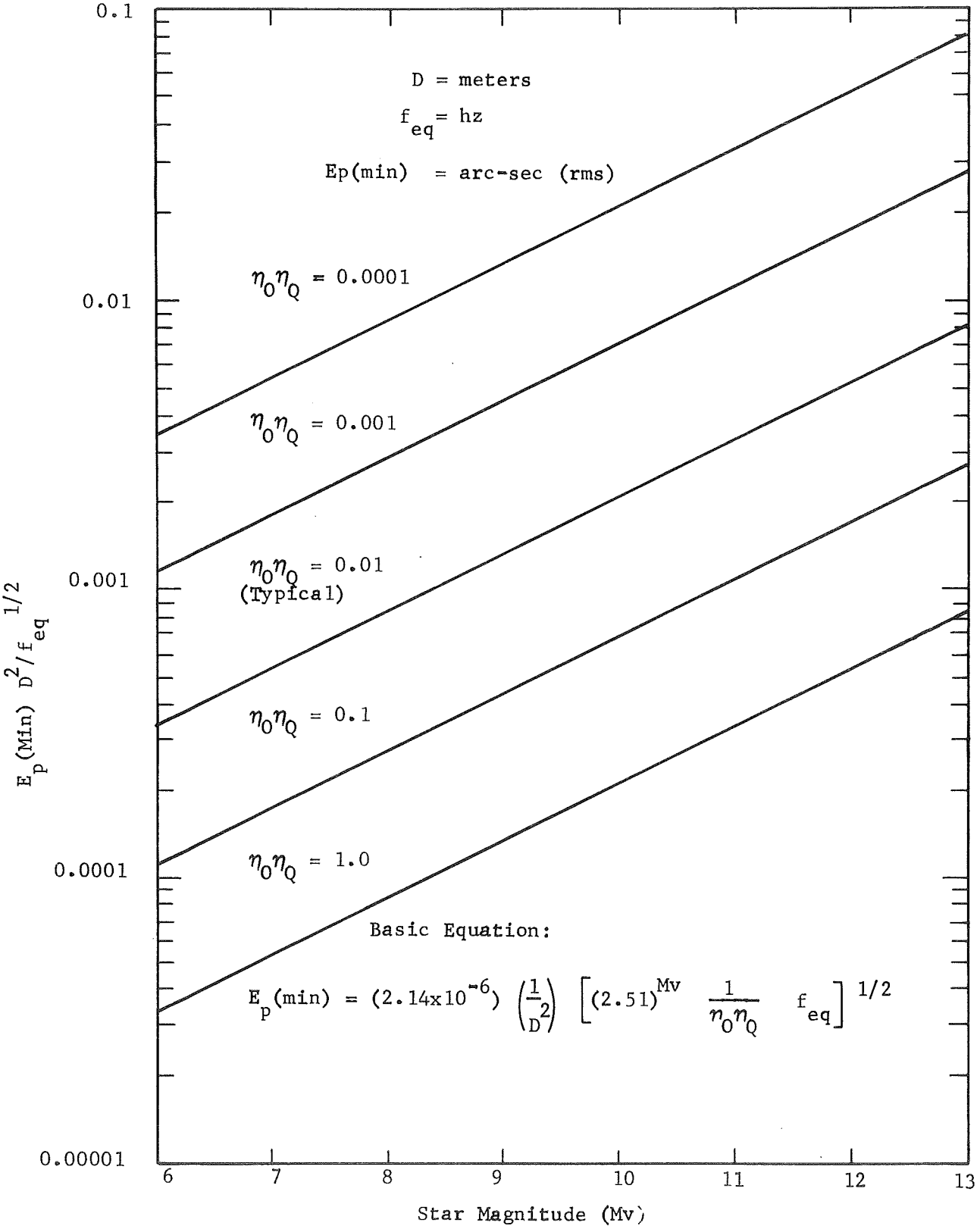

Figure 125. Minimum RMS Pointing Error (E_p) vs Stellar Magnitude

The focused guide star image is divided into four equal parts by the dividing prism as shown in Figure 126. The divided images are symmetrically spaced during perfect pointing and directed outward in four directions to mirrors which reflect the images onto the face of a spinning reticle. The divided images are shown in Figure 127 as they appear on the spinning reticle.

The reticle itself is located behind the dividing prism and it is circular. It is equally divided into a reflecting surface and a transparent surface. Two photomultiplier tubes are used to collect the energy from all four divided images. Consider the images of Figure 127 for instance, denoted by intensities I_1, I_2 I_3 and I_4. Images I_2 and I_3 are reflected into one photomultiplier (PM #1) while images I_1 and I_4 pass through the reticle to a second photomultiplier (PM #2) for the reticle position shown. One of the phototubes could fail and the star tracker would continue to operate. For a single failure however, a 2:1 reduction in signal intensity would result in an approximate $1/\sqrt{2}$ reduction in S/N.

The fundamental optical chopping and associated signal processing technique is best described by waveforms at the photomultiplier preamplifier outputs (see optical sensor electronics, Figure 128). As the reticle spins, the images are chopped producing square waves at the photomultiplier outputs. The phototube's outputs are ac coupled to a wideband ac preamplifier which rejects the phototube dc components and amplifies the square wave inputs.

The result is the preamplifier output waveforms shown in Figure 129. The amplitude of each waveform is still proportional to the intensity of each divided image as indicated in the four output waveforms for each photomultiplier (PM#1 and PM #2) preamplifier output. The angular error phasing, amplitude and correct axis information is obtained from these waveforms by:

1) Summing the two preamplifier output signals (reflected and transmitted, (i.e., PM#1 plus PM#2),

2) Applying these summed signals to two synchronous demodulators which are excited by horizontal and vertical synchronization signals from magnetic heads situated near the reticle. The horizontal and vertical synchronization signal frequencies are in quadrature.

3) Adding and subtracting the demodulator outputs.

The two demodulator outputs yield dc voltages proportional to pointing error in two axes respectively. Adding the demodulator outputs gives a dc voltage proportional to the vertical axis image position

$$V_{\phi}(\text{Vertical}) = (V_{I3} + V_{I2}) - (V_{I1} + V_{I4}) \qquad (5)$$

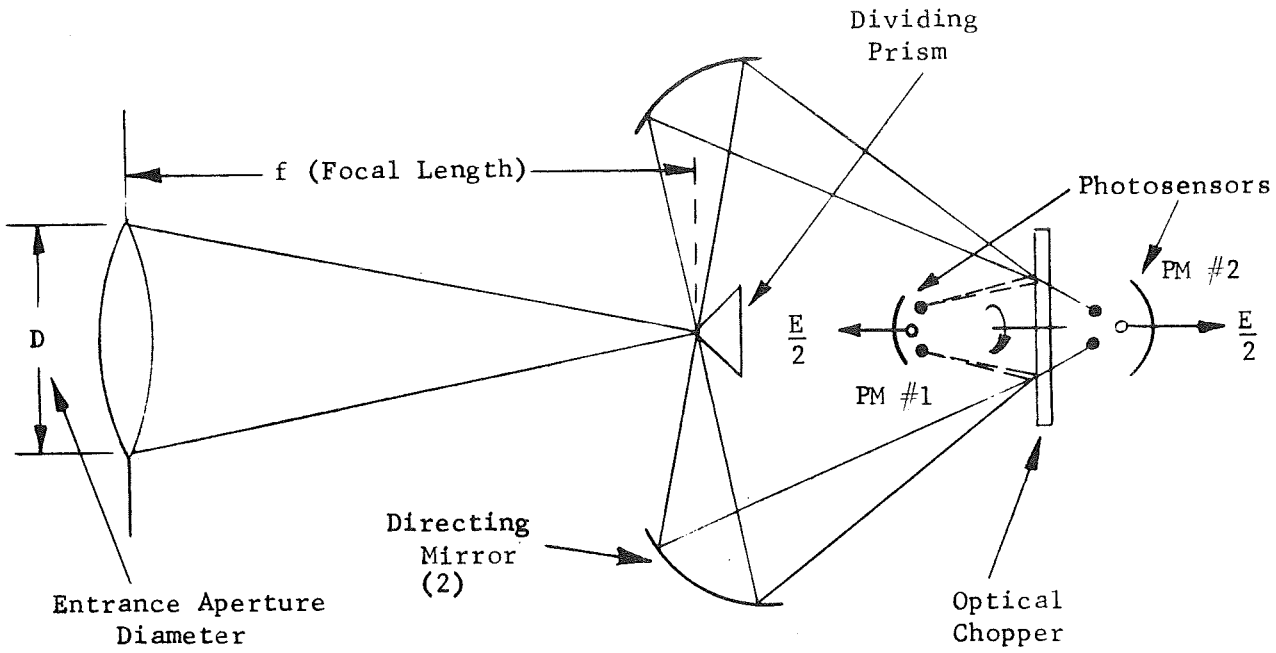

Figure 126. Single Axis Tracking Sensor Utilizing a Single Tube and Optical Chopper

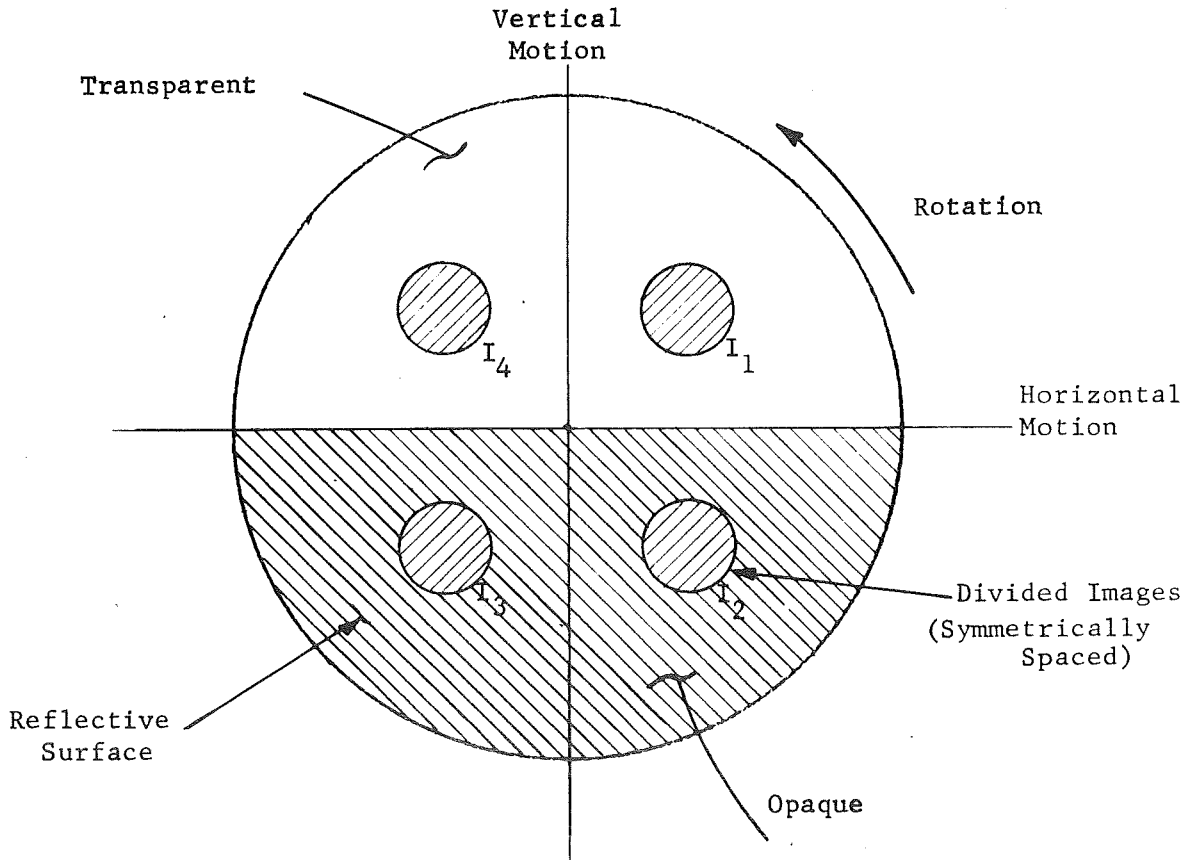

Figure 127. Image Location on Reticle Face

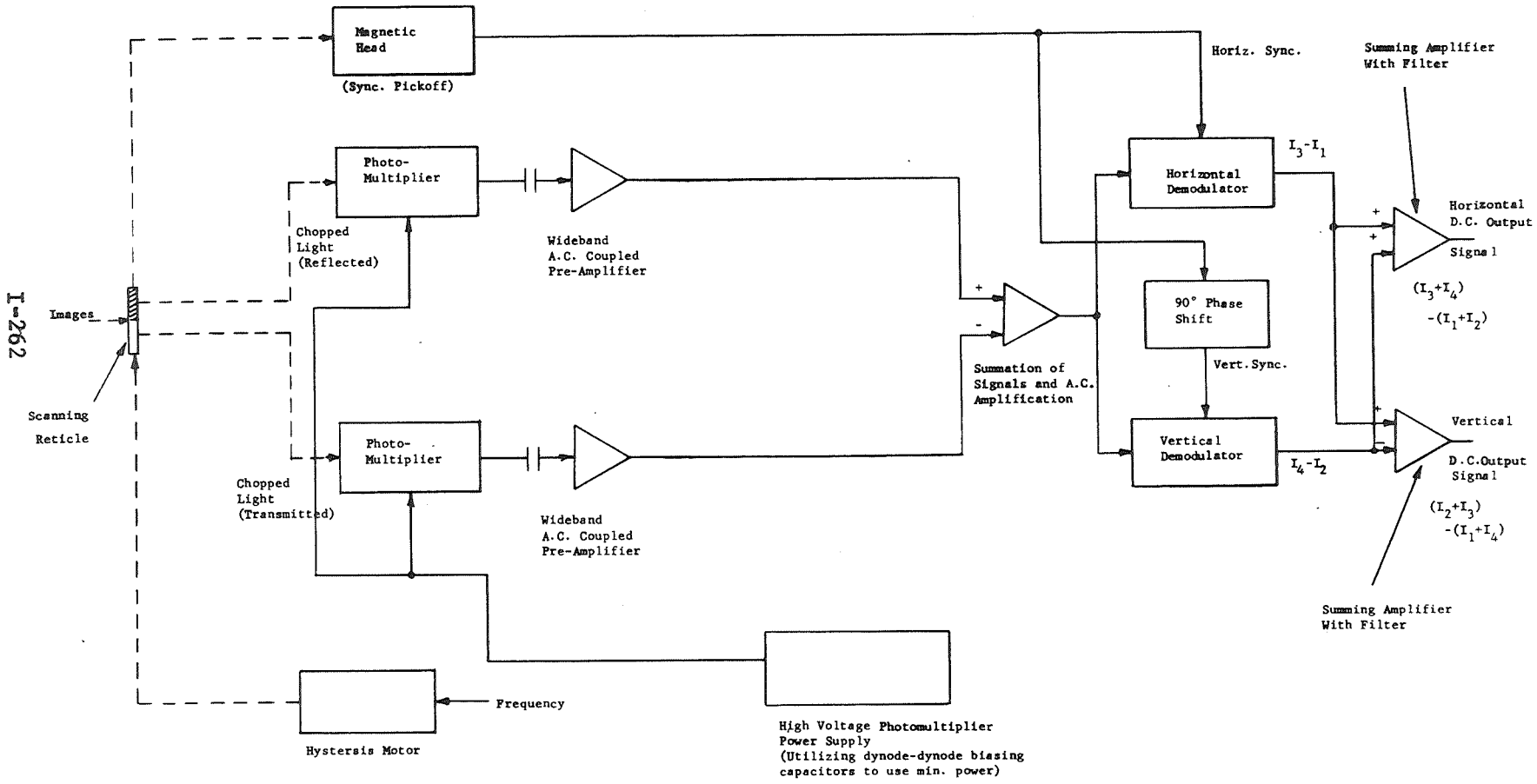

Figure 128. Sensor Electronics (Two Axis)

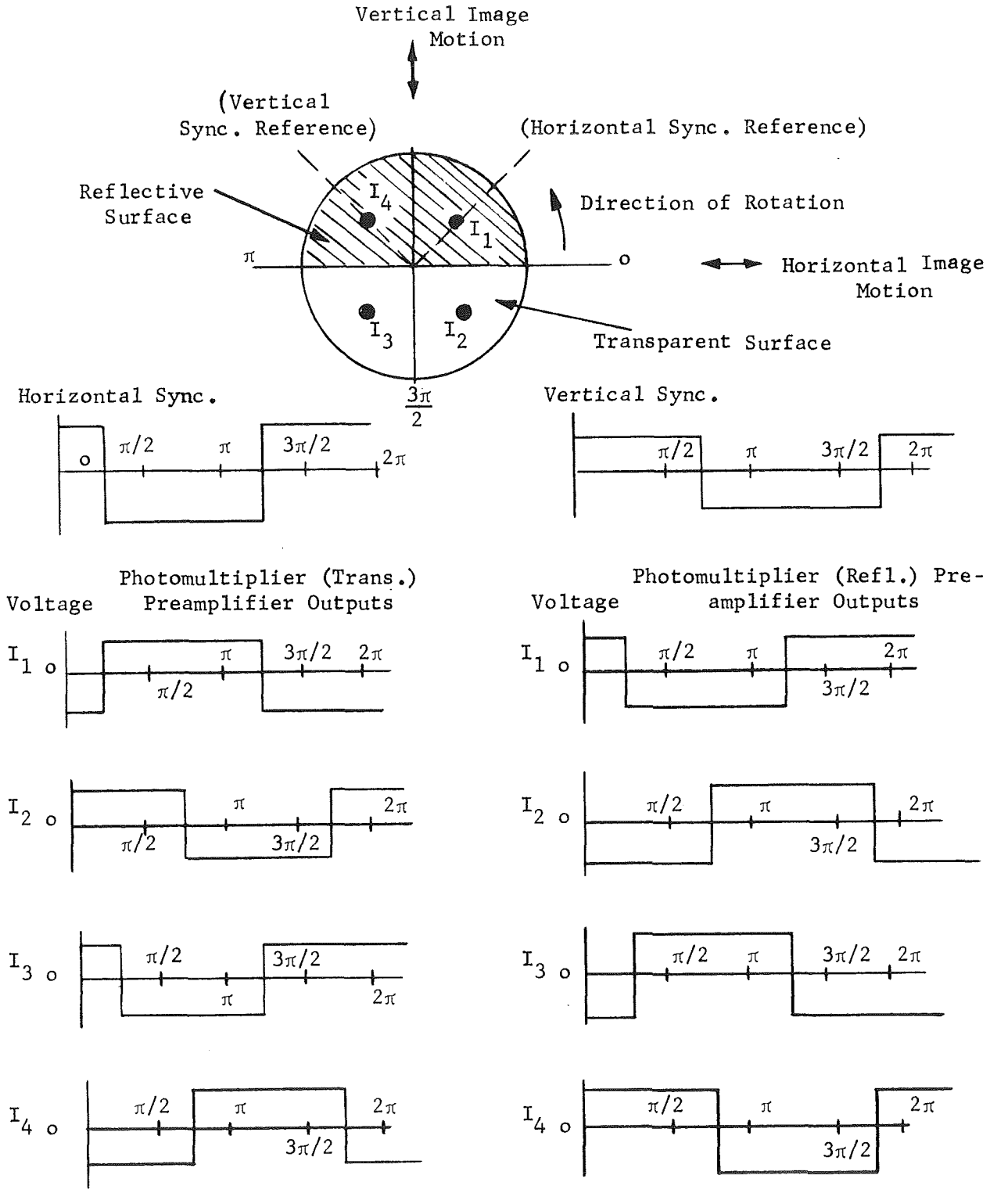

Figure 129. Typical Output Wave Forms

where

$V_{I3} - V_{I1}$ = Horizontal Demodulator output

$V_{I4} - V_{I2}$ = Vertical Demodulator output

V_{I1}, V_{I2}, V_{I3}, V_{I4} = Individual voltage components proportional to each divided image intensity.

Subtracting the demodulator output gives a dc voltage proportional to the horizontal axis image position,

$$V_{\psi}(\text{horizontal}) = (V_{I3} - V_{I2}) - (V_{I1} - V_{I4}) \qquad (6)$$

The voltages V_{ϕ} and V_{ψ} of Equations (5) and (6) are proportional to pointing error which can also be seen by considering what occurs to the divided images during mispointing. Assume an angular error exists in the vertical axis (upward). For this case, the division of light at the optical sensor dividing prism (See Figure 126) will cause the intensity in images I_1 and I_4 (see Figure 127) to equally increase and the intensity in images I_2 and I_3 to equally decrease. The demodulator voltage V_{ϕ} of Equation (5) will go positive since

$$V_{I3} + V_{I2} > V_{I1} + V_{I4}$$

The positive increase in voltage is equal to pointing error. On the other hand, the demodulator voltage V_{ψ} of Equation (6) should not change which is true since

$$V_{I3} = V_{I2}$$

and

$$V_{I1} = V_{I4}.$$

The optical chopper spinning reticle design is functionally superior to other types of choppers. It avoids a lot of problems. Choppers using vibrating reeds for instance, encounter design difficulties since relatively large motions are required at relatively high frequencies. Second, if phase modulation is used as discussed above to recapture the information in the dc output voltage form, at least two sets of reeds are required. Frequency modulation techniques reduce the amount of vibrating reeds to one set but this approach creates higher harmonics causing severe axis cross coupling errors.

The circular reticle spin rate can be quite low. The main requirement is to maintain an ac carrier frequency higher than the servo bandwidth frequencies. Servo bandwidth for the free float is very low (less than 1/5 Hz) so a chopping frequency of 10 Hz to 20 Hz is more than adequate.

A star tracker implemented with an optical chopper as described here does not alter the fundamental S/N relationship given by Equation (3).

Considering again, the pointing system noise-induced error (Ep) defined by $\frac{1.22\lambda}{D}\left(\frac{S}{N}\right)^{-1}$ and the S/N relationship of Equation (3), the controlling factor

in these equations, i.e., the parameter which can be easily varied, is Δt, the bandwidth period or sampling interval. The S/N ratio increases with larger Δt and proportionally reduces the noise-induced pointing error (Ep). Since by definition, $\Delta t = 1/2\,feq$, the "equivalent noise" bandwidth frequency Δfeq should therefore be as low as possible to minimize noise error. The equivalent noise bandwidth frequency term (feq), however, is directly dependent on and determined by, the free float closed-loop servo parameters. It therefore becomes necessary at this point to examine the free float servo system prior to calculating values for Δfeq. More important, values for Δfeq must be selected also keeping in mind the magnitude and frequency of external torque disturbances. A trade-off in servo loop gain and bandpass frequencies is required in order to simultaneously minimize pointing error due to noise and pointing error due to torque disturbance.

As stated previously, the free float system uses electrical integration in the signal paths. A typical servo loop for the CLOS and RLOS axes is shown in Figure 130 using two stages of integration.

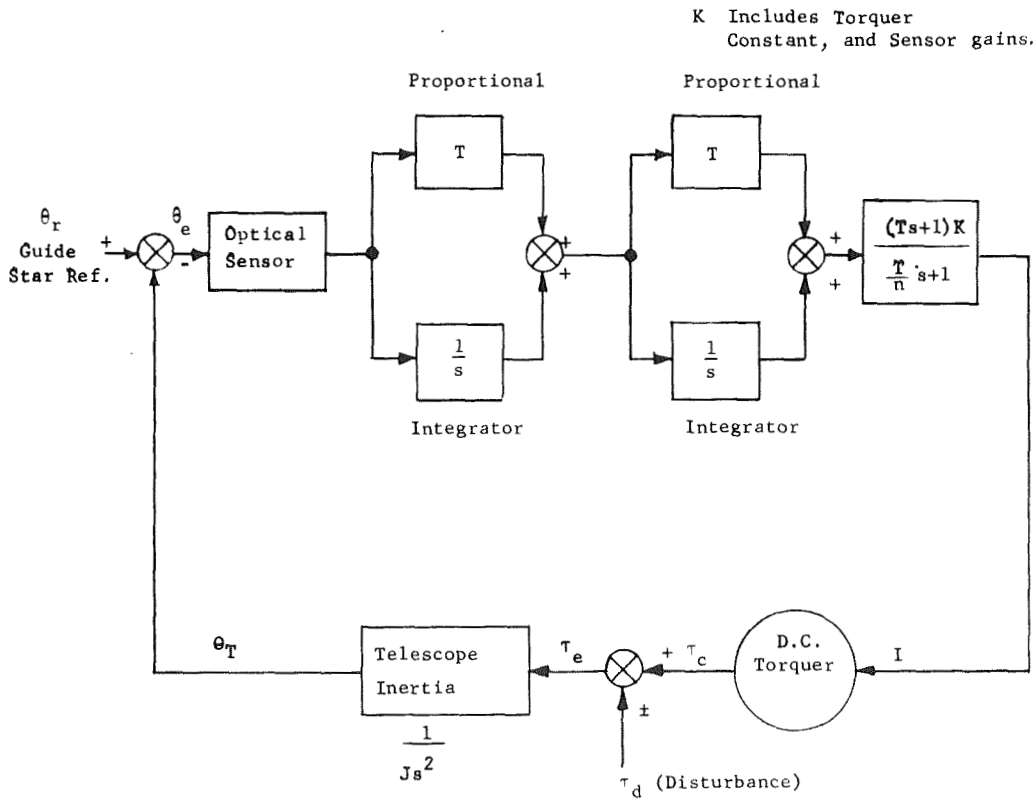

Figure 130. Servo Utilizing Integration (Single Axis)

The advantages of using integration, both from the viewpoint of minimizing pointing error due to disturbances and errors due to noise, can readily be seen by examining and comparing servo loop transfer functions with and without integration. Figure 131 shows a servo loop without integration using a lead-lag compensation network for stabilization identical to the lead networks used to stabilize the servo system of Figure 130 .

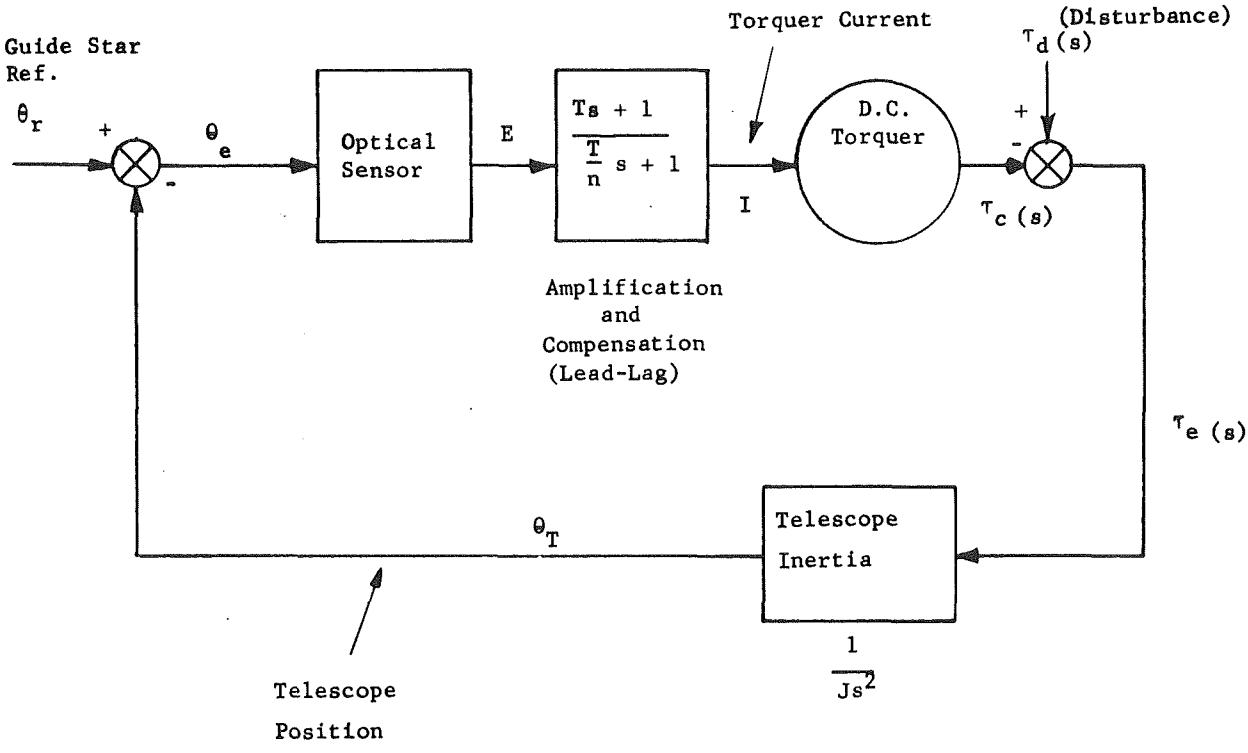

Figure 131. Fundamental Guidance Servo Loop (Single Axis)

Using feedback relationships, the servo error transfer function of Figure 130 (with integration) for input torque disturbances is

$$\tau_e(s) = \frac{\left(\frac{T}{n} s + 1\right) s^4 \tau_d(s)}{\left(\frac{T}{n} s + 1\right) s^4 + \frac{K}{J} (Ts + 1)^3} \tag{7}$$

and for Figure 131 (without integration), the transfer function is

$$\tau_e(s) = \frac{\left(\frac{T}{n} s+1\right) s^2 \tau_d(s)}{\left(\frac{T}{n} s + 1\right) s^2 + \frac{K}{J} (Ts + 1)} \tag{8}$$

Defining terms,

$\tau_e(s)$ = Torque error

$\tau_d(s)$ = Disturbance input torque

T = Proportional time constant

K = Torque-optical sensor-amplitude gain

J = Telescope Inertia

n = Integer

s = Laplacian operator

If $n \to \infty$ or $(T/n)^{-1}$ is, by design, large compared to the torque input disturbing frequency (ω) and if T also presents a frequency (i.e., $T = 1/2\pi f$) much higher than the input disturbing frequency, then terms containing these parameters can be neglected. Similarly, the remaining denominator terms J/Ks^4 and J/Ks^2 of Equations (7) and (8) are also by design, much smaller than unity. The error transfer functions reduce to

$$\tau_e(s) \cong \frac{J}{K} s^4 \tau_d(s) \tag{9}$$

or in terms of time

$$\tau_e(t) = \frac{J}{K} \frac{d^4\tau_d(t)}{dt^4} \quad \text{(with integration)} \tag{10}$$

and

$$\tau_e(s) \cong \frac{J}{K} s^2 \tau_d(s) \tag{11}$$

or in terms of time

$$\tau_e(t) = \frac{J}{K} \frac{d^2\tau_d(t)}{dt^2} \quad \text{(without integration)} \tag{12}$$

The result of adding two stages of integration is to add at least two orders of differentiation to the torque disturbance. Since the disturbing torque (τ_d) is a sinusoidal function, i.e.

$$\tau_d(t) = A \sin \omega t \tag{13}$$

then

$$\frac{d^4\tau_d(t)}{dt^4} = A\omega^4 \sin \omega t \tag{14}$$

At peak amplitudes, the torque error is

$$\tau_e(t) \Big|_{peak} = \frac{J}{K} (A\omega^4) \tag{15}$$

where

A = Peak amplitude of disturbing torque

$\omega = 2\pi/2700$ rad/second = Orbital frequency

The disturbing frequency (ω) is less than unity, so the torque error (τ_e) becomes rapidly reduced when ω is raised to higher powers. The pointing error (ϕ_e) is also reduced considerably with integration since it is proportional to τ_e

$$\theta_\epsilon(t)\Big|_{peak} = \frac{\tau_\epsilon}{J\omega^2} = \frac{A\omega^2}{k} \quad \text{(with integration)} \tag{16}$$

$$\theta_\epsilon(t)\Big|_{peak} = \frac{\tau_\epsilon}{J\omega^2} = \frac{A}{K} \quad \text{(without integration)} \tag{17}$$

The "equivalent noise bandwidth" (feq) can be calculated and compared for the servo loops of Figures 130 and 131. The bandwidth (feq) is unlike the bandwidth normally defined in linear networks theory and is derived from statistical theory. It is defined by relationship

$$2feq = \frac{1}{2\pi j}\int_{-j\infty}^{+j\infty} G(s)\, G(-s)\, ds \text{ Hz} \tag{18}$$

G(s) is the closed loop transfer function and G(-s) is the conjugate of G(s).

For Figure 130,

$$G(s) = \frac{(Ts+1)^3}{\frac{J}{K}s^4 + (Ts+1)^3} \tag{19}$$

For Figure 131,

$$G(s) = \frac{(Ts+1)}{\frac{J}{K}s^2 + (Ts+1)} \tag{20}$$

Equations (19) and (20) assumed T/n is small compared to T. Substituting Equations (19) and (20) into Equation (18) results in solutions for the equivalent bandwidth in terms of the servo loop parameters;

$$feq = \frac{1}{4}\,\frac{9T^8 + 15T^4\frac{J}{K} - 3\left(\frac{J}{K}\right)^2}{\frac{J}{K}(8T^5 - 9T\,J/K)} \text{ Hz (with integration)} \tag{21}$$

and

$$feq = \frac{1}{2}\,\frac{T^2\frac{K}{J} + 1}{2T} \text{ Hz (without integration)} \tag{22}$$

Comparing Equations (21) and (22) and reaching conclusions by inspection is difficult without values for T, K and J. However, based on known input disturbance torque levels and required pointing error requirements for modules C and D in the CLOS and RLOS axes, numerical values for these parameters can be easily derived.

The major torque disturbance (τ_d) has been specified as 29.5×10^{-3} lb-ft at 1/5400 Hz with the requirement to point to 0.0060 arc-second (peak) during application of these disturbances. The loop gain for the servo loop without integration (Figure 131) can be approximated from Equation (17)

$$K = \theta_\epsilon(t)\Big|_{peak} = \frac{29.5 \times 10^{-3}}{0.006} \times 2.06 \times 10^5$$

$$\cong 1.1 \times 10^6 \frac{\text{lb-ft}}{\text{rad}}$$

The servo open loop frequency response is as shown in the Bode stability plot of Figure 132 assuming a telescope inertia (J) of 15,000 slug-ft^2 with K = 1.1×10^6 lb-rad. A reasonable value for the time constant (T) is 0.22 second which results in a phase margin of 43 degrees. The equivalent bandwidth is calculated from Equation (22) which yields

$$feq = 5.10 \text{ Hz}$$

Similarly, values can be selected for servo loop with dual integrators in the signal paths (Figure 130). Referring to Equation (16),

$$K = \frac{A\omega^2}{\theta_\epsilon(t)/peak} = \frac{(29.5 \times 10^{-3})(2.06 \times 10^5)\left(\frac{2\pi}{5400}\right)^2}{0.006}$$

$$K = 1.36 \text{ lb-ft/rad}$$

The Bode stability plot is also shown in Figure 132 for K = 1.36 lb-ft/rad and J = 15,000 slug-ft^2. The time constant (T) is selected at 14 seconds which also results in a phase margin of 43 degrees. The equivalent bandwidth is determined from Equation (21).

$$feq = 0.14 \text{ Hz}$$

The noise-induced pointing error (Ep) can now be calculated for each type of servo given the above values for the equivalent bandwidth (feq). From Equation (2) and using Figure 125 , the pointing error for the servo system without integration is

$$Ep = 0.0089\ (5.1)^{1/2}/2^2 \cong 0.005 \text{ arc-second (rms)}$$

Assuming,

D = 2 meters

feq= 5.10 Hz

Mv = 13th (star magnitude)

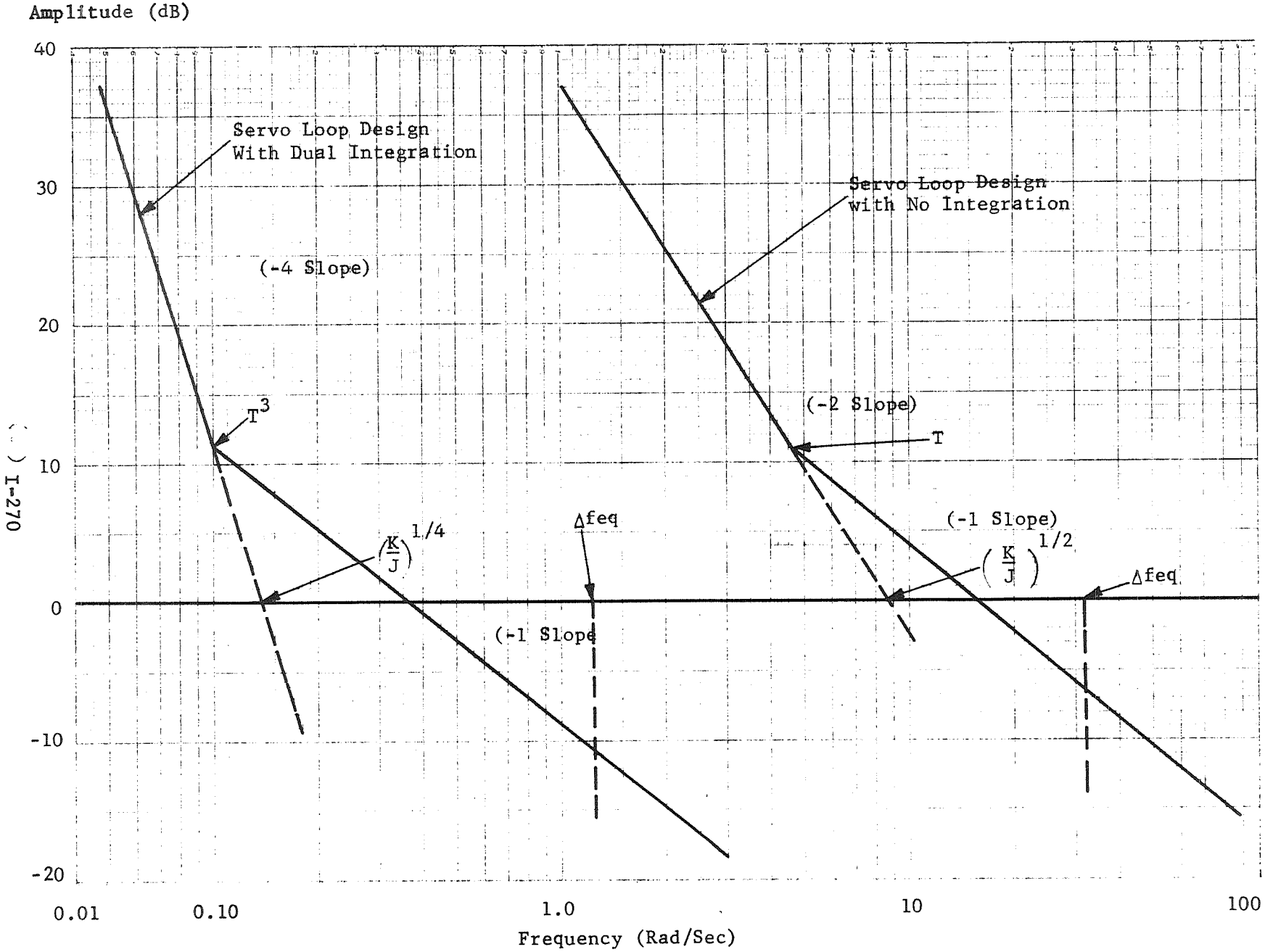

Figure 132. Comparison of Servo Loop With and With No Integration

No = 0.1 (optical efficiency)

Nq = 0.1 (quantum efficiency)

Using the above assumptions, a servo loop with dual integration yields,

$$Ep = 0.0089(0.14)^{1/2}/2^2 \cong 0.001 \text{ arc-second/(rms)}$$

The conclusions are obvious. By simply inserting electrical integration into the signal paths, the noise-induced pointing errors for the CLOS and RLOS axes can be markedly reduced (5:1 for the above example) without sacrificing error due to external torque disturbances (i.e., the torque disturbance errors are identical in both cases for the above examples).

EXPERIMENTAL RESULTS

Description

The line-of-sight stabilization method proposed for the Princeton Advanced (OAO) Experimental package, a one-meter telescope with ultraviolet imaging and spectral analysis capability, was the free float approach. This recommendation was one result of the OAO - Advanced Princeton Satellite Study (Phase I) performed by Perkin-Elmer. An extension of this program (Phase II) had as its goals the experimental verification of the feasibility of the concept and a reduction to hardware of the major required components. The following paragraphs describe the hardware and test arrangement together with results relevant to the performance attained with each.

The data is presented since the components are appropriate, with only straightforward modifications, for use on the LTEP telescope free float implementation. Furthermore, while the measurement precision was insufficient to verify potential pointing of accuracies greater than 0.1 arc-second rms, the results obtained

- Verified the practicality of the free float approach; i.e., that precise control of a magnetically suspended telescope is feasible and, that magnetic suspension offers a high decoupling from vehicle motional disturbances.
- Indicated no fundamental reason why higher precision should be unattainable; i.e., greater precision was not demonstrated due to the lack of an optical error sensor.

An experimental breadboard of the free float pointing system was constructed to determine the feasibility of achieving several of the pointing system requirements. Breadboard versions of the special electrical-mechanical components required for this system concept were constructed as part of this effort. These included the magnetic "pushers", capacitive sensors and the chain link transformer.

In the experimental setup, specially designed air bearings were used to "float" a 535-pound platform to simulate weightless conditions. The platform was approximately 6 feet in length and 2.5 feet wide and served to simulate the telescope structure.

The main goal of the experiment was to prove out the free float control system concepts for three of the possible six degrees of freedom (three angular and three translational) controlled by the pointing system. One CLOS rotational axis and the longitudinal (z) and lateral (x) translational degrees of freedom were selected for the test. The majority of actual tests were focused on the angular axis and the associated centering control. Proving out a combination of an angular and associated centering axis verifies nearly all of the critical free float pointing system concepts. A full scale, six-degree-of-freedom test would be more complete only in that an evaluation of the effects of axis-to-axis cross-coupling would be possible (although the difficulty of the test would be greatly magnified).

The prime concern in devising the experiment configuration itself was to develop a test device which would realistically simulate the weightless conditions of outer space. To accomplish this, a means of suspension had to be developed in which uncontrollable disturbance forces and torques were an order of magnitude less than those known to exist in the space environment. The approach used was to develop a frictionless surface (describing a plane exactly at right angles to the gravity vector) on which a mass representing the telescope could be supported. It was concluded that the best technique for generating a frictionless surface was to suspend the simulated telescope on a cushion of air. The technique is illustrated below in Figure 133 .

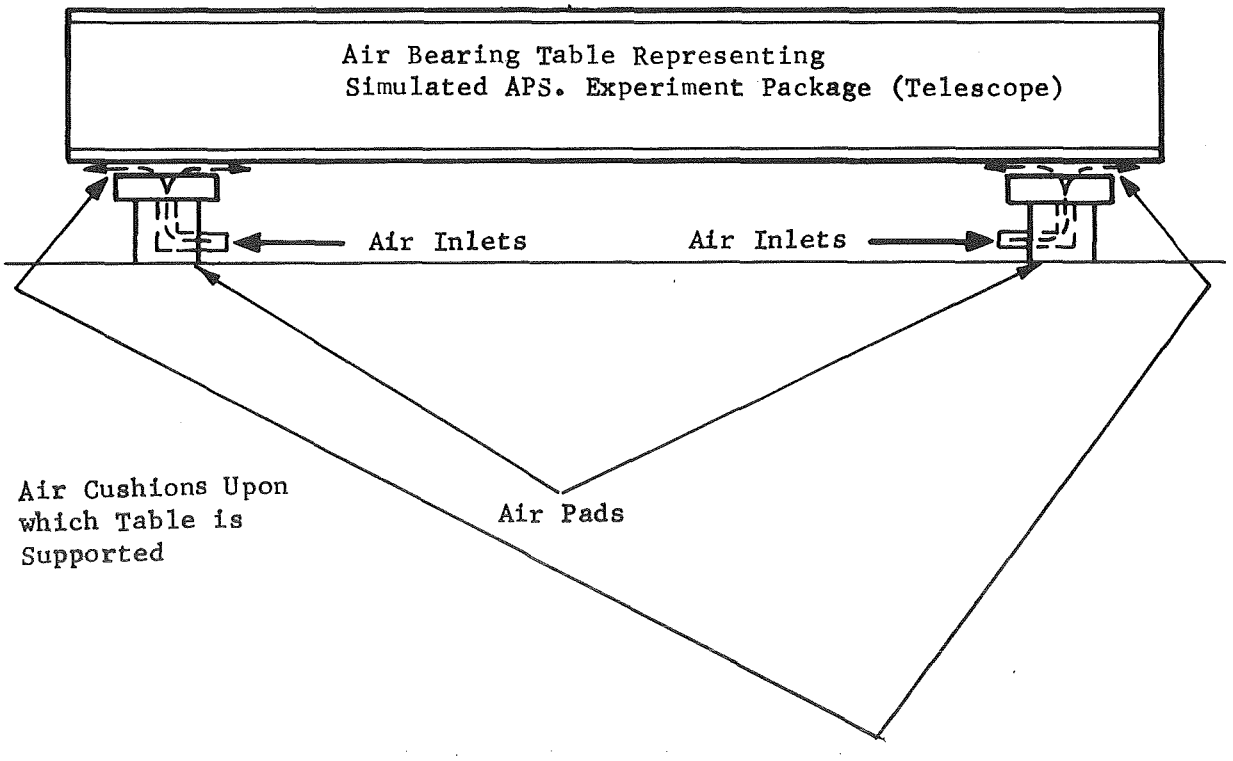

Figure 133. Air Bearing Table Concept

Located symmetrically beneath the table were four 6-inch diameter air pads which lifted the structure and suspended it on air. The only friction from such devices are the shearing force (viscous force) between the air pads and the table, but forces of this nature are very small. For the particular design used and telescope velocities of 0.050 inch/second, the force is only 1.8×10^{-5} pound. This was well below the external forces expected in space and weightless conditions in one plane were closely simulated.

Having established a weightless environment for the simulated experiment package in one plane, the remainder of the experiment was directed towards proving the magnetic suspension concepts. The first goal was to determine whether or not the system could be easily stabilized and remotely controlled. It was also necessary to determine whether the magnetic pushers, capacitive sensors and chain link transformers, developed during this program, could perform simultaneously and acceptably without creating unexpected detrimental effects. In summary therefore, the test effort was directed at

1) Determining angular pointing and linear displacement errors caused by purposely applied torque and force disturbances intended to simulate those expected in space.

2) Separate evaluation of the special components' performance when used in the system.

In regard to the control loops, the capacitive displacement sensor output signals were electrically added to produce output voltages proportional to angular errors in addition to deriving centering axis error signals. The test base stand or the earth was used as the pointing reference, which is identical in concept to using a stellar reference source and an optical sensor for control. Double electrical integration was incorporated in the CLOS axis servo loop with a bandwidth of approximately 1/5 Hz.

In addition, a stage of integration was used in each of the two centering servo loops to null out unwanted electrical offsets and provide a measure of the air bearing table unbalances. Any unbalance in this system would produce, by design, dc voltages at the centering servo loop integrator outputs in the correct proportion. These voltages were sent from the table to a remote automatic-balancing system which leveled the table to 0.005 arc-second with respect to a plane perpendicular to gravity. This auxiliary closed loop servo was switched out of the loop when actual data was taken. The automatic balancing subsystem utilized piezoelectric disks located beneath each air bearing. The height of each air bearing could therefore be varied in increments as small as 1μ in. by applying voltage to the piezodisks to precisely level the table. An artist's version of the actual table set-up is shown in Figure 134. Photographs of the experimental setup are shown in Figure 135.

Two laboratory rooms were also used for the experiment. One room contained the power supplies, control electronics, recording equipment, and the air supply for remote operation of the simulated pointing system which was located in an adjoining room and could be viewed from the control room through a window installed between the rooms. The room containing the air bearing table was isolated from

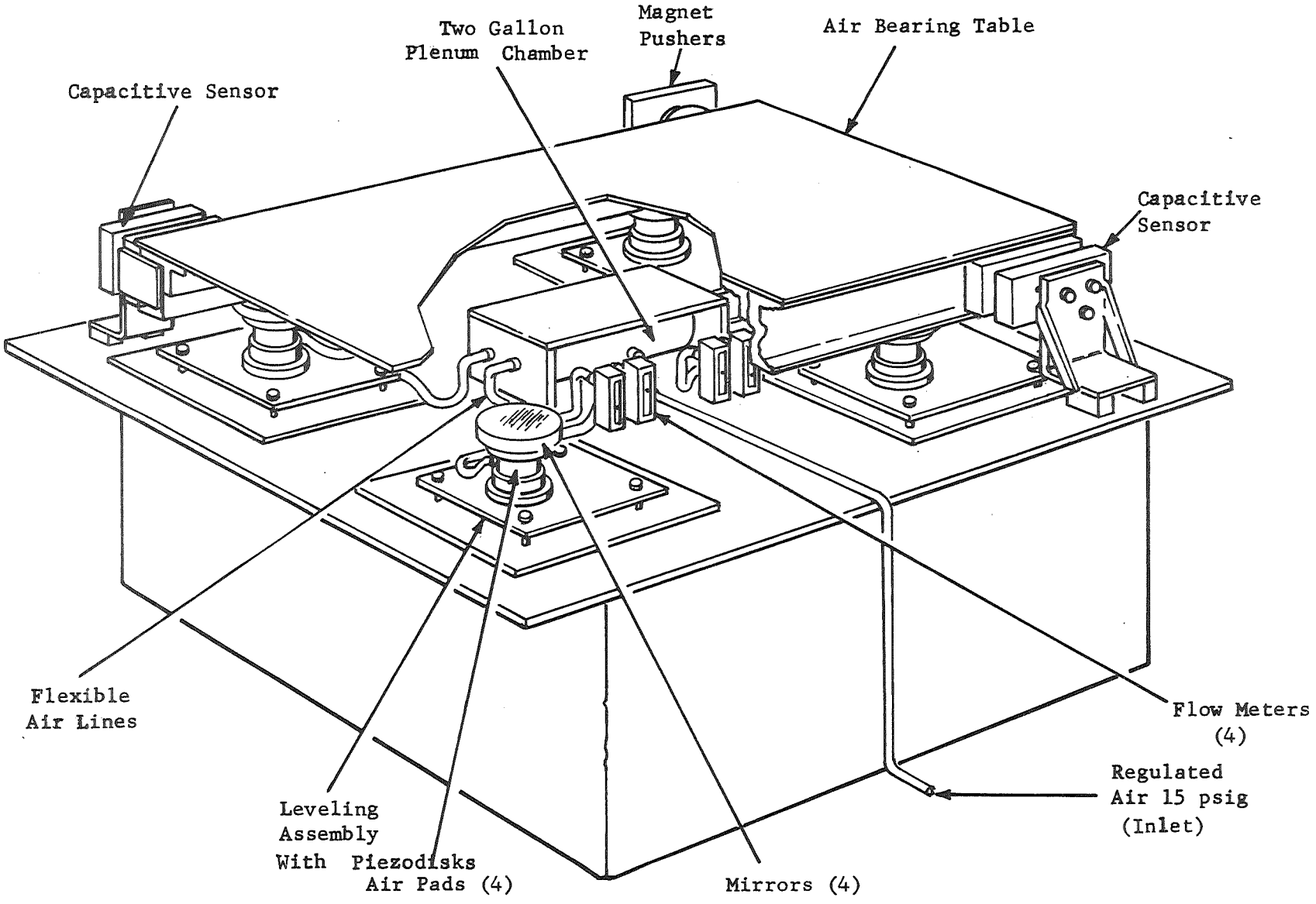

Figure 134. Automatic-Leveling Air Pad System

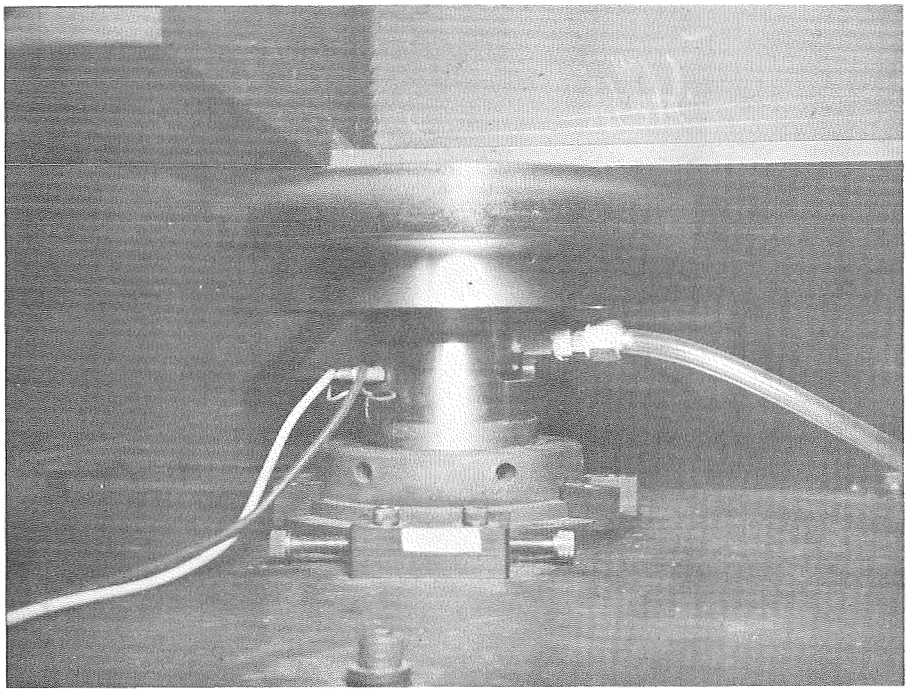

Air Pad Assembly

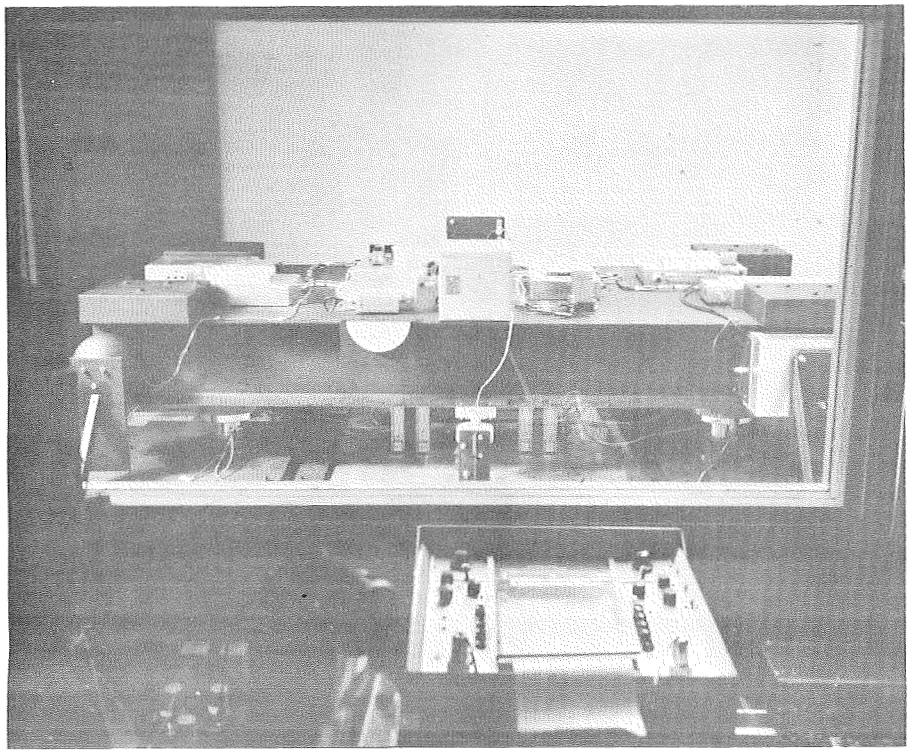

Table Viewed From Adjoining Room

Figure 135. Experimental Setup (Sheet 1 of 2)

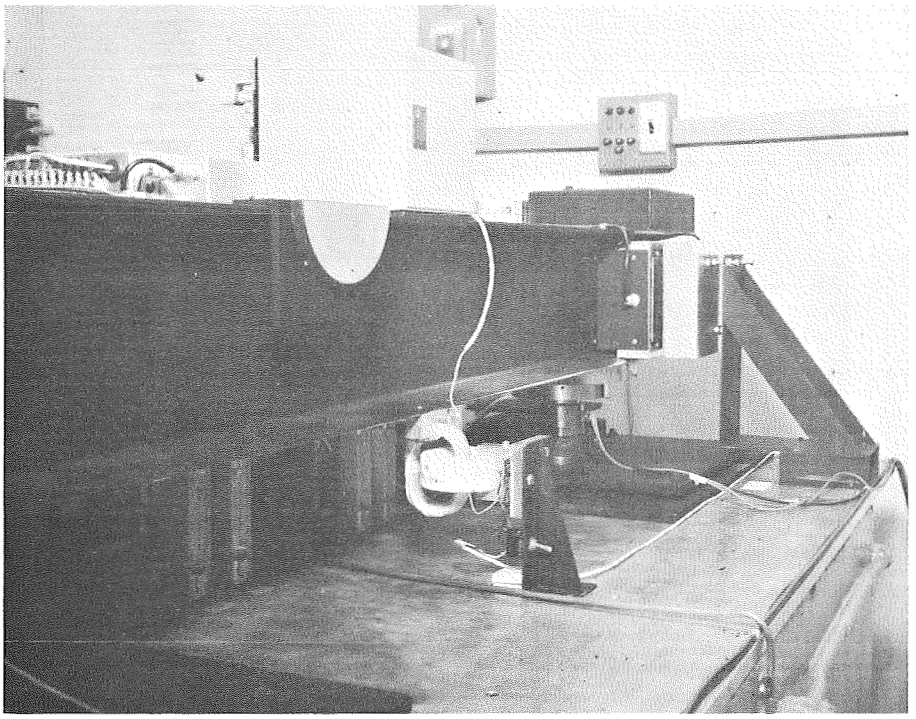

View of Power Chain Link Transformer and Capacitor Sensor

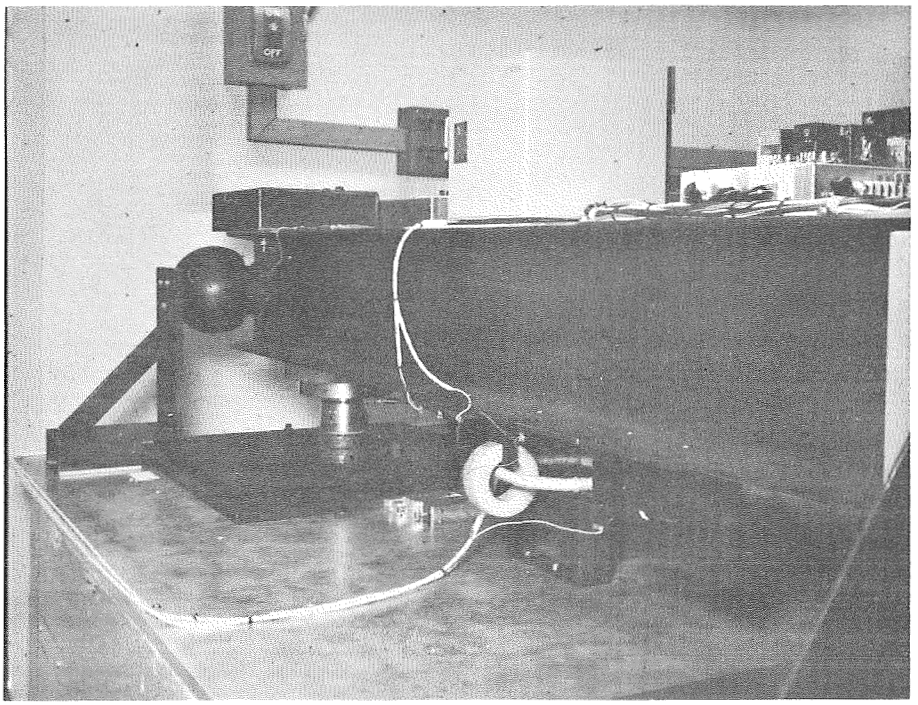

View of Signal Chain Link Transformers and Magnetic Pushers

Figure 135. Experimental Setup (Sheet 2 of 2)

the control room as well as from any surrounding areas for several reasons. Temperature uniformity of the air pads was required since differences in temperature among the pads creating uneven expansions would disturb the perpendicularity of the table with respect to the gravity vector. Also, differences in air viscosity might cause unwanted disturbances. Thermal measurements were made and variations from air pad to air pad stabilized to less than 0.05°C which was too small to create any problems. Isolating the air bearing table also aided in stabilizing air mass motions which would disturb the pointing system. Calculations indicated that the rate of flow of the surrounding air mass had to be held to 0.05 inch/second in order to avoid disturbances due to air drag in excess of 1×10^{-5} pound . In the case of vibrations, the air bearing table had to be left almost entirely vulnerable to the laboratory floor or building vibrations. Supporting the air bearing table and its pneumatic pad system on standard vibration isolators was not possible because of either the spring constants associated with vibration isolators or isolator repeatability problems for changing loads. The table was designed to travel ±1/2 inch in the horizontal plane and as the center of gravity of the table travels relative to the supporting pads, varying loads are imposed on each pad and isolators mounted beneath each pad would experience the same load. If the isolator consisted of spring mass damper devices, it would compress and upset the table level. The lack of precise (less than 1.0 microinch) position repeatability in some of the more advanced (high spring rate) servo-controlled isolating systems would incur the same detrimental results. Therefore the table and pads were hard mounted to the floor. Earlier seismic vibration measurements were made on the ground floor of the building - on the same floor level as the laboratory but removed approximately 350 feet - and consisted mostly of high-frequency (10 Hz and up) and extremely low-amplitude (0.10 microinch orders) perturbations. Since the pointing system is an ultra-low frequency servo system with a bandpass of 1/5 Hz, these vibrations did not affect the system.

COMPONENT EVALUATION

Three special components — the magnetic pusher, capacitive displacement sensor, and the chain link transformer — were developed and proven out in the laboratory. These components, specifically tailored to the free float pointing system, are required to perform three essential tasks:

1) Telescope Positioning - Accomplished with the magnetic pushers which develop controlling forces proportional to electrical input signal currents.

2) Telescope Position Sensing - Accomplished with the capacitor displacement sensors which develop dc output signal voltages proportional to displacement variations between two parallel capacitor plates.

3) Delivering electrical power to the Telescope - Accomplished with the chain link transformer. These transformers can also be used to transmit data to and from the telescope.

In considering each of the component design philosophies, there is one important goal that is common to all three. They are required to perform their specific

pointing system functions, while at the same time maintaining isolation, that is, no physical contact between the telescope and the outer spacecraft. In view of this goal, the reason for each of the specific component designs becomes apparent. The magnetic pusher consists of a permanent magnet designed with a gap that accepts a coil which does not make contact with the magnet. The magnet is located on the outer spacecraft and the coil is located on the telescope. Current is fed to the coil from the telescope position sensors to develop forces by magnetic repulsion or attraction. Similarly, the capacitive displacement sensor requires a gap between its two capacitor plates, one of which is located on the outer spacecraft and the other on the telescope. Again, no physical contact is made. The chain link transformer delivers power through a primary mounted on the outer spacecraft and a physically disconnected secondary mounted on the telescope. Isolation of the pointing system is therefore maintained by these "gaps". Conversely, these "gaps" also provide most of the difficulty. The 1-inch gap required in the permanent magnet of the magnetic pusher lends itself to flux leakage losses which tend to compromise trade-offs in other design areas such as size, weight, and electrical power. A similar situation exists for the chain link transformer in which efficiency is compromised. The capacitive sensors ultimately suffer from lack of resolution or the detection of small displacements between parallel plates in the presence of a large displacement (i.e., signal-to-noise), the nominal 0.60-inch gap.

One of the first components fabricated and tested was the magnetic pusher. A photograph of this unit is shown in Figure 136.

In testing the magnetic pusher, the major experimental goals were:

(a) The determination of the transfer function, force output versus current input, which results in linearity and sensitivity performance as well as proving out the basic concept or operation. A force output of 0.167 pound for a 1-A input was the main design goal in this area.

(b) The determination of resolution or the ability to perform at very small levels of force, 1×10^{-4} pound and less. Achieving linear operation in these lower force ranges is vital to the performance of the free float pointing system during fine tracking.

(c) The determination of other pertinent electrical and mechanical constants such as the magnetic field distribution, maximum power, size, and weight. The power allocated to each unit has been specified at 1 watt for 1 amp and/or 0.167 pound of force per axis.

The results of the tests as well as the design of the magnetic pusher are listed in Table 26 below.

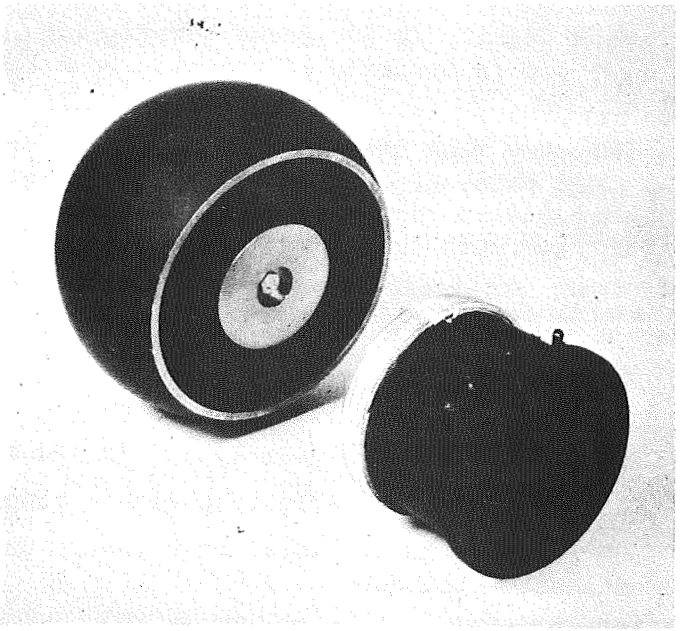

Figure 136. Magnetic Pusher

TABLE 26. MAGNETIC PUSHER SPECIFICATIONS

Permanent Magnet (a mechanical assembly is shown in Figure 137).

Size:-	Approximately spherical with a diameter of 6.00 inches
Weight:-	13.25 pounds. The lightweight version (3-4 lb) was not fabricated for this experiment.
Material:-	Alnico V and C1018 steel
Gap Size:-	The gap forms an annulus with an inside diameter of 2.322 inches and an outside diameter of 4.724 inches. The depth is 1.57 inches.
Gap Field Strength and Distribution:-	Flux density is 700 gauss (average) in the center of the gap and is distributed radially from the center.
External Fields:-	Magnetic flux lines protrude outside the gap forming a field external to the magnetic housing. In addition, fields also lie outside the perimeter of the housing but are much smaller in magnitude.

Coil (a mechanical assembly is shown in Figure 138).

Size:-	The coil and its mount form a cylinder 3.33 inches in diameter and 2.67 inches in height.
Weight:-	Coil and mounting assembly: 0.75 pound
Material:-	Aluminum mounting structure with a copper coil
Windings:-	80 turns of No. 20 wire, five layers on a 3.323-inch diameter cylinder
Resistance:-	0.768 ohm (nominal)
Inductance:-	9.0×10^{-4} henries
Maximum Current Rating:-	2.0 amperes

Performance as a Unit

Nominal Sensitivity:-	0.313 pounds/ampere at center. When specified as a torquer with a 3-foot moment arm, a pair of magnetic pushers would develop 1.88 pound-foot/ampere.
Linearity:-	Not greater than 5 percent for 0.185 pound force range and full left-right travel of ±0.50 inch.
Peak Force (maximum rating or saturation limit):-	0.63 pound. (When specified as a torquer with a 3-foot moment arm, pair of magnetic pushers develops a peak torque of 3.80 pound-feet.)

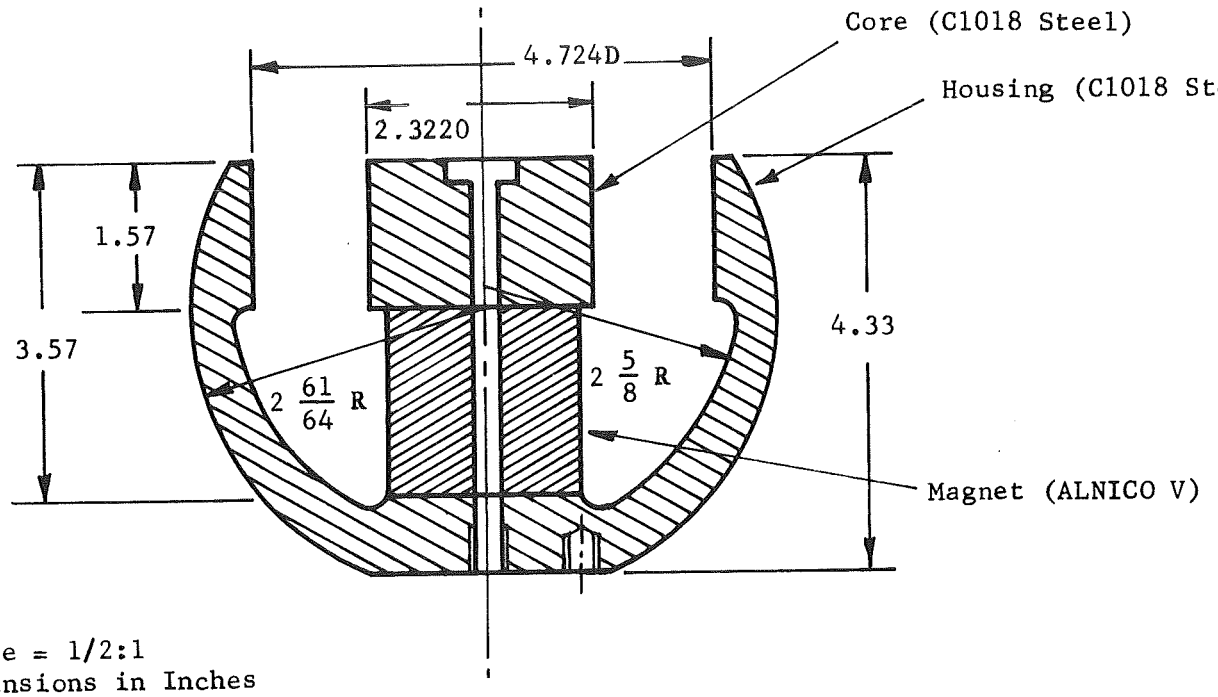

Note:
Scale = 1/2:1
Dimensions in Inches

Figure 137 . Magnetic Pusher Design

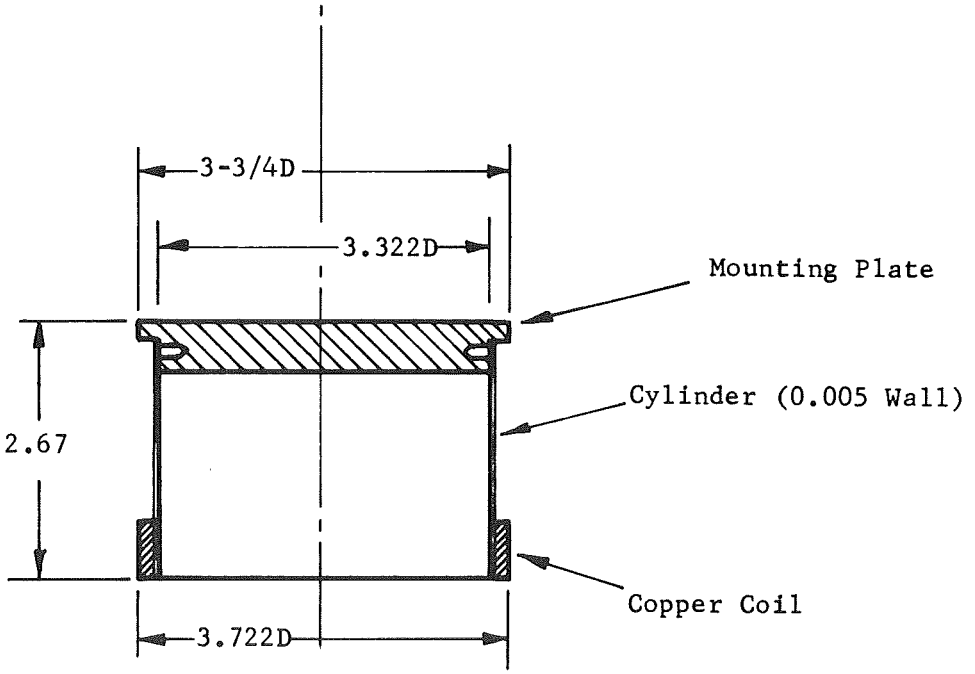

Note:
Scale = 1/2:1
Dimensions in Inches

Figure 138.. Coil Assembly

Maximum Power:-	3.10 watts at a peak force of 0.63 pound.
Resolution:-	Forces in the order of 1×10^{-5} pounds to 1×10^{-4} pounds were developed for specific current inputs based on the nominal sensitivity of 0.313 pounds/A.
Coil Travel Within the Magnet:-	Not less than ±0.50 inch in all directions

A plot of force output versus current input is also shown in Figure 139 for the lower magnetic pusher force range.

Various sized chain link transformers were also tested. Test data was consistent from transformer to transformer. Test results from one of these units is listed in Table 27 . A photograph of the unit is shown in Figure 140.

TABLE 27. CHAIN LINK TRANSFORMER SPECIFICATION

Size:-	The primary forms a hollow cylinder which has an outside diameter of 3.375 inches and an inside diameter of 2.125 inches. It is 1.375 inches in height. The secondary forms a solid ring with an equivalent circular diameter of 2.11 inches. The cross-sectional diameter is 0.7365 inch.
Travel:-	The secondary is free to travel a total distance of not less than 1.10 inches.
Weight:-	The combined weight of the primary and secondary is 2.13 pounds less mounting brackets.
Resistance:-	0.624 ohm - primary 1.625 ohms - secondary
Inductance:-	64.0 millihenries - primary (secondary open circuited) 3.24 millihenries - primary (secondary short circuited) 38.0 millihenries - secondary (primary open circuited) 4.02 millihenries - secondary (primary short circuited)
Maximum Power Capability:-	120 watts
Efficiency at 53 watts Input Power (110 volts ac 400-Hz sinusoidal input):-	87.6 percent
Force Levels Between the Primary and Secondary:-	See Figure 141.
Voltage Ratio:-	1.00:1.01 (115 volt ac primary; 116.5 volt secondary)

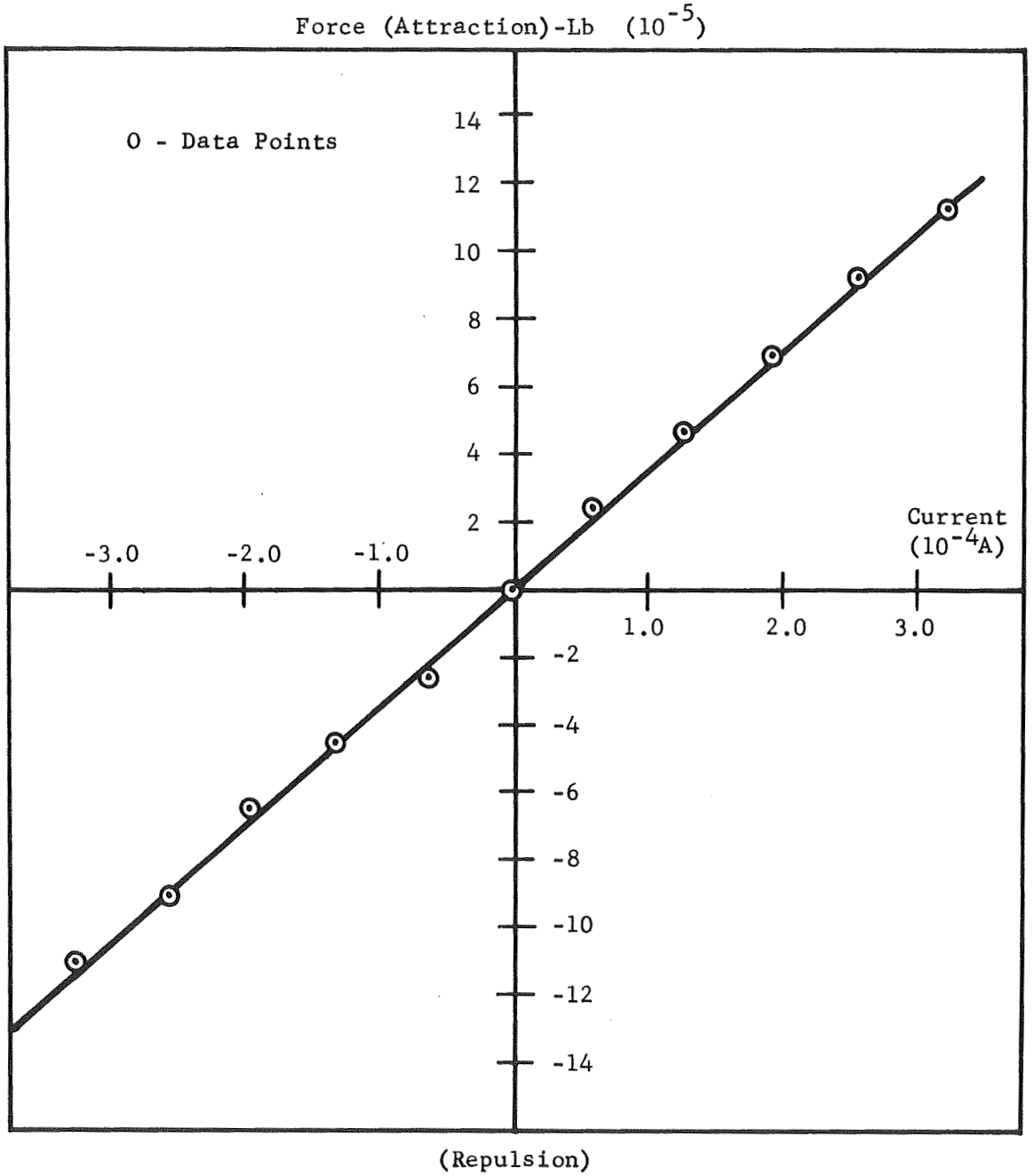

Figure 139. Lower Force Output Range Linearity (Magnetic Pusher)

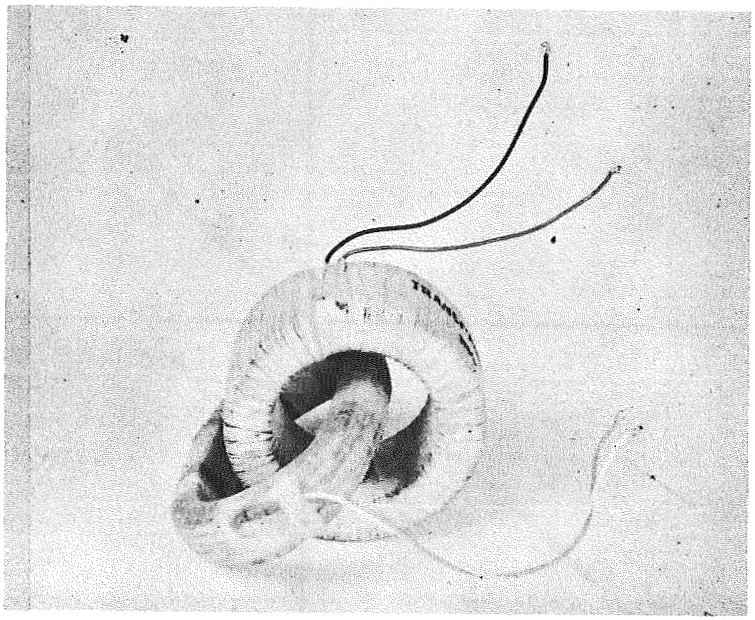

Figure 140. Chain Link Transformer

The force levels between primary and the secondary were dependent upon the relative location between the primary and secondary and also were dependent upon the primary and secondary current. As shown in Figure 141 for instance, the force of this chain link transformer varied -17×10^{-5} to 3×10^{-5} pounds for ±0.55 inch at 32-watt input power. At 60-watt input power, these forces varied -86×10^{-5} to $+25 \times 10^{-5}$ pounds for ±0.55 inch. These results also indicate that the force levels for a given position are proportional to the product of the primary and secondary currents.

The position at which the force goes to zero is not in the geometric center of the primary and secondary windings but occurs as the two windings become closely linked.

Several other tests were performed using this transformer. When efficiency measurements were made at various voltage and current levels some interesting results occurred. At lower voltage inputs, the efficiency definitely increased for a given input-output power ratio but indicated a net decrease at lower powers. Table 28 contains a list of measurements showing the variations in efficiency for various voltages and currents. Square wave inputs were also applied to the transformer and the efficiency was measured and compared to efficiency measurements using sinusoidal inputs. The input voltages (sine wave and square wave) were held to the same rms amplitude using low voltage, 80 volt ac (rms) which produces high efficiency. The efficiency using square waves was less - 84.5 percent by comparison to 88.6 percent for sinusoidal inputs.

TABLE 28. EFFICIENCY MEASUREMENTS

Voltage Input (VAC)	Voltage Output (VAC)	Current Input (A)	Current Output (A)	Power Input (watts)	Power Output (watts)	Efficiency %
120	121.5	0.537	0.442	64.2	54.0	84.0
110	111.0	0.483	0.420	53.2	46.8	87.6
100	102.0	0.450	0.397	45.0	40.5	90.0
90	90.5	0.420	0.375	37.8	34.0	90.0
80	80.8	0.390	0.350	31.3	28.3	90.2
70	70.2	0.363	0.330	25.5	23.2	91.0
120	122.8	0.295	0.198	35.4	24.6	69.3
110	112.0	0.262	0.188	28.7	21.2	73.8
100	102.0	0.233	0.177	23.3	18.2	77.3
90	92.0	0.214	0.166	19.2	15.3	80.0
80	81.0	0.193	0.154	15.4	12.5	81.0
70	71.0	0.179	0.146	12.5	10.4	82.5

Efficiency measurements were made for higher frequencies (sinusoidal) and again a decrease in efficiency was noted. For the conditions of 80-volt ac (rms) input voltage, 30-watt nominal power, the efficiency was 3 percent less at 800 Hz than at 400 Hz.

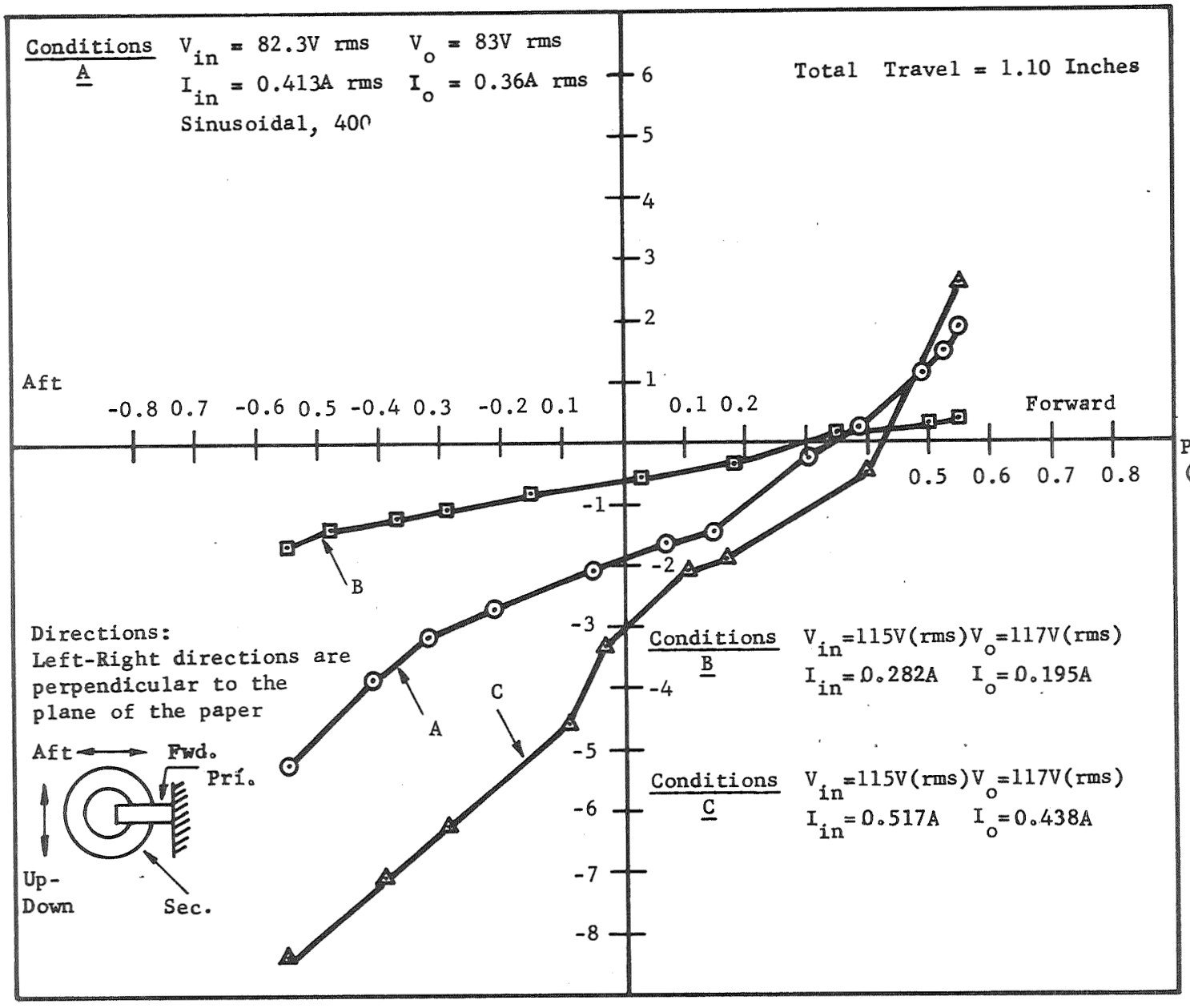

Figure 141. Chain Link Transformer Test Data

A final measurement was made to determine if the force levels varied when square wave inputs were used. A comparison was made with sinusoidal inputs for the conditions where the voltage, currents, and power output were held the same. The force was less in this case by nearly 14 percent.

The capacitive sensor was designed and tested with the results listed in Table 29 below. The size of the plates that were used in the design of the capacitor sensor are shown in Figure 142. The plates were made large to minimize losses such as fringing. The electronics associated with each set of capacitor sensors are shown in Figure 143. In this case, a pair of capacitive sensors produce output voltages proportional to both angle and linear displacement of the air bearing table.

TABLE 29. CAPACITIVE SENSOR SPECIFICATION

Travel:-	±0.50 inch from a nominal 0.60-inch plate displacement
Plate Area (total for two plates):-	45.0 inches^2
Resolution (at 0.60 inch):-	Less than 0.0001 inch
Linearity:-	2.0 percent for ±0.025 inch (see Figure
Sensitivity:-	Nominal 5 volts (dc)/inch
Drift:-	A single unit was tested for 24 hours in the laboratory and the maximum deviations in terms of displacement were less than 0.00050 inch (peak).
Frequency Response:-	The only normal limitation here is the data rate which is 10 kc and the filters used to smooth the 10 kc ripple at the demodulator output. These filters were arbitrarily selected at 100 Hz. (In the system, however, a twin 10-Hz filter was used at the demodulator output to minimize 60-Hz pickup.)

A plot of dc voltage output versus capacitive sensor plate displacement is also shown in Figure 144 for a single sensor.

Space qualification for each of these three component designs is not expected to be difficult since these components are inherently simple and reliable. In each case, there are no moving parts which rub, wear, or deteriorate in the normal mechanical sense.

POINTING SYSTEM TESTS

The experimental free float pointing system discussed in this section was subsequently operated in simulated performance situations. Results of these tests are enumerated here.

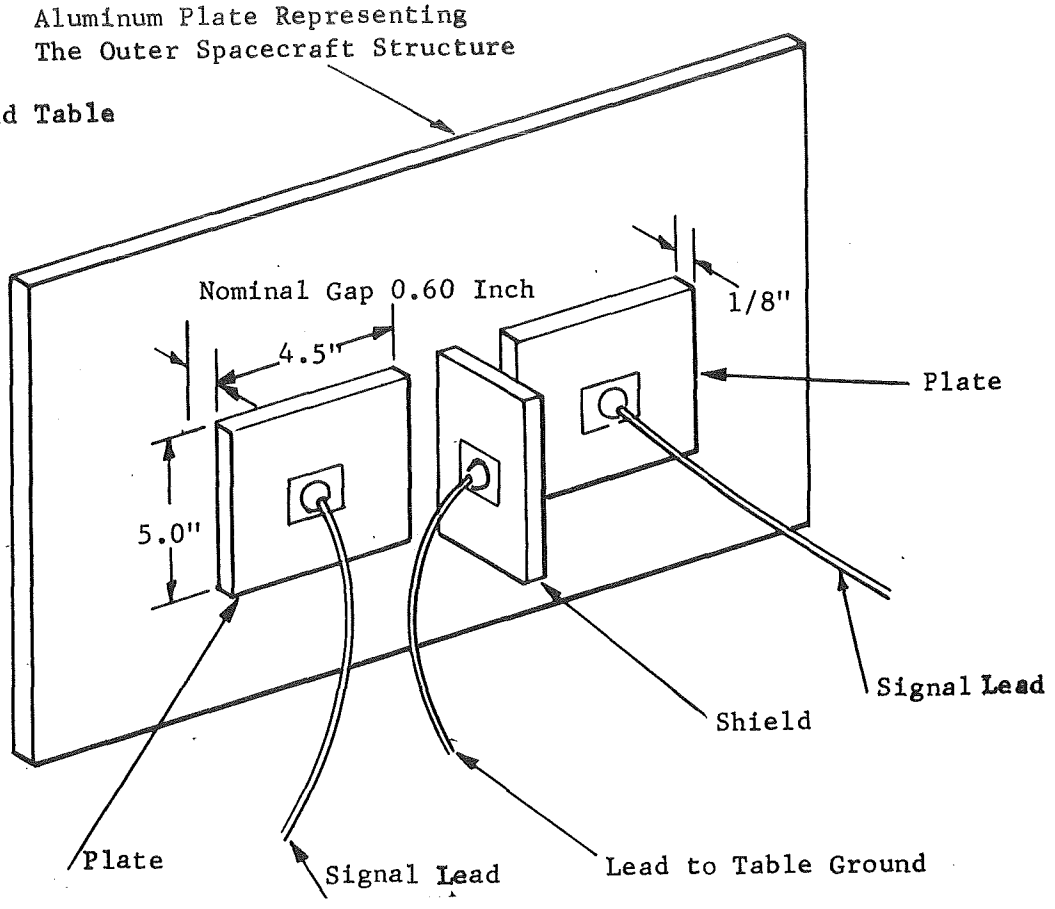

Figure 142. Grid Table

The performance evaluation procedure used in testing was straightforward. Controlled disturbances were applied to the pointing system and angular or displacement errors were recorded. Acquisition performance was evaluated for specific initial angular or linear displacement conditions. System noise was also measured at the capacitive sensor outputs in both linear and angular displacement. Pointing error was recorded independently by an optical instrument - an azimuth alignment theodolite.

Prior to evaluating the pointing system, tests were performed directed at an examination of errors created by disturbances from the test setup itself. Possible test bed disturbances can arise from unknown vibrations in the air bearing table, excessive building vibrations, room disturbances from air mass movements or large temperature variations, and internal disturbances from the system electronics, such as power supply transients. The tests involved noise measurements in the pointing and centering axes. Data was specifically obtained on angular noise, linear displacement noise, and magnetic pusher coil current variations which are a direct measure of force. In one test sequence, the table was balanced and the pointing system placed in the low gain or normal operating mode; the (angular) pointing axis pointing errors were then recorded over a period of 100 minutes (typical time for one orbit). An azimuth alignment theodolite was used to monitor pointing axis motions independent of the pointing system capacitive sensors. This theodolite is an optical instrument capable of consistently measuring angular deviations as low as 0.10 arc-second for long periods - 24 hours or more - over a 10-Hz bandwidth. Typical chart recording samples from this test run are shown in Figure 145.

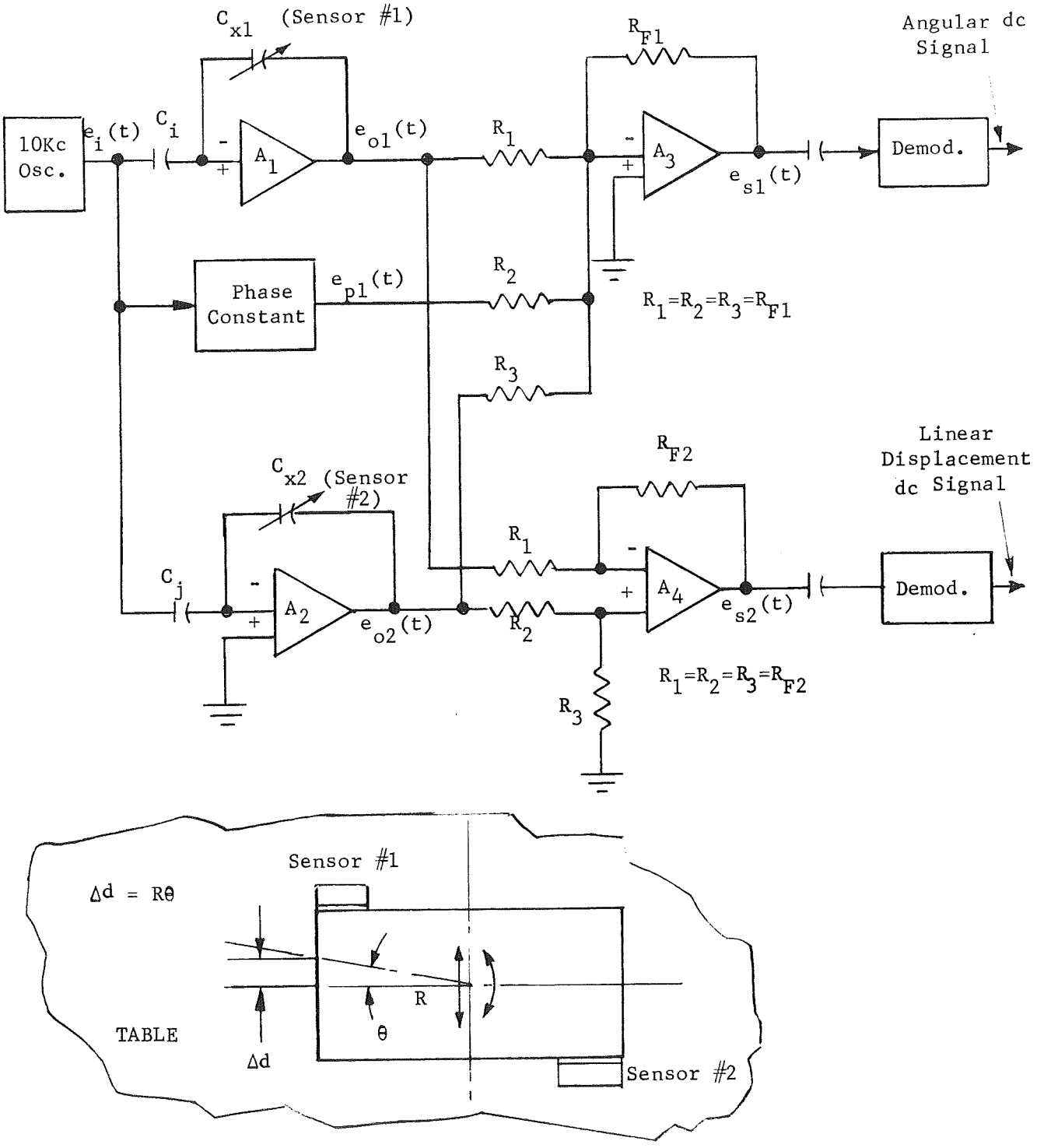

Figure 143. Capacitive Sensor Electronics

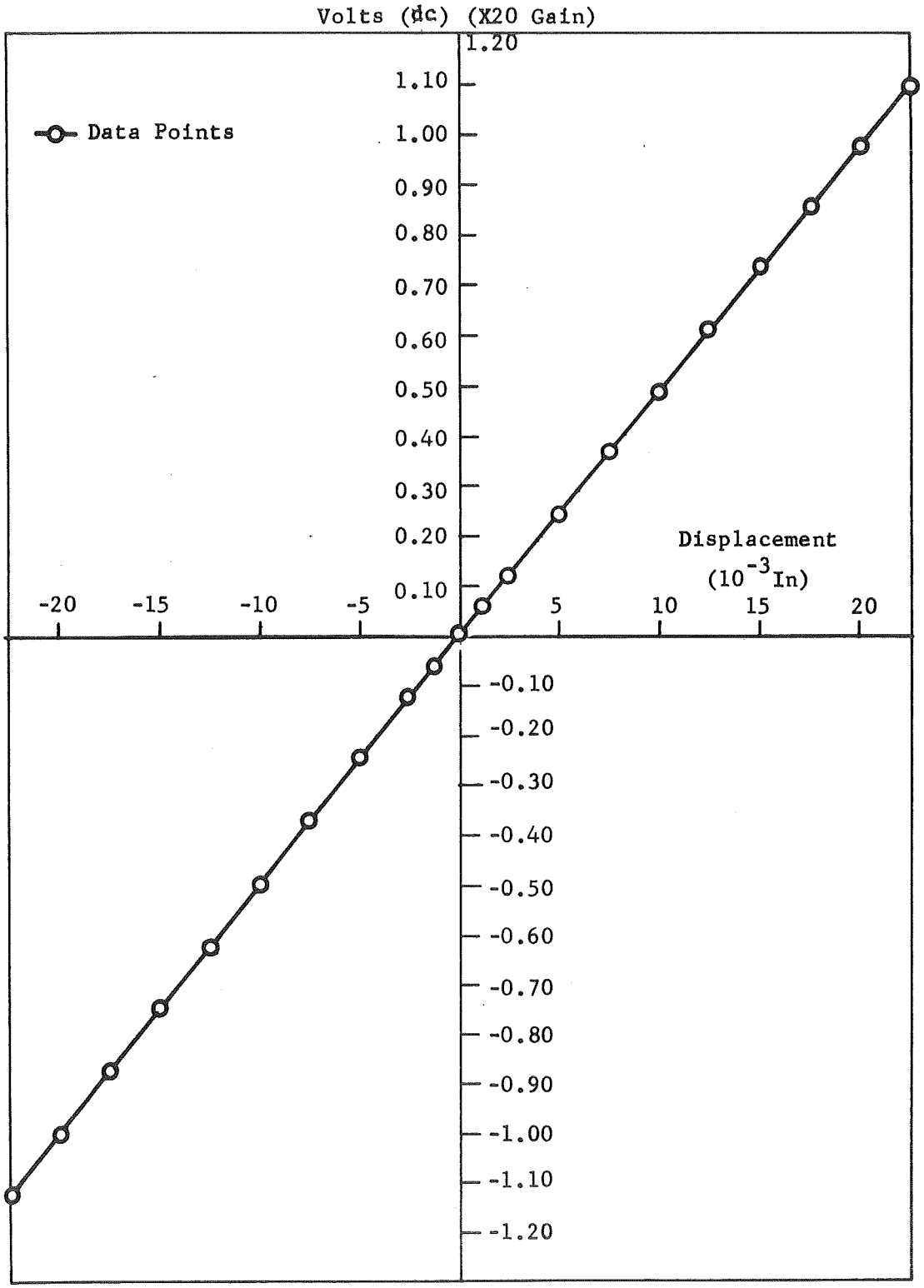

Figure 144. Capacitive Sensor Linearity

Pointing Errors
(Sample No. 1)

3730 Seconds
Into Run

Calibration: 13 mm/Arc-Second
1 mm/Sec

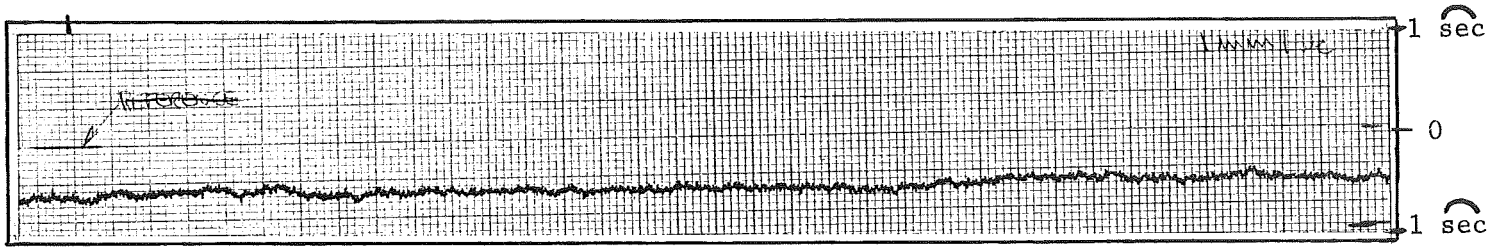

Pointing Errors
(Sample No. 2)

6085 Seconds
Into Run

Calibration: 13 mm/Arc-Second
1 mm/Sec

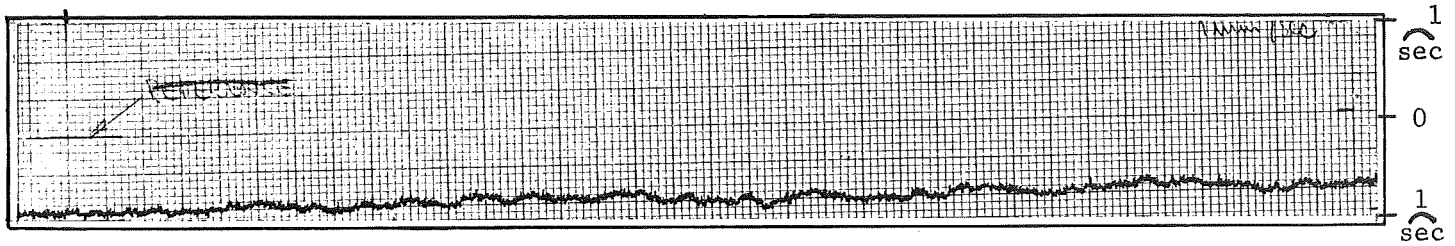

Pointing Errors
(Sample No. 3)
(System Turned Off)

6400 Seconds

Calibration: 13 mm/Arc-Second
1 mm/Sec

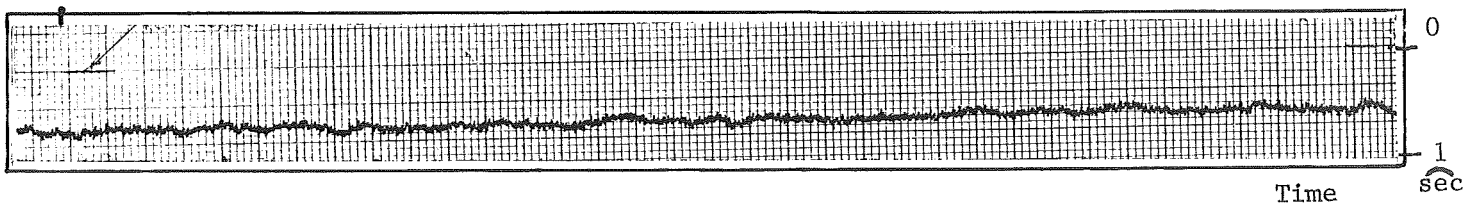

Figure 145. Long Term Stability and Vibration
Pointing Angular Error Measurements

The first two traces of Figure 145 are pointing errors sampled at 3730 seconds and again at 6085 seconds into the test run. The third sample is a plot of errors with the experimental pointing system and the air bearing table turned off. This latter trace provides a measure of the inherent theodolite noise, atmospheric disturbances and the building vibrations occurring between the air bearing table and the alignment theodolite. In some cases, such as sample No. 1, there is no distinguishable difference between the noise measurements with the pointing system active or inactive. The worst-case short-duration (15-second) peak-to-peak angular errors are equivalent to 0.077 arc-second in both instances. However, referring to sample No. 2 and other portions of the test run not shown, pointing system errors were detectable and noise errors of 0.10 to 0.15 arc-second (peak-to-peak) were measured. Again, these latter measurements included pointing system error plus the theodolite noise, building vibrations, and also power line variations. The pointing system was sensitive to random power supply fluctuations and/or 400-Hz line variations, and these electrical disturbances contribute to the pointing errors. In the final analysis, for errors of 0.14 arc-second (peak-to-peak) or less, it was difficult to determine the true angular pointing errors. Nevertheless, the free float experimental goals in terms of jitter were more than satisfied during these tests. Pointing errors of 1 to 3 arc-seconds (peak) were initially considered to be an optimistic design goal without an optical sensor and performance beyond this goal was left to further experimental programs.

Long-term drift was noticeable, amounting to 1×10^{-4} arc-second/second (time) or less. A comparison of samples No. 1 and No. 2 (Figure 145) clearly indicates the drift rate. The drift was attributed to temperature variations in the capacitor sensors and first stage operational amplifier integrators.* The rate of drift decreased with an increase in the amount of time that the room containing the air bearing table was left undisturbed.

The centering (x-axis) displacement errors were monitored in the second test for similar 100-minute periods, and samples of these recordings are shown in Figure 146. The capacitive sensors were used for these displacement measurements. The frequency bandwidth of the sensor and its associated data link was set at 1 Hz and the table was again precisely balanced. The first two samples shown were selected from the same run at 375 seconds and 2120 seconds respectively. A random, low-frequency variation was evident throughout each of the tests. This was attributed to the centering servo reacting to small random disturbances; and since the centering servo is under-damped, it will oscillate. The worst-case peak amplitude variations were no greater than 0.00053 inch during any portion of this run. Sample No. 2 is a typical worst-case fluctuation. These variations were detected by the capacitive sensors and are based on a linear interpolation of their sensitivity in the range of 0.0005 inch or less.

*Electrical components such as operational amplifiers were standard, commercially available items. It was concluded that better quality, temperature-stabilized components, would decrease drift rates.

Displacement (x-Axis) Errors
(Sample No. 1)

375 Seconds

Scale: 17.0 mm/0.001 In.

Run No. 1

1 mm/Sec

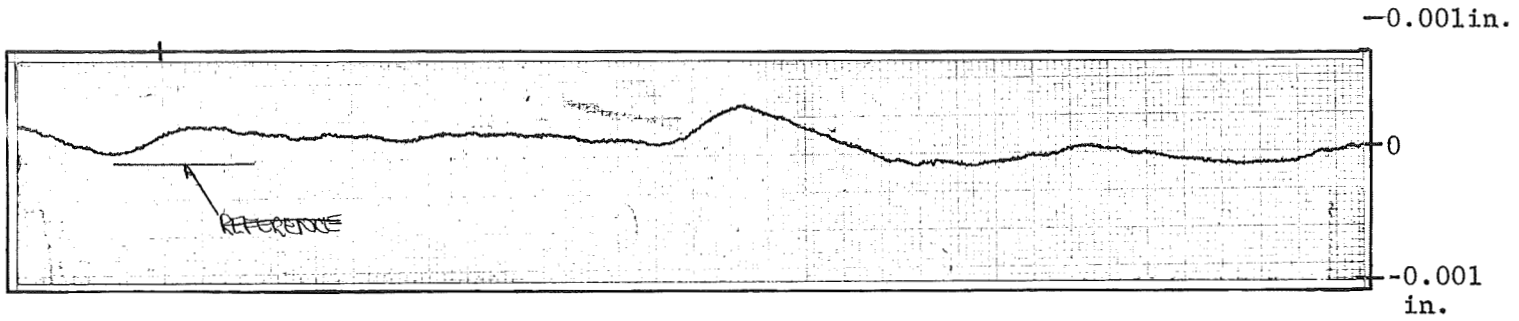

Displacement (x-Axis) Errors
(Sample No. 2)

2120 Seconds

Scale: 17.0 mm/0.001 In.

Run No. 1

1 mm/Sec

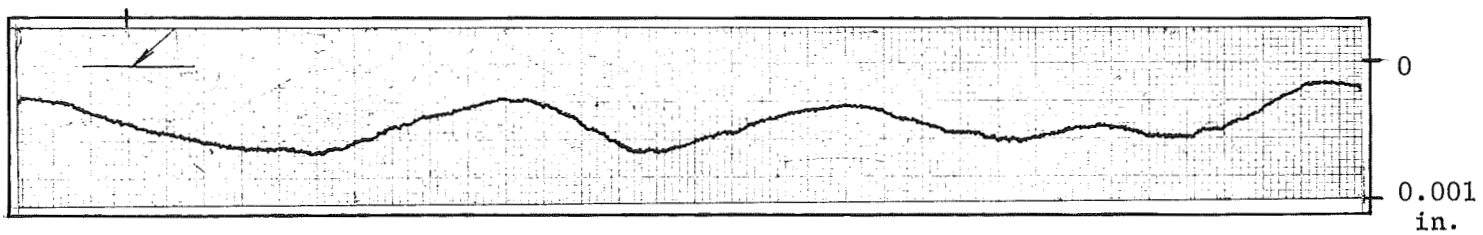

Displacement (x-Axis) Errors
(Sample No. 3)
(Increased Loop Gain)
Run No. 2

2480 Seconds

Scale: 34.0 mm/0.001 In.

1 mm/Sec

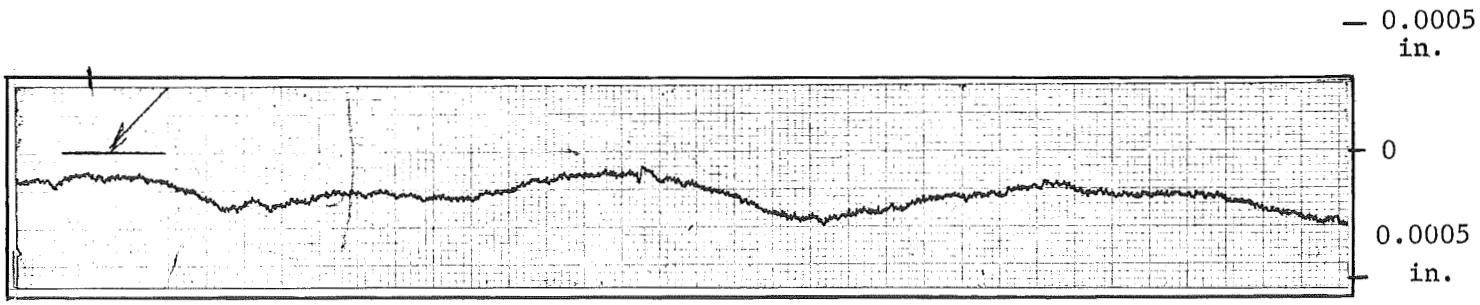

Figure 146. Long Term Stability and Vibration
x-Axis Displacement Error Measurements

The servo loop gain in the x axis was increased by 4:1 following the test run of samples No. 1 and No. 2, and a definite improvement was noted in the low-frequency variation. A second 100-minute run was recorded under these conditions and the data sample, sample No. 3, taken at 2480 seconds is shown in Figure 146. In this latter case, the short term worst-case peak amplitude variations were no greater than 0.00024 inch and generally less. Sample No. 3 is a worst-case sample (note the scale change).

Drift was detectable and can be seen by comparing the average displacement levels of sample No. 1 and sample No. 2. Typical average drift rates amounted to 0.17×10^{-6} inch/second in the first run, but were slightly larger in the second run, amounting to 0.29×10^{-6} inch/second.

In each of the previous stability tests, the air bearing table was precisely leveled or balanced to minimize offset forces in the magnetic pushers. The steady-state unbalance forces were separately measured for periods of 100 minutes by recording the magnetic pusher dc amplifier input voltage variations. These voltages are directly proportional to the current in the pusher coils. Sample data are given in Figure 147 from two runs. The first run is at normal gain settings and the second run is at increased (4:1) gain settings. The following performance was noted. The table could be leveled to 1 to 3×10^{-5} pounds of unbalance force. Long-term steady-state drift rates which would result in a slow buildup of steady-state force in the magnetic pushers were not detectable over periods of 100 minutes in the first run but were evident in the second run, amounting to an average drift rate of 5×10^{-8} pounds/second. The first run was at night while the second run was conducted during the daytime. The latter case was less ideal in terms of building vibration and room temperature variations and possibly accounts for the difference. Low-frequency variations were clearly evident. Variations in force were measured up to 8×10^{-5} pounds (peak) in run No. 1, occurring at frequencies identical to those shown in the samples. A representative 55-second sample recording was analyzed in this respect to determine the rms levels of force. Discrete values of force at 5-second intervals were used which resulted in an rms level of 2.75×10^{-5} pounds. The low-frequency variations were very slightly lower during the second run. High-frequency variations (approximately 1/2 Hz) were more predominant in this case with typical peak-to-peak amplitudes of 1 to 4×10^{-5} pounds.

An important consideration in the lower force ranges of the magnetic pushers and their magnetic amplifiers is the effect of dead zones or severe nonlinearities at null. A special test was therefore conducted to determine if any unusual effects were evident at the dc amplifier outputs. A sinusoidal input voltage was fed to the y-axis sensors and the current into the pusher coil was measured directly. The table was precisely balanced and the input voltage was set up to command the y-axis centering servo to swing the pointing system through the zero-force region. The results of the test are shown in the lower traces (samples Nos. 3 and 4) of Figure 147 . As shown, the current is very smooth through null, indicating adequate linearity in the null force regions. The magnetic pushers themselves are linear in the null force regions (see Figure 139).

The remaining tests and test results concentrated on evaluating the performance of the x-axis centering servo and the pointing axis - the two directly associated degrees of freedom.

Centering (x-Axis) Force Variations
(Sample No. 1)

3675 Seconds

Scale: 1.11×10^{-5} Lbs/mm

Run No. 1

1 mm/Sec

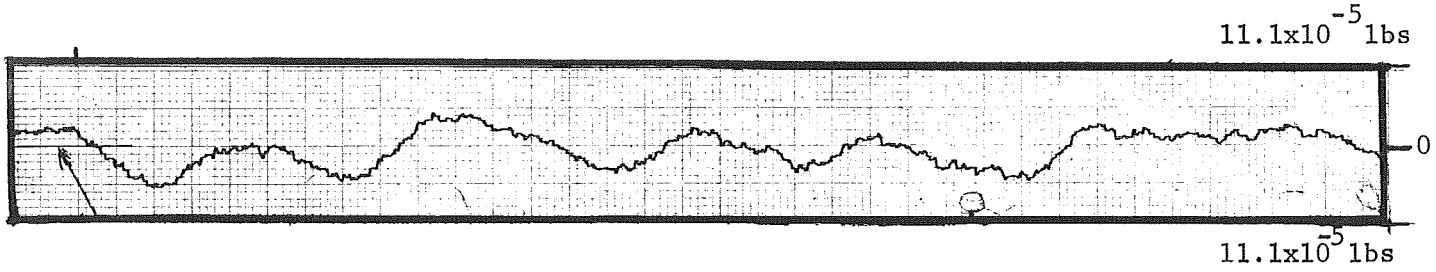

Centering (x-Axis) Force Variations
(Sample No. 2)

1715 Seconds

Scale: 1.11×10^{-5} Lbs/mm

Run No. 2

1 mm/Sec

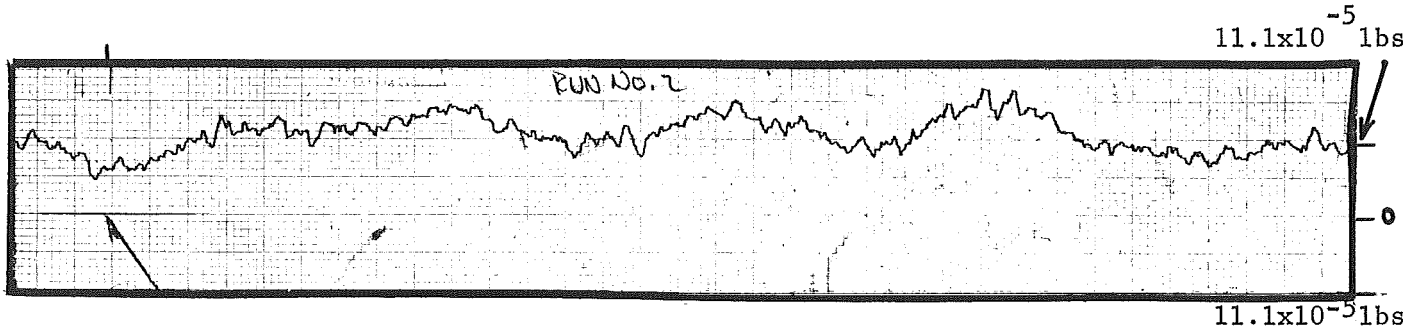

Coil Current (y-Axis)
(Sample No. 3)

Scale: 2×10^{-5} Lbs/mm

20 mm/Sec

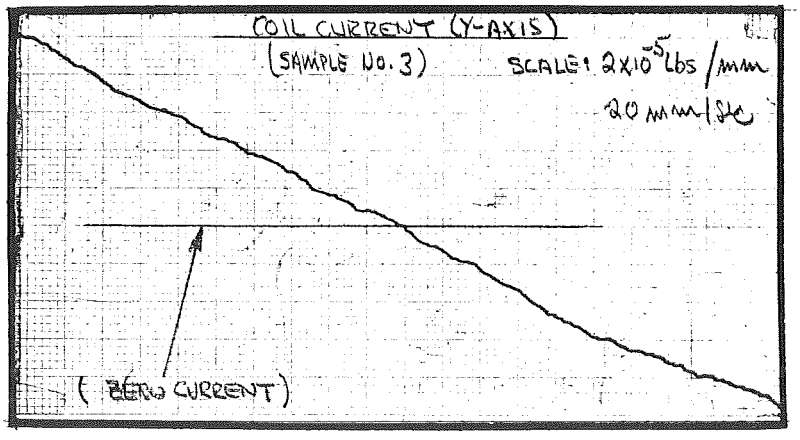

Coil Current (y-Axis)
(Sample No. 4)

Scale: 2×10^{-5} Lbs/mm

5 mm/Sec

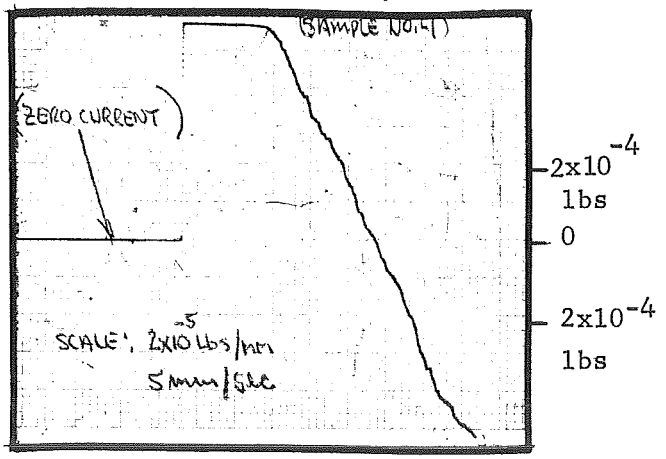

Figure 147. Magnetic Pusher Force Variations (x-Axis) and Resolution

The x-axis centering servo loop performance was evaluated in terms of displacement errors for known input force disturbances which were simulated by applying current to the pushers. In addition, force disturbances were applied by deliberately upsetting the table level with the piezoelectric balancing servo. Raising and lowering a pair of air pads with the piezoelectric stacks introduces horizontal components of force into the centering servo system. These disturbing forces were applied at the same sinusoidal periods and provided a cross-check against the results obtained with the simulated inputs. The final results of these tests are shown in Figure 148 which plots capacitive displacement sensor output errors versus the frequency of the input disturbance. Two levels of force were used - 0.33×10^{-3} pound and 1×10^{-3} pound — and the bandpass of the sensor and its associated data link was set at 1 Hz. There was good agreement between the theoretical and actual results.

Simulated spacecraft displacement motions or disturbances were also introduced into the x-axis displacement loop by feeding in sinusoidal electrical signals at the capacitive sensor summing point to the first-stage integrator. The same integrator output signals were then recorded; and, by knowing the integrator gain and the frequency of the disturbance, the error which represents the loop displacement errors due to spacecraft motions was determined. Two displacement amplitudes were used: 0.10 inch (peak) and 0.2 inch (peak) for a range of sinusoidal frequencies. The results of these tests are given in Figure 149. Errors were less than 0.002 inch (peak) for 0.1-inch (peak) input disturbance at 0.02 radian/second.

The pointing servo loop performance was evaluated in terms of angular pointing errors for known simulated torque disturbances. The torque disturbances were simulated electrically by feeding sinusoidal voltage into the dc pusher amplifiers. The angular errors were measured with the azimuth alignment theodolite and cross-checked using the capacitive sensors. Two levels of torque were used:— 7.5×10^{-3} pount-foot and 15×10^{-3} pound-foot for a range of input frequencies. The results of these tests are shown in Figure 150. Errors were undetectable at the 2700-second period (1/2 orbital period) torque disturbance rates since these conditions produce pointing errors less than 0.010 arc-second, which was beyond the measuring capability of the instruments used in this phase of the experiment.

The acquisition performance of the x-axis displacement loop and the pointing servo loop using the full linear capacitive sensor range (± 1/2 inch, ±30 arc-minutes) is shown in the time-base plots of Figures 151 and 152. Figure 151 represents the displacement loop recovery performance in the normal mode for initial conditions; (1) 0.35-inch, zero-pointing offset, and (2) 0.35-inch and 3 arc-minute pointing offset. The initial conditions in the adjacent axis provide a measure of the effects of cross-coupling. As shown, recovery time was less than 50 seconds. Recovery performance was also evaluated for combinations of initial conditions of displacement, and rate in the yaw axis. For initial conditions of 3.0-arc-minute displacement and estimated 0.50-to 1.50-arc-minute/second rates, typical recovery times ranged from 40 to 60 seconds.

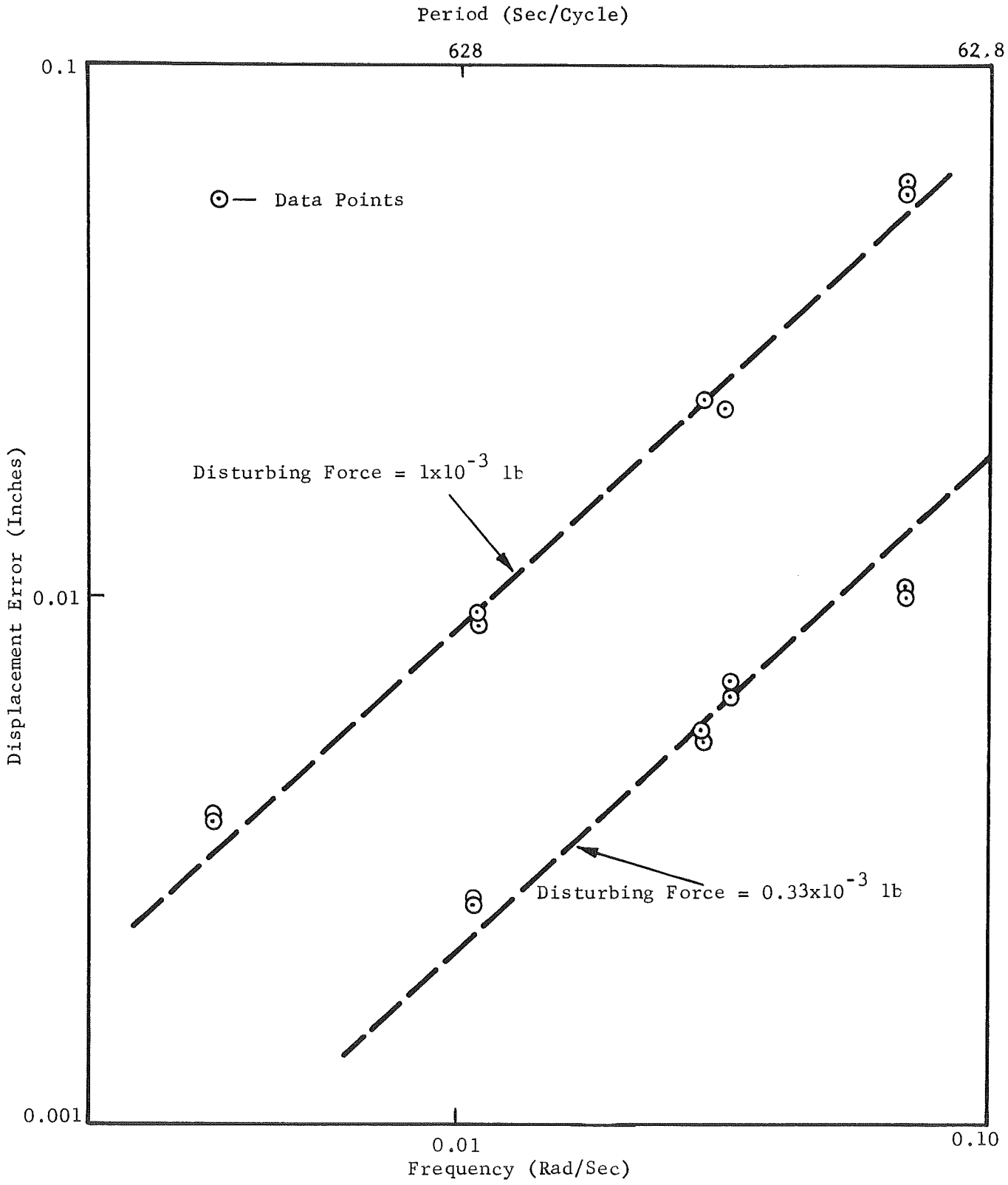

Figure 148. Centering Axis (x-Axis) Displacement Errors Versus Force Disturbance Inputs

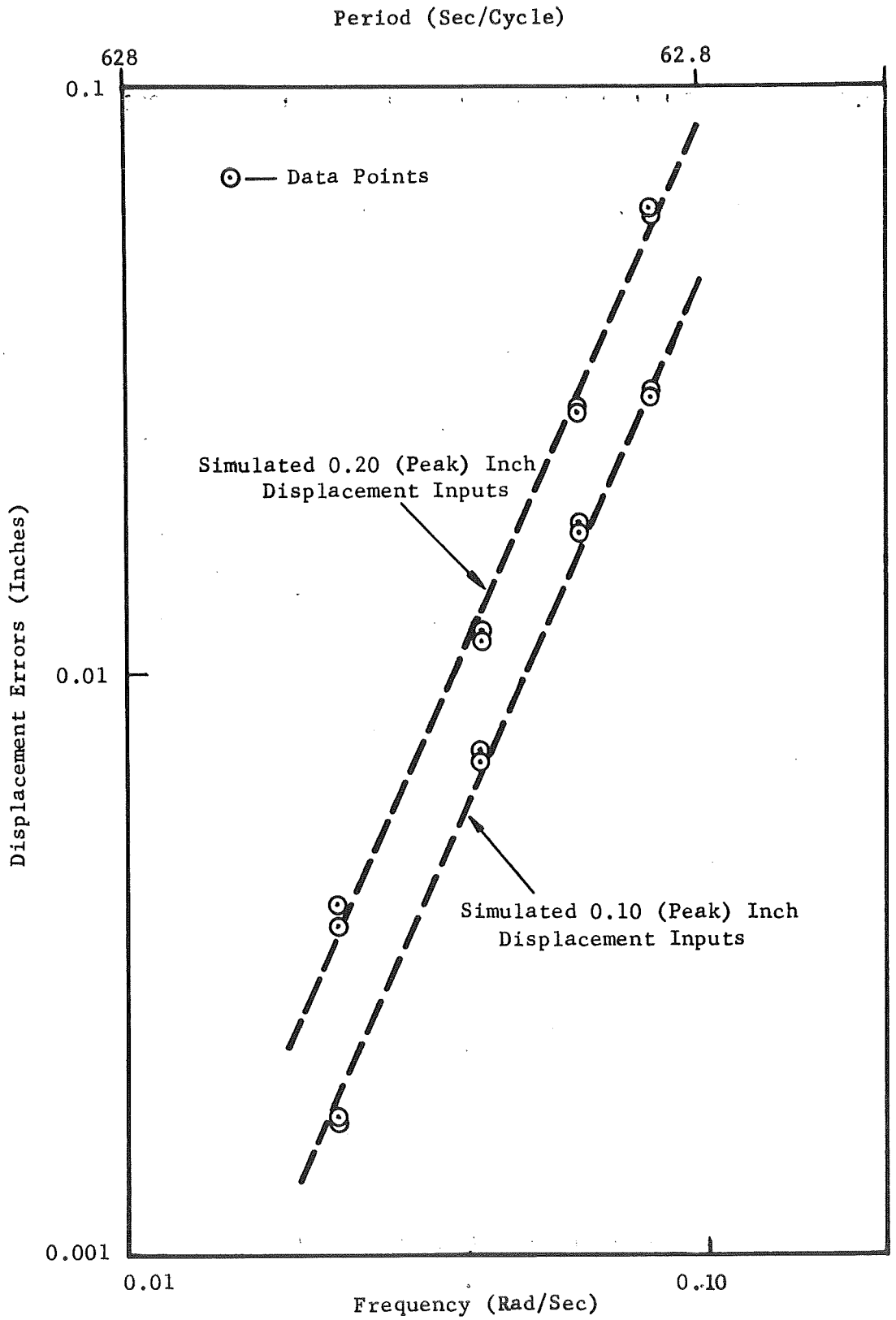

Figure 149. Centering Axis (x-Axis) Displacement Errors Versus Displacement Inputs

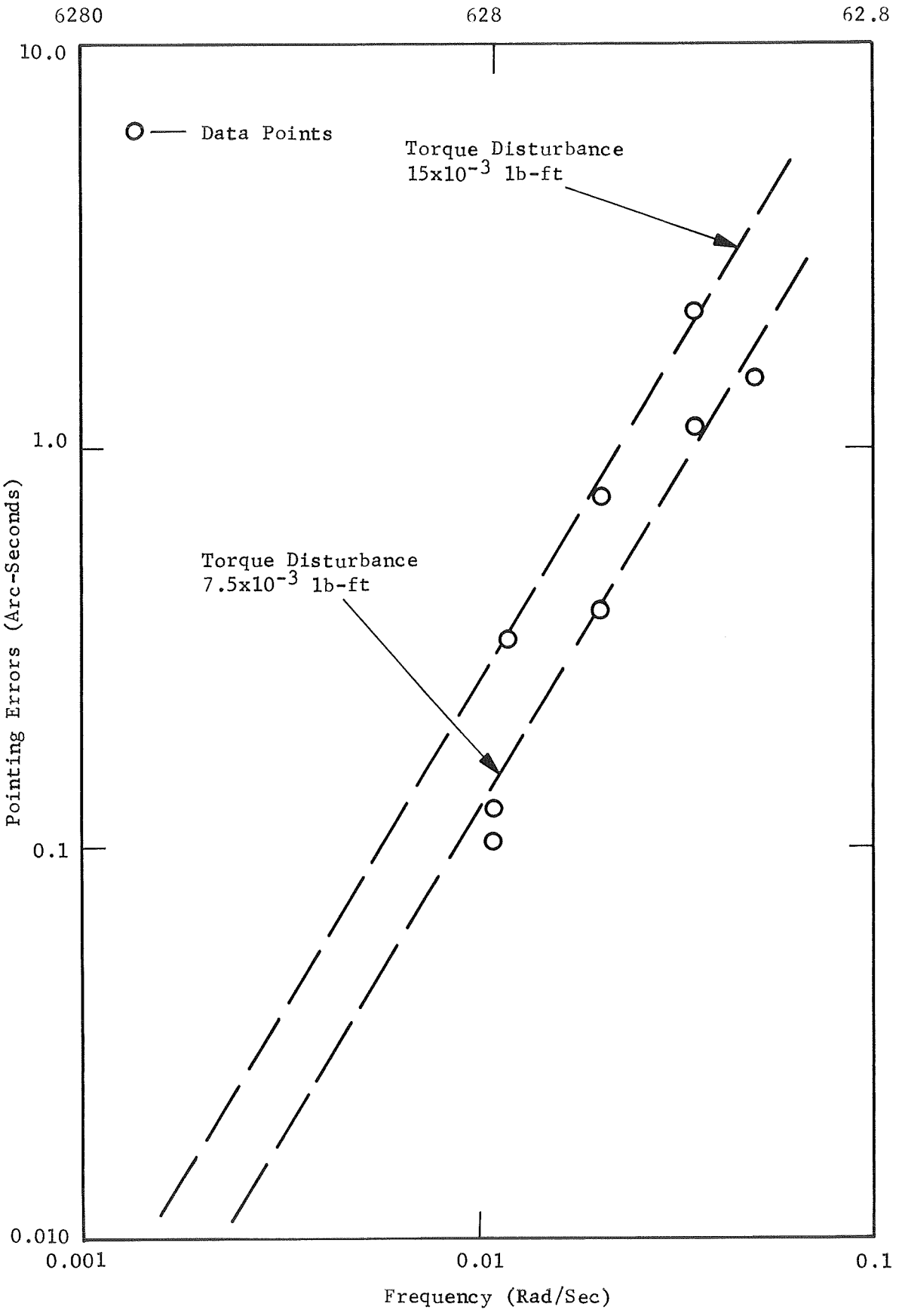

Figure 150. Pointing System Angular Errors Versus Torque Input Disturbances

Displacement (x-Axis)

Calibration:
2.97 cm/In.

1 mm/Sec

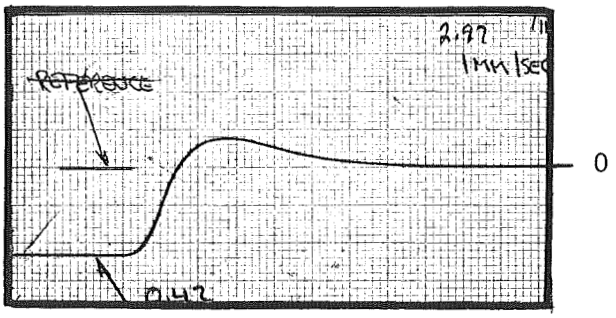

Displacement (x-Axis)

Calibration:
2.97 cm/In.

1 mm/Sec

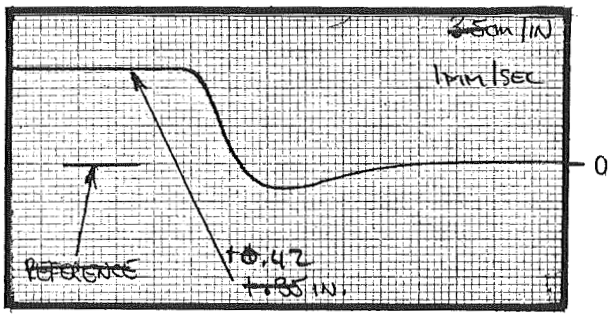

Sample No. 1

(Initial Conditions: 0.350 Inches, 0.00 Arc-Minutes)

Displacement (x-Axis)

Calibration:
2.97 cm/In.

1 mm/Sec

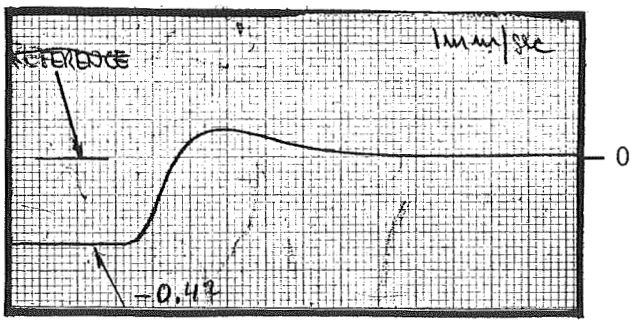

Displacement (x-Axis)

Calibration:
2.97 cm/In.

1 mm/Sec

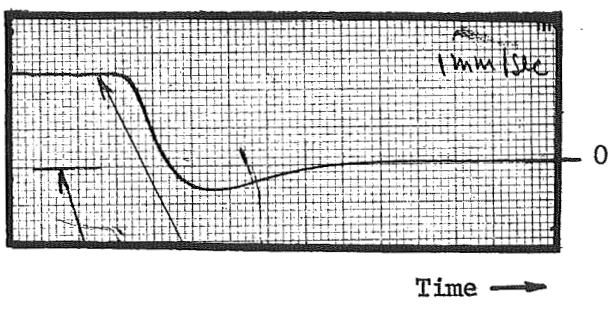

Sample No. 2

Initial Conditions: 0.350 Inches, 3.0 Arc-Minutes)

Figure 151. Centering Axis (-axis) Requisition Performance Runs

Yaw Axis Displacement

Calibration: 10 Arc-Sec/mm

1 mm/Sec

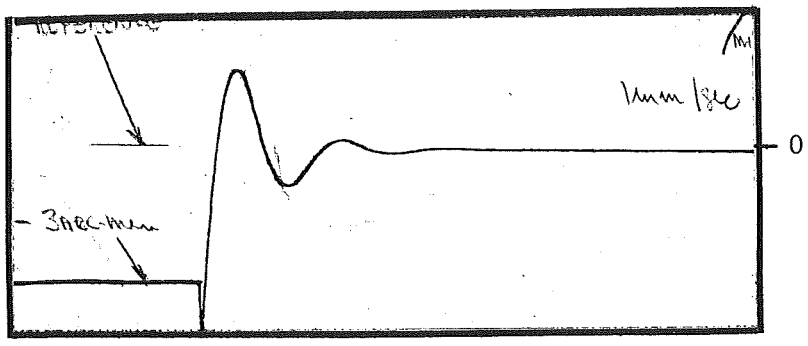

Sample No. 1

(Initial Conditions: -3 Arc-Minutes, 0 Displacement)

Yaw Axis Displacement

Calibration: 10 Arc-Sec/mm

1 mm/Sec

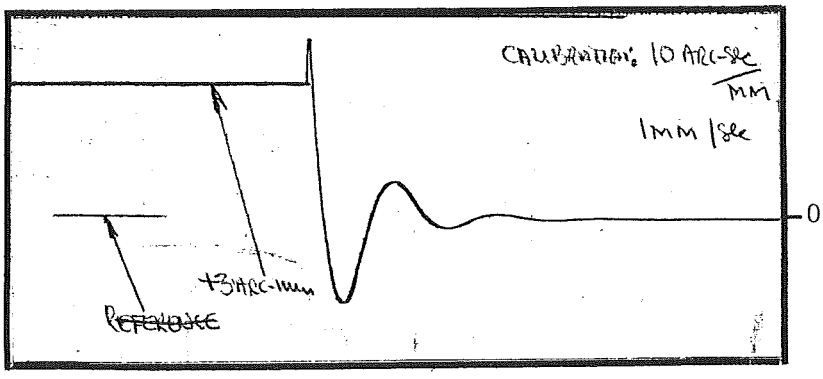

Sample No. 2

(Initial Conditions: +3 Arc-Minutes, 0 Displacement)

Figure 152 . Pointing Yaw Axis Acquisition Performance Runs

The test results agreed very closely with the expected or theoretical results, and a few examples illustrate this fact. The displacement errors plotted in Figure 148 should conform to the fundamental low-frequency servo (Type III) displacement error formula which states:

$$X_e(t) = \frac{\left[\frac{d}{dt} F_d(t)\right]}{M k_x}$$

where

$X_e(t)$ = displacement error (feet)

K_x = the x-axis servo open loop dynamic constant (first derivative of linear acceleration - second^{-3})

$F_d(t)$ = force disturbance input (pounds)

M = mass of the simulated telescope (slugs)

Tests were conducted in which the force disturbance input was sinusoidal:

$$F_d(t) = F_d \sin \omega t$$

where

F_d = peak amplitude of the force (pounds)

Selecting a sample point from Figure 148 at a frequency of 0.011 radian/second and a force input of 1×10^{-3} pounds, the peak error calculates to be:

$$X_e(t)_{peak} = \frac{\omega F_d}{MK_x} = \frac{(0.011)\ (1 \times 10^{-3})}{(16)\ (1 \times 10^{-3})} \text{ feet}$$

$$X_e(t)_{peak} = 0.00069 \text{ foot or } 0.00827 \text{ inch}$$

where

$K_x = 1 \times 10^{-3}$ second^{-3} — the constant used in the experimental setup

The mass (M) was calculated based on the known table weight.

The measured value was 0.0094 inch (peak), which is quite close to the predicted error.

The pointing errors of Figure 150 are predictable using the equation:

$$\theta_e(t) = \frac{\frac{d^2}{dt^2}\left[\tau_d\ (t)\right]}{K_a I}$$

where

$\theta_e(t)$ = pointing error (radians)

K_a = the pointing axis servo open loop dynamic constant (second derivative of angular acceleration - second^{-4})

I = inertia (pound-foot-second^2)

$\tau_d(t)$ = torque disturbance (pound-feet)

If sinusoidal inputs of torque are used, then:

$$\tau_d(t) = \tau_d \sin\omega t$$

where

τ_d = peak amplitude of torque disturbance (pound-feet)

The pointing error equation becomes:

$$\theta_e(t)_{peak} = \frac{\omega^2 \tau_d}{K_a I}$$

Selecting a sample point of 1.5×10^{-3} pound-foot (peak) torque disturbance input at 0.0233 radian/second, the error calculates to be:

$$\theta_e(t)_{peak} = \frac{(0.0207)^2(0.015)}{(0.012)(100)} = 5.30 \times 10^{-6} \text{ radians}$$

or

$$\theta_e(t)_{peak} = 1.10 \text{ arc-seconds}$$

The measured value indicates an error of 0.75 arc-second (peak). Thus, in this case, as well as the two previous examples, good correlation is achieved between theoretical and actual results. Any differences in error values are not considered system malfunctions but are rather attributed to calibration inaccuracies.

The basic free float isolation concepts were clearly proven during this experiment. The plots of Figure 149 for instance, proved, by simulated means, the system's ability to remain centered within the spacecraft when the spacecraft is moving. An important isolation test was also performed in this respect that was not discussed in the results. A magnetic pusher permanent magnet housing was removed from its mounting brackets and slowly moved (manually) 1 to 2 inches "in and out" with respect to the coil while the system was active. The magnet housing is considered part of the outer spacecraft and these motions would represent spacecraft motions. Theoretically, for this type of test, the experimental pointing system should not be disturbed since this is a direct demonstration of the isolation concept. The results were very successful. The pointing system did not follow the slow and very large 1- to 2-inch motions of the pusher permanent magnet.

This type of test should be repeated when the entire pointing system is simulated in a vacuum chamber, as recommended in the non-space experiments section.

CHAPTER 11 - TELESCOPE ROTATIONAL CONTROL

The Rowland circle spectrometer module and the modified echelle spectrograph (module A) are unique in that rotational control other than that provided by the CMG system is not required. This is because the target/guide star image is formed nominally on the optical axis. Since the rotation axis coincides with the optical axis, roll motions have no effect on pointing direction. In the practical case where small misalignments between these axes do exist, the roll motions will generate very small errors which are removed by x-y motions.

Each of the other modules differ in that its associated x-y guide star sensor is not nominally on the optical axis and therefore roll motions affect the x-y sensor output. Moreover, and more important, the x-y errors affect the output of the roll sensor (when this is of the stellar image-splitting variety) since the sensing axes cannot be mutually orthogonal in a common optical arrangement; i.e., the roll sensor cannot be so located due to limited field size.

The interaction between the servo loops must be given careful design consideration in order to avoid possible adverse effects on stability. Consider for example the system as depicted by Figure 153a. Here the corrective motions take place about the line of sight (α) and in the two orthogonal directions (x and y) as a consequence of signals generated by the two guide star image-splitting sensors shown. The block diagram for the arrangement is shown in Figure 153b and can be rearranged into the equivalent form of Figure 153c. This latter diagram places in clearer evidence the fact that interaction modifies the loop characteristics. In the case of the y loop for example, the unity negative feedback characteristic is seen to be modified by the x loop to

$$-\left[1 + \frac{Rx}{R_\alpha}\right]\left[\frac{G_\alpha}{1 + G_\alpha}\right]$$

so that the loop gain characteristic is changed from -Gy to

$$-Gy\left[1 + \frac{Rx}{R_\alpha}\right]\left[\frac{G_\alpha}{1 + G_\alpha}\right] \triangleq -Gy\left[1 + n\left[\frac{G_\alpha}{1 + G_\alpha}\right]\right.$$

Similarly, the α loop gain is changed from $-G_\alpha$ to

$$-\left[\frac{G_\alpha}{R_\alpha}\right]\left[R_\alpha + R_x\left[\frac{G_y}{1 + G_y}\right]\right] = -G_\alpha\left[1 + n\,\frac{G_y}{1 + G_y}\right]$$

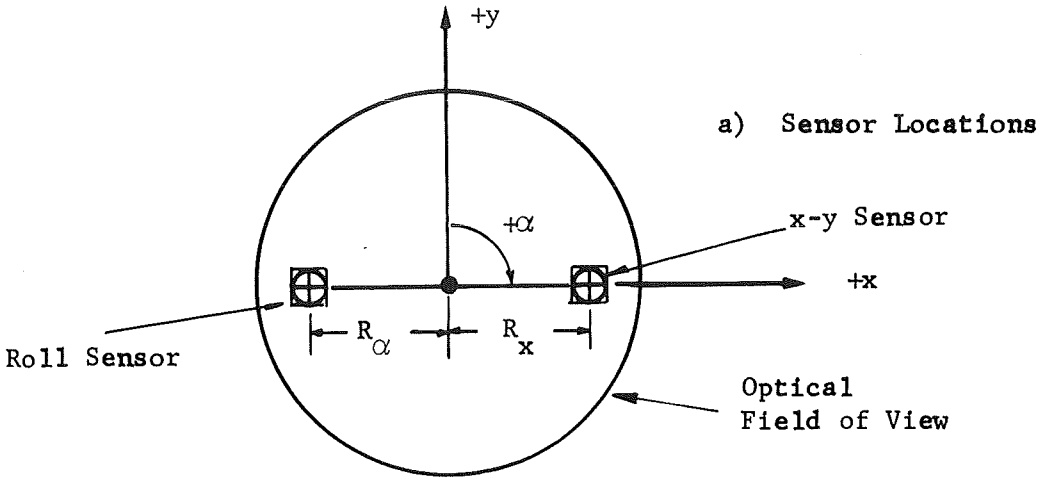

a) Sensor Locations

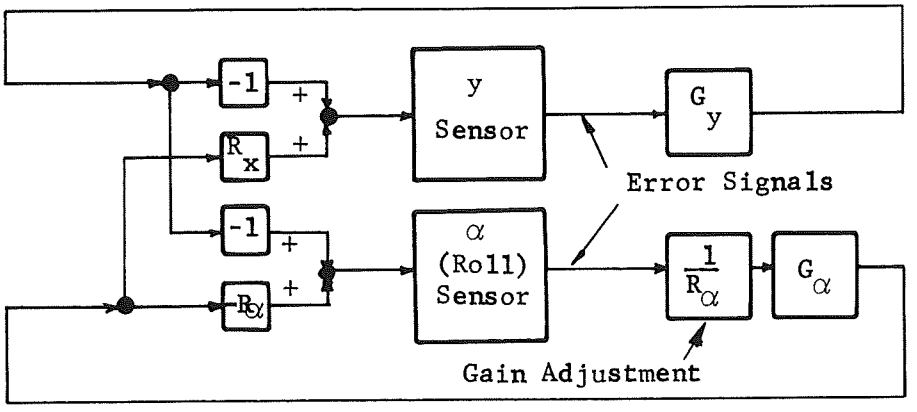

b) Control Loop Block Diagram Showing Interactions

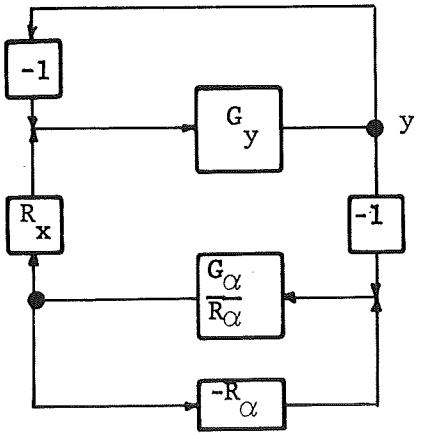

c) Equivalent Block Diagram

Figure 153. Typical Loop Interaction

The expressions, it should be noted, are for the particular sensor locations indicated in Figure 153a. These were chosen purposely to avoid coupling between the α and x loops and hence simplify the discussion to a consideration of a two-, rather than a three- interacting loop case. If, as a further simplification, it is assumed that $G_\alpha = Gy = 1/S$, then the coupling-induced changes to the open loop gain characteristics are as shown in Figure 154 and include a change of crossover frequency and phase margin. The amount of modification in this case depends upon the value of $Rx/R_\alpha (= n)$ and therefore upon the distances of the two guide stars from the center of the field. In the more general case where the two sensors do not both lie on the horizontal diameter (as shown), coupling between the α and both the x and the y loops will be present. Then the interaction will be a function of four parameters, the radial distances and angles to each sensor or, equivalently, the x and y locations of each, relative to the line of sight.

The result of interaction is clearly undesirable and is normally avoided by one of two methods. The first approach involves the mechanization of the loops with different bandwidths. Consider, for example, the system above in which the functions G_y and G_α are purposely chosen such that the y-loop bandwidth greatly exceeds that of the α loop. Then, the y-loop gain expression

$$-Gy \left[1 + n \left(\frac{G_\alpha}{1 + G_\alpha}\right)\right]$$

reduces to $-Gy$ in the vicinity of crossover since

$$n \left(\frac{G_\alpha}{1 + G_\alpha}\right) \ll 1$$

in this region. The y-loop stability under such circumstances will be only slightly influenced by the α-loop action. On the other hand the α-loop gain expression

$$-G_\alpha \left[1 + n \left(\frac{G_y}{1 + G_y}\right)\right]$$

reduces to

$$-G_\alpha \left[1 + n\right] = \left[G_\alpha\right] \left[\frac{R_\alpha + R_x}{R_\alpha}\right]$$

in the vicinity of crossover since

$$\frac{G_y}{1 + G_y} \approx 1$$

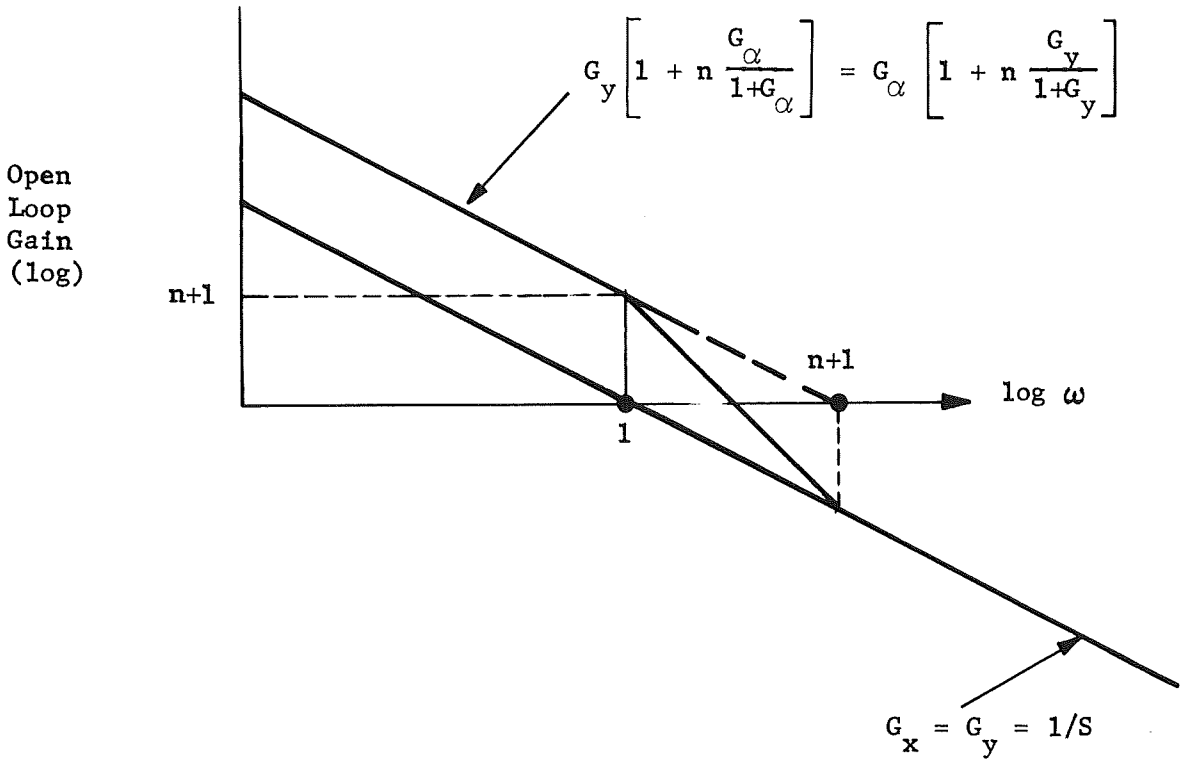

Figure 154. Typical Effect of Coupling on Open Loop Gain Characteristics

in this region. The dependence of loop gain on the factors R_α and R_x, moreover, can be nicely avoided by implementing a gain adjustment of $\frac{1}{R_x + R_\alpha}$ rather than $\frac{1}{R_\alpha}$ in the α loop as was assumed above. The action of the system under these conditions is to stabilize the x-y guide star image at its sensor apex with rotations (of the optical field) about this point due to roll motions. This technique is that of the Stratoscope guidance arrangement where the fast x-y corrections are made by moving a small transfer lens while the roll corrections are introduced via structural pointing loop of much lower bandwidth.

With such an arrangement the tracking error at the x-y sensor consists only of the x-y errors with no appreciable tracking error due to roll errors. For points removed from the x-y sensor, the error will consist of the x-y errors plus an additional component, due to roll error motion, proportional to the distance to the x-y sensor.

A different approach to avoiding loop interactions involves the introduction of compensating crossfeeds in the electronics following the sensors. Consider the general sensor arrangement as shown in Figure 155, where the indicated y, x, and θ_R axes are those of correctional movements. Positive up, right, and counterclockwise motions of the telescope will make the guide stars appear to move down, left and clockwise and the two sensors will respond by generating the following signals.

Sensor Output		Sensor Signal Components due to Motions of Telescope		
Signal Line		Up	Right	Counterclockwise
Left Sensor	y	-y	0	$+ \theta_R R_B \cos B$
	x	0	-X	$+ \theta_R R_B \sin B$
Right Sensor	x	0	-X	$+ \theta_R R_\alpha \sin\alpha$
	y	-y	0	$- \theta_R R_\alpha \cos\alpha$

Assuming now that the left sensor is used as a roll θ_R sensor which can only supply x or y signals, we can consider the two cases. When a y signal is available from the roll sensor, the two sensor y signals may be subtracted to obtain

$$-y + \theta_R R_B \cos B - \left[-y - \theta_R R_\alpha \cos\alpha\right] = \theta_R \left[R_B \cos B + R_\alpha \cos\alpha\right] = \theta_R \left[x_B + X_\alpha\right]$$

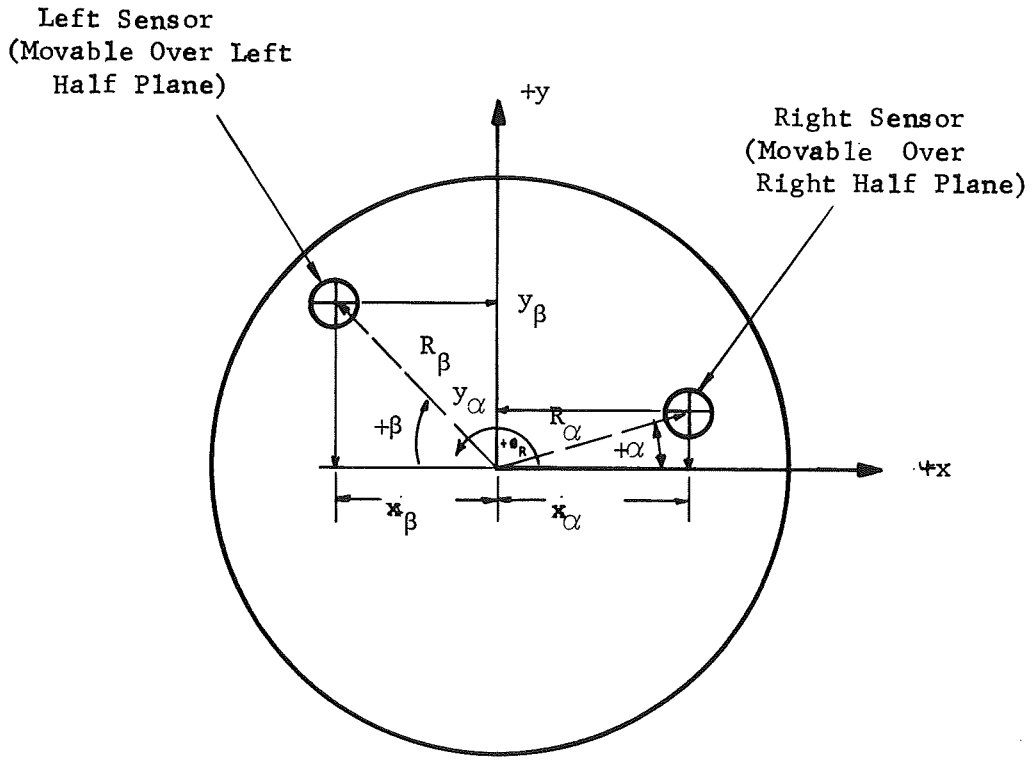

Figure 155. Geometry of Guide Star Image Sensor Location.

Hence, the resulting signal can be divided by $X_B + X_\alpha$ to obtain a θ_R signal which can be multiplied by $R_\alpha \sin\alpha = y_\alpha$ and $R_\alpha \cos\alpha = X_\alpha$ to obtain terms appropriate for correcting the x-y sensor output signals to obtain pure x and y error signals. When two x signals are available subtraction yields

$$-X + \theta_R R_B \sin B - \left[-X + \theta_R R_\alpha \sin\alpha\right] = \theta_R \left[R_B \sin B - R_\alpha \sin\alpha\right] = \theta_R \left[y_B - y_\alpha\right]$$

which can be divided by $y_B - y_\alpha$ to obtain θ_R. Multiplication by y_α and X_α yields terms suitable for correcting the x-y sensor output.

In the event that the left rather than the right sensor is selected as the x-y sensor, the signal processing would be similar. A block diagram for a typical mechanization is shown in Figure 156.

The upper block diagram indicates the operations required with either the left or right sensor selected (S1) to generate x-y information. In either case, the other (or roll) sensor output signal can be selected (S2) to be generated by either x or y motions of the guide star. Sensitivity to both axes of motion is generally assumed as not possible since this requires precise spacing, between the two sensor apexes, equal to the distance between the two guide star images. The y sensitivity is preferred when the line between the two apexes is within 45° of the x axis; otherwise, x sensitivity from the roll sensor should be chosen. This results in maximum sensitivity sensor output voltage per unit rotation; viz, consider for example the fact that $R_B \sin B - R_\alpha \sin\alpha$ becomes zero when both apexes lie on the x axis. The lower block diagram performs equivalent functions with G1 set equal to $\left[R_B \cos B + R_\alpha \cos\alpha\right]^{-1}$ or $\left[R_B \sin B - R_\alpha \sin\alpha\right]^{-1}$, by remote input commands, depending upon whether x or y sensitivity of the roll sensor is desired. The input command, moreover, must include sign data since either term of the latter expression, and therefore the expression itself, can be negative. The former expression is positive as should be expected since it represents the horizontal distance between the two apexes.

This method of decoupling the loops, by appropriate signal processing, differs from the approach described earlier in that the point about which rotations appear to take place is the line of sight rather than the x-y sensor apex. Moreover, the roll and cross line of sight loops, being effectively decoupled can be implemented with equal or greatly differing bandwidths.

Either of the two previously described methods of avoiding adverse interaction effects can be considered for the LTEP equipment. Reference to Table 19 , indicates, for example, that the roll to x-y bandwidth ratios are in the order of 1:5. This is not a sufficiently large separation to allow decoupling, as implemented in Stratoscope, to be achieved with reasonable safety, margin.

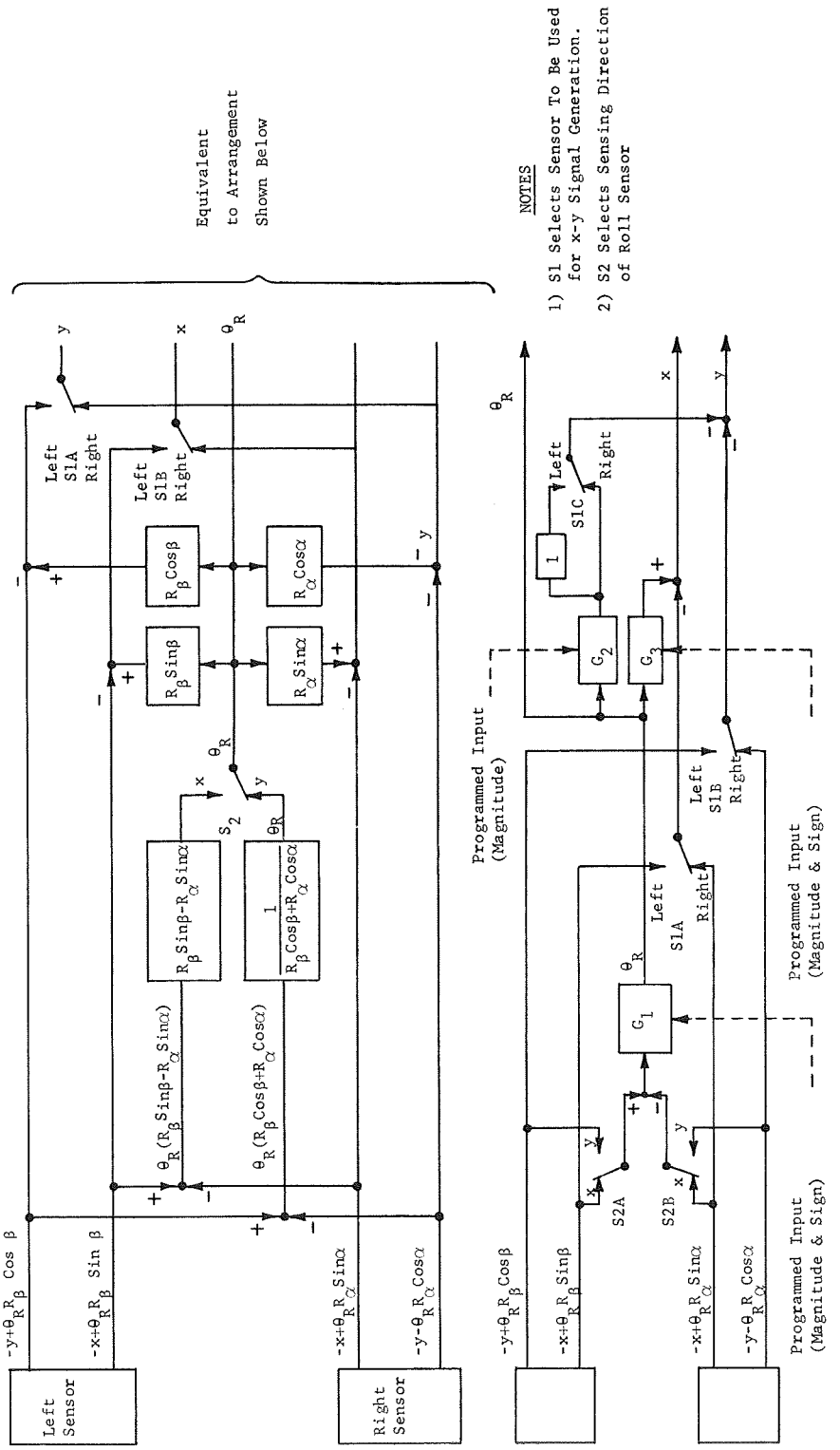

Figure 156. Block Diagram Showing Decoupling Computation and Associated Switching

Subsequent design efforts could include a consideration of appropriate changes to allow this approach and hence to avoid the complexity of decoupling via signal processing. However, the operational virtues of the signal processing approach make it the preferred technique; i.e., using this approach, bandwidth adjustments to a loop can be made at any time, without concern about interaction effects, to obtain, for example, optimum performance with the available guide star magnitude.

IMAGE PLANE EQUIPMENT ROTATION

Fine rotational control concurrent with transfer lens x-y control will be accomplished, as mentioned previously, by rotating the experiment modules. In effect then, the structural roll motions cause rotations of the optical image field and relative motion effects are avoided by moving the hardware to track the images. Means for doing this will be provided for the electronic and photographic imagery packages, modules F and C. It should be noted that during magnetic suspension operations with modules C and D (the Echelle package) roll stabilization is provided by torquing the whole LTEP structure to maintain correct attitude. Furthermore, the Rowland Circle Experiment (module E) requires only the fine x-y control provided by the gimbal system and the coarse CMG roll stabilization, a fine rotation control being unnecessary since the guide star is the target star and lies on axis.

The particular fine roll control requirements for modules C and F are reasonably similar. The control loop crossover frequencies are in the order of 0.0028 to 0.004 Hz and the roll accuracies must be within 0.73 and 0.31 arc-second, respectively. The minimum range of roll motion must be at least as large as the peak-to-peak roll excursions of the CMG system during track. More realistically, the roll range should be increased to allow correction for errors in precise positioning of the guide star splitting prisms as well as the ATM gimbal Roll Positioning Mechanism (RPM). In the former case, one could assume that the prisms are each mispositioned by 0.025 percent of the 30-arc-minute field diameter when spaced apart by a minimum amount (2 arc-minutes between apices). This corresponds to a roll error angle of

$$\theta_R = \frac{2 \times 0.025 \times 10^2 \times 30}{2} = 0.0075 \text{ rad} = 25 \text{ arc-minutes}$$

The specified accuracy in setting a roll angle via the RPM is about ±10 arc-minutes indicating that a total fine servo roll range of about ±1/2° would be appropriate. Several techniques to reduce this range could be considered. For example, one might modify the vehicle (CMG) or RPM roll angle to obtain a null from the experiment package roll error sensor prior to permitting the fine roll servo to drive off center. This is feasible since even a 1/2° error in roll about the x-y sensor in an extreme field position would misplace the data image at recording device by only

$$1/2^\circ \times \frac{1}{57.3} \times 15 \text{ arc-minutes} = 0.131 \text{ arc-minute}$$

For the purposes of the following discussion, reduction of the required roll range by such means will not be considered. This will place the most stringent requirements on the implementation as it is considered here.

A typical mechanization, appropriate for use with the f/10 photographic imagery package is shown in Figure 157. The rear flexure pivot provides three-axis translational constraint and allows roll motions as controlled by the concentric torquer motor. Two fixed roller supports, preloaded by an identical but spring-loaded third roller, provide appropriate motional constraints at the opposite end of the module. The control concept involves the use of a minor positioning loop of reasonably high bandwidth for good isolation against stray torques (viz, flexure pivot and interconnecting wire effects). The low bandwidth major loop can then be realized by commanding the minor loop with roll error signals, suitably processed through low frequency integration circuits. The details of the approach will now be examined.

Flexure pivots suitable for use in this application are Bendix types 6005-600 and 6006-800. The former has load ratings upwards of 19 pounds and is suitable for the rear pivot which must resist the radial decentering forces of attraction between the torquer motor rotor and stator. The bearing spring rate is 0.2 pound-inches per radian. The rate of the latter type is less ($\approx$0.041) as are the load capacities ($\geq$3.5 pounds) which are considered low but quite adequate to support the instrument in the essentially gravity-free environment. The total spring rate of the instrument about its roll axis is expressible as

$$0.2 + 3 \times 0.041 \frac{R_I}{R_R}$$

where R_I is the radius of the instrument to the point of roller contact and

R_R is the radius of the roller

This expression indicates that minimum spring action prevails when large rollers support the module at points close to its roll axis. Maximum roller radius in a given space is attained, as shown in Figure 157, by resorting to roller sectors of sufficient angle to permit the required limited motion. Sector gears attached to the rollers and meshing loosely with gear sectors attached to the module would be a simple expedient to prevent inadvertent gross roller slippage.

For the case of R_I = 5" and R_R = 2", the pivot torque at the $\pm 1/2^\circ$ angular extremes is $\pm$0.0712 in-oz. If now the minor loop gain is assumed to become unity at 1 Hz and the module inertia is 1/4 slug-ft^2, then the torque constant $\overline{T}$ of the loop can be expressed as

$$\overline{T} = JS^2 = 1/4\ (2\pi)^2 \approx 10\#\ \text{ft/rad} \approx 0.55\ \text{in-oz/min}$$

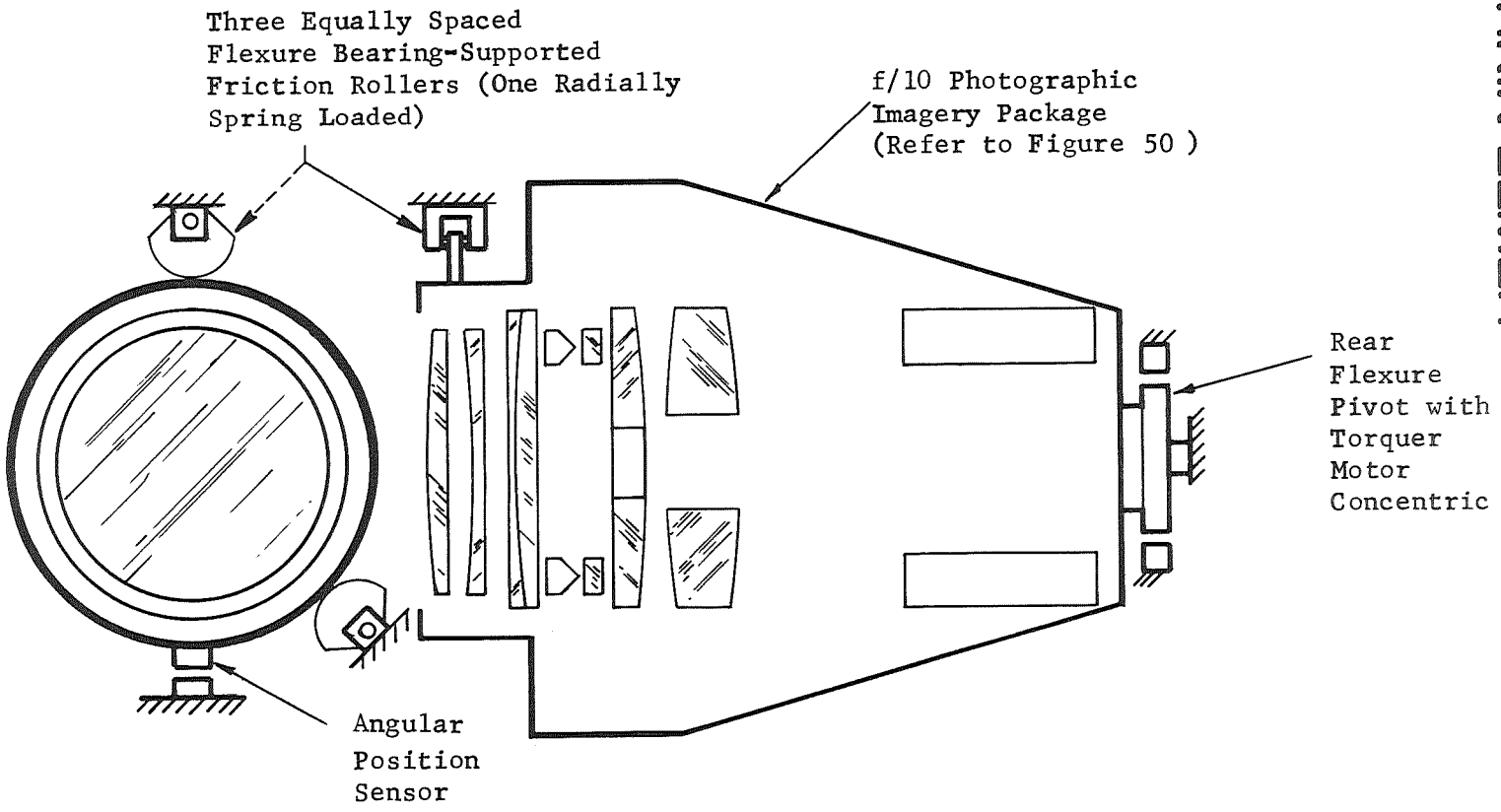

Figure 157 . Typical Mechanization for Introducing Roll Correction Motions into Experiment Package

Hence the torque disturbance will tend to cause a minor loop positioning error of

$$\frac{0.0712}{0.55} = 0.1292 \text{ min} = 7.76 \text{ arc-sec}$$

which can be reduced to lesser magnitude by the introduction of low frequency integration. This is shown in the circuitry of Figure 158(refer to amplifier A4) which also includes lead-lag stabilization. The integration enhances the minor loop gain at frequencies below 0.18 Hz at the rate of 6 dB/oct. This results in a sixtyfold increase of loop gain at 0.003 Hz with a proportional reduction of torque-induced positioning errors at this frequency. Static errors due to dc torques, moreover, are completely eliminated.

An appropriate torquer motor would be the Aeroflex TQ-2 brushless circular type rated at 3 oz-inch and 2 watts and with an outer diameter (o.d.) and thickness of only 1.63" and 0.65", respectively. With such a unit, the power required to maintain the positional extreme (i.e., overcome the 0.0712 in-oz) would be

$$2\left(\frac{0.0712}{3}\right) = 0.0475 \text{ watts}$$

This assumes that the torquer motor current is drawn via non-switching type electronics from a source capable of producing rated motor torque.

The minor loop transfer function, with the assumed 5V-per-30-arc-minute feedback scale factor, is essentially 6 arc-minutes per volt at low frequencies. Figure 158 also indicates the type of circuitry which might be used to realize the major loop characteristic with unity gain crossover at 0.003 Hz. The key components are the integrators with field-effect transistor input stages to minimize bias current effects, permit use of large summing resistors and, therefore, achieve the large required time constants (RC). Constant offset effects in amplifiers A_1 and A_2, it should be noted, will not cause major loop error since they are preceded by integration.

Constant offset effects associated with amplifier A_1, on the other hand, will not be troublesome provided they are small compared to the saturated value of the error signal, since the net effect will be a fixed roll error. It should be noted that the major open loop break from -6 to -12 dB/oct at 0.01 Hz is assumed due to a single order lag-type noise filter associated with the error sensor. The minor loop will introduce additional major loop breaks above about 1.8 Hz.

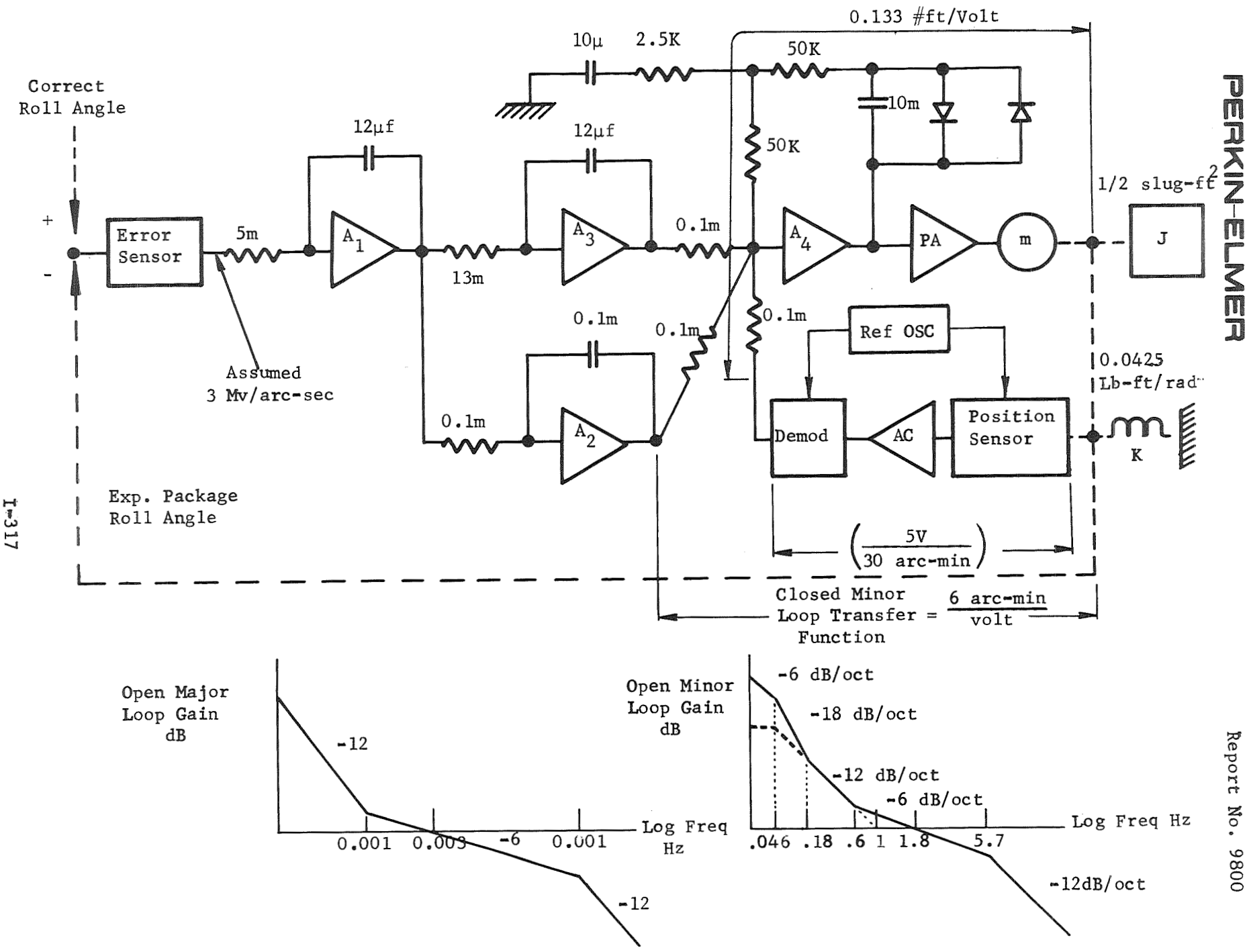

Figure 158. Roll Servo Block Diagram and Bode Diagram

The foregoing preliminary design calculations indicate the feasibility of roll controlling the modules in the manner described. Subsequent efforts should consider whether the proposed approach can be modified to avoid the need for a caging mechanism for launch survival. In this connection, the use of larger pivots and overcenter spring compensation offers a potential solution.

Table 30 presents a summary of the servo parameters as evolved above. The approach, which assumed the use of a minor positioning loop in order to achieve isolation against torque disturbance effects, appears to be adequate and non-critical.

TABLE 30. FINE ROLL SERVO ESTIMATED PARAMETERS

1.	Major Loop Crossover Frequency	0.003Hz [0.0028Hz Mod C; 0.004Hz Mod F]
2.	Accuracy	0.31 arc-second Mod F 0.73 arc-second Mod C
3.	Flexure Bearings	
	3.1 Roller	6006-800
	3.2 Rear Support	6005-600
4.	Angular Range of Module	±1/2°
5.	Net Spring Rate of Support (For roller to Module diameter ratio of 4"/10")	0.0024 in oz/min
6.	Pivot Torque at Angular Extreme	±0.0712 oz-in
7.	Servo Torque Constant (Minor loop without integration)	0.55 in oz/arc-min
8.	Minor Loop Crossover Frequency	1.8Hz
9.	Torquer Motor	
	9.1 Type	TQ-2 Aeroflex
	9.2 Rated Torque/power	3 oz-in/2 watts
	9.3 Outside Diameter/Thickness	1.65"/0.65"
10.	Power to Hold at Angular Extreme	0.05 watts
11.	Positioning Accuracy Required	
	11.1 RPM - Roll Positioning Mechanism	±10 arc-min
	11.2 Guide Star Sensors	±0.025% x 30 arc-min

CHAPTER 12 - LTEP MISSION PROFILE

The Large Telescope Experiment Program has the twin goals of achieving astronomical data retrieval in a precursor, two-meter telescope configuration and performing experiments in the technology required to advance to a three-meter telescope size. In the discussion of the mission profile, we shall cover a sequence of events which will give a slight priority to the acquisition of data for the astronomers, but will be interwoven with the technological experiments so that this data is also acquired. Technological experiments which carry with them the risk of preventing further astronomical observations will be late in the schedule of events. The LTEP sequence to be described below will commence at the stage at which all of the docking maneuvers and cluster stabilization, solar panel deployment, etc., have been accomplished. For the details of these operations, the reader is referred to Volume II of the study.

TELESCOPE EXTENSION

First the swing link will deploy the telescope and rack structure with the telescope still caged so that the axis of the telescope is perpendicular to the axis of the space station, as shown in Figure 159. The CMG's will be spun up and the orientation of the space station stabilized. Then the telescope tube extension mechanism will be activated so that the secondary mirror and figure sensor are moved to their operational positions. Either the protechnically actuated holding pins or the irreversible screw drives will hold the telescope tubes in the extended position. Upon satisfactory telemetry indication of completion of this sequence, the telescope uncaging sequence will be initiated.

TELESCOPE UNCAGING

During boost, docking, and deployment, the telescope will be caged to the supporting rack structure, either through vibration isolating structural members (similar to aircraft landing gear), or the individual glass elements will be supported on their own vibration isolators, and the main telescope will be restrained with rigid links. These links will be retracted (pyrotechnically or by mechanical actuators) and/or the various individual glass elements will be freed of their vibration isolators.

ACTIVATING ACTIVE OPTICS

The figure sensor laser and the primary mirror scanner will then be activated to control the position of the primary mirror. A pre-programmed sequence to check out each of the actuators of the primary mirror for freedom of motion is then executed. Backup modes would be activated if required. Coarse and fine closed-loop control of the segments is to be instituted to bring the mirror to a reasonable figure.

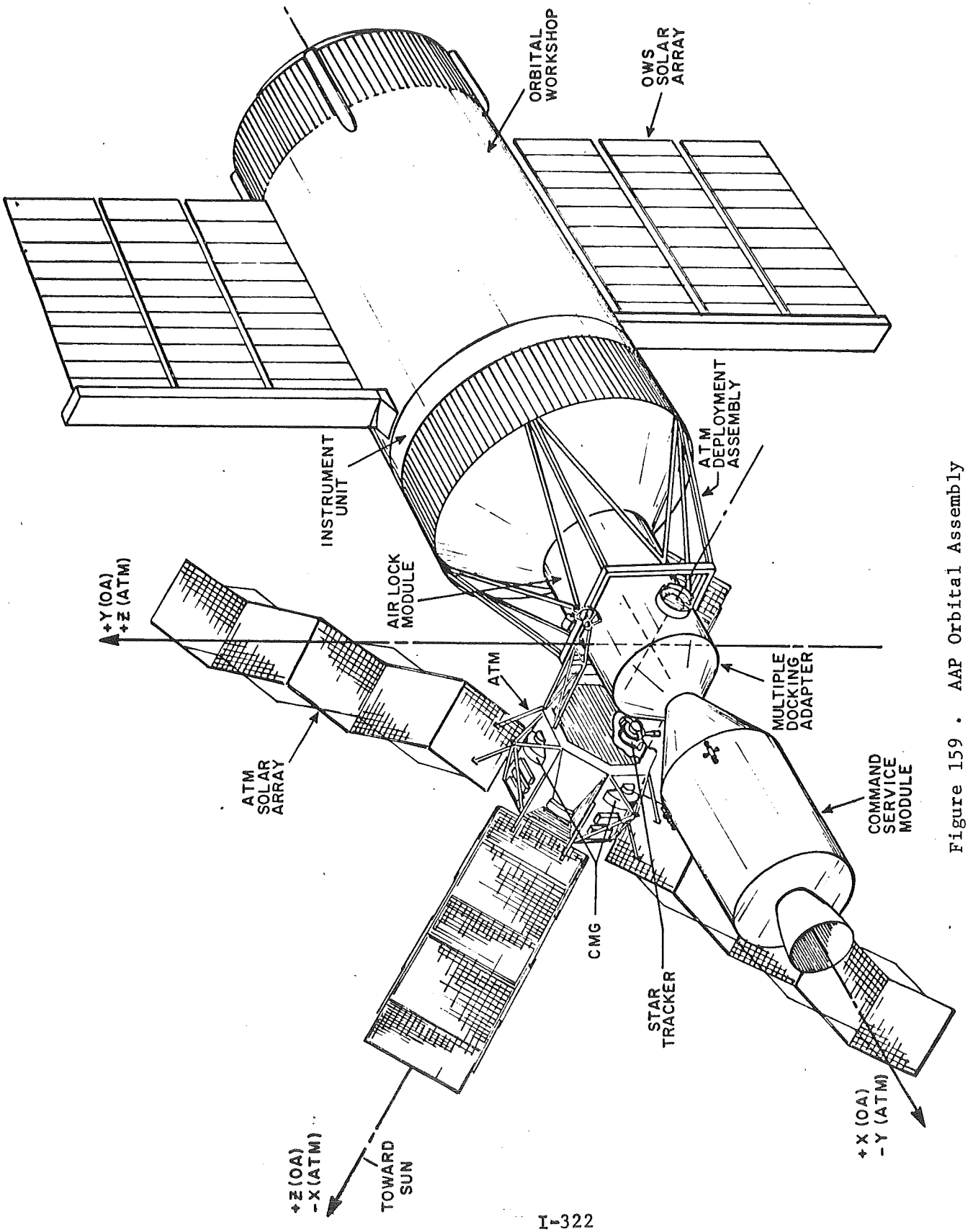

Figure 159 . AAP Orbital Assembly

ALIGNMENT PROCEDURES

At this time the figure sensor alignment control is activated and the figure sensor servoed to the center of curvature of the primary mirror. Upon completion of this sequence, control of the secondary mirror is instituted. Its position is controlled by servo so that its focal point lines up with the prime focus. of the primary mirror. Final trimming up of the primary mirror figure is then accomplished. Information on the rms figure error is telemetered to the ground with the phase-measuring interferometer acting as sensor. As early as possible, the optical scattering experiment (No. 34) is activated. It will be reactivated periodically to assess the changes in optical scattering.

EXPERIMENT PACKAGE ACTIVATION

Following mirror and telescope alignment, the first astronomy data acquisition package is activated. This checkout or positional presetting is first accomplished. Telemetry channels are also activated.

GUIDANCE STAR ACQUISITION

The image movers are programmed to precalculated positions for picking up the images of the guide star in the telescope field. A search mode causes the guide star images to fall within the image mover aperture. When this occurs, automatic guidance commences.

EVALUATION AND ADJUSTMENT OF POINTING SYSTEM

Once acquisition is accomplished, the pointing servo errors are telemetered to the ground for evaluation. If required, servo gain changes and bias offset adjustments would be accomplished. Proper setting of the image movers is checked and, if necessary, minor corrections in the image mover positions would be made. Once the object of interest is properly located to the entrance slit of the spectrometer, data collection commences.

ASTRONOMY DATA COLLECTION

The order in which the astronomy instrumentation modules are activated is set by the pointing accuracy required by each instrument, with the lowest accuracy requirements being executed first. Thus, the Rowland Circle Spectrometer (Module E) is activated first, using the EPC or stabilization followed by the f/10 photographic imagery module (C) using the transfer lens for image stabilization, then the f/50 electronic imagery module (F). Module A, the modified echelle is then actuated in this pointing mode, and the Princeton Experiment Package is activated simultaneously with the free float mode.

AUTONOMOUS MODE

At this point in the operation sequence the LTEP module is undocked from the space station and starts the autonomous mode operations. After the orientation sequence and locking onto the navigational stars with the star trackers, the telescope is set up for the ultraviolet imagery module and acquisition of guide stars is reaccomplished. Again, the television camera is the prime source of data acquisition. Interspersed with the acquisition of astronomical data is the thermal diagnostic experiment (Experiment Nos. 2, 12 and 13).

Following TV acquisition of ultraviolet imagery is high-resolution visible light imagery which is then followed by a photographic photometry (this implies an astronaut revisit for the purpose of loading the film and removing the exposed film). Finally, after the accomplishment of the photographic photometry are the experiments in astrometry (in which photographic plates are utilized and astronaut participation is required).

Experiment No. 34, Optical Scattering Environment, is performed intermittently during the autonomous mode.

REDOCKING

After completion of the autonomous mode astronomy and technology experiments, the LTEP is redocked with the space station. At this time the astronauts perform Experiment No. 3 in which a segment of the optical mirror is removed and taken into the orbital recoating facility. After installation of the new segment, the reflectivity in the ultraviolet region of the segment is compared with the reflectivity of the other segments. This gives a measure of the degradation of reflectivity. Experiment No. 34 would also be repeated. Any refurbishment or replacement of astronomy experiments would be accomplished at this time also.

ALTERNATE MODES

The above paragraphs cover the astronomy mission as it would occur for the astronomy experiment modules which are studied in this volume. Changes will occur as the Principle Investigators are identified and as their inputs alter and better define the instrumentation.

Lockheed, in Volume II, has studied many vehicle and orbital variations. Four operational modes are nominated, as shown in Figures 160 , 161 , 162 , 163 , 164, 165 , 166 , and 167. For the details of these operational modes, the reader is referred to Volume II. The LTEP telescope configuration and the astronomy mission profile will remain essentially unchanged regardless of which operational mode is selected.

LTEP-2-METER CONCEPT: EXTENDED CONFIGURATION

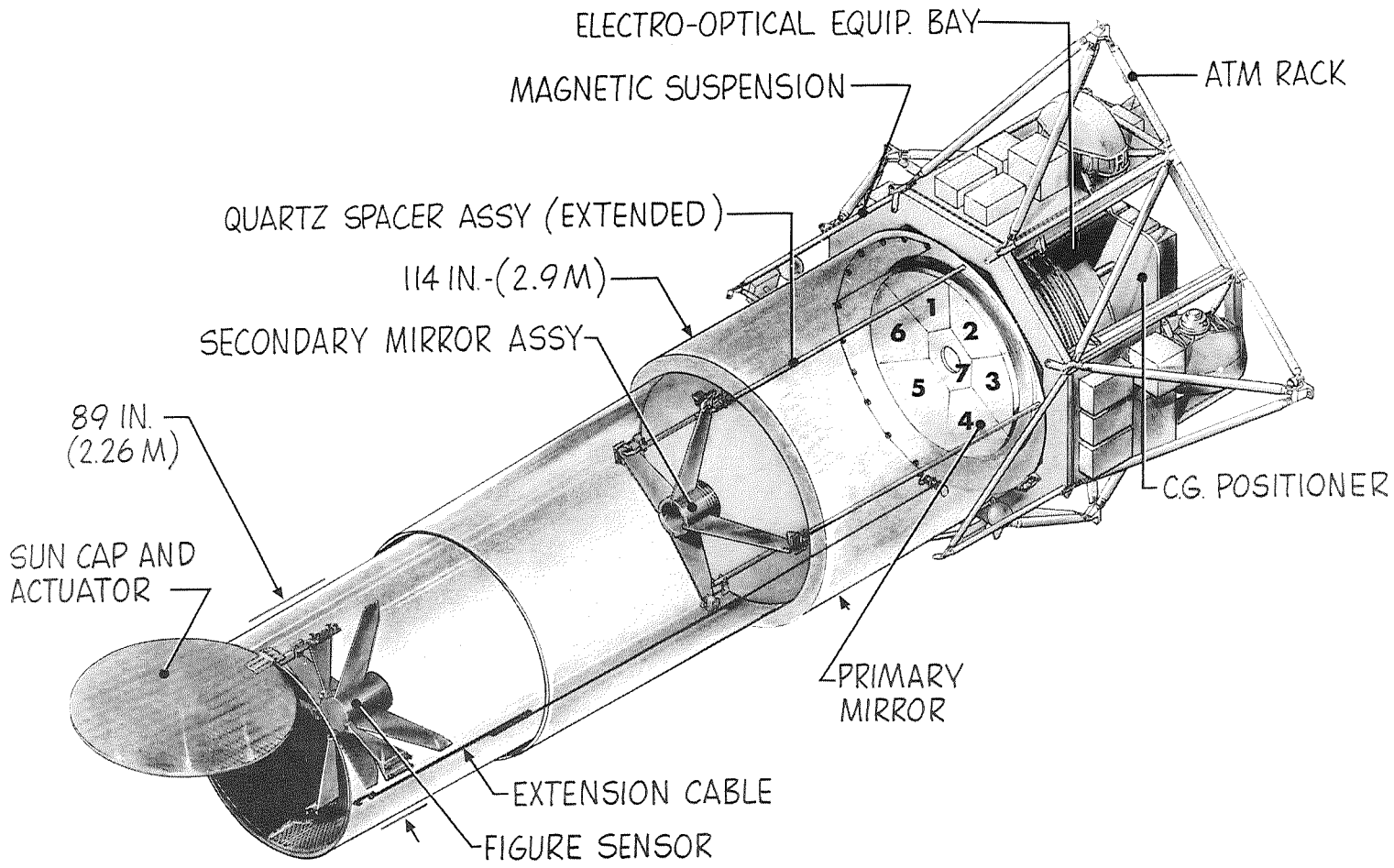

Figure 160. LTEP-2-Meter Concept: Extended Configuration

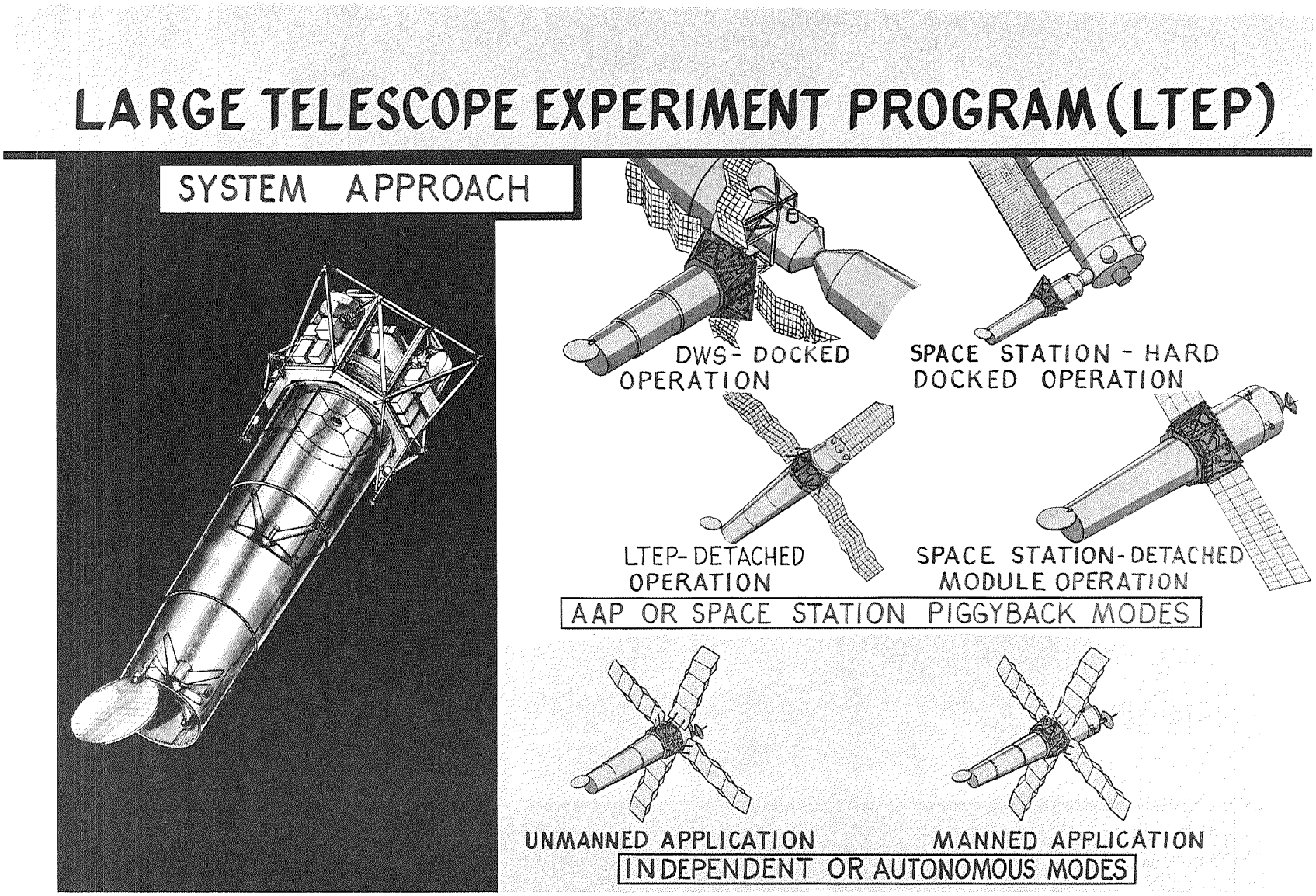

Figure 161. Large Telescope Experiment Program (LTEP)

LTEP OPERATIONAL MODES

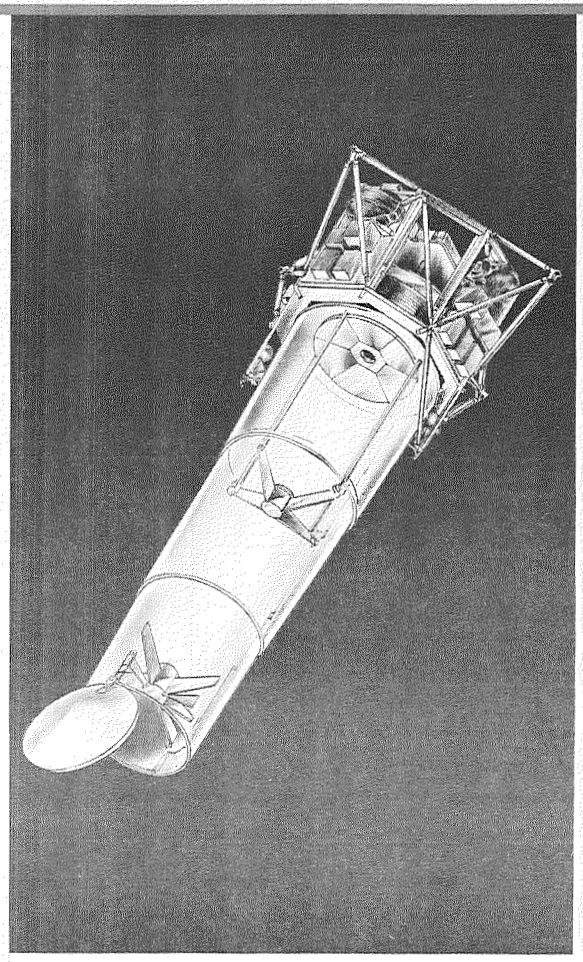

MODE	DESIGNATION	DEFINITION
1	THE SWS-II LTEP AAP SATURN WORKSHOP *	● LAUNCHED ON SAT. V WITH DWS-2 ● INITIAL OPERATION HARD-DOCKED: MANNED SUPPORT ● SUBSEQUENT OPERATION DETACHED (REMOTE) ● REDOCKING FOR MANNED RESUPPLY/ MAINTENANCE
2	THE TITAN III C LTEP INDEPENDENT/ UNMANNED	● LAUNCHED ON TITAN III C ● UNMANNED OPERATION (NO RESUPPLY OR FILM RECOVERY)
3	THE RENDEZVOUS LTEP INDEPENDENT LAUNCH-CLUSTER OPERATION	● LAUNCH ON TITAN III C ● DOCK TO AAP CLUSTER—MANNED OPERATION ● SEPARATE FOR UNMANNED REMOTE (DETACHED) OPERATION ● REDOCKING FOR MANNED RESUPPLY/ MAINTENANCE
4	THE SATURN IB LTEP INDEPENDENT LAUNCH-MANNED CAPABILITY	● LAUNCH ON SAT. IB WITH MOTEL ● MANNED OPERATION WITH CSM ● UNMANNED OPERATIONAL SPAN ● CSM RESUPPLY AND MAINTENCE

*THE CONCEPTUAL DESIGN IS INHERENTLY ADAPTABLE TO OPERATION AS A SPACE SHUTTLE OR SPACE STATION EXPERIMENT IN A MANNER SIMILAR TO THE SATURN/AAP SYSTEM

Figure 162. LTEP Operational Modes

LTEP SYSTEM CONFIGURATIONS

MODE →	THE SWS-II LTEP ① AAP SATURN WORKSHOP	THE TITAN IIIC LTEP ② INDEPENDENT UNMANNED	THE RENDEZVOUS LTEP ③ INDEPENDENT LAUNCH CLUSTER OPERATION	THE SATURN IB LTEP ④ INDEPENDENT LAUNCH MANNED CAPABILITY
LAUNCH ENVELOPE	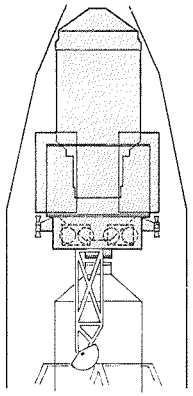	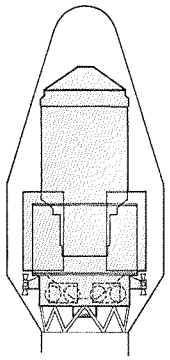	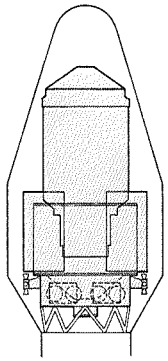	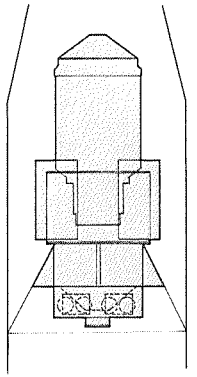
LAUNCH VEHICLE	SATURN V	TITAN IIIC	TITAN III C	SATURN I B
SYSTEM EQUIPMENT	2 METER TELESCOPE ATM RACK PROPULSION/SUPPORT MODULE	SAME AS MODE 1	SAME AS MODE 1	SAME AS MODE 1 PLUS MOTEL
MANNED SUPPORT	AAP SATURN IB LAUNCH	NONE	AAP SATURN IB LAUNCH	SATURN IB LAUNCH
KEY FEATURE	INTEGRAL CLUSTER EXPERIMENT	UNMANNED SIMPLIFIED EXPERIMENT	AAP EXPERIMENT AUTONOMOUS LAUNCH	AUTONOMOUS-MANNED SUPPORT CAPABILITY

Figure 163. LTEP System Configurations

MODE 1 - THE SWS-II LTEP

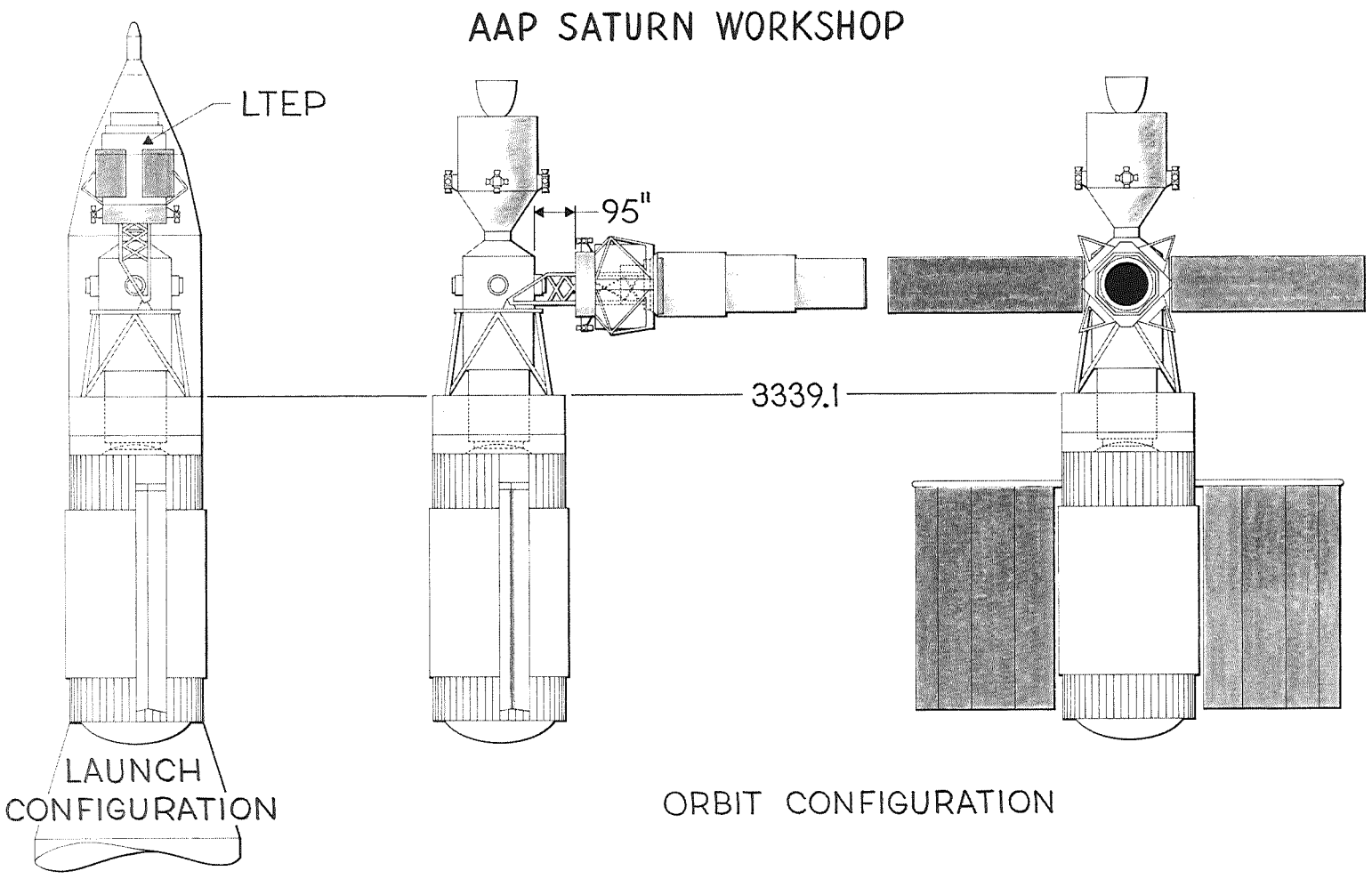

Figure 164. Mode 1 - The SWS-II LTEP

MODE 2 - THE TITAN IIIC LTEP

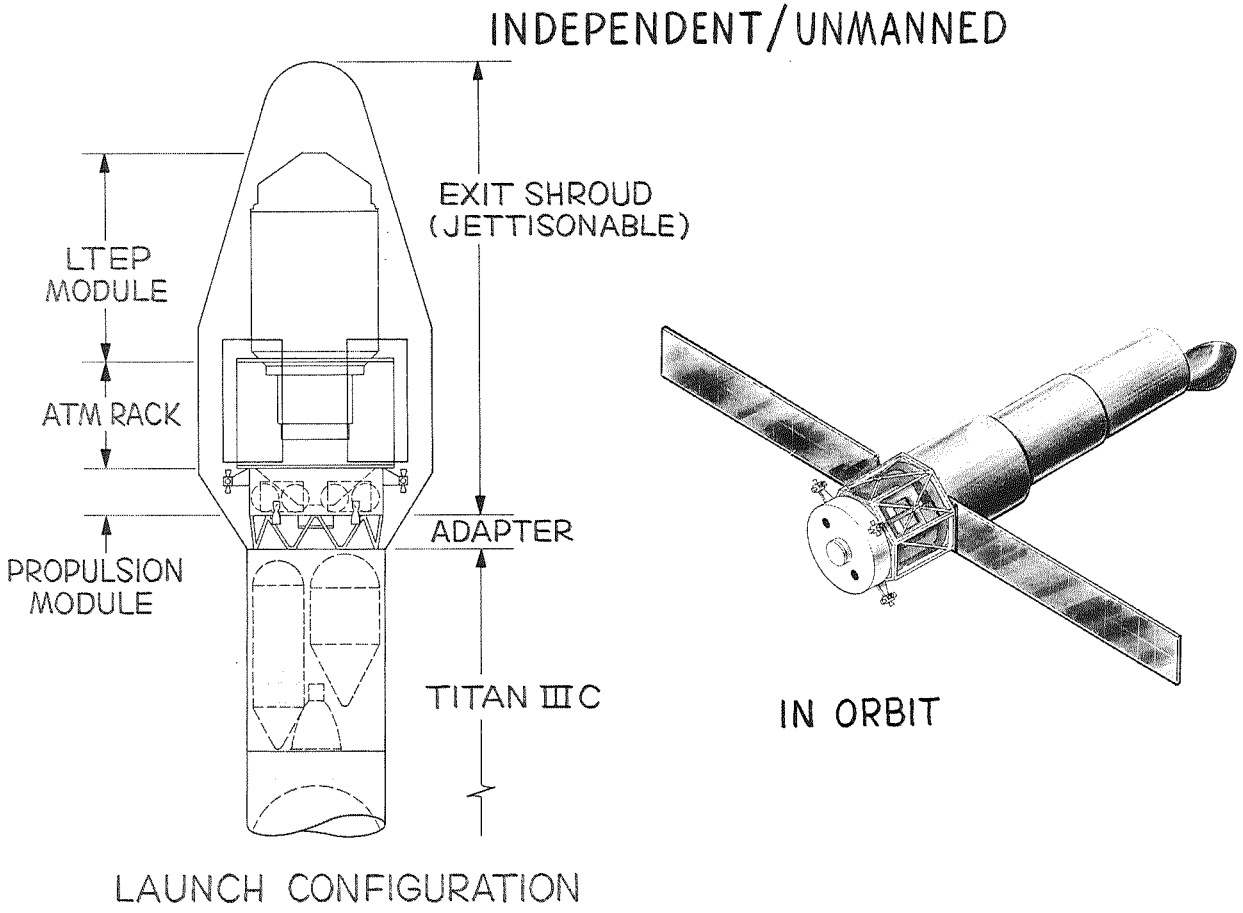

Figure 165. LTEP Mode 2-Independent/Unmanned

MODE 3 - THE RENDEZVOUS LTEP

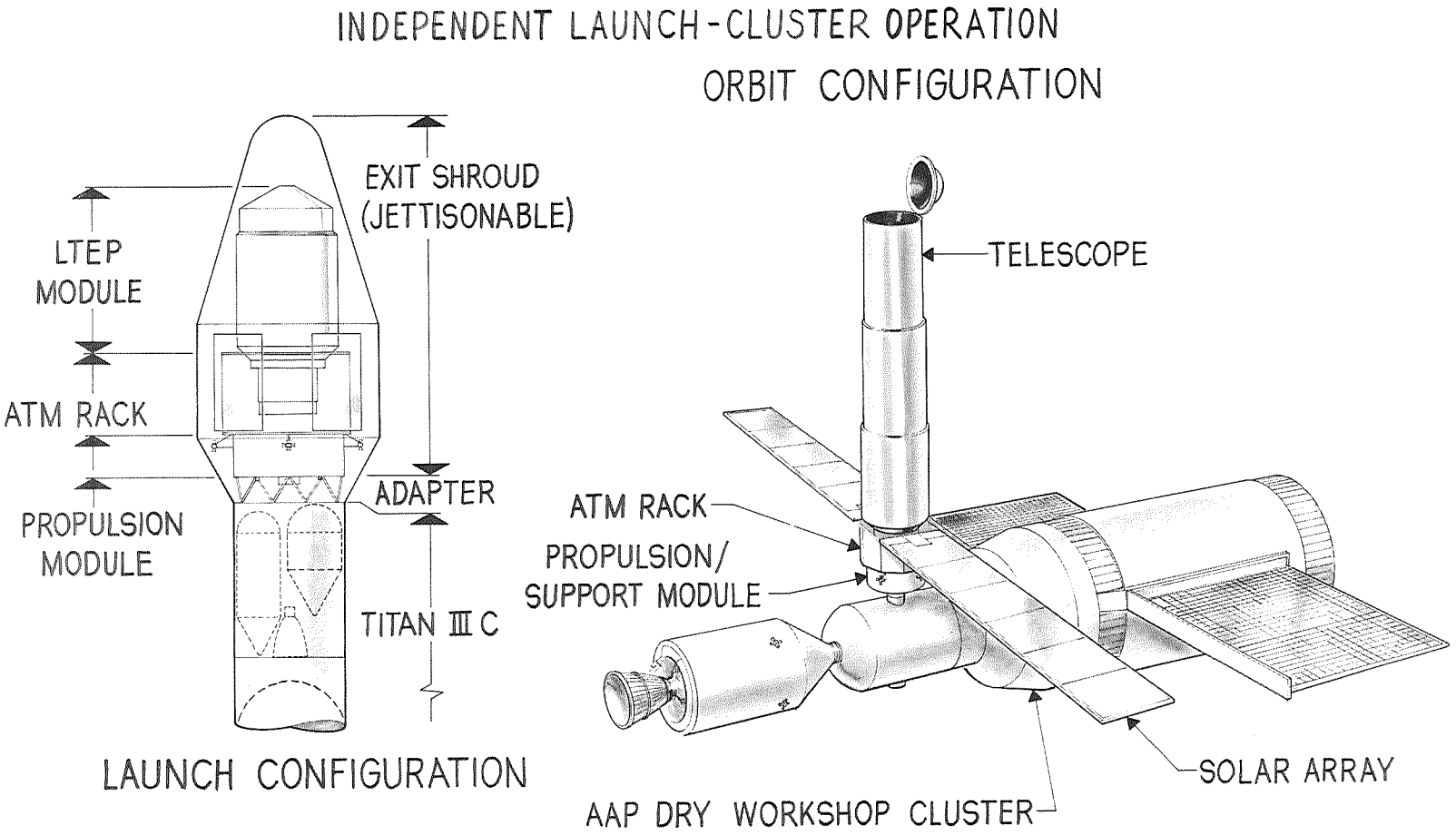

Figure 166. LTEP Mode 3-Independent Launch-Cluster Operation

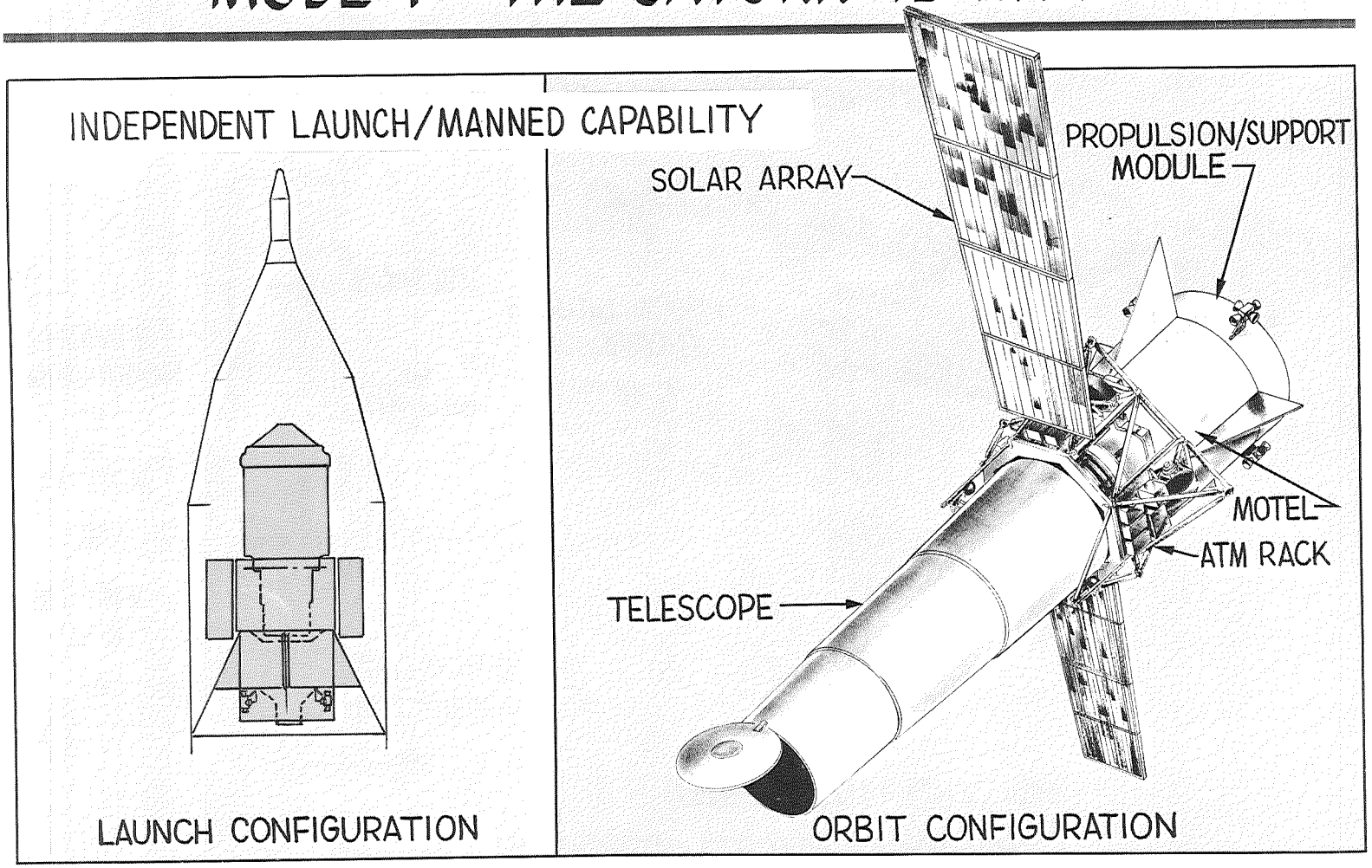

Figure 167. LTEP Mode 4-Independent Launch/Manned Capability